

2. SITE 504¹

Shipboard Scientific Party²

HOLE 504B

Date occupied: 1 October 1991
Date departed: 10 November 1991
Time on hole: 40 days, 20 hr, 20 min
Position: 1°13.611'N, 83°43.818'E
Bottom felt (rig floor; m, drill pipe measurement): 3474.0
Distance between rig floor and sea level (m): 11.30
Water depth (drill pipe measurement, from sea level, m): 3462.7
Water depth (sea level, corrected m, echo sounding): 3460
Total depth (rig floor; m): 5474.40
Penetration (m): 2000.4
Number of cores (including cores with no recovery): 57
Total length of cored section (m): 378.9
Total core recovered (m): 47.69
Core recovery (%): 12.6

Hard rock:

Depth sub-bottom (m): 1601.50
Nature: Diabase
Measured velocity (km/s): 5.64 ± 0.3

Principal results: Site 504 is located 201 km south of the Costa Rica Rift, the easternmost arm of the Galapagos Spreading Center (1°13.611'N; 83°43.818'W; water depth 3460 m), in 5.9-m.y.-old crust. Leg 140 is the seventh DSDP/ODP expedition to occupy Hole 504B and was devoted to drilling into or through the dike/gabbro and/or seismic Layer 2/3 transition. Leg 140 has established the most complete reference section to date through the upper oceanic crust, by deepening Hole 504B to a total depth of 2000.4 m below sea floor (mbsf). Hole 504B is now the deepest hole ever drilled by DSDP/ODP, and extends almost three times as deep into oceanic basement as any other hole.

JOIDES Resolution left Victoria, Canada, 15 September 1991, and started operations after arriving at Site 504 on 1 October. After 2 days of logging (temperature and formation microscanner, FMS), 10 days were needed to fish a core barrel lost at the bottom of the hole during the end of Leg 137, and to clean the hole for further coring. Coring (26 days) and more downhole measurements (3 days), including temperature, acoustic velocity, resistivity, digital borehole televiwer, geochemical combination, and a permeability test, were performed before the drill ship left Site 504 on 10 November for transit to Panama.

The temperature profile, which was recorded between 200 and 550 mbsf before operations were begun, is characterized by a gradient inversion between 283 and 288 mbsf, possibly due to local fluid inflow from the basement into the borehole. Below this section a downhole flow of ocean bottom water into the basement, which was also observed during earlier legs, is still active, but had decayed considerably since Leg 137. The linear temperature gradient in the deeper hole is still 61°C/km, which

extrapolates to a temperature of 195°C at 2000 mbsf. The FMS produced two good images from 290 to 940 mbsf and 1563 to 1575 mbsf, and the first shipboard data are given below.

Coring was straightforward without any unexpected drilling problems; however, the penetration rate of less than 2 m/hr and recovery of 13% were low but adequate. Hole 504B remains stable with negligible evidence of hole ellipticity and was left open and clean for further deepening.

At the end of Leg 140, Hole 504B extends through 274.5 m of sediment and 1725.9 m into basement, and is the only hole which clearly penetrates through the extrusive pillow lavas and into the sheeted dike complex predicted from studies of ophiolites. The Hole 504B basement section includes 571.5 m of pillow lavas and minor flows, underlain by a 209-m transition zone of mixed pillow lavas, thin flows and dikes, and 945.4 m of sheeted dikes and massive units.

Coring on Leg 140 recovered 47.7 m, of which 11.4% was aphyric, 18.6% sparsely phyrlic, and 70% moderately phyrlic plagioclase-pyroxene-olivine diabase, which has been divided into 59 lithological units. The coarsest unit identified has an average grain size of 1.5 mm, but in terms of texture and grain size it is clearly a diabase and not a gabbro. While there is not a simple systematic increase in grain size with depth, coarser grained diabases do become more common, whereas glassy chilled margins virtually disappear, an observation that is consistent with generally deeper dike emplacement at higher temperatures. Phenocrysts include plagioclase, augite, olivine, and Cr-rich augite. The groundmass is dominated by plagioclase, augite, and magnetite. In a few units Cr-spinel is present as inclusions in olivine and plagioclase. Most of the rocks examined are seriate porphyritic, a texture in which there is a continuous range of grain sizes from the phenocrysts down to the groundmass. A variety of "gabbroic" clots were observed in hand specimen and thin section. Some individual clots contain up to 20% Fe-Ti oxide minerals, and many contain small fine-grained patches with up to 50% Fe-Ti oxide minerals. These fine-grained patches are interpreted to be crystallized pockets of trapped Fe-Ti-rich magma.

In hand specimen there is no evidence for any pervasive deformation, and the rock exhibits well-preserved primary characteristics. The rocks are generally isotropic, both in hand specimen and in thin section, and there is no evidence for extensive recrystallization associated with ductile deformation. No significant fault-rocks have been recovered, and we see little evidence for local increases in the intensity of microfaulting, so it is unlikely that we have drilled through, but not recovered, a major fault zone.

Chemically, the Leg 140 rocks can be classified as olivine tholeiites with compositions that are similar to moderately evolved mid-ocean ridge basalts (MgO = 7.7%–10.1%, Fe₂O₃ total = 8.1%–11.4%, Ni = 79–189 ppm, Mg value = 0.60–0.75). However, they are strongly depleted in incompatible elements (TiO₂ = 0.67%–1.1%, Nb ≤ 0.3–0.7 ppm, Zr = 35–58 ppm). These characteristics encompass over 98% of all investigated samples recovered from Hole 504B, through 2000 mbsf. There appear to be no major igneous enrichment or depletion trends with depth, nor are there large-scale fractionation trends throughout this crustal section. There is, however, a systematic decrease in Zn content from an average of 70 ppm at 1500 mbsf to 30 ppm at 2000 mbsf.

All of the recovered rocks are mineralogically and chemically altered to some extent and exhibit a pervasive slight "background" alteration. Locally more extensively altered zones occur around veins and in centimeter-sized patches. The background alteration is characterized by a 10%–20% replacement of primary minerals by secondary phases. Olivine in most of

¹ Dick, H.J.B., Erzinger, J., Stokking, L.B., et al., 1992. *Proc. ODP, Init. Repts.*, 140: College Station, TX (Ocean Drilling Program).

² Shipboard Scientific Party is as given in the list of participants preceding the contents.

the rocks is completely altered, and pseudomorphs have been interpreted to reflect multiple stages of alteration, with early talc + magnetite followed by later chlorite or mixed-layer clay formation. Fresh olivine was present in some samples. Clinopyroxene in the rocks is partly replaced by actinolite. Plagioclase is generally only slightly altered to albite and chlorite along fractures and grain boundaries. A characteristic feature of Leg 140 rocks is the common presence of centimeter-sized, green to light gray "patches" of alteration, similar to those identified on previous legs. Irregularly shaped amygdules, 0.1–2.0 mm in size and filled with actinolite and chlorite, occur at the centers of many of these patches and are surrounded by alteration halos (2–10 mm wide) where the rock is extensively altered (about 80%) to actinolite, chlorite, albite, and titanite. These alteration patches comprise 8% of the core recovered.

Rocks from 1710 to 1790 mbsf, however, are characterized by generally slight alteration, with lower abundances of actinolite and chlorite, by the presence of talc replacing olivine, and by the presence of relict igneous olivine in the rocks. These rocks also lack the centimeter-sized "patches" of more extensively altered rock. These rocks are interpreted to reflect alteration at relatively low water-rock ratios. Such rocks occur sporadically in the lower portion of the hole, and the deepest sample recovered is among the least altered. Alteration is strongly influenced by local permeability. Although the secondary mineralogy of the Leg 140 and 111 rocks is generally the same, the proportion of actinolite is greater in the Leg 140 rocks, actinolite veins are more abundant, and the Leg 140 rocks are slightly more altered.

Penetration of hydrothermal fluids resulted in pervasive, but heterogeneous, veining of at least five macroscopic vein types (chlorite, chlorite/actinolite, actinolite, epidote/quartz and chlorite/pyrite) ranging from ≤ 0.5 mm to 2 mm in width. The only consistent crosscutting sequence established among these vein types is that the epidote/quartz veins are relatively late. An apparently random orientation suggests that vein genesis is mainly influenced by the local stress regime, dominated by contractional cooling. Dips of open fractures fall into two dominant groups, one shallow and one steep. Both seem to be late features, associated with the drilling process. The majority of the fractures are shallow, with dips less than 30° . Some of these exhibit the typical saddle morphology of discing fractures which may reflect the in-situ stress field. The borehole ellipticity measured by the FMS calipers is in good agreement with these interpretations. Steeply dipping fractures mostly strike to the east-southeast, a trend which again generally corresponds to the first interpretations of the FMS data, and perhaps also reflects the in-situ stress field.

Several chilled dike contacts were observed, and some have been oriented using stable paleomagnetic directions. Oriented dikes indicate an east strike, subparallel to the ridge-spreading axis. The dikes have dips between 79° and 85° to the north, so the crustal sequence has probably tilted by only a few degrees.

A similar indication can be drawn from the natural remanent magnetization of the Leg 140 samples, which is of moderate intensity (2.6–3.0 A/m) and stability. The range of the stable magnetic inclination values (-57° to 43°) is similar to that observed in the upper portion of the sheeted dike complex sampled in Hole 504B. The mean value of stable inclination observed in Leg 140 samples falls within the range predicted by normal variations of the geomagnetic field for Site 504, and does not indicate significant tilting or rotation of the crustal section.

The mean value of magnetic susceptibility (0.016 SI units) for these samples is nearly identical to the mean value from the upper part of the dike section (1055–1570 mbsf). However, the range in susceptibility values is much wider than that observed from the upper dikes. This suggests that, there is more variation in the degree of hydrothermal alteration experienced by rocks from the newly drilled section.

Compressional-wave velocities in 49 oriented and water-saturated minicore samples have a mean of 5719 ± 257 m/s. This average is lower than the values measured from samples obtained during the later stages of Legs 111 and 137. If two highly altered samples are excluded, the mean value of the average wet bulk density is $2.98 \text{ g/cm}^3 \pm 0.023 \text{ g/cm}^3$. This value is higher than the average determined during Leg 111 ($2.91 \text{ g/cm}^3 \pm 0.06 \text{ g/cm}^3$). Excluding the altered samples, the mean wet-porosity of the rocks is 0.52%

$\pm 0.60\%$. The average thermal conductivity of 2.410 W/m-K (homogenous samples) is considerably higher than the mean value of 2.01 W/m-K obtained during Leg 111. The downhole distribution of the physical rock properties shows an increase in velocity at 1660 mbsf, and a porosity and thermal conductivity minimum at 1720 mbsf and 1800 mbsf, respectively.

A vertical seismic profile experiment conducted in Hole 504B during Leg 111 shows a relatively weak seismic reflector between 1660 and 1860 mbsf. This reflector was interpreted as the transition between sheeted dikes in seismic Layer 2C and gabbros in Layer 3. Leg 140 clearly penetrated through this depth section. The observed changes in intensity of alteration and in physical rock properties may have caused an acoustic impedance difference somewhere around 1750 mbsf, which may have caused the observed reflector. This "boundary" was clearly not the transition from the dike complex into the gabbros at Site 504. The changes in alteration mineralogy, the increasing average grain size, the general increase in actinolite abundance, and the absence of glassy chilled dike margins in the newly drilled section of Hole 504B indicate that Leg 140 has reached the lower part of the sheeted dike section.

During the second program of downhole measurements an additional temperature log was run from seafloor to the bottom of the hole at 2000.4 mbsf to determine the temperature rebound after 5 weeks of operations. The maximum temperature recorded was 142°C , with a rate of increase of 1.96°C/hr at the bottom. Next, the geochemical combination tool logged from 1811 to 1896 and from 1350 to 1686 mbsf with good data recovery. The resistivity/sonic log was successfully conducted from 1990 to 275 mbsf. The first run with the digital borehole televiewer (BHTV) failed, but following a repair of the cable head the section from 1885 to 1985 and 1485 to 1685 mbsf was successfully logged. A flowmeter was then deployed to test the permeability of the upper basement, and finally the geochemical combination tool was run again to log the missing section of Hole 504B from 1648 to 1826 mbsf.

BACKGROUND AND OBJECTIVES

Introduction

The primary objective of Leg 140 was to revisit Hole 504B in the eastern equatorial Pacific (Fig. 1) to deepen it into the sheeted dike complex toward, and hopefully through, the dike/gabbro and/or seismic Layer 2/3 transitions. This hole is by far the deepest ever drilled into oceanic crust, and provides our most important in-situ reference section for shallow ocean crust structure (Fig. 2). It was temporarily abandoned at the end of Leg 111, ending within a thick section of sheeted dikes beneath a half kilometer of extrusive pillow lavas. A vertical seismic profile conducted in Hole 504B during Leg 111, however, indicated a reflector only 100–300 m below the bottom of the hole (Shipboard Scientific Party, 1988). This reflector was interpreted as the possible transition between sheeted dikes in seismic Layer 2C and gabbros in seismic Layer 3, providing a major incentive for the Ocean Drilling Program to return to Hole 504B. Although the sheeted dike-gabbro transition, believed by many to be the Layer 2/3 reflector, has been sampled and observed by submersibles in tectonic exposures in both the Atlantic and the Pacific (Auzende et al., 1990; Francheteau et al., 1990), this transition has never been sampled in an undisrupted section of oceanic crust, and its equivalence to the seismic Layer 2/3 transition has never been directly confirmed. As a result, the Planning Committee of the Ocean Drilling Program committed two legs to reoccupy Hole 504B in 1991. A short engineering leg (137) was assigned to clean out a coring assembly, including a diamond bit and other junk lost in the hole at the end of Leg 111, as well as to conduct a suite of downhole measurements. Leg 140 was then to make a major attempt to deepen the hole, ideally through the Layer 2/3 transition.

Drilling History

Leg 140 was the seventh leg of DSDP/ODP to occupy Hole 504B (Table 1). The hole was spudded in October 1979, during DSDP Leg 69, several hundred meters east of an earlier pilot hole which drilled

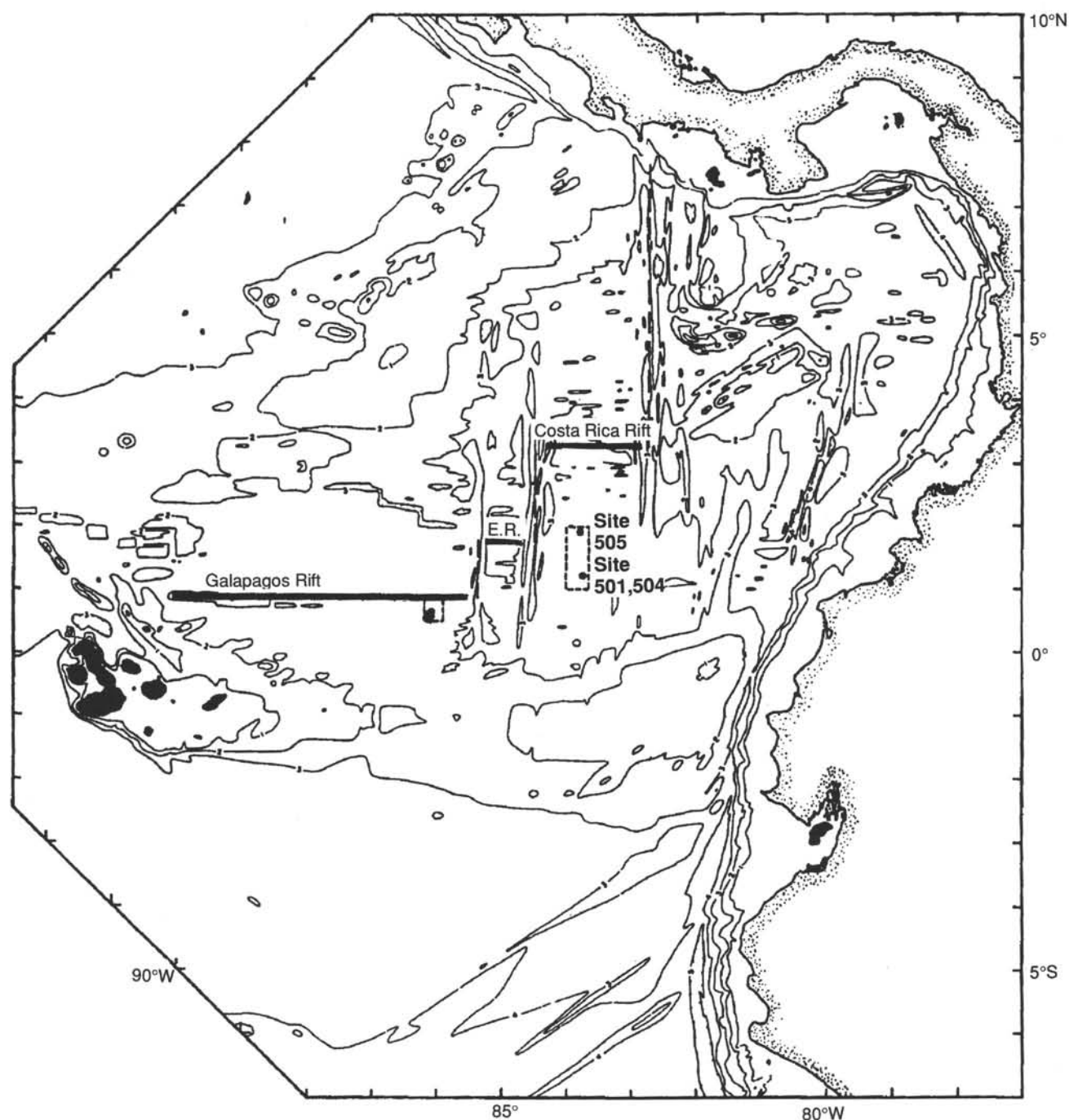


Figure 1. Location of DSDP/ODP Sites 501, 504, and 505 south of the Costa Rica Rift in the eastern equatorial Pacific Ocean from Hobart et al., (1985). E.R. = Ecuador Rift.

73 m into basement during Leg 68 (Hole 501). Hole 504B was subsequently deepened and/or logged during parts of five other legs, including Leg 70 (1979), Leg 83 (1981–1982), Leg 92 (1983), Leg 111 (1986), and Leg 137 (1991). These legs provided a wealth of scientific results, much of which are summarized by CRRUST, 1982; Cann, Langseth, Honnorez, Von Herzen, White, et al., 1983; Anderson, Honnorez, et al., 1982; Anderson, Honnorez, Becker, et al., 1985; Leinen, Rea, et al., 1986; Becker, Sakai, et al., 1988, 1989; Becker, Sakai, Anderson, et al., 1989; and Becker, Foss, et al., 1992.

Although previous coring, logging, and geophysical programs at Hole 504B achieved unprecedented scientific success, the operational history of the hole was marred by repeated downhole hardware losses

and by disappointing rates of core recovery (Fig. 3). These problems have increased with depth and were a particular problem during Leg 111, which experienced four significant losses of hardware in the hole, and a rash of premature bit failures. Leg 111 succeeded in deepening the hole by only 212 m with an overall recovery rate of 12.6%. During Leg 111, remedial work was successful in cleaning the hole on three occasions, however, when a diamond coring assembly was lost near the end of the leg, a lack of time and proper equipment forced the temporary abandonment of the hole before the lost junk could be removed.

Leg 137 returned to Hole 504B and successfully fished and milled the junk left in the hole from Leg 111, and succeeded in deepening it by 59.2 m. Operations throughout the leg showed no indication of

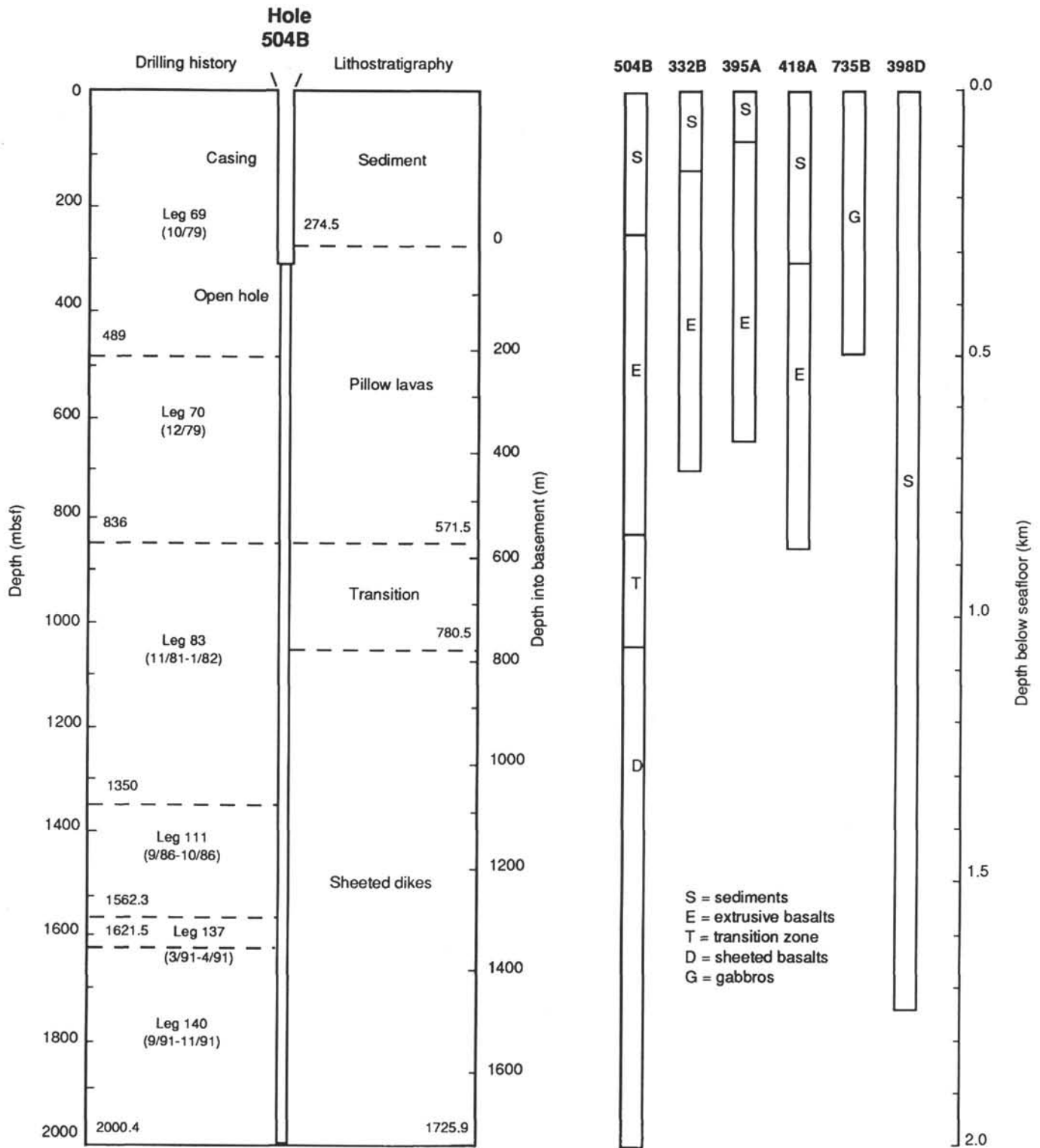


Figure 2. Generalized drilling history and lithostratigraphy of Hole 504B through Leg 140 and lithostratigraphy of selected DSDP/ODP holes.

previously supposed problems with the casing, although a borehole televiewer inspection during the last day on site showed flaws within the lower 30–40 m of casing. Unfortunately an 18-m outer core barrel with a diamond drilling bit broke off and was lost at the bottom of the hole near the end of Leg 137. Leg 137 was not able to fish this junk because of a defective fishing tool, and a lack of time to obtain and

deploy any further appropriate tools. As the new junk in the hole was not deemed a serious impediment, fishing operations were scheduled to be completed by Leg 140 which could return to the hole with new fishing tools and proceed with deepening the hole.

Leg 140 spent 38 days at Site 504: 3.5 days devoted to downhole measurements, 10.5 days to fishing operations, and 24.0 days to

Table 1. Drilling history of Hole 504B.

	Leg 69	Leg 70	Leg 83	Leg 92	Leg 111	Leg 137	Leg 140
Date	20/9/1979	19/12/1979	14/11/1981–5/1/1982	23/2–18/4/1983	27/8–20/10/1986	20/3–1/5/1991	15/9–12/11/1991
Basement penetration (m)	214.5	347.0	514.0	0.0	212.3	59.2	378.9
Cored (m)	214.5	347.0	514.0	0.0	209.1	48.6	378.6
Recovery (%)	35.7	26.4	20.8	0.0	12.6	18.1	13.0
Depth (mbsf)	489.0	836.0	1350.0	1350.0	1562.3	1621.5	2000.4
Depth sub-bottom (m)	214.5	561.5	1075.5	1075.5	1287.8	1343.8	1722.4
Coring (days)	4.8	8.9	21.3	0.0	17.0	6.9	26.0
Logging (days)	6.4	4.1	12.0	9.2	14.0	5.0	3.5
Fishing (days)	0	0	4.7	n.a.	12	10.8	10.5
Penetration rate (m/hr)	2	4	2.5	n.a.	2.3	^a 1.7	1.4
^b Total drilling (days) = 84.9							
Total logging (days) = 54.2							
Total fishing (days) = 38.0							
Overall core recovery (%) = 20.8							
Pillow lavas (%) = 29.8							
Dikes (%) = 14.3							
Transition (%) = 25.3							

^a Rotary coring bits only.

^b In computing drilling time, 16 hr was assumed for round trip of bit, and 4 hr for drilling first core.

coring. After an initial 12 hr of logging (formation microscanner and temperature logs), fishing operations were begun, proving to be considerably more challenging than originally anticipated. During the remaining 24 days, though drilling proved slow and at times difficult, the hole was successfully deepened 378.9 m without any major equipment failures to 2000.4 m below seafloor (mbsf). During the last 3 days on site additional downhole measurements were made, including acoustic velocity-resistivity log, digital borehole televiwer, geochemical combination tool, and a flowmeter experiment, and the ship departed 10 November, arriving in Panama on 12 November 1991.

Geology and Tectonic History

Hole 504B is located in the Panama Basin 200 km south of the Costa Rica Rift in 5.9 m.y. crust (Fig. 1). The Costa Rica Rift (Hey et al., 1977) is a 171-km east-west segment of the Cocos-Nazca Spreading Center. It is bounded by the Panama Fracture Zone to the east, which connects the spreading center to the Middle American Trench, and the Ecuador Fracture Zone to the west, which offsets it some 172 km north from the short Ecuador Rift segment. A well-developed pattern of near east-west linear magnetic anomalies south of the Costa Rica Rift, demonstrates the absence of fracture zones within the segment during the last 10 m.y. and

indicates a relatively simple plate-spreading history (Klitgord et al., 1975; Lonsdale and Klitgord, 1978).

The Cocos-Nazca Spreading Center (sometimes called the Galapagos Spreading Center) consists of the Galapagos, Ecuador, and Costa Rica Rifts. It was produced at approximately 27 Ma when the Farallon Plate into the Cocos and Nazca Plates split, forming the Galapagos Triple Junction (Hey et al., 1977; Lonsdale and Klitgord, 1978). This resulted in the creation of the Galapagos Gore (Holden and Dietz, 1972), a triangular wedge of rough terrain bisecting smoother crust formed along the East Pacific Rise. This crust was created as the Cocos-Nazca Spreading Center progressively increased in length due to westward propagation. The Cocos-Nazca Spreading Center is an intermediate-rate ridge, spreading asymmetrically, with a half rate of 3.6 cm/yr to the south and 3.0 cm/yr to the north (Hey et al., 1977) measured at the Costa Rica Rift segment.

A central feature of the ridge system is the Galapagos Hot Spot, currently located south of the Galapagos Spreading Segment, close to the westward limits of the Carnegie and Cocos Ridges. These aseismic ridges extend roughly east-west and north-east from the ridge near the Galapagos Islands, making an asymmetric V-shaped wake eastward across the gore. This is believed to represent the track of the Galapagos Hot Spot, and indicates that the hot spot was close to the ridge axis throughout the last 22 m.y. These tracks, then, imply steady eastward drift of the plate boundary over the asthenosphere in the hot-spot reference frame (Hey, 1977; Lonsdale and Klitgord, 1978). The asymmetric character of the V reflects both the northeastward-stepping morphology of the ridge and its asymmetric spreading history.

Schilling et al. (1982) found a strong geochemical gradient from enriched to normal MORB between 87.5° and 95.7°W along the Cocos-Nazca Spreading Center, centered on the ridge just north of the Galapagos Islands at 91°W. Based on the reconstruction of Hey (1977), however, the paleoposition of Hole 504B along the ridge at 5.9 m.y. would have been approximately 600–700 km from the hot spot: too far to show a significant influence of the mantle plume on the geochemistry of the basalts drilled there. This is consistent with the highly depleted character of the Hole 504B basalts and diabases (e.g., Autio and Rhodes, 1983; Marsh et al., 1983; Etoubleau et al., 1983; Autio et al., 1989).

It is important to note that Site 504 was originally chosen on the basis of its unusually high uniform heat flow for ocean crust of this age (Langseth et al., 1983). This heat flow is associated with (1) the high (50 m/m.y.) sedimentation rate, which produced a thick overlying 274.5-m blanket of sediments, preventing almost all advective heat loss due to open circulation of seawater through the basement

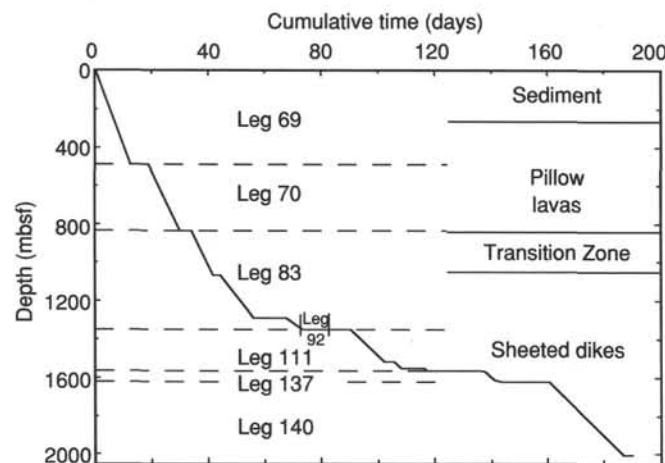


Figure 3. Summary of drilling operations in Hole 504B with respect to depth and time.

(Anderson and Hobart, 1976), and (2) the relatively low relief of the basement topography, such that there is no local excess heat flow around basement highs which would disrupt the regional thermal gradient. The original goal of DSDP Legs 69 and 70 was to investigate geothermal phenomena in basaltic basement and overlying sediments at two contrasting sites of different age and sediment cover in the same segment of an oceanic spreading center. The geothermal characteristics and degree of alteration in the basement of these sites were anticipated to differ sharply. Site 505 is situated on 3.9-m.y.-old crust, in an area of relatively high basement relief and low heat flow. More recent heat-flow surveys and coring in 1982 and 1986 showed that somewhat subdued convection must still occur in the crust around Hole 504B (Langseth and Mottl, 1982; Langseth et al., 1988).

These two site characteristics have important implications for generalizing the drilling results at Hole 504B. First, the geothermal gradient in Hole 504B is likely to be steeper than that encountered in normal ocean crust of the same age, with a higher temperature at shallower depth resulting from the capping of the advective circulation in the basement by the sediment cover. Second, the low relief of the basement topography implies a specific kind of basement structure and magmatic architecture at the ocean ridge which may have important implications for the chemical evolution of the lavas, and the character of plutonic Layer 3.

The well-known striking contrast of rift mountain topography between fast- and slow-spreading ridges is generally attributed to a difference in the tectonics at the ridge axis where the topography appears to be largely created by faulting. Slow-spreading ridges are characterized by rift valleys 1- to 3-km deep bounded by steep walls that mark the location of sets of large-throw normal faults. In contrast, fast-spreading ridges are marked by far more numerous, closely spaced normal faults that rarely exceed a hundred meters in total throw. This difference would appear to correspond to the presence of long-lived magma chambers beneath fast-spreading ridges and to the existence of only short-lived or ephemeral chambers beneath slow-spreading ridges (e.g., Detrick et al., 1987; Dick et al., 1991).

The inferred magmatic plumbing and crustal structures beneath fast- and slow-spreading ridges have important implications for magma evolution. At fast-spreading ridges, basalts tend to be relatively evolved often reaching ferrobasalt composition (e.g., Clague and Bunch, 1976), and may be locally more homogeneous than basalts from slower spreading ridges. In contrast, at very slow-spreading ridges, such as the Southwest Indian Ridge (le Roex et al., 1983; Dick, 1989), ferrobasalts are rare except near hot spots, and there is a remarkable local diversity of isotopic, and major- and trace-element compositions. On the Southwest Indian Ridge, for example, le Roex et al. (1983) report a single dredge haul containing basalts that span nearly the entire known range of strontium isotope ratios for ocean-ridge basalts. These differences can be reasonably attributed, in part, to the presence or absence of long-lived open-system magma chambers. Where long-lived chambers are present, mixing would homogenize magmas, whereas in their absence, solidification of intruding melts is likely to be rapid and mixing of melts infrequent.

This picture of magma evolution is consistent with the stratigraphy of the 500-m section of plutonic Layer 3 drilled at the very slow-spreading Southwest Indian Ridge in Hole 735B. This section suggests sequential crystallization of small intrusive bodies, successively working their way up through a largely solidified crust. These underwent rapid crystallization, with a complex interplay between igneous and tectonic processes (e.g., Dick et al., 1991). The gabbros exhibit numerous ductile shear zones, deep circulation of hydrothermal fluids, and amphibolitization evidencing downward migration of the brittle-ductile transition during amagmatic periods (Dick et al., 1991; Stakes et al., 1991; Cannat et al., 1991).

Basement relief south of the Costa Rica Rift is moderately rough for 170 km, then changes abruptly to a region of smooth basement

topography that includes Site 504 (Langseth et al. 1983; Hobart et al., 1985). The northern section contains several basement highs whose relief is 100–200 m and exhibits a total relief of 300 m (Fig. 4). Basement outcrops comprise 17% of the seafloor (Searle, 1983). These hills consist of numerous east-west lineated highs up to 30 km long, whose steep northward-facing scarps and gentle southward slopes suggest a series of normal faults and back-tilted blocks. In contrast, the southern area is almost devoid of basement outcrops, though smaller fault scarps, with throws typically less than 100 m buried under the sediment, are common. Site 504 is located on a generally flat featureless sediment plane. Three small lineated sedimented highs are located about 5 km to the south of the site, one of which may expose a small area of outcrop (0.1 × 2 km) (Searle, 1983).

All of this relief is relatively low compared to that found at most slow-spreading ridges. The sharp difference between the northern and southern areas south of the Costa Rica Rift, however, implies an abrupt change in the conditions of rifting. Klitgord et al. (1975) found that the spreading rate increased from 26 to 38 mm/yr about 4.1 m.y., and the change in basement relief may reflect this (Searle, 1983). Normally, as pointed out by Searle, increasing spreading rate is associated with smoother topography, not the reverse. However, the topography generated at intermediate-spreading-rate ridges may be either rough or smooth. Along the Southeast Indian and Pacific Antarctic Ridges, for example, the ridge axis may have either the morphology of a fast- or a slow-spreading ridge for long intervals and change abruptly for no apparent cause.

The differences in topography south of the Costa Rica Rift may reflect differences in the longevity and extent of magma chambers beneath the ridge. Overall, the smooth basement topography at Site 504 suggests a relatively long-lived chamber, and Natland et al. (1983) have proposed such a chamber based on the chemistry and petrology of the basalts. The rougher basement topography to the north, might reflect an effective change in the rate of magma supply, magma chamber geometry, and life brought about by the abrupt change in spreading at 4.1 Ma.

The vicinity of Site 504 has been studied using a wealth of seismic techniques, ranging from sonobuoys, single-channel and multichannel seismic surveys to oblique downhole seismic experiments, vertical downhole seismic experiments and downhole sonic logs. Four multichannel seismic lines showed a discontinuous, nearly horizontal reflector at about 1.6-s two-way traveltimes beneath basement which has been interpreted as the Mohorovicic discontinuity, indicating relatively thin, 5-km-thick, crust (Brocher et al., 1986; Collins et al., 1989; Becker, Sakai, et al., 1989; Becker, Sakai, Adamson, et al., 1989). Despite extensive processing to remove high-amplitude side-scattered arrivals, the multichannel data revealed no conclusive evidence for laterally coherent reflection events generated within the upper 1–2 km in the vicinity of Hole 504B (Collins et al., 1989), although intermittent reflectors at deep crustal depths may be similar to the Layer 3 dipping reflectors in the North Atlantic (Mutter et al., 1985). Numerous sonobuoys shot by Langseth et al. (1983) suggested considerable crustal heterogeneity in the region, although the crustal structure determined by averaging these matches the depth-velocity profile determined by an offset seismic experiment in Hole 504B remarkably well (Fig. 5) (Little and Stephen, 1985; Hobart et al., 1985). Little and Stephen (1985) note no sharp transitions in their velocity-depth curves that correspond to either rock type or velocity, though there is some indication of the Layer 2B/2C boundary at the depth of the transition to sheeted dikes. A vertical seismic profile shot during Leg 111 showed numerous seismic reflectors which were correlated with various lithostratigraphic horizons in the hole. However, the reflector immediately below the bottom of the hole, believed to be the dike/gabbro transition, did not clearly coincide with any observed change in lithology or mineralogy in the core recovered during Leg 140.

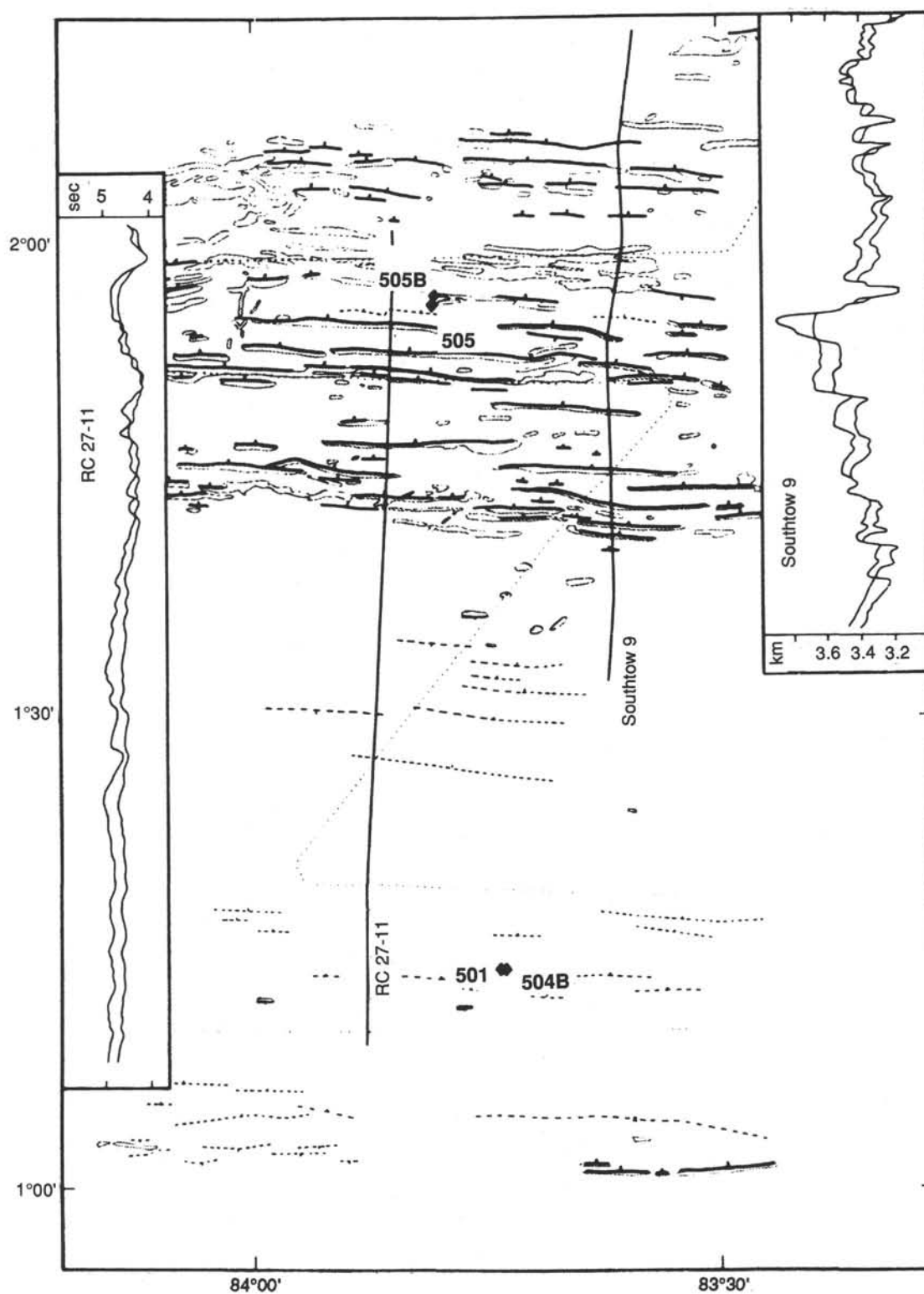


Figure 4. Regional geology south of the Costa Rica Rift from Searle (1983) based on GLORIA and seismic surveys, showing northward-facing fault scarps and basement highs in the areas of DSDP Sites 501, 504, and 505. Insets show tracings of seafloor bathymetry and basement topography from *Conrad* cruise 27 (Langseth et al., 1983) and Southtow 9 (Kiltgord et al., 1975). Stippled areas represent basement outcrops, heavy lines show fault scarps, and broken lines indicate relative steep sediment-covered slopes. From Searle (1983).

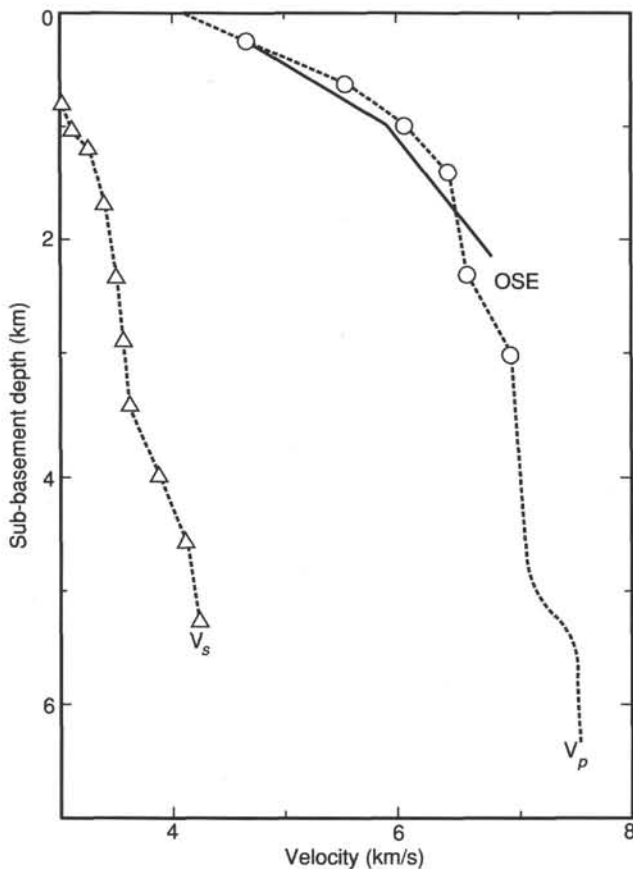


Figure 5. Comparison of the average compressional and shear-wave profiles (V_p and V_s , respectively) for the region around Hole 504B with the results of the Oblique Seismic Experiment in Hole 504B of Stephen (1983). From Hobart et al. (1985).

A common characteristic of most seismic studies in the vicinity of Hole 504B (Langseth et al., 1983; Hobart et al., 1985; Stephen, 1983; Little and Stephen, 1985) is an anomalously high shallow crustal velocity for Layer 2A, where the lowest velocity seems to be close to 4.3 km/s, as compared to the normal velocity for Layer 2A of 3–4 km/s (Houtz and Ewing, 1976). These authors generally attribute this to consolidation and healing of cracks resulting from the anomalously steep geothermal gradient and the unusually thick sediment cap, which effectively seals off the crustal section to open circulation of seawater. Thus, alteration in the shallow ocean crust here may be atypical for ocean crust of the same age.

The oblique seismic studies also show significant shallow crustal anisotropy of 4–4.8 km/s in the upper 100 m of the basement, with the higher velocity east-west, parallel to the lineation of the basement topography and the axis of the Cocos-Nazca Rift (Little and Stephen, 1985). This is attributed to faulting and the formation of east-west cracks in the basement on the scale of hundreds of meters adjacent to the hole.

Summary of DSDP/ODP Results from Hole 504B

An excellent summary of the scientific results at Hole 504B through Leg 111 has been presented by Becker, Sakai, Adamson, et al. (1989) (Fig. 6), and we only detail the highlights here. At the end of Leg 137, Hole 504B extended through 274.5 m of sediment and 1347 m of basement, for a total penetration of 1621.5 m, more than twice that of the second deepest hole (583 m in DSDP Hole 332B). Hole 504B is the only basement hole to clearly penetrate the extrusive

pillow lavas into the sheeted dikes predicted from studies of ophiolites. The Hole 504B section includes 571.5 m of pillow lavas and minor flows, underlain by a 209-m transition zone of mixed pillow lavas, thin flows and dikes, and 566.5 m of sheeted dikes and massive units (Fig. 2). The stratigraphy is based on an average core recovery of only 23.3% (29.8% in the pillows, 25.3% in the transition zone, and 14.8% in the dikes), but is generally corroborated by an extensive suite of geophysical logs, except that the Layer 2B/2C transition seen in the logs is sharper than the lithostratigraphic pillow lava-dike transition (Fig. 7). To date, the scientific results of Hole 504B are the best direct verification of the ophiolite model for the oceanic crust. However, this verification is only partial, as the lowermost 3–4 km of oceanic crust has never been sampled in situ.

Hole 504B is in a particularly interesting stage of physical and chemical evolution. Temperatures at the sediment-basement interface are high, which has promoted the formation of chert bands in sediments 30 m above basement and indurated limestones for 90 m above the cherts (Fig. 8). Recent detailed heat-flow work and numerical simulations indicate that some convection still occurs in the permeable uppermost 200–300 m of basement beneath the impermeable sediment cover, partly controlled by the presence of isolated basement faults and topographic highs (Langseth et al., 1988; Fisher et al., 1990).

The basement rocks recovered from Hole 504B range from aphyric to highly phyrlic tholeiitic basalts. Based on phenocryst assemblage, four major types occur: most abundant are aphyric basalts, followed by olivine-plagioclase-clinopyroxene basalts, olivine-plagioclase basalts, and olivine-plagioclase-clinopyroxene-spinel-bearing basalts. Olivine-clinopyroxene and plagioclase-clinopyroxene basalts occur deeper in the hole, and aphyric types are also more abundant with depth in the sheeted dike section. A singular feature of the Hole 504B basalts is the remarkably uniform major-element composition. Only small differences exist between the composition of the sheeted dikes and the pillow lavas, and essentially none, when the compositions of aphyric dikes and pillows are compared (Natland et al., 1983; Autio and Rhodes, 1983; Autio et al., 1989; Emmermann, 1985; Kempton et al., 1985). Only a few thin units, about 2% of the core, were enriched or transitional-type mid-ocean ridge basalts (Autio and Rhodes, 1983). The sonic and seismic data are generally consistent with a sharp Layer 2B/2C boundary at the top of the sheeted dikes. The sonic data, but not the much longer wavelength seismic data, indicate a thin Layer 2A, consisting of the uppermost 100–200 m of highly porous pillow lavas. This layer corresponds to a highly permeable, underpressured zone into which ocean bottom water has been drawn since the hole was drilled (Fig. 8). Layer 2B comprises the lowermost 500 m of pillows, in which the original porosity has been partially sealed by alteration products.

OPERATIONS

Transit to Hole 504B

Leg 140 began with the first mooring line on Victoria's Ogden Point dock at 1400 UTC, 11 September 1991. The 15-day transit to Hole 504B covered 4064 nmi in 369.0 hr at an average speed of 11.0 kt. Hurricane Kevin slowed progress to 6.5 kt; swells up to 20 ft and winds up to 40 kt required a course change to bypass the center of the storm by 65 nmi.

Leg 137 Operations Summary

The seafloor depth used on Leg 137 was 3475 m below rig floor (mbrf); however, on previous legs, a water depth of 3474 mbrf was reported. A depth of 3474 mbrf was measured at the start of Leg 140, consistent with most earlier legs at Hole 504B. The following summary of Leg 137 operations assumes a depth of 3474 mbrf.

Hole 504B was cleaned out, drilled, and cored during Leg 137. While using a Christensen large-diameter (6-3/4 in.) rotary core barrel with a 7-7/8 in. diamond-impregnated core bit, penetration stopped at 1621.5 mbsf. The drill string was retrieved and revealed that the

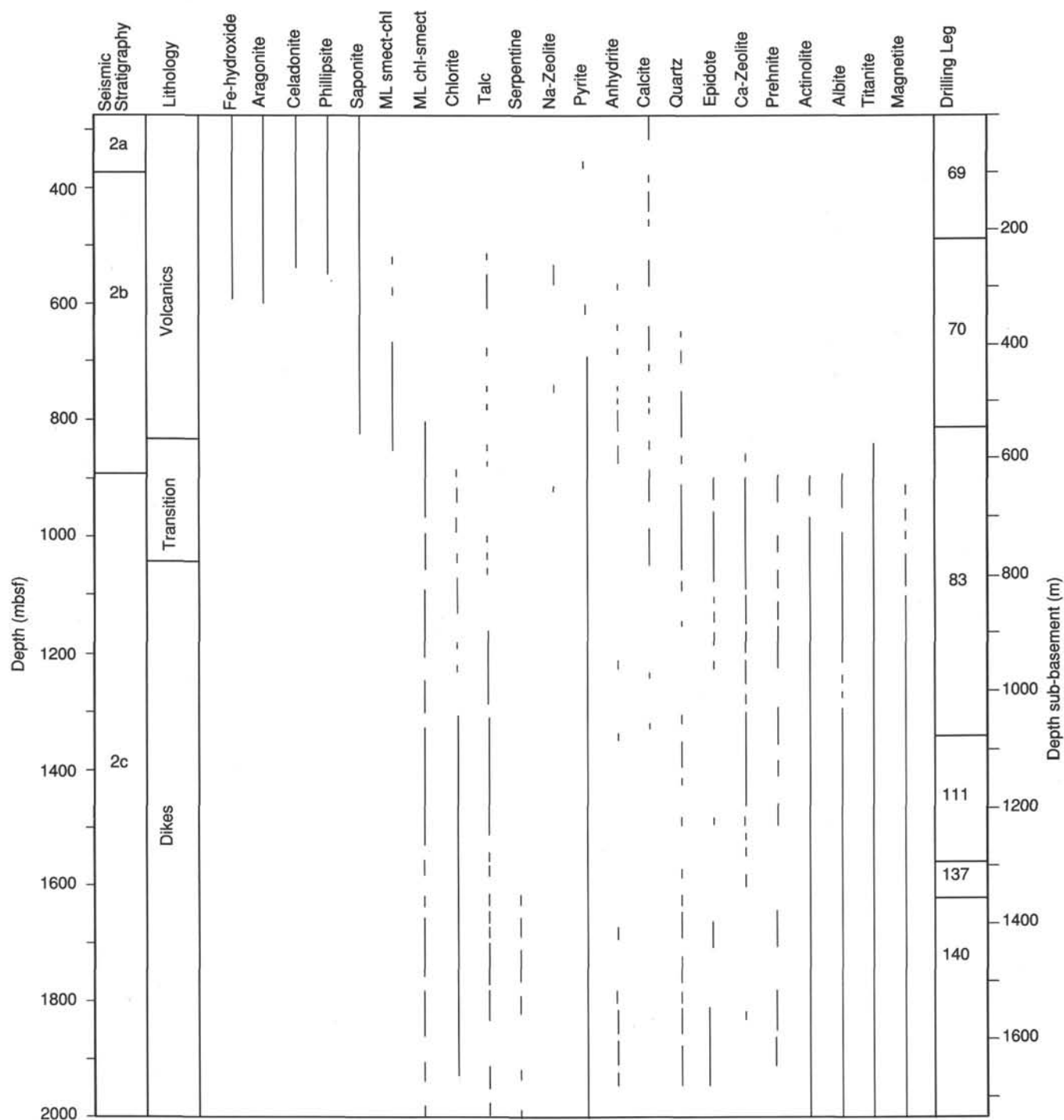


Figure 6. Distribution of seismic stratigraphy, lithology, and secondary mineralogy with depth in Hole 504B. From Becker, Sakai, Adamson, et al. (1989).

core barrel had parted below the inner barrel swivel. The drill string recovered the inner core barrel and core, but the outer core barrel and diamond-impregnated bit were left in the hole (Fig. 9A). A 9-1/2 in. slim-hole overshot dressed with an extension, 6-3/4 in. basket grapple, and cut lip guide, was run to attempt to engage the core barrel.

Apparently, the overshot swallowed the core barrel: the bottom of the overshot drive sub contained a perfect imprint of the core-barrel tube, and the top of the core-barrel fish was clearly marked by the overshot cut lip guide. Faint marks 18 in. down on the hard tube of the core barrel may have been made by the overshot grapple. The grapple teeth were dull and chipped, suggesting that the grapple could

have easily slipped off. The drive sub on top of the overshot pulled out of the extension bowl while being pulled up, possibly because of drag which may have been caused by the core barrel. The extension and overshot bowl were left in the hole on top of (and presumably connected to) the core-barrel fish.

In the short time remaining on Leg 137, an unsuccessful attempt was made to engage the overshot bowl using a shortened taper tap. The failure of the taper tap to engage the overshot bowl suggested again that the core barrel might have stuck above the basket grapple. The top of the overshot fish was tagged at 1589 mbsf. Assuming the overshot and core barrel were still together, the 18.4-m core barrel

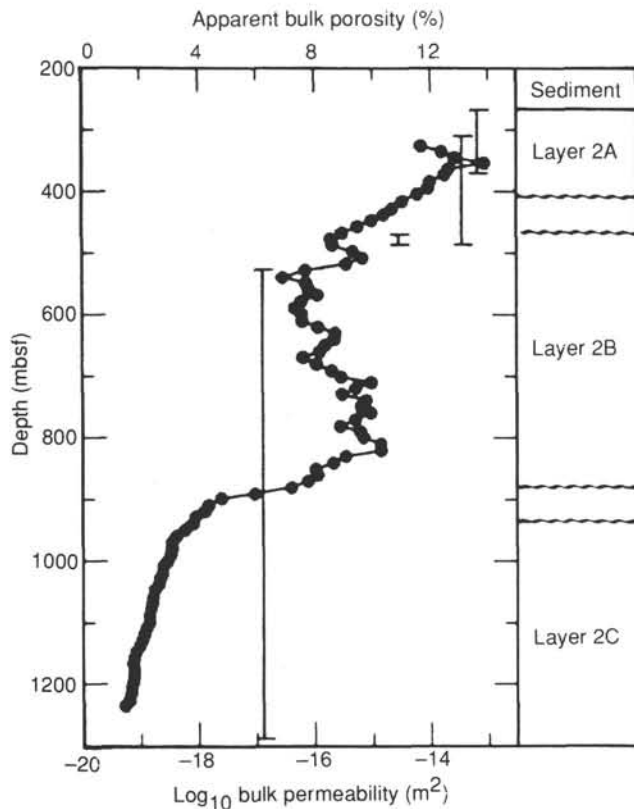


Figure 7. Variation of apparent bulk porosity of basement with depth in Hole 504B determined by applying Archie's Law to large scale electrical resistivity logs and bulk permeabilities measured over the intervals spanned by the vertical bars. Shown on right are approximate boundaries of seismic Layers 2A, 2B, and 2C based only on the apparent bulk porosity gradients. From Shipboard Scientific Party (1988).

would also have been above the bottom of the hole. The bit was probably resting on a ledge that had been reamed out at least four times during the leg (Fig. 9B). The overshot may not have moved the core-barrel fish up the hole, but might simply have fallen off and become jammed in the hole.

Leg 140 Operations

Hole 504B was approached at 1350 UTC, 1 October, and ship control was shifted to dynamic positioning (DP). A retrievable beacon was dropped on the global positioning system (GPS) location recorded during Leg 137 and hit bottom 55 m south-southeast of the reentry cone and 22 m southeast of the beacon drop point. The search and reentry into Hole 504B required 1.42 hr. The reentry bit was run to 58 mbsf for logging.

Logging: First Phase

A French Bureau de Recherche Géologique et Minières (BRGM) temperature tool logged 150–550 mbsf, and recorded a temperature of 90.5°C at 550 mbsf (see "Downhole Measurements" section, this chapter). A Schlumberger slim-hole formation microscanner (FMS) tool was run to 1576.6 mbsf (8 m above the top of the fish) and logged from 1570.6 to 1556 mbsf, where the telemetry failed, apparently because of the high temperature. The four spring-loaded arms could not be closed without telemetry, so the tool was pulled from the hole for repairs. At 1138 mbsf, it became stuck, and was eventually freed after 7800-lb pull (3500-lb overpull). The tool was pulled up to 946 mbsf, where telemetry was reestablished. The hole was logged up to

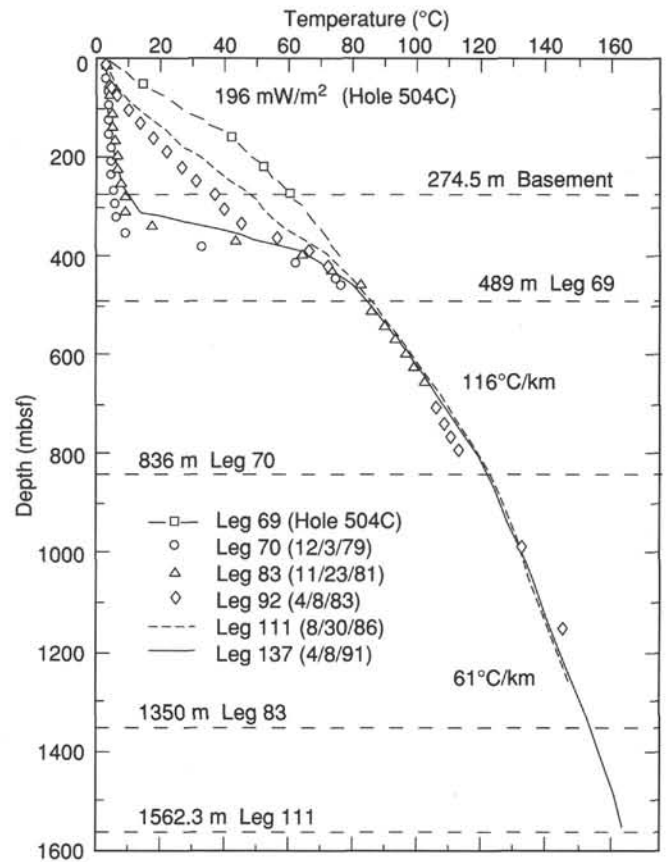


Figure 8. Temperatures measured in Hole 504B during Legs 69, 70, 83, 92, 111, and 137. The depressed temperatures in the upper 400 m reflect the downhole flow of cold ocean bottom water through the casing into the upper 100–150 m of the basement.

281 mbsf, but some of the readings were unreliable. The reentry into the casing and bottom-hole assembly (BHA) was normal, but the tool became stuck again about 20 m inside the BHA. About 2000-lb overpull was required to free the tool. The FMS tool had lost an arm, a bow spring, and pad parts. The bow spring of one pad had been bent upward to form a hook, which might have been caught in the BHA. The arms and hinge pins of this specially built slim-hole FMS are of light construction and are held open by bow-spring pressure (not by hydraulic pressure as in the normal FMS tool). The pads were built in three sections, and came apart in the hole. Hole 504B has a very rugose and hard wall, so a slim-hole FMS with a stronger arm, stronger hinge pin and non-segmented pad is needed before rerunning the tool in equivalent formations.

Fishing

Leg 140 fishing plans were predicated on the assumption that the outer core-barrel fish was still engaged in the overshot fish. The marks on the overshot drive sub indicated that the core-barrel fish had been above the grapple at one time; moreover, overshot basket grapples are known for their strong gripping power and seldom slip off. The fishing operation was expected to be straightforward and of little risk; however, the normal indicators of fishing problems, such as pressure drop, weight and torque changes, were masked by an open core barrel (inner diameter 5.38 in.) that may have been stuck above the bottom of the hole, a lightweight fish, a smooth diamond bit on a hard bottom, a fish that changed position in the hole, and loose rock rubble and junk. The fishing plan was to use an overshot tool first, a spear next, the taper tap last, and milling if required.

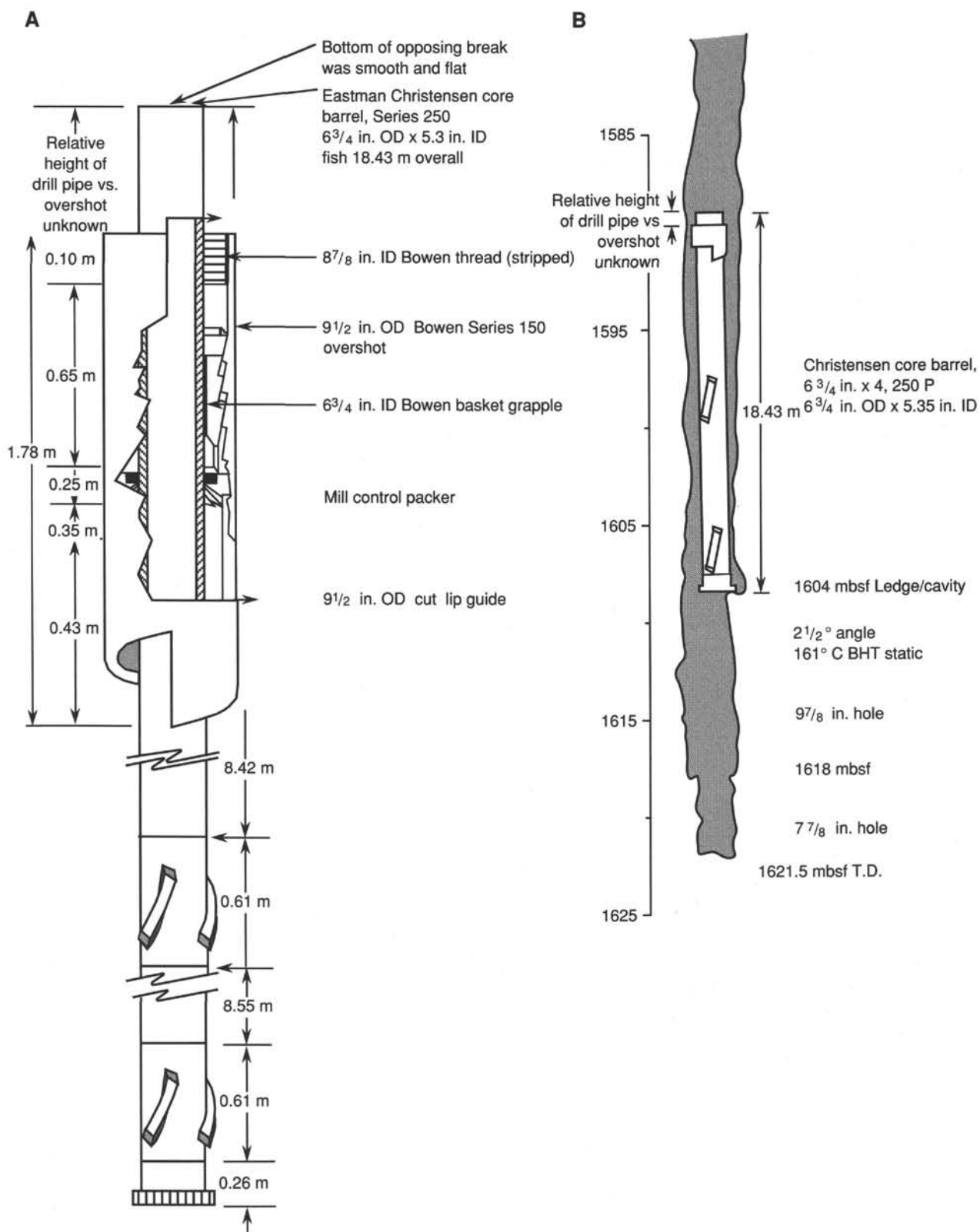


Figure 9. A. Schematic diagram of the Christensen core barrel and Bowen overshot grapple, which comprised (in part) the fish left in Hole 504B at the end of Leg 137. B. Assumed position of fish at the end of Leg 137.

The following fishing tools were purchased especially for Leg 140: a 9-1/2 in. slim-hole overshot with a cut lip guide and 6-3/4 in. basket grapple, an Itco 5-1/2 in. Bowen-type releasing spear with 5.367 in. grapple, a 5-3/8 in. × 7 in. taper tap, two 9-5/8 in. piloted junk mills, a 7-7/8 in. concave junk mill, a 9-5/8 in. lead impression block, and three reconditioned 9-5/8 in. concave junk mills.

The reentry bit had been run for temperature and FMS logging; it was therefore run to 1589 mbsf, where the fish was tagged. Little fill had collected above the fish, indicating that Hole 504B had been stable since Leg 137. Figures 10A and 10B summarize operations.

The reentry bit was pulled out of the hole, and a 9-1/2 in. slim-hole overshot, including a 6-3/4 in. basket grapple and flat shoe, was deployed. Initially it was thought that the overshot fish was further down the core barrel so that the fishing overshot could engage the core barrel. Eight unsuccessful attempts were made to engage the fish, and the overshot fish was bumped 9 m down the hole (top of fish now at 1600 mbsf). The fishing overshot contacted the fish, but the grapple did not engage. When the bottom of the overshot guide was examined later, it contained several indentation marks, indicating that it had been on the top rim of the overshot bowl. The inside of the overshot contained no marks, however, showing that it never got over the core barrel. Thus, the overshot fish must have been too far above the core barrel for the fishing overshot grapple to engage.

Next, a fishing spear was run to attempt to catch the core barrel through the overshot fish. An Itco releasing spear with a 5.367 in. nominal grapple was deployed to catch the core barrel (5.38 in. inner diameter). The spear was run to 1586 mbsf. The top of the fish was tagged again at 1590 mbsf, and unsuccessful attempts were made to engage the core-barrel fish. The spear had no marks on it, but showed some evidence of sliding on the kutrite shoe. The spear was probably not long enough to reach through the overshot fish to engage the core barrel.

A 7 in. × 4-1/4 in. taper tap was run next to engage the 6-3/4 in. basket grapple in the overshot fish, so the overshot could be removed to clear the top of the core barrel. The taper length of the tool should have been sufficient to engage both the 6-5/8 in. ID overshot grapple (and the 5.38 in. ID core barrel, if they were together). The taper tap tagged the fish at 1589 mbsf. The fish was engaged with 35,000 lb drag, but fell off after 2 m. The taper tap was hammered down, but would not reengage. The paint on the teeth of the tool was worn off from the tip up to a diameter of 5.33 in. (ID of core barrel) and also, 50 cm above, at a diameter of 6.75 in. (ID of the grapple) as if it had been washing through fill inside the core barrel. The marks on the taper tap were 19 in. apart, indicating that the core barrel top must have been just inside the overshot cut lip guide. The overshot fish prevented full engagement of the taper tap in the core barrel.

Another attempt was made to get both fish by running an extended spear through the overshot. A 1.88-m extension was constructed on the ship and added to the spear. The extended spear was run with a 5.367 in. nominal grapple (to catch the 5.38 in. ID core-barrel fish) and a milling nose. The top of the fish was tagged at 1599 mbsf, but the fish was not engaged. The spear advanced 0.3 m by rotation and was washed down 3.5 m with light rotation, but still did not engage. After pulling out the spear, mild wear was observed on the mill nose, and the grapple had been lost in the hole.

The next strategy was to shorten the nose of the taper tap so it could engage the overshot grapple without having to wash down into the core barrel. The lower 40 cm of the taper tap was cut off, leaving a 6-7/8 in. × 5-1/8 in. wicker. The top of the fish was tagged at 1602.8 mbsf, but attempts to engage the overshot grapple failed. Unsuccessful attempts were made to circulate the taper tap further down and use the jars to hammer down on the taper tap to engage it. When examined, the taper tap had no marks on the bottom, but the teeth at 6-3/4 in. to 7 in. diameter were polished and had some metal shavings. The taper tap appeared to have been driven down into the overshot fish grapple without engaging it.

Although the fish was engaged on several fishing runs, no solid connection had been achieved after 5.5 days of fishing. The overshot and core barrel were no longer together and were separated by rock rubble, making fishing much more difficult than originally anticipated. One more day of fishing was planned; if no progress were made, Hole 504B would be abandoned. An alternative fishing tool, designed to pass through the overshot grapple and open beneath it, was built on the ship for a last attempt.

The ship-built "double dog" fishing tool had three horizontal dogs activated by hydraulically shearing a forcing cone and two 45° flipper dogs built into a piece of 5-1/2 in. drill pipe. A 5-1/2 in. mill was built into the bottom in case the overshot or core barrel was full of debris. Six meters of fill was tagged at 1598.8 mbsf, and the fishing tool was washed down through fill. The fish was chased to 1604.6 mbsf and engaged, but came off at 35,000-lb overpull. An attempt was made to set the hydraulic dogs, and the fish was engaged again, but the tool slipped off at an overpull of 25,000 lb and could not be reengaged. The tool was spudded with 30,000–50,000 lb of weight, and was engaged successfully. However, the fish was stuck and could not be moved with 50,000-lb tension. After working the fish several times, it began to move and the drag slowly decreased to 20,000 lb. The overshot fish was recovered, and the bottom mill was found wedged into the outer core barrel, however, the core barrel broke off at the top of the bottom stabilizer unit. The diamond-impregnated bit, near-bit bottom stabilizer, formation microscanner parts, and miscellaneous small pieces of junk were left in the hole. A 9-7/8 in. tri-cone bit was run to clean out the fill to 1619 mbsf and open the 7-7/8 in. hole to 1620.1 mbsf. A 9-7/8 in. tri-cone bit (Bit Run 1) was used to open the hole and clean out fill to the top of the fish. The hole was then circulated clean.

Only a taper tap could recover the bit and stabilizer and collect the remaining small junk without milling. A mill nose was added to the taper tap so it could drill out any junk in the stabilizer before engagement. The taper tap was washed down to the top of the fish at 1620.1 mbsf and engaged. Increasing circulation pressures indicated the fish was packing off, therefore, a 50-bbl high-viscosity mud pill was pumped to the fish to reestablish circulation. The taper tap was engaged, 40,000-lb blows were struck to seat the tap firmly, and the fish was worked using 25,000-lb overpull while circulating the mud pill around the bit. Pump pressure broke back, and the fish was moved with 20,000-lb drag. The taper tap recovered the remainder of the fish: the 7-7/8" diamond bit, near-bit stabilizer, spear grapple parts, a FMS pad, and miscellaneous overshot junk.

Most of the junk in Hole 504B was recovered. A 9-7/8 in. bit (Bit Run 2) was run with two junk subs to open the remaining 7-7/8 in. hole to 9-7/8 in. (1621.8 mbsf) and to remove any remaining junk.

Coring Operations

Bits and Bottom-hole Assembly

During Leg 137, two 9-7/8 in. rotary coring bits were pulled after coring 25.3 m at a rate of 1.7 m/hr and 20.2 m at a rate of 1.8 m/hr to reveal that the outer driver-row inserts had broken off. The hard fractured basalt caused the driver-row (outer) cutting structure of these bits to fail. To deepen Hole 504B during Leg 140, 15 Security H87F bits were built with ovoid inserts (teeth) and more ductile (but less abrasion-resistant) tungsten carbide inserts.

The bottom-hole assembly used during Leg 140 consisted of a 9-7/8 in. × 2-7/16 in. four-cone rotary coring bit and core barrel, 11 8-1/4 in. drill collars, hydrolex jars, 2 8-1/4 in. drill collars, and a 7-1/4 in. drill collar. Six joints of 5-1/2 in. transition drill pipe and 120–130 stands of 5 in. drill pipe were connected to the bottom-hole assembly; the remainder of the string consisted of 5-1/2 in. drill pipe. The bottom-hole assembly design provided 250,000-lb overpull with 6° roll and 10,000-lb heave load. Rotary coring started at 1621.8 mbsf on 13 October. Table 2 summarizes coring operations.

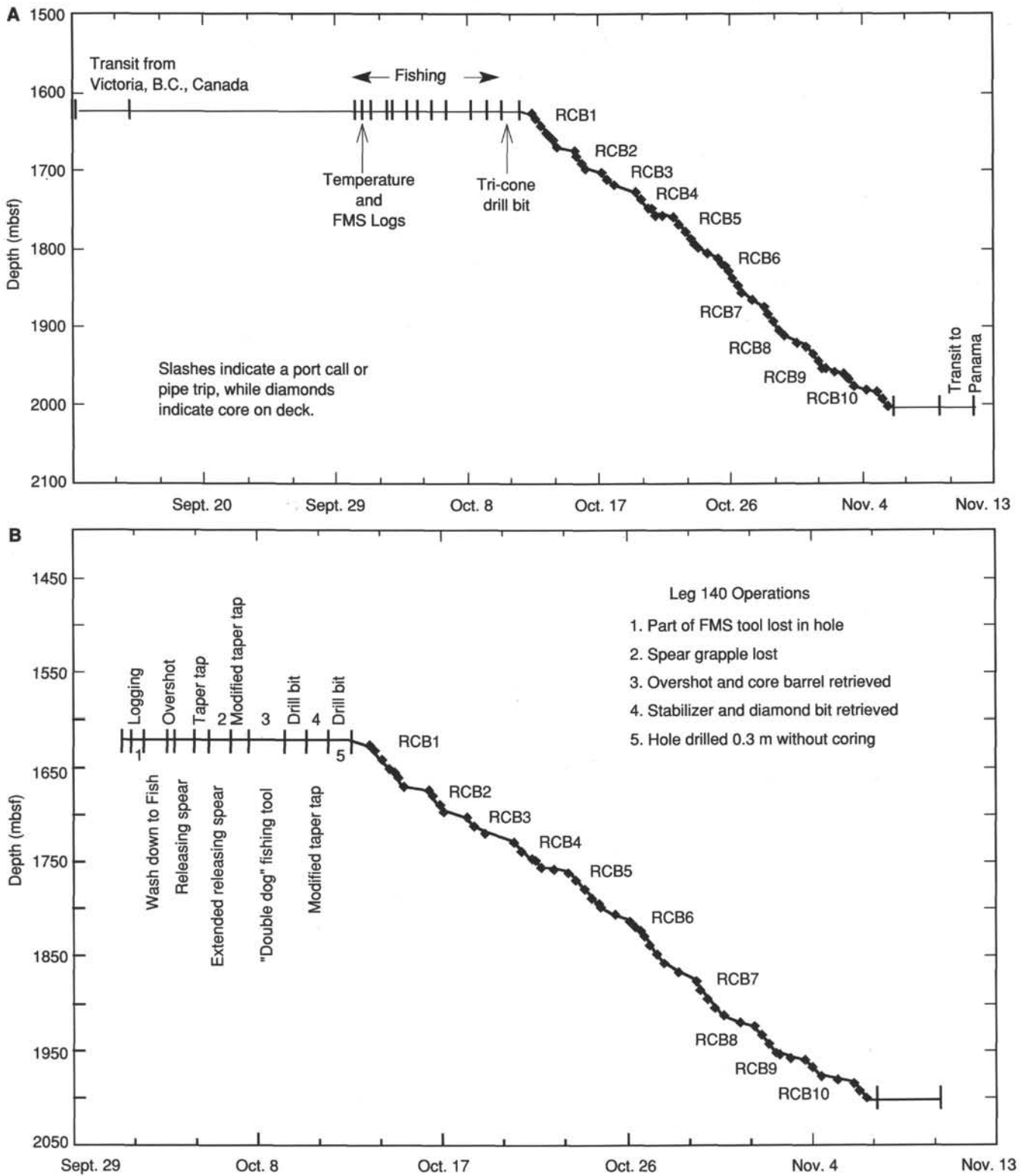


Figure 10. A. Detailed summary of fishing, drilling, and logging operations at Hole 504B. B. Summary of the sequence of operations conducted during Leg 140. RCB = rotary coring bit.

Bit Run 3

A 9-7/8 in. rotary coring bit was run from 1621.8 to 1655.1 mbsf and cored 33.3 m in 27.28 hr for a penetration rate of 1.22 m/hr. The bit was run at 50 revolutions per minute (rpm), with 20,000–32,000 lb weight on bit. The penetration rate was 0.9 m/hr with 30%–49% recovery in unfractured basalt, and 1.8 m/hr with 5% recovery in fractured basalt. The bit run was terminated after 27 hr because it was the first bit of its type ever tested. The core catcher and liner sleeve were jammed with wedge-shaped fractured core; the bit was re-runnable.

Bit Run 4

A 9-7/8 in. rotary coring bit was run from 1655.1 to 1696.5 mbsf, coring 41.4 m in 26.58 hr for a penetration rate of 1.56 m/hr. Brief drilling tests running the bit at 50–70 rpm with 20,000–35,000 lb weight on bit indicated that the best penetration rate was obtained at 50 rpm and a weight on bit of 35,000 lb. The penetration rate was 0.9 m/hr with 30%–49% recovery in unfractured basalt and 1.8 m/hr with 5% recovery in fractured basalt. Two cores were jammed when the butyrate core liner was deformed by core wedging, and the liner sleeve jammed with wedge-shaped fractured rocks on one core. The bit was re-runnable. The butyrate core liners were removed for Core 193R and for the remainder of the leg with the consent of the shipboard scientific party.

Bit Run 5

A 9-7/8 in. rotary coring bit was run from 1696.5 to 1719.4 mbsf, coring 22.9 m in 16.0 hr for a rate of penetration of 1.43 m/hr. The bit was run at 30,000–35,000 lb weight on bit, 50 rpm, and was pulled for an unexplained pressure drop, or "washout." The rate of penetration was 1.9–1.30 m/hr with 6%–19% recovery in fractured basalt. The bit was re-runnable.

Bit Run 6

A 9-7/8 in. rotary coring bit was run from 1719.4 to 1757.0 mbsf, coring 38.6 m in 34.25 hr for a penetration rate of 1.13 m/hr. The bit was run with 28,000–35,000 lb weight on bit, at 50 rpm. The bit was pulled for a drop in both pump pressure and penetration rate, and was re-runnable. The penetration rate was 0.45–1.67 m/hr, with 2%–86% recovery in altered fractured and unfractured basalt.

Bit Run 7

A 9-7/8 in. rotary coring bit was run from 1757.0 to 1806.0 mbsf, coring 45.3 m in 39.1 hr, and a penetration rate of 1.16 m/hr. The bit was run with 28,000–40,000 lb weight on bit, and 50 rpm. The bit was not re-runnable, and was pulled because of irregular torque. The driver-row inserts on all four cones were badly chipped, however, the ductile tungsten carbide was still providing some cutting surface. The rate of penetration was 1.10–1.73 m/hr with 5%–45% recovery in altered fractured and unfractured basalt.

Bit Run 8

A 9-7/8 in. rotary coring bit was run from 1806.0 to 1865.5 mbsf, coring 59.5 m in 40.75 hr for a penetration rate of 1.46 m/hr. The bit was run with 35,000 lb weight on bit, at 50 rpm. The bit was not re-runnable and was pulled because of irregular torque. Several of the driver-row inserts were chipped about 50%, however, the ductile tungsten carbide was still providing some cutting surface. The penetration rate was 0.89–2.00 m/hr, with 2%–55% recovery in altered

Table 2. Coring summary, Hole 504B.

Core	Date (Oct.-Nov. 1991)	Time	Depth (mbsf)	Cored (m)	Recovered (m)	Recovery (%)
Hole 504B						
182M	9	1540	277.0–1621.5	–	–	–
183M	10	1600	277.0–1621.5	–	–	–
184M	12	1300	1621.5–1621.8	0.3	–	–
185R	13	0955	1621.8–1626.3	4.5	0.18	4.0
186R	13	1625	1626.3–1632.0	5.7	1.70	29.8
187R	14	0105	1632.0–1641.5	9.5	0.34	3.6
188R	14	1055	641.5–1651.0	9.5	0.47	5.0
189R	14	1705	1651.0–1655.1	4.1	2.00	48.8
190R	14	2005	1655.1–1661.4	6.3	0.94	14.9
191R	15	0225	1661.4–1670.9	9.5	0.96	10.1
192R	16	0745	1670.9–1674.5	3.6	0.32	8.9
193R	16	1235	1674.5–1680.4	5.9	0.55	9.3
194R	16	2010	1680.4–1689.6	9.2	1.16	12.6
195R	17	0200	1689.6–1696.5	6.9	0.09	1.3
196R	18	0425	1696.5–1702.8	6.3	0.37	5.9
197R	18	1330	1702.8–1712.2	9.4	1.81	19.2
198R	19	0150	1712.2–1719.4	7.2	0.80	11.1
199R	19	1120	1719.4–1728.6	9.2	1.48	16.1
200R	20	2025	1728.6–1737.8	9.2	4.23	46.0
201R	21	0800	1737.8–1747.2	9.4	0.18	1.9
202R	21	1350	1747.2–1749.0	1.8	0.59	32.8
203R	21	2020	1749.0–1756.5	7.5	0.63	8.4
204R	22	0950	1756.5–1757.0	0.5	0.43	86.0
205R	23	0315	1757.0–1760.7	3.7	0.74	20.0
206R	23	1155	1760.7–1768.4	7.7	0.47	6.1
207R	23	2115	1768.4–1778.0	9.6	0.45	4.7
208R	24	0715	1778.0–1787.5	9.5	2.65	27.9
209R	24	1445	1787.5–1794.9	7.4	2.63	35.5
210R	24	1820	1794.9–1798.5	3.6	1.63	45.3
211R	25	0950	1798.5–1806.0	7.5	1.25	16.6
212R	26	0300	1806.0–1812.5	6.5	0.43	6.6
213R	26	0915	1812.5–1818.6	6.1	1.04	17.0
214R	26	1545	1818.6–1823.0	4.4	2.44	55.4
215R	26	2015	1823.0–1827.9	4.9	0.63	12.8
216R	27	0230	1827.9–1837.4	9.5	0.60	6.3
217R	27	1020	1837.4–1846.9	9.5	0.29	3.1
218R	27	1845	1846.9–1856.2	9.3	0.20	2.2
219R	28	1135	1856.2–1865.5	9.3	0.14	1.5
220R	29	0845	1865.5–1875.0	9.5	0.33	3.5
221R	29	1415	1875.0–1884.6	9.6	0.57	5.9
222R	29	2305	1884.6–1894.2	9.6	1.01	10.5
223R	30	0650	1894.2–1903.7	9.5	0.34	3.6
224R	30	1640	1903.7–1912.2	8.5	0.61	7.2
225R	31	1255	1912.2–1920.0	7.8	2.32	29.7
226R	1	0420	1920.0–1924.5	4.5	3.02	67.1
227R	1	1400	1924.5–1934.0	9.5	1.51	15.9
228R	1	2210	1934.0–1943.5	9.5	0.58	6.1
229R	2	0645	1943.5–1953.0	9.5	0.47	5.0
230R	2	1120	1953.0–1953.5	0.5	0.20	40.0
231R	3	0030	1953.5–1957.3	3.8	0.09	2.4
232R	3	1635	1957.3–1960.0	2.7	0.14	5.2
233R	4	0110	1960.0–1967.4	7.4	0.24	3.2
234R	4	1030	1967.4–1976.1	8.7	0.00	0.0
235R	5	0600	1976.1–1980.7	4.6	0.24	5.2
236R	6	0145	1980.7–1983.7	3.0	0.72	24.0
237R	6	0805	1983.7–1992.1	8.4	0.24	2.9
238R	6	1650	1992.1–2000.4	8.3	0.24	2.9
Coring totals				378.9	47.69	12.6

fractured and unfractured basalt. Recovery, however, averaged only 3.2% in the last four cores.

Bit Run 9

A 9-7/8 in. rotary coring bit was run from 1865.5 to 1920.0 mbsf, coring 54.5 m in 41.53 hr for a penetration rate of 1.31 m/hr. The bit was run with 30,000 lb weight on bit, at 50 rpm. The bit was not re-runnable. Most of the driver-row inserts were chipped about 50%, however, the ductile tungsten carbide was still providing some cutting surface. The rate of penetration was 2.62–0.87 m/hr, with 4%–30%

recovery in altered fractured and unfractured basalt. Recovery, however, averaged only 9.5% for the bit run.

Bit Run 10

A 9-7/8 in. rotary coring bit was run from 1920.0 to 1957.3 mbsf, coring 37.3 m in 30.57 hr for a penetration rate of 1.22 m/hr. The bit was run with 30,000 lb weight on bit, at 50 rpm. The bit was not re-runnable and was pulled because of unexplained pressure drop. The 300-psi pressure loss was the result of a core-barrel check valve that had sheared out (probably when the inner barrel was pumped down after getting caught in cuttings inside the outer core barrel). The cuttings apparently got into the core barrel when a roll pin slipped in and jammed the float. The core was washed out and only two cobbles were recovered in Core 231R. Almost 100% of the driver-row inserts on all four cones were chipped about 80%. The penetration rate was 1.48–1.12 m/hr, with 5%–67% recovery in altering fractured and unfractured basalt. Recovery, however, averaged 15.7% for the bit run.

Bit Run 11

A 9-7/8 in. × 2-7/16 in. rotary coring bit was run from 1957.3 to 1980.7 mbsf. The bit was run with 30,000 lb weight on bit, at 50 rpm. The bit exhibited junk damage on shirt-tail, hence was not re-runnable. It was pulled for erratic torque. The inner 80% of each cone was missing, whereas only the outer-gauge row rings of all four cones were still on the bit. Spear points from two cones were recovered on a subsequent coring run. The spear points had been cut off just before the thrust bearings. The penetration rate was 1.16–0.66 m/hr, with a 3.2%–5.2% recovery in fractured and unfractured basalt.

Bit Run 12

A 9-7/8 in. × 2-7/16 in. rotary coring bit was run from 1980.7 to 2000.4 mbsf, coring 19.7 m in 14.88 hr for a penetration rate of 1.32 m/hr. The kelly was measured out with no weight on bit to confirm the depth measurement at intermediate tide. The bit was run with 26,000–30,000 lb weight on bit, at a rate of 50 rpm. Junk caused gauge damage and broken and chipped teeth on the driver rows. The bit was pulled because of time limitations. The bit was drilling at 2.0 m/hr, with normal torque, when coring was terminated. The bit was pulled with normal 20,000-lb overpull; hole conditions were normal. Damage to the driver rows was moderate to severe. The teeth on the inner rows were moderately chipped. All four cones of the outer gauge inserts were worn 20%. The gauge ring indicated that the bit was 3/16 in. under gauge, therefore, it would be advisable to ream the lower 20 m of the hole before any future coring. The rate of penetration was 0.86–1.81 m/hr, core recovery was 2.9%–24% in fractured basalts. Recovery averaged only 6.1% for the bit run.

Bit Summary

Ten 9-7/8 in. × 2-7/16 in. bits were run and performed significantly better than previous bits in hard fractured basalt, with an overall record of coring 378.6 m in 294.77 rotating hours for an average penetration rate of 1.28 m/hr with 12.6% recovery. Rate of penetration and recovery correlated directly with the type of basalt being cored. The penetration rate was 1.3–1.8 m/hr in fine-grained, fractured basalt and chilled margins with recovery of 6% or less. The penetration rate was 0.9 m/hr in coarser grained, relatively unfractured basalt, but recovery was 30%–50%. The driver-row and spearpoint inserts need to be harder formation (ball-type) cutters in future designs.

Hole Conditions and Hydraulics

The hydraulics were maintained at 120 strokes per minute at 1800 pounds per square inch (psi; with bit seals) to 2300 psi (without bit seals). Hole cleaning while coring with single 50-bbl sweeps proved inadequate, even at 700 gallons per minute. Therefore, two 50-bbl viscous mud sweeps were circulated during each core. Additional sweeps were circulated whenever abnormal drag, fill, torque, or penetration rate were noted. Bit nozzle plugging (from inner core-barrel drop stones or cuttings from failed floats) was a frequent problem. Core jamming occurred in every conceivable part of the core barrel: the core catcher (jamming and wedging), butyrate core liner (swelling the walls), core liner sleeve, and steel inner barrel.

The hole was circulated at 500-m intervals when running in to cool the hole and to reduce thermal stresses, and also to cool the bit and jar seals. The hole appeared to be relatively stable; however, stress breakout chips (thermal or tectonic) were found in junk subs, cores were disced and fractured, and hand-sized wall breakouts (curved to hole diameter) were recovered in the core barrel. Fill on trips was negligible, and a few cobbles (mostly from the pillow lava section) were recovered in the tops of some cores. Drag on pipe trips was consistently 10,000–20,000 lb (normal for this depth). The drill string was occasionally trapped by what appeared to be small cobbles or boulders falling in the hole, but the string was eventually freed by working the pipe uphole with rotation, 40,000-lb overpull, and pumping 50-bbl viscous mud sweeps. Occasional ledges, light bridges, and under-gauge hole required reaming with 2,000 lb weight on bit and light torque. Torque was monitored carefully to core as little under-gauge hole as possible (so future bits would not be destroyed by the under-gauge hole).

Logging: Second Phase

Prior to logging, at 0500 UTC, 7 November, a re-entry logging bit was run to 104 mbsf. An additional temperature log was run initially, using the French Bureau de Recherche Géologique et Minières (BRGM) temperature tool, to determine the temperature rebound after circulation. (See "Downhole Measurements" section, this chapter, for a detailed discussion of logging results.) The tool logged temperature while running into the hole, and tagged the bottom at 2000.4 mbsf. The maximum temperature recorded was 142°C, because of cooling from circulation. While recording temperature built up, the logging winch failed. The temperature tool failed after 90 min, but recorded a temperature increase of 1.96° C/hr. The logging winch was subsequently repaired and the tool was pulled out of the hole.

Next, the geochemical tool string was run to 700 mbsf, but was pulled out to switch cartridges. The tool was then run in and logged from 1896 to 1811 mbsf, where the "minitron" failed. While being pulled, the tool revived, and logging continued from 1686 to 1350 mbsf.

A resistivity/sonic log was run next, but failed at 526 mbsf. The tool was pulled, and water was found in the cable head. The tool was rerun, and logged successfully from 275 to 1990 mbsf.

The digital borehole televiewer was the fourth logging tool employed. It was run to 1980 mbsf, but was pulled because of bad readings. The cable head was damaged and the conductors had shorted to ground. The tool was repaired and logged successfully from 1985 to 1885 mbsf and from 1685 to 1485 mbsf.

The flowmeter was then deployed and logged four passes from 256 to 468 mbsf. The geochemical tool string was deployed for a final run from 1826 to 1648 mbsf, ending the logging program. Plans to load sodium bromide in the hole as a borehole fluid tracer were cancelled because of time limitations.

The drill string was pulled out of the hole with the corrosion inhibitor inside, clearing the seafloor at 0350 UTC, 10 November. The two beacons on bottom were recalled and recovered. The vessel was underway for Panama City at 1200 UTC, 10 November for the 530-nmi transit to Panama City, Panama.

IGNEOUS PETROLOGY

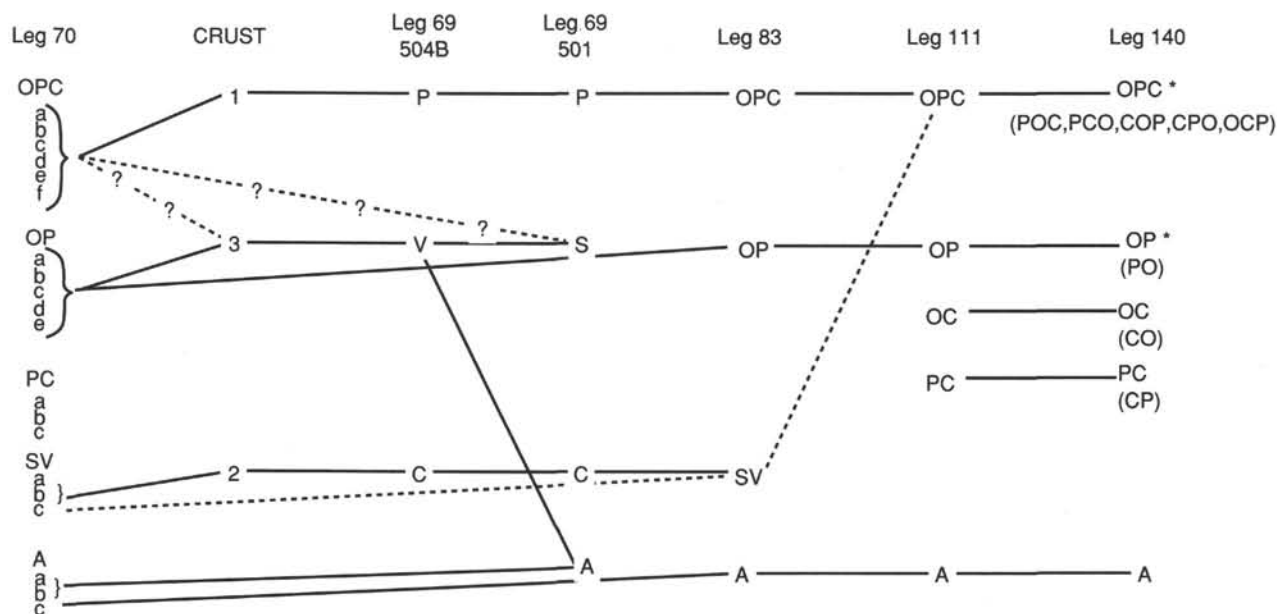
Lithologic Units

Lithologic units were classified on the basis of the abundance of phenocrysts identified in hand specimen or by binocular microscope. Units with less than 1% phenocrysts are called "aphyric," units with 1%–2% are called "sparsely phyric," units with 2%–10% are called "moderately phyric," and units with greater than 10% are called "highly phyric." The prefixes "P," "O," and "C" are added to indicate plagioclase, olivine, and clinopyroxene phenocrysts, respectively, in order of relative abundance. On Legs 83 and 111, initial classification was made purely on the basis of the phenocryst phases present and not on their relative proportions (i.e., previous legs used "OPC" for rocks with these three phenocrysts regardless of which phase was most abundant). Previous legs also classified all rocks as basalts due to their characteristic mineral assemblage, and used the term "dike" only when an intrusive contact was recognized. While the rocks drilled on Leg 140 fall into the general chemical classification of basalts and contain a "basaltic" mineral assemblage, this rock type is generally recognized as "diabase," and we use this term to describe the majority of cored samples. The term "basalt" has been reserved for samples with a very fine-grained groundmass (average grain size < 0.25 mm). We have used the term "doleritic" to describe the typical texture of diabase, rather than the term "diabasic" used on previous legs to this site. Figure 11 is a diagram showing the correspondence of lithologic classification schemes employed by different DSDP and ODP legs to Hole 504B. This diagram is an extension of that presented in DSDP Volume 83 (Anderson, Honnorez, Becker, et al., 1985, p. 26, fig. 6) in a discussion of the previous classification schemes, and a detailed description of the nomenclature used by Legs 69/70, CRRUST (1982), and Leg 83 is presented on pages 26–31 of that volume (Anderson, Honnorez,

Becker, et al., 1985). The classification scheme employed on ODP Leg 111 is described on pages 50–52 of the *Initial Reports* volume (Becker, Sakai, et al., 1988).

Drilling on Leg 140 recovered 56.86 m of rock (archive length) of which 6.46 m (11.4%) is aphyric, 10.57 m (18.6%) is sparsely phyric, and 39.83 m (70.0%) is moderately phyric. These rocks have been divided into 59 units, 10 of which are represented by a single piece of core. Unit boundaries were placed wherever there was an abrupt change in lithology (grain size, phenocryst assemblage, or phenocryst abundance) or wherever a chilled contact between two units was observed. Individual pieces with distinct lithologies within otherwise homogeneous units were not assigned to separate units if they appeared to have fallen from a higher level in the hole (particularly common as the first piece recovered after a bit change), or if they were only separated from a nearby unit of like lithology by small fragments of the host unit. Unit boundaries may represent the transition from one dike to another, or they may represent lithologic changes within the same dike. Owing to the poor recovery in some sections, it was not always possible to distinguish between these two possibilities.

The mineralogy and grain size of each unit was estimated from hand-specimen examination and is recorded in the igneous mineralogy log (Appendix A). The lithology, texture, color, sulfide mineral content, and oxide mineral content of each unit were estimated from hand-specimen examination and are recorded in the igneous lithology log (Appendix B). The nature of the contacts between units is recorded in the igneous contacts log (Appendix C). Of the 59 units described, 19 are aphyric, 14 are sparsely phyric, and 26 are moderately phyric. Most units (47) are fine-grained basalts, but several (3) have average grain sizes > 1.0 mm and were classified as medium-grained diabase, and several (9) have microcrystalline groundmasses (average grain size < 0.25 mm) and were classified as basalt. The medium-grained basalts presumably represent the central parts of thick dikes, and the basalts are believed to represent either chilled marginal facies of dikes or material which has fallen down the hole from higher stratigraphic levels. The majority of the porphyritic units (36 of 40) were multiply saturated in plagioclase, olivine, and clinopyroxene (POC, PCO, OPC, OCP, CPO, or COP). Two



* The order of phenocrysts in the lithologic unit name indicates the relative abundances of those phases in the rock as determined by macroscopic examination.

Figure 11. Comparison of rock classification schemes used on Legs 69, 70, 83, 111, and 140. Abbreviations are explained in the "Petrography" section of the "Explanatory Notes" chapter (this volume).

porphyritic units contained only plagioclase and olivine phenocrysts (PO and OP), and two contained only plagioclase and clinopyroxene phenocrysts (PC). The rock names applied to thin-section descriptions do not necessarily correspond to the rock names used in the lithologic log, which is based solely on hand-specimen descriptions. The thin-section descriptions represent a much smaller volume of rock and used different criteria for determining phenocryst percentages and grain sizes than the hand-specimen descriptions.

The 378.9 m drilled at Hole 504B on Leg 140 (1621.5–2000.4 mbsf) appears to be a continuation of the sheeted dike complex previously described from Leg 83 (Anderson, Honnorez, Becker, et al., 1985) and Leg 111 (Becker, Sakai, et al., 1988). All rocks recovered (with the exception of fragments that appear to have fallen down the hole during bit changes) are interpreted as rocks which crystallized from magmas as dikes. These rocks have been subsequently altered by subsolidus processes, with the result that the original igneous minerals have been partly replaced by metamorphic minerals. The degree of alteration in individual samples ranges from a few percent to almost 100%. None of the samples recovered are interpreted as in-situ extrusive rocks or plutonic rocks. The coarsest unit identified (260) has an average grain size of 1.5 mm and in terms of both texture and grain size is clearly a diabase and not a gabbro.

Phenocryst Phases

Introduction

Phenocrysts in Units 211–269 include plagioclase, augite, olivine, and Cr-rich augite (Fig. 12). Although not texturally a phenocryst, Cr-Al spinel is an early-formed mineral in these rocks and is described with the phenocryst phases. The groundmass is dominated by plagioclase, augite, and magnetite. Some of the rocks examined are seriate porphyritic, a texture in which there is a continuous range of grain sizes from the phenocrysts down to the groundmass. In most of the porphyritic samples, however, a clear distinction can be made between phenocryst and groundmass minerals. Although alteration in these rocks ranges from a few percent to almost 100%, the original igneous textures and mineral assemblages can be determined for most samples, and for all units. The igneous features of the recovered rocks are described below, whereas subsolidus alteration is described in the "Alteration and Metamorphism" section (this chapter).

Plagioclase

Plagioclase feldspar is commonly the most abundant mineral phase in basalts and this is true for basalt and diabase from Hole 504B. Plagioclase is present in the groundmass, as phenocrysts, and in glomeroporphyritic clots and all together makes up between 43% and 68% of the primary mode in the diabase recovered on Leg 140. Gabbroic xenoliths also contain plagioclase, but these are a minor contribution to the total plagioclase abundance.

Plagioclase phenocrysts make up 3% or less of the diabase (Fig. 12) and are commonly the most abundant phenocryst (the abundance of plagioclase phenocrysts reported from hand specimen is usually less than that reported from thin-section descriptions because different criteria are used to define phenocrysts in the two methods). The average size of plagioclase phenocrysts ranges from that of the groundmass up to about 4 mm, and a few grains are more than 10 mm long. They are mostly euhedral with subhedral overgrowths, but some are anhedral, as a result of resorption or fracturing of preexisting subhedral grains. Fractured grains can be recognized by their angular appearance and by zoning patterns that truncate against an edge.

Plagioclase phenocrysts can be divided into three regions, core, mantle, and rim, that may be interpreted as corresponding to three stages of crystal growth. Not all crystals have all three zones. The rims of phenocrysts represent the final stage of cooling and crystal growth, whereas the core may represent a prolonged stage of crystal growth under stable conditions. The mantle is interpreted as a region of

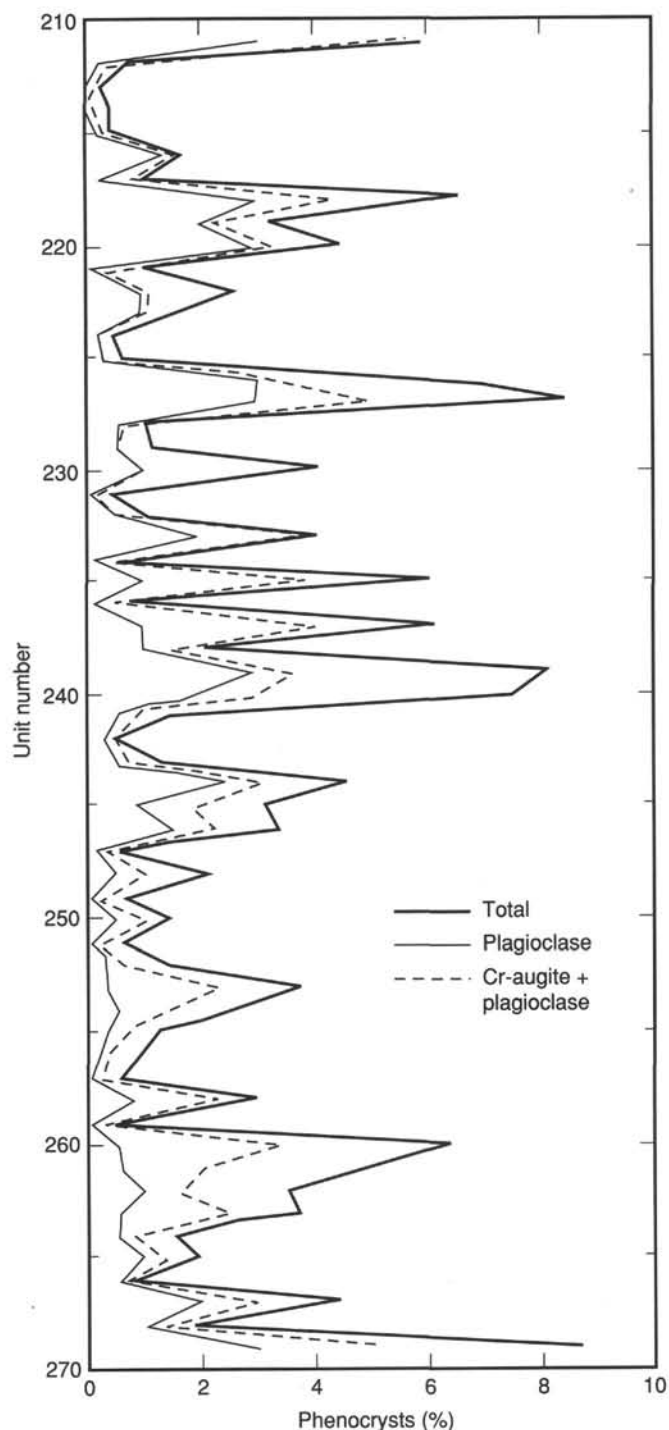


Figure 12. Plagioclase phenocrysts, plagioclase + Cr-augite phenocrysts, and total phenocryst abundance, by unit number.

transition from stable growth in a magma chamber to rapid growth in a dike (see "Plagioclase Zoning Patterns," this section).

Inclusions in plagioclase consist of all the phenocrysts phases, spinel, sulfide minerals, opaque oxide minerals, and glass. Round to elongate glass inclusions ranging from 0.005 to 0.1 mm are the most common, but all have been altered to microcrystalline aggregates. Glass inclusions are usually randomly concentrated in dense patches in the cores of phenocrysts, but they also occur in the mantle, and rarely in the rim. Glass inclusions are sometimes aligned along twin

planes or distributed in bands within the core or mantle. As many as three concentric bands of inclusions (each about 0.1 mm wide) can be present in a single phenocryst. Large (0.1–0.2 mm) irregular glass inclusions are also present in some crystals. Spinel inclusions are commonly present and may occur within the core or mantle of phenocrysts. Spinel is only rarely present within rims (this was only observed in samples from the upper units drilled on Leg 140; Units 211–227). Augite, olivine, and small rounded subhedral plagioclase crystals are common inclusions in the cores and mantles of plagioclase phenocrysts, but are not common in the rims.

Glomeroporphyritic clots are composed of plagioclase, augite, olivine, and rarely spinel, but plagioclase is generally the dominant mineral. Plagioclase may form aligned mats of laths with no intergranular spaces or may be randomly oriented. Individual grains within clots range from rounded subhedral to euhedral in shape, but some are anhedral crystal fragments. Plagioclase grains included in the center of glomerocrysts often have no compositional zoning, but grains at the margins of glomerocrysts have complex zoning similar to that of the phenocrysts, and individual grains may have numerous glass inclusions, whereas adjacent grains are free of inclusions. These observations suggest that grains in some glomerocrysts formed in different environments and later came together to form a clot.

Pyroxene

Four color varieties of pyroxene phenocrysts were observed in hand specimen: (1) pale, translucent grass-green, (2) black, (3) deep emerald-green, and (4) milky blue green. The most abundant (0.05%–3.0% in 49 of the 59 units) is the pale, translucent green variety which is believed to be equivalent to the high-Cr, low-Ti augite described in the Leg 111 diabases (Becker, Sakai, et al., 1988) and is referred to in the mineralogical log as Cr-augite. The next most abundant (0.05%–1.5% in 46 units) pyroxene phenocryst is the black variety which is believed to be equivalent to the low-Cr, high-Ti augite described in the Leg 111 diabase and is referred to in the mineralogical log as augite. The deep emerald-green pyroxene was observed as a few crystals (<0.1%) in only two samples and may represent Cr-diopside xenocrysts. The milky blue-green pyroxene was observed as a phenocryst in only two samples where it is texturally similar to the augite phenocrysts (black pyroxene) and probably represents a localized alteration of that phase.

The Cr-augite phenocrysts typically occur as euhedral to subhedral elongate laths (1.0–6.5 mm in length, aspect ratio 3:1 to 6:1), and most optically include groundmass plagioclase in their outer rims, suggesting that the pyroxene phenocrysts continued to grow during groundmass crystallization. Many Cr-augite phenocrysts have inclusion-free cores, but some enclose rounded, stubby, subhedral to euhedral plagioclase laths texturally distinct from those in the groundmass, and a few have Cr-spinel and/or olivine inclusions. Cr-augite phenocrysts only rarely show resorption textures or contain melt inclusions. Some of the Cr-augite phenocrysts are compositionally zoned with simple-zoning, oscillatory-zoning, or sector-zoning patterns (Figs. 13 and 14).

Augite phenocrysts typically occur as black, subhedral to anhedral, ophitic to poikilitic, equant crystals (0.4–1.5 mm in diameter). In most samples they are texturally very similar to the groundmass pyroxene and probably represent unusually large crystals in a groundmass that is seriate porphyritic with respect to the black augite. Thin-section examination indicates that in many samples the grain size of augite is much larger than that reported in the igneous mineralogy log (Appendix A) which is based on hand-specimen measurements, where the extent of individual poikilitic crystals is not always apparent. Some of the poikilitic augite phenocrysts have patchy extinction suggesting disruption of the pyroxene lattice by the growth of included plagioclase laths. Some of the augite phenocrysts are zoned, with simple zoning patterns the most common. In some cases the largest augite crystals in a seriate porphyritic rock were counted

as phenocrysts during hand-specimen examination but were counted as groundmass crystals during thin-section examination where the continuous range of grain sizes is more apparent.

Olivine

Olivine is a common phenocryst phase (0.1%–4.0% in 54 units) in the porphyritic diabases recovered on Leg 140, but unaltered olivine cores are only preserved in a few units (227, 260, and 269 in particular). Although it has been completely replaced by alteration minerals in most samples (see “Alteration and Metamorphism” section, this chapter), the original crystal outline and textural relationships are often preserved. Olivine typically occurs as equant, subhedral to euhedral crystals, 0.5–2.5 mm in diameter. Olivine in many samples has an ophitic or skeletal crystal outline with inclusions of plagioclase and rarely Cr-spinel.

Spinel

Oxide minerals in mid-ocean ridge basalts can be broadly grouped as either iron-titanium oxides (usually magnetite) or as chrome-aluminum oxides. In oceanic basalts the chrome-aluminum oxide minerals have been called spinels, chromites, chrome spinels, magnesiochromites, and titaniferous magnesiochromites (Sigurdsson and Schilling, 1976), depending on their chemical composition, but in the absence of chemical information they will be referred to collectively as spinel in this report.

Spinel is a minor phase in oceanic basalts, rarely making up more than 1% of the rock and in the Leg 140 diabase, spinel was rarely observed in hand specimen. In thin section, however, it is apparent in about half of the lithologic units (Appendix D) as microscopic phenocrysts and inclusions in plagioclase, olivine, and augite oikocrysts. Spinel is by far most abundant in plagioclase phenocrysts, but is not common in plagioclase grains in glomerocrysts. Spinel makes up much less than 1% of these units and is always represented by fewer than 10 grains per 2 cm² of thin section. Spinel commonly occurs as equant grains 0.05–0.07 mm in diameter but may be as large as 0.2 mm. The color is distinctive, ranging from reddish-brown and reddish-yellow to black in transmitted light and from light to dark gray in reflected light. Some grains are zoned from reddish cores to black rims which corresponds with dark to light gray, respectively, in reflected light. These colors are probably related to chemical composition (Fisk and Bence, 1980). Black implies high iron content and reddish-yellow implies high chrome content (Furuta and Tokuyama, 1983). The black rims of some spinels may be a result of reaction of an early-formed crystal with the residual liquid during cooling of the diabase.

Morphologically, spinel in Leg 140 diabases occurs as equant, anhedral to euhedral grains, but in some samples it occurs as irregular, anhedral cylinders up to 0.1 mm long. The shape in some samples correlates with color, with reddish-brown euhedral grains and reddish-yellow anhedral grains. A few grains appear to have reacted with the host liquid resulting in a symplectitic texture with glass infiltrating the rim of the crystal. These symplectitic zones are black in transmitted light and more reflective than the spinel core in incident light. The rims, however, are generally not as reflective as groundmass magnetite. Some spinel crystals have round inclusions 0.02–0.05 mm in diameter of plagioclase, glass, sulfide minerals, or possibly olivine (see “Cr-spinel Stability in Basalts and Diabase,” this section).

Groundmass

The groundmass in the diabases recovered on Leg 140 is composed of plagioclase, augite, and magnetite, with or without minor amounts of devitrified glass, quartz, apatite, spinel, and sulfide minerals. Olivine is a groundmass mineral in some samples, but owing to the degree of alteration typical of this section, the number of units containing groundmass olivine can not be determined with any certainty. The groundmass is composed primarily of plagioclase and augite in proportions ranging from 1:1 to 2.5:1, with plagioclase



Figure 13. Sector-zoned Cr-augite phenocryst in Sample 140-504B-181M-2, 148–150 cm.

always equal to or greater than augite. The average grain size of the groundmass, as determined from macroscopic description of all rocks (except chilled contacts), ranges from 0.1 mm to 1.5 mm but is most commonly 0.3 to 0.8 mm with plagioclase having a slightly larger grain size than augite (Fig. 15).

Groundmass plagioclase occurs in a variety of textural types: euhedral to subhedral laths (aspect ratio 3:1 to 5:1), acicular crystals (aspect ratio 10:1 to 20:1), skeletal crystals (aspect ratio 10:1 to 15:1), and splays of complex branching crystals (Figs. 16 and 17). Individual samples may contain one, two, three, or all four of these textural types. Some of the euhedral to subhedral laths contain zoned cores and may represent microphenocrysts. The acicular, skeletal, and branching morphologies are typical of phases that precipitate from oversaturated melts in which the growth rate is large relative to the diffusion rate. Plagioclase is the most abundant groundmass mineral (41%–55%) in samples that are coarse enough for the groundmass mineralogy to be accurately determined.

Augite is typically present in the groundmass as subhedral to anhedral crystals, and is the second most abundant groundmass mineral (31%–46%). In most samples augite is ophitic to poikilitic with numerous plagioclase inclusions (Fig. 18). Crystals with abundant large plagioclase inclusions typically have patchy extinction patterns in which sections of what appear to be originally continuous crystals reach extinction at slightly different orientations. In some samples augite occurs as intergranular inclusion-free crystals with subhedral prismatic morphologies



Figure 14. Normally zoned Cr-augite phenocryst showing ophitic overgrowth in Sample 140-504B-181M-2, 40–44 cm.

(Fig. 19). In a few samples augite is sheaf-like to plumose, suggesting rapid growth under supersaturation conditions. An unusual texture results where plagioclase forms complex branching crystals enclosed within a single poikilitic groundmass augite (Figs. 17 and 19).

Fe-Ti oxide minerals are a ubiquitous groundmass phase. They typically form equant grains 0.05–0.30 mm in diameter and, in many samples, have distinct skeletal morphologies. In most samples a magnetite host has exsolved ilmenite lamellae during cooling, and has subsequently been partly replaced by titanite.

Some samples contain scattered (1%–4%) interstitial patches of quartz-albite granophyric intergrowths with minor pyroxene, Fe-Ti oxide, and sulfide mineral inclusions. Some of these patches may be the result of alteration, but most appear to represent late-stage interstitial pockets of trapped trondhjemitic liquid. Similar textures were reported by Sinton and Byerly (1980) in basalts recovered from DSDP Sites 417 and 418 in the western Atlantic.

Crystal Clots

Oceanic basalts and diabases recovered from sites in the Atlantic, Indian, and Pacific oceans contain crystal aggregates of various origins that may record processes of magma evolution and solid rock-melt interaction during generation, fractionation, and emplacement of magmas in the oceanic crust. The variety of crystal aggregates observed is thought to be representative of the compositional heterogeneities created in

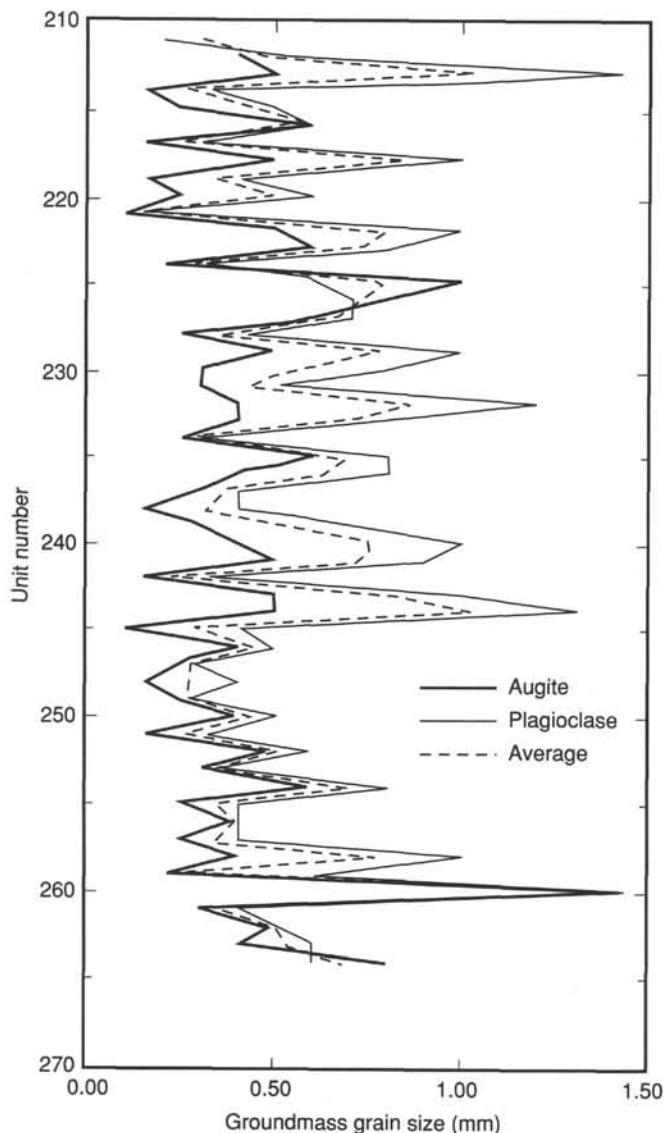


Figure 15. Groundmass grain size from hand-speciman descriptions. The weighted average of plagioclase and augite is given by the dashed line.

magmatic conduits by a complex combination of petrogenetic processes involving crystal fractionation, magma mixing, cumulate compaction, and interaction between the crystal mush and the residual liquid (Sato et al., 1979; Natland, 1980; Saunders et al., 1982).

Crystal clots in oceanic basalts have been reported from a number of Pacific Ocean sites at minor spreading ridge centers (Costa Rica Rift, Galapagos Spreading Center, Guaymas Basin, OCP Ridge) (Donaldson et al., 1976) and abyssal basins (Panama Basin, Central Pacific Basin) (Yeats et al., 1973). Very few crystal clots have been reported from the East Pacific Rise itself, but zero-age basalts dredged from the East Pacific Rise axial valley contain crystal clots and mafic cumulate xenoliths which may have formed in the sub-axial magma chamber (Natland, 1980; Thompson and Humphris, 1980).

A variety of crystal clots and xenoliths were reported from basalts recovered from Hole 504B during Leg 69. They include clinopyroxene and plagioclase megacrysts and xenocrysts, clinopyroxene-plagioclase-olivine-spinel glomeroporphyritic clots, and gabbroic xenoliths (Natland et al., 1983). These authors report textural evidence for considerable resorption of clinopyroxene-bearing crystal clots and of xenoliths of various mineralogic composition. They also report the presence in some clots of clinopyroxene that is more



Figure 16. Skeletal groundmass plagioclase in Sample 140-504B-208R-1, 0-3 cm.

Fe-rich, and plagioclase that is more Na-rich than those that would be in equilibrium with the host basaltic glass.

Diverse terminology has been used to describe textural and compositional microheterogeneities in oceanic basalts. The terms for mineral aggregates include glomeroporphyritic clusters, glomeroporphyritic clots, glomerophyric clusters, glomeroporphyritic patches, glomerocrysts, stellate clusters, xenocrysts, xenolithic fragments, xenoliths, and cognate clots. In this study all the mineral aggregates are referred to as crystal clots, of which two major types have been recognized: (1) syngenetic clots that are genetically related to the host rock, and (2) xenolithic clots trapped by upwelling magma and unrelated to the evolution of the host magma or its associated plumbing system (Fig. 20). Single crystals can be referred to as xenocrysts (derived from disaggregated xenoliths), megacrysts (derived from the host magma at greater depths and under different P - T - f_{O_2} conditions), or phenocrysts (derived from the host magma under P - T conditions similar to those of its emplacement).

Syngenetic clots include oikocrysts, proto-clots, and mature clots. Oikocrysts are poikilitic crystals filled with mineral inclusions (chadacrysts) and may represent an early stage of clot formation. Proto-clots and mature clots are aggregates of discrete grains. The major distinction between them is the higher degree of compaction and the occurrence of cumulate textures in the mature clots. Syngenetic clots can be dunitic (olivine-dominated), wehrlitic (olivine-clinopyroxene), pyroxenitic (clinopyroxene-dominated), gabbroic (olivine-clinopyroxene-plagioclase-magnetite), Fe-gabbroic (significantly enriched in Fe-Ti



Figure 17. Branching groundmass plagioclase in Sample 140-504B-212R-1, 4–7 cm.



Figure 18. Anhedral, poikilitic augite with groundmass plagioclase chadacrysts in Sample 140-504B-199R-1, 105–110 cm.

oxide minerals), troctolitic (olivine-plagioclase), or anorthositic (plagioclase-dominated).

Xenolithic clots usually show clear reaction relationships with the surrounding groundmass and are commonly partially resorbed by the host basalt. Subdivisions of the xenolithic clots are based on the occurrence of one (simple) or more than one (composite) rock lithologies in the same enclave, and generally follow the classification scheme of Dawson et al. (1980) and Kepezhinskas (1989).

The majority of diabase dikes in the Leg 140 core contain small (1–3 mm) crystal clots. Rare clinopyroxene-dominated clots exceed 7 mm in diameter, and a few gabbroic clots exceed 2 cm in diameter. Most of the clots are rounded to oval in shape, although some are irregular in shape as a result of thermomechanical and/or chemical interaction with the host basalt creating dissolution structures, glass pockets, resorbed and corroded surfaces, and crosscutting veins with a groundmass mineralogic assemblage. Some gabbroic clots have elongated or lens-like shapes suggesting compaction or deformation. Textural evidence for clot compaction includes plagioclase and clinopyroxene with zones of adcumulate growth penetrated by late plagioclase laths and Fe-Ti oxide grains corresponding to the crystallization of the plagioclase + augite + Fe-Ti oxide groundmass assemblage of the host basalt.

Dunitic, wehrlitic, and pyroxenitic syngenetic clots are relatively rare and always show a reaction relationship with the surrounding groundmass. In several cases, clear thin (0.01 mm in thickness)

reaction rims are present. Some are well compacted and probably represent the early crystallization stages in the parental magma (syngenetic clots). Others have cumulate textures with olivine and clinopyroxene as major cumulus phases, and plagioclase as a later intercumulus phase along with minor clinopyroxene and rare magnetite. Texturally and mineralogically, these clots appear to represent a cumulate dunite-wehrlite-pyroxenite-gabbro sequence derived from a previous magma reservoir not directly related to the one associated with the host diabase (xenolithic clots) (Figs. 21 and 22). Troctolitic clots are widespread and texturally resemble cumulate clusters formed through fractionation of olivine and plagioclase in a lower crustal level magma chamber. Some, however, may have crystallized at higher levels in the magmatic conduit, as suggested by the textural similarity between the clots and the host diabase.

Gabbroic clots composed mainly of clinopyroxene, plagioclase, and Fe-Ti oxide show various degrees of compaction as expressed by the relative abundance of Fe-Ti oxide minerals. Some ferrogabbroic crystal clots contain significant amounts of primary-textured opaque oxide grains which appear to have crystallized simultaneously with plagioclase and augite from a highly evolved residual liquid (Figs. 23 and 24). These liquids may be similar to the Fe-Ti basaltic liquids erupted along the Galapagos Spreading Center, and may represent a late stage of the liquid line of descent for oceanic tholeiite magma. Some olivine-bearing gabbroic clots are heterogeneous with respect to the distribution of the major mineral constituents, and have a



Figure 19. Subhedral, prismatic groundmass augite (A) and anhedral, poikilitic augite enclosing branching plagioclase (B) in Sample 140-504B-200R-1, 103–107 cm.

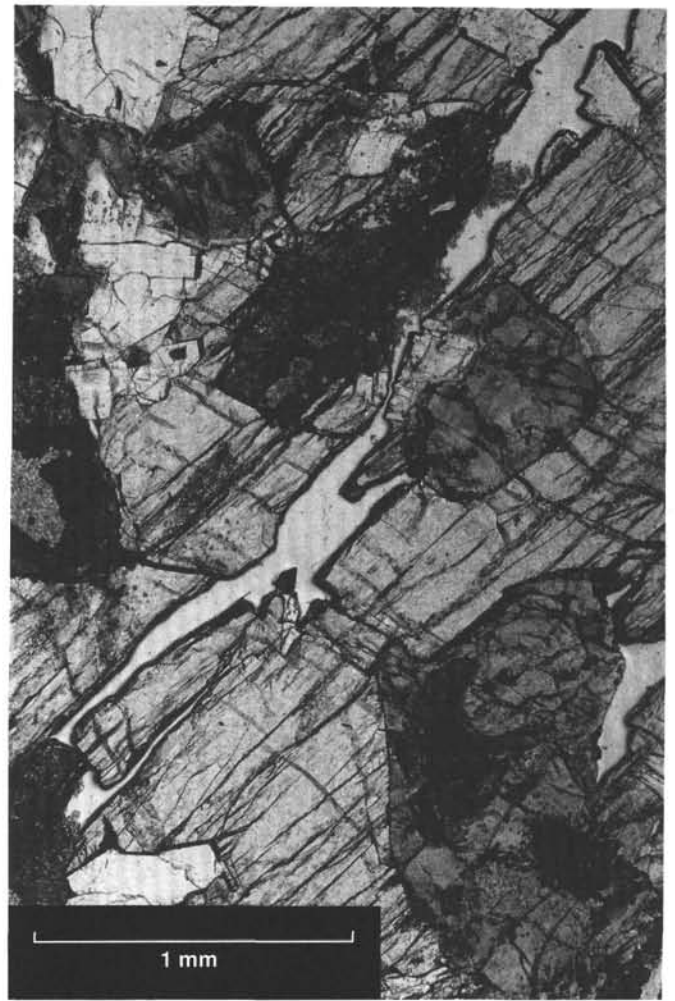


Figure 21. Wehrlite clot in Sample 140-504B-200R-3, 125–130 cm.

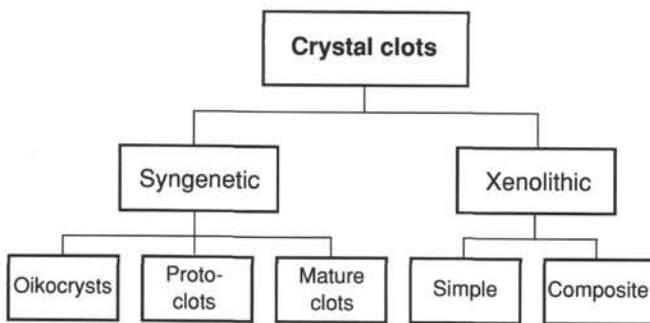


Figure 20. Classification scheme for crystal clots in oceanic basalts. Modified from Alt et al. (1989); Alt, Anderson, and Bonnell (1989); Alt, Anderson, Bonnell, and Muehlenbachs (1989); Shipboard Scientific Party (1985, 1988, 1992).

preferred orientation of plagioclase laths. These textures may have resulted from compaction of the clots with the resulting removal of any previously trapped liquid from inter-grain boundaries. Olivine-bearing proto-gabbroic clots are commonly depleted in the Fe-Ti oxide phase in comparison with typical gabbroic clots. This process may be similar to that proposed for gabbros from Hole 735B (Natland

et al., 1991). A few gabbroic clots appear to have a reaction relationship to the host diabase and may be gabbro xenoliths (Fig. 25).

Plagioclase Zoning Patterns

Zoning of plagioclase in the groundmass, in phenocrysts, and in clots takes numerous forms even within the same unit and thin section. The groundmass, by definition, represents the liquid portion of the magma so normal compositional zoning in groundmass plagioclase (as inferred from petrographic observation) presumably reflects decreasing temperature and evolving residual liquid composition during cooling of the dikes. A rim is present on almost all surfaces of phenocrysts in contact with the groundmass and corresponds to the same stage of crystal growth as the groundmass plagioclase.

Cores and mantles of phenocrysts take on a variety of forms in the Leg 140 diabase. Cores may be euhedral or subhedral, they may have no zoning or they can show slight oscillatory, undulatory, or patchy zoning, and they may have inclusions of glass, smaller euhedral or subhedral rounded plagioclase laths, or spinel. Mantles generally are about 0.1 mm wide and are characterized by an abrupt change in composition relative to the core. This change in composition may represent normal zoning (mantle with lower albite content than the core) or reversed zoning. The mantle commonly has fine oscillatory zoning that outlines the core, and these oscillations may be present as single or multiple 0.05–0.10 mm broad increments. The mantle may

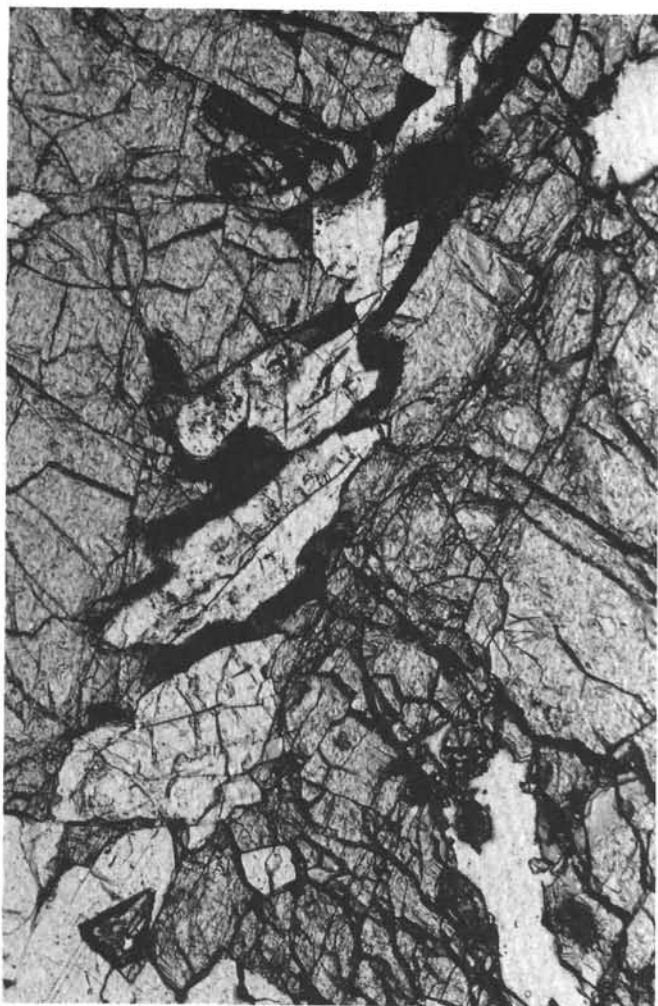


Figure 22. Plagioclase vein in a pyroxenite clot in Sample 140-504B-200R-3, 125–130 cm.

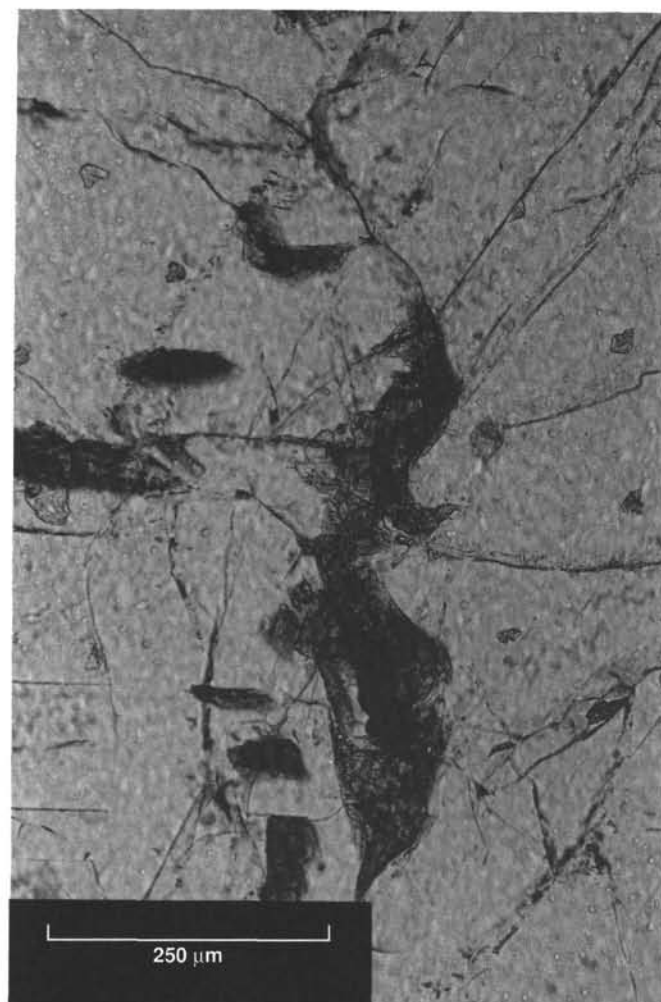


Figure 23. Pocket of the trapped residual liquid in an anorthositic crystal clot in Sample 140-504B-200R-3, 59–63 cm.

form euhedral overgrowths on a rounded core or the oscillations may follow the outline of a rounded and corroded core. The mantle may also contain glass, plagioclase, spinel, olivine, or augite inclusions. The type of zoning in the core appears to be independent of that in the mantle and rim, so there are numerous combinations of zoning patterns possible. The dominant zoning pattern is a uniform, euhedral core surrounded by a euhedral mantle with two to four fine oscillations surrounded by a normally zoned rim. Three common variations of this pattern are cores with glass inclusions, anhedral rounded cores, and cores with minor undulatory or oscillatory zoning.

The core usually represents the bulk of a phenocryst and probably formed in the magma chamber prior to emplacement. The compositional zoning, size, and inclusions in the core may record conditions in the magma chamber prior to the emplacement of a dike. The simplest form of zoning observed would be a compositionally uniform, euhedral core free of inclusions surrounded by a uniformly zoned mantle and rim. This may be interpreted as a crystal initially grown in a stagnant magma chamber (core), that continued to grow during magma transport and emplacement (mantle), and during final solidification in situ in the crust (rim). This simple zoning, however, is the exception for plagioclase phenocrysts in the Leg 140 diabase dikes. Complex zoning suggests that plagioclase growth responded to a variety of changing conditions within the magma chamber, and during subsequent transport, emplacement, and solidification. Fine-scale oscillations can be interpreted as crystal growth under rapidly

changing conditions of temperature, pressure, or magma chemistry. The more uniform phenocryst cores suggest that they formed in an environment without fluctuations of the magnitude seen by the phenocryst mantle. Zoning is observed in crossed polarized light if variations in composition are more than about 1 mol% anorthite, and in these magmas a 1 mol% change in anorthite corresponds to the fractional crystallization of about 8% plagioclase of An_{80} , and a cooling of the magma by about 15°C (based on the empirical crystallization model of Nielsen (1990)). Oscillations observed in the Leg 140 phenocrysts typically represent >5 mol% anorthite variations, suggesting that oscillatory zones are unlikely to be produced by simple magma differentiation. Possible causes for these oscillations include (1) convective overturn within the magma carrying crystals repeatedly from cooler to hotter parts of the chamber, (2) mixing of a new hot magma with a magma already containing plagioclase phenocrysts, (3) rapid fluctuations of volatile content due to the introduction of a new wet magma or by assimilation of hydrated crust, or (4) episodic periods of movement and stagnation as the magma is transported through the crust.

Grain-size Variations

Downhole variations in the maximum grain size of plagioclase and magnetite in groundmass have been examined. Measurement of the grain size is carried out as follows: Twelve domains with an area

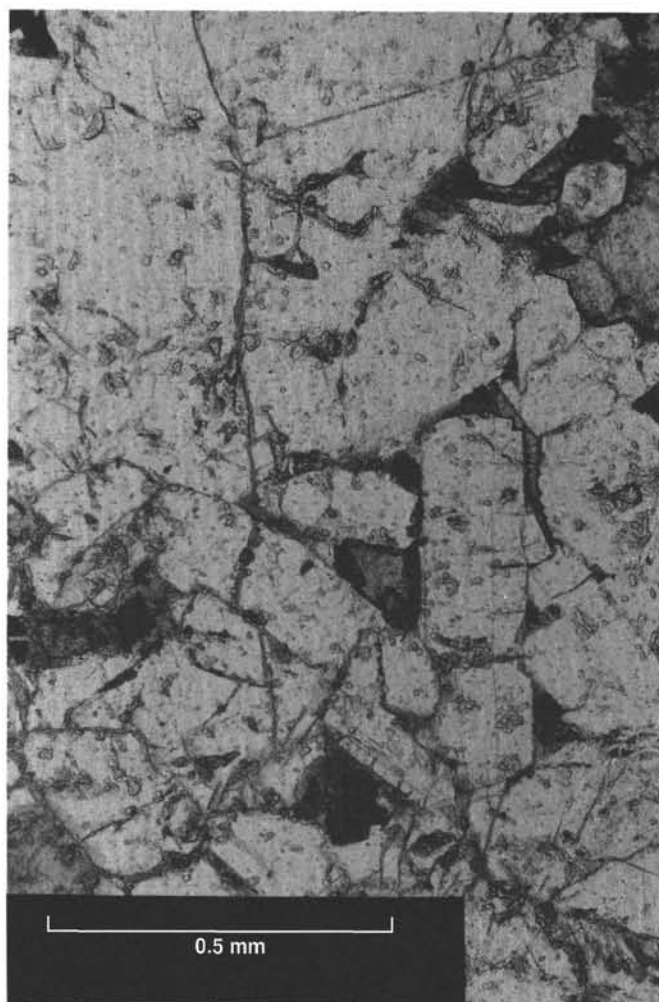


Figure 24. Pockets of the trapped liquid in a cumulate-textured gabbrioc crystal clots in Sample 140-504B-185R-1, 15–19 cm.

of approximately 23.3 mm^2 were selected from each thin section. Selection of domains was made so as not to overlap each other. In samples that are highly porphyritic and in which the number of crystals within an individual domain is small, domains were chosen to minimize the area occupied by phenocrysts. The length and width of the largest crystals of plagioclase and magnetite were measured, and the largest and smallest values among the 12 domain measurements were excluded. Averages of the remaining 10 values are reported as the average maximum grain size. The length and width data were used to calculate the average area per grain, which is reported as the diameter of a circle with the equivalent area (E.Q.D.). Very fine-grained or aphanitic samples taken from the chilled margins of dikes were not measured. Grain-size measurements are listed in Appendix E.

Although there is some scatter in the data, the length and E.Q.D. of plagioclase are positively correlated with those of magnetite (Fig. 26). Downhole variations in the grain size of plagioclase and magnetite from the present leg, together with Legs 83 and 111, are shown in Figure 27. The maximum length of plagioclase is highly variable but shows a gradual decrease from 900 mbsf down to 1400 mbsf. Data points are lacking between 1400 mbsf and 1580 mbsf because thin sections were not available. Below 1570 mbsf the data points are scattered about a crude zigzag pattern (Fig. 28). The length of plagioclase appears to decrease from 1.3 mm to 0.9 mm with depth from 1570 mbsf to 1650 mbsf where it jumps to 1.6 mm and then

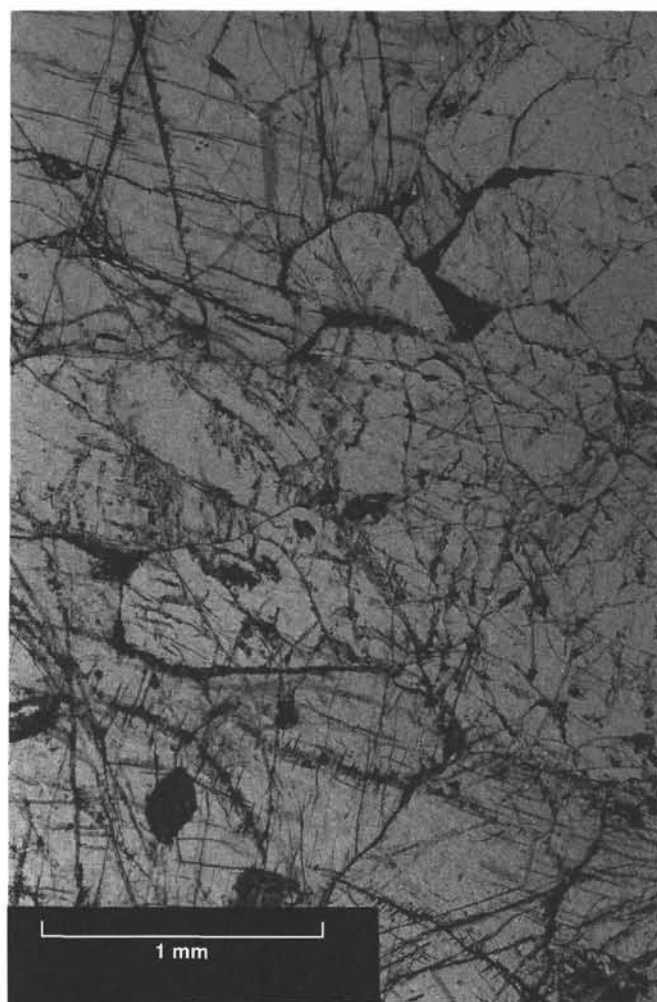


Figure 25. Gabbrioc clots in Sample 140-504B-186R-1, 13–14 cm.

decreases again downhole. The decrease in plagioclase length from 1709 mbsf to 1718 mbsf occurs within a single lithologic unit (232), and hence, it probably represents a variation in grain size within a single dike. The overall zigzag pattern, however, includes many dikes within each cycle. Major changes in plagioclase length are observed between Units 211–213, 213–218, 230–232, 232–233, 235–236, 244–245, 247–252, 252–254, and 254–258. The maximum grain size of magnetite does not show as clear a zigzag pattern as does that of plagioclase, but with one exception (between 230 and 232), the major changes in plagioclase length correlate with those of magnetite.

The size of minerals crystallizing in a dike is a function of the chemical composition of the melt, the cooling rates, and the initial magma–host rock temperature contrast (ΔT). All of the samples studied have similar basaltic compositions and the same mineral assemblage, and the growth rate of plagioclase is reported to be independent of melt compositions in basaltic to andesitic magmas (Cashman, 1990). ΔT is a kinematic driving force of crystallization and affects the growth rate and textures of rocks. At extreme ΔT values, such as occur when a magma near or above the liquidus temperature is emplaced in rocks far below the solidus temperature, the melt will be quenched and crystal growth greatly inhibited. Chilled margins of dikes are examples. In the central part of dikes, however, ΔT is thought to remain small because cooling by conduction and the latent heat of crystallization cancel each other out (Brandeis and Jaupart, 1987). Although the estimated growth rates of plagioclase decrease from the margins to the centers of dikes, grain

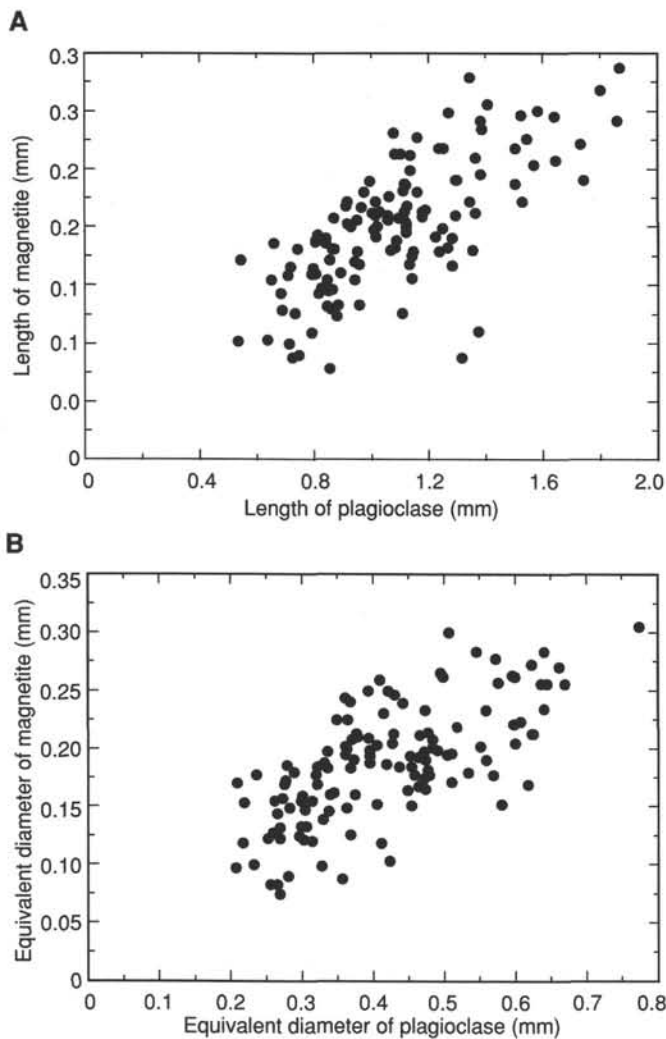


Figure 26. **A.** Maximum length of groundmass plagioclase vs. maximum length of groundmass magnetite from diabase recovered on Leg 140. **B.** Equivalent diameter of groundmass plagioclase vs. equivalent diameter of groundmass magnetite from diabase recovered on Leg 140.

sizes in relatively narrow dikes generally increase toward the center, because grain size is determined by the product of growth rate and time. Ikeda (1977) has shown that peak grain size within individual dikes is well correlated with the calculated cooling rate at the center of the dike. Cooling rates are governed by the width of dikes and the temperature difference between the melt and the surrounding rocks. Most estimates of oceanic dike widths are in the range of 0.5–1 m (Becker, Sakai, et al., 1988), and therefore, the cooling rate at the center of dikes should differ by less than an order of magnitude (Ikeda, 1977). The temperature of the wall rocks at a spreading axis will increase downward, and therefore, the cooling rate should decrease downward and the grain size in the coarsest sample from each unit should increase downward. The inter-unit variations observed, however, exhibit steady decreases followed by abrupt jumps, yielding a zigzag pattern which cannot be explained by simple cooling models. These grain-size variations appear to represent several cooling units, each composed of several dikes that were emplaced during short periods of intermittent crustal extension, forming single cooling units. Such multiple dikes are common in the sheeted dikes of ophiolites and continental flood basalt provinces which were formed under extensional regional stress fields. In a multiple dike, new batches of

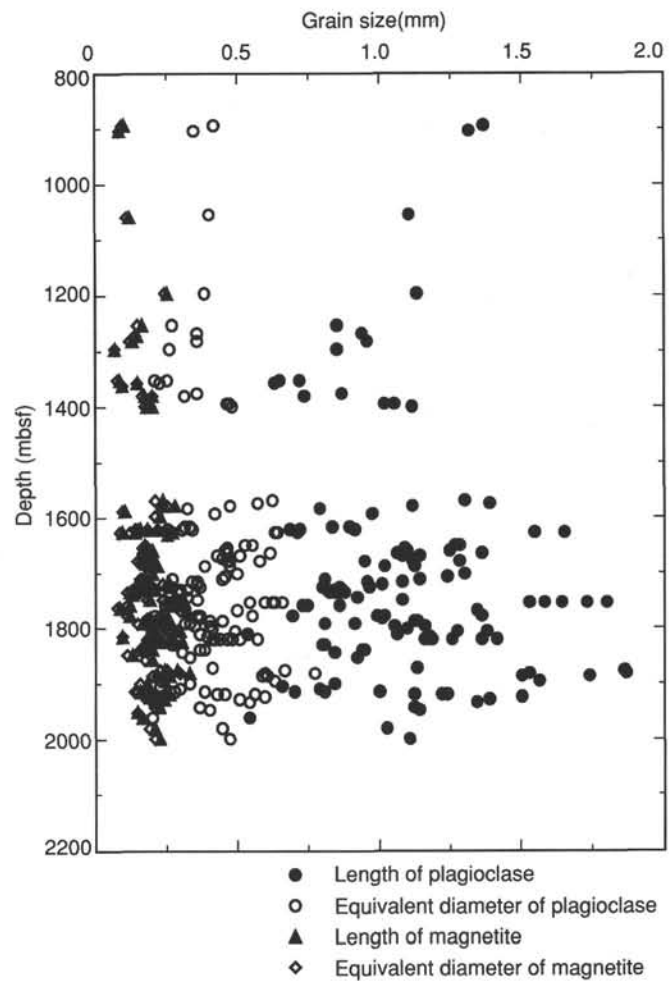


Figure 27. Downhole variation in the average maximum length of groundmass plagioclase and groundmass magnetite in Hole 504B from 800 to 2000 mbsf.

magma successively intrude previous dikes before they completely solidify. The later dikes are emplaced in rocks at or near the solidus temperature and the composite dike width progressively increases with time. This process has the effect of reducing the cooling rate of the later dikes, resulting in a coarsening toward the center of the multiple dike units. The inter-unit grain-size variations in Hole 504B may represent such a series of multiple dike units.

Historical volcanic activity and crustal movements in Iceland indicate that rifting events are episodic and associated with intermittent dike intrusions (Bjornsson et al., 1977; Sigurdsson and Sparks, 1978). Although there is no direct observation of volcanic eruptions and tectonic movements in mid-oceanic spreading axes, it is plausible that rifting in slow-to-moderate spreading oceanic ridges is also episodic and is associated with the successive intrusion of dikes during a short interval, followed by comparatively long magmatically quiescent periods (Pockalny et al., 1988; Scott and Stevenson, 1989). Thus, each cooling unit may represent a minimum amount of crustal extension during an individual rifting event. An estimated dip of 79° for the dikes yields a 10 m minimum for the width of the largest cooling unit proposed for the Leg 140 section. If we assume an average spreading rate of 7.2 cm/yr for the Cocos Ridge, the time interval for a 10 m rifting event is 140 years, which is comparable to the 100–150 yr intervals proposed for rifting events in Iceland (Bjornsson et al., 1977).

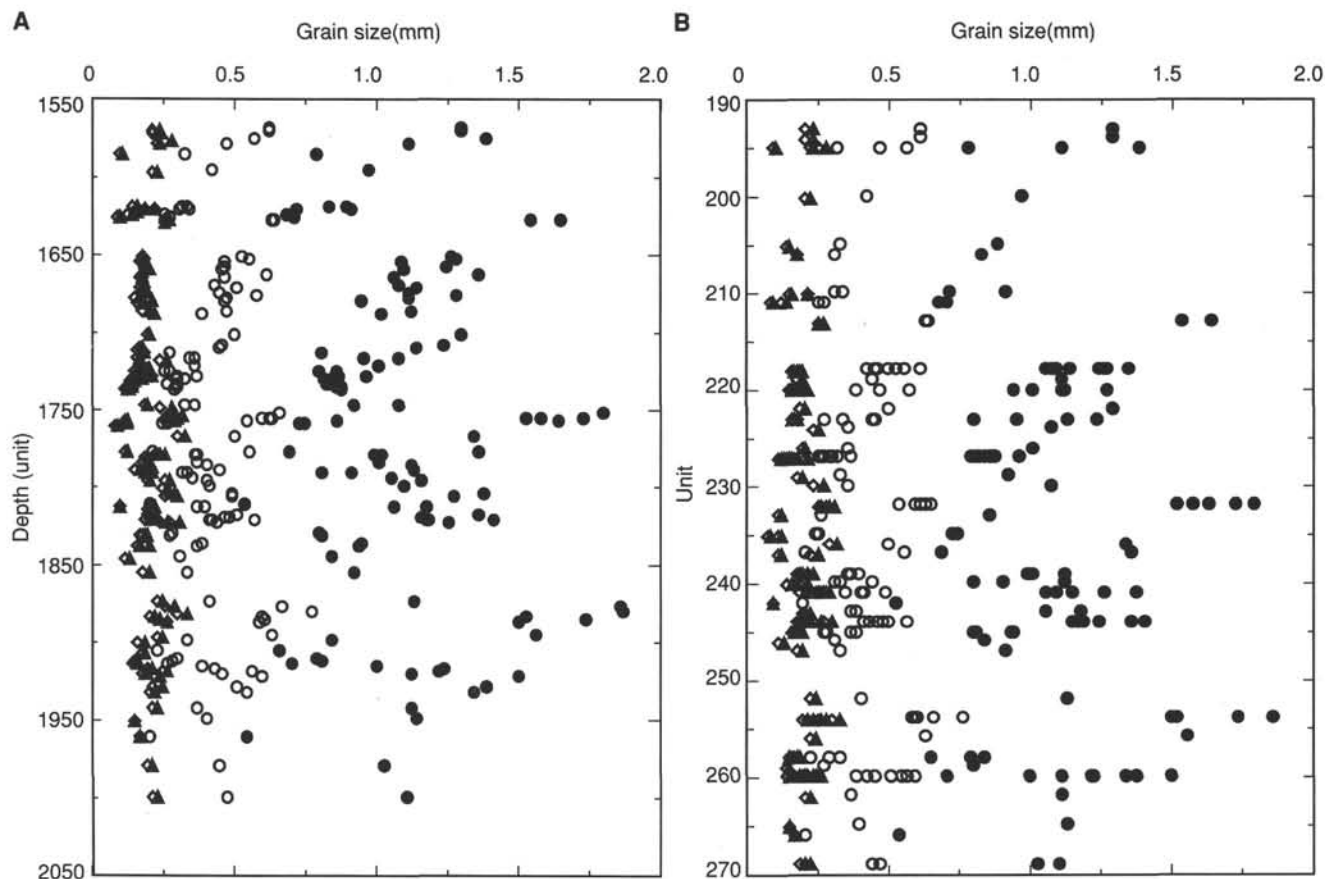


Figure 28. A. Downhole variation in the average maximum length of groundmass plagioclase and groundmass magnetite in Hole 504B from 1550 to 2000 mbsf. B. Downhole variation in the average maximum length of groundmass plagioclase and groundmass magnetite in Hole 504B for Units 190 to 270. Symbols as in Figure 27.

Cr-spinel Stability in Basalt and Diabase

The crystallization of spinel is strongly dependent on the chrome content of the coexisting magma (Hill and Roeder, 1974, Roeder and Reynolds, 1991) and it appears that there is a rough correlation between the occurrence of spinel in Leg 140 diabase dikes and the chrome content of these dikes as determined by shipboard X-ray fluorescence analysis (Fig. 29). Spinel was rarely found in diabase samples with less than 300 ppm Cr (3 of 23), but was found in the majority of samples with more than 300 ppm Cr (27 of 42). The 300 ppm dividing line between spinel-absent and spinel-phyric is equal to the experimentally determined saturation limit of Cr in basalts (Hill and Roeder, 1974).

Spinel is found in only two of the upper 13 units of Leg 140 diabase, and is absent in the 4 lithologic units from Leg 137 for which we have thin sections. These dikes with little or no spinel may represent a period of eruption from a chamber with more evolved Cr-depleted magma.

In the pillow lavas of Sites 504 (Natland et al., 1983) and 505 (Furuta and Tokuyama, 1983) spinel is most commonly found in the glassy rims and groundmass and is less abundant as inclusions in olivine and plagioclase. This contrasts with the Leg 140 diabase dikes where the most common mode of occurrence of spinel is as inclusions in plagioclase. This textural difference may be the result of (1) separate, unrelated batches of magma for the dikes and the pillow lavas, (2) a reaction relationship between spinel and the residual liquid during crystallization of the dikes, or (3) the crystallization of spinels in the pillow lavas at low pressure due to changing physical and chemical conditions in the magma. The bulk rock chemistry of the

pillow basalts (Natland et al., 1983) is the same as that of the dikes (see "Geochemistry" section, this chapter), and therefore, it is unlikely that whole-rock composition alone can be responsible for the difference in spinel occurrence. Spinels in contact with the groundmass of the diabase sometimes show symplectic resorption textures, but more commonly they have iron-rich rims grading to magnetite, suggesting that although the spinel rims have reequilibrated with the cooling magma, the crystals were not completely resorbed. Decompression melting of chrome-rich augite during its ascent from the magma chamber to the surface could increase the Cr content of the residual liquid while maintaining a constant bulk rock composition. Natland et al. (1983) suggest that olivine grows at the expense of augite in the pillow basalts, and rounded, resorbed augites are observed in the pillow basalts and in some diabase dikes. Resorption of 1% augite (about 1 wt% Cr_2O_3) could result in the crystallization of about 0.03 modal% spinel (about 33 wt% Cr_2O_3). The crystallization of 0.1% spinel in the pillow basalts (a typical value) would require the dissolution of 3% chrome-rich augite (a typical Cr-augite phenocryst abundance in the dikes).

Crystallization Sequence

In general, the inferred crystallization sequence in the Leg 140 diabase is plagioclase as the first mineral to crystallize followed by a brief period of plagioclase and spinel crystallization. In some units the next mineral to crystallize is olivine but in others it is augite. The crystallization of augite usually coincides with the disappearance of spinel because spinel stability is strongly dependent on the abundance of Cr in the host liquid and, as a result of a high $D_{\text{augite/liquid}}^{\text{Cr}}$, augite

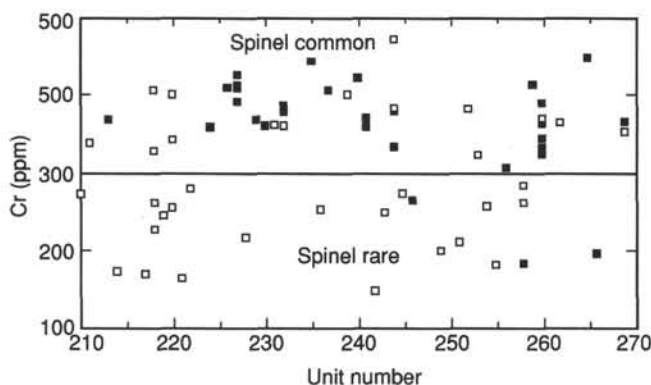


Figure 29. Cr content of diabase dikes analyzed by X-ray fluorescence analysis on Leg 140 plotted against lithologic unit number. Open symbols, spinel absent; solid samples, spinel present.

depletes the liquid in Cr and thus inhibits spinel crystallization. Spinel was found included in augite in only one unit of the Leg 140 diabase.

Inclusions within phenocrysts and coexisting minerals within clots suggest that several crystallization sequences may exist within the diabase. Throughout the sequence olivine phenocrysts are present but the timing of their appearance is uncertain because there are few instances where they are included in other phenocrysts or have inclusions of plagioclase or augite. Where such relationships are observed they are ambiguous. In Unit 221 olivine is enclosed by plagioclase but in Units 222 and 223 olivine encloses laths of plagioclase and in Unit 224 olivine contains a single spinel inclusion. In these upper units spinel is also enclosed in plagioclase but most frequently in their rims rather than the cores. These relationships suggest that plagioclase was usually the first mineral to crystallize, followed by spinel and olivine. The inclusion of plagioclase laths in augite phenocryst indicates that the cores of augite phenocrysts crystallized simultaneously with plagioclase but the relationship of augite and olivine is not constrained. The following crystallization order for Units 211 to 224 is proposed:

plagioclase → plagioclase + spinel → plagioclase + spinel + olivine → plagioclase + olivine + augite (± spinel).

In Units 226 and 227 spinel continues to crystallize even after the onset of pyroxene crystallization and is found in augite oikocrysts, and in groundmass plagioclase. In some of the lower units recovered during Leg 140 spinel is enclosed in the cores of plagioclase phenocrysts and plagioclase grains in the center of glomerocrysts, and is not found in augite phenocrysts or oikocrysts. In these units spinel probably precedes plagioclase and ceases to crystallize with the onset of augite crystallization.

The crystallization order shown above is consistent with that determined in melting experiments on five of seven basalts from the pillow lava sequence collected on Leg 69 (Autio and Rhodes, 1983). The crystallization sequence calculated using the empirical computer crystallization model of Nielsen (1990) and the bulk chemical composition (determined by shipboard XRF) of a depleted unit (218) is consistent with the melting experiments of Autio and Rhodes (1983) and the crystallization order shown above. The computer calculations give the following crystallization order:

plagioclase (1216°C) → plagioclase + olivine (1208°C) → plagioclase + olivine + augite (1193°C), for Unit 218.

The crystallization of the trace mineral spinel is not well constrained by the experimental data used in the computer model and therefore does not appear in the crystallization sequence.

Most mid-ocean ridge basalts have olivine as the first mineral to crystallize and reports of plagioclase crystallizing first in experiments have often been attributed to the use of a starting composition containing accumulated plagioclase and/or the incomplete melting of the starting material. The Hole 504B basalts and diabases have lower abundances of Na₂O and K₂O, and higher Al₂O₃ and CaO than many mid-ocean ridge basalts. This combination of low total alkalis and high Al₂O₃ and CaO favors the formation of anorthite-rich plagioclase with a relatively high crystallization temperature. Hole 504B basalts are known for their anomalous anorthitic feldspar, up to An₉₄ (Natland et al., 1983) which is compatible with the basalt chemistry and with the observed crystallization sequence (plagioclase before olivine).

In one of the basalts experimentally melted and recrystallized by Autio and Rhodes (1983) olivine crystallized before plagioclase. A few samples of diabase from Leg 140 have calculated crystallization sequences in which olivine precedes plagioclase:

olivine (1194°C) → olivine + plagioclase (1192°C) → olivine + plagioclase + augite (1183°C), calculated for Unit 214.

The 2°C interval separating the appearance of olivine and plagioclase is not significant, and this sample may have been derived from a magma with chemistry similar to Unit 218 by plagioclase and olivine crystallization. The lowest units of the Leg 140 diabase dikes, however, appear to follow this crystallization sequence as they have numerous olivine phenocrysts with spinel inclusions, but the olivine is free of plagioclase inclusions.

The order of crystallization of the groundmass is generally determined by textural relationships. The first phases to crystallize are the subhedral zoned or unzoned microphenocrysts of plagioclase and the subhedral inclusion-free prisms of augite. These are followed by more acicular plagioclase, subophitic to ophitic augite, and magnetite. Skeletal and branching plagioclase crystals formed next probably coprecipitating with the surrounding poikilitic augite. Finally, interstitial fine-grained plagioclase-augite aggregates, granophyric quartz-albite patches, apatite, and other trace accessory minerals crystallized from pockets of enriched melt.

Igneous Summary

The 378.9 m drilled at Hole 504B during Leg 140 appear to represent the lower part of a sheeted dike complex. The units recovered contained significantly less chilled margin material and were in general coarser grained than those recovered in the upper part of the complex on Legs 83 and 111 (Anderson, Honnorez, Becker, et al., 1985; Becker, Sakai, et al., 1988). Grain-size variations within the section suggest that multiple dike units may have formed during brief episodes of magma injection separated by longer periods of repose. The order of crystallization recorded in the phenocryst assemblage of most samples indicates that plagioclase was the first phase to crystallize followed by spinel, olivine, and augite. The crystallization of augite depleted the magma in Cr and, as a result, spinel ceased to crystallize shortly after augite became a liquidus phase. Zoning patterns in plagioclase record a three-part crystallization history that may represent initial crystallization in a magma chamber, followed by continued crystallization during magma transport and emplacement, followed by final crystallization in situ in the lower crust. A variety of plagioclase zoning patterns are present within individual thin sections indicating that the magmas from which these basalts formed underwent a complex mixing process as a result of convection within a lower crustal magma chamber and/or transport through the crust. A number of syngenetic and xenolithic crystal clots are present in the diabase recovered on Leg 140 and may provide insight into magmatic processes that occurred at lower levels in the crust. Xenolithic clots are particularly rare in basalt and diabase recovered from higher levels of the oceanic crust. Interstitial patches of quartz-albite-pyroxene-magnetite in some of the samples recovered on Leg 140

may represent crystallized pockets of trondhjemite liquid produced by in-situ crystal fractionation of the host diabase.

ALTERATION AND METAMORPHISM

Introduction

Alteration of basement down to 1621.5 mbsf in Hole 504B has already been documented in detail based on the combined efforts of previous drilling legs (Alt et al., 1986; Alt, Anderson, Bonnell, and Muehlenbachs, 1989; Shipboard Scientific Party, 1992). The core can be divided into three zones (Fig. 30): the upper 320 m of the volcanic section affected by "seafloor weathering" at low temperatures (0°–100°C); the lower portion of the volcanic section affected by low temperature (<150°C), reducing alteration; and the transition zone and dikes, which were hydrothermally altered under greenschist and superimposed zeolite conditions. A sequence of hydrothermal alteration in the transition zone and dikes was established on the basis of crosscutting vein relationships. This sequence can be briefly summarized in three basic stages. First, chlorite and actinolite followed by quartz and epidote formed in veins and greenschist minerals formed in the rocks during axial hydrothermal alteration at temperatures of 250°–380°C. Later, as the crust moved off-axis into a recharge zone, penetration of seawater into still-warm rocks resulted in precipitation of anhydrite in cracks and local replacement of plagioclase by anhydrite. Finally, zeolites formed in fractures and rocks during later off-axis alteration at lower temperatures (less than about 150°C).

Some variations in proportions of secondary minerals with depth in the dike section were recognized on Leg 111. The abundance of actinolite replacing clinopyroxene generally increases with depth in the dikes, whereas calcic plagioclase is less extensively altered to albite as depth increases. This increase in actinolite and decrease in alteration of plagioclase was interpreted to reflect higher temperatures at depth, with conditions approaching the upper greenschist facies, where more calcic plagioclase and actinolite are stable.

We report here on the alteration and metamorphism observed in rocks recovered from Hole 504B during Leg 140. Also included in this report are updated and slightly revised descriptions of cores taken from Hole 504B during Leg 137, using the new core description logs devised during Leg 140 as well as new observations from additional shipboard thin sections of the Leg 137 cores taken during Leg 140.

Rocks recovered during Leg 140 exhibit a pervasive slight "background" alteration, with locally more extensively altered zones around veins and in irregular patches, up to several centimeters across. This alteration is described below based on observations of the core and study of approximately 140 thin sections. Detailed documentation of alteration effects and vein abundances and types are given in the "Alteration Log" (Appendix F) and "Vein Log" (Appendix G, back pocket), and thin-section modal data on alteration phases is given in Appendix H.

Phyllosilicate minerals are important secondary phases in the Leg 140 rocks, particularly as pseudomorphs of olivine, and were divided into different types on the basis of previous work (Alt, Anderson, and Bonnell, 1985; Alt, Anderson, Bonnell, and Muehlenbachs, 1989). Electron microprobe and X-ray diffraction analyses of phyllosilicate minerals in altered diabases sampled from Hole 504B during previous legs can be divided into the following types: chlorite, mixed-layer chlorite-smectite, smectite, talc, and talc-smectite. Besides these phyllosilicate minerals identified from Hole 504B on previous legs, serpentine was also observed in rocks sampled during Leg 140. Optical properties used to distinguish these minerals are given in Table 3. Chlorites in rocks from Leg 140 include the anomalous blue to gray chlorite identified on Legs 83 and 111, but more commonly range from anomalous blue to purple and brown interference colors, suggesting a more magnesium-rich composition. Minerals that were identified as talc on Leg 140 may also include some colorless Mg-smectite.

Pervasive Background Alteration

The background alteration is generally characterized by 10%–20% replacement of primary minerals by secondary phases (Appendix H and Fig. 31). The higher modal percentages of secondary minerals in Figure 31 generally occur in locally more extensively altered patches and alteration halos around veins (see "Alteration Patches" and "Veins and Associated Alteration Halos" this section).

Olivine

Olivine occurs in the rocks as completely or, in some cases, partly altered phenocrysts (1–5 mm diameter), or as totally altered grains in the groundmass (<1 mm diameter). Replacement minerals after olivine include chlorite, talc, talc-smectite, serpentine, smectite, actinolite, mixed-layer chlorite-smectite, magnetite, hematite, pyrite, chalcocopyrite, and quartz. Based on petrographic observations, these alteration minerals were divided into seven commonly occurring associations replacing olivine:

talc + magnetite ± pyrite ± chalcocopyrite;
 chlorite ± magnetite ± pyrite ± chalcocopyrite;
 chlorite + actinolite ± pyrite ± chalcocopyrite;
 mixed-layer chlorite-smectite ± magnetite ± pyrite ± chalcocopyrite;
 serpentine + hematite;
 serpentine + magnetite ± pyrite ± chalcocopyrite;
 smectite ± hematite or magnetite.

Quartz may occur together with all of the above mineral associations. Anhydrite is also present in olivine pseudomorphs in a few samples (e.g., 140-504B-227R-1, 83–85 cm). In many samples, olivine grains are completely replaced by single phyllosilicate minerals, including chlorite, mixed-layer chlorite-smectite, talc, or serpentine (Appendix I). Significant variations in replacement assemblages were observed on the thin-section scale, however. The altered olivine phenocrysts are generally replaced by one or more phyllosilicate minerals, whereas the groundmass olivine is generally replaced by a single phyllosilicate phase.

Replacement textures in olivines also commonly show a more or less systematic mineralogical zonation from rim to core. The spatial distribution or zonation from rim to core of various replacement minerals within individual olivine grains is documented in Appendix I and Figures 32 through 35. Talc commonly replaces the rim of olivine grains and forms an interconnected network, enclosing "islands" of other minerals, which include talc, talc-smectite, chlorite, smectite, or serpentine. Accessory oxide and sulfide minerals exhibit characteristic associations with the phyllosilicates. Fine-grained magnetite (<1 to about 5 µm) is always associated with talc, and pyrite is generally present with talc as 1–350 µm grains, typically intergrown with the magnetite. Patches of serpentine and smectite enclosed by talc rims sometimes contain small magnetite grains, but more commonly contain hematite as 1–10 µm grains or spherulitic aggregates. The hematite grains in some cases enclose magnetite, suggesting that the hematite may be derived from oxidation of magnetite. In some cases, at the boundary between talc and smectite or serpentine, hematite encloses both magnetite and pyrite. It is not clear why one oxide dominates over the other, although in the replacement assemblages that contain significant number of pyrite and/or chalcocopyrite grains, magnetite is the dominant oxide, whereas when sulfides are absent, hematite predominates. One possible explanation for the ubiquitous association of magnetite with sulfide minerals may be that the sulfides create a localized reducing environment and act as a buffer preventing the oxidation of associated magnetite.

Although most olivine phenocrysts have been totally replaced by secondary minerals, some olivine relics were identified in Cores 140-504B-197R, -199R, -200R, -208R, -210R, -214R, and -225R through -227R (Appendix I). The olivine relics comprise 5%–95%

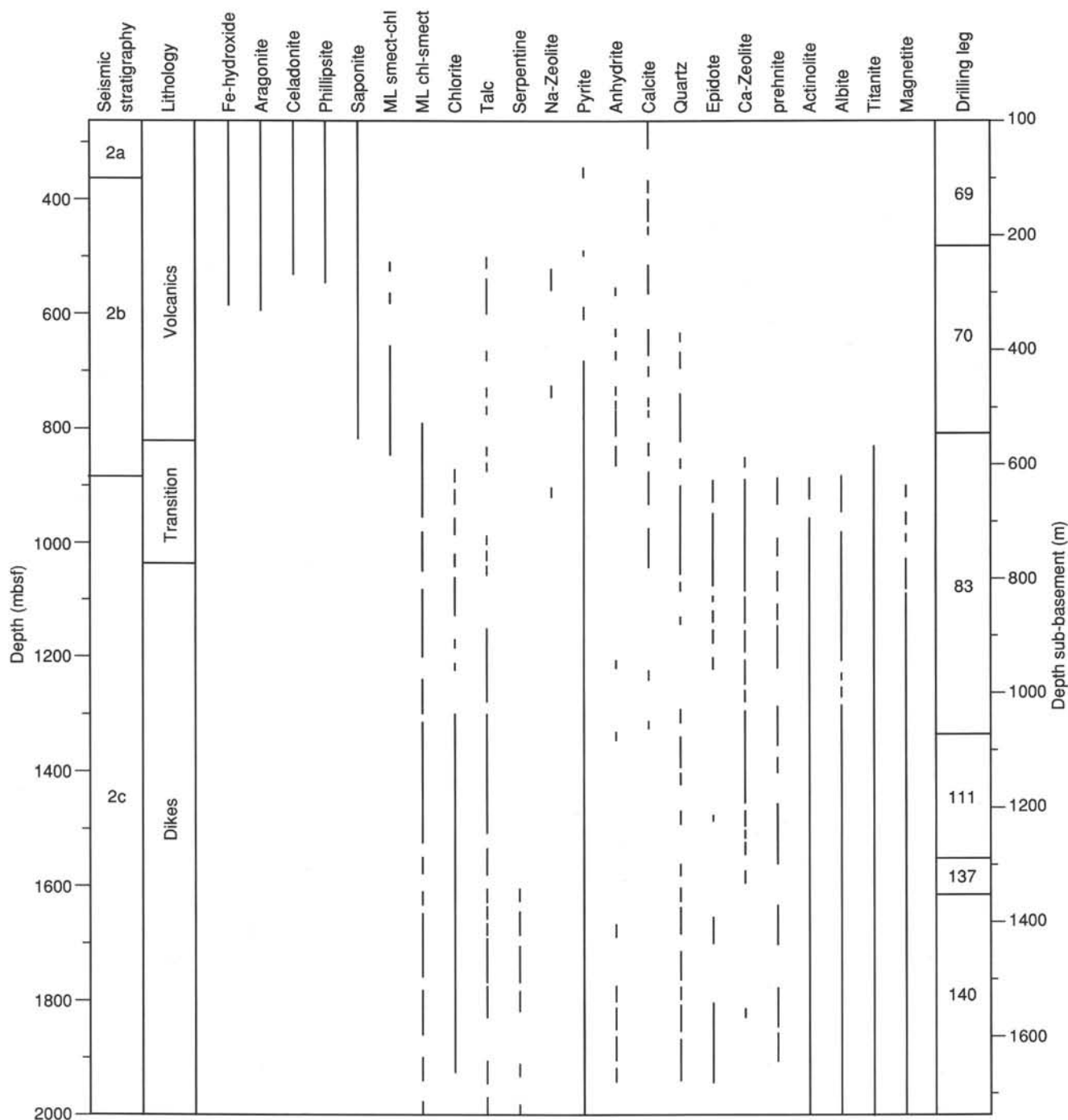


Figure 30. Distribution of secondary minerals with depth in Hole 504B (modified from Alt, Anderson, and Bonnell, 1985; Alt, Anderson, Bonnell, and Muehlenbachs, 1989). Lithostratigraphy, seismic stratigraphy, and drilling legs also shown (Shipboard Scientific Parties, 1985, 1988, 1991). ML smect-chl, mixed-layer smectite-chlorite; ML chl-smect, mixed-layer chlorite-smectite; Na-zeolite includes analcite, natrolite, stilbite, and epistilbite; Ca-zeolite includes laumontite, heulandite, and scolecite.

(averaging about 50%) of the volume of olivine phenocrysts originally present in these samples. These relict grains have 10–100 μm wide rims consisting of talc + magnetite \pm pyrite surrounding unaltered olivine cores, which may be cut by small (1–10 μm) veinlets of talc + magnetite \pm pyrite. In several samples, serpentine and/or smectite occur between the talc rim and the central olivine relics.

Where the rims of olivine grains are replaced by chlorite, the following alteration zonation toward the center may be present: talc then serpentine; talc then mixed layer chlorite-smectite; chlorite +

quartz; mixed layer chlorite-smectite \pm quartz or \pm serpentine, or quartz \pm serpentine (Appendix I). Less common zonations are (from rim to core) mixed-layer chlorite-smectite to serpentine, and actinolite to chlorite. In some cases phyllosilicate minerals are intergrown with quartz. The quartz occurs as 50–100 μm equant grains, commonly cloudy or with diffuse or irregular boundaries with the phyllosilicate minerals, or as elongate, curved grains, interleaved with chlorite. Such textures suggest that in many cases the quartz may be a replacement product of the phyllosilicate minerals.

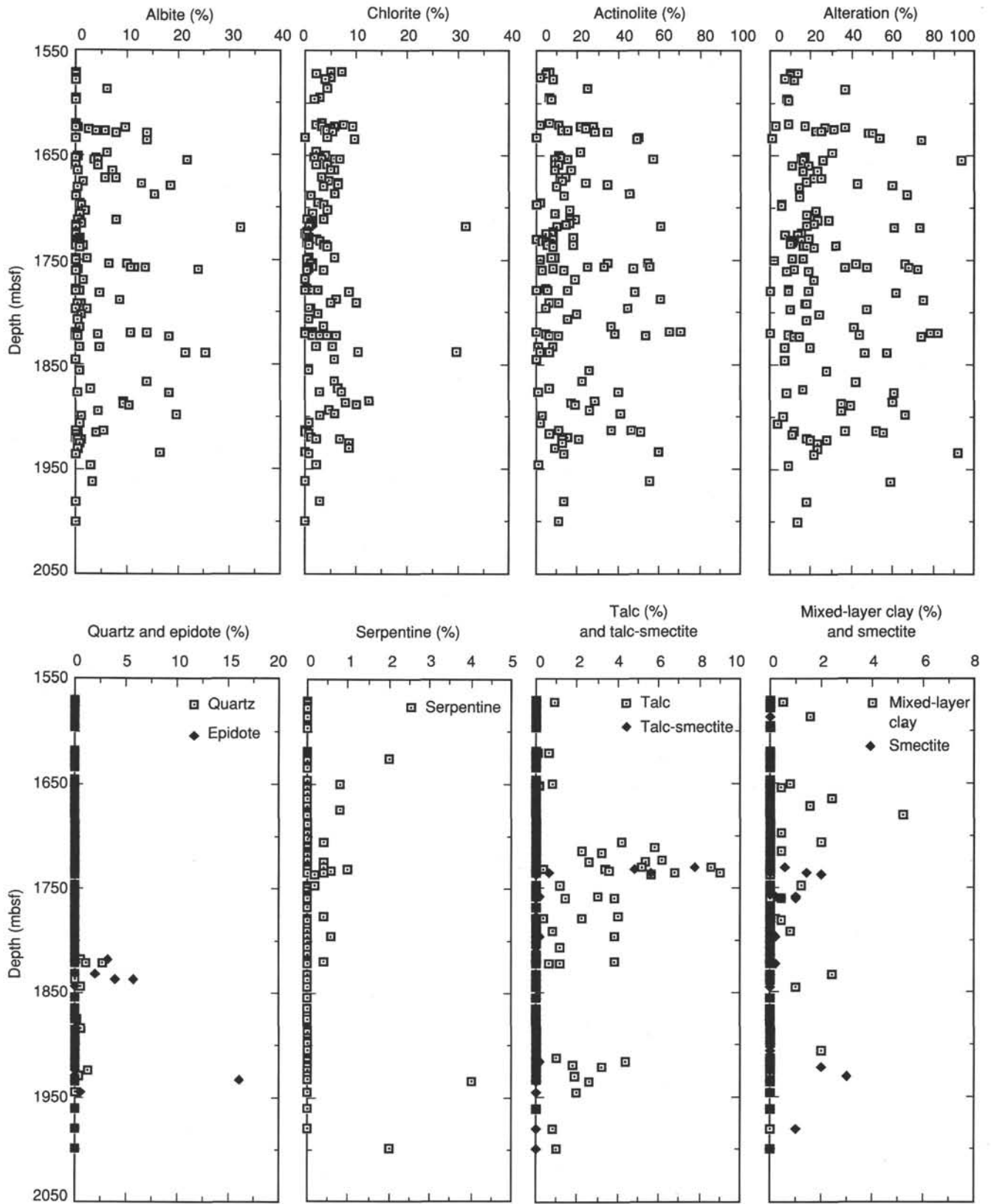


Figure 31. Modal mineralogy of secondary phases in Legs 137 and 140 core. Data from Appendix H.

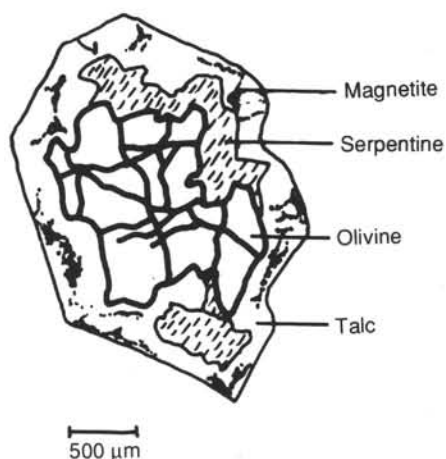


Figure 32. Replacement zonation in partly altered olivine. From rim to core: talc, serpentine + magnetite, relict olivine. Sample 140-504B-179R-2, 33–38 cm.

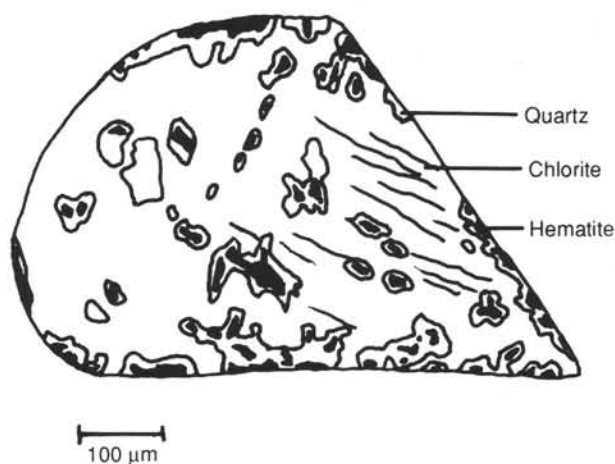


Figure 34. Replacement of olivine by chlorite + quartz + hematite, Sample 140-504B-221R-1, 0–4 cm.

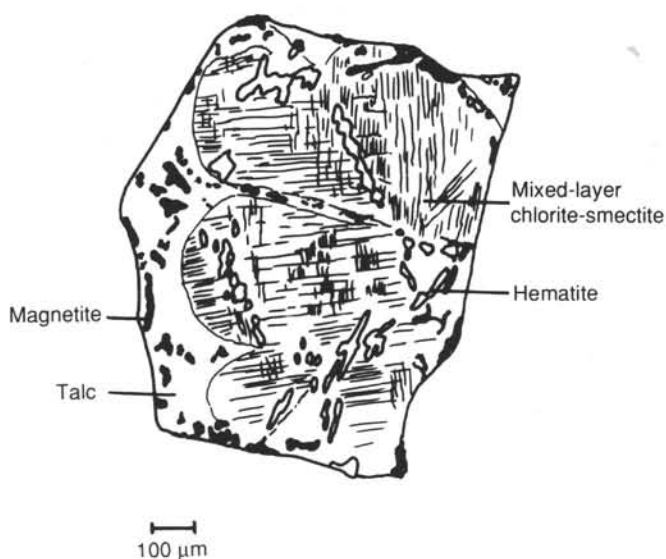


Figure 33. Replacement of olivine by discontinuous rim of talc + magnetite, and mixed-layer chlorite-smectite + hematite. Sample 140-504B-205R-1, 95–97 cm.

Although replacement minerals in some olivine grains form well-developed concentric zones consisting of different phyllosilicate minerals, in most olivine this zoning is irregular and replacement minerals occur in small domains within a single grain. Many of the above described mineral associations coexist within individual thin sections. Small grains in the matrix are always pervasively altered, whereas phenocrysts may be only partially altered. This suggests that the size of olivine grains may affect the extent of their alteration, with the larger grains not always completely reacting. The overall extent of alteration in the rocks however, is often independent of the grain size.

The replacement of olivine by serpentine involves the breakdown of olivine to serpentine + magnetite in the presence of fluid. At the initial stage of serpentinization magnetite grains are randomly dispersed within the serpentinized olivine, and commonly occur in olivine fractures (Fig.

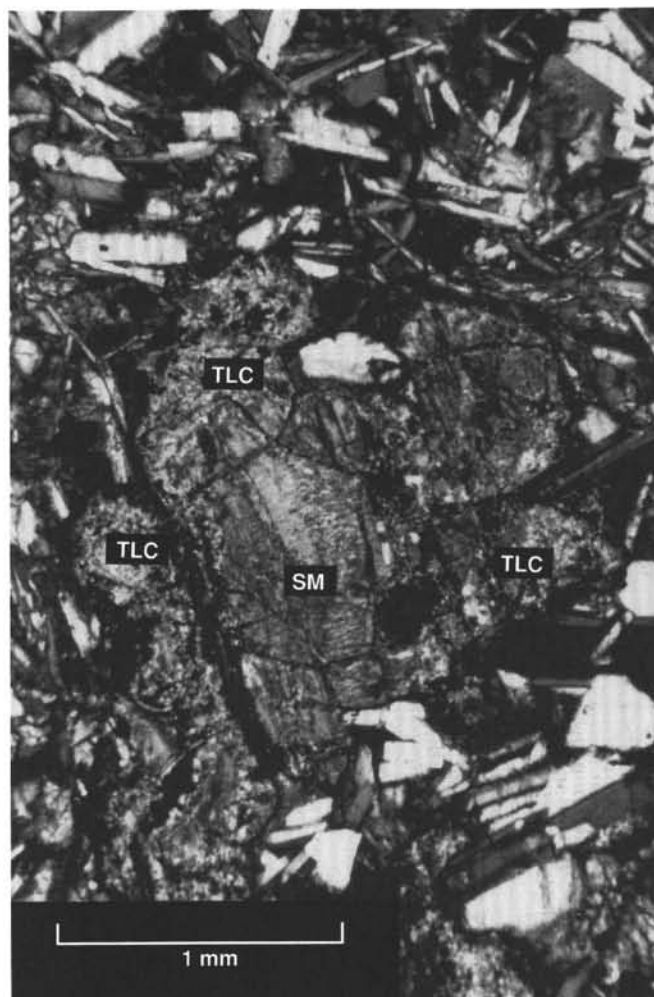


Figure 35. Photomicrograph of replacement zonation in altered olivine. Rim, talc (TLC) + magnetite; core, smectite (SM). Sample 140-504B-198R-1, 21–25 cm.



Figure 36. Photomicrograph of serpentinized olivine with fine-grained magnetite. Plane polarized light. Sample 137-504B-181M-2, 40–44 cm.



Figure 37. Photomicrograph of hourglass texture in serpentinized olivine. Sample 140-504B-205R-1, 87–89 cm.

Table 3. Optical classification of phyllosilicate minerals rocks from Legs 137 and 140.

Mineral	Color in plane-polarized light	Color under crossed nicols
Chlorite	Pleochroic green to pale yellow or colorless	Anomalous blue-gray to blue to purple or brown
Mixed-layer chlorite-smectite	Pleochroic green to pale yellow	First-order gray to yellow, with "anomalous" green color
Smectite	Yellowish to olive brown	To upper second order
Talc	Colorless	Third order
Serpentine	Not pleochroic, colorless to slightly yellowish or pale green	First-order gray to yellow

36). With the subsequent recrystallization of serpentine however, the secondary magnetite recrystallizes, it becomes coarser, and migrates toward the grain boundaries. The fine-grained magnetite in some serpentinized olivine forms a discontinuous band parallel to the olivine grain boundaries, suggesting recrystallization after initial formation. Recrystallization of serpentine is apparent from the partial replacement of lizardite by interpenetrating antigorite (Wicks and Whittaker, 1979), although some relict pseudomorphic replacement texture such as hourglass (Fig. 37) and mesh textures are preserved in some serpentinized olivine. The absence of serpentine veins (such as serrate veins) in the olivine suggests the lack of shearing and deformation in the rocks during and after serpentinization.

Small (100–300 μm) patches of chlorite \pm actinolite and talc \pm actinolite occur in many samples, and these are commonly difficult

to distinguish from similarly sized pseudomorphs of olivine. In extensively altered patches containing abundant actinolite (see "Alteration Patches" below), olivine pseudomorphs are also difficult to distinguish. Replacement of olivine by actinolite must occur in these patches, because olivine replaced by chlorite can be traced in hand specimen up to the edge of the patch, where the visible olivine pseudomorphs disappear.

In order to determine if specific alteration types are controlled by bulk-rock chemistry, grain size, or by the abundance of phenocrysts, the alteration minerals replacing olivine were compared between various lithological units, using the igneous lithology log and the olivine alteration sheet (Appendix I). No apparent relationship between lithological units and the types of secondary minerals replacing olivine was found.

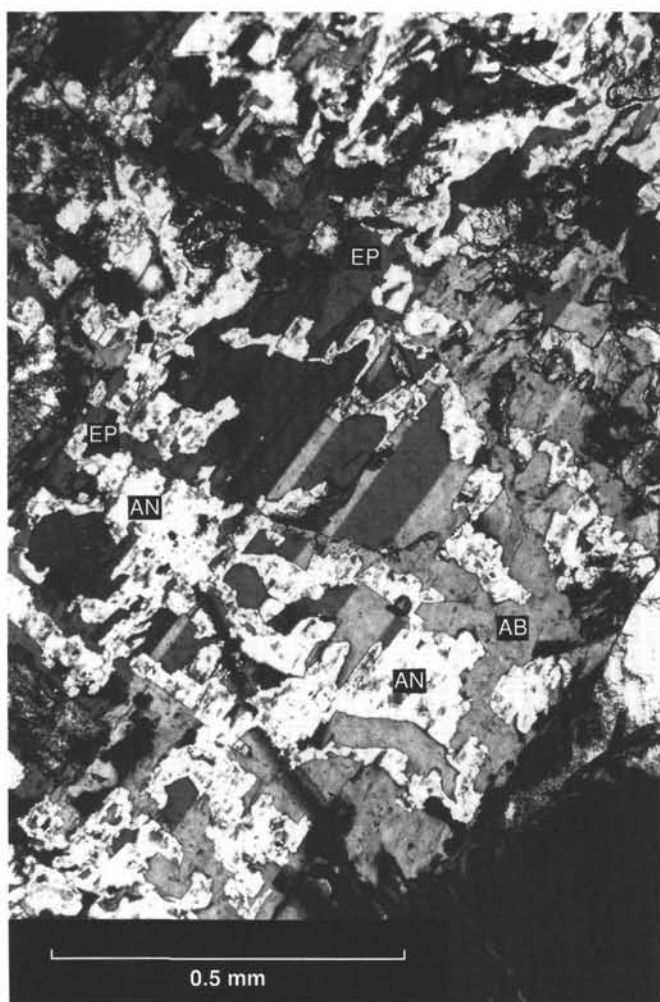


Figure 38. Photomicrograph of plagioclase phenocryst partly replaced by albite (AB), epidote (EP), and anhydrite (AN). Sample 140-504B-217R-1, 0–2 cm.

Pyrite and chalcopyrite are common in altered olivine, where they occur as 1–305 μm grains or aggregates. They are most common near olivine rims but also occur at the center of olivine pseudomorphs. Some pyrite and chalcopyrite inclusions were found in relict olivine grains as well (Sample 140-504B-200R-2, 26–31 cm). Inclusions of sulfide minerals also occur in silicate minerals and primary magnetite, as well as intergrown with secondary magnetite in olivine. It appears that during the alteration and breakdown of silicates (and magnetite) sulfide was locally mobilized and concentrated in phyllosilicate mineral pseudomorphs of olivine.

From 1570 to 1700 mbsf, olivine is generally replaced by chlorite or mixed-layer chlorite-smectite associations, along with trace amounts of serpentine and talc (Appendix I and Fig. 31). A zone of abundant talc replacing olivine occurs in Cores 140-504B-197R through -200R, at 1710–1740 mbsf (Fig. 31). Talc-rich olivine alteration also occurs sporadically at greater depths (1760, 1778, 1800, and 1919–1930 mbsf). Chlorite \pm quartz or mixed-layer chlorite-smectite \pm quartz associations are generally common olivine alteration products below 1790 mbsf (below Core 140-504B-209R), alternating with talc-rich and other olivine alteration mineral associations.

Clinopyroxene

Clinopyroxene in the rocks is partly to totally replaced by actinolite, with the extent of alteration to actinolite approximated by the abun-

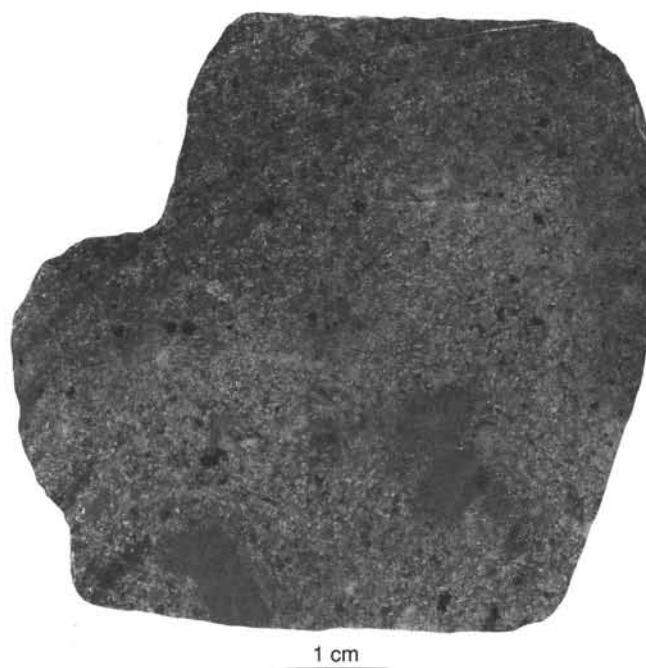


Figure 39. Extensively altered greenish patch (lighter gray) around 5-mm diameter actinolite-filled vugs (dark gray spots) in Sample 140-504B-189R-2, 10–16 cm. Patch grades into dark gray rock affected by pervasive slight background alteration.

dance of actinolite in Figure 31. Trace amounts of epidote also appear to replace clinopyroxene in one sample (140-504B-226R-1, 61–63 cm). Fine (<1–5 μm) magnetite grains occur in actinolite and at the boundary between unaltered clinopyroxene and actinolite, and small (<1–5 μm) grains of pyrite and chalcopyrite are also present in altered clinopyroxene in many samples. In the least altered rocks, clinopyroxene is only slightly corroded around the rims and in irregular patches, with fine secondary magnetite in the corroded areas.

Plagioclase

Plagioclase is generally only slightly altered to albite and chlorite along fractures and grain boundaries, but is locally more extensively altered to albite, which typically contains abundant fluid inclusions. Epidote, prehnite, and anhydrite also replace plagioclase locally in small amounts. Small (50–100 μm) grains of epidote rarely replace plagioclase in several samples below 1814 mbsf (Fig. 38, Appendix H). Anhydrite occurs as fifty to several-hundred-micrometer patches replacing plagioclase, mainly below 1790 mbsf (Fig. 38). Prehnite is present in small (10–50 μm) patches and in narrow veinlets cutting plagioclase, again mainly below 1790 mbsf.

Titanomagnetite

Titanomagnetite generally exhibits ilmenite exsolution lamellae, and is partly to extensively altered to titanite. The extent of alteration of titanomagnetite to titanite appears to correlate well with the extent of alteration of the silicate minerals.

Sulfide Minerals

Recrystallized igneous sulfide minerals are commonly present as inclusions in plagioclase and rarely in clinopyroxene and titanomagnetite. They were also observed as inclusions in single crystals of Cr spinel and olivine, and occur in interstitial areas and in late-stage

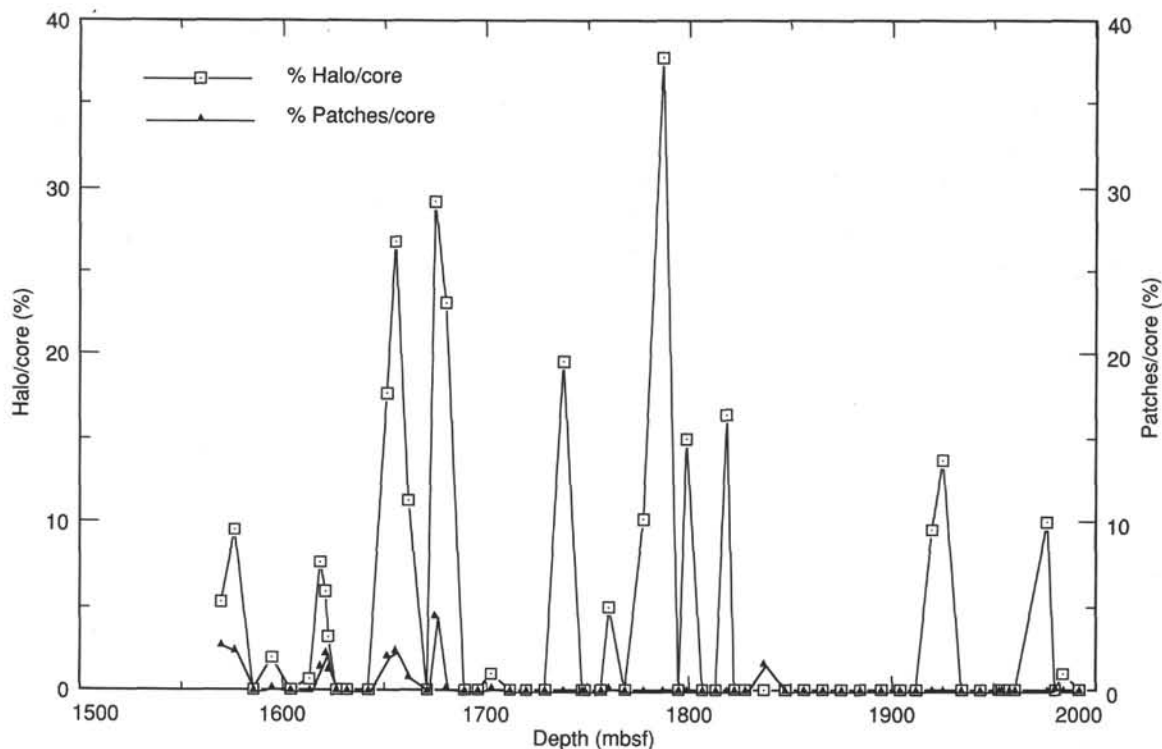


Figure 40. Distribution of extensively altered patches and amygdules vs. depth. Data from Appendix F. Patches and amygdules plotted as percent of recovered material for each core.

granophyric intergrowths of albite + quartz. The sulfide minerals occur as 2- to 40- μm equant to globular grains of pyrite + chalcopyrite + magnetite, or chalcopyrite alone. Hematite was also rarely observed associated with recrystallized igneous sulfides in some samples. Secondary pyrite is present in trace amounts as pseudomorphs of igneous sulfides, as 10- to 800- μm equant to irregular, porous grains in interstitial areas, and replacing silicates. Pyrite is present in some cases as overgrowths on and replacing igneous titanomagnetite or as small (<20 μm) veinlets in the groundmass. Secondary chalcopyrite is often present intergrown with or as inclusions in the pyrite. Secondary chalcopyrite is also present in trace amounts as 2- to 100- μm anhedral grains in interstitial areas and replacing silicates.

Alteration Patches

A characteristic feature of Leg 140 rocks is the common presence of greenish "patches," up to several centimeters across, where the rock is extensively altered (Fig. 39, Appendix F). Such features were also observed shallower in Hole 504B (Alt, Anderson, and Bonnell, 1985; Alt, Anderson, Bonnell, and Muehlenbachs, 1989). The patches are 70%–90% replaced by actinolite, chlorite, albite, titanite, and traces of epidote, anhydrite, and prehnite. In particular, plagioclase is more extensively replaced by albite than chlorite in the patches, in contrast to the background alteration where albite and chlorite replace plagioclase in subequal amounts (Appendix H). The greater extent of alteration of these patches can be seen in Figure 31, where the rocks affected by background alteration generally contain about 10%–20% secondary phases, whereas the patches range up to much greater amounts of secondary minerals. Sulfide minerals are also essentially absent from these patches. These alteration patches or halos average about 10% of the core recovered, and range from none present to about 40% of individual cores (Fig. 40). The peaks in patch abundance in Figure 40 generally correspond to more massive, coarser grained units, and the absence of patches correlates with finer grained intervals.

In many cases these patches or halos occur around amygdules, whereas in others, no amygdules are visible (Fig. 39, Appendix F). The amygdules are irregularly shaped, with crystals of igneous minerals protruding from the walls. Amygdules range from 0.1 to 2.0 mm in size, are filled with actinolite and chlorite, and are surrounded by 2- to 10-mm alteration patches or halos. Amygdules typically make up <1%–5% of individual pieces, but range up to about 20% of individual thin sections (Appendix F; "Thin-Section Descriptions" section, "Explanatory Notes" chapter, this volume). The surrounding halos often coalesce, resulting in extensively altered patches up to 5 \times 10 cm in size in some pieces. Amygdules are common from 1621 to 1750 mbsf, but occur only rarely in small amounts below 1750 mbsf (Fig. 40).

The origin of the amygdules is somewhat uncertain. They may be primary pore spaces (vugs) that are filled with secondary minerals. Several samples contain zoned amygdules, with chlorite and actinolite lining the margins and with the cores filled by epidote, quartz, or laumontite. Such amygdules are consistent with progressive filling of open space by secondary minerals. Alternatively, the amygdules may represent areas of glassy or fine-grained groundmass that have been totally recrystallized. Amygdules consisting of fine-grained actinolite may fit with this interpretation, although these could also be explained as filling of open pore space. Titanite is commonly present in smaller (100 μm) interstitial areas consisting of actinolite and chlorite. These likely represent areas of recrystallized fine interstitial material that originally contained titanomagnetite, which typically alters to titanite. Hydrothermally altered basalt glass also commonly contains small granules of titanite (Alt, Anderson, and Bonnell, 1989), and recrystallized areas around actinolite veins also characteristically contain titanite. The amygdules in Leg 140 rocks lack titanite, which would appear inconsistent with derivation of these amygdule minerals from recrystallized fine-grained or glassy interstitial material.

Above 1750 mbsf in the core, halos or patches are sometimes present but no amygdules are observed. In these cases it is inferred that splitting of the core simply passed through the outer edge of an

Table 4. Vein types in Leg 137 and 140 rocks.

Type	Major minerals	Number logged	Percent of total
Dark green	Chlorite	330	44.1
Medium green	Actinolite	40	5.3
Light green	Actinolite	188	25.1
Dark/light green	Chlorite + actinolite or actinolite	140	18.7
Light blue green	Actinolite	15	2.0
Pistachio	Epidote ± chlorite, sulfide minerals	13	1.7
White, translucent	Quartz ± chlorite, epidote	23	3.1
Total		749	100.0

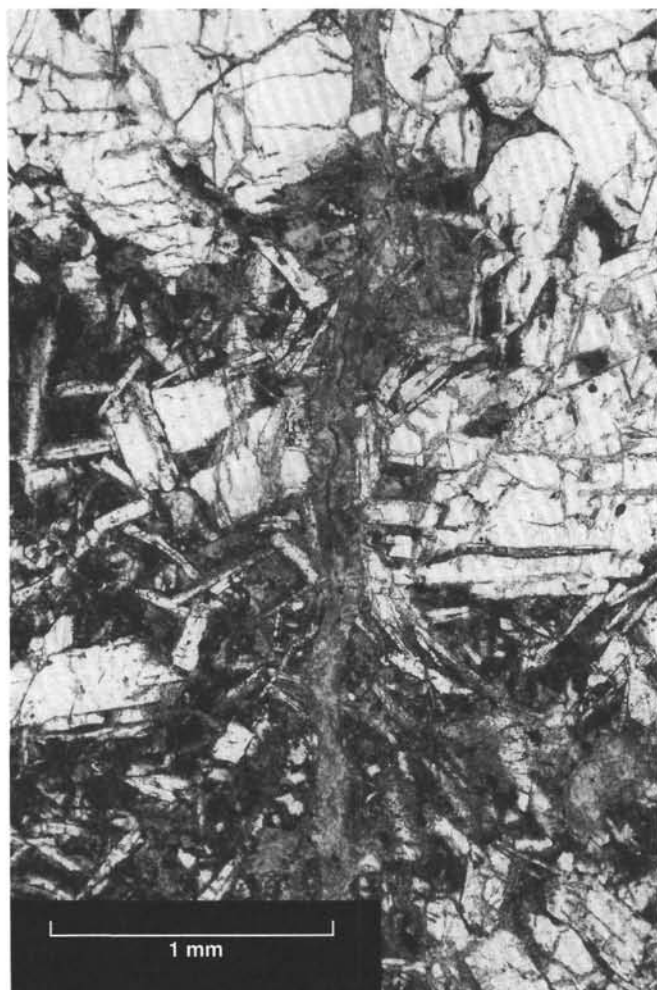


Figure 41. Photomicrograph of a 0.08-mm-wide chlorite vein cutting a diabase/crystal clot boundary. The chlorite consists of a fine-grained mat of fibrous crystals. An opaque seam at the vein core is discontinuous. Groundmass clinopyroxene is extensively altered to actinolite and chlorite. Plane-polarized light. Scale bar = 1 mm. Sample 140-504B-186R-1 (Piece 4, 13–14 cm).

alteration halo, missing the central amygdale. Below 1750 mbsf amygdules are rare, and such variations in splitting of the cores cannot account for their absence in the observed alteration patches. The alteration patches are interpreted to have been zones of enhanced primary porosity that allowed more extensive interaction of surrounding rock with hydrothermal fluids in pore spaces, resulting in the observed local intense alteration in the patches or halos, both around the amygdules and in cases where amygdules are absent. There is no

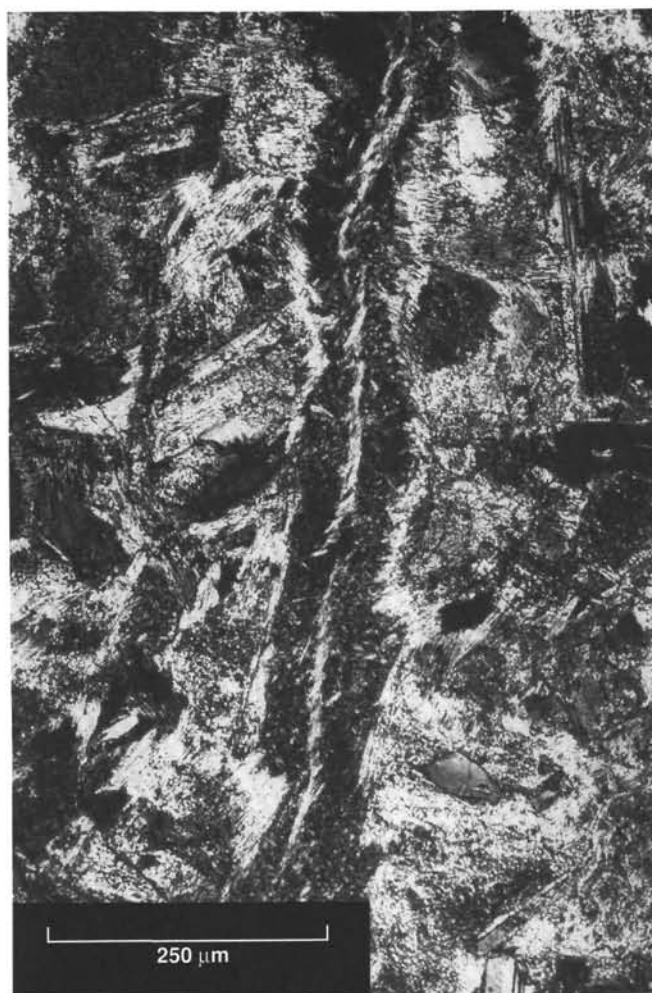


Figure 42. Photomicrograph of a 0.12-mm-wide chlorite-actinolite vein in diabase. Clear actinolite occupies the center, with matted chlorite on either side. Additional clear actinolite occurs discontinuously at the vein edge, grown epitaxially on wallrock clinopyroxene and actinolite after clinopyroxene. Cross-polarized light. Scale bar = 250 μm . Sample 140-504B-186R-1 (Piece 4, 13–14 cm).

observable increase of fracturing, either on a macroscopic or microscopic scale, within or around the alteration patches, suggesting that fluid and solute movement in the rocks occurred through percolation and diffusion along grain boundary porosity.

Several pieces from Core 140-504B-189R, -193R, -209R, -214R, and -217R contain irregularly shaped patches of actinolite up to about 1 cm in size. These actinolite patches are interconnected, covering areas of several square centimeters, and are surrounded by green alteration halos like those around the amygdules. These patches are termed amygdules, but they have smooth outlines in contrast to the more jagged edges of other amygdules. Such amygdules in Section 140-504B-214R-1 contain 2- to 5-mm radiating clusters of epidote, that appear to fill open space. The smooth-walled amygdules are also much larger than the more common smaller amygdules described above. Two possible origins for these larger amygdules are suggested. One is that they represent primary pore space produced by exsolution of volatiles (CO_2) from saturated melts. A second hypothesis is that the amygdules represent solution cavities, where hydrothermal fluids dissolved the igneous phases and precipitated actinolite. Like the smaller, irregular amygdules, these large actinolite-filled ones lack titanite, leading to problems concerning the fate of titanium originally present in these zones. Chemical analyses of alteration patches con-



Figure 43. Photomicrograph of actinolite vein in diabase. Coarse fibrous actinolite crystals, oriented perpendicular to the vein wall, form the outer zone of the vein. Fibrous actinolite with vein-parallel orientation forms the core. Discontinuous opaque seams, parallel to the vein, occur at various positions. The host diabase is heavily altered to albite, chlorite, and actinolite. Plane-polarized light. Scale bar = 1 mm. Sample 140-504B-197R-1, 99–101 cm.

taining these amygdules indicate a decrease in titanium in the rock, suggesting that titanium may have been removed from the alteration patches (see “Geochemistry” section, this chapter). There may exist a gradation between the two types of amygdules described here, from the smaller, irregular amygdules to the larger, smooth-walled ones.

Dark bluish-green, fine-grained areas, up to 1 cm in size, occur in several cores (Sections 140-504B-200R-3, -200R-4, -206R-1, -209R-1, -211R-1; 83-504B-137R-1, and -138R-1). In thin section these are areas of fine, fibrous actinolite, and may represent areas of completely recrystallized fine groundmass.

Variations with Depth

Variations in type of alteration are reflected in the distribution of olivine alteration products (Fig. 31). Cores 140-504B-197R–200R, at 1710–1740 mbsf, are characterized by generally slight alteration, with generally lower abundances of actinolite and chlorite than other cores, by the presence of talc replacing olivine, and by the presence of relict igneous olivine in the rocks. These rocks also lack the centimeter-sized “patches” of more extensively altered rock. Alteration effects similar to these also occur sporadically in underlying rocks (Fig. 31). These

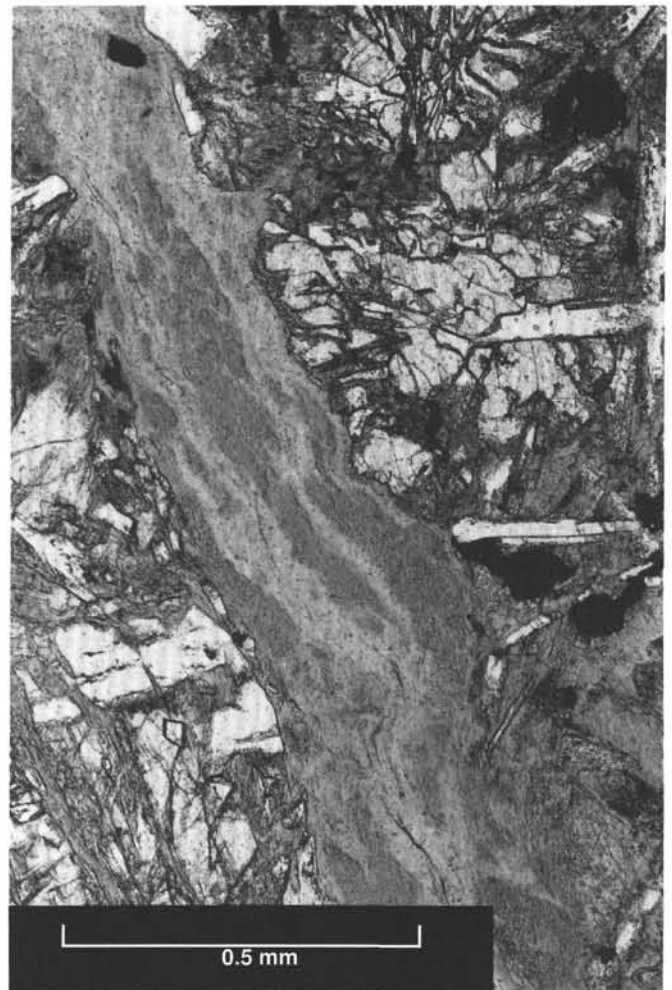


Figure 44. Photomicrograph of actinolite vein. Two different shades of fibrous actinolite occur interbraided. Discontinuous opaque seams occur at the vein center. Plane-polarized light. Scale bar = 0.5 mm. Sample 140-504B-200R-1, 105–107 cm.

rocks are interpreted to reflect reaction at relatively low water/rock ratios, and it is inferred that these zones may be less fractured than elsewhere in the hole, which would have restricted access of hydrothermal fluids.

Epidote is somewhat more abundant in several samples from Cores 214R, 216R, and 217R, at 1820–1840 mbsf (Fig. 31). Epidote occurs in veins, replacing plagioclase, and partly filling amygdules in several samples from this interval. Also present in slightly greater than normal quantities are quartz, prehnite, and anhydrite, in both veins and in the rocks. It is suggested that this may be a zone of relatively late fracturing, allowing greater access of late-stage, evolved hydrothermal fluids and seawater. Epidote is also particularly abundant in Sample 140-504B-227R-2, 14–16 cm, at 1934 mbsf (Fig. 31), where it occurs filling actinolite-rimmed amygdules.

Somewhat coarser grained rocks occur in Cores 213R and 214R, but alteration of these rocks appears generally similar to that in the finer grained diabase.

Veins and Associated Alteration Halos

Introduction

Veins were observed in the archive half of every core from Legs 137 and 140, and were recorded on the Vein Log (see Appendix G, back pocket). Some veins present in the working half but not in the

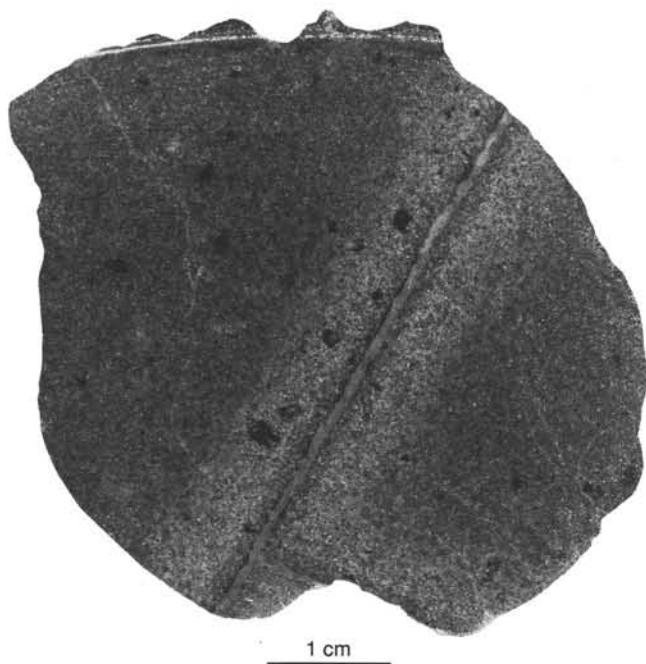


Figure 45. Actinolite veins, meeting at 90°, with well-developed compound halos. Sample 140-504B-197R-1 (Piece 22, 100–104 cm).

Table 5. Alteration halos around veins in Legs 137 and 104 rocks.

Halo type	Average vein width (mm)	Average halo width (mm)
Dark green (N = 49)	0.45	1.8
Light green (N = 110)	0.56	2.8
Medium green (N = 12)	0.73	2.9
Compound dark/light (N = 19)		
dark inner halo	1.0	1.5
outer light halo		3.2
Gray halos (N = 12)	0.25	1.7

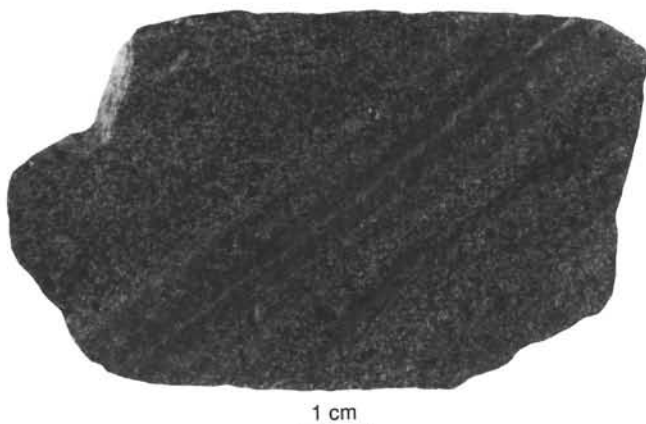


Figure 46. Actinolite vein with a complex compound halo. The zones, from inside out, are dark green (2.5 mm), light green (2.0 mm), dark green (2.0 mm), and light green (2.0 mm). Sample 140-504B-208R-1 (Piece 19, 82–91 cm).

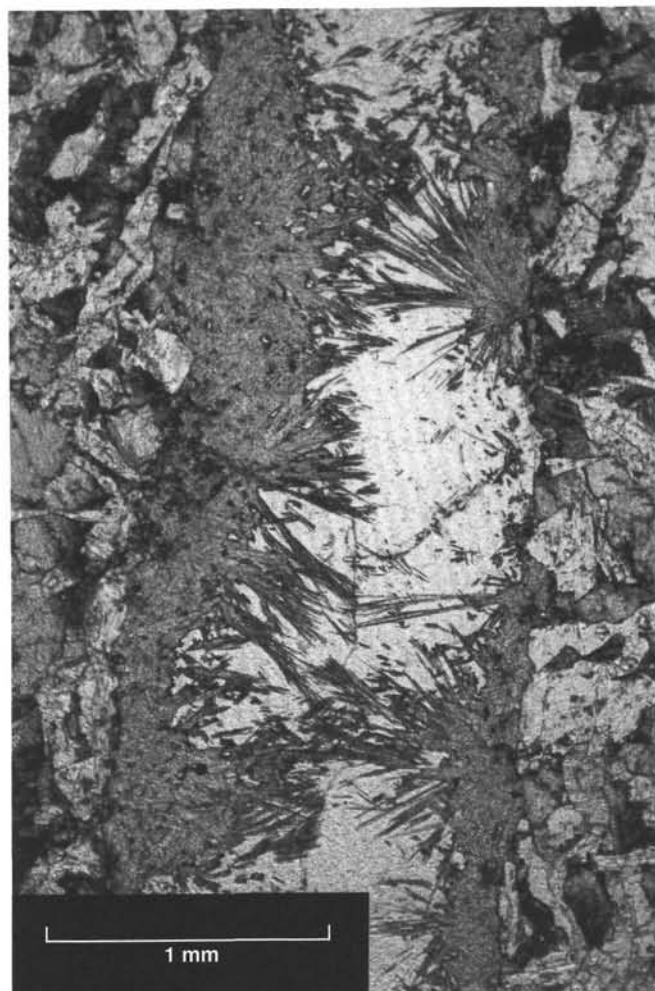


Figure 47. Photomicrograph of a quartz-epidote vein in diabase, showing radial acicular habit of the epidote and the equant granular clear quartz. Plane-polarized light. Field of view is 3.7 mm wide. Sample 140-504B-192R-1 (Piece 4, 13–15 cm).

archive half were noted. These represent a minor percentage of the total, because the cores were oriented by a structural geologist before splitting in such a way as to cut the major veins perpendicular to their strike. The veins are interpreted as evidence for brittle failure of the rocks and subsequent fracture-filling by a variety of minerals. The textures and mineralogy of these veins reveal details about the physical and chemical conditions of rock alteration, and cross cutting relations provide information about the timing of fracturing and vein filling and evolution of hydrothermal conditions (see also “Structure and Deformation” section, this chapter).

Based on their color in hand specimen, veins were classified in one of the following categories: dark green, light green, dark/light green, medium green, blue green, pistachio, and translucent. Other combinations or variants (e.g., medium/light green, apple green) occur infrequently. Thin-section observations indicate that most of the veins are composed of amphibole. Further studies will allow a more detailed classification based on compositional determinations of the vein amphiboles. To be consistent with descriptions and data from the overlying dikes (e.g., Leg 111), the amphibole is generally referred to as actinolite. However, hand-specimen descriptions are

insufficient to distinguish actinolite from actinolitic hornblende (using the terminology of Leake, 1978).

Vein Types

Approximately seven vein types occur, bearing from one to about six vein minerals. Eleven minerals in all have been identified in veins: chlorite, actinolite (amphibole), albite, quartz, epidote, prehnite, anhydrite, titanite (sphene), pyrite, chalcopyrite, and diopside. The most common veins contain actinolite, chlorite, and actinolite + chlorite (with 0–5 vol% other minerals). Table 4 summarizes the vein types recorded in the “Vein Log.”

Chlorite

Logged as “dark green” veins, in thin section these veins contain fine-grained matted chlorite (Fig. 41), usually with anomalous blue and purple-brown interference colors. Chlorite veins are narrow; most were logged in hand specimen as <0.5 mm, and thin-section measurements are typically 50–100 mm across. These veins are often pure chlorite, but may contain small amounts (<5%) of actinolite, titanite, albite, prehnite, epidote, and sulfide minerals. Approximately 25% of the chlorite veins exhibit alteration halos.

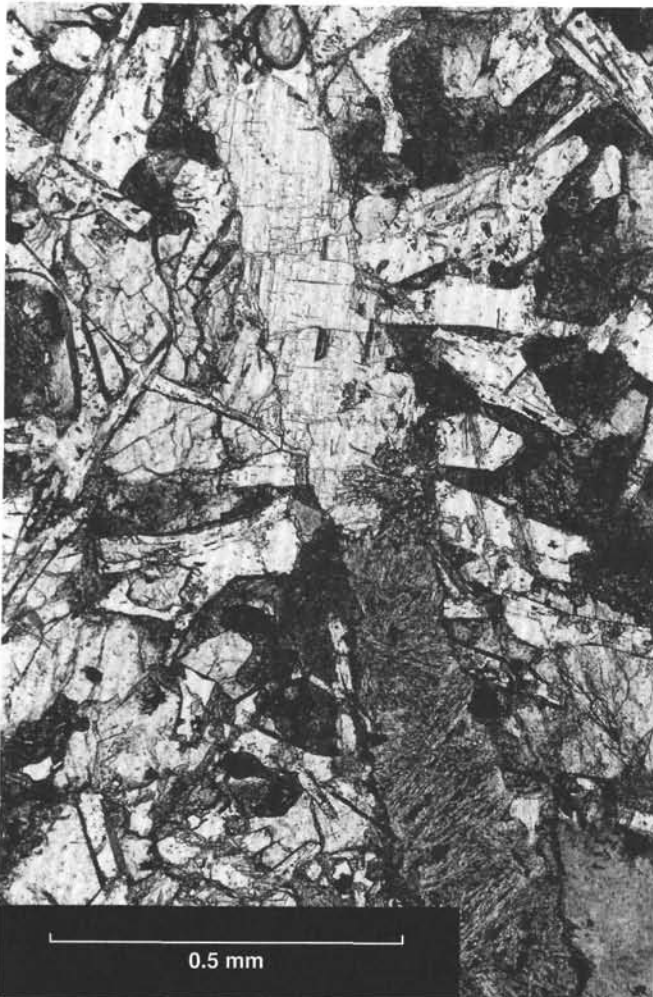


Figure 48. Photomicrograph of vein anhydrite. Anhydrite completely fills the vein at the top. Along strike downward, the vein also contains epidote, chlorite, albite, and quartz. Cross-polarized light. Scale bar = 0.5 mm. Sample 140-504B-217R-1, 0–2 cm.

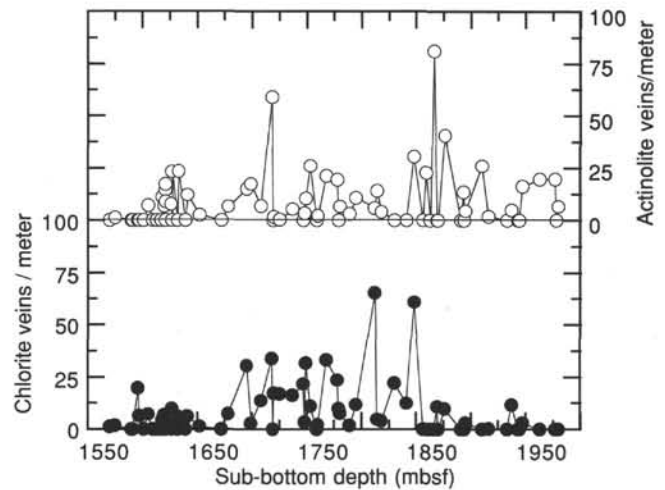


Figure 49. Plot of vein density, in veins per meter, calculated for each lithologic unit.

One subset of the chlorite veins consists of chlorite + sulfide mineral coatings on rock faces. In hand specimen, these appear as planar broken rock surfaces coated with soft dark green chlorite and a few percent millimeter-sized sulfide mineral aggregates (mostly pyrite). These chlorite veins rarely exhibit an alteration halo. When the veins are observed to continue into a sample, they are less than 0.5 mm wide. The chlorite + sulfide mineral veins possess steep dips (see “Structure and Deformation” section, this chapter).

Actinolite-chlorite

Logged as “dark/light green” or “light/dark green,” these thin veins, typically less than or equal to 0.5 mm wide, contain both actinolite and chlorite in varying proportions. The distribution of these minerals commonly reflects the primary igneous mineral in the wallrock: chlorite when the wall is plagioclase, and actinolite when the wall is clinopyroxene (or actinolite after clinopyroxene). The actinolite has usually grown epitaxially on the clinopyroxene, with identical prismatic cleavage orientation.

Actinolite and chlorite may be arranged symmetrically within veins. In some samples an actinolite central zone is flanked by chlorite (Fig. 42), and in other samples a chlorite center is flanked by actinolite. Such textures are interpreted as evidence for re-opening of the veins at different times.

Thin (<0.5-mm-wide) actinolite-chlorite veins, particularly those with wallrock-controlled mineral distribution, lack alteration halos. Thicker actinolite-chlorite veins range up to 2 mm in width, may be zoned texturally and mineralogically, and may possess halos up to 8 mm wide. An example is Sample 140-504B-208R-1, 85–87 cm, where zones from the outside to the center of the vein are chlorite, brown granular actinolite, pyrite, chalcopyrite, and prismatic actinolite.

Actinolite

These veins were logged as “light green,” “medium green,” and “light blue green,” and based on thin-section observations, they contain actinolite. The light blue-green color of some actinolite may be due to enrichment in iron (ferro-actinolite) or alumina (actinolitic hornblende). An unknown proportion of the veins logged as “dark/light” and “light/dark” are also actinolite veins, containing various textural types of actinolite.

Actinolite veins vary from less than 0.5 mm (as thin as 0.1 mm in thin section) to 2 mm wide, averaging about 0.5 mm. Most veins are nearly monomineralic, but include small proportions (to 5%) of other minerals such as chlorite, albite, quartz, and sulfide minerals.

Actinolite in veins exhibits a variety of textures. For example, in Sample 140-504B-197R-1, 99–101 cm, light green drusy needles form the

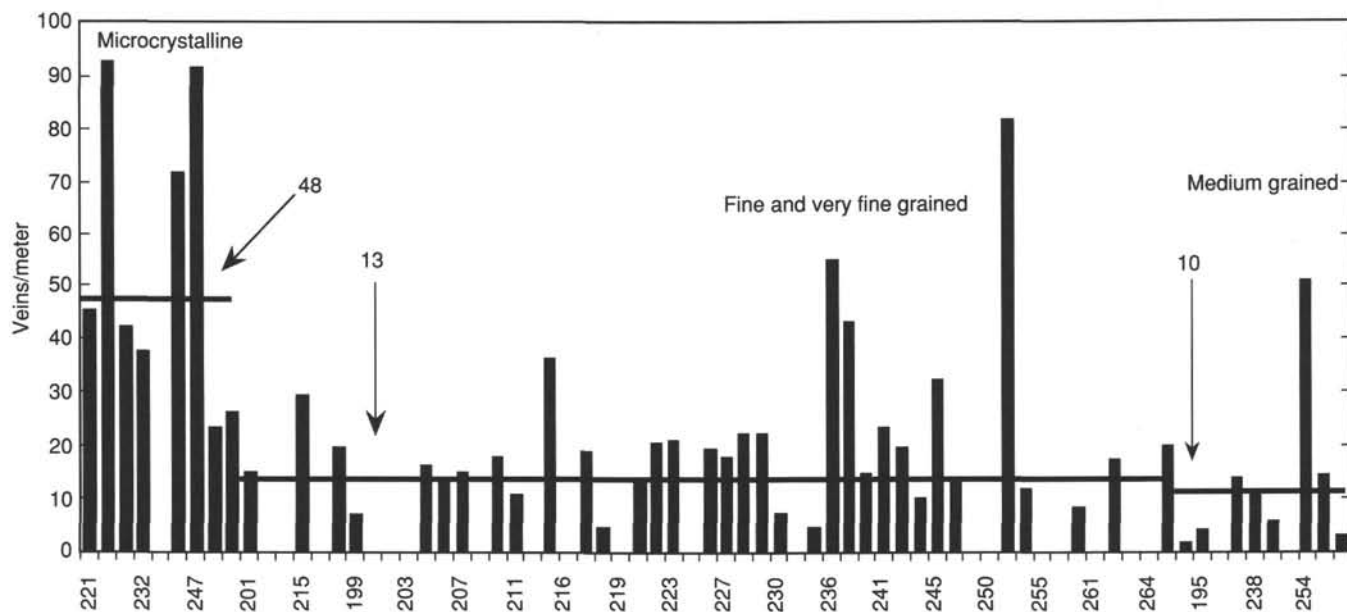


Figure 50. Plot of vein density calculated for each lithologic unit. The units have been re-grouped on the basis of their texture. There is no depth significance. Horizontal lines represent the average for each labeled textural type. Microcrystalline units have over three times the number of veins per meter as the crystalline diabase units.

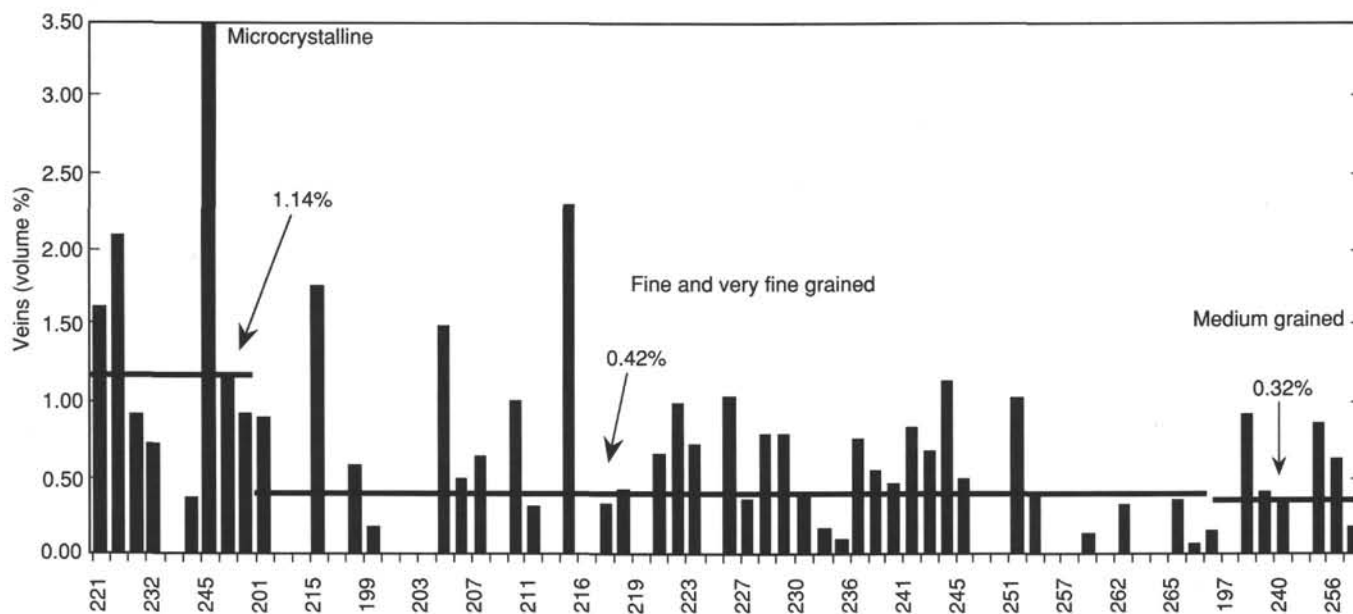


Figure 51. Plot of vein volume, expressed as volume % of veins in each igneous unit. The units have been sorted into similar textural types (see Fig. 50). Microcrystalline units have, on average, 1.14 vol% veins, whereas the crystalline diabase contains about 0.4 vol% veins.

vein wall and light green needles parallel to the vein edges occur in the center (Fig. 43). Other types of actinolite textures occur (Fig. 44), and cross-fiber actinolite has also been observed. The variable textures observed in individual veins suggest different stages of crystallization, perhaps linked to multiple episodes of vein re-opening.

Alteration Halos

The contact of actinolite veins with the host rock is commonly diffuse, because actinolite needles that have grown on or replaced clinopyroxene in the wallrock extend into and sometimes merge with the vein actinolite. On a larger scale, most actinolite veins, as well as many actinolite-chlorite

and chlorite veins, possess an alteration halo. Halos can be simple light, dark, or medium green discolorations of the wallrock wherein recrystallization of magmatic minerals is more extensive (typically 40%–90%) than in adjacent wallrock (typically 5%–40% altered) (Fig. 45). Average dimensions of halos are given in Table 5.

Compound halos generally consist of a dark inner zone and a light outer zone. For example, Sample 140-504B-192R-1, 75–79 cm, contains a 2-mm-wide actinolite vein with a compound halo. The inner dark halo zone is 3 mm wide and contains plagioclase crystals, 75% replaced by albite, set in a mat of well-crystallized actinolite plus minor chlorite and titanite (for a total of about 95% recrystallization of the diabase). The outer light halo is 5 mm wide, with less altered plagioclase (about 40%

recrystallized to albite), relict pyroxene, and “dirty” brown actinolite. The total amount of recrystallization in the outer halo is about 60%, whereas that in the host rock outside of the halo is only 10% (in the host rock plagioclase is slightly altered to albite and chlorite (2%), clinopyroxene to actinolite (15%), olivine to chlorite, magnetite, pyrite, and mixed-layer clays (100%), and titanomagnetite to titanite (2%). In one vein, a double compound halo exists, with the sequence (inner to outer zone) dark-light-dark-light (Fig. 46).

Epidote

Veins containing epidote were logged as pistachio or apple green. Associated minerals include one or more of the following: quartz, prehnite, chlorite, albite, actinolite, sulfide minerals, and anhydrite. These veins vary from 0.2 to 0.25 mm wide, averaging 0.8 mm, and occur in restricted intervals of the dike section drilled during Legs 137 and 140. The epidote is generally acicular, extending in radial aggregates from points along the vein wall (Fig. 47), or granular. In epidote-quartz veins, centrally-located quartz may be flanked by epidote.

Quartz

Twelve examples of quartz-bearing veins (Fig. 47) occur with width ranging from less than 0.5 mm to 2 mm. Associated minerals are epidote, chlorite, prehnite, pyrite, and chalcopyrite. Quartz occurs as equant mosaic grains, usually with straight extinction. Wavy extinction and included arrays of secondary fluid inclusions are rare or absent, indicating that these quartz veins are essentially undeformed on an intragrain scale. Primary fluid inclusions, however, do occur with low frequency. These are small (5–15 mm) and contain liquid + vapor or liquid + vapor + one birefringent, unidentified daughter crystal.

Diopside

A small (0.15- to 0.4-mm-wide) veinlet of fine granular diopside occurs in Sample 140-504B-206R-1, 47–50 cm. The veinlet appears to be restricted to a centimeter-scale patch of clinopyroxene-rich host rock, in which the clinopyroxene is recrystallized at the core to granular diopside, similar to that in the veinlet. This patch may be a recrystallized xenolith of hydrothermally altered (to diopside) diabase that has undergone partial assimilation by the host diabase. Alternatively, the groundmass and veinlet may represent in-situ alteration.

In addition to this example, diopside may occur in a vein (0.3 mm wide) in Sample 140-504B-213R-1, 3–6 cm, as small crystals associated with magnetite and minor actinolite(?). The boundary of the vein with the host rock is gradational.

Albite

One albite (plus minor actinolite, magnetite, and titanite) vein was observed in Sample 140-504B-213R-1, 3–6 cm. It is 0.4 mm wide, and is partly rimmed by fine-grained diopside(?). The crosscutting relationship of the albite vein with the diopside vein is not clear and no strong argument regarding the relative timing of the two veins is possible. Further chemical investigation of this occurrence should help place constraints on the origin and significance of diopside and albite veining.

Anhydrite

The single occurrence of anhydrite in a vein is in the epidote-quartz-chlorite-albite-diopside(?)-anhydrite vein of Sample 140-504B-217R-1 (0–2 cm). The anhydrite (Fig. 48) occurs along a 1.6-mm length of this 0.2 mm-wide vein, in crystals measuring up to 0.9 mm. The anhydrite is associated with adjacent rock alteration that involves actinolite (6 vol%), chlorite (10%), albite (22%), epidote (6%), prehnite (1.4%), and anhydrite (0.4%). This is the only example of anhydrite in a vein from Leg 140 samples, although anhydrite replacement of plagioclase is observed in several thin sections.

Vein Abundance

The summary of veins (Table 4) that are recorded in the Vein Log (Appendix G, back pocket) gives an overall view of the relative abundance of the vein types. The distribution of veins downhole (Fig. 49) generally shows no major trends, although there is a distinct reduction in chlorite veins below 1850 mbsf. The overall average number of veins recorded per meter of recovered core is 15 (ranging from 0 to 90 veins/meter). No significant intervals (over three successive igneous units) of the cored section are free of veins. The lithologic units with unusually high vein abundances are almost invariably associated with chilled margins composed of microcrystalline diabase. Many of the spikes in vein abundance in Figure 49 correspond to chilled margins.

The abundance of veins per meter for each lithologic unit is displayed in Figure 50, where the igneous units have been regrouped according to their texture. Microcrystalline units have higher vein abundance, averaging about 50 veins per meter. Very fine-grained, fine-grained, and medium-grained igneous units have a uniformly lower average of about 12 veins per meter (with a few exceptions).

Figure 51 shows the calculated volume percent of veins for each igneous unit, and grouped according to textural type. These calculations show that the aphanitic microcrystalline units, with an average of 1.14 vol% veins, contain over twice the volume of veins (about 0.4 vol%) in the very fine-grained, fine-grained, and medium-grained igneous units. The weighted average volume of veins in cores from Legs 137 and 140 is 0.57 vol%.

Medium-green veins are restricted to depths of approximately 1781, 1796–1821, 1913–1941, and 1954–1983 mbsf. Light blue-green veins are restricted to depths of 1803–1830, 1896, 1914–1915, and 1966 mbsf. The increase in frequency of occurrence of medium-green and light blue-green veins in the lower part of the drilled section could be due to a subtle increase in metamorphic grade, or related to the slight increase in average grain size observed in the igneous units downhole.

Epidote-bearing veins have a restricted occurrence, in Cores 140-504B-186R-1, -186R-2, -192R-1, -193R-1, -195R-1, -214R-1, -216R-1, and -217R-1. The development of epidote veining is closely related to a chilled margin in Core 216R-1, Pieces 2, 3, 5, 7, 8, 13, and 18.

Quartz veins are similarly restricted in occurrence. In Cores 186R-2 and 192R-1, quartz-bearing veins (with epidote) cut a fine-grained phaneritic diabase. In Core 216R-1 and Core 222R-1, quartz-bearing veins are associated with chilled margins.

Temporal Relations

Crosscutting relations were documented during Leg 140 (for a more detailed discussion, see also “Structure and Deformation” section, this chapter). In general, the following observations can be made:

Chlorite, actinolite-chlorite, and actinolite veins are mutually crosscutting. That is, integrated over many samples, each possible type of crosscutting relation has been observed.

In general, light-green or light blue-green actinolite veins tend to be later than dark-green veins. Many exceptions to this generality have been observed, however.

In all cases, quartz- and epidote-bearing veins are the latest veins in a sample, crosscutting actinolite- and chlorite-bearing veins.

Lithologic contacts such as chill margins and xenolith boundaries are cut by veins, and do not crosscut veins. In only one case has evidence, somewhat equivocal, been described for a chilled dike margin following a pre-existing vein or fracture (see “Structure and Deformation” section, this chapter).

Despite the fact that no clear examples of a dike margin cutting a vein network were observed, the existence of mutually crosscutting chlorite, actinolite, and actinolite-chlorite veins, and of multiply re-opened veins, may suggest an episodic nature to the fracturing and fracture-filling process. This could be attributed to local episodic tectonic or magmatic events, such as individual dike injections.

Discussion

The alteration effects observed in the Leg 140 rocks are generally similar to those in the overlying Leg 111 section of the dikes, but some significant differences suggest higher temperatures of alteration in the Leg 140 rocks. The secondary mineralogies of the Leg 140 and 111 rocks are generally the same, but the Leg 140 rocks contain a greater proportion of actinolite, more abundant actinolite veins, and are generally more extensively altered. These observations appear consistent with a trend noted in Leg 111 rocks. There, plagioclase is more extensively altered to albite in the upper section of the dikes and clinopyroxene is relatively unaltered, whereas the reverse is true at the base of the Leg 111 section, where clinopyroxene is more extensively altered to actinolite and plagioclase is less altered. This was interpreted to reflect increasing temperatures downward in the dike section, approaching the stability of more calcic plagioclase plus actinolite rather than albite plus chlorite (Shipboard Scientific Party, 1988). The Leg 140 rocks also contain more strongly pleochroic amphibole, which is suggested to be actinolitic hornblende. Also, on the basis of optical properties, the Leg 140 rocks may contain more magnesian chlorite than the overlying dikes. Such differences in mineral composition would provide additional evidence for higher alteration temperatures in the Leg 140 dikes than shallower in the dike section. Epidote occurs locally in veins in the Leg 140 dike rocks, but is also present in trace amounts replacing plagioclase at depths below 1814 mbsf. In contrast, epidote has only been observed in veins in the overlying Legs 83 and 111 dike sections. These mineralogical changes and implied increases in temperatures of alteration in the Leg 140 dike section are consistent with the changes that take place toward the base of sheeted dike sections in many ophiolites, suggesting that Hole 504B may penetrate close to the base of the sheeted dike complex.

One similarity between the Leg 140 section and the overlying dikes is the general sequence of vein minerals and implied alteration conditions (Alt, Anderson, and Bonnell, 1989; Alt, Anderson, Bonnell, and Muehlenbachs, 1989). Crosscutting relationships of veins in Leg 140 rocks indicate that the formation of actinolite and chlorite in veins, and of greenschist minerals in host rocks, was followed by later quartz and epidote in veins and local formation of small amounts of epidote within the rocks. The presence of actinolite indicates temperatures greater than about 300°C, and actinolitic hornblende would be consistent with even higher temperatures. The mutually crosscutting actinolite, actinolite + chlorite, and chlorite veins may be related to fluctuations in temperatures and fluid compositions. Such variations may simply be due to episodic fracturing of the rocks, which may in turn be related to periodic dike injection.

Because Mg is rapidly taken up from seawater during hydrothermal alteration of basaltic rocks, the presence of chlorite in veins is taken as an indicator for the presence of Mg-bearing seawater fluids circulating in the rocks. The presence of quartz and epidote in later veins and of traces of epidote replacing plagioclase indicate more evolved hydrothermal fluids, depleted in Mg and enriched in Ca. These occurrences appear to be the only indication that could possibly be related to upwelling hydrothermal fluids in the Leg 140 rocks. Temperatures estimated for formation of these minerals from shallower depths in the hole range from 230°–380°C (Alt, Anderson, and Bonnell, 1989; Alt, Anderson, Bonnell, and Muehlenbachs, 1989). The small amounts of prehnite in veins and replacing plagioclase may have formed simultaneously with quartz and epidote at similar temperatures, although prehnite has been observed partly replacing quartz in a vein in Sample 140-504B-222R-1, 129–132 cm, suggesting at least locally a somewhat later formation of prehnite.

Only small amounts of laumontite have been tentatively identified filling pore space interstitial to chlorite, epidote, and actinolite in Leg 140 rocks. This suggests a relatively late-stage formation of laumontite. The upper thermal stability of laumontite is about 230°C (Liou, 1971), supporting a relatively late-stage, lower temperature origin for this mineral, as in the upper dikes.

The presence of trace amounts of anhydrite in the rocks below 1679 mbsf provides evidence for the penetration of relatively unaltered

seawater to depths of nearly 2 km bsf (or 1625 m sub-basement). Simple heating of seawater as it penetrates into hot rocks will precipitate anhydrite at temperatures of about 150°C, but only about one third of the sulfate present can precipitate because of the limitation by the amount of Ca in seawater. Ca released from the rocks can cause precipitation of additional seawater sulfate as anhydrite, however, and the occurrence of anhydrite replacing plagioclase may be attributed to local Ca-enriched microenvironments in the rocks. Timing of anhydrite formation in Leg 140 rocks is poorly constrained, but a single occurrence of anhydrite in a vein in Sample 140-504B-217R-1, 0–2 cm, indicates that anhydrite formed later than quartz in veins. This is consistent with anhydrite at shallower depths, where it is interpreted to have formed during a "pulse" of seawater recharge as the crust moved away from the spreading axis (Alt et al., 1986). An alternative is that anhydrite could have formed in Leg 140 rocks through mixing of sulfate-bearing seawater with Ca-enriched hydrothermal fluids. Penetration of relatively unaltered seawater to 2000 mbsf could account for the presence of oxidation effects in the rocks (i.e., the small amounts of hematite in altered olivine). Anhydrite in shallower cores was mainly recovered from veins, with only one occurrence reported replacing plagioclase (Alt, Anderson, and Bonnell, 1989), whereas the reverse is true for anhydrite in Leg 140 rocks. The paucity of anhydrite veins from Leg 140 may be caused either by a true lack of anhydrite in veins at this depth, or by grinding up and loss of such vein material during drilling.

The zonation of secondary minerals in olivine pseudomorphs, particularly around relict olivine grains, provides evidence for the timing and conditions of formation of the various phyllosilicate minerals replacing olivine. Where talc is present, talc + magnetite + pyrite were generally first, forming along grain boundaries and in small fractures, followed by later formation of smectite, talc-smectite, and serpentine, probably at lower temperatures, from the islands of relict olivine surrounded by talc. Where chlorite rims the olivine grains, chlorite was first, generally followed by mixed-layer chlorite-smectite or serpentine replacing remaining olivine, possibly with later quartz replacing the phyllosilicate minerals. Talc (plus magnetite) can form by simple hydration (and oxidation) of olivine, whereas formation of chlorite from olivine requires a source of Al. This variation in olivine replacement has been interpreted to reflect variations in water/rock ratios and kinetic effects (Alt, Anderson, and Bonnell, 1989; Alt et al., 1986). Alteration of olivine to talc occurred at low water/rock ratios, in zones of low permeability and small amounts of fracturing (or in portions of the rock far removed from fractures), with little or no alteration of other phases in the rocks. In contrast, chlorite formed at relatively higher water/rock ratios, with corresponding breakdown of plagioclase providing the Al required for chlorite formation. Mixed-layer chlorite-smectite may reflect intermediate water-rock ratios, where insufficient Al is available to form chlorite. Alternatively, the mixed-layer phyllosilicates may form at somewhat lower temperatures, or, perhaps less likely, may represent a replacement reaction of smectite to chlorite or of chlorite to smectite. Like talc, serpentine can form from olivine simply by addition of water, suggesting relatively low water/rock ratios during formation of serpentine.

Temperature may also play a role in controlling phyllosilicate distribution. Talc and chlorite can form at the inferred alteration temperatures of 250°–350°C, but talc is stable up to much greater temperatures (500°–600°C), and may have formed during initial cooling and penetration of seawater into the diabases (Alt, Anderson, and Bonnell, 1989). Serpentine is generally stable over a temperature range from about 250°C to 450°C (O'Hanley et al., 1989), whereas smectite generally forms at temperatures less than about 200°C. Ambient temperatures in the Leg 140 section range from 165°C to 195°C, suggesting that smectite may currently be forming from olivine, as witnessed by the presence of smectite between unaltered olivine relics and talc rims. The details of phyllosilicate mineral textural relationships and the sequences of their formation and reaction relationships are complicated, however, and the extreme variability within individual thin sections is puzzling. Access of fluids to minerals may have been locally heterogeneous on a millimeter to centimeter scale, with secondary

Table 6. Shipboard chemical analyses of Hole 504B basalts and diabases, Leg 140.

Leg	137	137	137	137	137	137	140	140	140
Site	504B	504B	504B	504B	504B	504B	504B	504B	504B
Core and section	175R-1	180M-1	180M-2	181M-1	181M-1	181M-2	185R-1	186R-1	187R-1
Interval (cm)	19–21	Volcanic	29–31	7–9	90–92	45–47	15–19	135–137	5–9
Piece #	3	1	3	1	12	4	3	17A	2
Lithologic unit	197	-----	205	206	210	210	211	213	214
Depth (mbsf)	1566.4	-----	1568.8	1570.9	1574.5	1575.6	1622.0	1627.7	1632.1
Unit rock name							M-PCO	A	A
Average grain size							F	F	F
Thin-section interval			35–39		3–5				81–84
% Alteration	37	n.d.	9	3	17	37	31	50	1
Sample wt (g)	n.d.	n.d.	n.d.	n.d.	n.d.	n.d.	22.0	21.8	16.7
SiO ₂ (wt%)	50.40	49.79	50.35	50.80	50.73	50.99	50.38	48.28	49.92
TiO ₂	0.89	0.97	0.86	0.97	0.96	0.86	0.89	0.97	1.08
Al ₂ O ₃ *	15.35	14.56	14.67	14.59	14.65	14.59	14.65	15.90	14.40
Fe ₂ O ₃	10.51	10.97	10.25	11.17	11.12	10.37	10.56	10.05	11.34
MnO	0.18	0.21	0.17	0.18	0.18	0.17	0.17	0.16	0.19
MgO	7.94	8.35	8.39	8.05	8.12	8.43	8.63	9.25	8.07
CaO	12.83	12.54	13.08	12.60	12.49	12.79	12.96	13.42	12.53
Na ₂ O	1.76	2.10	1.75	1.81	1.82	1.88	1.75	1.66	2.23
K ₂ O	<0.005	0.01	<0.005	<0.005	<0.005	<0.005	<0.005	0.01	0.01
P ₂ O ₅	0.08	0.12	0.10	0.07	0.05	0.05	0.06	0.08	0.07
Total (anhydrous)	99.93	99.62	99.62	100.24	100.12	100.13	100.05	99.70	99.77
H ₂ O ⁺	1.37	1.40	1.30	1.16	1.21	1.80	1.15	1.99	1.19
CO ₂	0.07	0.07	0.06	0.04	0.05	0.05	0.04	0.05	0.05
Nb (ppm)	<0.3	0.6	<0.3	<0.3	0.3	0.5	0.3	0.4	0.7
Zr	42.6	47.1	39.7	45.0	44.7	38.7	42.4	58.5	56.0
Y	23.3	25.2	22.9	25.8	25.3	22.5	23.5	25.5	28.5
Sr	44.1	54.3	42.5	44.1	43.3	43.5	43.9	63.0	60.6
Rb	0.4	<0.4	<0.4	<0.4	<0.4	0.8	<0.4	<0.4	0.7
Zn	59.0	77.0	56.0	68.0	70.0	56.0	62.0	43.2	78.6
Cu	81.0	91.0	66.0	83.0	80.0	87.0	51.0	20.6	90.5
Ni	95.0	96.0	89.0	80.0	83.0	87.0	102.0	131.6	78.7
Cr	252	265	293	189	212	273	339	369	173
V	308	334	312	320	338	306	305	291	346
Mg'-value	0.624	0.626	0.643	0.613	0.616	0.641	0.643	0.670	0.610
CaO/Na ₂ O	7.290	5.971	7.474	6.961	6.863	6.803	7.406	8.084	5.619
Zr/Y	1.828	1.869	1.734	1.744	1.767	1.720	1.804	2.294	1.965

Unit rock names and average grain size data are from the igneous lithologic log (Appendix A). The rock names have been abbreviated for this table: aphyric (A), sparsely phyrlic (S), moderately phyrlic (M), highly phyrlic (H), plagioclase (P), olivine (O), and clinopyroxene (C). Grain size data are abbreviated as follows: microcrystalline (m), fine-grained (F), medium-grained (M). Percent alteration figures are from the alteration log (Appendix F) and refer to the total modal percentage of secondary minerals in each thin section representing a given sample. Thin sections are usually taken from the same interval as the bulk-rock sample, but when the interval is different, it is noted in the row marked "Thin section interval." The amount of sample that was crushed for analysis is recorded under "Sample Weight." Fe₂O₃* is the total amount of iron expressed as Fe₂O₃, and Mg'-value is the molar ratio MgO/MgO + FeO, where FeO is calculated to be 90% of the total iron as FeO. Potassium analyses on all samples prior to 140-504B-193R-1, 28–31 cm, were determined to only two significant figures and recorded as either 0.01 or <0.005%. All subsequent potassium analyses are reported with three significant figures. n.d. - Not determined.

mineralogy controlled by local microscale variability in water/rock ratio and fluid compositions: for example localized microfractures in plagioclase controlling availability of aluminum.

Recovery throughout the dike section in Hole 504B averages only about 10%–15%, and it has generally been assumed that the cores recovered are representative of the drilled section. The potential effect of low sample recovery should be kept in mind when evaluating the plots of mineralogy or vein abundance, etc. vs. depth. On the other hand, the material that has been recovered from the dike section at Site 504 has been studied in great detail, so it is unlikely that significant features were overlooked in the recovered core.

While there is a general trend toward increasing extents of alteration and increasing proportions of actinolite with depth in the Hole 504B dike section (from the Legs 83 and 111 sections to the Legs 137 and 140 sections), the extent of alteration and the secondary mineralogy are heterogeneous throughout. Moreover, the deepest sample recovered is among the least altered rocks from the Hole 504B dike section. Such variations emphasize the critical influence of fracturing and permeability on alteration of oceanic crust. Other important factors that contribute to the heterogeneity of alteration include spatial and/or temporal variations in water/rock ratio, temperature, solution

chemistry, and the kinetics of reaction of the various primary phases with hydrothermal fluids.

GEOCHEMISTRY

Introduction

This section summarizes the major and trace element characteristics of the diabase samples recovered from Hole 504B during Leg 140. Representative samples from 75 percent of the 58 igneous lithologic units defined by the Shipboard Scientific Party were analyzed for major and trace elements, including structural water and carbon dioxide (see "Geochemistry" section, "Explanatory Notes" chapter, this volume). The results of these analyses are presented in Table 6. Included in this table are six analyses from the Leg 137 cores that were re-sampled by the Leg 140 Shipboard Scientific Party. Estimates of precision and calculated detection limits are given in Table 7. For estimates of analytical accuracy, the analyses of well-characterized geochemical standards obtained during the Leg 140 calibrations are recorded in the "Explanatory Notes" chapter (Tables 5, 6, and 7). An inter-laboratory standard was prepared from a 1-kg portion of Sample 137-504B-182M-3, 7–20 cm (see "Geochemistry"

Table 6 (continued).

Leg	140	140	140	140	140	140	140	140	140	140	140
Site	504B	504B	504B	504B	504B	504B	504B	504B	504B	504B	504B
Core and section	188R-1	189R-1	189R-2	191R-1	192R-1	193R-1	193R-1	193R-1	194R-1	194R-1	196R-1
Interval (cm)	21–23	13–16	83–86	60–62	0–3	7–10	28–31	44–46	5–9	115–118	0–3
Piece #	7A	4	12	8	1	3	9	13A	2	2	21
Lithologic unit	217	218	218	218	218	219	220	220	220	220	221
Depth (mbsf)	1641.7	1651.1	1653.3	1662.0	1670.9	1674.6	1674.8	1675.0	1680.5	1681.6	1696.5
Unit rock name	S-CPO	M-POC	M-POC	M-POC	M-PCO	M-PCO	M-PCO	M-PCO	M-PCO	M-PCO	A
Average grain size	F-M	M	M	M	M	M	M	M	M	M	m
Thin section interval											
% Alteration	30	17	26	16	21	18	43	60	14	14	5
Sample Wt (g)	20.7	21.7	30.2	34.7	27.7	17.5	22.3	23.4	25.7	20.7	30.6
SiO ₂ (wt%)	50.66	50.43	50.08	50.08	50.18	50.07	50.45	50.16	49.98	50.26	50.50
TiO ₂	0.98	0.94	0.86	0.77	0.93	0.94	0.43	0.94	0.82	0.95	1.10
Al ₂ O ₃	14.51	14.88	15.54	15.75	15.21	14.96	15.61	15.35	15.91	15.01	14.45
Fe ₂ O ₃ *	11.20	10.60	9.91	9.50	10.33	10.60	8.95	9.91	9.74	10.80	11.21
MnO	0.17	0.18	0.17	0.16	0.18	0.19	0.15	0.19	0.17	0.18	0.18
MgO	7.98	7.81	8.20	8.73	7.74	7.87	9.12	8.08	8.36	7.85	8.06
CaO	12.56	12.64	12.99	13.04	12.73	12.75	12.50	13.02	13.06	12.83	12.18
Na ₂ O	1.73	1.74	1.63	1.80	1.91	1.84	2.06	1.93	1.80	1.79	2.03
K ₂ O	<0.005	<0.005	<0.005	<0.005	<0.005	0.01	0.015	0.006	0.010	0.002	0.002
P ₂ O ₅	0.08	0.10	0.05	0.06	0.09	0.05	0.02	0.10	0.05	0.06	0.08
Total (Anhydrous)	99.79	99.32	99.43	99.89	99.30	99.28	99.31	99.68	99.90	99.73	99.79
H ₂ O ⁺	1.44	1.42	1.17	1.53	1.31	1.51	3.68	1.99	1.62	1.34	1.45
CO ₂	0.04	0.05	0.05	0.05	0.03	0.07	0.03	0.03	0.03	0.04	0.02
Nb (ppm)	0.3	0.4	0.4	0.3	<0.3	0.5	<0.3	<0.3	0.3	0.03	0.05
Zr	45.9	44.8	41.5	36.4	45.4	44.4	18.4	46.3	39.4	46.4	54.8
Y	25.7	24.4	22.8	20.6	24.8	24.7	12.8	25.3	22.3	25.7	28.1
Sr	43.3	45.1	45.3	47.4	47.6	45.8	50.8	48.8	46.5	46.8	48.2
Rb	<0.4	0.4	<0.4	<0.4	<0.4	0.6	<0.4	<0.4	<0.4	<0.4	<0.4
Zn	65.3	63.7	60.8	54.4	70.7	70.0	63.0	61.7	57.6	69.7	102.9
Cu	79.1	143.8	83.6	85.5	81.2	85.6	11.7	100.9	89.5	79.9	79.1
Ni	81.4	82.1	108.8	121.5	86.6	85.0	112.7	96.6	109.2	86.7	86.6
Cr	170	229	330	407	262	245	402	278	345	255	164
V	325	338	286	277	317	333	225	317	293	332	345
Mg ⁺ -value	0.611	0.619	0.646	0.669	0.623	0.620	0.692	0.642	0.654	0.615	0.613
CaO/Na ₂ O	7.260	7.264	7.969	7.244	6.665	6.929	6.068	6.757	7.256	7.168	6.000
Zr/Y	1.786	1.836	1.820	1.767	1.831	1.798	1.438	1.830	1.767	1.805	1.950

section, "Explanatory Notes" chapter, this volume). The shipboard analysis of this standard is recorded in Table 8.

Many of the analyzed samples exhibit a moderate to high degree of alteration (H₂O⁺ up to 3.68%), which can obscure many primary igneous compositional trends. Some measure of the intensity of alteration must be made before igneous compositional trends can be intelligently assessed. To this end, we have selected the first-order approach of only using compositions with H₂O⁺ less than 1.5 percent and defining them as "fresh." This somewhat arbitrary category was chosen by plotting elemental abundance vs. water content and selecting the point at which some elements (notably Cu) became depleted or enriched compared to less altered samples within the same lithologic unit. Only the arbitrary "fresh" samples will be used when the text refers to igneous processes. Later in this section, the chemical characteristics of the highly altered samples will be described.

Description of Igneous Chemistry

The analyzed samples range from aphyric basalts to moderately phyrific diabases, most of which are multiply-saturated with respect to olivine, plagioclase, and clinopyroxene (see "Igneous Petrology" section, this chapter). Chemically, the Leg 140 dike samples can be classified as olivine to slightly quartz-normative tholeiites with compositions that are similar to moderately evolved mid-ocean ridge basalts (MgO = 7.7%–10.1%, Fe₂O₃* = 8.1%–11.4%, Ni = 79–189 ppm). They are unusually depleted in incompatible element abundances (TiO₂ = 0.67%–1.1%, Nb ≤ 0.3–0.7 ppm, Zr = 35–58 ppm, Rb ≤ 0.4 ppm) (Fig. 52), yet their incompatible element ratios (e.g., Zr/Nb > 30) are comparable to normal Type-I mid-ocean ridge basalts as defined by Bryan et al. (1976). As shown in Figure 53, these depleted compositions are consistent with the D-group classification of Autio and Rhodes (1983). This group encompasses over 98% of all samples recovered from

Hole 504B, through 2000 mbsf. No samples from groups M, E, or T (Autio and Rhodes, 1983) representing normal Type-I, Type-II enriched (Bryan et al., 1976) or transitional basalts, were identified by the Leg 140 Scientific Party. Another unusual chemical feature of Group D compositions is their refractory nature. Measured bulk-rock CaO/Na₂O ratios (5–8) are in equilibrium with plagioclase compositions of up to An₉₀ (Drake, 1976), which is consistent with microprobe analyses of plagioclase (up to An₉₀) by Natland et al. (1983) and Kempton et al. (1985). Figure 54 depicts the unusual CaO/Na₂O ratios in the Leg 140 dike samples compared to normal aphyric and sparsely phyrific mid-ocean ridge basalt compositions.

Two models have previously been proposed to explain the depleted, refractory nature of the Costa Rica Rift Zone basalts. Natland et al. (1983) suggested that they were highly primitive basalts, whereas Autio and Rhodes (1981, 1983), Kempton et al. (1985), and Autio et al. (1989) have argued persuasively that the basalts were produced from the multistage melting of a normal ocean ridge mantle source, followed by moderately extensive crystal fractionation. The compositional similarity between the Leg 140 shipboard data and previous legs to Hole 504B sheds no new light on these models.

With the exception of mobile elements (K, Zn, Cu, and, to a lesser extent, Sr), Leg 140 dike compositions are not significantly different from the previously analyzed basalts of the sheeted dike section and overlying pillow lavas (e.g., Autio and Rhodes, 1983; Etoubleau et al., 1983; Hubberten et al., 1983; Marsh et al., 1983; Sharaskin et al., 1983; Emmermann, 1985; Kempton et al., 1985; Tual et al., 1985; Shipboard Scientific Party, 1988; Autio et al., 1989). Compared with aphyric basalts from the four previous legs to Hole 504B (Table 9), the mean compositions of the aphyric basalts from Leg 140 display nearly complete overlap, particularly if the standard deviations from each mean are taken into account. In order to minimize laboratory bias, the data from Legs 69, 70, 83, and 111 (Autio and Rhodes, 1983;

Table 6 (continued).

Leg	140	140	140	140	140	140	140	140	140	140	140
Site	504B	504B	504B	504B	504B	504B	504B	504B	504B	504B	504B
Core and section	196R-1	197R-2	198R-1	199R-1	199R-1	200R-1	200R-2	200R-3	200R-4	201R-1	202R-1
Interval (cm)	39–42	33–38	61–64	71–76	106–110	86–88	26–31	59–63	23–27	19–23	25–29
Piece #	9	6	16	17	25A	17A	4A	8B	6	5	7
Lithologic unit	222	223	223	226	227	227	227	227	227	228	229
Depth (mbsf)	1696.9	1698.4	1712.8	1720.1	1720.5	1729.5	1730.4	1732.2	1733.4	1738.0	1747.5
Unit rock name	S-OPC	S-POC	S-POC	M-PCO	M-POC	M-POC	M-POC	M-POC	M-POC	A	S-PO
Average grain size	m	F	F	F	F	F	F	F	F	F	F
Thin section interval											
% Alteration	22	23	18	15	13	13	1.1	16	21	19	11
Sample Wt (g)	29.9	53.6	30.6	21.4	30.3	23.9	36.8	31.5	22.6	24.4	28.3
SiO ₂ (wt%)	49.83	49.30	49.39	49.59	49.31	49.12	49.22	49.33	50.44	49.45	49.62
TiO ₂	0.93	0.75	0.78	0.76	0.74	0.72	0.71	0.73	0.93	0.71	0.82
Al ₂ O ₃	15.18	15.89	15.66	16.17	16.32	16.31	16.11	16.46	14.63	16.24	15.50
Fe ₂ O ₃ *	10.45	9.72	9.94	9.47	9.09	8.96	9.08	9.05	10.57	8.99	9.99
MnO	0.18	0.16	0.17	0.15	0.15	0.15	0.15	0.15	0.19	0.15	0.18
MgO	8.10	9.35	9.27	9.48	9.14	9.27	10.01	9.28	8.27	9.57	8.76
CaO	12.80	12.91	12.85	13.00	13.23	13.13	12.95	13.23	12.71	13.15	13.12
Na ₂ O	1.98	1.81	1.74	1.79	1.77	1.81	1.76	1.79	2.01	1.72	1.81
K ₂ O	0.002	0.006	<0.001	0.004	0.003	0.004	0.003	0.003	0.004	0.004	0.002
P ₂ O ₅	0.07	0.04	0.07	0.09	0.05	0.05	0.04	0.05	0.08	0.08	0.04
Total (Anhydrous)	99.52	99.94	99.87	100.51	99.81	99.52	100.04	100.08	99.83	100.06	99.84
H ₂ O ⁺	1.50	1.40	1.08	1.16	1.02	1.35	1.30	1.48	1.27	1.16	0.97
CO ₂	0.04	0.05	0.03	0.06	0.03	0.03	0.02	0.02	0.03	0.03	0.04
Nb (ppm)	0.4	0.5	<0.3	0.5	0.5	0.3	<0.3	<0.3	0.4	0.3	<0.3
Zr	45.4	36.5	39.3	39.9	39.2	39.1	37.5	38.6	37.3	44.7	40.5
Y	24.5	20.9	21.8	18.7	19.0	19.1	18.4	18.7	18.0	23.8	23.0
Sr	49.2	51.1	52.9	63.4	65.9	65.8	66.2	64.6	62.5	54.0	51.4
Rb	<0.4	<0.4	<0.4	<0.4	<0.4	<0.4	<0.4	<0.4	<0.4	<0.4	<0.4
Zn	53.4	56.5	54.5	59.5	53.5	52.6	49.6	64.3	61.9	42.5	53.3
Cu	77.6	95.1	96.0	89.0	87.2	88.0	86.6	89.0	89.0	80.0	136.4
Ni	90.7	154.6	147.5	168.7	154.5	161.2	188.9	160.0	177.4	85.6	114.8
Cr	280	352	359	412	414	428	427	392	409	217	369
V	325	247	260	241	241	230	218	225	233	326	282
Mg'-value	0.630	0.679	0.672	0.688	0.689	0.695	0.708	0.693	0.633	0.701	0.659
CaO/Na ₂ O	6.465	7.133	7.385	7.263	7.475	7.254	7.358	7.391	6.323	7.641	7.249
Zr/Y	1.853	1.746	1.803	2.134	2.063	2.047	2.038	2.064	2.072	1.878	1.761

Kempton et al., 1985; Autio et al., 1989) selected for this comparison were produced in one laboratory.

The addition or subtraction of phenocryst phases in Leg 140 diabases does not impose a large degree of chemical variability. The compositional ranges of fresh phyruc and aphyric samples are roughly equivalent, although the more phyruc samples exhibit somewhat more variability (Fig. 55 and Table 10). Higher Al₂O₃ abundances and CaO/Na₂O ratios in the phyruc samples is consistent with small amounts of plagioclase accumulation. Increased variability could be also be attributed to sample sizes that are too small to be representative of a moderately phyruc lithologic unit. To help evaluate this type of variation (e.g., Clanton and Fletcher, 1976), the weights of samples prior to grinding are recorded in Table 6 and appropriate petrographic information is given in the "Igneous Petrology" section, this chapter.

Chemical Variability with Depth

With the extension of Hole 504B to 2,000 mbsf, several general observations can be made about compositional variations with depth. The first is that there appears to be no major igneous enrichment or depletion trends with depth, nor are there large-scale trends reflecting increased or decreased fractionation throughout the sampled crustal section (Figs. 56 and 57). Secondly, there are distinct trends of shorter duration (200–400 m), the origins of which are unclear at this time. Two such trends appear to converge near 1550 mbsf, where it appears that the scatter in the Mg'-value (molar MgO/MgO + FeO) is increasing with depth, a trend that is the reverse of that observed in the previous 200 m. Similar inflections occur in SiO₂, Fe₂O₃*, TiO₂, and MnO abundances at 1550 mbsf. Calcium, on the other hand, appears to be increasing gradually over the 1400 mbsf to 2000 mbsf interval. Compatible trace elements Ni and Cr co-vary in concert with the

Mg'-value, indicating increased variability in olivine and possibly Cr-spinel. The variation of Cr and its relationship with the presence of Cr-spinel is discussed further in the "Igneous Petrology" section, this chapter. Incompatible element Zr and the ratio Zr/Y exhibit slight decreases at the 1550 mbsf depth, followed by little or no change with depth. This variation, however, is small enough to be the result of analytical differences between the shipboard and shorebased laboratory. The apparent decrease in the scatter of Sr data at 1550 mbsf is probably due to plotting only "fresh" Sr values for the Leg 140 data, whereas no water data were available to help sort out the altered samples from the previous legs. Coordinating data from the geophysical logs, grain-size data, and alteration logs could provide clues to determining which factors control these trends.

The Effect of Alteration on Bulk-rock Chemistry

As previously noted, alteration processes play an important role in the overall composition and variability of the Leg 140 samples. This section will describe the general bulk-chemical trends observed by the Leg 140 Shipboard Scientific Party. For more detailed treatments, the reader is referred to the "Alteration and Metamorphism" section of this chapter, as well as studies from previous legs to Hole 504B (e.g., Alt et al., 1986; Ishizuka, 1989; Kusakabe et al., 1989).

The chemical and mineralogic effects of high temperature alteration can be manifested in various ways. Because secondary minerals are mainly hydrous phases (actinolite, phyllosilicates) we have chosen the bulk structural water content as an indicator of the extent of alteration. When plotted against water content (H₂O⁺), certain "alteration" trends emerge (Fig. 58). With increasing water content, the abundance of Cu, Ti, Zr, and the Zr/Y ratio decreases. In the case of Cu the decrease is from approximately 90 ppm to 10 ppm at about

Table 6 (continued).

Leg	140	140	140	140	140	140	140	140	140	140	140
Site	504B	504B	504B	504B	504B	504B	504B	504B	504B	504B	504B
Core and section	202R-1	203R-1	203R-1	204R-1	205R-1	206R-1	207R-1	208R-1	208R-1	208R-2	208R-3
Interval (cm)	41-45	4-7	39-42	28-32	10-13	47-50	0-4	0-3	50-53	61-65	7-10
Piece #	11	2	12	7	1	1.1	1	1	13	10B	1
Lithologic unit	230	231	232	232	232	235	236	237	239	239	239
Depth (mbsf)	1747.6	1749.1	1749.4	1756.8	1757.1	1761.2	1768.4	1778.0	1778.5	1780.1	1781.1
Unit rock name	M-OP	A	S-PCO	S-PCO	S-PCO	M-COP	A	M-COP	M-OPC	M-OPC	M-OPC
Average grain size	F	m	m-F	m-F	m-F	m-F	F	F	F	F	F
Thin section interval	14-17										
% Alteration	16	2	42	37	72	19	21	9	9	19	75
Sample Wt (g)	19.7	15.2	19.9	23.9	38.3	22.2	42.4	35.3	18.6	24.7	16.6
SiO ₂ (wt%)	48.35	49.80	48.92	48.66	48.66	49.47	50.34	49.11	49.66	49.52	50.00
TiO ₂	0.81	0.89	0.97	0.95	0.94	0.76	0.99	0.72	0.77	0.69	0.56
Al ₂ O ₃	16.10	14.72	15.85	15.92	16.17	16.08	14.42	16.29	16.38	16.52	16.35
Fe ₂ O ₃ *	9.90	10.26	9.54	9.82	9.33	9.11	10.84	8.94	9.22	8.71	10.03
MnO	0.18	0.18	0.16	0.16	0.15	0.16	0.19	0.15	0.17	0.15	0.16
MgO	9.52	8.33	8.94	8.95	8.99	9.02	8.21	9.47	8.41	8.94	8.69
CaO	12.97	13.13	13.62	13.21	13.82	13.21	12.65	13.10	13.33	13.40	11.86
Na ₂ O	1.87	1.94	1.81	1.74	1.73	1.76	1.91	1.81	1.76	1.83	1.83
K ₂ O	0.001	0.008	0.016	0.013	0.014	0.003	0.006	0.002	0.003	0.002	0.012
P ₂ O ₅	0.04	0.06	0.07	0.11	0.12	0.05	0.05	0.04	0.04	0.04	0.03
Total (Anhydrous)	99.74	99.32	99.89	99.53	99.91	99.61	99.60	99.62	99.74	99.80	99.52
H ₂ O ⁺	2.34	1.11	1.69	2.31	1.86	1.92	1.12	1.13	1.07	1.73	3.05
CO ₂	0.06	0.04	0.04	0.05	0.02	0.04	0.04	0.03	0.03	0.04	0.07
Nb (ppm)	<0.3	<0.3	0.9	0.6	0.3	<0.3	<0.3	0.5	0.4	<0.3	<0.3
Zr	39.1	44.3	59.7	59.5	57.2	40.2	49.0	38.1	39.2	33.7	30.6
Y	22.3	24.1	25.2	25.4	24.3	20.3	25.4	18.5	20.4	18.0	13.9
Sr	52.4	51.3	66.0	65.6	64.5	56.8	53.0	65.3	56.2	55.5	57.3
Rb	<0.4	0.4	<0.4	<0.4	<0.4	0.5	<0.4	<0.4	<0.4	<0.4	<0.4
Zn	140.1	61.7	36.7	46.8	56.5	51.5	45.8	53.4	57.6	45.6	54.0
Cu	105.2	92.4	26.6	32.3	18.1	89.8	63.9	86.5	89.1	111.5	12.1
Ni	138.5	95.4	127.0	133.6	143.1	144.6	88.9	166.9	112.2	121.6	125.1
Cr	362	363	380	388	361	445	253	406	403	375	396
V	259	313	300	288	289	259	327	221	264	236	202
Mg'-value	0.679	0.641	0.673	0.667	0.680	0.686	0.625	0.700	0.668	0.693	0.656
CaO/Na ₂ O	6.936	6.767	7.532	7.583	8.007	7.521	6.623	7.244	7.574	7.342	6.481
Zr/Y	1.753	1.838	2.369	2.343	2.354	1.980	1.929	2.059	1.922	1.872	2.201

1.5%–2% water, whereas Ti and Zr abundances are lowered by a factor of two at higher water contents. It is likely that the progressive depletion of Cu is due to the breakdown and removal of sulfide minerals. However, it is unclear which mechanism(s) are responsible for variability of Ti and Zr (and Y), elements that are normally thought of as being largely resistant to alteration effects, particularly the Zr/Y ratio. It is possible that the breakdown of titanomagnetite to titanite or the formation of chlorite and actinolite after clinopyroxene play important roles. Some analyzed samples exhibit small degrees of Ti, Zr, and Y enrichment, and we currently suspect that these three elements are mobile only on a limited scale (centimeter to meter?). Detailed post-cruise examinations of mineralogy and mineral chemistry are required to define the proper mechanisms and constrain the extent of these processes.

We have observed the beginning of an important Zn depletion trend with depth (Fig. 59A). Between 1600 and 2000 mbsf, the Zn abundance in “fresh” samples decreases from approximately 70 to 25 ppm. Although only “fresh” samples were used to construct this figure, Zn may mobilize at lower water contents than our arbitrary upper limit (H₂O⁺ = 1.5 wt%) for “fresh” rocks. We have not observed a clear relationship between Zn abundance and water content (Fig. 60), so perhaps the increased temperature at this level of the oceanic crust becomes an important contributor to the mobilization and loss of Zn from the rocks. This Zn loss from the lower part of the sheeted dike complex may be a source of Zn to hydrothermal fluids analogous to those responsible for the stockwork sulfide mineralization, and corresponding Zn, Cu, and Mn enrichments in the transition zone, approximately 1000 mbsf. A similar Mn depletion trend has not yet been detected, however (Fig. 59B).

Major components SiO₂ and CaO (Fig. 61) do not decrease with increased water content, as was observed in the Leg 83 basalts by

Emmertmann (1985). The silica content in Leg 140 diabases appears to decrease between 2% and 3% H₂O⁺, and then increase in samples containing over 3% H₂O⁺. Similarly, the Mg'-values display no consistent trend with increased water content. Table 11 compares the compositional ranges and means for samples with H₂O⁺ ≤ 1.53% (“fresh”) with the analyses for the altered samples containing more than 1.53% H₂O⁺.

The observed differences between the Leg 140 and Leg 83 data may be the result of different styles of metamorphism acting at these two different levels of the oceanic crust (e.g., Alt et al., 1986). These generalized observations point out the difficulty in characterizing the effects of high-temperature alteration processes by using bulk-chemical analyses.

Brief Discussion of Inter-laboratory Reproducibility

A large volume of geochemical data for rocks from Hole 504B has been generated by various laboratories since drilling began on Leg 69. To ensure uniformity, inter-laboratory standards were established using designated samples from each leg. Nevertheless, significant inter-laboratory variability is observed for samples from the same lithologic units and stratigraphic levels in the hole. To help potential users of the vast data set for Hole 504B and in the interest of accuracy and consistency, we briefly report selected results of a comparative examination of data reported by the various participating laboratories (not shipboard analyses) in DSDP *Initial Reports* and ODP *Scientific Results* volumes. Some results from inter-laboratory standards from Leg 83 are presented, along with an example of all reported analyses for TiO₂, Zr, and Ti/Zr from the hole for illustrative purposes. The reader is referred to a similar comparison, involving a large number of analytical laboratories, in the *Initial Reports* for Leg 69 (Cann et al., 1983). We emphasize that this treatment is for information pur-

Table 6 (continued).

Leg	140	140	140	140	140	140	140	140	140	140	140
Site	504B	504B	504B	504B	504B	504B	504B	504B	504B	504B	504B
Core and section	209R-1	209R-2	210R-1	211R-1	212R-1	213R-1	213R-1	214R-1	214R-1	214R-2	214R-2
Interval (cm)	98-102	30-33	36-39	136-140	4-7	3-6	79-83	24-28	126-129	29-32	100-103
Piece #	14	4	4	30	IB	2	2.1	5A	1.8	7	22
Lithologic unit	240	240	241	241	241	242	243	244	244	244	244
Depth (mbsf)	1788.5	1789.3	1795.3	1799.9	1806.1	1812.5	1813.3	1818.9	1819.9	1818.9	1821.1
Unit rock name	M-OPC	M-OPC	S-POC	S-POC	S-POC	A	S-POC	M-POC	M-POC	M-POC	M-POC
Average grain size	F	F	F	F	F	m	F	m	m	m	m
Thin section interval	48-51										
% Alteration	18	10	24	18	0	8	2	9	4	4	12
Sample Wt (g)	42.2	36.1	30.3	42.5	17.5	15.1	19.4	28.3	21.6	25.1	28.3
SiO ₂ (wt%)	49.34	48.96	49.73	49.33	49.34	50.47	49.89	49.13	49.05	49.36	49.02
TiO ₂	0.39	0.67	0.82	0.78	0.80	1.07	0.98	0.53	0.80	0.69	0.79
Al ₂ O ₃	15.99	17.87	15.78	15.59	15.58	14.30	14.79	15.92	16.66	17.16	16.16
Fe ₂ O ₃ *	11.15	8.14	9.55	9.82	9.81	11.06	10.76	9.86	9.57	8.12	9.60
MnO	0.16	0.14	0.16	0.16	0.16	0.17	0.18	0.13	0.15	0.12	0.16
MgO	9.22	8.25	8.65	8.77	8.84	7.79	8.29	9.67	8.29	9.12	8.70
CaO	11.54	13.61	13.11	12.96	13.05	12.73	12.86	12.10	13.00	13.65	13.12
Na ₂ O	1.82	1.83	1.92	1.83	1.83	1.91	2.04	1.73	1.81	1.93	1.77
K ₂ O	0.024	0.004	0.001	0.001	0.005	0.007	0.005	0.016	0.004	0.006	0.002
P ₂ O ₅	0.01	0.04	0.04	0.04	0.04	0.13	0.07	0.10	0.11	0.04	0.09
Total (Anhydrous)	99.64	99.51	99.75	99.28	99.45	99.63	99.87	99.19	99.44	100.19	99.42
H ₂ O ⁺	3.00	1.46	0.99	1.24	1.29	1.80	1.09	2.31	1.51	1.84	1.69
CO ₂	0.03	0.04	0.04	0.04	0.04	0.03	0.02	0.03	0.05	0.02	0.02
Nb (ppm)	<0.3	<0.3	0.4	0.7	0.3	0.4	0.4	<0.3	0.3	<0.3	<0.3
Zr	19.4	34.7	41.5	39.0	39.4	54.6	50.7	26.0	41.1	31.2	39.8
Y	11.0	18.1	21.0	22.2	22.4	27.9	25.8	14.8	22.2	18.1	22.2
Sr	51.7	56.9	57.7	53.3	52.2	52.1	53.3	49.0	55.8	57.8	52.4
Rb	<0.4	<0.4	<0.4	<0.4	<0.4	<0.4	<0.4	<0.4	<0.4	<0.4	<0.4
Zn	60.7	43.8	48.7	46.9	48.8	36.8	68.9	39.3	43.4	34.6	46.3
Cu	13.1	92.5	117.7	98.4	103.0	54.4	89.5	11.2	86.4	13.9	93.9
Ni	134.5	136.7	121.1	124.3	122.4	75.9	92.8	166.0	137.0	149.3	143.7
Cr	418	424	361	361	373	149	250	473	335	384	381
V	198	221	249	269	271	340	315	213	267	245	251
Mg ⁺ -value	0.645	0.690	0.666	0.663	0.665	0.608	0.628	0.683	0.656	0.713	0.666
CaO/Na ₂ O	6.341	7.421	6.826	7.082	7.151	6.668	6.304	7.006	7.198	7.084	7.412
Zr/Y	1.764	1.917	1.976	1.757	1.759	1.957	1.965	1.757	1.851	1.724	1.793

poses only and we make no judgments concerning accuracy of the various data sets. In many cases, the research papers themselves report results on analyses of international reference standards, which should be referred to by potential users to assess the accuracy of the data. We also emphasize that while all of the data are relatively precise, they are not consistently accurate. Therefore, we recommend using data from one laboratory group whenever possible when making inferences about chemical groups or downhole variations, as our example will illustrate. Table 12 summarizes analytical information for the various laboratories reporting data in the DSDP and ODP publications.

Inter-laboratory standards for Leg 83 were 83-504B-77R-1, 44-53 cm, 83-504B-97R-2, 74-89 cm, and 83-504B-130R-2, 44-58 cm. Data from the standards were reported by Kempton et al. (1985) (K), Emmermann (1985) (E), and Tual et al. (1985) (T) and these data are used for Figures 62 through 65. For some elements, Tual et al. (1985) reported both XRF and instrumental neutron activation analysis (INAA) data for the standards which is indicated in the plots. Significant variation is observed between laboratories analyzing splits from the same standards and in all cases, results from at least one laboratory are outside of reported analytical uncertainty for the plotted elements. In general, the data are consistently displaced relative to one another implying that the values are internally precise, but plot outside of the reported limits of analytical precision.

To illustrate the practical impact of such data disagreement, we plot Ti, Zr, and Ti/Zr vs. depth in Figure 66. TiO₂ does not show any significant variation as a function of laboratory, but differences become evident in the plot of Zr vs. depth, and are strikingly pronounced in the plot of Ti/Zr vs. depth. Elemental ratios are commonly used in geochemical discussions and modeling to point out fundamental differences in source composition, melting proportions, assimilation components, and fractional crystallization effects. Samples from the

same stratigraphic levels and lithologic units analyzed by different laboratories produce a bimodal variation in Ti/Zr in the lower part of Hole 504B. This variability is almost certainly artificial and petrogenetic inferences made on the basis of data from different laboratories should be made with a great deal of caution.

STRUCTURE AND DEFORMATION

Introduction

This report is largely based on observations from hand specimens and thin sections from the core recovered in Legs 137 and 140, complemented by additional information from paleomagnetic and logging studies. The methodology adopted in making these observations and measurements is described in the "Explanatory Notes" chapter, this volume. The structure log is included as Appendix J. The hand-specimen descriptions and the thin-section descriptions are available from the ODP database.

Gross Structure

Two oriented chilled dike contacts have been recovered on Leg 140 (Fig. 67), which yield true dips of 79° and 84°, consistent with the steep (70° to vertical) dike dips recorded on Leg 111. Application of the paleomagnetic technique suggests that these dikes strike approximately east (094° and 074°, respectively), parallel to the spreading axis and to trends in the local bathymetry, and dip to the north, toward the axis. The seismic-reflection data over Hole 504B (Langseth et al., 1988; Fig. 68) support this, as they can be interpreted as representing a series of half-graben structures, with faults dipping towards the axis, and crustal blocks that tilt gently (<5°) away from the spreading axis.

Table 6 (continued).

Leg	140	140	140	140	140	140	140	140	140	140	140
Site	504B	504B	504B	504B	504B	504B	504B	504B	504B	504B	504B
Core and section	215R-1	216R-1	217R-1	219R-1	220R-1	220R-1	221R-1	221R-1	222R-1	221R-1	221R-1
Interval (cm)	0-4	66-68	23-26	7-11	2-5	27-30	4-7	40-44	9-12	101-104	129-132
Piece #	1	14	6	3	1	7	2	10ID	1	9	24
Lithologic unit	244	245	246	249	251	252	253	254	254	255	256
Depth (mbsf)	1823.0	1828.6	1837.6	1856.3	1865.5	1865.8	1875.1	1875.4	1884.7	1885.6	1885.9
Unit rock name	M-POC	M-COP	M-PO	A	A	S-COP	M-COP	M-COP	M-COP	S-OCF	A
Average grain size	M	F	F	m	F	F	F	F	F	F	F
Thin section interval											
% Alteration	14	7	7	20	42	16	8	n.d.	3	5	66
Sample Wt (g)	22.4	21.9	11.9	14.6	13.2	12.2	14.0	28.8	4.9	20.2	24.3
SiO ₂ (wt%)	49.30	49.47	50.22	50.46	50.62	48.54	49.71	47.96	50.34	50.44	48.68
TiO ₂	0.78	0.87	0.88	0.85	1.04	0.80	0.87	1.05	0.88	1.00	1.05
Al ₂ O ₃	15.90	15.15	15.42	14.29	14.56	16.18	15.75	16.40	14.92	14.52	16.73
Fe ₂ O ₃ *	9.75	10.56	10.15	10.93	10.26	10.07	9.82	9.83	9.87	11.23	9.96
MnO	0.16	0.18	0.17	0.19	0.17	0.17	0.16	0.16	0.19	0.18	0.15
MgO	8.70	8.46	8.05	8.35	7.74	8.93	8.23	9.16	7.80	8.07	9.03
CaO	12.94	13.09	13.06	12.88	12.89	13.21	13.31	13.47	13.27	12.60	12.78
Na ₂ O	1.78	1.77	1.82	1.93	2.23	1.86	1.85	1.63	2.11	1.92	1.76
K ₂ O	0.006	0.003	0.004	0.009	0.021	0.007	0.006	0.006	0.008	0.006	0.010
P ₂ O ₅	0.12	0.05	0.05	0.07	0.06	0.04	0.06	0.08	0.06	0.06	0.07
Total (Anhydrous)	99.44	99.59	99.82	99.96	99.58	99.80	99.76	99.75	99.43	100.03	100.21
H ₂ O*	1.51	1.90	1.69	1.32	1.30	2.24	1.76	2.85	1.33	2.46	2.70
CO ₂	0.02	0.02	0.03	0.04	0.04	0.04	0.05	0.03	0.13	0.03	0.03
Nb (ppm)	0.4	<0.3	<0.3	<0.3	0.6	0.3	<0.3	0.8	n.d.	<0.3	0.9
Zr	37.3	42.8	45.3	38.6	51.8	39.9	45.2	66.0	n.d.	48.7	65.6
Y	21.1	24.1	23.8	23.5	26.8	22.4	23.9	26.5	n.d.	26.7	25.5
Sr	52.1	49.1	52.6	43.4	60.6	51.3	52.6	61.0	n.d.	50.9	66.3
Rb	<0.4	<0.4	<0.4	<0.4	<0.4	<0.4	<0.4	<0.4	n.d.	<0.4	<0.4
Zn	43.9	76.1	67.5	59.4	28.0	61.0	55.9	35.9	n.d.	43.6	31.7
Cu	87.7	100.2	90.1	134.3	21.3	96.3	76.6	16.9	n.d.	94.4	14.1
Ni	144.1	99.8	97.1	83.4	77.7	136.5	102.4	154.8	n.d.	79.2	140.4
Cr	365	274	265	200	211	383	324	258	n.d.	182	308
V	263	297	294	329	343	270	293	273	n.d.	326	286
Mg'-value	0.662	0.638	0.636	0.627	0.624	0.661	0.648	0.672	0.635	0.613	0.666
CaO/Na ₂ O	7.270	7.409	7.185	6.674	5.775	7.114	7.214	8.264	6.289	6.563	7.261
Zr/Y	1.768	1.776	1.903	1.643	1.933	1.781	1.891	2.491	-----	1.824	2.573

No significant fault rocks (i.e., cataclasites, slickensided phacoids, etc.) have been recovered, and we see little evidence for local increases in the intensity of microfaulting, so it is unlikely that we have drilled, but not recovered, a major fault zone.

Structural features recorded from the recovered core are restricted to some primary igneous fabrics, crystal fracturing, dike margins, veins, and fractures.

Primary Igneous Characteristics

All the samples from Leg 140 cores which were selected for thin-section descriptions exhibit well-preserved primary (igneous) characteristics (Table 13). The primary igneous textures are only lost in alteration halos around veins and patches where recrystallization may be extensive.

From Core 140-504B-187R to -238R, the recovered rocks do not exhibit any evidence for pervasive deformation or for incipient recrystallization, so that the ophitic to intergranular texture of the diabase is well preserved (see "Igneous Petrology" section, this chapter).

The fabric of the recovered rocks, as seen in thin section, is characterized by the absence of any planar or linear anisotropy, although a systematic measurement of the crystal orientations has not been carried out. However, in some samples, preferred orientation of subprismatic plagioclase groundmass laths (140-504B-186R-1, 53-57 cm (Piece 10)) or phenocrysts (140-504B-208R-1, 0-3 cm (Piece 1); 140-504B-213R-1, 32-34 cm (Piece 11)) has been observed. In the first case, this arrangement of plagioclase seems to be localized in a very restricted area of the thin section, and the laths are aligned vertically (Fig. 69). This may suggest the occurrence of flow orientation of the plagioclase laths and, accordingly, it must be regarded

as a primary feature and not as a later anisotropy related to ductile deformation. Preferential orientation of plagioclase laths has also been observed in samples recovered from close to a chilled margin (Sample 140-504B-219R-1, 7-11 cm, (Piece 3)). The rock exhibits a very fine grained porphyritic texture, with the plagioclase phenocrysts oriented subparallel to the chilled margin.

In addition to "flow texture," other characteristics apparently related to localized strain fields have been detected. Augite crystals in the groundmass show undulose extinction in most of the observed thin sections. These features are usually associated with hourglass structures or with radially arranged clinopyroxene crystals of different optical orientation. The hourglass structures are a primary feature resulting from rapid crystal growth. The radial segmentation of augite crystals is interpreted as resulting from fracturing of the crystals as the rock crystallized (Augustithis, 1978 and references therein). Similarly, the occurrence of curved plagioclase groundmass laths in most of the recovered samples, especially in Cores 140-504B-198R to -205R, is considered to be a primary characteristic of the rock, related to its crystallization.

A slight fabric development has been observed in some samples from Core 140-504B-205R down, characterized by (1) localized stretching of the radially arranged augite-plagioclase aggregates (Samples 140-504B-205R-1, 14-17 cm (Piece 1), and 140-504B-205R-1, 87-89 cm (Piece 21)), yet without imparting a preferred orientation; (2) reorientation of plagioclase groundmass laths and amphibole (replacing augite) imparting a very weak, poorly defined preferred orientation (Sample 140-504B-205R-1, 14-17 cm (Piece 1)); and (3) preferred orientation of mineral phases (amphibole, plagioclase) in a narrow band at the contact between the host rock and the chilled margin (Fig. 70), and weak preferred reorientation

Table 6 (continued).

Leg	140	140	140	140	140	140	140	140	140	140	140
Site	504B	504B	504B	504B	504B	504B	504B	504B	504B	504B	504B
Core and section	223R-1	224R-1	224R-1	225R-1	225R-2	226R-1	226R-2	227R-1	227R-2	227R-2	228R-1
Interval (cm)	20-23	21-24	59-62	40-44	46-49	16-20	69-74	90-94	0-5	14-16	52-54
Piece #	6	4	14	10	7	3	10	11	1	2	13
Lithologic unit	258	258	258	259	260	260	260	260	260	260	262
Depth (mbsf)	1894.4	1903.9	1904.3	1912.6	1914.2	1920.2	1920.7	1925.4	1926.0	1926.2	1934.5
Unit rock name	M-CPO	M-CPO	M-CPO	A	M-COP	M-COP	M-COP	M-COP	M-COP	M-COP	M-OCF
Average grain size	F	F	F	F	M	M	M	M	M	M	F
Thin section interval					42-45				76-78	76-78	82-85
% Alteration	6	4	37	52	12	18	20	2	3	2	3
Sample Wt (g)	21.9	27.0	25.7	23.3	38.3	36.6	49.7	49.8	38.7	34.5	29.3
SiO ₂ (wt%)	50.12	49.90	50.17	49.69	49.81	49.08	48.93	49.23	48.80	50.80	49.43
TiO ₂	0.88	0.91	1.02	0.95	0.79	0.76	0.80	0.76	0.78	0.57	0.78
Al ₂ O ₃	15.14	15.14	14.44	15.35	15.63	16.46	16.67	16.56	16.96	16.32	15.73
Fe ₂ O ₃ *	10.27	10.55	11.38	10.09	10.00	9.62	9.78	9.51	9.56	8.85	9.86
MnO	0.18	0.18	0.18	0.17	0.17	0.17	0.16	0.16	0.16	0.14	0.17
MgO	8.32	8.25	8.19	8.65	8.94	8.92	8.69	8.74	8.85	8.30	9.54
CaO	12.84	12.93	12.34	13.11	13.08	12.96	12.90	13.12	13.06	11.91	12.95
Na ₂ O	1.75	1.83	2.08	1.94	1.86	1.80	1.84	1.83	1.91	2.52	1.89
K ₂ O	0.004	0.001	0.009	0.010	0.005	0.005	0.007	0.006	0.005	0.016	0.006
P ₂ O ₅	0.06	0.05	0.07	0.06	0.08	0.05	0.08	0.08	0.06	0.03	0.06
Total (Anhydrous)	99.56	99.74	99.87	100.03	100.37	99.81	99.85	100.00	100.14	99.45	100.42
H ₂ O*	1.76	1.35	0.84	0.91	1.18	1.17	1.58	1.17	1.96	1.97	1.14
CO ₂	0.03	0.03	0.03	0.04	0.02	0.02	0.03	0.02	0.02	0.02	0.02
Nb (ppm)	<0.3	0.5	0.4	0.3	<0.3	<0.3	<0.3	<0.3	<0.3	0.4	0.3
Zr	44.6	46.5	48.4	57.5	38.1	37.6	40.5	38.4	38.9	27.8	39.1
Y	24.2	24.6	27.5	23.5	21.8	21.0	22.1	21.3	21.8	15.2	22.0
Sr	53.5	54.8	50.7	75.7	56.0	57.2	57.3	58.1	57.1	77.0	54.7
Rb	<0.4	<0.4	<0.4	0.9	<0.4	0.4	<0.4	<0.4	<0.4	<0.4	<0.4
Zn	67.7	63.9	34.2	26.0	53.0	39.3	39.7	36.9	40.0	30.7	49.2
Cu	88.9	86.2	75.0	73.6	89.6	88.6	121.9	118.8	139.7	9.6	92.3
Ni	99.5	100.4	86.0	112.1	129.2	144.4	157.7	154.4	151.6	135.7	136.6
Cr	284	262	184	415	371	346	326	364	332	391	366
V	301	300	342	282	252	251	245	241	240	221	259
Mg'-value	0.641	0.632	0.613	0.654	0.663	0.671	0.662	0.669	0.671	0.674	0.680
CaO/Na ₂ O	7.333	7.066	5.931	6.758	7.017	7.216	7.011	7.169	6.838	4.732	6.853
Zr/Y	1.843	1.890	1.760	2.447	1.748	1.790	1.833	1.803	1.784	1.829	1.777

of plagioclase laths in the adjacent area (host rock). These occasional (related to the recovery percentage) occurrences of fabric anisotropy are probably related to dike intrusion.

The occurrence of well-preserved igneous characteristics and the homogeneity of the rock fabric, the absence of any pervasive foliation, and incipient recrystallization suggest that the recovered rocks have not been affected by pervasive ductile deformation, which should occur in the transition from brittle to ductile behavior.

Crystal Fracturing

Brittle deformation affects the recovered rocks not only by structures cutting through the rock (veins, fractures) but also by deforming the rock-forming crystals. Plagioclase laths and phenocrysts are usually more extensively fractured than clinopyroxene groundmass grains and phenocrysts.

Plagioclase crystals are cut by (1) curvilinear and radiating cracks, of micrometer thickness, which are usually unfilled and are more concentrated in the upper Leg 140 cores; and (2) planar microfractures, (5–30 μm wide) orthogonal to the elongation direction of the crystals. They are usually filled by chlorite or amphibole (± anhedral albite), and sometimes associated with granulation of opaque minerals.

Clinopyroxene crystals exhibit (1) cracks which were probably formed by differential contraction during cooling are arranged radially from the cores some of which enclose plagioclase; and (2) microfractures (several micrometers thick) with different orientations, some of which were influenced by the cleavage of the crystals.

These fractures are possibly the result of contraction during cooling followed by dilational growth of alteration products (e.g., Agar, 1990).

The downhole distribution of the cracks and microfractures affecting the crystals (see also Table 13), is quite homogeneous, perhaps

with a slight concentration in the upper cores, although it should be taken into account that thin section observations are not entirely uniformly distributed downhole and are not truly representative of the recovered rocks.

Intrusive Contacts

Several dikelets and chilled margins between diabase dikes have been recovered in the Leg 140 cores. Two of the chilled margins have been oriented (see "Gross Structure," this section).

The chilled margins are characterized by abrupt and planar (Sample 140-504B-213R-1, 45–47 cm (Piece 15)) to highly irregular (Sample 140-504B-221R-1, 0–4 cm (Piece 1)) contacts that in general lack primary brecciation, but may be disrupted by later veining. An exception is Sample 140-504B-187R-1, 11–14 cm (Piece 3), where a complex brecciated and microfaulted contact is developed (Fig. 71).

Evidence for post-emplacement movement on chilled margins is seen in several samples. In Sample 140-504B-203R-1, 33–36 cm (Piece 10), a fractured chilled zone abuts a thin brecciated and sheared zone of fractured plagioclase in a matrix of fine actinolite with a moderately well-developed preferred orientation. The majority of veins in the chilled margin are terminated by the contact with the sheared zone, although a thick chlorite-actinolite vein appears to cut, but is offset within, the faulted zone (Fig. 72). A zone, up to 6 mm wide, of fine-grained actinolite and chlorite, with weakly developed preferred orientation, enclosing lenses of fractured chilled margin and brecciated and sheared diabase separates two chilled margins in Sample 140-504B-219R-1, 7–11 cm (Piece 3) (Fig. 73). A third example comes from Sample 140-504B-221R-1, 11–15 cm (Piece 4) (Fig. 74), where the chilled margin is separated from host rock by a zone of fine-grained actinolite, with brecciated porphyroclasts of

Table 6 (continued).

Leg	140	140	140	140
Site	504B	504B	504B	504B
Core and section	229R-1	233R-1	236R-1	238R-1
Interval (cm)	34–37	4–7	0–4	22–25
Piece #	10	2	1	8
Lithologic unit	265	266	269	269
Depth (mbsf)	1943.9	1967.5	1980.7	1992.3
Unit rock name	S-POC	A	M-POC	M-POC
Average grain size	F	F	F	F
Thin section interval				
% Alteration				
Sample Wt (g)	23.1	14.1	22.9	26.3
SiO ₂ (wt%)	50.27	50.00	49.17	50.00
TiO ₂	0.87	0.87	0.76	0.85
Al ₂ O ₃	14.99	14.65	16.64	15.70
Fe ₂ O ₃ *	9.24	10.23	8.86	9.77
MnO	0.17	0.16	0.15	0.17
MgO	8.63	8.53	8.41	8.46
CaO	13.52	13.18	13.41	13.03
Na ₂ O	1.78	1.87	1.79	1.89
K ₂ O	0.005	0.011	0.004	0.006
P ₂ O ₅	0.06	0.10	0.13	0.08
Total (Anhydrous)	99.54	99.60	99.33	99.96
H ₂ O*	1.30	1.29	1.35	0.83
CO ₂	0.03	0.03	0.02	0.02
Nb (ppm)	0.5	<0.3	<0.3	<0.3
Zr	46.1	40.9	39.1	43.1
Y	23.4	24.2	20.6	22.6
Sr	53.5	47.5	61.8	59.1
Rb	<0.4	<0.4	<0.4	<0.4
Zn	22.9	23.7	35.9	52.5
Cu	16.4	19.4	114.2	83.4
Ni	104.5	91.6	127.7	106.4
Cr	450	196	354	367
V	304	329	241	208
Mg'-value	0.673	0.647	0.676	0.656
CaO/Na ₂ O	7.596	7.048	7.483	6.898
Zr/Y	1.970	1.690	1.898	1.907

Table 7. Calculated detection limits and estimates of precision for Leg 140 shipboard analyses.

	Mean	Standard deviation (1 σ)	Maximum	Minimum	Detection limit (2 σ)
(wt%)					
SiO ₂	49.56	0.12	49.76	49.27	n.d.
TiO ₂	0.77	0.01	0.78	0.76	0.004
Al ₂ O ₃	16.35	0.06	16.46	16.24	n.d.
Fe ₂ O ₃	9.09	0.02	9.12	9.06	n.d.
MnO	0.15	0.00	0.16	0.15	0.005
MgO	8.38	0.05	8.45	8.29	n.d.
CaO	13.20	0.02	13.23	13.17	n.d.
Na ₂ O	1.94	0.05	2.04	1.84	n.d.
K ₂ O	0.006	0.001	0.007	0.004	0.001
P ₂ O ₅	0.11	0.01	0.12	0.10	0.004
H ₂ O*	0.92	0.08	1.09	0.78	n.d.
CO ₂	0.07	0.01	0.08	0.06	n.d.
(ppm)					
Nb	0.5	0.1	0.7	0.3	0.3
Zr	39.7	0.2	40.2	39.2	0.4
Y	19.8	0.2	20.1	19.4	0.4
Sr	60.3	0.4	61.1	59.7	0.4
Rb	<0.4	0.2	-	-	0.4
Zn	59.1	0.6	59.7	58.2	0.5
Cu	89.4	0.6	90.3	88.2	0.5
Ni	128	1	129	127	0.6
Cr	359	4	367	353	1.4
V	244	3	249	239	4.2

Precision estimates were made by running shipboard standard BASill (Hole 504B basalt) with each run, and therefore reflect the precision at typical Hole 504B compositions. n.d. – Not determined.

Table 8. Analysis of the Leg 140 inter-laboratory geochemical standard (Sample 137-504B-182M-3, 7–20 cm).

	Mean (n = 12)	Standard deviation	Maximum	Minimum
(wt%)				
SiO ₂	50.59	0.13	50.77	50.37
TiO ₂	0.97	0.00	0.98	0.97
Al ₂ O ₃	14.59	0.05	14.65	14.50
Fe ₂ O ₃ *	11.16	0.07	11.26	11.04
MnO	0.18	0.00	0.19	0.18
MgO	8.02	0.05	8.10	7.93
CaO	12.51	0.03	12.56	12.46
Na ₂ O	1.84	0.04	1.94	1.77
K ₂ O	0.003	0.003	0.010	<0.001
P ₂ O ₅	0.06	0.01	0.09	0.04
Total (anhydrous)	99.94	0.25	100.29	99.47
Mean (n = 8)				
H ₂ O*	1.25	0.06	1.42	1.15
CO ₂	0.03	0.01	0.04	0.01
Mean (n = 6)				
(ppm)				
Nb	0.5	0.1	0.6	0.3
Zr	45.4	0.5	46.2	44.9
Y	25.9	0.2	26.3	25.6
Sr	44.5	0.3	44.8	44.0
Rb	<0.4	0.2	-	-
Zn	75.8	0.4	76.3	75.1
Cu	82.6	0.5	83.6	82.2
Ni	84.1	0.5	84.8	83.2
Cr	175	1.3	177	173
V	331	5.4	336	322

Six separate splits were analyzed. Major elements were determined on duplicate samples, trace elements were determined on single pellets.

plagioclase, which passes into a discontinuous zone of deformed plagioclase and actinolite.

Veining and brecciation of chilled margins are common, often with the majority of fractures confined to the chilled material (e.g., Sample 140-504B-213R-1, 45–47 cm (Piece 15)). Veining may also develop at the contact between chilled material and host lithology, often subparallel to this contact, while minor brecciation may be related to veining (Sample 140-504B-221R-1, 11–15 cm (Piece 4)), or, rarely, the result of cracking due to devitrification and infill by secondary minerals (e.g., Sample 140-504B-222R-1, 0–4 cm (Piece 1)). Intense hydrothermal brecciation of chilled margins has been recorded in two samples. In Sample 140-504B-195R-1, 7–10 cm (Piece 3), chilled material passes through a highly irregular contact into a breccia of altered diabase and three textural types of chill material set in a chloritic matrix. Similar brecciation is observed in Samples 140-504B-216R-1 (Pieces 7 and 8).

At least two dikelets have been recovered: Samples 140-504B-213R-1, 32–34 cm (Piece 11), and 140-504B-201R-1, 10–13 cm (Piece 3). The former appears to terminate in an actinolite vein and has an alteration halo similar to that of the vein, suggesting it intruded the vein (Fig. 75), but as a thin vein of amphibole can be traced along the margin of the dikelet, it seems probable that the vein postdates the dikelet.

The well-defined chilled dike margins indicate that the host diabase had cooled sufficiently to allow quenching. Furthermore, the lack of high-temperature alteration minerals (see "Alteration and Metamorphism" section, this chapter) suggests that subsequent heat from the new dikes was dissipated very rapidly, attesting to a very efficient heat-removal mechanism; probably convective cooling by hydrothermal fluids.

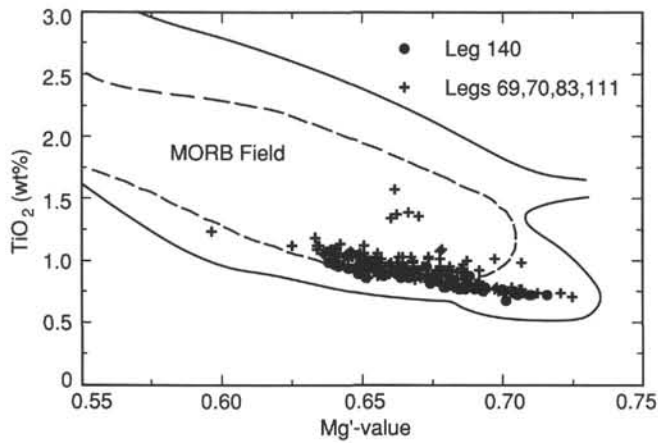


Figure 52. TiO₂ vs. Mg'-value, Hole 504B. The Hole 504B compositions have much lower levels of TiO₂ than most ocean ridge basalts with similar Mg'-values. MORB field constructed from over 1300 analyses of aphyric to sparsely aphyric basalt compositions from Bass et al. (1973), Frey et al. (1974), Melson et al. (1976), Rhodes et al. (1976; 1978), Ballard et al. (1979), Tarney et al. (1979), Byerly and Sinton (1979), Bender et al. (1984), Drake et al. (1985), and J. M. Rhodes (unpubl. data). The solid line denotes the full MORB field, the dashed line encloses 95% of the field. MORB field after Autio et al. (1989). References for Leg 69, 70, 83, and 111 data given in text. Leg 140 shipboard analyses contain less than 1.53 wt% H₂O⁺.

Veins

Interpretation of True-dip Data

In this study we have acquired a large body of true-dip data without corresponding azimuthal control. In their interpretation, the geometry of spherical data must be considered.

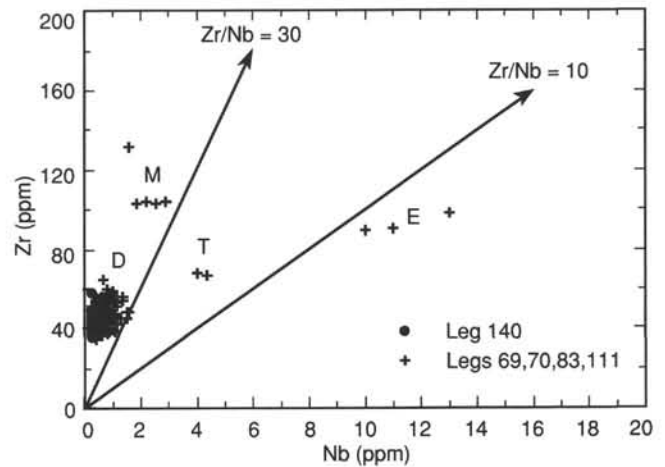


Figure 53. Zr vs. Nb, Hole 504B. Leg 140 compositions all lie within the D-group of Autio and Rhodes (1983). They are extremely depleted in incompatible elements Nb and Zr, but Zr/Nb ratios are similar to those of normal Type I oceanic basalts of Bryan et al. (1976). Data for the enriched E-group lavas from Hole 504B are from Emmermann (1985). Leg 140 shipboard analyses contain less than 1.53 wt% H₂O⁺.

Consider first a purely random distribution of planes. If these are represented by poles, then any given area on a unit hemisphere will, on average, contain the same number of poles, independent of its position on the unit sphere. Within any given interval of dip, the number of poles will depend on an area described by the corresponding arc on the unit sphere. By integration, it can be shown that n, the number of planes with a given dip, a, is given by:

$$n = C \sin \alpha$$

Table 9. Statistics of aphyric basalts and diabbases, Hole 504B.

	Legs 69 and 70 (aphyric only)				Leg 83 (aphyric only)			
	Standard deviation	Average	Maximum	Minimum	Standard deviation	Average	Maximum	Minimum
Major elements (wt%)								
SiO ₂	50.3	0.3	50.7	49.8	50.1	0.5	50.8	48.8
TiO ₂	0.94	0.04	1.00	0.88	1.00	0.08	1.14	0.84
Al ₂ O ₃	15.61	0.56	16.70	14.90	14.83	0.38	16.08	14.31
Fe ₂ O ₃ ⁺	9.97	0.56	10.69	8.83	10.68	0.60	11.62	9.67
MnO	0.18	0.02	0.23	0.16	0.21	0.02	0.26	0.17
MgO	8.28	0.18	8.55	7.99	8.49	0.37	9.09	7.72
CaO	12.68	0.24	12.98	12.17	12.86	0.25	13.18	12.25
Na ₂ O	1.99	0.13	2.20	1.80	1.99	0.19	2.44	1.68
K ₂ O	0.14	0.09	0.36	0.04	0.02	<0.01	0.03	<0.01
P ₂ O ₅	0.08	0.01	0.10	0.06	0.09	0.01	0.11	0.08
Trace elements (ppm)								
Nb	0.5	0.1	0.7	0.4	0.7	0.2	1.1	0.4
Zr	47.5	3.0	53.0	43.0	50.6	5.5	59.0	38.0
Y	23.3	1.4	25.6	21.5	24.7	2.2	28.0	20.5
Sr	66.9	6.0	78.0	57.0	53.4	6.1	66.0	43.0
Rb	2.2	2.0	7.3	0.4	0.5	0.1	0.9	0.4
Zn	78	7	90	66	85	11	104	67
Cu	n.d.	----	----	----	n.d.	----	----	----
Ni	106	19	144	76	93	7	102	76
Cr	362	45	463	282	274	59	355	168
V	279	28	347	231	292	24	326	245
Mg'-value	0.647	0.012	0.671	0.628	0.636	0.021	0.666	0.594
CaO/Na ₂ O	6.39	0.43	7.09	5.66	6.54	0.61	7.73	5.02
Zr/Y	2.04	0.09	2.18	1.90	2.06	0.26	2.84	1.60

Reference for Legs 69, 70, 83, and 111 data are given in the text. Leg 140 aphyric data are for samples containing less than 1.53 wt% H₂O⁺. n.d. - Not determined.

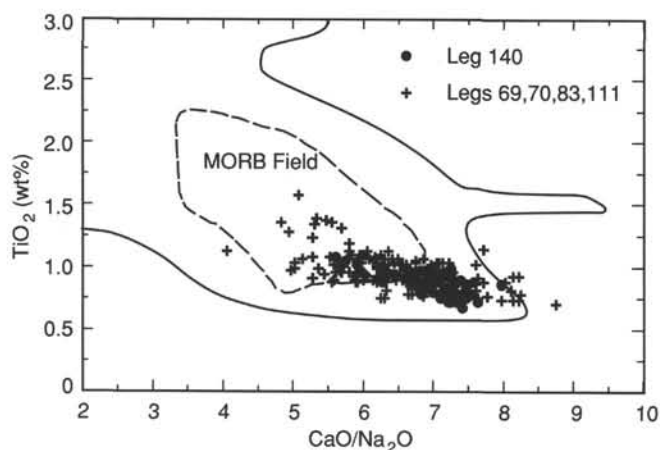


Figure 54. TiO_2 vs. $\text{CaO}/\text{Na}_2\text{O}$, Hole 504B. Basalts and diabases from Hole 504B have $\text{CaO}/\text{Na}_2\text{O}$ ratios greater than most basalts in the MORB field. MORB field constructed as in Figure 53. Leg 140 shipboard analyses contain less than 1.53 wt% H_2O^+ .

where C is a constant. A histogram for a theoretical, random data set is shown in Figure 76. The data are biased to the steeper dips, so a real data set with a similar distribution of true dips may represent a random data set, if the azimuths are random.

A second consideration is the effect of the sampling bias introduced by a vertical borehole, discussed by Newmark, Anderson, Moos, and Zoback et al. (1985). Consider a regularly spaced set of planes. If the planes are horizontal, then the number of planes within a length, l , of borehole is given by:

$$n = l/s$$

where s is the spacing of the planes. For vertical planes, either 1 or 0 planes are encountered. For the general case of dipping planes

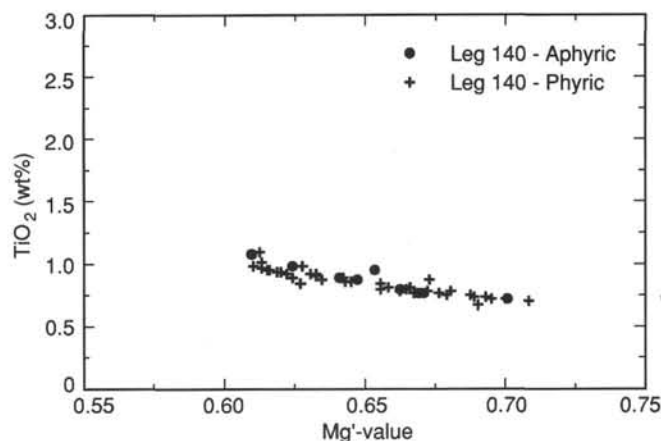


Figure 55. TiO_2 vs. Mg' -value for "fresh" phyrice and "fresh" aphyric Leg 140 basalts. Aphyric and phyrice samples display nearly the same range of Mg' -values and TiO_2 content. Only analyses containing less than 1.53 wt% H_2O^+ are plotted.

$$n = l \cos(\alpha)/s.$$

So this effect tends to bias the data in favor of shallow dips (Fig. 76). If these two effects are combined we arrive at a relationship of the form:

$$n = K \sin(\alpha) \cos(\alpha)$$

which gives a distribution with a peak at 45° inclination (Fig. 76).

Vein Orientations

Orientations of 307 veins have been obtained from Leg 137 and 140 cores. The hand-specimen identification and classification of these veins has been confirmed with the aid of the Vein Log (see "Veins" subsection, "Alteration and Metamorphism" section, this

Table 9 (continued).

	Leg 111 (aphyrice only)				Leg 140 ("fresh" aphyric only)			
	Standard deviation	Average	Maximum	Minimum	Standard deviation	Average	Maximum	Minimum
Major elements (wt%)								
SiO_2	50.3	0.6	51.1	48.9	50.2	0.4	50.6	49.5
TiO_2	0.96	0.12	1.24	0.75	0.95	0.14	1.10	0.71
Al_2O_3	15.23	0.85	16.90	13.80	14.73	0.68	16.24	14.29
Fe_2O_3	10.46	0.84	12.50	9.26	10.55	0.81	11.34	8.99
MnO	0.18	0.01	0.21	0.15	0.18	0.02	0.19	0.15
MgO	8.33	0.41	9.18	7.16	8.33	0.58	9.57	7.74
CaO	12.72	0.40	13.17	11.70	12.77	0.35	13.15	12.18
Na_2O	1.90	0.16	2.22	1.59	2.00	0.18	2.23	1.72
K_2O	0.01	<0.01	0.02	<0.01	0.009	0.006	0.021	0.002
P_2O_5	0.06	0.01	0.08	0.05	0.07	0.01	0.08	0.05
Trace elements (ppm)								
Nb	0.8	0.3	1.5	0.3	0.4	0.2	0.7	0.3
Zr	48.3	5.9	64.4	38.4	48.5	6.3	56.0	38.6
Y	24.5	2.6	30.4	20.1	25.7	2.1	28.5	23.5
Sr	57.9	6.4	66.4	43.7	53.0	6.3	60.6	43.4
Rb	0.4	-	0.4	-	<0.4	----	0.7	<0.4
Zn	74	10	99	55	60	25	103	28
Cu	n.d.	----	----	----	80	34	134	21
Ni	104	28	164	55	85	6	95	78
Cr	252	106	388	26	226	67	363	164
V	271	36	345	213	333	12	346	313
Mg' -value	0.637	0.029	0.686	0.558	0.634	0.031	0.701	0.610
$\text{CaO}/\text{Na}_2\text{O}$	6.75	0.74	8.21	5.27	6.44	0.70	7.64	5.62
Zr/Y	1.97	0.10	2.12	1.78	1.88	0.11	1.96	1.64

Table 10. Comparison of “fresh” phryic and aphyric basalts, Leg 140, Hole 504B.

	Leg 140 “fresh” aphyric				Leg 140 “fresh” phryic			
	Standard deviation	Average	Maximum	Minimum	Standard deviation	Average	Maximum	Minimum
(wt%)								
SiO ₂	50.2	0.4	50.6	49.5	49.9	0.5	50.8	49.0
TiO ₂	0.95	0.14	1.10	0.71	0.85	0.10	1.10	0.67
Al ₂ O ₃	14.73	0.68	16.24	14.29	15.48	0.79	17.87	14.29
Fe ₂ O ₃	10.55	0.81	11.34	8.99	10.00	0.78	11.38	8.14
MnO	0.18	0.02	0.19	0.15	0.17	0.01	0.19	0.14
MgO	8.33	0.58	9.57	7.74	8.54	0.57	10.01	7.74
CaO	12.77	0.35	13.15	12.18	12.95	0.29	13.61	12.18
Na ₂ O	2.00	0.18	2.23	1.72	1.84	0.10	2.11	1.63
K ₂ O	0.009	0.006	0.021	0.002	0.003	0.003	0.010	<0.001
P ₂ O ₅	0.07	0.01	0.08	0.05	0.07	0.02	0.13	0.04
H ₂ O ⁺	1.24	0.13	1.45	1.11	1.27	0.18	1.53	0.83
CO ₂	0.04	0.01	0.05	0.02	0.04	0.02	0.13	0.02
(ppm)								
Nb	0.4	0.2	0.7	0.3	0.4	0.1	0.7	0.3
Zr	48.5	6.3	56.0	38.6	41.8	4.3	54.8	34.7
Y	25.7	2.1	28.5	23.5	22.5	2.7	28.1	18.0
Sr	53.0	6.3	60.6	43.4	52.9	7.5	66.2	42.5
Rb	<0.4	-----	0.7	<0.4	<0.4	-----	0.6	<0.4
Zn	60	25	103	28	57	13	103	23
Cu	80	34	134	21	89	21	144	16
Ni	85	6	95	78	118	32	189	80
Cr	226	67	363	164	324	84	450	164
V	333	12	346	313	281	42	345	208
Mg ⁺ -value	0.634	0.031	0.701	0.610	0.652	0.029	0.708	0.611
CaO/Na ₂ O	6.44	0.70	7.64	5.62	7.07	0.45	7.97	5.93
Zr/Y	1.88	0.11	1.96	1.64	1.87	0.12	2.13	1.64

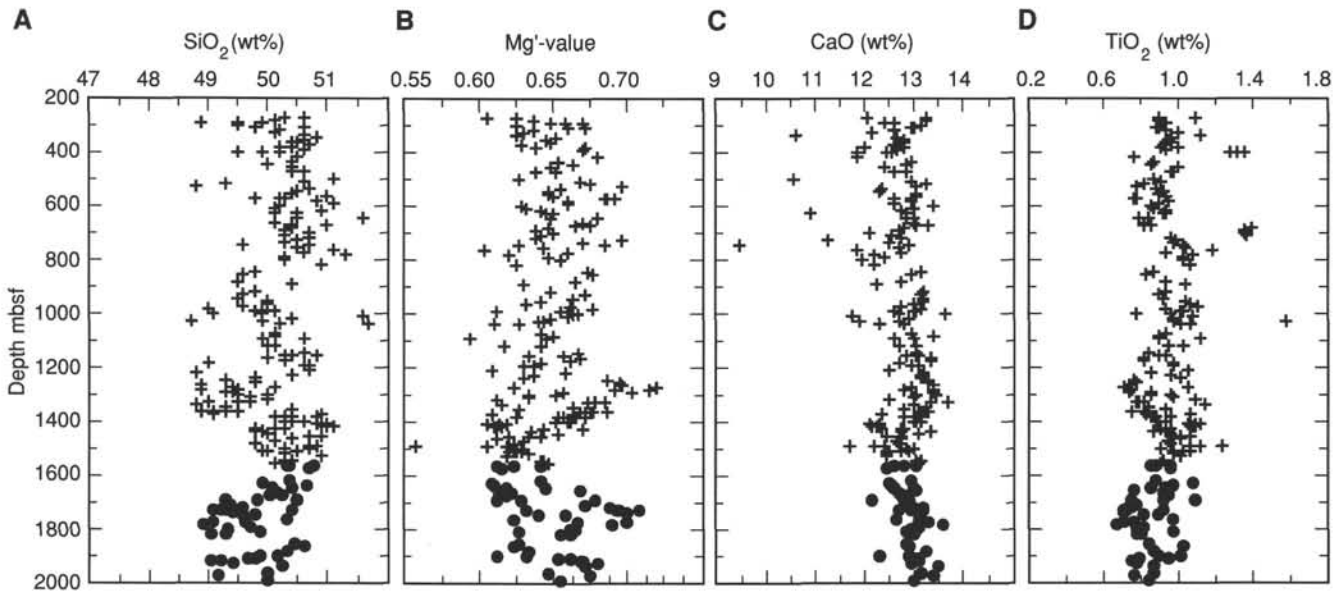


Figure 56. Depth vs. (A) SiO₂, (B) Mg⁺-value, (C) CaO, and (D) TiO₂ for Hole 504B. Symbols are the same as in Figure 52. References for Leg 69, 70, 83, and 111 data given in text. Leg 140 shipboard analyses contain less than 1.53 wt% H₂O⁺.

chapter). These break down into five categories: (1) chlorite-bearing veins, (2) chlorite- and actinolite-bearing veins, (3) actinolite-bearing veins, (4) chlorite- and pyrite-bearing veins, and (5) epidote-bearing veins. However, the relative abundances and occurrences of veins given here should not be taken to be definitive, since many veins occur on pieces that cannot be oriented with respect to the vertical. Of the five categories, the epidote veins are the least abundant, with only nine

measured. These do not exhibit any preferred dip angles (Fig. 77A), therefore they cannot be used to determine the state of stress that existed during their generation.

In hand specimen, the veins appear fairly uniform morphologically. The majority (77%) are planar in shape, with the remaining veins approximately split evenly between curvilinear and sinuous in shape. Few veins were found to be anastomosing or branching. As for

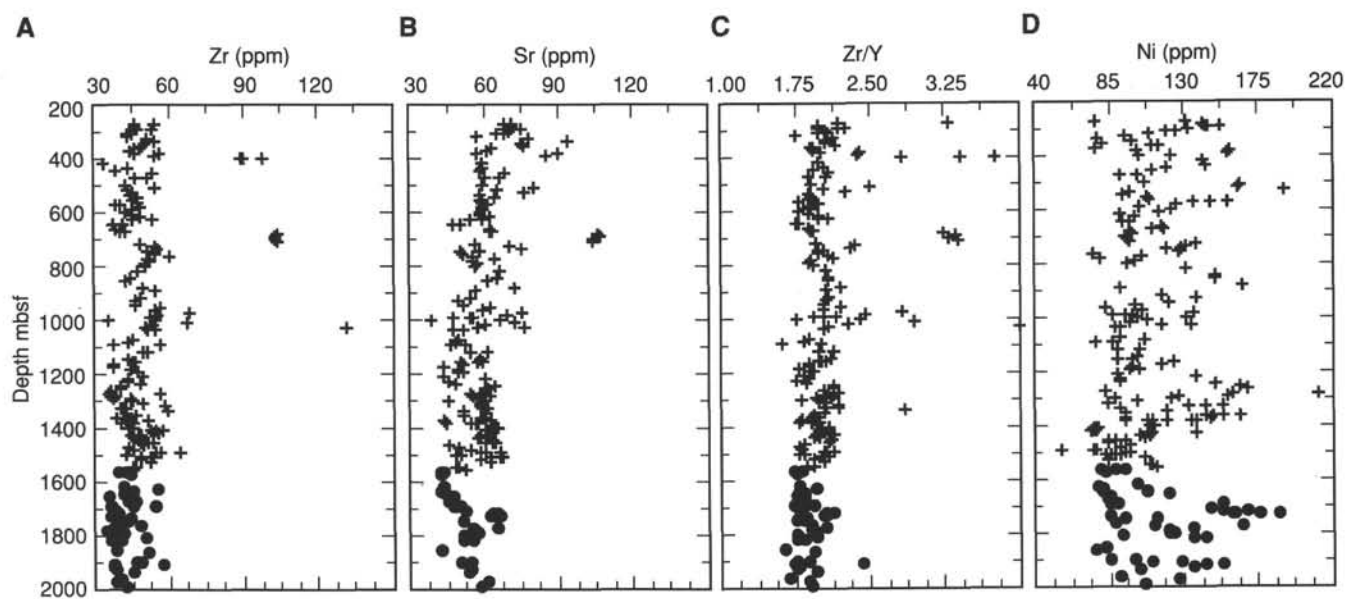


Figure 57. Depth vs. (A) Zr, (B) Sr, (C) Zr/Y, and (D) Ni for Hole 504B. Symbols are the same as in Figure 52. References for Leg 69, 70, 83, and 111 data given in text. Leg 140 shipboard analyses contain less than 1.53 wt% H_2O^+ .

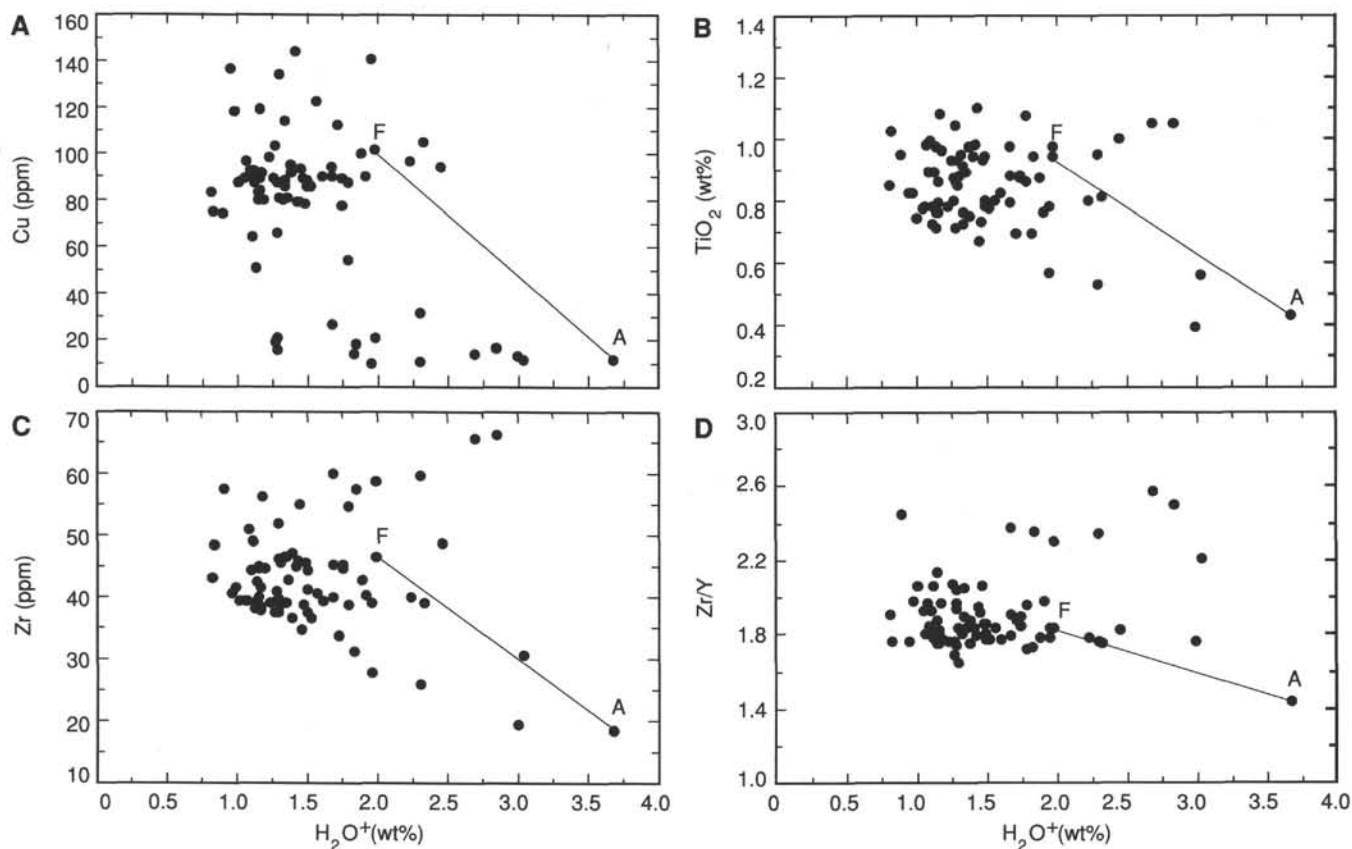


Figure 58. H_2O^+ vs. (A) Cu, (B) TiO_2 , (C) Zr, and (D) Zr/Y for Leg 140 diabases. Symbols A and F denote Samples 140-504B-193R-1, 28–31 cm ($H_2O^+ = 3.68\%$), and 140-504B-193R-1, 44–46 cm ($H_2O^+ = 1.99\%$), respectively. Both of these samples are from Unit 220.

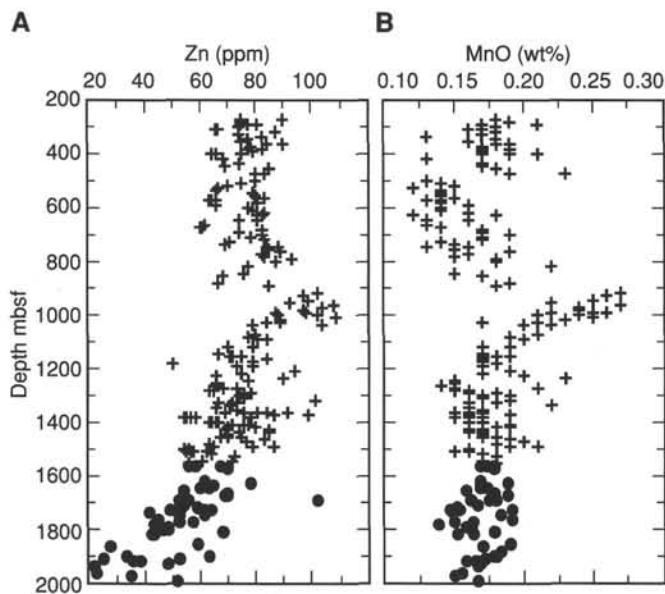


Figure 59. Depth vs. (A) Zn and (B) MnO, Hole 504B. Symbols are the same as in Figure 52. References for Leg 69, 70, 83, and 111 data given in text. Leg 140 shipboard analyses contain less than 1.53 wt% H₂O⁺.

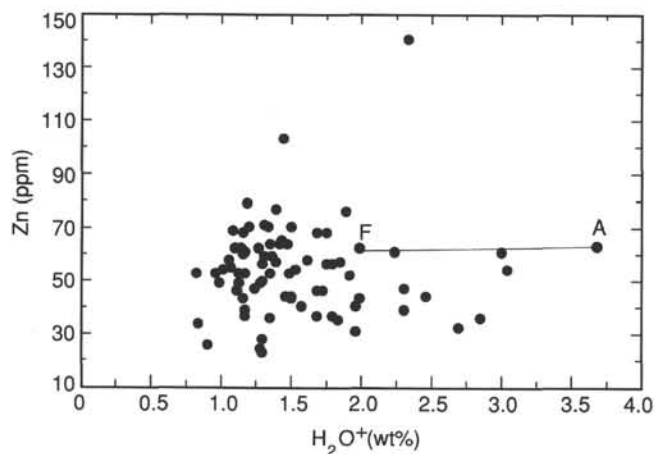


Figure 60. H₂O⁺ vs. Zn, Leg 140 diabases. Symbols A and F are the same as in Figure 58.

the degree of unevenness, most (88%) are smooth, with the rest being irregular, and none were found to be stylolitic.

An analysis of different vein distributions with respect to depth would be at best incomplete here, as the veins noted here are only those from pieces that could have their vertical axis identified (see "Structure and Deformation" section, "Explanatory Notes" chapter, this volume). However, a preliminary investigation showed that the distribution based on the oriented data was similar to the distribution-based data from the Vein Log (see "Veins" subsection, "Alteration and Metamorphism" section, this chapter).

Chlorite Veins

The largest number of veins measured were chlorite-filled veins, with a population of 126. There is a strong mode in their dip angle of between 25° and 30° (Fig. 77B), with a smaller population at 80°–85°.

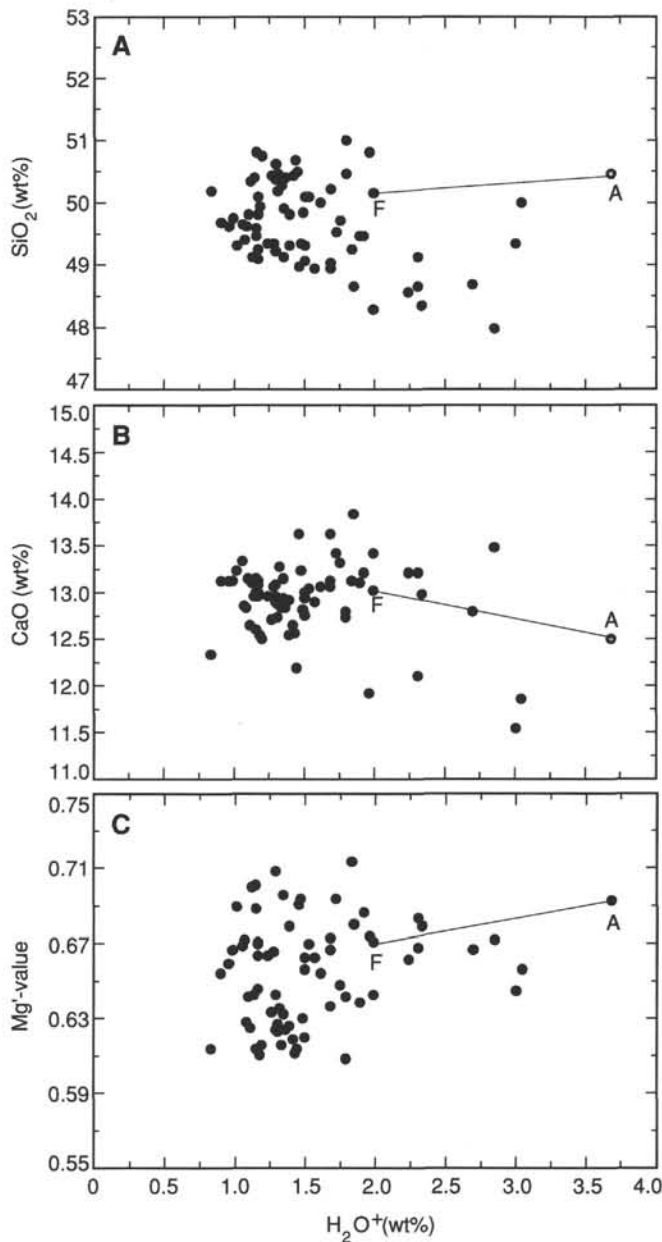


Figure 61. H₂O⁺ vs. (A) SiO₂, (B) CaO, and (C) Mg'-value for Leg 140 diabases. Symbols A and F are the same as in Figure 58.

Chlorite and Actinolite Veins

Seventy-five chlorite and actinolite veins were measured, showing equal modes at 25°–30° and 35°–40° and a smaller peak at 70°–75°, similar to that of chlorite veins (Fig. 77C).

Actinolite Veins

The measurement of 73 actinolite veins shows an overall even distribution of dip angles, with small identical peaks at 10°–15° and 25°–30° (Fig. 77D). The orientation of the actinolite veins is not random despite the evenness of the dip angle distribution, as that would manifest itself as a distribution centered on angles of 45°. However, because of the evenness of the data collected it would be

Table 11. Comparison of "fresh" and "altered" basalts, Leg 140, Hole 504B.

	Leg 140 "Altered"				Leg 140 "Fresh"			
	Standard deviation	Average	Maximum	Minimum	Standard deviation	Average	Maximum	Minimum
(wt%)								
SiO ₂	49.4	0.8	51.0	48.0	49.8	0.5	50.8	49.0
TiO ₂	0.81	0.18	1.07	0.39	0.86	0.10	1.10	0.67
Al ₂ O ₃	15.90	0.70	17.16	14.30	15.43	0.80	17.87	14.29
Fe ₂ O ₃ *	9.83	0.71	11.23	8.12	10.04	0.76	11.38	8.14
MnO	0.16	0.02	0.19	0.12	0.17	0.01	0.21	0.14
MgO	8.75	0.47	9.67	7.79	8.54	0.55	10.01	7.74
CaO	12.94	0.55	13.82	11.54	12.95	0.28	13.61	12.18
Na ₂ O	1.84	0.16	2.52	1.63	1.86	0.13	2.23	1.63
K ₂ O	0.008	0.006	0.024	<0.001	0.004	0.004	0.021	<0.001
P ₂ O ₅	0.06	0.03	0.13	0.01	0.07	0.02	0.13	0.04
H ₂ O*	2.12	0.52	3.68	1.58	1.25	0.18	1.53	0.83
CO ₂	0.03	0.01	0.07	0.02	0.04	0.02	0.13	0.02
(ppm)								
Nb	0.4	0.2	0.9	0.3	0.4	0.1	0.7	0.3
Zr	42.8	12.7	66.0	18.4	42.7	5.2	57.5	34.7
Y	21.7	4.5	27.9	11.0	22.8	2.7	28.5	18.0
Sr	55.8	7.3	77.0	43.5	53.8	7.6	75.7	42.5
Rb	0.4	0.1	0.8	<0.4	0.4	0.1	0.9	<0.4
Zn	52.9	21.0	140.1	30.7	54.4	15.0	102.9	22.9
Cu	62.2	42.7	139.7	9.6	85.9	24.0	143.8	16.4
Ni	125	25	166	76	115	31	189	78
Cr	339	74	473	149	316	84	450	164
V	270	38	340	198	286	42	346	208
Mg'-value	0.662	0.024	0.713	0.608	0.651	0.028	0.708	0.610
CaO/Na ₂ O	7.06	0.68	8.26	4.73	6.99	0.51	7.97	5.62
Zr/Y	1.94	0.28	2.57	1.44	1.88	0.14	2.45	1.64

difficult to constrain the state of stress at the time of generation by their use.

The distribution of chlorite-actinolite veins more closely mirrors that of the chlorite veins than that of the actinolite veins. It is therefore proposed that the chlorite formed first, with a distinct orientation, and subsequently formed actinolite veins either reopened preexisting chlorite veins (and thus have a similar distribution of true dips) or filled fresh fractures. This would be consistent with a crack-seal mechanism of formation (Ramsay, 1980), although, this order of generation cannot be confirmed by the crosscutting relationships seen in either hand specimen or thin section (see "Crosscutting Relationships," this section).

Chlorite and Pyrite Veins

Twenty-four chlorite and pyrite veins have been measured, mostly on the fractured planar surfaces of cores. These dip very steeply (Fig. 77E). This one set of veins is clearly oriented differently than the others, and give the probability curve, the true maximum is likely to be subvertical, reflecting a significantly different stress field.

Paleomagnetic Corrections

Determining the true-dip direction by using the stable paleomagnetic declination (see "Structure and Deformation" section, "Explanatory Notes" chapter, this volume) for 70 veins shows an overall random distribution of dip directions (Fig. 78), with a dominantly shallow orientation, as suggested by the true-dip data. These data may represent the superposition of two sets; one essentially shallowly dipping, and another, random set. This essentially random fabric may reflect a genesis not controlled by a regionally or temporally continuous stress regime, but rather by local stress conditions dominated by high fluid pressures, which may be expected to be active in a hydrothermal field. The shallowly dipping veins are difficult to reconcile in terms of an extensional stress system, and may indicate the presence

of a compressive regime. Of course, it is possible that the randomness of the vein set is artificial, resulting from the application of the paleomagnetic correction. However, the restoration of steeply inclined fractures (see below) and dikes to a consistent strike direction give some confidence in this technique.

Microstructural Characteristics

Several sets of veins crosscutting the diabase have been observed in thin section (Table 13). They represent only selected examples of the veins measured in hand specimen. Under the microscope they show a planar to curvilinear form, occasionally changing morphology and exhibiting branching or anastomosing shapes. Almost all the veins are characterized by irregular walls, very often inheriting the shape of the replacement minerals. Crystals of the host rock that project into the vein have been observed.

The most common vein minerals are chlorite, amphibole, epidote, and quartz, with titanite, laumontite, and pyrite present in minor amounts. Five categories of veins have been recognized on the basis of these filling minerals (see above).

Consideration of the arrangement of the minerals filling the veins is important for understanding how they formed. Different examples from thin sections have been described as follows: (1) random orientation of the crystals, especially of amphiboles, which frequently exhibit bent and folded shapes; (2) regular orientation of the crystals with elongation direction perpendicular to the vein edges (quartz + epidote vein in Sample 140-504B-192R-1, 13–14 cm (Piece 4). In this example, however, quartz crystals are locally elongated oblique to the vein edges (Fig. 79); and (3) zoning patterns defined by different orientations of the crystals growing along the vein walls to those in the middle. Two examples of this category are represented by Samples 140-504B-197R-1, 99–101 cm (Piece 22), and 140-504B-198R-1, 70–71 cm (Piece 18). In the first example, amphibole crystals are arranged along the walls with their cleavages orthogonal to the walls. The core of the vein is filled by chlorite flakes parallel to the vein

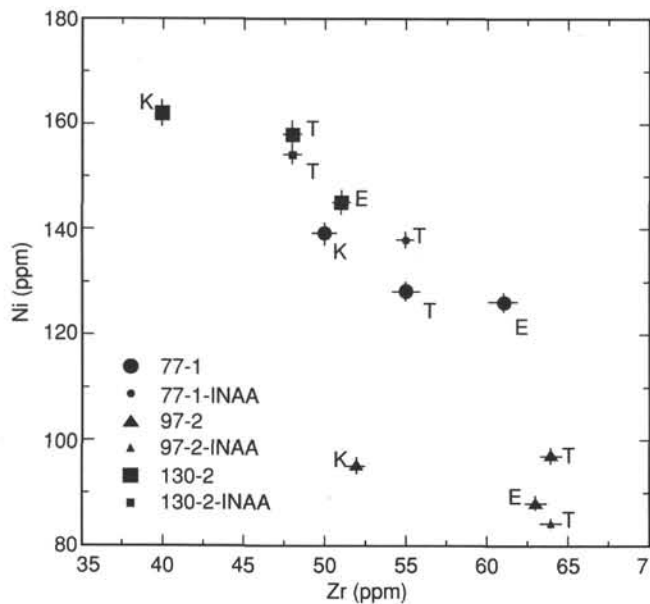


Figure 62. Ni vs. Zr, Leg 83 inter-laboratory standards. See text for explanations.

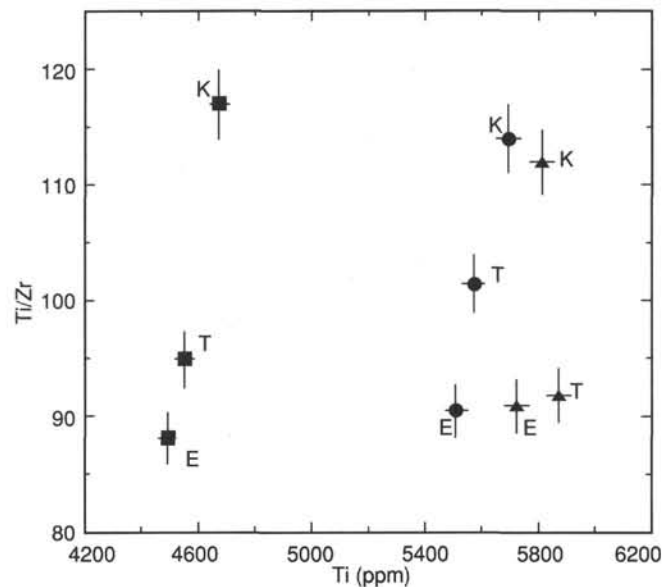


Figure 64. Ti/Zr vs. Ti, Leg 83 inter-laboratory standards. See text for explanations.

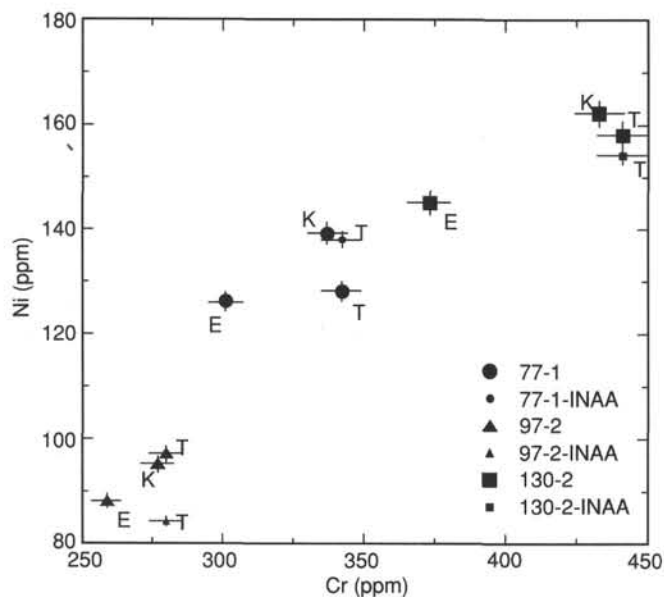


Figure 63. Ni vs. Cr, Leg 83 inter-laboratory standards. See text for explanations.

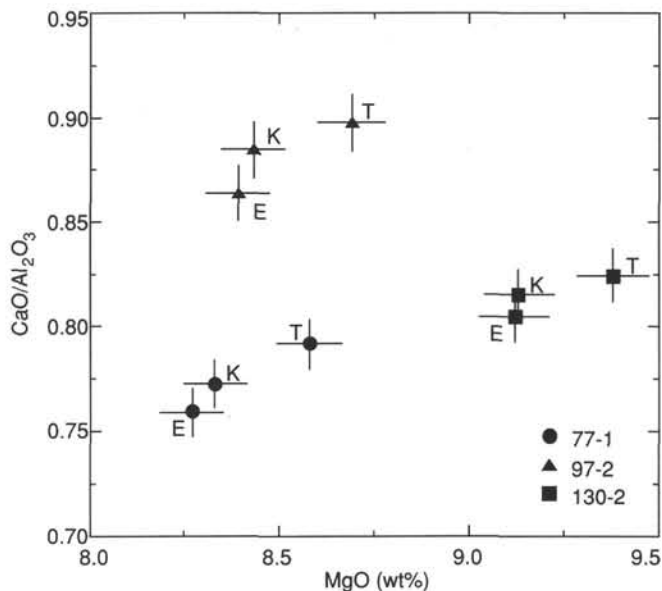


Figure 65. CaO/Al₂O₃ vs. MgO, Leg 83 inter-laboratory standards. See text for explanations.

trend. Locally, the chlorite flakes seem to be arranged into ribbons parallel to the vein trend, and they are underlain by fine-grained opaque minerals. In the second case, chlorite is arranged irregularly along the wall; deformed amphibole crystals with variable orientations fill the core of the vein (Fig. 80), but mostly with cleavage oriented at high angles to the vein edges.

Although in many veins the filling minerals seem to have grown under static conditions, in other cases evidence of deformation inside the veins has been detected. This deformation is strictly localized to the vein and does not seem to affect the host rock. Only in one thin section (Sample 140-504B-186R-1, 53–57 cm (Piece 10)) do crystals of the host rock exhibit preferred orientation parallel to the external walls of an open fracture.

Evidence of ductile deformation inside the veins is represented by bent and/or folded amphibole crystals (Sample 140-504B-189R-1, 105–106 cm (Piece 21B)) (Fig. 81). They exhibit wavy extinctions and sometimes appear to be broken. Their shape seems to suggest the occurrence of shearing deformation, although the sense of movement is not well constrained. Shearing is suggested by the opening of small “pull-aparts” inside a vein which cuts a centimeter-sized clinopyroxene phenocryst (Fig. 82) (Sample 140-504B-186R-1, 17–24 cm (Piece 5)). These voids are filled by chlorite and amphibole crystals (replacing pyroxene clasts?) exhibiting different orientations. The edges of the vein are lined by small amphibole crystals with their cleavages parallel to the vein trend. In the middle of the vein, amphibole crystals (replacing clinopyroxene) are randomly oriented,

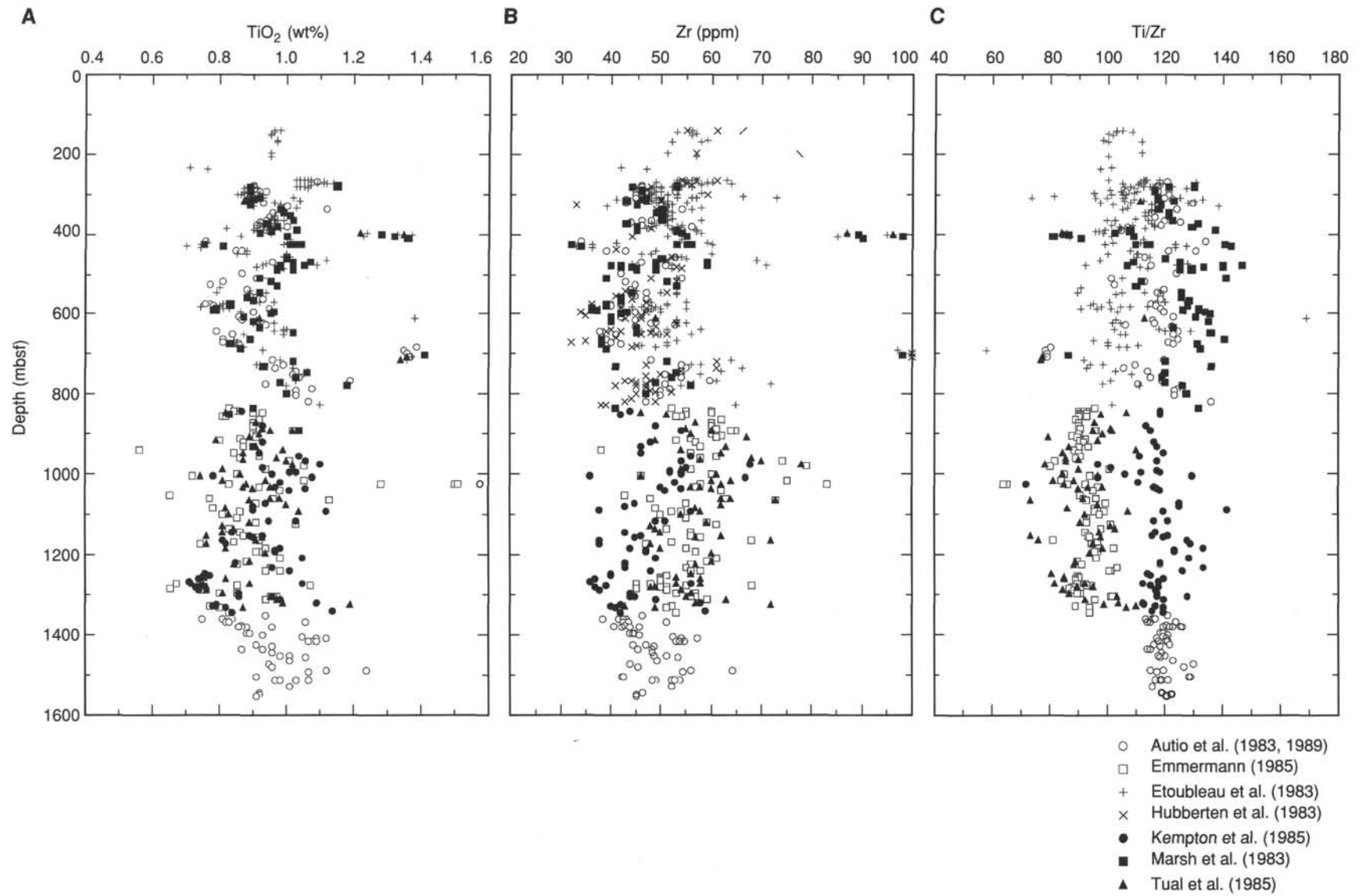


Figure 66. Depth vs. (A) TiO_2 , (B) Zr, and (C) Ti/Zr, Hole 504B, various laboratories.

A



B

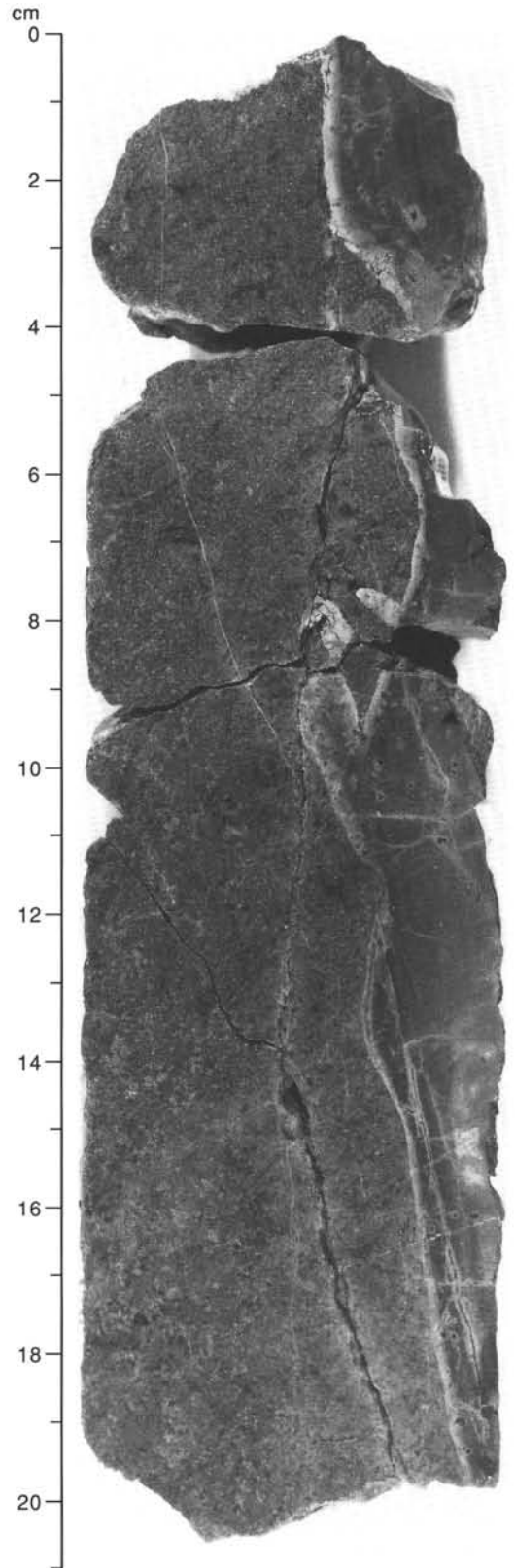


Figure 67. Chilled contacts between dikes in core. (A) Sample 140-504B-213R-1, 45–52 cm (Piece 15). (B) Sample 140-504B-222R-1, 0–23 cm (Piece 1, A–E). Note that apparent dips on cut halves are steep.

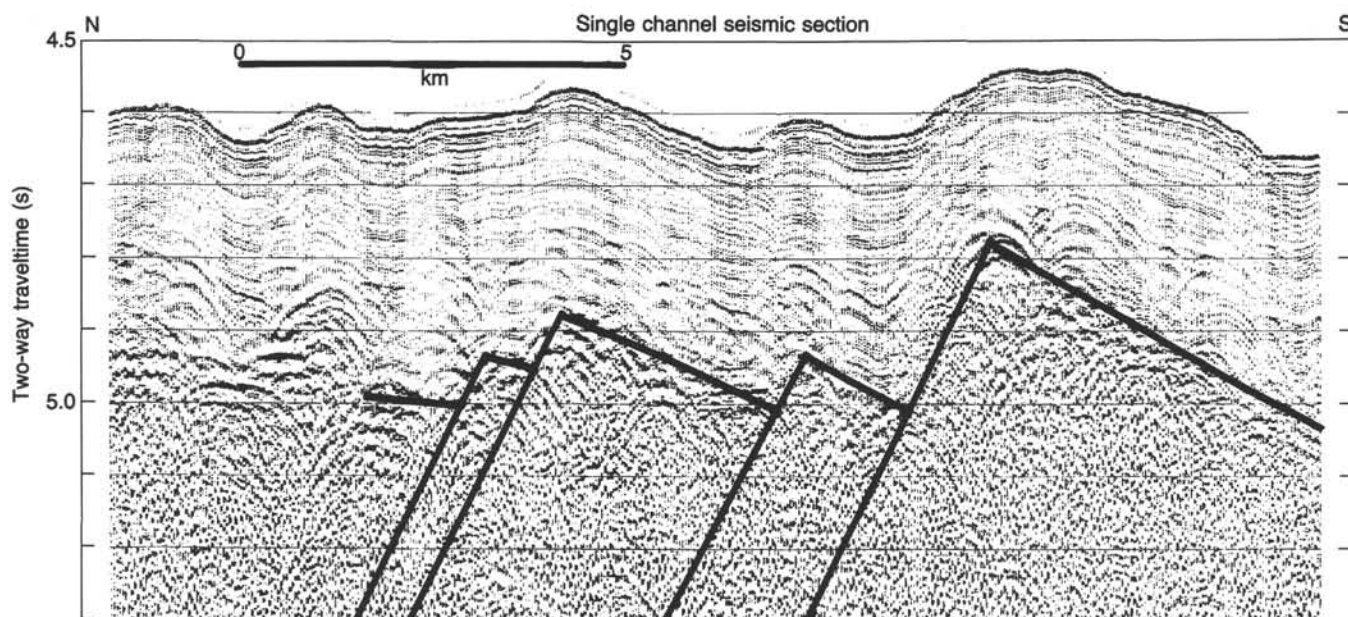


Figure 68. Interpretation of the 3.5-kHz seismic-reflection record which passes close to Hole 504B (from Langseth et al., 1988), as a series of gently ($< 5^\circ$) dipping normal fault blocks.

with their cleavages usually at a high angle to the vein edges. In addition, they sometimes exhibit wavy extinctions. The matrix of the vein is composed of chlorite and small needles of actinolite. Cracking inside the clinopyroxene phenocryst seems to be consistent with the inferred shear movement, which is approximately horizontal.

Evidence for shear is also seen in another oriented thin section (Sample 140-504B-186R-1, 53–57 cm (Piece 10)), where the direction of movement is again close to the horizontal. The vein is filled by amphibole (locally bent crystals), titanite, and laumontite. Shear deformation is inferred by the occurrence of small tension gashes filled by quartz or albite (indistinguishable under the microscope) (Fig. 83). These openings are associated with S-shaped cracks consistent with the inferred sense of movement. In Sample 140-504B-203R-1, 0–3 cm (Piece 1), a vein cutting a chilled margin is apparently deformed by shear and is filled by highly deformed amphibole crystals. The relative sense of movement (the sample is unoriented) seems to be consistent with the offset of a vein in the same chilled margin (see below), suggesting the occurrence of shear deformation even if probably restricted to the segmented chilled margin. On the other hand, this evidence might be consistent with deformation inferred for the host rock/chilled margin contact (see “Intrusive Contacts,” above). The two subhorizontal surfaces characterized by shear deformation correspond to depths of about 1626 mbsf (for Sample 140-504B-186R-1, 53–57 cm (Piece 10)) and 1651 mbsf (for Sample 140-504B-189R-1, 105–106 cm (Piece 21B)).

Brittle deformation during the veining processes is indicated by the occurrence of mineral clasts filling the vein. These clasts are frequently rounded and arranged in a fine-grained chlorite matrix. The best example is represented by Sample (140-504B-186R-1, 13–14 cm (Piece 4)) (Fig. 84). The rock is cut by a vein (0.3–2.0 mm thick) which is filled by chlorite where it cuts the groundmass, by plagioclase clasts and with fine-grained chlorite + amphibole matrix where it cuts plagioclase phenocrysts, and by clasts of clinopyroxene where it cuts the clinopyroxene phenocryst. The occurrence of mineral clasts, which are probably derived from the groundmass or phenocrysts of the host rock inside a vein, suggests that the clasts were brecciated by brittle deformation and/or the action of fluids under high pressure. Even for the vein exhibiting pull-aparts (Sample 140-504B-

189R-1, 105–106 cm (Piece 21B)), some brecciation during formation can be inferred, if only restricted to the clinopyroxene phenocryst, suggested by the shape of the filling minerals (round clasts, prismatic crystals included in a fine-grained matrix). All these features must be taken into account for a better understanding of the evolution and formation mechanism of the veins.

Mode of Vein Formation

The morphology, crystal arrangement, and structural features of the veins observed in thin section may furnish some indication of the formation mechanism of the veins. Considering the different features exhibited by the veins, a unique mechanistic model cannot be constrained, and here the clearest examples are examined, suggesting some possibilities.

The occurrence of highly contorted, folded, and sheared fibrous amphiboles (although in most cases the shear sense is chaotic and cannot be related to a shear displacement along the vein) suggests one possible scenario for the development of these structures (Fig. 85). Fractures are initiated, and open long enough for fine fibrous amphiboles to form. Once the rock returns to the normal stress condition, and the weakened vein suffers compression which deforms the amphibole fill.

Other mechanisms are suggested by the following examples. In Sample 140-504B-190R-1, 75–79 cm (Piece 17), a vein shows a multiple-stage history. The vein itself is about 1 mm wide and is surrounded by a broad alteration halo. It is composite, with a margin of chlorite and a center of actinolite. In two places the vein branches, in one case leaving an isolated “island” of altered groundmass, in the other an isolated branch of chlorite vein. The morphology of the vein is typical of overlapping crack systems described by Pollard and Aydin (1984). The crack probably initiated as a linked, overlapping system, and was filled by chlorite (Fig. 86). Further fracturing allowed the propagation of the vein through the rock as a single, throughgoing system, which was then filled by actinolite.

In Sample 140-504B-197R-2, 9 cm (Piece 2), a small, relatively planar vein is cut by a larger vein, both filled with actinolite. There is no apparent offset of the small vein by the larger one, an observation which can be reconciled with forcible opening of the later vein only

Table 12. Summary of analytical techniques at various laboratories.

Leg	Analyst	Crushing	Technique	Sample preparation	Elements	Standards
69/70	Autio and Rhodes (1983)	W-carbide shatterbox	XRF	Glass disks; pressed-powder pellets	Major elements except Na (Cr-tube). Trace elements: Y, Sr, Rb, Ga (Mo tube); Zr, Nb, Ni, Cr, V (Au tube).	BCR-1
69/70	Autio and Rhodes (1983)	W-carbide shatterbox	Flame photometry	HF/boric acid dissolution	Na	AGV-1, PCC-1
69/70	Autio and Rhodes (1983)	W-carbide shatterbox	Isotope dilution	Flux fusion + acid dissolution	Ce, Nd, Sm, Eu, Gd, Dy, Er, Yb	
69/70	Marsh et al. (1983)	Agate TEMA swingmill	XRF	Powder briquettes	Si, Ti, Al, Fe, Mn, Mg, Ca, Na, K, P, Zr, Nb, Ni, Cr (Rh tube); Y, Sr, Rb, Th, Pb, Ga, Zn, Ba (Mo tube); La, Ce, Nd (W tube)	BOB-1, BCR-1, JB-1
69/70	Etoubleau et al. (1983)		XRF		Major elements, Ti, V, Cr, Mn, Fe, Co, Ni, Zn, Rb, Sr, Y, Zr, Nb	
69/70	Etoubleau et al. (1983)		INAA		Sc, Co, Ni, Sb, Cs, La, Eu, Tb, Hf, Ta, Th	
69/70	Sharaskin et al. (1983)		Wet chemistry		Major elements, H ₂ O ⁺	
69/70	Sharaskin et al. (1983)		XRF		Major elements, Cr, V	
69/70	Sharaskin et al. (1983)		Flame photometry		K, Na, Li	
69/70	Sharaskin et al. (1983)		RNAA		REE	
69/70	Sharaskin et al. (1983)		INAA		Cs, Co, Cu, Zn, Cd, Sb, Au, Ag, Sc, Ta, Hf	
69/70	Hubberten et al. (1983)	Agate mill	XRF	Fused glass disks	Major elements, Na, K, P, Zr, Y, Sr, Zn, Ni	BCR-1, BHVO-1
69/70	Hubberten et al. (1983)		INAA		Fe, Mn, Na, Sc, Cr, Co, Hf, Ta, La, Ce, Nd, Sm, Eu, Gd, Tb, Yb, Lu	BCR-1, BHVO-1
69/70	Hubberten et al. (1983)		AAS		V, Cr, Ni, Cu, Zn	BCR-1, BHVO-1
69/70	Hubberten et al. (1983)		Coulometric titration		CO ₂ , S	BCR-1, BHVO-1
69/70	Hubberten et al. (1983)		Karl Fischer titration		H ₂ O ⁺	BCR-1, BHVO-1
69/70	Hubberten et al. (1983)		Manganometric titration		Fe ²⁺	BCR-1, BHVO-1
83	Kempton et al. (1985)	W-carbide shatterbox	XRF	Glass disks; pressed-powder pellets	Major elements except Na. Trace elements: Y, Sr, Rb, Ga (Mo tube); Zr, Nb, Zn, Ni, Cr, V (Au tube).	BCR-1
83	Kempton et al. (1985)	W-carbide shatterbox	INAA		REE: La, Ce, Nd, Sm, Eu, Tb, Na, Yb, Lu, Co, Hf, Ta, Sc, Na	BCR-1, BHVO, DTS-1

if the apparent extension direction is coincidentally parallel to the small vein. A more probable explanation is that the vein was formed by recrystallization and assimilation of the groundmass adjacent to a microfracture which allowed fluid percolation.

Further evidence for assimilation comes from Sample 140-504B-197R-1, 99–101 cm (Piece 22) (see above). In this sample one chlorite-actinolite vein abruptly terminates against another (Figs. 82 and 87). The corners are rounded, not sharp, as may be expected from a crack-seal opening mechanism, and the internal, laminar structure follows around one of the corners. Dark-green (chlorite?) crystals within the vein may represent relict phenocrysts of altered clinopyroxene, which were either detached from the marginal groundmass into the vein, or the remnants of a completely recrystallized and mobilized groundmass.

Whatever the formation mechanism, the veins clearly localized and channeled fluid circulation which in turn produced extensive alteration within, and in the host rock next to, the veins.

Crosscutting Relationships

Crosscutting relationships between veins of differing composition and orientation were recorded in the structural core log, the vein log and on hand-specimen drawings (see Table 14 for summary) and in thin-section descriptions (Table 15).

In hand specimen, epidote and quartz-epidote veins crosscut earlier vein sets (i.e., chlorite, chlorite-actinolite, and actinolite); but within these earlier veins no consistent crosscutting sequence was determined. No crosscutting relationships have been determined for chlorite-pyrite veins. The belief that chlorite is an early vein-filling phase is supported by microscopic evidence; i.e., filling of fractures in plagioclase, and overprinting relationships in Sample 140-504B-190R-1, 71–79 cm (Piece 17A), discussed below.

Intersections of veins are of three types: one vein overprints an earlier vein (no apparent offset); a vein apparently terminates against a second vein and thirdly a vein is offset by a later vein. Most observed

Table 12 (continued).

Leg	Analyst	Crushing	Technique	Sample preparation	Elements	Standards
83	Kempton et al. (1985)	W-carbide shatterbox	Flame photometry	HF/boric acid dissolution	Na	AGV-1, PCC-1
83	Emmermann (1985)		XRF	Glass disks; pressed-powder pellets	Major elements, Cr, BIR-1, BM, BE-N, BHVO-1 Co, Ni, Cu, Zn, Ga, Sr, Y, Zr, (Rh compton peak)	
83	Emmermann (1985)		Manganometric titration		Fe ²⁺	BIR-1, BM, BE-N, BHVO-1
83	Emmermann (1985)		Coulometric titration		CO ₂ , S	BIR-1, BM, BE-N, BHVO-1
83	Emmermann (1985)		Karl Fischer titration		H ₂ O ⁺	BIR-1, BM, BE-N, BHVO-1
83	Emmermann (1985)		AAS		Mg, Na	BIR-1, BM, BE-N, BHVO-1
83	Emmermann (1985)		Flameless AAS		K	BIR-1, BM, BE-N, BHVO-1
83	Emmermann (1985)		Ion-selective electrode	Separation by pyrohydrolysis	F	BIR-1, BM, BE-N, BHVO-1
83	Emmermann (1985)		ICP	REE separation by chromatographic columns	La, Ce, Pr, Nd, Sm, Eu Gd, Tb, Dy, Ho, Er, Yb, Lu	BIR-1, BM, BE-N, BHVO-1
83	Tual et al. (1985)		XRF		Major elements, Ti, V, Cr, Co, Ni, Cu, Zn, Ga, Rb, Sr, Y, Zr, Nb	
83	Tual et al. (1985)		INAA		Sc, La, Ce, Eu, Tb, Hf, Ta, Th, Co, Ni	
111	Autio et al. (1989)	W-carbide shatterbox	XRF	Glass disks; pressed-powder pellets	Major elements (end window Rh tube); Y, Sr, Rb, Ga (Mo tube); Nb, Zr, Zn, Ni, Cr, V, (Au tube)	BHVO-1
111	Kusakabe et al. (1989)	W-carbide	AAS	Acid dissolution in sealed teflon bombs	Na, K	
111	Kusakabe et al. (1989)	W-carbide	ICP	Acid dissolution in sealed teflon bombs	Ca, Mg, Al, Ti, Fe, Mn, Cr, Co, Ni, Cu, Sr	
111	Kusakabe et al. (1989)	W-carbide	Colorimetry-Mo yellow method	Na ₂ CO ₃ fusion	Si	
111	Kusakabe et al. (1989)	W-carbide	Mass spectrometry	Acid dissolution in sealed teflon bombs; chromatographic column separation of elements	Sr and Nd isotopes	
111	Shimizu et al. (1989)		Mass spectrometry	Acid dissolution; chromatographic column separation of elements	REE, Ba, Sr abundances; Sr, Nd, and Ce isotopic compositions	

XRF = X-ray fluorescence, INAA = instrumental neutron activation analysis, RNAA = neutron activation analysis, AAS = atomic absorption spectroscopy, ICP = inductively coupled plasma, REE = rare-earth elements.

intersections are without apparent offset, and where an offset is observed it is small (<10 mm) with no dominant sense of movement. Another general observation is that, where true dips are recorded, veins with steeper dip cut, terminate, or offset veins of shallower dip. This is particularly apparent for chlorite + actinolite and actinolite veins.

In thin section (see Table 15), it is not easy to recognize the timing relationships between the veins in all the samples, especially if offsets are missing or not well preserved. Where offset is evident (for example, Fig. 88), timing relationships between crosscutting veins are better constrained. Where displacement does occur, it is usually on a scale of millimeters.

The best examples are represented by crosscutting veins in Samples 140-504B-198R-1, 70–71 cm (Piece 18), and 140-504B-186R-1, 53–57 cm (Piece 10). In the first example, a vein filled by amphibole, cutting a chilled margin, is cut by a later amphibole-chlorite vein (Fig. 89). Chlorite flakes are arranged along the edges of the vein while the amphibole crystals are randomly oriented in the center of the vein.

The first vein is also cut by a very thin chlorite-filled vein, which dies out near the second vein. The two offsets show the same sense of movement and are related to shear deformation. The arrangement of “en-echelon” cracks in the chilled margin seem to be consistent with the inferred shear displacement.

In the second example, a vein filled by amphibole + chlorite is offset by a later vein filled by amphibole (Fig. 90) in an oriented thin section. In both veins amphibole crystals are randomly oriented and sometimes deformed. The sense of displacement in this case was vertical, though unfortunately, most of the samples showing offset of the crosscutting veins are not oriented.

Open Fractures

Deformation in the lower section of the sheeted dike complex of Hole 504B is dominated by fracturing on all scales. The nature and timing of this fracturing was investigated with the aim of defining the



Figure 69. Preferred orientation of plagioclase groundmass laths in Sample 140-504B-186R-1, 53–57 cm (Piece 10). Cross-polarized light.

deformation history of this sequence. The results described below are a combination of observations, both macro- and microscopic, on cores from both Leg 137 and 140 with some input from a preliminary interpretation of FMS images (see “Downhole Measurements” section, this chapter) covering part of the interval cored during Leg 137.

Published structural data on fracturing from Hole 504B includes the results of downhole logging experiments during Legs 83 (Newmark, Anderson, Moos, and Zoback, 1985; Newmark, Zoback, and Anderson, 1985) and 111 (Morin et al., 1989; Pezard and Anderson, 1989) and detailed studies of fracture evolution in the pillow lavas, transition zone and upper dikes (Agar, 1990). Fracturing is dominantly without significant offset, although small apparent offset between fractures has been observed, and no faults or fault zones have been recovered.

Previous core descriptions suggest that the orientation of small-scale fracturing in the sheeted dike section is random (J.H. Natland, pers. comm., 1983, in Newmark, Anderson, Moos, and Zoback, 1985; p. 484), with dips varying from vertical to horizontal (Shipboard Scientific Party, 1988). These fractures are largely filled and open fractures are not common until the Leg 137 core. Instrumental techniques suggest fractures are both steeply dipping, as indicated by electrical experiments (Pezard and Anderson, 1989), and shallowly dipping ($<30^\circ$), with a minimum spacing of 10.0 cm, as defined by borehole televiwer (BHTV) surveys (Newmark, Anderson, Moos, and Zoback, 1985). However, the predominance of shallow dips in the BHTV data may be the result of difficulty in interpreting steeply

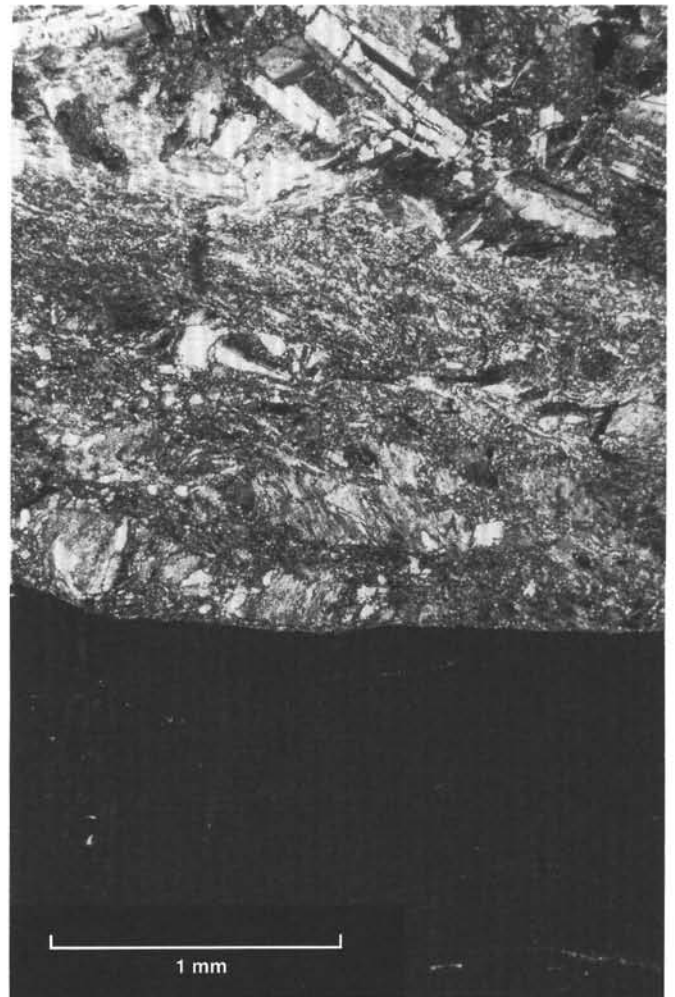


Figure 70. Preferred orientation of amphibole, plagioclase in a band parallel to the chilled margin/host rock contact in Sample 140-504B-203R-1, 33–36 cm (Piece 10). Cross-polarized light, scale bar = 1 mm. Dark gray at bottom: chilled margin; fine-grained at middle: band with preferred orientation of crystals. Coarse-grained at top: host rock.

dipping structures using this system. Comparisons of fracture orientation and spacing between the BHTV and visual core description are also affected by the scale of resolution of the BHTV data which images structures of approximately 1.0 cm thickness whereas fractures measured in the cores are generally <1.0 mm thick.

True dips for 226 measured open fractures from the Leg 137 and 140 cores are shown on Figure 91. Two populations are defined, a shallowly dipping (10° – 25°) and a steeply dipping (70° – 90°) set with a less well-defined intermediate (45° – 55°) grouping. These represent a significant departure from a predicted random distribution (Fig. 76).

The shallowly, and probably many of the moderately, dipping fractures form two types, incipient and well developed. The incipient type is most common fractures are generally best observed on the cut face of the core as there is often little, if any, expression on the outer surfaces. They appear white in hand specimen, were often logged as “thin white cracks” (TWC), and have thicknesses of <0.2 mm.

The geometry of incipient fractures varies from planar to sinuous, but fractures are generally smooth and may branch. Very few of these structures extend across the entire cut face of the core; many appear to initiate at the edge of the core, often on veins or large phenocrysts, and extend toward the interior. Other examples may have begun in the center of the core (Fig. 92). These fractures appear to rupture phenocrysts and groundmass minerals at a hand-specimen scale, and

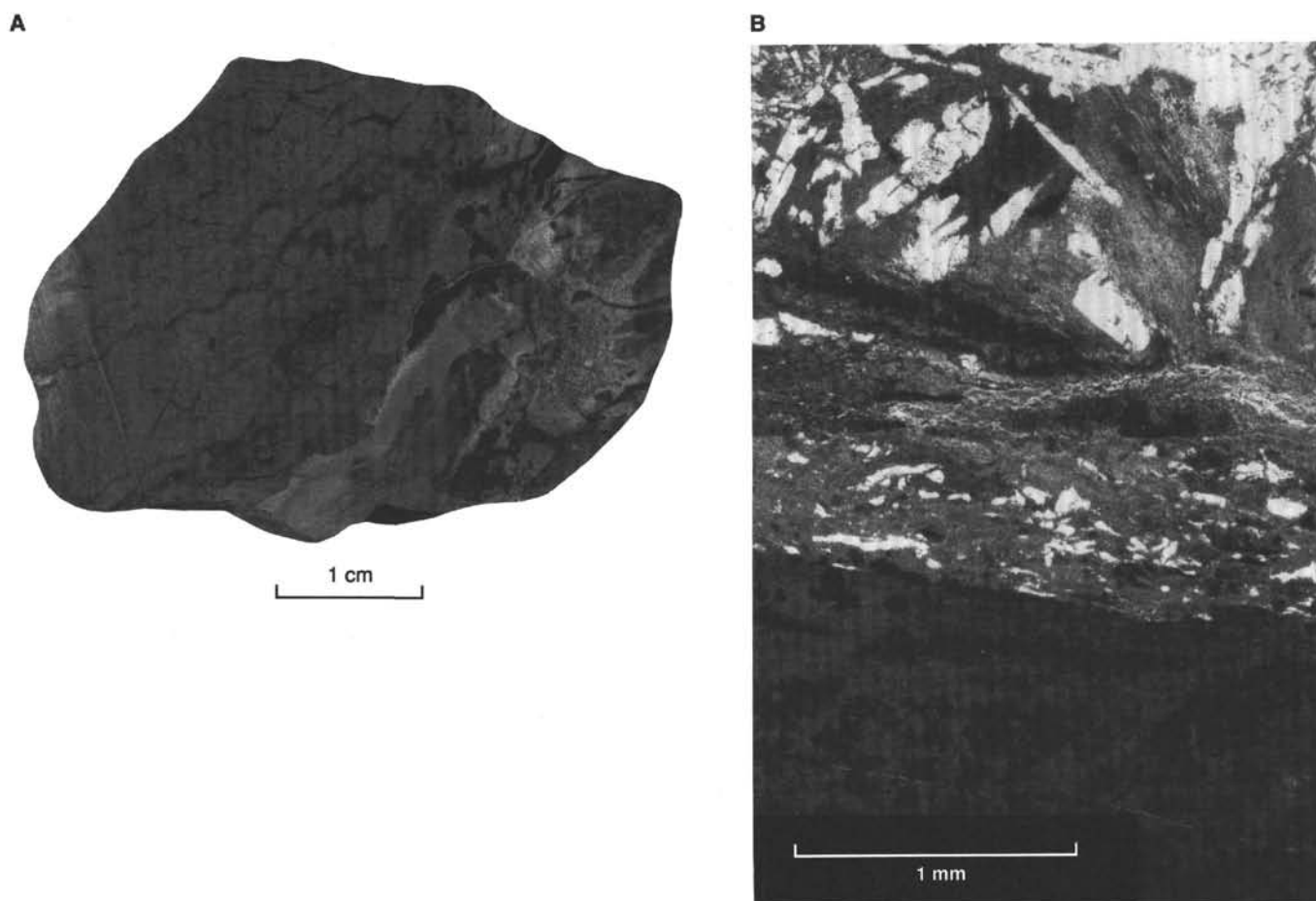


Figure 71. Brecciated and microfaulted chilled dike contact, Sample 140-504B-187R-1, 11–14 cm (Piece 3). **A.** Hand specimen. **B.** Photomicrograph, plane-polarized light. Chilled margin at bottom; fine-grained shear zone in middle and coarse-grained protholite at top.

this is confirmed in thin section. In some cases fractures divert around small crystals or follow cleavage planes. The well-developed fractures generally have the same morphology as the incipient type but are wider, up to approximately 0.5 mm, and make curvilinear traces on the rounded outer surface of the core.

These characteristics invite correlation with “discing” fractures recorded from the KTB pilot hole (Wolter et al., 1990) and elsewhere. Incipient fractures of this type occur in lithologies with little tectonic fabric at depths of 1180 m in the KTB pilot hole, whereas well-developed saddle-shaped discs occur below 3574 m as a result of unloading during drilling. The morphology of the discs reflects the in-situ stress field with the trough in the disc parallel to the orientation of maximum horizontal in-situ stress. Very few well-developed disc fractures (e.g., 140-504B-186R-1 (Piece 16A), 140-504B-186R-2 (Pieces 10A and B)) have been recorded in Hole 504B and these have not been oriented to true geographic coordinates by paleomagnetic methods and thus no estimate of stress direction can be made.

Measurements of spacing for all low- and moderate-angle fractures indicate an average and mode of 2.0 cm, with a range of 0.4 to 17.0 cm (Fig. 93). These measurements were taken from core pieces >6.0 cm in length, assuming the top and bottom of each piece to represent fracture surfaces. More continuous fractures are more widely spaced than incipient fractures. There is some indication that average and maximum fracture spacing increases in Cores 140-504B-211R to -238R; however, zones of extremely poor recovery, often associated with fine-grained lithologies, may affect these results.

Steeply dipping fractures also form three distinct morphological types: incipient “thin white cracks” closely spaced joints, and more

continuous fractures that often form the broken face of core pieces. The incipient type are generally difficult to trace on the rounded section of core, but may be more obvious on the broken upper surfaces of core pieces. They are also discontinuous on the cut core face, often being terminated by low angle fractures. Similar fractures are associated with discing in the KTB pilot hole and are attributed to hydraulic fracturing during drilling (Wolter et al., 1990). The more continuous style of fracture often occur on both cut and rounded surfaces and appear to terminate or offset low-angle fractures. Many of these fractures are interpreted to have formed on pre-existing veins, in particular chlorite and chlorite + pyrite types, as they are coated by vein minerals and in some cases have alteration haloes. Timing of fracturing is unclear but fracturing may have occurred both before and during drilling. Closely spaced (2–3 mm) subvertical and more widely spaced shallow (<10°) incipient fractures are developed in some chilled margin samples, e.g., 140-504B-221R-1, (Piece 19). These fractures appear blocky in hand specimen, and are interpreted to have formed during cooling. Some fractures do not penetrate across chilled margins into host rock, whereas others lead into incipient disc fractures, possibly the result of the initiation of these drilling-induced structures on the cooling joints.

A total of 55 fractures have been re-oriented paleomagnetically (Fig. 94). Shallowly and moderately dipping data show no preferred strike, as would be expected to result from the form and discontinuous nature of these fractures. Strikes of the steeply dipping fractures have an east-south-east (133°) trend. If these fractures are dominantly related to drilling processes then theoretical considerations (Wolter et al., 1990) suggest they should parallel the direction of minimum horizontal in-situ stress.

Table 13. Thin-section observations for Legs 137 and 140.

Core, section, interval (cm)	Piece	Oriented?	Primary character	Primary ductile	Flow fabric	Micro-fractures	Veins			Open fracture	Cross-cutting	Chilled contacts	Description included	Additional comments
							amphibole	chlorite	Other					
Leg 137														
173R-1, 7	2	N	Y	Y	N	Y	N	N	N	N	N	N	N	
173R-2, 24	3	N	Y	Y	N	N	N	N	N	N	N	N	N	
173R-1, 103	11	N	Y	Y	N	Y	N	Y	N	N	N	N	N	
174R-1, 50	8	N	N	Y	N	Y	N	N	N	N	N	N	N	
174R-2, 85	14	N	Y	Y	N	Y	N	Y	N	N	N	N	N	
175R-1, 19	3B	N	N	Y	N	Y	Y	Y	Y	N	N	N	N	Y
176R-1, 74	14	N	Y	Y	N	Y	N	Y	N	N	N	N	N	
176R-1, 126	23	N	Y	Y	N	Y	N	N	N	N	N	N	N	
180M-1, 4	1	N	Y	Y	N	Y	N	N	N	N	N	N	N	
180M-2, 35	3	N	Y	Y	N	Y	N	N	N	N	N	N	N	
181M-1, 3	1	N	Y	Y	N	Y	N	N	N	N	N	N	N	
181M-1, 90	8	N	Y	Y	N	Y	N	N	N	N	N	N	N	
181M-2, 40	4	N	Y	Y	N	Y	Y	Y	Y	N	N	N	N	Y
181M-2, 148	12	N	Y	Y	N	Y	N	N	N	N	N	N	N	
Leg 140														
185R-1, 15	3	N	Y	Y	N	Y	Y	Y	N	N	N	N	N	
186R-1, 13	4	N	Y	Y	N	Y	Y	Y	Y	N	N	N	N	
186R-1, 17	5	Y	Y	Y	N	Y	Y	Y	N	N	N	N	N	
186R-1, 53	10	Y	N	Y	N	Y	Y	Y	N	Y	Y	N	N	Tension gashes in vein
186R-1, 81	13B	N	Y	Y	N	Y	Y	Y	N	Y	Y	N	N	
187R-1, 5	2	N	Y	N	N	Y	N	N	N	N	N	N	N	
187R-1, 11	3	N	N	N	N	N	Y	Y	Y	N	N	N	N	
187R-1, 24	6	N	Y	N	N	Y	N	Y	N	N	Y	N	N	Shear deformation
188R-1, 21	7A	N	Y	Y	N	Y	N	Y	Y	N	N	N	N	
189R-1, 105	21B	N	N	Y	N	Y	Y	Y	N	N	N	N	N	Deformed amphibole in vein
189R-2, 39	5C	N	Y	Y	N	Y	N	N	N	N	N	N	N	
189R-2, 83	12	N	Y	Y	N	Y	N	N	N	N	N	N	N	
189R-1, 13	4	N	Y	Y	N	Y	Y	Y	N	Y	N	N	N	
189R-1, 96	21A	N	Y	Y	N	Y	N	N	N	N	N	N	N	
190R-1, 75	17	N	Y	Y	N	Y	N	N	N	N	N	N	N	
190R-1, 95	19	N	Y	Y	N	Y	N	N	N	N	N	N	N	
191R-1, 48	7B	N	Y	Y	N	Y	N	N	N	Y	N	N	N	
191R-1, 60	8	N	Y	Y	N	Y	N	N	N	N	N	N	N	
192R-1, 1	1	N	Y	Y	N	Y	N	N	N	N	N	N	N	
192R-1, 13	4	N	Y	Y	N	N	Y	Y	Y	N	Y	N	N	
193R-1, 7	3	N	Y	Y	N	Y	N	N	N	N	N	N	N	
193R-1, 28	9	N	Y	Y	N	Y	N	N	N	N	N	N	N	
193R-1, 44	13A	N	N	N	N	Y	Y	N	Y	N	N	N	N	
194R-1, 5	2	N	Y	Y	N	Y	N	N	N	Y	N	N	N	
194R-1, 95	18	N	Y	N	N	Y	N	N	N	N	N	N	N	
194R-1, 115	22	N	Y	Y	N	Y	N	N	N	N	N	N	N	
195R-1, 7	3	N	Y	N	N	Y	N	Y	Y	N	N	N	N	
196R-1, 0	1	N	Y	N	N	N	N	N	N	N	N	N	N	
196R-1, 39	9	N	Y	Y	N	Y	N	N	N	Y	N	N	N	
197R-1, 99	22	N	Y	N	N	Y	Y	Y	Y	N	N	N	N	
197R-1, 131	28	N	Y	Y	N	Y	N	N	N	Y	N	N	N	
197R-2, 33	6	N	Y	Y	N	Y	N	N	N	N	N	N	N	
198R-1, 21	6	N	Y	Y	N	N	Y	N	N	N	N	N	N	
198R-1, 61	16	N	Y	Y	N	N	Y	Y	N	Y	N	N	N	
198R-1, 70	18	N	N	Y	N	N	Y	Y	N	N	Y	N	N	En-echelon cracks
199R-1, 71	17	N	Y	Y	N	Y	N	N	N	N	N	N	N	
199R-1, 106	25A	N	Y	Y	N	Y	N	N	N	N	N	N	N	
199R-1, 121	26B	N	Y	Y	N	Y	N	N	Y	N	N	N	N	
200R-2, 26	4A	N	Y	Y	N	Y	N	N	Y	Y	N	N	N	
200R-2, 44	6	N	Y	Y	N	Y	N	N	N	N	N	N	N	
200R-3, 13	2C	N	Y	Y	N	Y	N	N	N	N	N	N	N	
200R-3, 59	8B	N	Y	Y	N	Y	N	N	N	N	N	N	N	
200R-3, 125	6	N	N	N	N	N	Y	Y	N	N	N	N	N	
200R-4, 23	6	N	Y	Y	N	Y	N	N	N	N	N	N	N	
201R-1, 19	5	N	N	Y	N	Y	Y	Y	N	N	N	N	N	
202R-1, 25	7	N	Y	Y	N	Y	N	N	N	N	N	N	N	
202R-1, 41	11	N	Y	Y	N	Y	N	N	N	N	N	N	N	
203R-1, 4	2	N	Y	N	N	N	N	Y	N	N	N	N	N	
203R-1, 33	10	N	Y	N	N	Y	Y	Y	N	N	Y	Y	N	
203R-1, 39	12	N	Y	Y	N	Y	Y	Y	N	N	N	N	N	
203R-1, 57	15B	Y	N	N	N	Y	Y	Y	N	N	N	N	N	
204R-1, 12	3	N	N	N	N	N	Y	Y	N	N	Y	N	N	
204R-1, 28	7	N	Y	Y	N	Y	N	N	N	N	N	N	N	
205R-1, 14	1	Y	Y	Y	N	N	Y	Y	Y	N	N	N	N	
205R-1, 64	14	N	Y	Y	N	N	Y	Y	N	N	N	N	N	
205R-1, 87	21	N	Y	N	N	Y	N	N	N	N	N	N	N	

Table 13 (continued).

Core, section, interval (cm)	Piece	Oriented?	Primary character	Primary ductile	Flow fabric	Microfractures	Veins			Open fracture	Cross-cutting	Chilled contacts	Description included	Additional comments
							amphibole	chlorite	Other					
206R-1.47	11	N	Y	N	N	Y	N	N	N	N	N	N		Crystal clot
207R-1.0	1	N	Y	N	N	N	Y	N	N	N	N	N		
208R-1.4	1B	Y	Y	Y	N	N	N	N	N	N	N	N		
208R-1.30	7	N	N	N	N	Y	N	N	N	Y	N	N		
208R-1.36	9	N	Y	Y	N	Y	N	N	N	N	N	N		
208R-1.50	13	N	Y	N	N	N	N	N	N	N	N	N		
208R-1.85	19	Y	Y	N	N	Y	Y	Y	Y	N	N	N		
208R-2.61	10B	N	Y	N	N	Y	N	N	N	N	N	N		
208R-3.7	1	Y	N	N	N	Y	N	N	N	N	N	N		
209R-1.98	14B	N	N	N	N	Y	Y	Y	N	N	N	N		
209R-2.9	2	N	N	N	N	Y	N	N	N	N	N	N		
209R-2.30	4	Y	Y	N	N	N	N	N	N	N	N	N		
210R-1.36	4C	N	Y	N	N	N	Y	Y	N	N	N	N		
210R-1.73	11	Y	N	N	N	Y	Y	N	N	N	N	N		
211R-1.48	11	N	N	N	N	N	Y	Y	Y	Y	Y	N		
211R-1.129	29B	Y	Y	N	N	N	N	N	N	N	N	N		
212R-1.4	1B	Y	Y	N	N	Y	N	N	N	N	N	N		
213R-1.3	2	N	Y	N	N	N	Y	N	Y	N	Y	N		
213R-1.45	15	N	Y	N	N	Y	N	N	Y	N	N	Y		
213R-1.32	11	N	N	N	N	Y	Y	Y	N	N	Y	Y		
213R-1.79	21	N	Y	N	N	N	N	N	N	N	N	N		
214R-1.24	5A	N	N	N	N	Y	N	N	N	N	N	N		
214R-1.76	8	Y	N	Y	N	Y	N	N	N	N	N	N		
214R-1.126	18	N	Y	Y	N	Y	N	N	N	N	N	N		
214R-1.130	25	Y	N	N	N	Y	N	N	N	N	N	N		
214R-2.29	7	N	N	N	N	Y	N	N	N	N	N	N		
214R-2.88	20	N	Y	N	N	Y	N	N	N	N	N	N		
214R-2.100	22	N	Y	N	N	Y	N	N	N	N	N	N		
215R-1.0	1	N	Y	N	N	Y	N	N	N	N	N	N		
216R-1.58	13	N	N	N	N	N	Y	N	Y	N	N	N		
216R-1.66	14	N	Y	N	N	Y	N	N	N	N	N	N		
217R-1.23	6	N	Y	Y	N	Y	N	N	N	N	N	N		
217R-1.4	1	Y	Y	N	N	N	N	Y	Y	N	N	N		
217R-1.0	1	Y	Y	N	N	N	Y	Y	Y	N	Y	N		
218R-1.24	7	N	Y	N	N	Y	Y	N	N	N	N	N		
219R-1.7	3	N	Y	N	N	N	Y	N	Y	N	N	N		
220R-1.2	1	N	Y	N	N	Y	N	Y	Y	N	N	N		
220R-1.27	7	N	Y	N	N	N	N	N	Y	N	N	N		
221R-1.4	2	N	Y	N	N	Y	N	N	N	N	N	N		
221R-1.11	4	N	Y	N	N	N	Y	Y	Y	N	Y	Y		
221R-1.40	10	N	Y	N	Y	N	Y	Y	N	N	Y	Y		
222R-1.0	1	N	Y	N	N	Y	N	Y	Y	N	Y	Y		
222R-1.17	1E	Y	N	N	N	Y	N	N	N	N	N	N		
222R-1.37	6	Y	N	N	N	Y	Y	Y	N	N	N	N		
222R-1.100	19	N	Y	N	N	N	Y	N	N	N	N	N		
222R-1.129	24	N	Y	N	N	Y	Y	Y	Y	N	N	N		
223R-1.20	6	N	Y	N	N	N	N	N	N	N	N	N		
223R-1.59	14	N	Y	Y	N	N	Y	Y	N	N	N	N		
224R-1.21	4	N	Y	N	N	Y	N	N	N	N	N	N		
224R-1.59	14	N	Y	Y	N	N	Y	Y	N	N	N	N		
225R-1.40	10	N	Y	Y	Y	N	Y	Y	N	N	N	N		
225R-1.59	14	N	Y	Y	N	Y	Y	Y	N	N	N	N		
225R-1.137	34	N	Y	N	N	N	N	Y	N	N	N	N		
225R-2.42	7	N	Y	N	N	N	N	N	N	N	N	N		
226R-1.16	3	N	Y	N	N	N	N	N	N	N	N	N		
226R-1.61	12	Y	N	N	N	N	N	N	N	N	N	N		
226R-2.77	10	Y	Y	Y	N	Y	N	N	N	N	N	N		
227R-1.83	10	Y	Y	Y	N	Y	N	N	N	N	N	N		
227R-2.0	1	N	Y	N	N	Y	N	N	N	N	N	N		
227R-2.14	2	N	N	N	N	N	N	N	N	N	N	N		
228R-1.55	13	N	Y	Y	N	Y	N	Y	N	Y	N	N		
229R-1.34	10	N	Y	Y	N	Y	Y	N	N	Y	N	N		
229R-2.7	3	N	Y	N	N	Y	N	N	N	Y	N	N		
233R-1.4	2	N	N	N	N	N	Y	Y	N	N	Y	N		
236R-1.0	1	N	Y	Y	N	Y	Y	Y	N	N	N	N		
238R-1.22	8	N	Y	Y	N	Y	N	N	N	N	N	N		

Primary character: reflects degree of recrystallization due to alteration. Primary ductile: evidence for ductile deformation during crystallization; curved plagioclase laths, undulose extinction in clinopyroxene, etc.

Flow fabric: presence of preferred orientation of plagioclase laths.

Microfractures: presence of intracrystalline microfractures. Presence or absence of the following: Veins—amphibole, chlorite, others; open fractures; crosscutting relationships; chilled contacts.

Table 14. Summary of vein crosscutting relationships in hand specimen.

		Younger vein				Total
		Chlorite	CHL/AC	Actinolite	Epidote	
Older vein	Chlorite	(4)	6	4	1	11
	CHL/AC	3	(5)	6	0	9
	Actinolite	4	3	(5)	1	8
	Epidote	0	0	0	(2)	0
	Total	7	9	10	2	28

Value in table indicates number of cases where veins of a particular composition intersect; e.g., there are four recorded actinolite veins that cut or offset chlorite veins. Values in brackets indicate intersecting veins of identical composition.

This data would also agree with results from BHTV studies of Newmark, Anderson, Moos, and Zoback (1985) and Morin et al. (1989) which suggest trends for the minimum horizontal stress direction of $112^{\circ} \pm 16^{\circ}$ and 123° degrees, respectively. The effectiveness of the paleomagnetic correction in improving the clustering of the strikes of these fractures suggests that the technique is appropriate.

It is concluded that the fractures measured in cores recovered from Legs 137 and 140 are largely the result of drilling-induced cracking and unloading and are consistent with previous estimates of in-situ stress. Earlier open fractures probably comprise part of the 87% of the sequence that was not recovered. Information on these fractures is only obtainable by use of geophysical techniques such as the formation microscanner (FMS).

Initial interpretation of the FMS data (see "Downhole Measurements" section, this chapter) from 1563.2 to 1574.8 mbsf has defined 81 large open fractures (Table 16) that have true dips ranging from 10° to 70° , although steeper dips are probably poorly represented due to detection problems, covering the range of fractures measured in the core (Fig. 95). The low-angle fractures most probably do not correlate with the discing fractures recorded in the core, but appear to have a random distribution of strikes. Strikes of the steeper structures are also variable, but a contour plot suggests three main orientations. These three trends all have moderate dips (51° – 57°) and strikes of 22° , 96° , and 156° . Comparison with the BHTV data (Morin et al., 1989; Moos and Zoback, 1990) indicate that the 96° and 22° trends are comparable to the predominant $117^{\circ} \pm 20^{\circ}$ and secondary 27° breakout modes. We have not observed any fracture set in the cores that corresponds to the 156° set.

It should be emphasized that this is a preliminary interpretation of these data. A more rigorous analysis requires processing and interpretational facilities not available on board ship.

Summary

Oriented dikes indicate an east strike, subparallel to the ridge axis, as would be predicted from models of oceanic crust formation. The dikes have dips between 79° and 85° , so the crustal sequence has probably been tilted by only a few degrees.

The earliest signs of deformation are associated with ductile deformation during magmatic crystallization, intrusion, cooling, and initial hydrothermal alteration of minerals and include ductile deformation of plagioclase and clinopyroxene, fracturing of plagioclase laths, in some cases filled by chlorite and opaque minerals, and formation of cooling joints in fine-grained chilled material.

Penetration of hydrothermal fluids resulted in pervasive, but heterogeneous, veining of at least five recognizable macroscopic types. No consistent crosscutting sequence has been established between these vein types. An apparent random orientation, from 70 paleomagnetically corrected measurements, suggest that their genesis is influenced by a local stress regime, dominated by contractional cooling, rather than by a regional tectonic regime. Zones of brecciation are developed on some dike margins, as are minor shear zones and microfaults that offset veins. The amount of movement on these

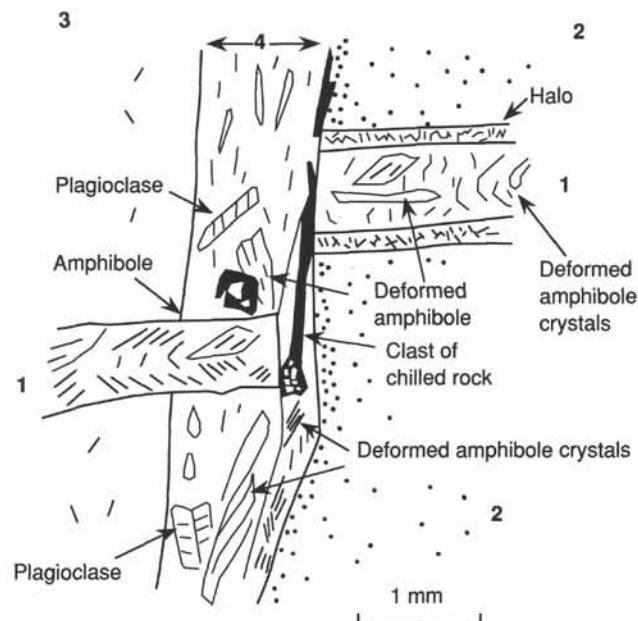


Figure 72. Offset of vein in the brecciation zone. 1. Vein with the halo in chilled margin and without the halo in altered diabase. 2. The chilled margin rock. 3. Diabase. 4. Zone of brecciation and altered diabase. Sample 140-504B-203R-1, 33–36 cm (Piece 10).

structures is not known but is probably quite small. There is no evidence for any major faults or shear zones in the recovered core.

Some veins have been re-fractured, whereas FMS data indicate three possible sets of fractures not obvious in the core. A final stage of fracturing occurred during the drilling process where unloading resulted in the formation of subhorizontal disc fractures.

PALEOMAGNETISM

Paleomagnetic measurements were made on 48 minicores sampled from drill core recovered during Legs 137 and 140 in order to examine the variation in magnetic properties with alteration, lithology, and depth in the crustal section. In general, the results of these measurements (Tables 17 and 18) indicate that the magnetic properties of the newly drilled sheeted dikes are similar to those of the dikes sampled during DSDP Leg 83 and ODP Leg 111 (Smith and Banerjee, 1986; Pariso and Johnson, 1991).

Natural Remanent Magnetization

The intensity of natural remanent magnetization (J_n) measured on Leg 137/140 samples is plotted vs. depth in Figure 96. The mean value for the samples is 3.0 A/m and this compares to 1.6 and 5.5 A/m, respectively, for the upper 500 m of the dike section and extrusive basalts sampled within Hole 504B (Furuta and Levi, 1983; Pariso and Johnson, 1991). The behavior of the samples during alternating field (AF) demagnetization, or magnetic cleaning, indicates that the natural remanent magnetization (NRM) of these rocks is of low to moderate stability. Values of the median demagnetizing field (MDF), the field required to remove one half of the J_n , were determined graphically using the demagnetization curve for each sample and are plotted vs. depth in Figure 97. A mean MDF value of 9.6 mT was calculated for the 48 minicores and is substantially lower than the mean MDF value for the upper part of the dike complex (21.0 mT). Following stepwise AF demagnetization, individual components of magnetization were identified using a least-squares fit through each component of magnetization identified on an orthogonal vector diagram (Zijderveld,

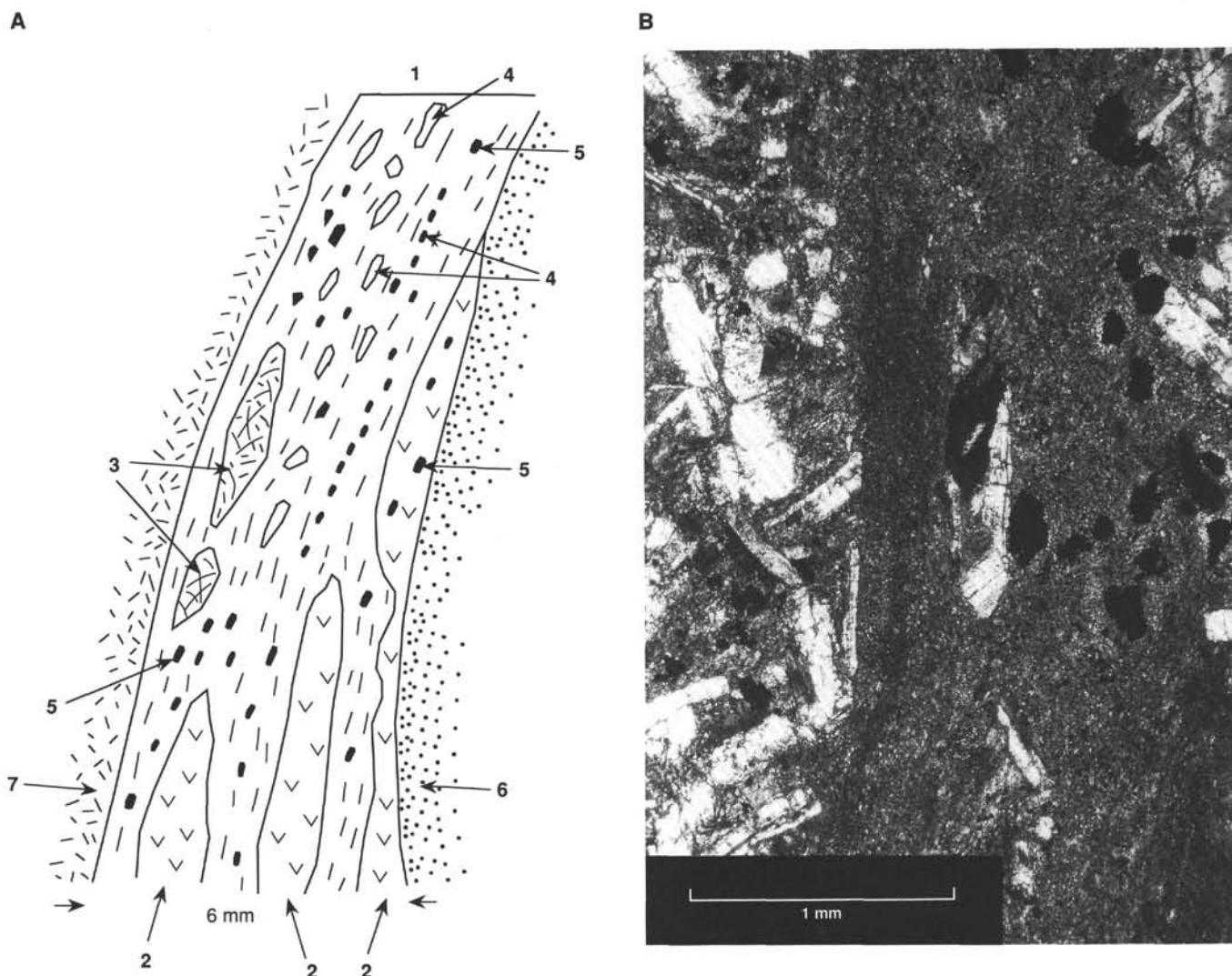


Figure 73. A. (1) Sheared zone with (2) microlenses of amphibolized diabase and (3) altered chilled rock, (4) fragments of plagioclase crystals, and (5) crystals of magnetite have developed between (6) altered chilled margin of Unit 249 and (7) fresh chilled margin of Unit 250, Sample 140-504B-219R-1, 7–11 cm (Piece 3). B. Photomicrograph, plane-polarized light.

1967). The natural remanent magnetization of each minicore was observed to have two components: a stable, or "hard," magnetization and a secondary magnetization. The inclination and declination of the NRM, the stable, and the secondary components of magnetization are listed in Table 18 and show that for nearly all of the samples, the secondary magnetization is nearly vertical and upward (also see Fig. 98). This type of secondary magnetization has been previously observed on samples recovered during DSDP/ODP Legs 34, 45, and 118 and is most likely induced during the drilling process (Ade-Hall and Johnson, 1976; Lowrie and Kent, 1978; Johnson, 1978; Pariso et al., 1991). In comparison, samples drilled during Legs 83 and 111, which have similar magnetic properties, did not acquire a substantial component of secondary magnetization. These observations suggest that the acquisition of the drilling remanent magnetization is a result of changes in the drilling system itself (e.g., a difference in the bottom-hole assembly) rather than changes in the intrinsic magnetic properties of the recovered diabase. In a prior study, magnetization acquired during drilling was observed to have a higher intensity and a lower stability than laboratory induced thermal remanent magnetization (Pariso, 1991). These results suggest that the NRM observed on Leg 137/140 samples may have slightly higher J_0 and lower MDF values than were present prior to drilling.

The stable magnetic inclination (I_s) values determined for Leg 137/140 minicores are plotted vs. depth in Figure 99. The mean I_s value is $-14^\circ \pm 18^\circ$ and the observed range in I_s values (-57° to 43°) is similar to that observed from the upper portion of the drill hole (Fig. 100). Assuming the remanent magnetization was acquired in a geocentric axial dipole field, the predicted magnetic inclination for Site 504B is 0° . Models of secular variation, that is, variations of the geomagnetic field with time, show that up to 17° of angular dispersion can be expected at this latitude (McFadden and Merrill, 1975). Therefore, the mean I_s value observed in Leg 137/140 samples falls within the range predicted by normal variations of the geomagnetic field for Site 504 and does not indicate significant tilting or rotation of the crustal section ("Structure and Deformation" section, this chapter).

Induced Magnetization

Magnetic susceptibility (K) is a measure of the instantaneous magnetization induced in a sample in the presence of an external field and it is a function of composition, concentration, and grain size of the magnetic minerals within a rock. Values of K determined for Leg 137/140 samples are plotted vs. depth in Figure 101 and have a mean value of 0.016 SI units. This is very close to the mean K value of the

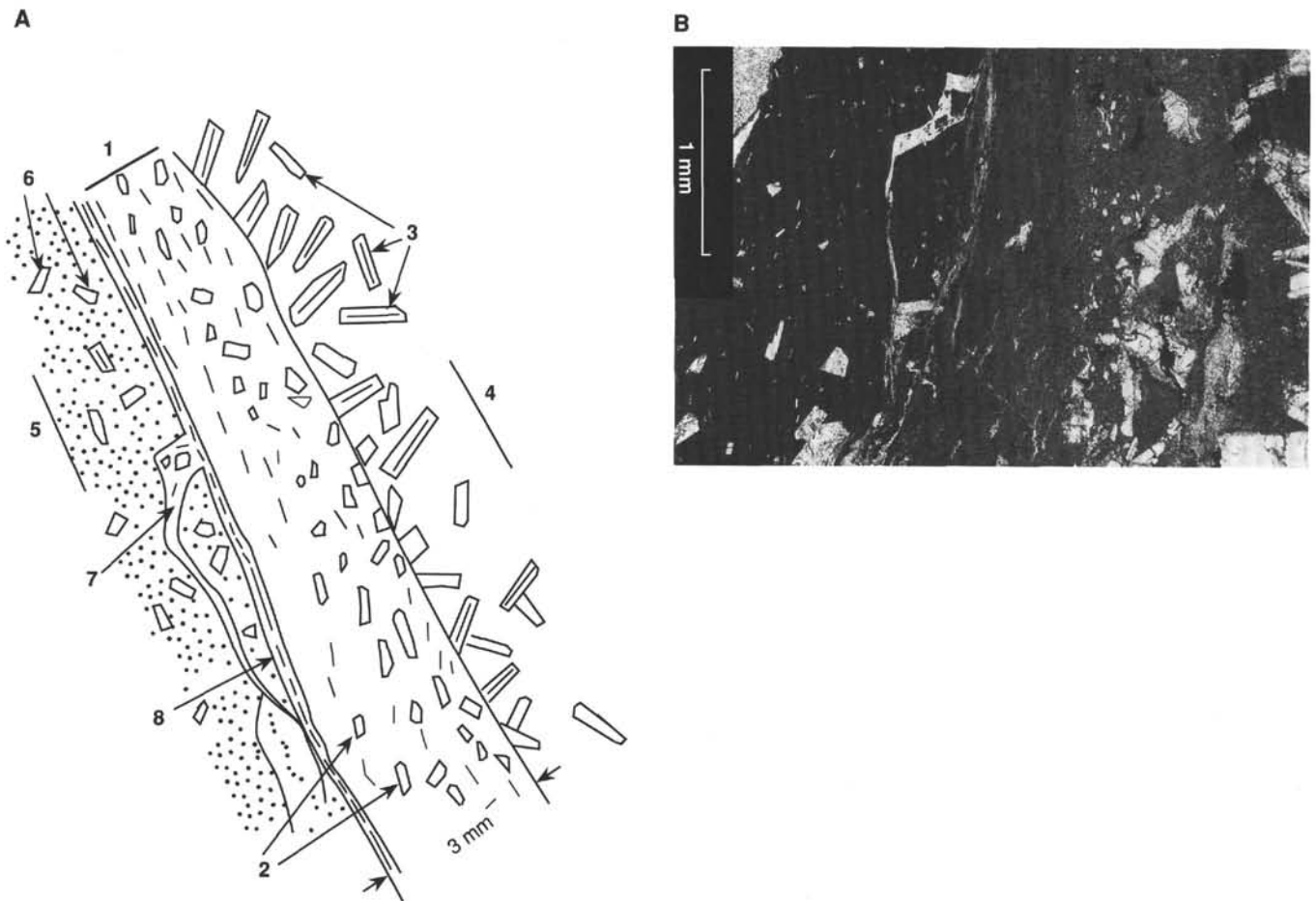


Figure 74. **A.** (1) Sheared zone with fragments of (2) plagioclase laths. (3) Well-preserved plagioclase laths in (4) strongly amphibolized diabase; (5) fresh chilled margin with (6) plagioclase phenocrysts; (7) coarse-grained epidote vein with fragments of plagioclase phenocrysts; (8) fine-grained pyrite-epidote vein. Sample 140-504B-221R-1, 11–15 cm (Piece 4). **B.** Photomicrograph, plane-polarized light.

upper dikes (0.018 SI units) and, like the K values from the upper portion of the dike complex, the K values determined for Leg 137/140 samples are bimodally distributed (Fig. 102). The variation in susceptibility of Hole 504B dikes was previously observed to correlate with the type of alteration experienced by opaque minerals (Pariso and Johnson, 1991) and suggests that magnetite is more stable under hydrothermal conditions than titanomagnetite. High K values are associated with primary titanomagnetite grains which experienced deuteric alteration to magnetite and ilmenite. As a result of this high temperature mineralogical change, the opaque minerals experienced low degrees of hydrothermal alteration. Low K values are characteristic of samples in which primary titanomagnetite grains have experienced less deuteric alteration (i.e., a higher rate of subsolidus cooling) and high degrees of hydrothermal alteration. One interpretation of these results is that samples with low magnetic susceptibility values are characteristic of dikes which had a high initial permeability and thus cooled quickly and, as a result, experienced extensive alteration by hydrothermal fluids. This interpretation is consistent with the observation that approximately 10% of the studied samples have very low susceptibilities and, similarly, about 10% of the recovered drill core has experienced high degrees of hydrothermal alteration (see "Alteration and Metamorphism" section, this chapter).

The Koenigsberger, or Q ratio, uses the ratio of J_0 and K to compare the strength of the remanent magnetization to the magnetization induced in the rock by the Earth's magnetic field (0.033 mT at Site 504). The Q values determined for Leg 137/140 samples are plotted vs. depth in Figure 103. The mean Q value of these samples

is 6.9 indicating that, like the upper dikes and extrusive basalts, this portion of the Hole 504B crustal section is dominated by the remanent, rather than induced, component of magnetization. It should be noted that the Q values may be biased because of the secondary magnetization induced during drilling.

Rock Magnetic Measurements

To determine the coercivity spectra, and to aid interpretation, measurements of anhysteretic remanent magnetization (ARM) were conducted on 24 Leg 137/140 samples; an example is shown in Figure 104. In all cases the magnetization does not saturate by the highest AF field applied (90 mT). Values of the median acquisition field, the field at which one half of the anhysteretic magnetization is acquired, are listed in Table 19. The median acquisition field values are consistently higher than the observed median demagnetizing field values; this may be because the drilling remanence, which strongly controls the MDF value, has a lower coercivity (is less stable) than the stable magnetization. Values of the intensity of magnetization (J_a) at the maximum AF field (90 mT) were compared to the intensity of NRM (J_0) by calculating the ratio J_a/J_0 , and are listed in Table 19. As expected, J_a is positively correlated with J_0 .

An isothermal remanent magnetization (IRM) was induced in a step-wise fashion in five samples to examine the magnetic behavior of diabase in the presence of a saturating field. The results of these measurements are displayed in Table 20 and typical curves are plotted in Figure 105. For most samples, saturation was reached by 170 mT,

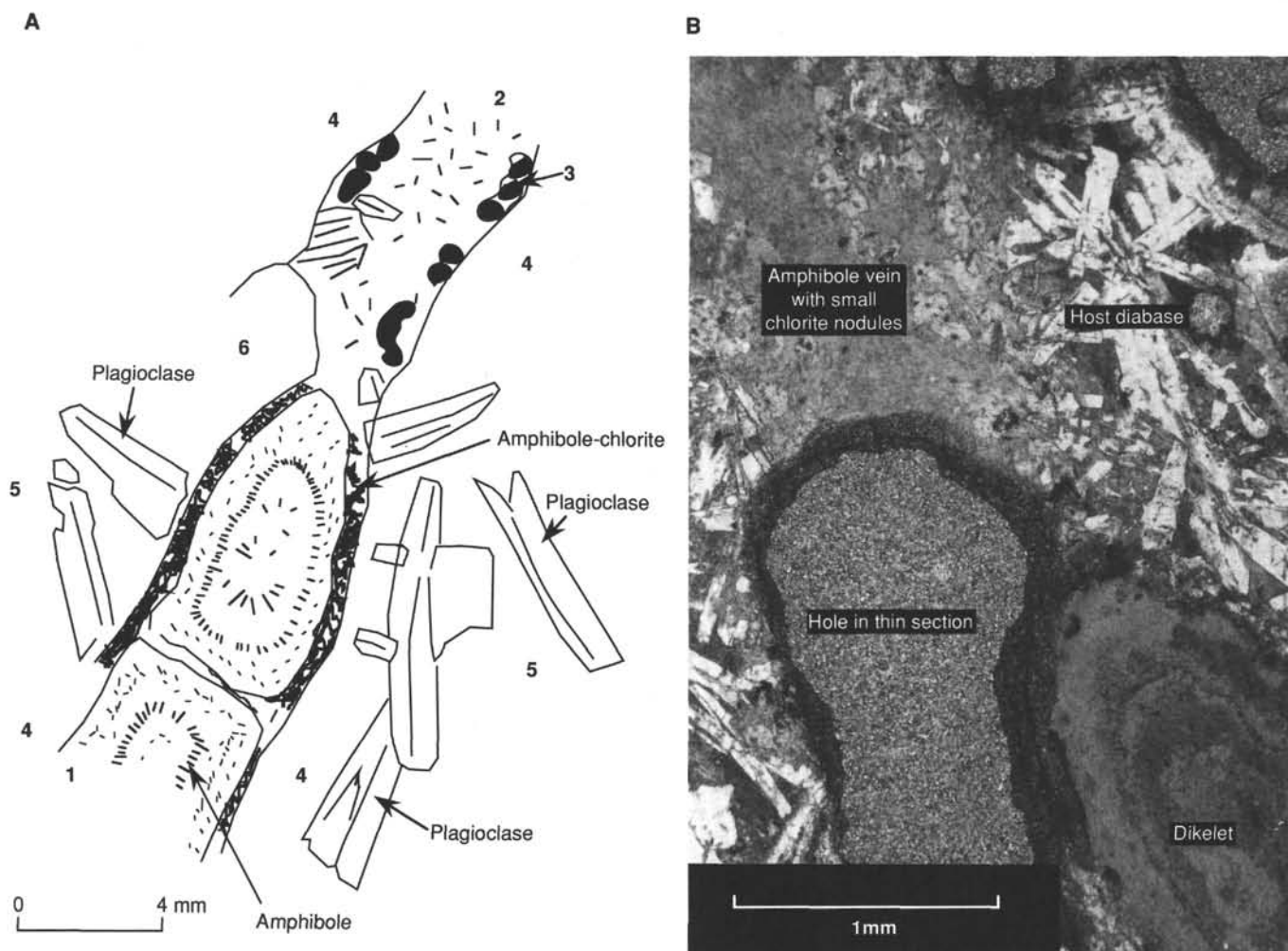


Figure 75. A microdiike intruding an amphibole vein. **A.** Sketch: (1) Chilled microdiike. (2) Amphibole vein with (3) small chlorite nodules. (4) Light-colored halo. (5) A host diabase. (6) A hole in the thin section. Sample 140-504B-213R-1, 32–34 cm (Piece 11) **B.** Photomicrograph, plane-polarized light.

which is within the range of values reported for titanomagnetite (Tarling, 1983). These results are consistent with Curie temperature measurements on samples from the upper portion of the sheeted dikes sampled during Leg 111 (Pariso and Johnson, 1991).

Magnetic Fabric

Anisotropy of anhysteretic remanence measurements were completed, as described in the “Explanatory Notes” chapter (this volume), on a total of 18 samples (see Table 21). One sample, 140-504B-193R-1, 48–51 cm, gave unusual results for this, and other measurements, and will be discussed individually below. Two samples, 140-504B-180R-2, 29–31 cm, and 140-504B-191R-1, 48–51 cm, have errors greater than 10% of the magnitude of the intermediate axis of the anisotropy ellipse, and are not considered further here. The remaining samples have errors < 6%. Four samples have a foliation ($K_{\text{int}}/K_{\text{min}}$) or a lineation ($K_{\text{max}}/K_{\text{min}}$) > 1.1, and may be considered to have a significant anisotropy ($K_{\text{max}}/K_{\text{min}}$ > 1.18), but the rest have $K_{\text{max}}/K_{\text{min}}$ < 1.16, and therefore, do not have a measurable anisotropy (see Fig. 106).

Three of the four samples that exhibited a measurable anisotropy have a steeply inclined (>69°) K_{max} direction. This may reflect a steeply inclined magmatic fabric, which has been observed in some thin sections, but not from those corresponding to the paleomagnetic samples. The rest of the samples have highly scattered anisotropy axes.

Self-reversal Behavior of Sample 140-504B-193R-1, 48–51 cm

One highly altered sample showed some unusual magnetic properties which were considered worthy of separate comment. This sample also proved to be anomalous in terms of its chemical and physical properties. In addition to having low susceptibility and J_0 values compared to the mean values, the sample exhibited self-reversal in an anhysteretic remanent magnetization acquisition experiment; i.e., when a low (0.1 mT) steady direct current (DC) field was applied in the +X axis over an AF cycle, the sample acquired a magnetization in the -X direction. This acquired, negative, magnetization reached a maximum at 30 mT AF, and subsequently decreased, with a gentle slope. This behavior suggests that at least two magnetic phases are present in this rock: a relatively low coercivity phase that exhibits self-reversal, and a higher coercivity phase that does not.

In addition to measurements of anhysteretic remanent magnetization, measurements of anisotropy of anhysteretic remanence were made. The sample gave a negative fabric (i.e., a field in +X yields a magnetization in -X) in the XY plane, and a positive fabric in Z. The axes are close to parallel to the arbitrary coordinate system. The standard error is low, so the results are repeatable in the 3 position at 45° to the X, Y, and Z axes, and the relative differences in the magnitudes of the axes are very large. It should, perhaps, be empha-

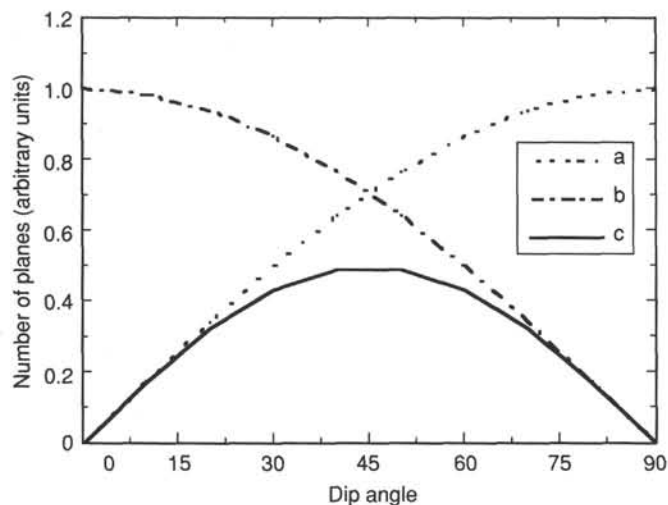


Figure 76. Interpretation of true dip data: line a depicts the effect of the spherical geometry on true dip data, line b shows the effect of bias introduced by a vertical borehole, and line c gives the combination of these effects; this is the predicted distribution of a random set of planes in a vertical borehole.

sized that the acquisition of anhysteretic remanent magnetization and the anisotropy experiments were conducted in batches with other samples, which showed no abnormal behavior. These experiments were made within about 24 hr of the sample taken from the core. The samples were then left overnight in a μ -metal shield. When experimentation was resumed in the morning, the sample did not show any self-reversing properties. It was then passed on for physical property measurements. Subsequent to physical property measurements, a second ARM acquisition experiment was conducted, which showed magnetic behavior very different from that suggested by the original results; acquiring a magnetization in the same direction as the applied field. Another sample, 140-504B-214R-2, 130–132 cm, showed self-reversing behavior during acquisition of anhysteretic remanent magnetization, in much the same manner as Sample 140-504B-193R-1, 48–51 cm. However, above an AF field of 30 mT, the behavior of the sample during acquisition of anhysteretic remanence was “normal.”

Self-reversing behavior has been reported from certain compositions of titanohematites (90% hematite), in pyrrhotite, and some titanomagnetites. However, an IRM acquisition experiment on both of the samples which showed self-reversing behavior resulted in magnetic saturation at about 175 mT. This is consistent with the primary magnetic phase being magnetite or titanomagnetite. No higher coercivity phase, such as hematite, was detected.

Comparison with Other Lithologies

Diabase samples recovered from Hole 504B have magnetic properties similar to those observed in dikes from ophiolites. Specifically, values of the intensity of magnetization are moderate, magnetic susceptibility values are high, and the magnetic stability, as described by MDF values, is moderate to low (Pariso and Johnson, 1989; Luyendyk et al., 1982). The average J_0 and K values of the Leg 137/140 samples (3 A/m and 0.018 SI units, respectively) are lower than those observed in extrusive basalts from the upper part of Hole 504B or other DSDP drill sites (Lowrie, 1974; Furuta and Levi, 1983). The intensity of magnetization of the dikes is similar to that observed in oceanic gabbros. However, gabbros are typically more stable and are observed to have lower magnetic susceptibility values than dike rocks (Pariso and Johnson, 1989; Kikawa and Pariso, 1991).

Table 15. Summary of vein crosscutting relationships in thin-section.

Core, section, interval (cm)	Piece	Cutting vein	Cut vein	Offset
140-504B-				
193R-1, 28–31	9	CHL	CHL-AMPH-AB	N
200R-3, 125–130	20	AMPH	AMPH	N
204R-1, 12–14	3	CHL-AMPH	AMPH	N
210R-1, 73–77	11	AMPH-CHL	AMPH-CHL	N
213R-1, 3–6	2	AMPH-CHL	PLAG-AMPH	N
186R-1, 53–57	10	AMPH-CHL	AMPH	Y
192R-1, 13–14	4	EP-QTZ	AMPH	Y
203R-1, 33–36	10	AMPH	AMPH	Y
198R-1, 70–71	18	AMPH-CHL	AMPH	Y
198R-1, 70–71	18	CHL	AMPH	Y

AMPH = amphibole; CHL = chlorite; PLAG = plagioclase; AB = albite; QTZ = quartz; EP = epidote; N = no; Y = yes.

PHYSICAL PROPERTIES

Index properties and compressional-wave velocities, in both wet and dry states, were obtained as part of the shipboard analyses from the core sections recovered during Legs 137 and 140. A detailed study of the physical properties of these rocks provided valuable information for the understanding of the composition and seismic nature of the oceanic crust within Hole 504B and the Costa Rica Rift. The measurements obtained from the Leg 137 cores provided the necessary resources to calibrate the shipboard instruments and complemented the observations made during Leg 140.

Index Properties

Measurements for index properties were taken on 75 samples from Legs 137 and 140. Wet/dry weights and volumes were used to calculate bulk and grain densities, porosity, and water content. A salt correction assuming 3.5% interstitial fluid salinity was applied (Hamilton, 1971). Results are given in Table 22.

The average wet bulk density of the samples measured from Legs 137 and 140 was $2.96 \text{ g/cm}^3 \pm 0.055 \text{ g/cm}^3$, whereas the grain density determinations gave a mean value of $2.95 \text{ g/cm}^3 \pm 0.056 \text{ g/cm}^3$. Wet and dry porosity values center on a mean values of $0.52\% \pm 0.60\%$ and $0.74\% \pm 0.73\%$, respectively, whereas the corresponding water content determinations have a mean value of $1.32 \text{ wt}\% \pm 0.98 \text{ wt}\%$. These percentages are comparable to previously reported values (Shipboard Scientific Party, 1988, 1992). The similarity between bulk and grain densities can be attributed to the low porosity and water content values observed in the samples. Evidently, the porosity has a direct effect on the water content.

The wet bulk density values for these samples are consistent with the mineralogical composition of the rocks and in several zones, a decrease in density has been observed with increasing porosity values (Fig. 107). A comparison between bulk density and porosity values of the samples cored throughout the entire section of Hole 504B indicates that some of the highest density zones at this site were encountered near the base of the section drilled during Leg 137 and the cores recovered from Leg 140 (Fig. 108). Some of these samples have higher density values than the $2.96 \text{ g/cm}^3 \pm 0.017 \text{ g/cm}^3$ mean obtained during Leg 137 (Shipboard Scientific Party, 1992). Several explanations can account for this difference. First, problems can arise when measuring wet volumes because helium tends to dissolve in the pore water, giving low volume readings and, consequently, high density measurements. In order to address this possibility and achieve a steady-state condition, purge times of 3, 5, and 10 minutes were used for the same samples. The results were $\pm 0.006 \text{ g/cm}^3$ from the previous measurements, which is within the accuracy of

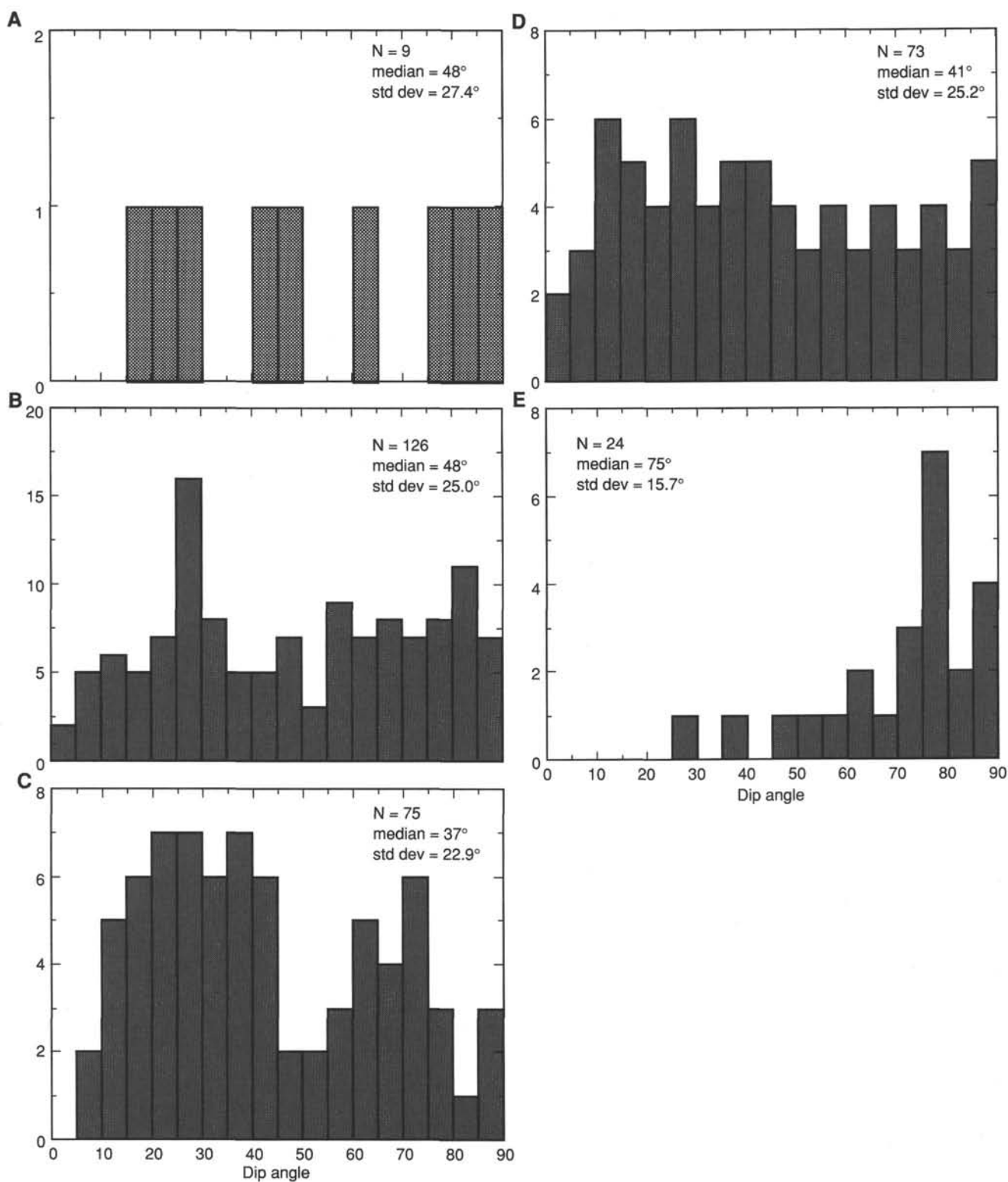


Figure 77. **A.** Histogram of epidote vein dips. No dominant dip angle emerges. **B.** Histogram of chlorite vein dips. A strong mode is present at 25°–30°, with an additional peak at 80°–85°. **C.** Histogram of chlorite and actinolite vein dips. Modes at 25°–30° and 75°–80° reflect a possible crack-seal method of formation. See text for discussion. **D.** Histogram of actinolite vein dips. A mostly even distribution of dip angles is seen. **E.** Histogram of chlorite and pyrite vein dips, showing a very strong mode between 75° and 80°.

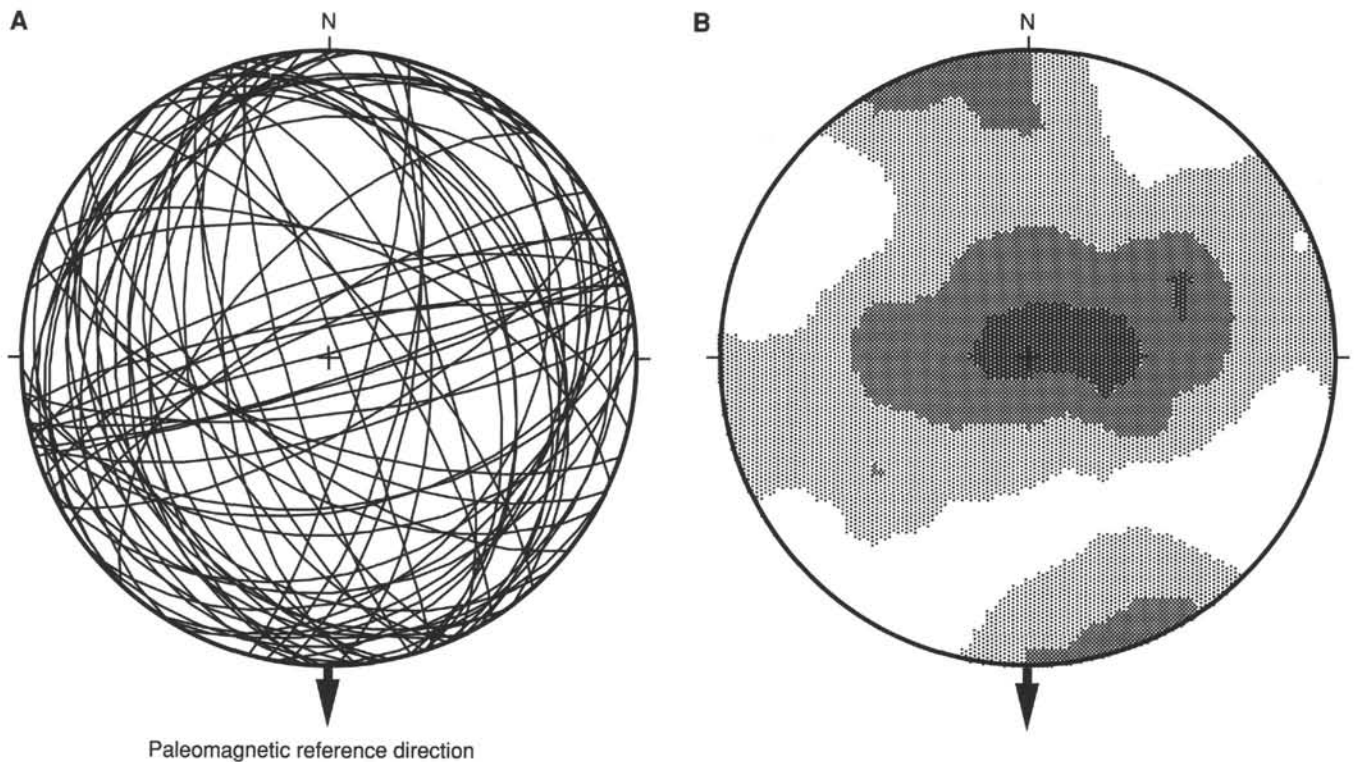


Figure 78. Equal-area lower hemisphere stereographic projections of 70 vein orientations corrected paleomagnetically. **A.** Great circle plot. **B.** Kamb contour plot of the poles to those great circles. Arrow indicates paleomagnetic reference direction to which magnetic remanence directions are collected.

the measurements (see “Explanatory Notes” chapter, this volume). Similar results were obtained by calculating volumes from careful measurement of the minicore dimensions, implying that the original values are reasonable. Also, the low percentages of porosity and water content measured suggest that the amount of helium being dissolved might be minimal. Sampling bias introduced by avoiding veins and fractures is improbable because similar porosity and water content values were obtained during Leg 137. A more likely explanation is directly related to the percentage of actinolite and chlorite alteration. Actinolite has a reported mean grain density of 3.20 g/cm^3 whereas the mean for chlorite is 2.80 g/cm^3 (Johnson and Olhoeft, 1984). Thin-section observations of the samples from both Legs obtained for shipboard studies during Leg 140 revealed a slightly higher actinolite content than in the shallower intervals. Hence, the increase in amphibole alteration can very simply account for the slightly higher densities. A more detailed study between physical properties and composition is needed and may also indicate a correlation with a more mafic composition.

Compressional-wave Velocities

While sampling, care was taken to avoid major veins and fractures in order to determine the effect of the mineral composition on the velocities; in some cases this proved to be a difficult task because of the amount of veins and microfractures throughout the core. Forty-seven samples were cut horizontally (perpendicular to the splitting plane, transmission direction C) and two were cut vertically (parallel to the core, direction A) for velocity measurements. Minicores were saturated in seawater and placed in a vacuum for 12 hr to achieve in-situ wet conditions and dried at 110°C for 24 hr to measure the dry properties. The traveltime of a 500 kHz pulse was measured using a Nicolet 320 oscilloscope and the calculated compressional-wave velocities (V_p) are given in Table 23.

The mean V_p for wet horizontal samples centers around $5719 \pm 257 \text{ m/s}$, whereas the mean V_p for the dry samples is $5097 \pm 835 \text{ m/s}$. A plot of velocity as a function of depth shows a considerable amount of scatter throughout the cores sections recovered during Leg 140 (Fig. 109). A comparison of velocity as a function of depth throughout the entire section drilled at Hole 504B (Fig. 110) shows significantly lower values obtained during Legs 137 and 140 than those from Leg 83 and the top section of Leg 111. The difference in velocities may be due to different types of localized alteration zones and the presence of a significant amount of microcracks and veins within the samples recovered. Velocity-density systematics tend to support both lines of evidence (Fig. 111). A group of high density and low velocity measurements imply the effects of microcracks whereas the lower density and velocity values suggest the presence of more altered zones. A cross-correlation between velocity and porosity (Fig. 112) shows a decrease in velocity with increasing porosity as well as the effects of different types of alteration. Thin-section observations from a high porosity and velocity sample (140-504B-214R-2, 130–132 cm) indicate a 50% actinolite alteration which will counterbalance the porosity effect. These observations imply a relationship between the amount and type of alteration and the velocities. Hence, a detailed correlation between mineralogical composition, porosity and in-situ seismic velocities may produce the necessary acoustic impedance contrast to produce the vertical seismic profile (VSP) reflector interpreted as the possible layer 2-3 boundary at an approximate depth of 1658 mbsf (Shipboard Scientific Party, 1988).

Anisotropy measurements were limited by the generally poor recovery and the difficulty in obtaining vertically oriented minicores. One of the vertical samples (140-504B-180M-1, 94–99 cm) shows a significant variation in wet V_p when compared with a horizontal sample from the same interval. The large discrepancy (490 m/s) is attributed to the presence of significant horizontal and subhorizontal



Figure 79. Quartz crystals arranged obliquely to the vein edges in a quartz-epidote vein (Sample 140-504B-192R-1, 13–14 cm (Piece 4)). Photomicrograph: crossed polars. Qtz: quartz; EP: epidote.

microcracks and 45° alteration veins propagating across the sample. Differences between wet and dry velocity measurements (Fig. 113) are also attributed to microcracks caused by expansion during the drying period. This observation is further confirmed by the higher dry porosity values obtained from the same samples (Table 22).

Thermal Conductivity

Horizontal and vertical thermal conductivity measurements were carried out on 36 samples having lengths between 5 and 19 cm (Table 24). The samples were polished on the cut face to ensure good thermal coupling between the needle probe and the sample. A period of 1 hr was chosen for reaching thermal equilibrium between the conductivity bath and the samples.

Most samples were classified as homogeneous or heterogeneous in composition. Homogeneous samples consisted of uniform mineralogical assemblages (i.e., altered or relatively fresh primary mineralogy) whereas heterogeneous specimens were composed of random altered and unaltered patches. Upon inspection, some measurements were performed along altered and unaltered bands, veins, and fractures in order to isolate the thermal properties of specific features (Table 24). Organizing the values in this manner showed that the lowest values are associated with cracks whereas the highest conductivity was obtained within homogeneous compositions (Fig. 114).

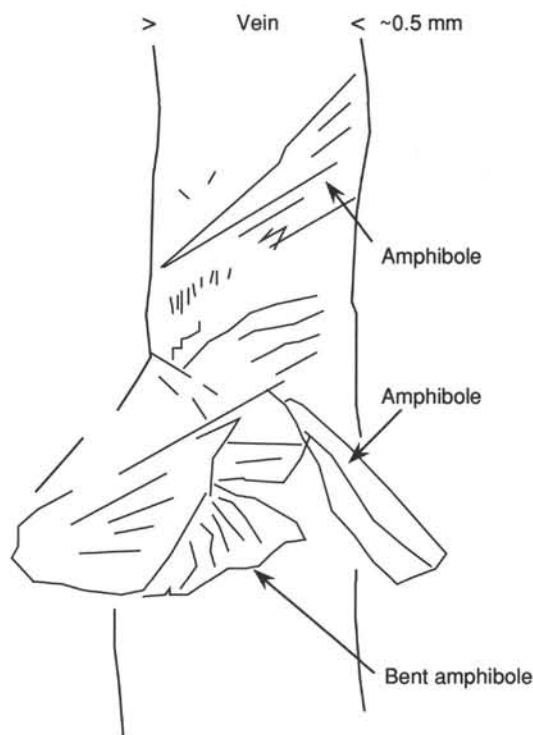


Figure 80. Deformed amphibole crystals filling a vein (Sample 140-504B-198R-1, 70–71 cm (Piece 18)).

Most open cracks, which are caused by drilling and unloading of the in-situ stress within the rock, tend to dissipate heat and produced low conductivity values. Thus, these values do not represent the thermal properties of the rocks within this section of the hole. Heterogeneous samples have a mean value of $2.22 \text{ W/m}\cdot\text{K} \pm 0.16 \text{ W/m}\cdot\text{K}$ and homogeneous samples center around a mean value of $2.59 \text{ W/m}\cdot\text{K} \pm 0.13 \text{ W/m}\cdot\text{K}$. The difference between these mean values may be attributed to lateral variations in thermal properties within heterogeneous specimens caused by changes in mineralogy.

The thermal conductivity measurements obtained during Leg 140 are higher than those reported during Leg 111 ($2.01 \text{ W/m}\cdot\text{K} \pm 0.10 \text{ W/m}\cdot\text{K}$) and slightly higher than the values from Leg 137 ($2.16 \text{ W/m}\cdot\text{K} \pm 0.14 \text{ W/m}\cdot\text{K}$). Based on these results, the thermal conductivity of Hole 504B has been gradually increasing as a function of depth, perhaps due to a gradual increase in grain size and a more mafic composition. The degree of alteration as well as the presence of microcracks within these samples can explain the variability between vertical and horizontal measurements. Furthermore, the lack of a strong fabric or preferred mineral orientation implies that any degree of thermal conductivity anisotropy is caused by heterogeneous compositions and fractures.

DOWNHOLE MEASUREMENTS

Introduction

During Leg 140, the downhole measurements program in Hole 504B consisted of two phases. The first phase preceded fishing operations and included two separate measurement runs: (1) the recording of temperature data and (2) the formation microscanner (FMS), magnetometer, and natural gamma-ray (GR) log. This short program of downhole measurements was run immediately after the first re-entry in order to investigate the thermal structure in the upper part of the basement. It was mainly aimed at monitoring the renewed vigorous downflow of ocean-bottom water detected 6 months earlier

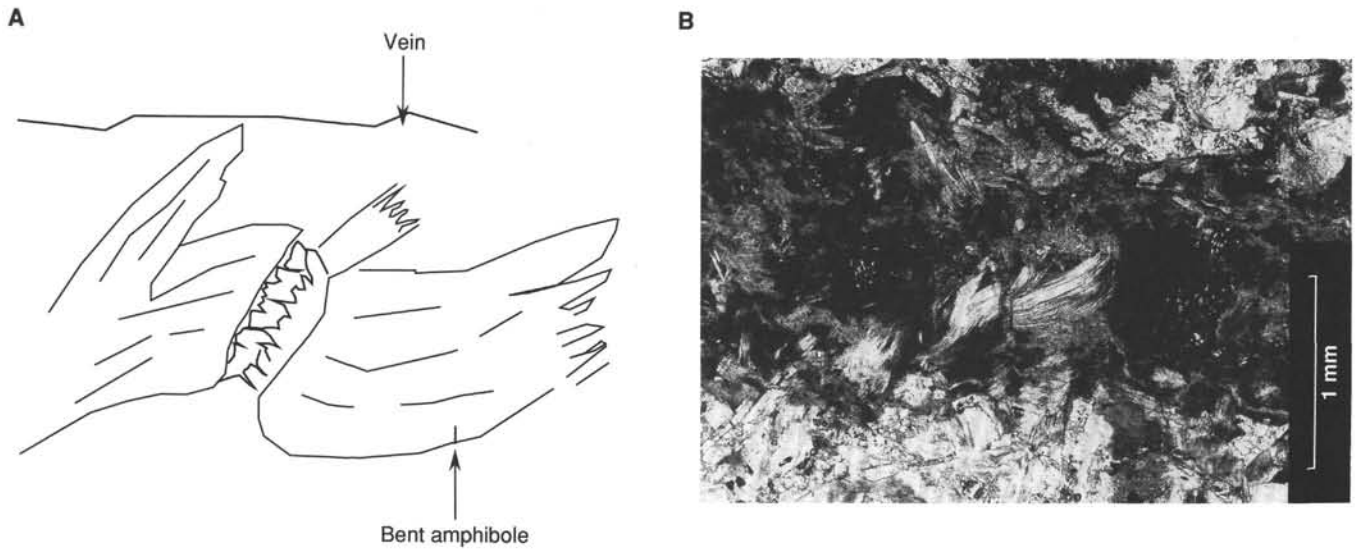


Figure 81. A. Bent amphibole crystals (white crystals at the middle) filling a vein (dark gray) (Sample 140-504B-189R-1, 105–106 cm (Piece 21B)). B. Photomicrograph: plane-polarized light.

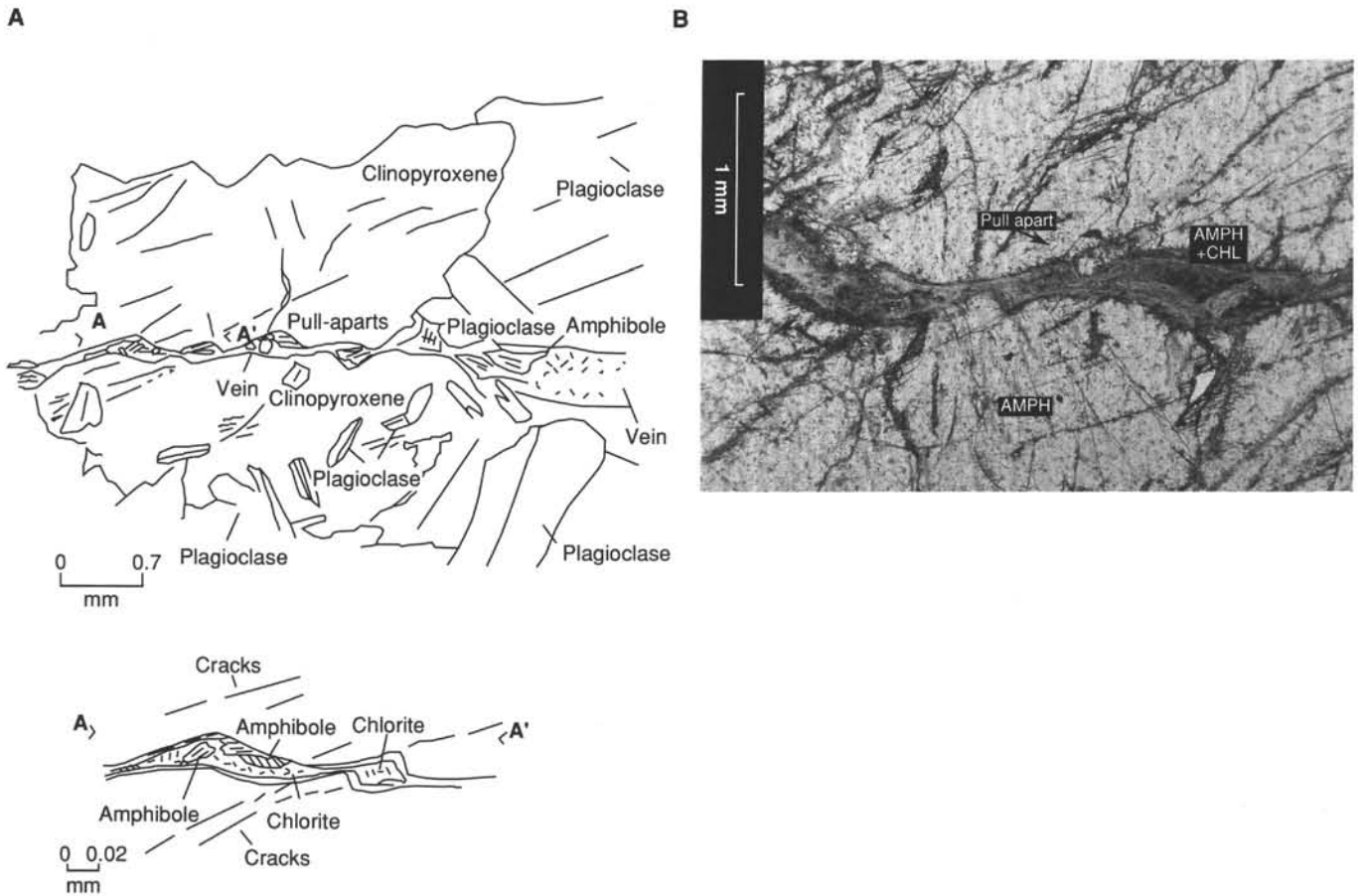


Figure 82. A. Pull-apart structures in a vein cutting a centimeter-sized clinopyroxene phenocryst (Sample 140-504B-186R-1, 17–26 cm (Piece 5)). B. Photomicrograph: plane-polarized light. AMPH: amphibole; AMPH + CHLO: amphibole + chlorite in the matrix of the vein.

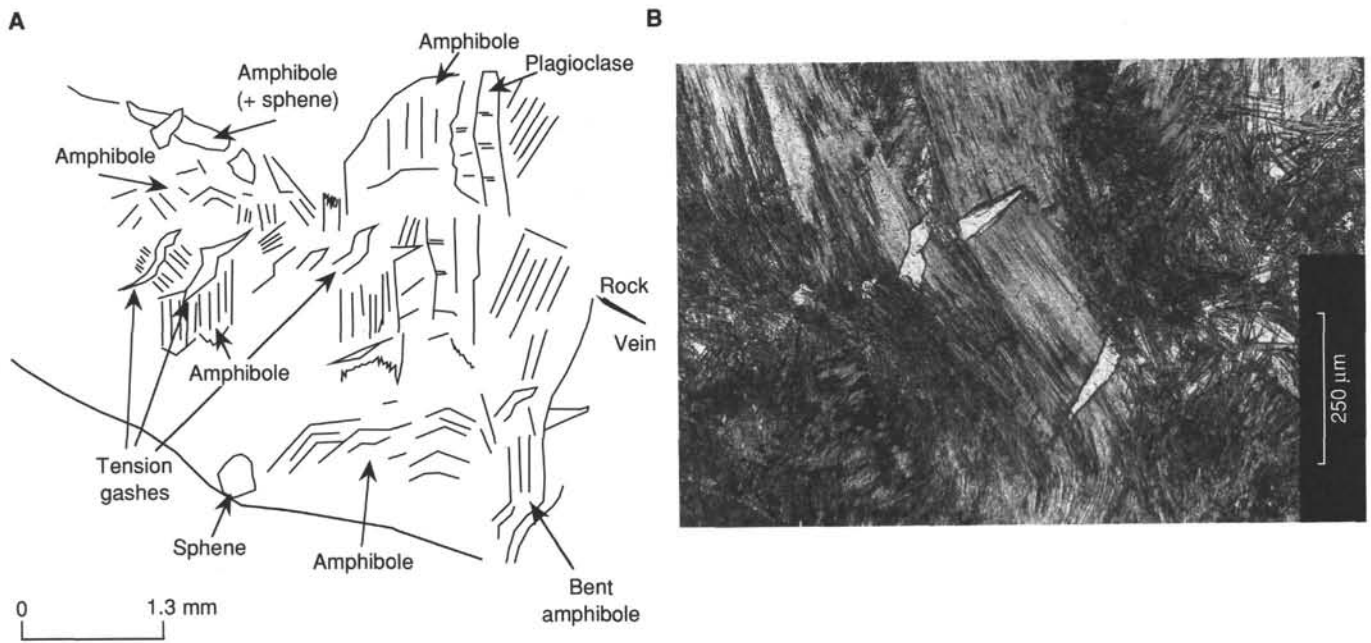


Figure 83. A. Tension gashes (quartz-filled) inside an amphibole-vein (Sample 140-504B-186R-1, 53–57 cm (Piece 10)). B. Photomicrograph: plane-polarized light.

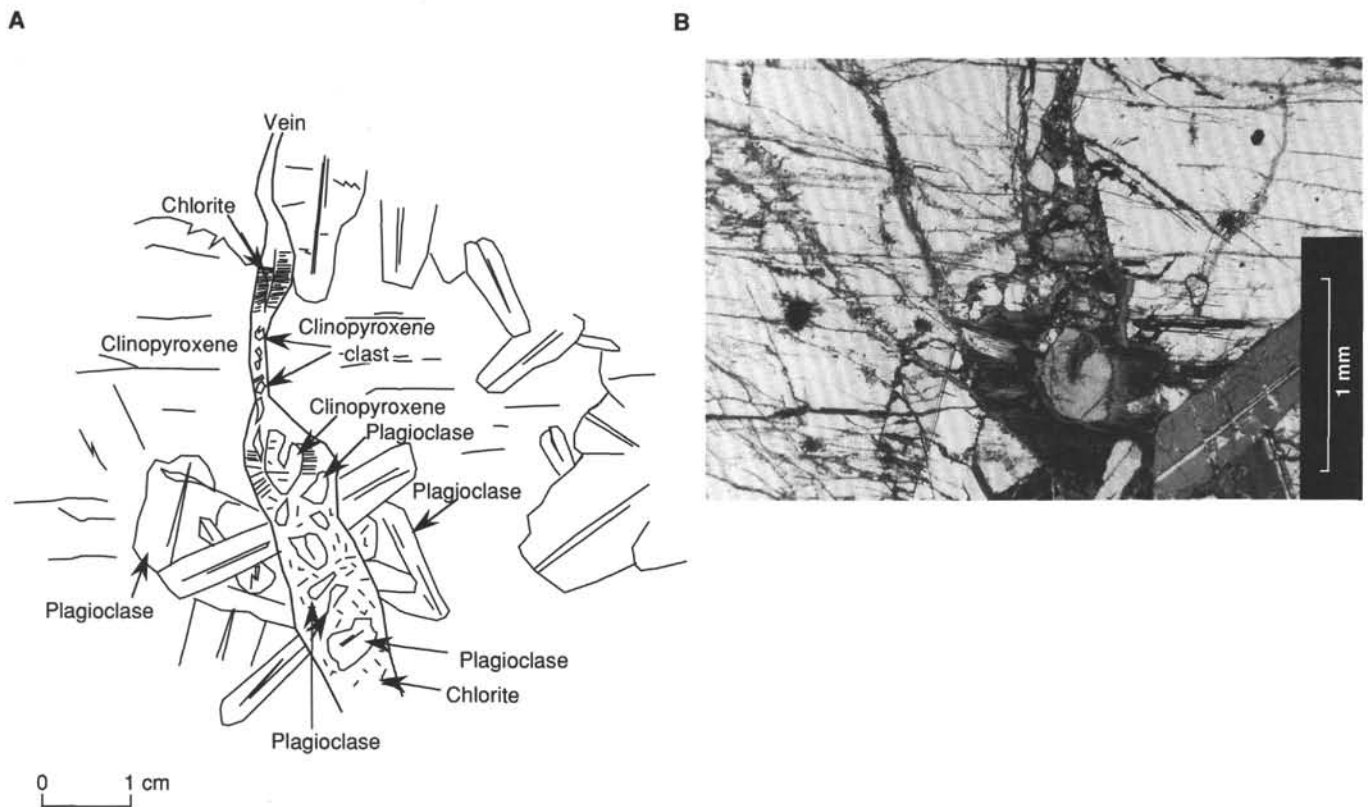


Figure 84. A. Mineral clasts filling a vein (Sample 140-504B-186R-1, 13–14 cm (Piece 4)). B. Photomicrograph: cross-polarized light.

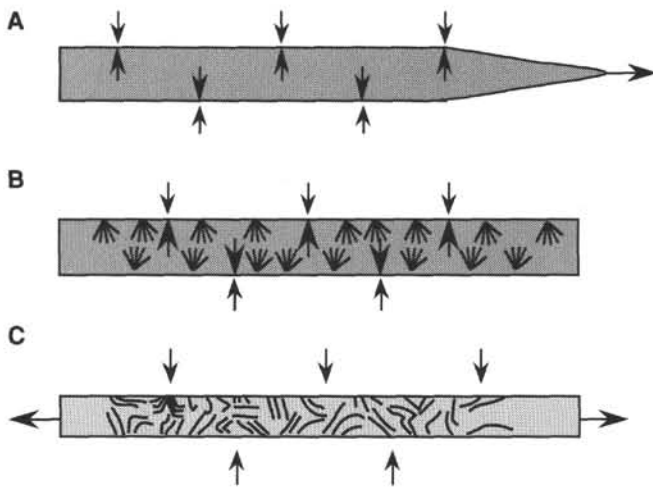


Figure 85. Model for the formation and deformation of amphibole veins. **A.** Fracture propagates. **B.** Fibrous minerals precipitate. **C.** Pressure on the walls closes the vein, deforming the fibrous crystals inside in a chaotic manner.

during Leg 137. The temperature sensor was lowered into the hole first, with the drill bit located inside casing at a depth of 3534.5 mbsf (60 mbsf).

The second phase of the downhole measurements program followed coring and consisted of six measurement runs. These included a high-resolution temperature run, the geochemical combination, the geophysical combination, the recording of borehole televiwer (BHTV) images, and a flowmeter experiment. Except for the flowmeter, whose measurements were restricted to the upper 200 m of the basement, all downhole measurements included the newly drilled section of the hole.

Data Acquisition after Re-entry

Run 1 (High-resolution Temperature)

This downhole tool was essentially the same as that used to record temperature data during Leg 111 (Gable et al., 1989), except for the use of different thermistors to improve the resolution capability of the tool. The temperature tool was lowered into Hole 504B at a velocity of 15 ft/min (4.57 m/min), with the re-entry bit located inside casing at a depth of 60 mbsf. Measurements were recorded every 0.1 m, from 200 mbsf to 550 mbsf. The operation was stopped at 550 mbsf, where the recorded temperature was identical to that measured at the same depth during Legs 111 and 137, in order to minimize operational time. To check the stability of the downhole probe, a 15-min stationary recording was made at 550 mbsf.

Run 2 (FMS Electrical Images–Magnetometer–Natural Gamma Ray)

The formation microscanner (FMS) produces high-resolution borehole images and, thus, allows visual characterization of the structures located in the near vicinity of the borehole wall (Ekstrom et al., 1986). The natural gamma sonde was used for depth correlation.

As the FMS was being lowered near the bottom of the hole, the current used to power the tool increased suddenly. The sonde was stopped and recording started at 1575.0 mbsf, well above the top of the fish at the bottom of the hole. Data acquisition started at a tool velocity of 1500 ft/min (500 m/min), and shortly thereafter, the telemetry link between the tool and the surface computer was lost at 1563.0 mbsf. This telemetry failure was probably due to the high downhole temperature (about 165°C). Without a communication link with the tool, it was impossible to close the sonde. From this depth, the tool was slowly pulled out of the hole (at logging velocity), and

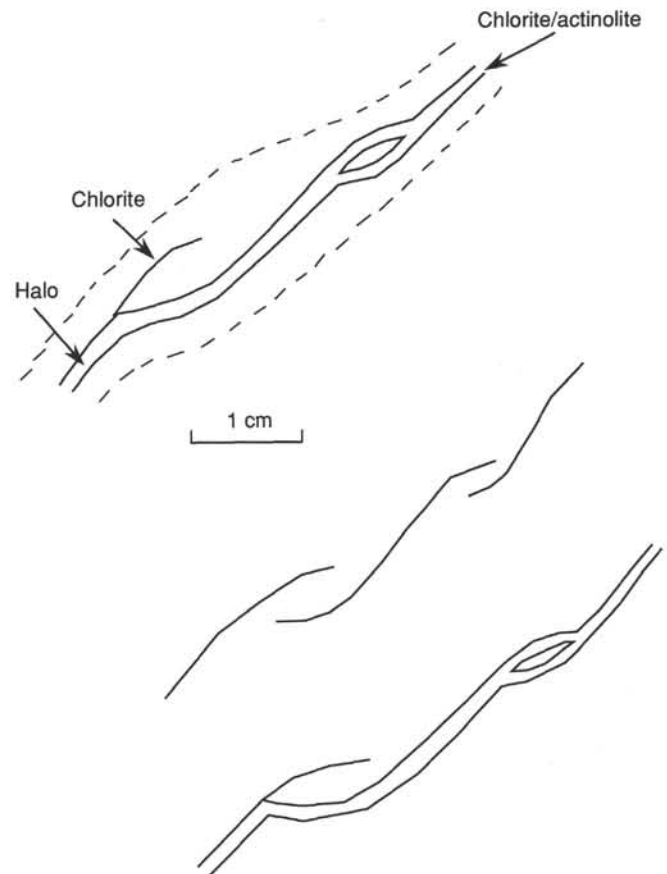


Figure 86. Overlapping system of veins (Sample 140-504B-190R-1, 75–79 cm (Piece 17)). Sketch of vein morphology (working half) and stages of development from (top) chlorite-filled en-echelon cracks to (bottom) throughgoing chlorite/actinolite vein.

every effort was made to regain control of the operation sonde. An overpull of 3600 lb was experienced at 1137.5 mbsf before communication was re-established at 1000.5 mbsf. This overpull probably damaged the sonde, as the data quality from two of the four electrode arrays were seriously affected when recording was resumed at 985.5 mbsf. The electronic circuits controlling the measuring currents also appeared to be affected by this initial series of problems.

While retrieving the sonde out of the hole, a second overpull was experienced inside the drill pipe, when passing by the “Kinley-cutter” restriction near the lower part of the bottom-hole assembly. As a consequence of this series of problems, one FMS arm, one complete bow-spring, and two electrode arrays (pads #1 and #4) were left in the hole. As good images were recorded up to basement top with pad #1, at least one pad was lost after the end of the recording, probably due to overpull in the drill pipe at 1137.5 mbsf. The other pad (#4) could have been lost during the first overpull. The wireline heave-compensator was used to perform each of these downhole measurements.

Data Acquisition after Coring

Run 1 (High-resolution Temperature)

The downhole sensor used for this measurement was the same as that used to record temperature data at the beginning of Leg 140 and during Leg 137. The temperature tool was lowered into Hole 504B at a velocity of 15 ft/min (4.57 m/min), with the re-entry bit located inside casing at a depth of 104 mbsf. Measurements were recorded every 0.1 m, from 15 to 2000 mbsf. Expected equilibrium tempera-

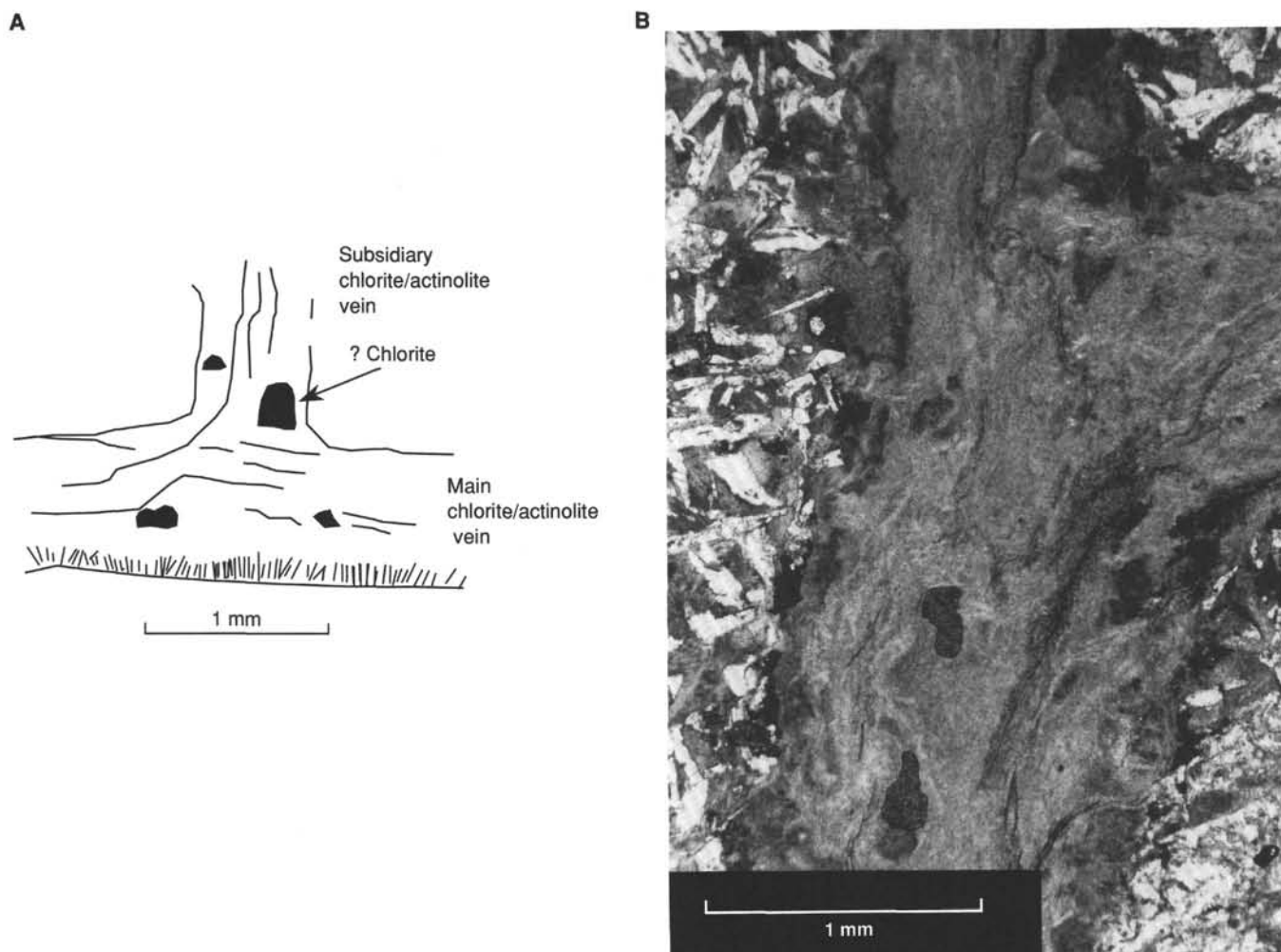


Figure 87. A. Chlorite-amphibole vein abruptly terminating against another vein (Sample 140-504B-197R-1, 99–101 cm (Piece 22)). B. Photomicrograph: plane-polarized light.

tures at total depth from previously measured gradients were of the order of 192°C, well beyond the maximum operating temperature of Schlumberger sensors (175°C). This measurement was made first, because of the expected cooling of the hole after 4 weeks of coring in order to evaluate the thermal status of the hole, and then set up a strategy for further downhole measurements. In order to evaluate the equilibrium temperature at total depth, and because mechanical problems with the winch, a 1-hr-long temperature recording was made, indicating a temperature increase of 2.0°C/hr. The wireline heave-compensator was used during the temperature run and for all subsequent downhole measurements.

Run 2 (Geochemical Combination–Natural Gamma Ray)

The geochemistry tool was the most heat-sensitive downhole sensor used during Leg 140, so it was run immediately after the temperature tool. As the geochemistry tool was being lowered in the hole, the GST cartridge failed at 700 mbsf, and the tool had to be pulled out of the hole to change the cartridge. The geochemical combination was run again, from 1896 to 1811 mbsf at a recording velocity of 200 m/hr. The GST minitron stopped operating at 1811 mbsf, probably due to high borehole temperature. While being pulled out of the hole, hence into a cooler environment, the minitron revived and logging continued from 1686 to 1350 mbsf.

Run 3 (Resistivity–Acoustic Velocity–Natural Gamma Ray)

The geophysical combination composed of the dual laterolog (DLL) resistivity sensor, the long-spacing acoustic velocity sensor (LSS), and natural gamma sensor (NGS) was run next. Unfortunately, communications with the tool were lost at 526 mbsf as water leaked into the bridle-head specially adapted to run the DLL. The tool was subsequently pulled out, repaired, and run again successfully from 275 to 1990 mbsf at a recording velocity of 600 m/hr. In order to improve the sonic data quality, two passes were made in the newly drilled section of the hole, from 1990 to 1480 mbsf.

Run 4 (Borehole Televier–Magnetometer)

The digital borehole televier was deployed next. It was run down to 1980 mbsf, operating properly, but communications with the tool were suddenly lost at this depth. The tool was pulled out, and the Gearheart-Owen cable-head was found to be damaged. A new cable-head was built, and the hole was successfully logged from 1985 to 1885 mbsf, and from 1685 to 1485 mbsf at a recording velocity of 200 m/hr. Constant communication problems between the surface panel and the downhole sensor obliged us to record the acoustic borehole images in small sections, and finally prevented us from logging the entire interval drilled during Leg 140.

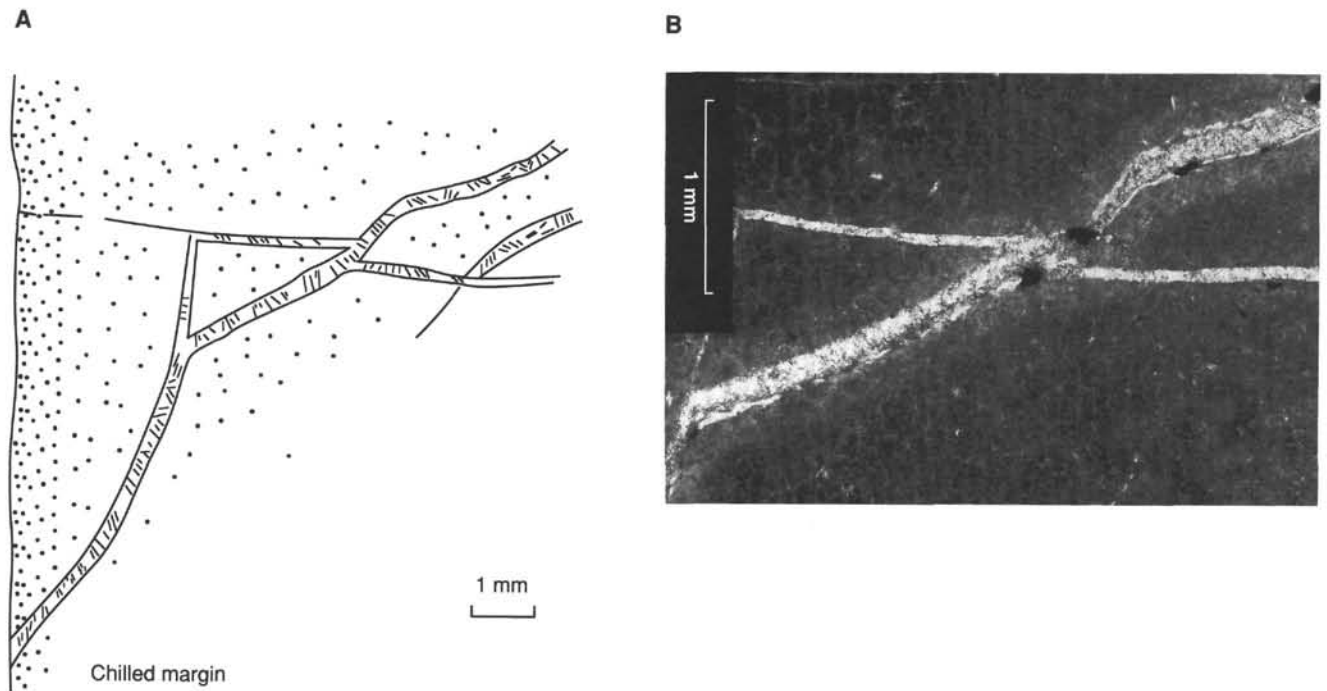


Figure 88. A. Crosscutting relationships with offset between veins cutting a chilled margin (dark gray) (Sample 140-504B-203R-1, 33–36 cm, (Piece 10)). B. Photomicrograph: plane-polarized light.

Run 5 (Flowmeter Experiment)

As initially planned, a flowmeter experiment was performed in the upper part of the basement. Four passes (two upward, and two downward) were recorded at different logging velocities over the most permeable part of the crust, between 256 and 468 mbsf. This experiment was followed by a calibration made in the pipe, where the tool was pulled out successively at six different cable velocities in order to evaluate the sensitivity of the spinner. As the wireline heave-compensator was being disconnected, a larger spread of data was recorded, showing the importance of the wireline heave-compensator for downhole measurements and the influence of ship's heave even as deep as 3500 m below the drill floor.

Run 6 (Geochemical Combination–Natural Gamma)

Because 6 hr were left prior to departing from Site 504, the geochemical combination was repeated in order to fill the gap in the data caused by the minitron failure encountered during Run 2. The tool was logged successfully from 1826 to 1648 mbsf at a velocity of 200 m/hr, hence effectively covering the section omitted during Run 2. Continuous geochemical data were thus recorded during Leg 140 from 1896 to 1350 mbsf.

Data Analysis

Temperature (Recorded Prior to Drilling)

The temperature profile recorded prior to drilling on Leg 140 between 200 and 550 mbsf (Fig. 115) is characterized by a gradient inversion in the upper part of the basement (283 to 288 mbsf; Fig. 116), probably due to local fluid inflow from the basement into the borehole. Below this upper section, the temperature gradient reaches values as high as 500°C/km, which can be explained by borehole fluid intake into the fractured basement. The three temperature profiles recorded at Hole 504B over the past 5 years, during ODP Legs 111, 137 and 140 (Fig. 117), vary widely with time of the hydrological activity in the upper basement. A strong downward flow of cold ocean

bottom water into the hole is outlined by the Leg 137 profile (Fig. 117). However, the Leg 111 and 140 profiles show a much weaker downflow in the cased sedimentary section, with a value on the order of 1.2 m/hr (Gable et al., 1989). Below 250 mbsf, differences between data recorded during Leg 140 and that recorded during Leg 111 (Fig. 117) suggest the presence of cold fluid inflow from the upper basement into the borehole. This fluid activity at the very top of the basement appears to be in contrast to the previous gradual re-equilibration of the underpressure observed between 1979 and 1986 (Gable et al., 1989). Such rapid and possibly short-lived variations may be related to modifications of the hydraulic “connectivity” of the upper basement, and may result from local tectonic activity. Below 450 mbsf (Fig. 117), the three temperature profiles coincide to describe a relatively constant thermal regime in the least permeable section of the basement during the past 10 years.

The Leg 140 temperature gradient recorded prior to drilling can be compared to the fracture porosity profiles derived from the analysis of electrical resistivity data obtained with the Dual Laterolog (DLL) during Leg 111 (Becker, Sakai, et al., 1988; Pezard, 1990). The principal mode of fracturing (either horizontal or vertical) was characterized by this method, and a minimum value for the volume fraction (or “porosity”) of the detected mode was computed (Becker, Sakai, et al., 1988). The lower sedimentary column and the upper basement zone (from 200 to 315 mbsf), where important fluid exchanges between the borehole and the basaltic basement were recently discovered, are described separately (Fig. 118) from that recorded in the deeper basement section (320–500 mbsf, Fig. 119). In this lower section, fluid flow into a depressurized aquifer was discovered and investigated as early as Leg 70 (Anderson and Zoback, 1982; Anderson et al., 1985). This porous aquifer was recently shown to be located below a thick and impermeable massive unit (Pezard, 1990), which is used here as a boundary to present the result of this comparison between fracture distribution and the temperature profile.

The zone of thermal gradient inversion located in the upper 15 m of the basement corresponds to a region where horizontal fractures dominate (Fig. 118). Similarly, a 1.0-m-thick pillow unit located just above a massive flow (lithologic Unit 2D) and characterized by

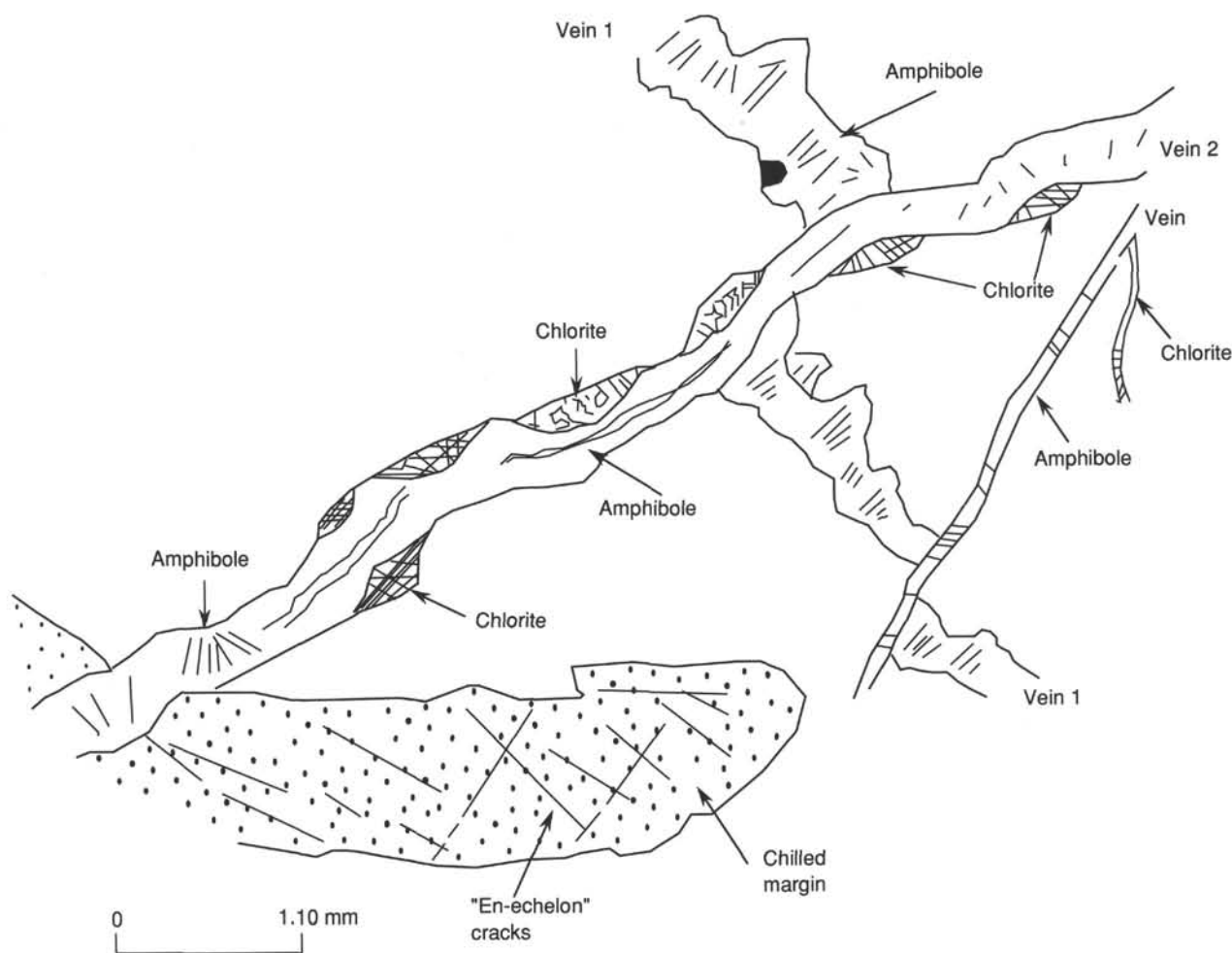


Figure 89. Crosscutting relationships between veins with offset (Sample 140-504B-198R-1, 70–71 cm (Piece 18)).

horizontal fracturing (310 mbsf) was the location of the abrupt change in temperature gradient recorded during Leg 137 (Fig. 117). However, this thin and fractured pillow unit was not the site of an abrupt temperature gradient in the Leg 140 profile (Fig. 118). In contrast, no particular inflow was noticed from 300 to 310 mbsf, where the presence of vertical fracturing is outlined by the resistivity data. The movement of fluids (in or out of the basement) is thus apparently favored by the presence of a horizontal fracture network. In the cased sedimentary section, the temperature gradient directly reflects the variations in thermal conductivity measured on the sediments from Holes 501 and 504. The bottom of the nanofossil ooze observed in Holes 501 and 504 (Cann et al., 1983) appears to be located in Hole 504B at 252 mbsf. In this upper sedimentary section, the temperature gradient recorded at the beginning of Leg 140 is nearly constant.

In nearby Holes 501 and 504, limestone with calcareous chert horizons (with increasing values of thermal conductivities with increasing depth) was cored at the base of the sedimentary section. The decreasing thermal gradient recorded in this interval (Fig. 118) follows the thermal conductivity increase with depth in Holes 501 and 504 (Cann et al., 1983). At the sediment-basement interface, a nearly constant value ($-0.25^{\circ}\text{C}/10\text{ m}$) is recorded over a 5-m-long interval. This interface, as in Holes 501, 504A and 505, is the zone of higher than average natural gamma-ray values (Cann and Von Herzen, 1983). These intervals have high gamma-rays values relative to the underlying basement, reflecting the presence of K, Th, and/or U, and are indicative of more altered basalt due to past and/or present fluid

circulation. The constant values recorded over this short interval during the Leg 140 re-entry argue against fluid circulation along this sediment-basement interface at the time of the experiment.

The basement interval located from 320 to 550 mbsf is characterized by the presence of several horizontal and vertical fractures (Fig. 119), with maximum fracture densities recorded within Layer 2A (Pezard, 1990). Horizontal fractures are uniformly distributed within the 30-m-thick aquifer (Cann et al., 1983; Pezard, 1990) located below massive Unit 2D, whereas the number of vertical fractures tends to decrease with increasing depth away from Unit 2D. The highly fractured zone is the site of a large positive anomaly of the thermal gradient, and probably indicates fluid intake from the borehole into the formation. Within Layer 2B, from 400 to 550 mbsf, the thermal gradient values tend to be nearly constant in steps defining three zones. These three zones are the sites of mostly vertical fractures, but appear to be separated by regions of horizontal fractures located at about 400, 450, and 510 mbsf. The deepest zone is characterized by a distinct paleoflow regime, with the presence of sodic and calcic alteration (mostly zeolites) observed in rocks from this interval (Alt et al., 1986). Such a detailed analysis provides a means to analyze the porosity structure of the upper basement in great detail, and to compare it with either past or present dynamic geological parameters, such as secondary alteration and temperature. The vertical resolution of such an analysis is that of standard downhole measurements on the order of a meter. The analysis of FMS electrical images should improve this detailed study due to the spatial orientation of the images, and the centimeter-scale resolution of the electrode array.

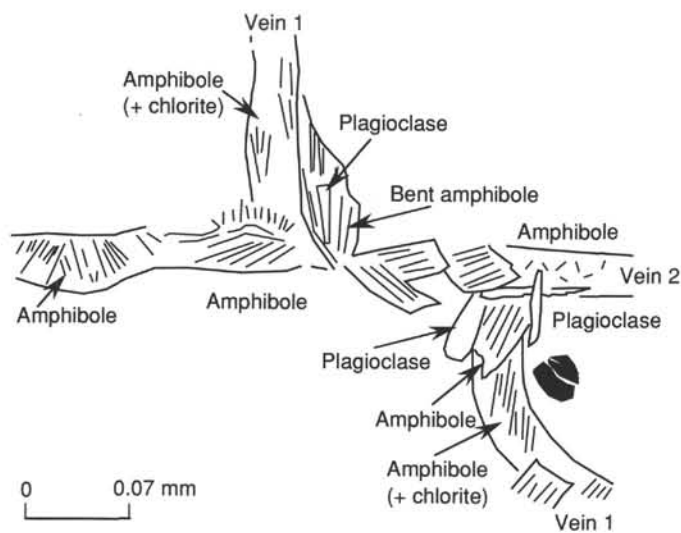


Figure 90. Crosscutting relationships with offset between veins (Sample 140-504B-186R-1, 53–57 cm (Piece 10)).

Electrical Images

The initial processing of the raw FMS data into electrical images was carried out on board ship during Leg 140 using proprietary Schlumberger software on the L-DGO VAX 3100 workstation. Once created, the electrical images were transformed into resistivity maps of the borehole wall using the calibrated shallow-laterolog (LLs) measurements obtained during Leg 111 (Becker, Sakai, et al., 1988). An example of this calibration is presented on Figure 120 over a short interval (306–324 mbsf) located in the upper part of the basement. This interval is composed of a massive unit (with high electrical resistivity values), and with pillows located above and below (with low electrical resistivity values). The resistivity values computed for one of the FMS electrodes (button B4) is compared to deep and shallow laterolog measurements (LLd and Ll). The three data sets generally agree well, considering the fact that the vertical resolution of the FMS is approximately 200 times higher than that of the dual laterolog (DLL). In order to reflect this large difference in vertical resolution, the DLL data are presented here as dots and the FMS-derived curve is plotted as a continuous trace. Thin and conductive fractures appear on the FMS-derived trace but are averaged out in the laterolog dataset.

In the short lower interval (1563–1575 mbsf), where three good FMS images were recorded, 61 individual fracture traces were identified, then mapped by hand on board the ship using a specially designed transparent overlay. Once represented on a stereoplot (Fig. 121), most of these fractures appear to be steep, and to dip toward the south and southeast (Fig. 122). A comparison of this dataset to direct observations from the core is provided in the structural section. In addition, the borehole ellipticity outlined by the FMS calipers over this interval was oriented toward N105.0°, in good agreement with the minimum horizontal stress direction (117.5°) derived from the analysis of BHTV images in the upper part of the hole by Morin et al. (1990).

Further processing and analysis of the FMS images will be performed on shore and will be aimed at producing a detailed lithostratigraphy, and detecting, mapping, and identifying fractures and faults (Pezard and Luthi, 1988; Pezard et al., 1988). The cored sections will be oriented whenever core recovery allows. Also, the FMS electrical images will be used whenever possible to determine the principal horizontal stress directions in conjunction with the BHTV images (Bell and Gough, 1979; Morin et al., 1990).

The three-components magnetometer data (F_x , F_y , F_z) extracted from the FMS dataset will be compared to those recorded during Leg

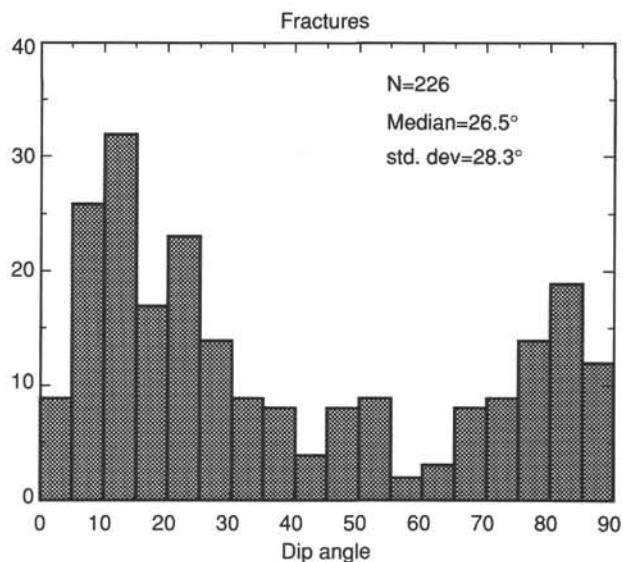


Figure 91. Histogram of true dip for measured fractures. Std dev = standard deviation.

111 using the General Purpose Inclinometry Tool (GPIT). Figure 123 is an example of the magnetic field measurements from Leg 140.

Temperature (Recorded After Coring)

The temperature profile recorded at the end of Leg 140 in Hole 504B shows lower temperatures with respect to equilibrium values than those recorded directly after first re-entry (Fig. 124) due to cooling during the coring. Active fluid movements were still detected in the upper basement, which is also the most permeable portion of the hole (Fig. 125). Negative temperature gradient values are obtained in discrete sections of the dikes. Such intervals most probably correspond to fractured and permeable zones where fluid was injected during coring. These zones were therefore efficiently cooled. In the bottom 200 m of Hole 504B, a sharp gradient increase was observed (Fig. 125) over the same interval where significant zinc leaching is reported (Fig. 126). The 1-hr-long temperature record at total depth (2000.4 mbsf) will allow the computation of the equilibrium temperature at this depth in Hole 504B (Fig. 127).

SUMMARY AND CONCLUSIONS

Introduction

JOIDES Resolution (SEDCO BP 471) returned to Hole 504B during Leg 140 of the Ocean Drilling Program and deepened it to 2 km, making this the deepest hole drilled in the ocean crust. This was the result of a two-leg effort during 1991, with 100 days at sea, culminating over 12 years of off-again, on-again drilling to reach a depth of 2 km below the seafloor. Three times deeper than any previous penetration into oceanic basement, Hole 504B is the only drill hole to penetrate the layer of sheeted dikes beneath the thick sequence of lava flows that pave the seafloor at ocean ridges.

Leg 140 deepened Hole 504B by 378.9 m, well in excess of the targeted 300 m for the leg, thereby overcoming numerous problems besetting previous attempts to deepen the hole. The deteriorating hole conditions, the high temperatures, poor rock recoveries, numerous breakouts observed during logging, apparent problems with the casing at the top of the well, and the perceived difficulty in clearing the large amount of metal at the bottom of the hole had previously left the status Hole 504B in serious doubt.

Leg 140 began with a successful, though time-consuming, attempt to fish an overshot, core barrel, and diamond bit from the hole. As a

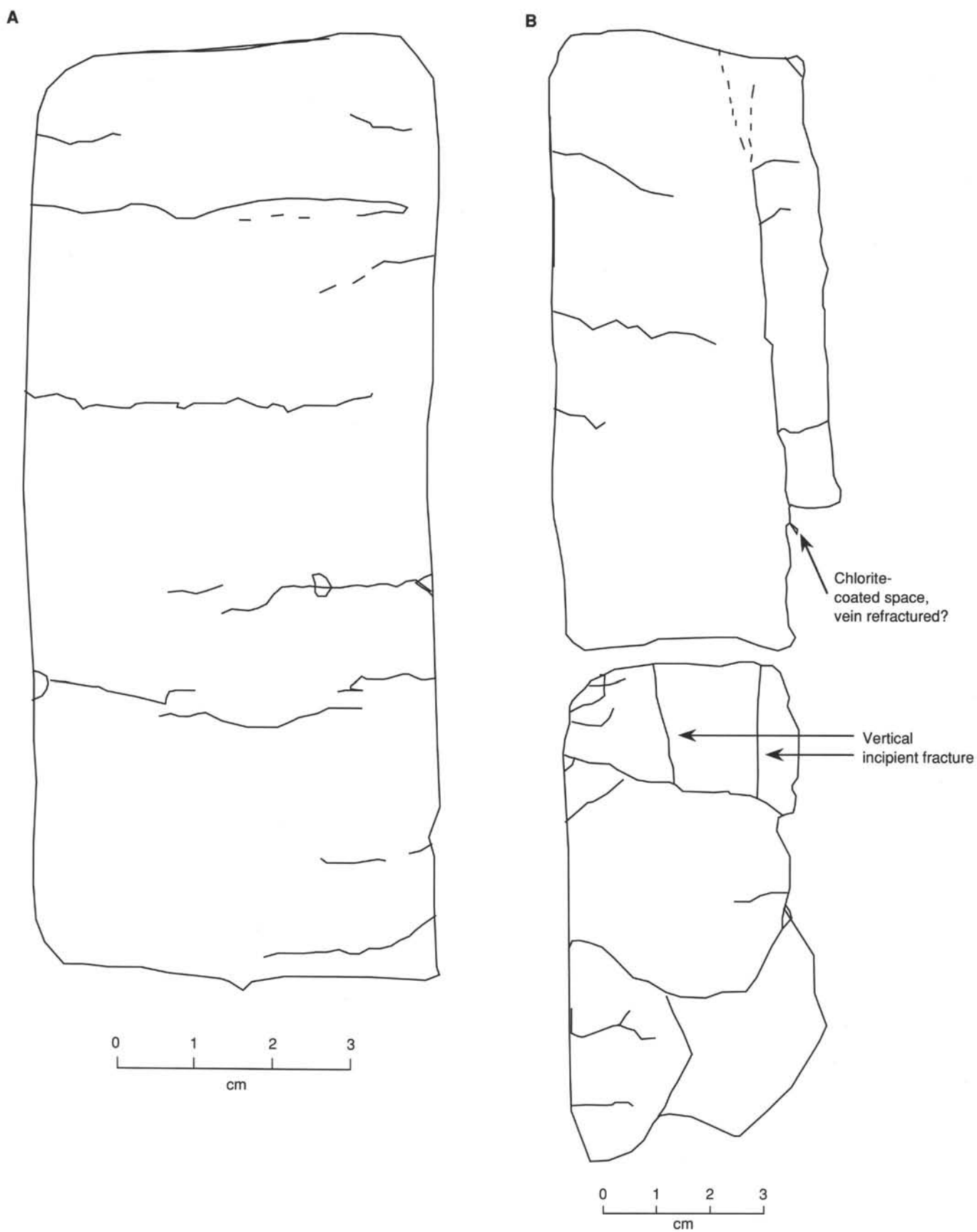


Figure 92. Sketches of fracture morphology. **A.** Low-angle incipient discing fractures. Interval 140-504B-200R-1, Piece 17B, working half. Incipient shallow fractures may result from discing. **B.** Low-angle incipient discing fractures and steeply dipping fracture developed on chlorite vein.

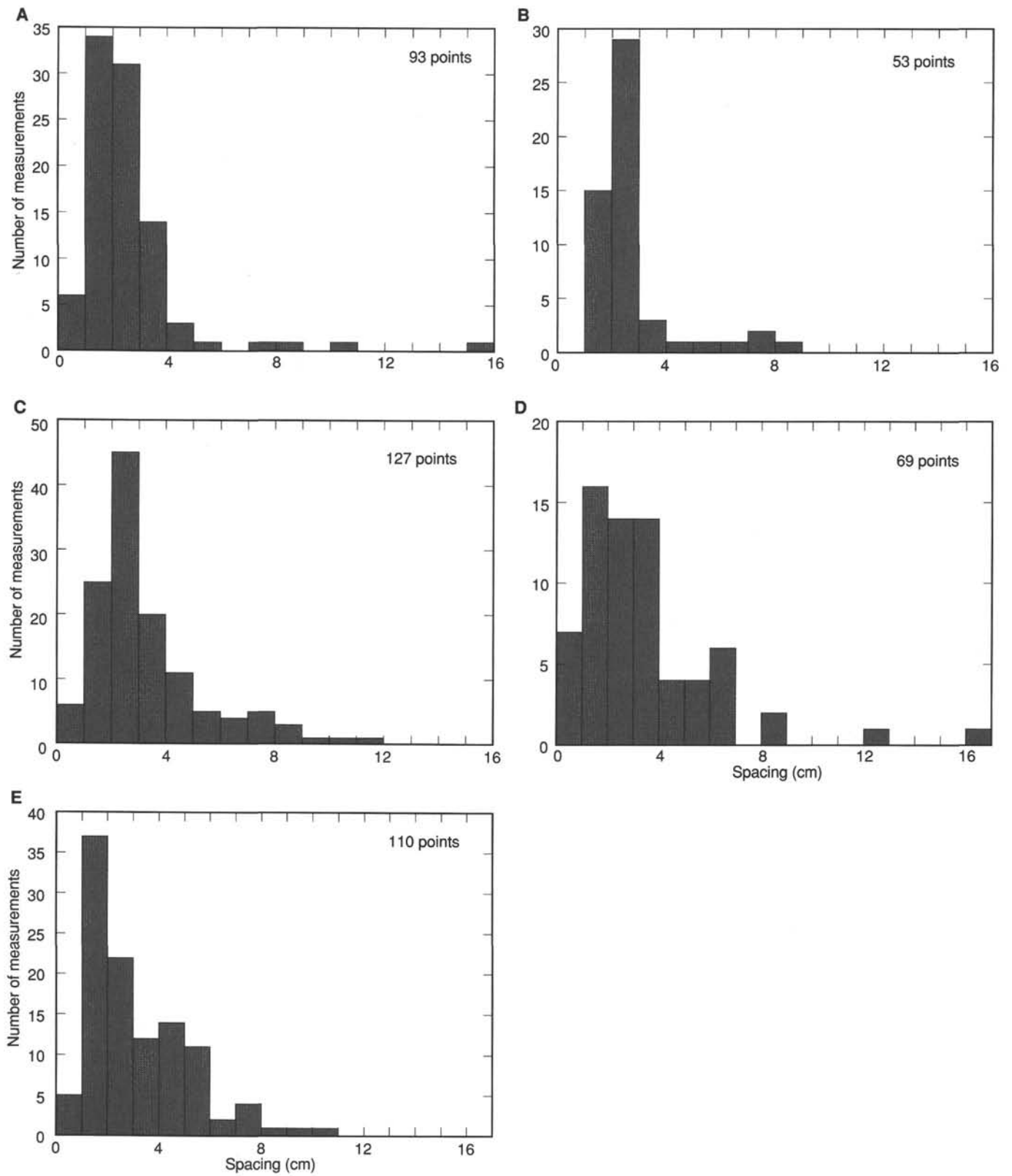


Figure 93. Downhole variations of fracture spacing, low- and moderate-angle dipping structures. **A.** Cores 137-504B-175R to 140-504B-199R. **B.** Cores 140-504B-200R to -207R. **C.** Cores 140-504B-208R to -211R. **D.** Cores 140-504B-212R to -217R. **E.** Cores 140-504B-218R to -228R.

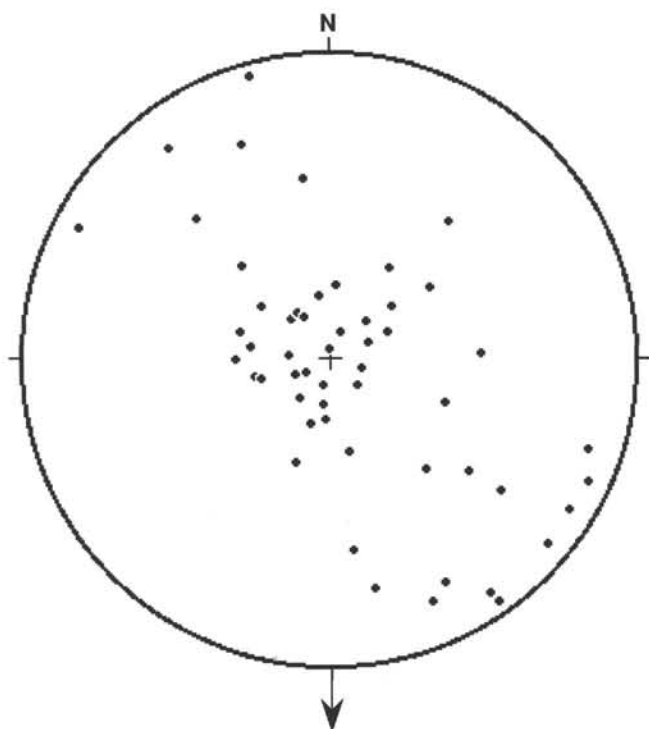


Figure 94. Poles to fractures. Equal-area lower hemisphere stereographic projection. Large arrow indicates paleomagnetic reference direction.

consequence, the time available for drilling was reduced by 10.5 days. Fortunately, no further failures occurred, and the hole was deepened continuously by slow but steady drilling over the next 24 days. Prior to departing the site, a suite of downhole measurements were made on the new section of hole, including an acoustic velocity-resistivity log, and runs with the digital borehole televiewer and geochemical combination tool followed by a flowmeter permeability test.

Leg 140 was a great technical success, and clearly demonstrated the value of persistence in deep crustal drilling. Building on the experiences of Leg 111 and engineering Leg 137, new bits were designed which proved far more durable, lasting over three times as long as the average bit on Leg 111. In no case did a total catastrophic bit failure occur. Increased pumping of mud to sweep cuttings and debris from the hole, and carefully maintaining its gauge, greatly improved drilling conditions. Hole stability proved to be good, with special care taken to cool it at 500 m intervals by pumping sea water to reduce thermal shock during pipe trips. At the end of the leg, the RCB was coring at a rate of 1.8 m/hr, torque was normal, and the hole was stable with negligible evidence of hole ellipticity and back-fill problems. The hole was left open and clean. The leg has demonstrated that ocean drilling can advance deep crustal holes to considerable depth with current technology, and it is anticipated that further improvements in bit cutting structure should further enhance future performance.

Igneous Petrology

The 379 m section drilled during Leg 140 is clearly a continuation of the sheeted dikes drilled on previous DSDP/ODP legs. Large grain-size variations exist between units, ranging from very-fine to medium-grained. These variations suggest a cyclicity of intrusion:

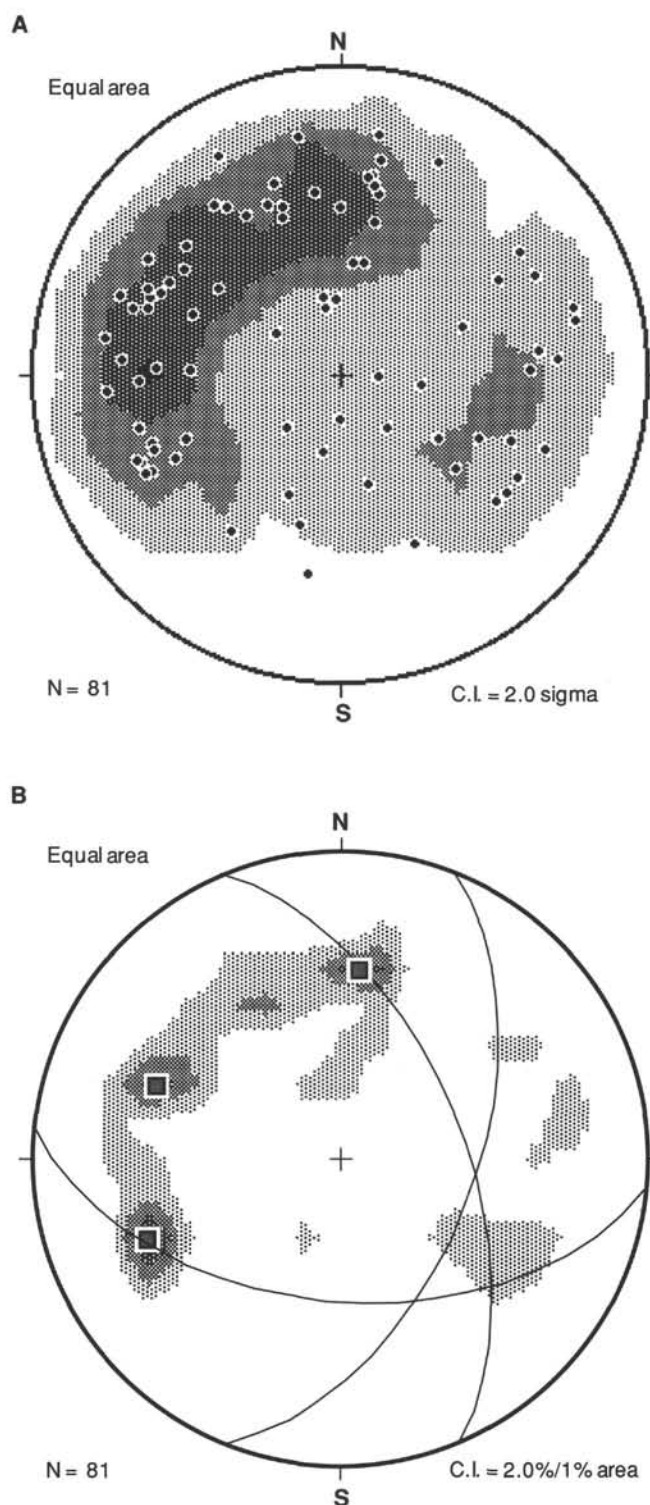


Figure 95. A. Poles to fractures, measured from initial interpretation of FMS images, superimposed on a Kamb contour plot for the same data. Equal-area lower hemisphere stereographic projection. B. Contoured fracture measurements with great circles for major trends superimposed. Equal-area lower hemisphere stereographic projection. C.I. = contour interval, N = number of measurements.

Table 16. Fractures observed in EMS data.

Depth (mbsf)	Dip (°)	Azimuth	Class
1563.5	60	63	3
1563.68	55	70	3
1563.9	55	68	3
1563.99	50	157	2
1564.12	55	130	3
1564.28	60	236	2
1564.37	48	161	2
1564.55	68	254	2
1564.81	40	309	2
1564.81	50	63	3
1565.1	19	319	2
1565.11	58	63	2
1565.14	58	143	3
1565.23	55	146	2
1565.25	62	121	2
1565.3	67	257	2
1565.5	60	66	2
1565.76	50	239	3
1565.81	45	67	2
1566.05	50	149	2
1566.08	60	243	3
1566.08	35	249	2
1566.13	10	272	2
1566.27	61	67	2
1566.5	70	151	2
1566.88	55	88	2
1567.01	52	269	3
1567.02	60	94	1
1567.14	50	336	2
1567.37	55	161	2
1567.42	45	160	3
1567.62	40	125	2
1567.65	30	346	2
1567.72	50	172	2
1567.85	57	75	2
1568.02	60	266	3
1568.25	60	191	2
1568.25	65	205	2
1568.33	50	92	2
1568.39	65	86	2
1568.5	43	112	2
1568.62	67	170	2
1568.82	66	99	2
1569.43	60	108	1

Depth (mbsf)	Dip (°)	Azimuth	Class
1569.75	65	110	2
1569.75	55	9	2
1570.07	45	180	2
1570.07	55	189	2
1570.18	42	15	1
1570.25	30	186	2
1570.28	21	12	2
1570.3	30	192	2
1570.32	53	118	2
1570.37	20	177	2
1570.38	18	168	2
1570.38	21	167	2
1570.62	68	189	2
1570.71	22	278	3
1570.79	40	92	3
1570.91	56	305	2
1570.93	50	192	3
1571.09	35	23	2
1571.14	52	35	2
1571.16	55	263	2
1571.2	56	300	2
1571.37	52	190	3
1571.58	50	291	2
1571.78	56	112	2
1571.79	20	44	3
1571.79	56	109	2
1571.82	12	360	2
1571.83	54	114	2
1572.07	58	114	3
1572.15	60	290	1
1572.26	55	309	2
1572.53	41	295	3
1572.63	54	188	2
1573.16	51	124	2
1573.19	31	303	2
1573.22	42	193	2
1573.57	20	123	2

NOTE: Class: 1. Fracture well defined on all traces. 2. Feature well defined on two traces with slight contrast on the third. 3. Feature well defined on one trace with slight contrast on the others.

dikes intruded early in a cycle, after an intrusion hiatus, are finer-grained, with mean grain-size increasing toward the end of the cycle as dikes cooled more slowly due to higher wall rock temperatures. Systematic grain-size analysis of representative thin sections suggests that Leg 140 may have cored three such intrusion cycles.

Contacts between dikes were rarely seen in the Leg 140 section, and, where observed, the chilled portions are inferred to be narrow apophyses on terminations of dikes. Almost no glassy or aphanitic material was recovered and the margins of individual dikes differed from those most often seen in ophiolite complexes. In the latter, dike margins consist of 0.1–5.0 cm glassy, aphanitic, or very fine-grained chill zones (e.g., Lippard et al., 1986) with an abrupt change to coarser-grained rock in the dikes interior occurring over a scale of centimeters. The Leg 140 dikes had a more gradual decrease in grain size on a scale of tens of centimeters from medium or fine-grained basalt in the interior to fine or very fine-grained basalt at their margins. An absence of well-developed chill margins characterizes some dikes near the dike-gabbro transition in ophiolites (e.g., Baragar et al., 1990). This is coupled with the appearance of medium-grained dikes and a coarser average grain size than dikes drilled on earlier legs at higher level. These features suggest higher mean wall-rock temperatures and slower cooling, which could be expected near the dike-gabbro transition.

Fifty nine igneous units were described, including 19 aphyric diabases, 14 sparsely phyrlic, and 26 moderately phyrlic. Three are medium grained, 47 fine grained, and only 9 are microcrystalline diabase (mostly chill margin material or backfill stones from higher

in the hole). Thirty six of these units are triply saturated plagioclase-olivine-pyroxene phyrlic diabases, while two contained only olivine and plagioclase and two plagioclase and clinopyroxene phenocrysts. The sequence of crystallization inferred from the phenocrysts is plagioclase first, followed by spinel, olivine, and then augite. Crystallization of augite appears to have depleted the melt in chrome, and terminated spinel crystallization. This differs from that for normal MORB chemistry, where olivine generally precedes plagioclase on the liquidus.

Zoning patterns in plagioclase, though quite variable, suggest a three-part crystallization history that may represent (1) early crystallization in a magma chamber (large uniform or slightly zoned cores with numerous melt and mineral inclusions), (2) crystallization during magma transport and emplacement (mantles with an abrupt change in composition and 2–4 fine oscillatory zones), and (3) in-situ crystallization following dike injection (normally zoned rims). The early zoning patterns indicate that the magmas underwent a complex mixing process as a result of convection within a lower crustal magma chamber and/or during transport through the crust.

A complex suite of cognate and xenolithic crystal clots are common in the diabases. These crystal aggregates are thought to reflect the compositional heterogeneities created in magmatic conduits deep in the crust including the complex combination of processes involving crystal fractionation, magma-mixing, cumulate compaction, and melt/wall-rock interaction. Both syngenetic clots, related to the host rock, and xenocrystic aggregates trapped by upwelling magma and unrelated to the host rock occur. The latter include wehrlitic, pyroxenitic, and gabbroic varieties,

Table 17. Magnetic properties of Leg 137/140 minicores.

Core, section, interval (cm)	Depth (mbsf)	Piece #	J_0 (A/m) (A/m)	MDF (mT)	K (SI units)	χ Q (SI units)
140-504B						
173R-1, 114	1577.47	11	2.16E+00	14.5	1.79E-02	4.6
175R-1, 19	1585.99	3	4.03E+00	11.0	2.68E-02	5.7
180R-1, 92	1619.32	8	1.49E+00	17.5	2.81E-02	2.0
180F-2, 29	1620.19	3	5.20E-01	24.0	1.74E-02	1.1
181F-2, 148	1623.38	12a	7.81E-01	17.0	1.42E-02	2.1
186R-1, 54	1626.84	5	1.63E+00	8.0	5.00E-03	12.4
186R-1, 81	1627.11	13b	7.21E-01	14.0	1.28E-02	2.1
186R-2, 42	1628.22	9	4.52E+00	6.0	1.64E-02	10.5
189R-1, 96	1651.96	21a	2.90E+00	5.0	3.14E-02	3.5
189R-2, 39	1652.89	5c	2.60E+00	5.0	1.52E-02	6.5
190R-1, 95	1656.05	19	1.03E+00	6.0	4.80E-03	8.2
191R-1, 48	1661.88	7b	3.83E+00	6.0	2.62E-02	5.6
193R-1, 48	1674.98	13a	3.00E-02	6.0	4.90E-04	2.3
194R-1, 92	1681.32	18	1.10E+00	7.5	8.11E-03	5.2
197R-1, 131	1704.11	28	5.82E+00	6	2.68E-02	8.3
199R-1, 121	1720.61	26b	3.81E+00	6	1.80E-02	8.1
200R-1, 128	1729.88	21	4.80E+00	5.5	2.57E-02	7.1
200R-2, 44	1730.54	6	3.61E+00	6	1.82E-02	7.5
200R-2, 140	1731.5	22	4.21E+00	6	1.98E-02	8.1
200R-3, 13	1731.73	2c	4.43E+00	6	1.88E-02	9.0
203R-1, 57	1749.57	15b	1.44E+00	9	9.10E-03	6.0
204R-1, 8	1756.58	3	7.32E-01	14	5.78E-03	4.8
205R-1, 3	1757.03	1	2.02E+00	7	8.81E-03	8.7
206R-1, 19	1760.89	4c	2.36E+00	6	1.52E-02	5.9
208R-1, 4	1778.04	1	5.55E+00	6	1.74E-02	12.1
208R-1, 85	1778.85	19a	5.53E-01	7	2.32E-03	9.1
208R-2, 99	1780.49	18	6.26E+00	7	1.64E-02	14.5
209R-1, 103	1788.53	14b	3.82E-02	8	6.66E-04	2.2
209R-2, 9	1789.09	2	8.73E-02	4.5	6.78E-04	4.9
210R-1, 18	1795.08	4A	7.47E+00	7.5	2.31E-02	12.3
211R-1, 129	1799.79	29B	7.18E+00	5.5	2.69E-02	10.2
213R-1, 49	1812.99	15	4.31E+00	6	1.47E-02	11.2
214R-1, 31	1818.91	5a	4.61E-02	32	8.04E-04	2.2
214R-1, 132	1819.92	19	6.86E+00	6	3.31E-02	7.9
214R-2, 88	1820.98	20	9.00E-02	9.5	3.76E-04	9.1
214R-2, 130	1821.4	25	6.20E+00	6	3.10E-02	7.6
217R-1, 4	1837.44	1	4.27E-02	20	7.91E-04	2.1
221R-1, 44	1875.44	10	3.49E+00	8	2.15E-02	10.6
222R-1, 17	1884.77	1	5.45E-01	26	3.59E-03	5.8
222R-1, 37	1884.97	6	8.19E-01	17	4.64E-03	6.7
225R-1, 137	1913.57	34	5.89E+00	5.5	2.78E-02	8.1
225R-2, 42	1914.12	7	5.24E+00	5	1.97E-02	10.1
226R-1, 61	1920.61	12	2.12E+00	5	8.24E-03	9.8
226R-2, 72	1922.22	10	5.55E+00	5	3.40E-02	6.2
226R-3, 2	1923.02	1	6.15E+00	5.5	3.16E-02	7.4
227R-1, 83	1925.33	10	6.26E+00	5.5	3.15E-02	7.6
227R-2, 10	1926.1	1	6.24E-02	25	7.66E-04	3.1
228R-1, 55	1934.55	13	3.61E+00	7	2.20E-02	6.3

NOTE: The intensity of natural remanent magnetization (J_0) is in A/m, the median demagnetizing field (MDF) is in mT, and magnetic susceptibility (K) is in SI units. Dec = declination; Inc = inclination.

and could represent a cumulate dunite-wehrlite-pyroxenite-gabbro crystallization sequence from an intrusion deep within the crust: a crystallization sequence, however, at odds with that inferred from the phenocryst assemblage in the Leg 140 dikes.

Geochemistry

The rocks recovered during Leg 140 are similar in most respects to those drilled during the latter half of DSDP Leg 83 and ODP Leg 111. All of the samples are altered to some degree with water contents ranging from 0.83 to 3.68 wt%. Since alteration can mask original igneous chemical characteristics, only the "freshest" samples (<1.5 wt% H₂O) were used to interpret igneous petrogenesis. The chemistry of these dikes is virtually identical to that of the overlying pillow lavas and dikes. They are olivine to slightly quartz-normative tholeiites, with moderately evolved compositions reflecting moderate degrees of fractional crystallization. The unusual chemical uniformity is very similar to that found in the overlying sheeted dikes and pillow lavas, and is consistent with a hypothesized long-lived near-steady-state magma chamber (Natland et al., 1983). The Leg 140 diabases are all

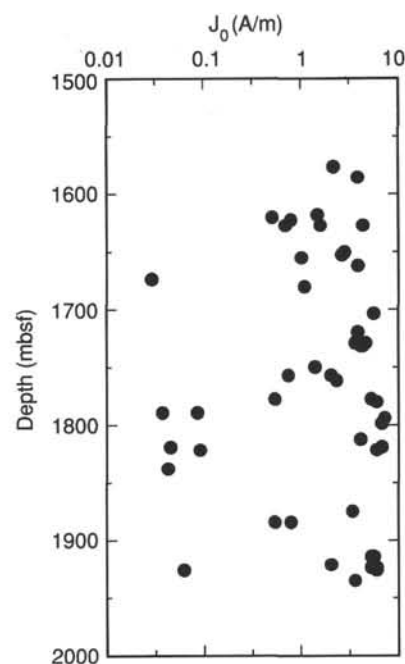


Figure 96. Intensity of NRM (J_0) plotted vs. depth in Hole 504B.

unusually depleted in incompatible element abundances, with low TiO₂, Nb, Zr, and Rb, yet with incompatible element ratios (e.g., Zr/Nb) similar to normal abyssal tholeiites. The diabases also have unusually high CaO/Na₂O ratios, and are in equilibrium with exceptionally calcic plagioclase at liquidus temperatures. These characteristics have been previously attributed to multi-stage melting of a normal ocean ridge mantle source followed by moderate fractional crystallization (Autio and Rhodes, 1983; Kempton, et al., 1985; Autio et al., 1989).

With the exception of mobile elements (K, Zn, Cu) Leg 140 diabase compositions are not significantly different from those higher in the section. Incompatible trace elements (Ti, Zr, Y, and Nb) are marginally lower, and the mean Mg/(Mg + Fe) ratio is slightly lower as well. As found higher in the hole, there is no major igneous enrichment or depletion trend with depth.

All the diabases have been altered to some degree. One notable effect is that, at the relatively high temperatures existing in the hole, alteration may have locally affected Zr/Y, a ratio normally thought not to be sensitive to alteration processes. When plotted against water content, it is evident that the abundances of Cu, Ti, and Zr and Zr/Y ratio decrease with the degree of alteration. A major finding is a large systematic decrease in Zn content between 1500 and 2000 m. Examined with the data from previous legs, this trend may actually have started at 1000 m (Fig. 126). A clear relationship between Zn and water content was not found, which suggests that the depletion with depth reflects changing conditions of metamorphism (increased temperatures). This Zn trend raises intriguing questions as to the overall Zn budget in the oceanic crust, and suggests that the dikes at deeper levels may be a source of the Zn in hydrothermal fluids analogous to those seen at black smoker deposits at mid-ocean ridges.

Alteration and Metamorphism

The alteration mineralogy of the Leg 140 dikes is similar in most respects to that in the dike section higher up: all of which show strong evidence of alteration at greenschist facies conditions. First, chlorite and actinolite, followed by quartz and epidote, formed in veins while greenschist minerals formed in the rocks during axial hydrothermal alteration at temperatures of 250°–380°C. Later, as the crust moved

Table 18. Inclination and declination (in degrees) of each observed component of remanent magnetization (NRM, stable, and secondary). n.d. = no data.

Core, section, interval, (cm)	Depth (mbsf)	Piece	Dec (°)	Inc (°)	Stable dec (°)	Stable inc (°)	Second dec (°)	Second inc (°)
140-504B								
173R-1, 114	1577.47	11	126.9	-66.1	129.6	-32.4	96.6	-75.1
175R-1, 19	1585.99	3	29.6	-73.6	29.7	-41.6	111.1	-86.5
180R-1, 92	1619.32	8	275.2	9.4	-65.5	42.5	-122.5	-54.9
180F-2, 29	1620.19	3	304.4	-20.8	-30.9	-32.4	-170.5	37.1
181F-2, 148	1623.38	12A	93.6	-9.6	72.2	28.1	148	-51.7
186R-1, 54	1626.84	5	359.1	72.3	-94.9	39.7	24	66.3
186R-1, 81	1627.11	13B	146.1	-69.5	105.5	-25.5	72.3	-83
186R-2, 42	1628.22	9	20.8	-66.9	42.3	-32.1	23.2	-80
189R-1, 96	1651.96	21A	311.0	-82.6	-46.4	-57.2	-50.2	-81.7
189R-2, 39	1652.89	5C	287.8	-79.2	-160.2	-11.2	-66.4	-79.4
190R-1, 95	1656.05	19	16.4	-63.1	-2.5	-27.3	16	-64.6
191R-1, 48	1661.88	7B	48.2	-76.1	47	-9.7	45.7	-75.9
193R-1, 48	1674.98	13A	190.8	-13.9	74.8	1.9	-163.3	-9.4
194R-1, 92	1681.32	18	0.9	-76.1	75.6	-14.2	-13	-74.7
197R-1, 131	1704.11	28	359.6	-77.0	16.9	-23.5	-8.1	-77
199R-1, 121	1720.61	26B	47.1	-66.6	71.3	-33.8	43.8	-67.3
200R-1, 128	1729.88	21	48.3	-85.7	153.9	-30.1	52.3	-83.4
200R-2, 44	1730.54	6	35.5	-79.4	59.5	-31.7	28.9	-77.4
200R-2, 140	1731.5	22	350.5	-75.6	-38	-24.5	5.7	-74.9
200R-3, 13	1731.73	2C	38.8	-78.4	130.4	-32.7	28.3	-76.5
203R-1, 57	1749.57	15B	286.1	-72.3	-107.2	-4.8	-23.3	-80.4
204R-1, 8	1756.58	3	352.2	-45.2	-21.8	11.2	-9.3	-67.6
205R-1, 3	1757.03	1	256.0	-76.9	-124.1	-3.7	72.4	0.2
206R-1, 19	1760.89	4C	292.3	-86.2	-118.3	-9.9	49.6	-80.7
208R-1, 4	1778.04	1	43.7	-76.1	-114	-24.3	50.1	-69
208R-1, 85	1778.85	19A	274.8	-81.5	-30.4	-8.4	-97.4	-81
208R-2, 99	1780.49	18	346.0	-81.9	158.2	-33.2	-12.3	-79.9
209R-1, 103	1788.53	14B	117.2	-22.5	58.9	-4.4	36.4	-68.8
209R-2, 9	1789.09	2	151.3	-36.3	-154.6	-13.9	116	-58.7
210R-1, 18	1795.08	4A	337.7	-77.0	n.d.	n.d.	-24.9	-73.9
211R-1, 129	1799.79	29B	348.8	-71.6	-21	4	-17.5	-68.9
213R-1, 49	1812.99	15	35.3	-82.0	-111.5	-13.6	45.5	-79.7
214R-1, 31	1818.91	5A	74.6	-56.8	69.4	2.7	-158.9	-55.6
214R-1, 132	1819.92	19	108.0	-79.1	130.6	-9.7	109.2	-76.6
214R-2, 88	1820.98	20	194.6	-11.4	32.3	-13	-170.3	-13.5
214R-2, 130	1821.4	25	24.7	-70.0	45.2	-5.5	23.8	-65.4
217R-1, 4	1837.44	1	37.6	-56.0	58.9	-2.6	24.2	-72.7
221R-1, 44	1875.44	10	211.4	-80.6	-161.9	-12.8	-32.7	-86
222R-1, 17	1884.77	1	105.1	-52.0	104.6	-10.9	-18	-85.4
222R-1, 37	1884.97	6	43.2	-46.7	47.7	-11.7	34.2	-74.3
225R-1, 137	1913.57	34	19.1	-79.1	58.3	-15.2	15.4	-77.4
225R-2, 42	1914.12	7	280.2	-75.7	-126.2	-18	-52.4	-76.1
226R-1, 61	1920.61	12	199.8	-81.2	-143.8	-16.3	-159.8	-87.6
226R-2, 72	1922.22	10	36.8	-68.2	41.7	-12.6	32.9	-71.8
226R-3, 2	1923.02	1	341.5	-70.8	-41.7	-13.9	-14.7	-69.2
227R-1, 83	1925.33	10	206.3	-80.7	-162.6	-19.9	-136	-82.2
227R-2, 10	1926.1	1	196.1	-40.7	-159.3	-17.5	n.d.	n.d.
228R-1, 55	1934.55	13	63.9	-71.5	74.1	-10.1	53.1	-76.1

off-axis, penetration of seawater into the warm rocks precipitated anhydrite in cracks and caused local replacement of plagioclase by anhydrite. Finally, zeolites formed in fractures and rocks during later off-axis alteration at lower temperatures. Only small amounts of laumontite were tentatively identified in the Leg 140 rocks, however, filling pore-space interstitial to chlorite, epidote, and actinolite, indicating a fairly late-stage formation, consistent with the 230° upper thermal stability of the mineral.

Because magnesium is rapidly taken up from seawater during hydrothermal alteration of basaltic rock, the presence of chlorite in veins is taken as evidence of Mg-bearing seawater-like fluids. The presence of quartz and epidote in later veins, and of traces of epidote replacing plagioclase in the Leg 140 diabases, indicate more evolved fluids (depleted in Mg and enriched in Ca through water-rock interaction). These few quartz-epidote occurrences are the only indication of any possible upwelling of hydrothermal fluids in the Leg 140 cores.

All the Leg 140 dikes are affected by 10%–20% background alteration, but extensively altered greenish patches, up to several centimeters across, are common. There, the rock is 70%–90% re-

placed by actinolite, chlorite, albite, titanite, and traces of epidote, anhydrite, and prehnite. Plagioclase is more extensively replaced by albite than chlorite in the patches, in contrast to the background alteration, where chlorite and albite replace plagioclase in nearly equal amounts. Sulfide minerals are essentially absent from these patches. In all, about 10% of the recovered core consists of these patches, constituting 0%–40% of individual pieces. The patches are most abundant in the coarser-grained diabases, and are absent in finer-grained intervals.

A complex and heterogeneous zonation of secondary minerals replacing olivine phenocrysts was observed in the Leg 140 diabases. Where talc occurs, talc + magnetite + pyrite generally formed first, followed by smectite, talc-smectite, and serpentine—probably at lower temperatures. Where chlorite rims olivine, it formed first, followed by mixed-layer chlorite-smectite or serpentine. Whereas talc or serpentine can form from olivine by simple addition of water, chlorite requires a source of alumina. The diversity and complexity of the olivine pseudomorphs, thus, probably reflects a diversity of water-rock ratios, temperatures, and kinetic effects, with the chlorite

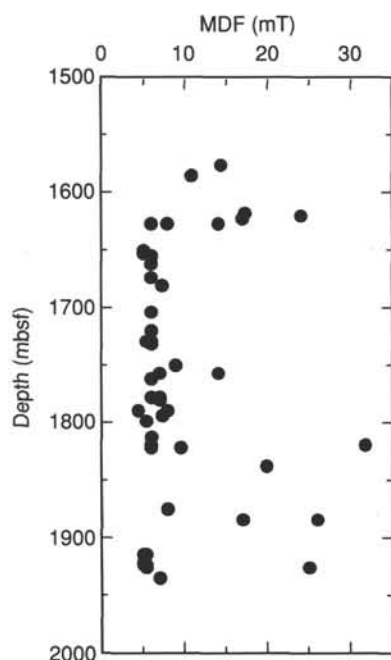


Figure 97. Median demagnetizing field (MDF) plotted vs. depth in Hole 504B.

assemblages forming at higher water-rock ratios accompanied by breakdown of plagioclase to provide alumina.

The Leg 140 diabases contain trace amounts of epidote replacing plagioclase at depths below 1814 mbsf, whereas epidote only occurs in veins near the top of the dike section. This and the appearance of more strongly pleochroic amphibole, suggested to be actinolitic hornblende, and apparently more magnesian chlorite than in the overlying dikes are consistent with higher maximum alteration temperatures for the Leg 140 dikes. In addition, the Leg 140 rocks have a greater proportion of actinolite than the dikes higher in the hole, and are generally more extensively altered. These differences are consistent

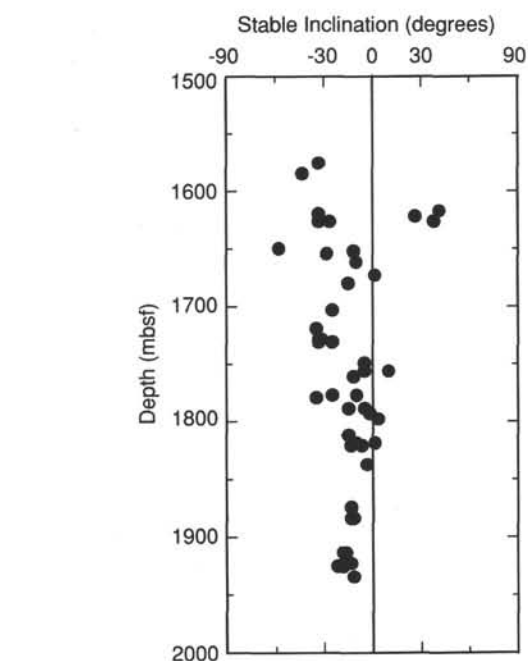


Figure 99. Stable magnetic inclination plotted vs. depth in Hole 504B.

with the changes that take place toward the base of sheeted dike sections in many ophiolites.

Alteration effects are heterogeneous, however, and rocks that are only slightly altered and contain relict olivine are present from 1710 to 1740 mbsf and sporadically to the bottom of the hole. These were altered at relatively low water-rock ratios.

Structural Geology

Careful examination of the Leg 140 diabases revealed abundant evidence of brittle deformation, but little evidence of ductile deformation, except that associated with magmatic intrusion. At least five recognizable types of macroscopic veins with greenschist facies mineralogies were recognized: chlorite, chlorite-actinolite, actinolite, chlorite-pyrite, and epidote-bearing veins. Except for quartz-epidote veins, which crosscut all other types, there are no consistent crosscutting

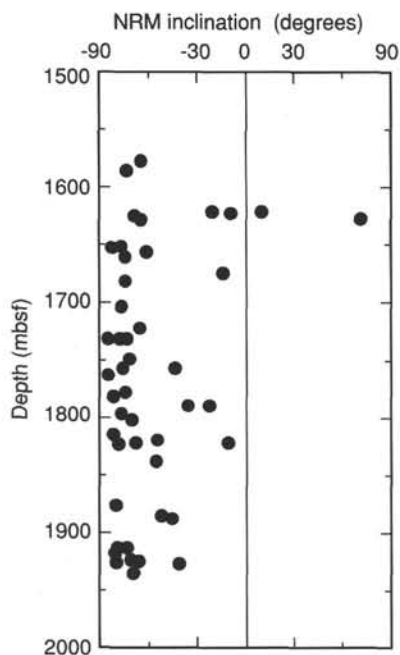


Figure 98. Inclination of NRM plotted vs. depth in Hole 504B.

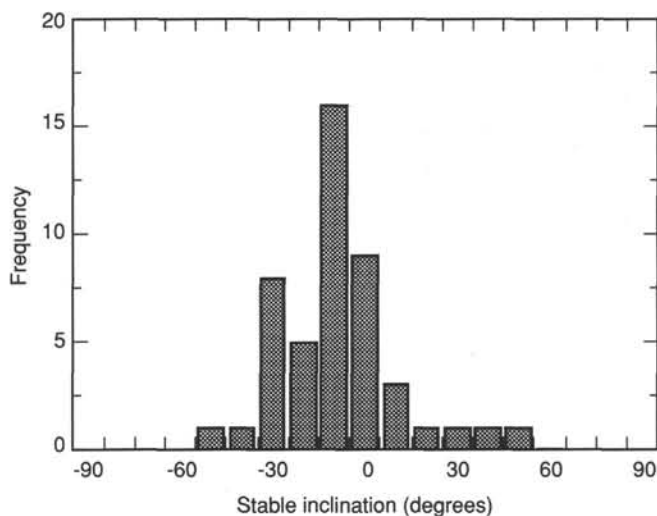


Figure 100. Histogram of stable magnetic inclination values for Leg 137/140 samples.

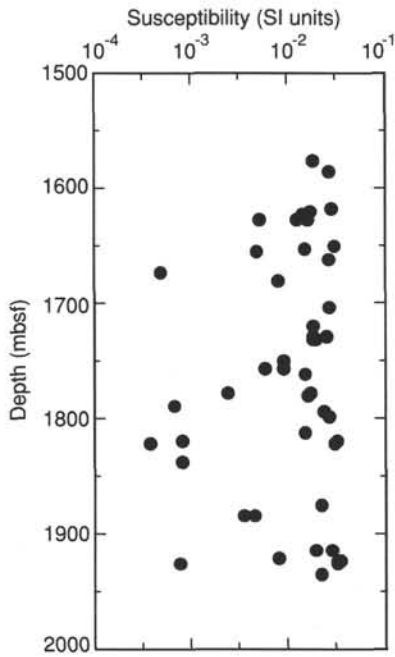


Figure 101. Magnetic susceptibility plotted vs. depth in Hole 504B.

relationships between them. With the exception of the chlorite-pyrite veins, which are oriented subvertically, the veins have an apparently random orientation, suggesting that their formation was strongly influenced by local stresses associated with dike injection and thermal stresses during cooling, rather than the regional tectonic regime. The only evidences of faulting encountered were millimeter-scale microfaults and minor shear zones offsetting veins found at some dike margins. No evidence was found of any major fault in the recovered core.

Two oriented dike margins, with dips of 79° and 84°, were reoriented using paleomagnetic vectors to give true strikes of 94° and 74°: roughly parallel the east-west axis of rifting on the paleo-Costa Rica Rift. This is entirely consistent with seismic reflection data (Langseth et al., 1988) showing Hole 504B situated in a gently back-tilted (5° southward) fault block or half graben.

Numerous unmineralized open fractures, with an average spacing of about 2 cm, were observed in the core, and appear to have been produced during drilling. True dips for 226 open fractures from Leg 137 and Leg

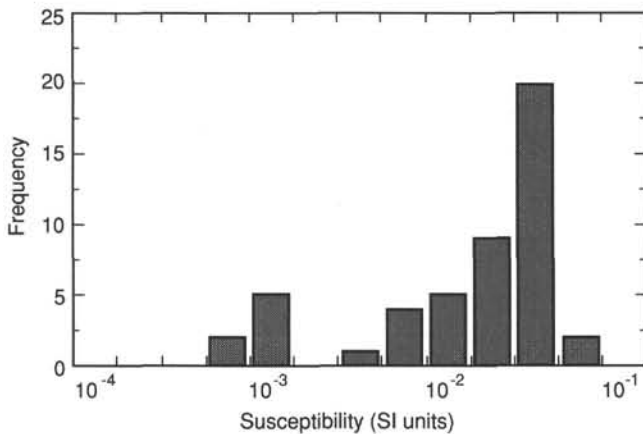


Figure 102. Histogram of magnetic susceptibility values for Leg 137/140 samples.

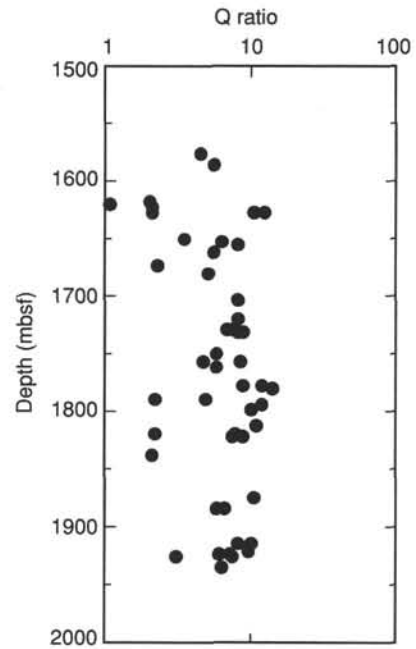


Figure 103. Q, or Koenigsberger, ratio plotted vs. depth in Hole 504B.

140 cores define shallowly dipping (10°–25°) and steeply dipping (70°–90°) sets. Unlike fractures observed previously, these sets are not randomly oriented. The open fractures include incipient fractures, termed “thin white cracks” (TWC) visible on the cut face of the cores, and a similarly oriented set of well-developed fractures that commonly split the core. These fractures were not as evident in cores from previous legs, and may be associated with unloading stresses during deep drilling: they closely resemble the “discing” fractures found in other deep boreholes. The more steeply dipping fractures include “thin white cracks,” closely spaced joints, and continuous fractures that often form the face of broken core pieces. Many have formed on pre-existing veins, in particular those filled with chlorite. These may have formed both before and during drilling.

Fifty five fractures were re-oriented paleomagnetically, and while the shallow dipping ones show no preferred strike, the steeply dipping ones have a strong preferred east-southeast trend (133°). This agrees with previous results from borehole televiewer studies at Hole 504B (Newmark, Zoback, and Anderson, 1985; Morin et al., 1989) and appears to reflect the present day in-situ state of stress in the hole.

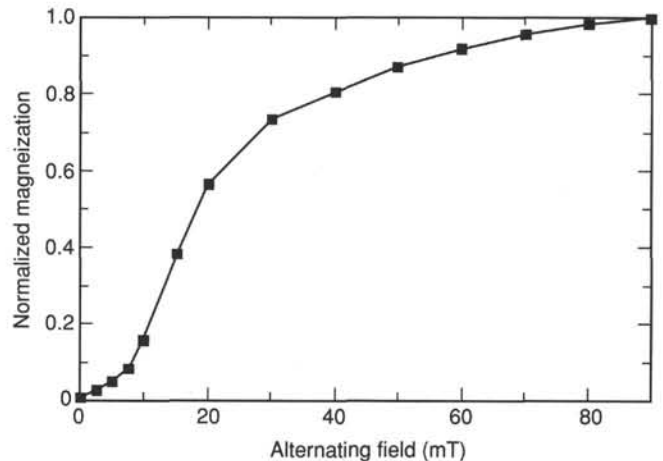


Figure 104. ARM acquisition for Sample 104-504B-181R-2, 148–150 cm.

Table 19. Results of anhysteretic remanent magnetization (ARM) measurements on selected minicore samples.

Core, section interval (cm)	Depth (mbsf)	J_a (A/m)	MAF (mT)	J_a/J_o	Comments
140-504B					
173R-1, 114	1577.47	5295	22.5	2.45	
180R-1, 92	1619.32	7833	18	5.27	
180F-2, 29	1620.19	2733	46	5.25	
181F-2, 148	1623.38	4760	18	6.09	
186R-1, 81	1627.11	2510	16	3.48	
186R-2, 42	1628.22	4174	16	0.92	
190R-1, 95	1656.05	461	11	0.45	
191R-1, 48	1661.88	2800	9	0.73	
193R-1, 48	1674.98	55	0	1.84	self-reversing
194R-1, 92	1681.32	699	12	0.63	
197R-1, 131	1704.11	5820	14	1.00	
199R-1, 121	1720.61	4440	13.5	1.16	
200R-1, 128	1729.88	4140	12	0.86	
203R-1, 57	1749.57	2650	34	1.84	
204R-1, 8	1756.58	1690	43	2.31	
205R-1, 3	1757.03	2943	31		
208R-1, 4	1778.04	3999	12.5	0.72	
208R-2, 99	1780.49	4288	12.5	0.68	
213R-1, 49	1812.99	2460	10	0.57	
214R-1, 132	1819.92	5360	11	0.78	
214R-2, 130	1821.4	58	62	0.01	self-reversing
217R-1, 44	1837.84	315	66	7.39	
221R-1, 4	1875.04	3860	24	1.11	
222R-1, 17	1884.77	1380	46	2.53	

The ratio J_a/J_o compares the intensity of the two different magnetizations. The median acquisition field (MAF) is the field by which one half of the maximum ARM is acquired.

Paleomagnetism

In general, the magnetic properties of the Leg 140 diabases are very similar to those of the upper part of the sheeted dike complex. The average stable inclination is -14° , falling within the range expected for normal variations of the geomagnetic field at this latitude. Consistent with the structural observations on the core, this average inclination cannot be taken as an indication of any significant tectonic rotation of the crustal section. The average NRM value is 3 A/m, about half the value of the overlying extrusives. The intensity of magnetization and magnetic susceptibility appear to be controlled by the degree of hydrothermal alteration experienced by primary titanomagnetite. A small percentage of samples studied (10%) have low intensities as a result of extensive hydrothermal alteration. Given that the drilled dike section is nearly twice as thick as, and contains far less scatter in magnetic direction than, the extrusive section, it is possible that the dikes make a significant contribution to the marine magnetic anomaly at the site today.

Physical Properties

The densities measured during the cruise on Leg 137 and 140 samples indicate that some of the highest density zones at this site were encountered at the base of the section drilled on Leg 137 and in the Leg 140 section. The most likely explanation for these zones is the relatively high proportion of actinolite observed in many of the rocks (mean grain density of 3.2 g/cm^3).

Porosity measurements show a continued steady decrease from the top of the hole, and the Leg 83 and 111 measurements. The average porosity of the Leg 140 dikes was 0.5% compared to roughly 2% in the upper sheeted dikes drilled during Leg 83, and close to 4% in the Leg 69 pillow basalts. Thermal conductivities also increase in the Leg 140 diabases, continuing a trend of steadily increasing conductivity in Hole 504B with depth. The weighted mean of the freshest diabases is $2.59 \text{ W/m}\cdot\text{K}$, while it is 2.22 in the more heterogeneous heavily

Table 20. Results of isothermal remanent magnetization measurements on selected minicore samples.

Core, section interval (cm)	Sat. IRM (A/m)	H_{sat} (mT)	H_{back} (mT)	Comments
140-504B				
173R-1, 114	403.82	140	37	
193R-1, 48	0.4	180	19	self-reversing
199R-1, 121	223	150	20	
203R-1, 57	41.8	180	32	
214R-1, 132	269.3	175	8	
214R-2, 130	1.01	175	8	self-reversing

Sat. = saturated.

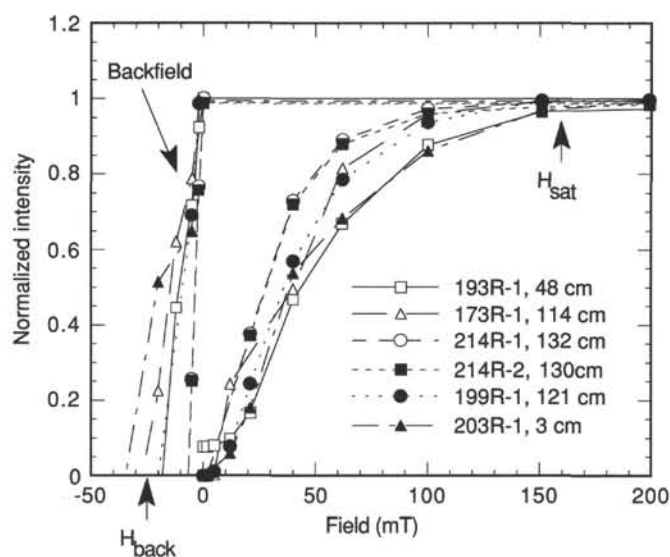


Figure 105. IRM acquisition for several Leg 140 samples. H_{back} is reversed IRM field, H_{sat} is saturation remanence.

altered diabases. This compares to a conductivity value of $2.01 \text{ W/m}\cdot\text{K}$ found for the Leg 111 diabases.

Wet compressional-wave velocity measurements at atmospheric pressure made on board ship show a sharp drop from about 1525 to 1650 mbsf, from which point they remain low to the bottom of the hole. This apparent sharp velocity inversion may account for the "E₅" reflector observed in the Leg 111 vertical seismic profile experiment and attributed to the dike/gabbro transition (Little and Stephen, 1985; Collins, 1989; Collins et al., 1989; Shipboard Scientific Party, 1988). Leg 140 clearly cored through the interval containing this reflector, but no gabbros were recovered. The most likely explanation for this reflector, then, is rapidly changing proportions and volumes of alteration phases interspersed with zones of relatively fresh rock in the lowermost section of the hole.

Downhole Measurements

Downhole measurements were made in two phases on Leg 140. The first phase included two runs, and was made immediately after the first re-entry prior to thermal disturbances resulting from operations. One run consisted of a temperature log and the other comprised the formation microscanner, magnetometer, and natural gamma logs. This short program investigated the thermal structure in the upper basement following the renewed vigorous downflow of ocean-bottom water detected 6 months earlier during Leg 137. The temperature log was run from 200 to 550 mbsf, where the observed temperature profile

Table 21. Results of anisotropy of anhysteretic remanence measurements on selected minicore samples.

Core, section interval (cm)	K_{max} intensity	K_{max} dec	K_{max} cor dec	K_{max} inc	K_{int} intensity	K_{int} dec	K_{int} cor dec	K_{int} inc	K_{min} intensity	K_{min} dec	K_{min} cor dec	K_{min} inc
140-504B												
173R-1, 114	466.0	320.00	190.40	20.0	448.0	102	333.0	66.0	439.0	225	95.40	14
180M-1, 92	690.0	279.00	344.50	29.0	650.0	142	207.5	53.0	634.0	21	86.50	21
180M-2, 29	181.0	294.00	324.90	75.0	133.0	154	184.9	11.0	61.0	62	92.90	9
181M-2, 148	397.0	245.00	172.80	43.0	380.0	145	72.8	16.0	361.0	38	-34.20	47
186R-1, 81	215.0	302.00	196.50	76.0	196.0	154	48.5	12.0	162.0	63	-42.50	7
186R-2, 42	342.0	280.00	237.70	69.0	370.0	138	95.7	16.0	252.0	45	2.70	12
190R-1, 95	470.0	322.00	324.50	81.0	412.0	127	129.5	9.0	396.0	218	220.50	2
191R-1, 48	3146.0	179.00	132.00	18.0	2460.0	84	37.0	13.0	741.0	321	274.00	68
194R-1, 92	648.0	285.00	209.40	71.0	616.0	77	1.4	17.0	564.0	170	94.40	8
197R-1, 131	5030.0	51.00	34.10	36.0	4888.0	299	282.1	27.0	4706.0	182	165.10	41
199R-1, 121	4294.6	3.00	292.00	24.0	4223.7	288	216.7	57.0	3852.8	103	31.70	20
200R-1, 128	4231.5	293.00	139.10	52.0	3942.4	190	36.1	10.0	3655.1	93	-60.90	36
203R-1, 57	1915.3	352.00	459.20	59.0	1831.2	197	304.2	29.0	1733.4	101	208.20	11
204R-1, 8	1126.3	238.00	259.80	19.0	1002.4	340	361.8	31.0	878.9	121	142.80	53
205R-1, 3	2203.1	27.00	151.10	15.0	2108.8	326	450.1	81.0	1955.4	128	252.10	37
208R-1, 4	3785.8	27.00	141.00	16.0	3658.0	280	394.0	46.0	3447.1	131	245.00	40
208R-1, 85	4206.8	338.00	368.40	40.0	4133.3	222	252.4	28.0	3749.9	109	139.40	37

Dec = declination; Inc = inclination; Cor = corrected.

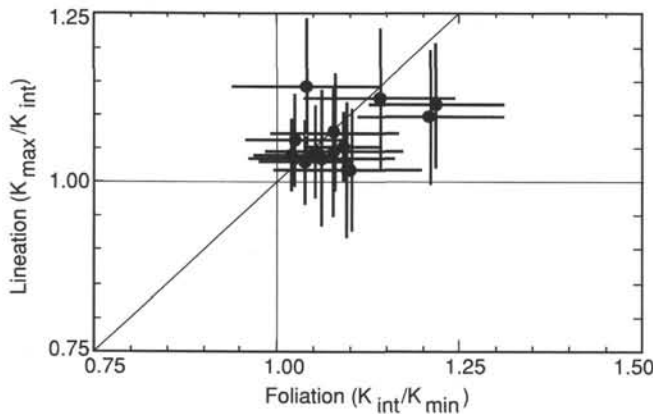


Figure 106. Results of anisotropy of anhysteretic remanence measurements are plotted for Leg 137/140 minicores. Anisotropy is considered to be present if lination (K_{max}/K_{int}) and foliation (K_{int}/K_{min}) values are > 1.1.

converged with that obtained on previous legs. A temperature gradient inversion was found in the upper basement and is different in detail from that observed on previous legs (283–288 mbsf), and may be attributed to local fluid inflow from the basement into the borehole. The variability of fluid flow with time observed during Legs 137 and 140 reflects large variations of hydrological activity in the upper basement. Such rapid and probably short-lived variations may be related to modifications of hydraulic connectivity in the upper basement, possibly associated with local tectonic activity. The observed temperature gradient above 450 m correlates with variations in vertical and horizontal fracture distributions and density. Below 450 mbsf, the Leg 140, 137, and 111 temperature profiles converge, indicating a near-steady-state thermal regime over the last 5 years.

The formation microscanner had technical problems, but recorded two images from 985.5 to 280.5 mbsf and four images from 1575.0 to 1563.0 mbsf. In the lower interval, 61 individual fracture traces were identified and mapped. On a stereo plot, these show three strong loci of preferred orientation, some of these sets were not identified from structural studies of the recovered core. The fractures are mostly steep and dip south-southeastward. In addition the borehole ellipticity outlined by the FMS calipers over this interval was oriented N105°,

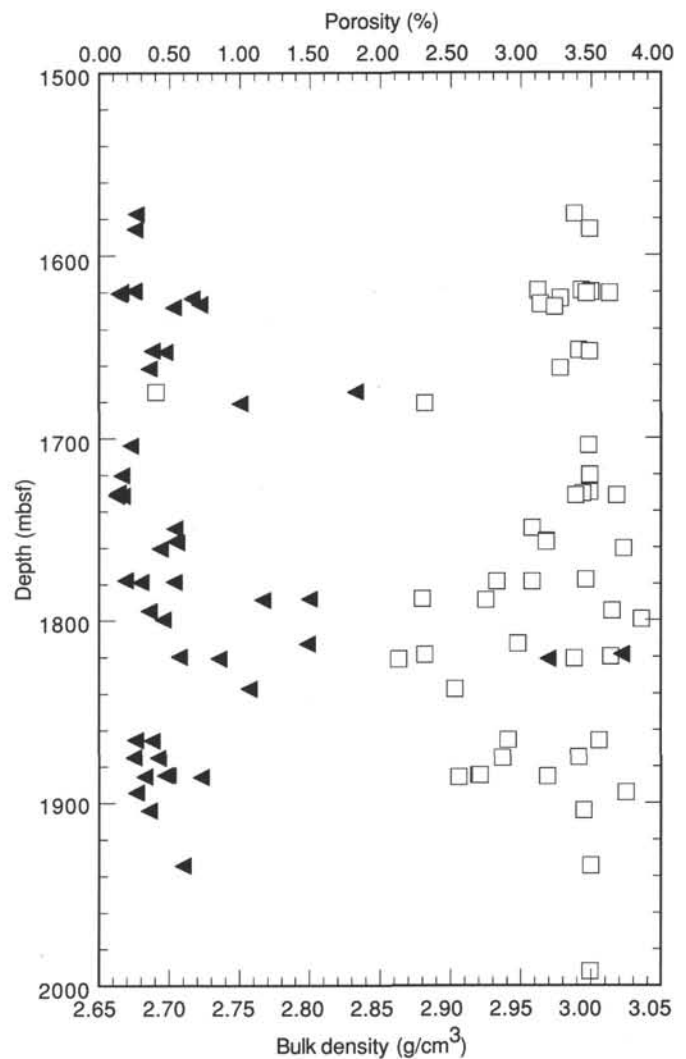


Figure 107. Bulk density (triangles) vs. porosity measurements (squares) as a function of depth for samples recovered during Legs 137 and 140.

Table 21 (continued).

Core, section interval (cm)	Standard error	Lineation (K_{max}/K_{int})	Foliation (K_{int}/K_{min})	Anisotropy (K_{max}/K_{min})	Error (%)
140-504B					
173R-1, 114	11.5	1.040	1.02	1.06	2.6
180M-1, 92	21.8	1.062	1.03	1.09	3.4
180M-2, 29	17.5	1.361	2.18	2.97	13.2
181M-2, 148	12.7	1.045	1.05	1.10	3.3
186R-1, 81	9.6	1.097	1.21	1.33	4.9
186R-2, 42	13.9	1.114	1.22	1.36	4.5
186R-2, 42	13.9	1.114	1.22	1.36	4.5
190R-1, 95	20.7	1.141	1.04	1.19	5.0
191R-1, 48	1000.0	1.279	3.32	4.25	40.7
194R-1, 92	15.2	1.052	1.09	1.15	2.5
197R-1, 131	149.3	1.029	1.04	1.07	3.1
199R-1, 121	210.0	1.017	1.10	1.11	5.0
200R-1, 128	168.0	1.073	1.08	1.16	4.3
203R-1, 57	95.0	1.046	1.06	1.10	5.2
204R-1, 8	51.0	1.124	1.14	1.28	5.1
205R-1, 3	98.3	1.045	1.08	1.13	4.7
208R-1, 4	180.0	1.035	1.06	1.10	4.9
208R-1, 85	183.0	1.018	1.10	1.12	4.4

in good agreement with the minimum horizontal stress direction (N117.5°) derived from the analysis of BHTV images from the upper part of the hole (Morin et al., 1990).

The second phase of downhole measurements followed coring, and consisted of six runs, including a high-resolution temperature run, the geochemical combination tool, the geophysical combination tool, the recording of BHTV images, and a flowmeter experiment. Except for the flowmeter, all measurements were in the newly drilled section of the hole.

Comparison to Ophiolites

The Leg 140 diabases differ significantly from those in ophiolite dike complexes in several important respects. Chemically, for example, the sheeted dikes in ophiolites typically range in composition from basalt to andesite or rhyolite (Troodos Ophiolite, Baragar et al., 1990; Semail Ophiolite, Pearce et al., 1981; Lippard et al., 1986; Josephine Ophiolite, Harper et al., 1988). This contrasts sharply with the chemical uniformity of the Hole 504B dikes and extrusives, and that of seafloor basalts in general.

In addition, the Leg 140 dikes are generally not altered to the same degree as those from many ophiolites. In the Semail Ophiolite, the primary igneous assemblage of calcic plagioclase, clinopyroxene, and Fe-Ti oxide minerals is almost completely replaced by greenschist facies assemblages of actinolite, chlorite, epidote, albite quartz, titanite, and secondary Fe-Ti oxide minerals, plus prehnite and pumpellyite (Lippard et al., 1986; Nehlig and Juteau, 1990). In the Troodos Ophiolite, the dikes consist of mostly chlorite, quartz, albite, actinolite, and plagioclase, with sporadic epidote (Baragar et al., 1990; Gillis and Robinson, 1990). Similarly, in the Josephine, Harper et al. (1988) report nearly complete replacement of the dike sequence to a greenschist facies assemblage, with epidote common in veins and replacing other minerals. In contrast, the Leg 140 and shallower dikes exhibit only about 20% recrystallization, ranging from 0% to 95% alteration products (Alt et al., 1986). This marked contrast cannot be attributed to the present-day thick sedimentary cap at Site 504, as Alt et al. (1986) have pointed out that the high temperatures of alteration required a magmatic heat source, and thus, must have occurred at or very close to the spreading axis where little or no sediment was present.

Some significant similarities between the 504B sheeted dikes and those in ophiolites do exist. The range of dike compositions in both the Semail and Troodos ophiolites closely reflects those of the overlying pillows, as is also the case for Hole 504B. In the Leg 140 section, systematic variations in grain size indicate dike injection in swarms.

Similarly, but based on packets of dikes with similar chemistry, Baragar et al. (1990) have suggested the presence of dike swarms in the Troodos sheeted dike complex. The Hole 504B dikes are altered largely under greenschist facies conditions, and lower temperature conditions occur near the transition zone from dikes to pillow basalts, similar to the trend observed in some ophiolites (Gillis and Robinson, 1990). Significantly, actinolitic hornblende, representing higher temperature conditions, occurs locally at the base of the Oman sheeted dikes whereas hornblende and amphibolite facies conditions occur at the base of the Josephine dikes, and actinolite is only present in the lower dikes in the Troodos Ophiolite. In Hole 504B, pleochroic amphibole, believed to be actinolitic hornblende, appears in quantity only in the Leg 140 dikes. Some rocks at the base of the sheeted dikes in ophiolites are depleted in certain metals and sulfur, and are interpreted to be the source of these constituents in hydrothermal vents at the seafloor (Richardson et al., 1987; Schiffman et al., 1987; Harper et al., 1988). Experimental evidence and thermodynamic modeling suggest that hydrothermal vent fluids acquire their signature where seawater-derived fluids penetrate into and interact with fresh rock in the so-called "reaction zone" (Seyfried, 1987). The striking zinc depletion zone at the bottom of Hole 504B appears to be analogous, in part, to the lower dikes in ophiolites and may be part of a former "reaction zone."

Significance of Leg 140 Results

The evidence outlined above suggests that Hole 504B now penetrates into the layer 2/3 transition. The Leg 140 sheeted dikes appear to represent direct sampling of rocks altered in the boundary layer between predominantly conductive cooling of the lower crust and convective cooling by open hydrothermal circulation of the shallow crust beneath a ridge axis (e.g., Lister, 1974; Nicolas and Bondier, 1991). This boundary layer is conceptually not a single physical contact, such as may locally exist between gabbro and dikes, but is a transition of finite thickness from ductile to brittle behavior, and from predominantly conductive to convective hydrothermal cooling. It is characterized by a steepening of the thermal gradient, and a rapid change in rock permeabilities with depth.

This boundary layer, unlike the gabbro-dike contact, is not fixed in space and time, and its imprint may be found at many levels in an old crustal section. The boundary layer, however, is most likely to leave a significant geologic and physical imprint in the rocks beneath the ridge axis. The heat supplied there by magmatism and active faulting drives a vigorous hydrothermal circulation, and the boundary layer will mark a major change in the rate of cooling and intensity of rock alteration. At the axis, magmas solidify rapidly to fine-grained basalt above the boundary layer; below it to coarse-grained gabbro. The imprint of the boundary layer off-axis, as it moves to deeper levels in the cooling crust, is likely less noticeable because less faulting, lower permeabilities, reduced flow of seawater, and a more subdued geothermal gradient produce less striking geological contrasts.

At Site 504, this boundary layer is likely to have existed within a relatively narrow zone close to the base of the sheeted dikes beneath the rift axis. This is anticipated from the smooth basement topography, which suggest high rates of magma supply, as at fast-spreading ridges, and the uniform chemistry of the dikes and lavas, which indicate homogenization of lavas in a long-lived magma chamber or crystal mush zone (e.g., Natland et al., 1983). At slower spreading ridges, the location of the cracking front limiting hydrothermal circulation is likely to vary significantly, rising and sinking deep into lower crust with the waxing and waning of magmatism. Thus, at a very slow-spreading ridge, gabbros are likely to show the effects of deep circulation of seawater near the ridge axis (e.g., Dick et al., 1991; Stakes et al., 1991).

In this context, the rocks recovered during Leg 140 are potentially significant for the earth science community: that is, they should help constrain the nature, thickness, and evolution of the critical boundary

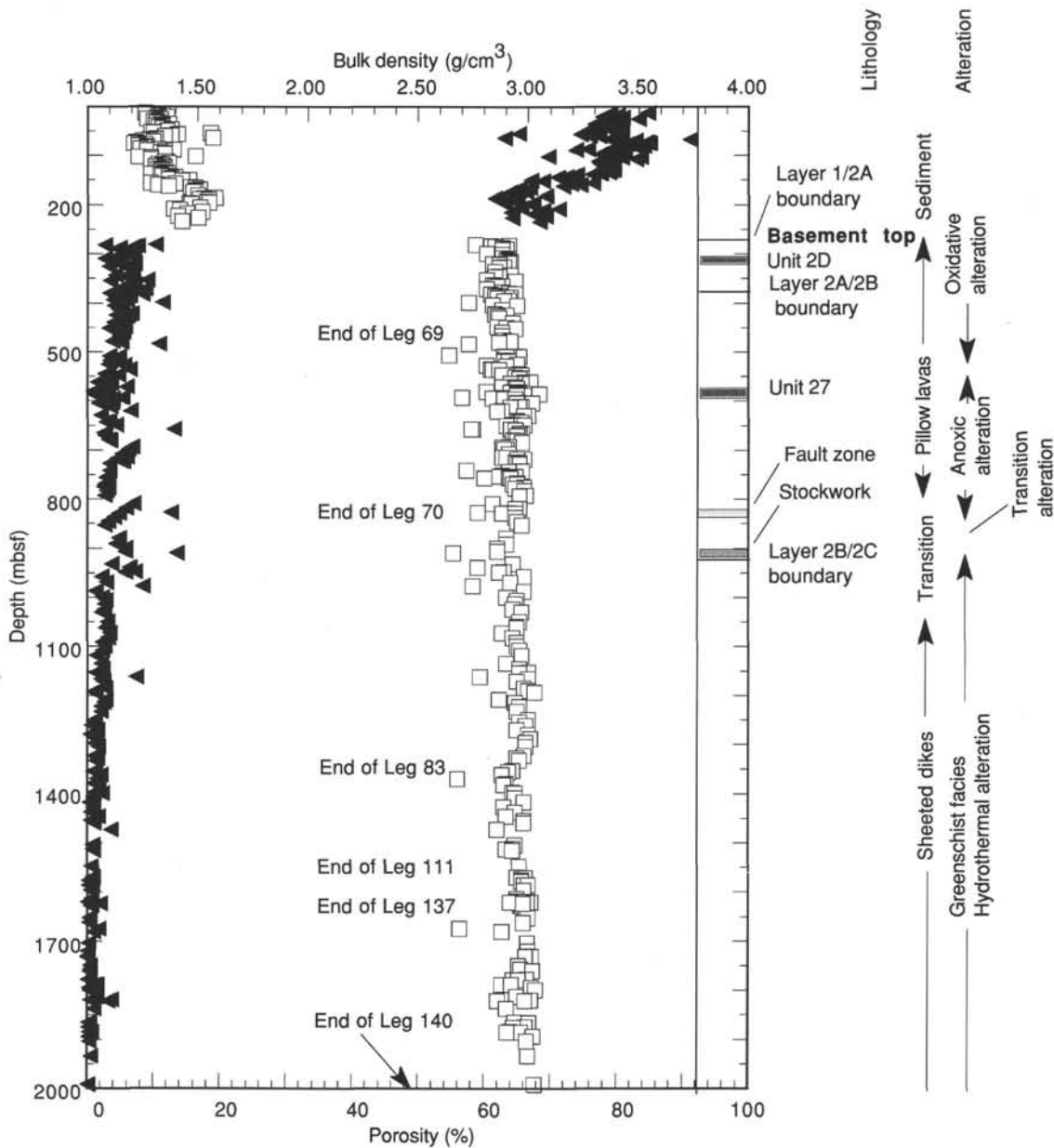


Figure 108. Bulk density (triangles) and porosity (squares) profiles vs. depth for the entire section Hole 504B. Sedimentary section added from Hole 504.

layer defining the igneous and metamorphic stratigraphy of the ocean crust. Interpretation of the results of Leg 140, and a simple lithologic progression as might be expected for a one-dimensional boundary layer (Lister, 1974), however, are likely to be complicated by the inherently heterogeneous, three dimensional, and time transgressive character of magmatism, dike injection, alteration, and faulting in the ocean crust.

That the Leg 140 rocks record the imprint of the boundary layer, however, is evident from the recovery of the first significant intervals where olivine, nearly absent in shallower dikes, is preserved in quantity. As olivine pseudomorphs are common throughout the rest of the dike section, its preservation demonstrates dramatically lower water-rock ratios at the bottom of the hole, which would be anticipated for hydrothermal alteration at reduced permeabilities within the boundary layer. This is also consistent with the resistivity log, which shows the highest overall resistivity in the Leg 140 dikes, indicating less fractures and the lowest permeabilities anywhere in Hole 504B. In addition, the reaction zone

supplying the source of trace metals for black smokers in ophiolites, like the zone of zinc depletion in Hole 504B, occurs at the base of the sheeted dike section (e.g., Richardson et al., 1987; Harper et al., 1988), presumably due to the higher temperatures of alteration in the boundary layer. The absence of well-developed chilled margins in the Leg 140 dikes is consistent with such inferred higher temperatures. Moreover, systematic variation from fine to medium-grained dikes, which indicate cycles of dike injection in the Leg 140 section were not seen in the Leg 83 and 111 sequences. Such cycles may in fact exist in these sections, but cooling was always sufficiently rapid that no medium-grained rocks formed there. Early in a cycle, the contrast between wall rock temperature and intrusive was large enough to cool the dike to a fine-grained basalt, similar to dikes seen higher in the hole. As the cycle proceeded, however, the medium-grained diabases show that the dikes cooled more slowly, and thus that the wall rocks were becoming hotter. The absence of medium-grained diabases in the Leg 83 and 111 sections, however, shows that this did not

occur higher up in the dike complex. This demonstrates less efficient heat dissipation during a cycle of intrusion at the base of the dike sequence than higher up, and therefore lower overall permeabilities and convective heat transport—consistent with dike intrusions in a boundary layer.

Conclusions

Leg 140 sampled the deepest section of ocean crust ever drilled in-situ. Moreover, the scientific results document a series of changes of mineralogy, chemistry, texture, and structure with depth which indicate rapidly changing conditions of alteration and crystallization of magma. These observations suggest that Hole 504B now penetrates to the depth of the seismic layer 2/3 transition, and that the physical contact between sheeted dikes and gabbro may lie well within a few hundred meters of the bottom of the hole.

REFERENCES

- Ade-Hall, J.M., and Johnson, H.P., 1976. Paleomagnetism of basalts, Leg 34. In Yeats, R.S., Hart, S.R., et al., *Init. Repts. DSDP*, 34: Washington (U.S. Govt. Printing Office), 513–532.
- Agar, S.M., 1990. Fracture evolution in the upper ocean crust: evidence from DSDP Hole 504B. In Knipe, R.J., and Rutter, E.H. (Eds.), *Deformation mechanisms, rheology and tectonics*. Geol. Soc. Spec. Publ. London, 54:41–50.
- Alt, J.C., Anderson, T.F., and Bonnell, L., 1989. Geochemistry of sulfur in a 1.3 km section of hydrothermally altered oceanic crust. *Geochim. Cosmochim. Acta*, 53:1011–1023.
- Alt, J.C., Anderson, T.F., Bonnell, L., and Muehlenbachs, K., 1989. Mineralogy, chemistry, and stable isotopic composition of hydrothermally altered sheeted dikes: ODP Hole 504B, Leg 111. In Becker, K., Sakai, H., et al., *Proc. ODP, Sci. Results*, 111: College Station, TX (Ocean Drilling Program), 27–40.
- Alt, J.C., Honnorez, J., Laverne, C., and Emmermann, R., 1986. Hydrothermal alteration of a 1-km section through the upper oceanic crust, Deep Sea Drilling Project Hole 504B: the mineralogy, chemistry and evolution of basalt-seawater interactions. *J. Geophys. Res.*, 91:10309–10335.
- Alt, J.C., Laverne, C., and Muehlenbachs, K., 1985. Alteration of the upper oceanic crust: mineralogy and processes in DSDP Hole 504B, Leg 83. In Anderson, R.N., Honnorez, J., Becker, K., et al., *Init. Repts. DSDP*, 83: Washington (U.S. Govt. Printing Office), 217–241.
- Anderson, R.N., and Hobart, M.A., 1976. The relation between heat flow, sediment thickness and age in the eastern Pacific. *J. Geophys. Res.*, 81:2968–2989.
- Anderson, R.N., Honnorez, J., Becker, K., et al., 1985. *Init. Repts. DSDP*, 83: Washington (U.S. Govt. Printing Office).
- Anderson, R.N., Honnorez, J., et al., 1982. DSDP Hole 504B, the first reference section over 1 km through Layer 2 of the oceanic crust. *Nature*, 300:589–594.
- Anderson, R.N., and Zoback, M.D., 1982. Permeability, underpressures, and convection in the oceanic crust near the Costa Rica Rift, eastern equatorial Pacific. *J. Geophys. Res.*, 87:2860–2868.
- Anderson, R.N., Zoback, M.D., Hickman, S.H., and Newmark, R.L., 1985. Permeability versus depth in the upper oceanic crust: in situ measurements in DSDP Hole 504B, eastern equatorial Pacific. *J. Geophys. Res.*, 90:3659–3669.
- Augustithis, S.S., 1978. *Atlas of the Textural Patterns of Basalts and Their Genetic Significance*: Amsterdam (Elsevier).
- Autio, L.K., and Rhodes, J.M., 1981. Basalts from Holes 501 and 504B (Costa Rica Rift Zone): a possible source for high anorthite phenocrysts in ocean-floor basaltic magmas. *Eos*, 62:309. (Abstract)
- , 1983. Costa Rica Rift Zone basalts: geochemical and experimental data from a possible example of multistage melting. In Cann, J.R., Langseth, M.G., Honnorez, J., Von Herzen, R.P., White, S.M., et al., 1983. *Init. Repts. DSDP*, 69: Washington (U.S. Govt. Printing Office), 729–745.
- Autio, L.K., Sparks, J.W., and Rhodes, J.M., 1989. Geochemistry of Leg 111 basalts: intrusive feeders for highly depleted pillows and flows. In Becker, K., Sakai, H., et al., *Proc. ODP, Sci. Results*, 111: College Station, TX (Ocean Drilling Program), 3–16.
- Auzende, J.-M., Bideau, D., Bonatti, E., Cannat, M., Honnorez, J., Lagabrielle, Y., Malavielle, J., Mamaloukas-Frangoulis, V., and Mevel, C., 1990. The MAR-Vema Fracture Zone intersection surveyed by deep submersible, *Nautile. Terra Nova*, 2:68–73.
- Ballard, R., Bryan, W., Dick, H., Emery, K.O., Thompson, G., Uchupi, E., Davis, K.E., Boer, J., Delong, S., Fox, P., Malcolm, F., Spydell, R., Stroup, J., Melson, W., and Wright, R., 1979. Geological and geophysical investigation of the Midcayman Rise Spreading Center: initial results and observations. In Talwani, M., Harrison, C.G., and Hayes, D.E. (Eds.), *Deep Drilling Results in the Atlantic Ocean: Ocean Crust*. Am. Geophys. Union, 66–93.
- Baragar, W.R.A., Lambert, M.B., Baglow, N., and Gibson, I.L., 1990. The sheeted dike zone in the Troodos Ophiolite. In Malpas, J., Moores, E.M., Panayiotou, A., Zenophontos, C. (Eds.) *Ophiolites: Oceanic Crustal Analogues*, 37–52.
- Bass, M.N., Moberly, R., Rhodes, J.M., Shih, C., and Church, S.E., 1973. Volcanic rocks cored in the central Pacific, Leg 17, Deep Sea Drilling Project. In Winterer, E.L., Ewing, J.I., et al., *Init. Repts. DSDP*, 17: Washington (U.S. Govt. Printing Office), 429–446.
- Becker, K., 1985. Large-scale electrical resistivity and bulk porosity of the oceanic crust, Deep Sea Drilling Project Hole 504B, Costa Rica Rift. In Anderson, R.N., Honnorez, J., Becker, K., et al., *Init. Repts. DSDP*, 83: Washington (U.S. Govt. Printing Office), 419–427.
- Becker, K., Foss, G., et al., 1992. *Proc. ODP, Init. Repts.*, 137: College Station, TX (Ocean Drilling Program).
- Becker, K., Sakai, H., Adamson, A.C., Alexandrovich, J., Alt, J.C., Anderson, R.N., Bideau, D., Gable, R., Herzig, P.M., Houghton, S., Ishizuka, H., Kawahata, H., Kinoshita, H., Langseth, M.G., Lovell, M.A., Malpas, J., Masuda, H., Merrill, R.B., Morin, R.H., Mottl, M.J., Pariso, J.E., Pezard, P., Phillips, J., Sparks, J., and Uhlig, S., 1989. Drilling deep into young oceanic crust, Hole 504B, Costa Rica Rift. *Rev. Geophys.*, 27:79–102.
- Becker, K., Sakai, H., et al., 1988. *Proc. ODP, Init. Repts.*, 111: College Station, TX (Ocean Drilling Program).
- , 1989. *Proc. ODP, Sci. Results*, 111: College Station, TX (Ocean Drilling Program).
- Bell, J.S., and Gough, D.I., 1979. Northeast-southwest compressive stress in Alberta: evidence from oil wells. *Earth Planet. Sci. Lett.*, 45:475–482.
- Bender, J.F., Langmuir, C.H., and Hanson, G.N., 1984. Petrogenesis of the basalt glasses from the Tamayo region, East Pacific Rise. *J. Petrol.*, 24:213–254.
- Bjornsson, A., Salmundsson, K., Einarsson, P., Tryggvason, E., and Gronvold, K., 1977. Current rifting episode in North Iceland. *Nature*, 266:318–323.
- Brandeis, G., and Jaupart, C., 1987. The kinetics of nucleation and crystal growth and scaling laws for magmatic crystallization. *Contrib. Mineral. Petrol.*, 96:24–34.
- Brocher, T.M., Geist, E.L., Collins, J.A., and Mutter, J.C., 1986. Seismic structure of the oceanic crust in the vicinity of DSDP Site 504. *Eos*, 67:1083.
- Bryan, W.B., Thompson, G., Frey, F.A., and Dickey, J.S., 1976. Inferred geologic settings and differentiation in basalts from the Deep Sea Drilling Project. *J. Geophys. Res.*, 81:4285–4304.
- Byerly, G.R., and Sinton, J.M., 1979. Compositional trends in natural basaltic glasses from Deep Sea Drilling Project Holes 417D and 418A. In Donnelly, T., Francheteau, J., Bryan, W., Robinson, P., Flower, M., Salisbury, M., et al., *Init. Repts. DSDP*, 51, 52, 53 (Pt. 2): Washington (U.S. Govt. Printing Office), 957–972.
- Cann, J.R., Langseth, M.G., Honnorez, J., Von Herzen, R.P., White, S.M., et al., 1983. *Init. Repts. DSDP*, 69: Washington (U.S. Govt. Printing Office).
- Cann, J.R., and Von Herzen, R., 1983. Downhole logging at deep sea drilling project sites 501, 504, and 505, near the Costa Rica Rift. In Cann, J.R., Langseth, M.G., Honnorez, J., Von Herzen, R., White, S.M., et al., *Init. Repts. DSDP*, 69: Washington (U.S. Govt. Printing Office), 281–299.
- Cannat, M., Mével, C., and Stakes, D., 1991. Normal ductile shear zones at an oceanic spreading ridge: tectonic evolution of Site 735 gabbros (Southwest Indian Ocean). In Von Herzen, R.P., Robinson, P.T., et al., *Proc. ODP, Sci. Results*, 118: College Station, TX (Ocean Drilling Program), 415–430.
- Cashman, K.V., 1990. Textural constraints on the kinetics of crystallization of igneous rocks. In Nicholls, J., and Russell, J.K. (Eds.), *Modern Methods of Igneous Petrology: Understanding Magmatic Processes*. Mineral. Soc. Am., 259–314.
- Clague, D.A., and Bunch, T.E., 1976. Formation of ferrobasalt at east Pacific mid-ocean spreading centers. *J. Geophys. Res.*, 81:4247–4256.
- Clanton, U.S., and Fletcher, C.R., 1976. Sample size and sampling errors as the source of dispersion in chemical analyses. *Proc. Lunar Sci. Conf.*, 7:1413–1428.
- Collins, J.A., 1989. A Search for Layering in the Oceanic Crust. [Ph.D. dissert.]. Woods Hole Oceanogr. Inst., Woods Hole, MA.
- Collins, J.A., Brocher, T.M., and Purdy, G.M., 1989. Seismic-reflection structure of the upper oceanic crust: implications from DSDP/ODP Hole 504B,

- Panama Basin. In Becker, K., Sakai, H., et al., *Proc. ODP, Sci. Results*, 111: College Station, TX (Ocean Drilling Program), 177–191.
- CRRUST (Costa Rica Rift United Scientific Team), 1982. Geothermal regimes of the Costa Rica Rift, east Pacific, investigated by drilling, DSDP-IPOD Legs 68, 69, and 70. *Geol. Soc. Am. Bull.*, 93:862–875.
- Dawson, J.B., Smith, J.V., and Hervig, R.L., 1980. Heterogeneity in upper mantle lherzolites and harzburgites. *Philos. Trans. R. Soc. London*, A297:323–331.
- Detrick, R.S., Buhl, P., Vera, E., Mutter, J., Orcutt, J., Madsen, J., and Brocher, T., 1987. Multichannel seismic imaging along the East Pacific Rise. *Nature*, 326:35–41.
- Dick, H.J.B., 1989. Abyssal peridotites, very slow spreading ridges and ocean ridge magmatism. In Saunders, A.D., and Norry, M.J. (Eds.), *Magmatism in the Ocean Basins*. Geol. Soc. Spec. Publ. London, 42:71–105.
- Dick, H.J.B., Meyer, P.S., Bloomer, S., Kirby, S., Stakes, D., and Mawer, C., 1991. Lithostratigraphic evolution of an *in-situ* section of oceanic layer 3. In Von Herzen, R.P., Robinson, P.T., et al., *Proc. ODP, Sci. Results*, 118: College Station, TX (Ocean Drilling Program), 439–540.
- Donaldson, C.H., Brown, R.W., and Reid, A.M., 1976. Petrology and chemistry of basalts from the Nazca plate: Part I. Petrography and mineral chemistry. *Init. Repts. DSDP*, 34: Washington (U.S. Govt. Printing Office), 227–238.
- Drake, M.J., 1976. Plagioclase-melt equilibria. *Geochim. Cosmochim. Acta*, 40:457–466.
- Drake, N.E.R., Rhodes, J.M., and Autio, L.K., 1985. The geochemistry of the Leg 82 Basalts. In Bougault, H., Cande, S.C., et al., *Init. Repts. DSDP*, 82: Washington (U.S. Govt. Printing Office), 421–438.
- Ekstrom, M.P., Dahan, C.A., Chen, M.-Y., Lloyd, P.M., and Rossi, D.J., 1986. Formation imaging with microelectrical scanning arrays. *Trans. SPWLA 27th Annu. Logging Symp.*, Pap. BB.
- Emmermann, R., 1985. Basement geochemistry, Hole 504B. In Anderson, R.N., Honnorez, J., Becker, K., et al., *Init. Repts. DSDP*, 83: Washington (U.S. Govt. Printing Office), 183–199.
- Etoubleau, J., Corre, O., Joron, J.L., Bougault, H., and Treuil, M., 1983. Costa Rica Rift: variably depleted basalts in the same hole. In Cann, J.R., Langseth, M.G., Honnorez, J., Von Herzen, R.P., White, S.M., et al., 1983. *Init. Repts. DSDP*, 69: Washington (U.S. Govt. Printing Office), 765–773.
- Fisher, A.T., Becker, K., Narasimhan, T.N., Langseth, M.G., and Mottl, 1990. Passive, off-axis convection through the southern flank of the Costa Rica Rift. *J. Geophys. Res.*, 95:9343–9370.
- Fisk, M.R., and Bence, A.E., 1980. Experimental crystallization of chrome spinel in FAMOUS basalt 527-1-1. *Earth Planet. Sci. Lett.* 48:111–123.
- Francheteau, J., Armijo, R., Cheminee, J.L., Hekinian, R., Lonsdale, P., and Blum, N., 1990. 1 Ma East Pacific Rise oceanic crust and uppermost mantle exposed by rifting in Hess Deep (equatorial Pacific Ocean). *Earth Planet. Sci. Lett.*, 101:281–295.
- Frey, F.A., Bryan, W.B., and Thompson, G., 1974. Atlantic Ocean floor: geochemistry and petrology of basalts from Legs 2 and 3 of the Deep Sea Drilling Project. *J. Geophys. Res.*, 79:5507–5527.
- Furuta, T., and Levi, S., 1983. Basement paleomagnetism of Hole 504B. In Cann, J.R., Langseth, M.G., Honnorez, J., Von Herzen, R.P., White, S.M., et al., *Init. Repts. DSDP*, 69: Washington (U.S. Govt. Printing Office), 697–703.
- Furuta, T., and Tokuyama, H., 1983. Chromian spinels in Costa Rica basalts, Deep Sea Drilling Project Site 505, a preliminary interpretation of electron microprobe analyses. In Cann, J.R., Langseth, M.G., Honnorez, J., Von Herzen, R.P., White, S.M., et al., *Init. Repts. DSDP*, 69: Washington (U.S. Govt. Printing Office).
- Gable, R., Morin, R.H., Becker, K., 1989. Geothermal state of Hole 504B: ODP Leg 111 overview. In Becker, K., Sakai, H., et al., *Proc. ODP, Sci. Results*, 111: College Station, TX (Ocean Drilling Program), 87–96.
- Gillis, K.M., and Robinson, P.I., 1990. Patterns and processes of alteration in the lavas and dikes of the Troodos Ophiolite, Cyprus. *J. Geophys. Res.*, 95:21523–21548.
- Hamilton, E.L., 1971. Prediction of *in-situ* acoustic and electric properties of marine sediments. *Geophysics*, 36:266–284.
- Harper, G.D., Bowman, J.R., Kuhns, R., 1988. A field, chemical and stable isotopic study of subseafloor metamorphism of the Josephine Ophiolite, California-Oregon. *J. Geophys. Res.*, 93:4625–4656.
- Hey, R., 1977. Tectonic evolution of the Cocos-Nazca spreading center. *Geol. Soc. Am. Bull.*, 88:1404–1420.
- Hey, R., Johnson, L., and Lowrie, A., 1977. Recent plate motions in the Galapagos area. *Geol. Soc. Am. Bull.*, 88:1385–1403.
- Hill, R., and Roeder, P., 1974. The crystallization of spinel from basaltic liquids as a function of oxygen fugacity. *J. Geol.*, 84:709–729.
- Hobart, M.A., Langseth, M.B., and Anderson, R.N., 1985. A geothermal and geophysical survey of the south flank of the Costa Rica Rift: Sites 504 and 505. In Anderson, R.N., Honnorez, J., Becker, K., et al., *Init. Repts. DSDP*, 83: Washington (U.S. Govt. Printing Office), 379–404.
- Holden, J.C., and Dietz, R.S., 1972. "Galapagos Gore, NazCoPac Triple Junction and Carnegie/Cocos Ridges." *Nature*, 235:266–269.
- Houtz, R., and Ewing, J., 1976. Upper crustal structure as a function of plateage. *J. Geophys. Res.*, 81:2490–2498.
- Hubberten, H.-W., Emmermann, R., and Puchelt, H., 1983. Geochemistry of basalts from Costa Rica rift Sites 504 and 505 (Deep Sea Drilling Project Leg 69 and 70). In Cann, J.R., Langseth, M.G., Honnorez, J., Von Herzen, R.P., White, S.M., et al., *Init. Repts. DSDP*, 69: Washington (U.S. Govt. Printing Office), 791–804.
- Ikeda, Y., 1977. Grain size of plagioclase of the basaltic andesite dikes, Iritono, central Abukuma plateau. *Can. J. Earth Sci.*, 14:1860–1866.
- Irvine, T.N., 1965. Chrome spinel as a petrogenetic indicator, 1: Theory. *Can. J. Earth Sci.*, 2:648–671.
- Ishizuka, H., 1989. Mineral paragenesis of altered basalts from Hole 504B, ODP Leg 111. In Becker, K., Sakai, H., et al., *Proc. ODP, Sci. Results*, 111: College Station, TX (Ocean Drilling Program), 61–76.
- Johnson, G.R., and Olhoeft, G.R., 1984. Density of rock and minerals. In Carmichael, R.S. (Ed.), *Handbook of Physical Properties of Rocks* (Vol. 3): Boca Raton, FL (CRC Press), 1–38.
- Johnson, H.P., 1978. Paleomagnetism of igneous rock samples—DSDP Leg 45. In Melson, W.G., Rabinowitz, P.D., et al., *Init. Repts. DSDP*, 45: Washington (U.S. Govt. Printing Office), 387–396.
- Kempton, P.D., 1985. An interpretation of contrasting nucleation and growth histories from the petrographic analysis of pillow and dike chilled margins, Hole 504B, Deep Sea Drilling Project, Leg 83. In Anderson, R.N., Honnorez, J., Becker, K., et al., *Init. Repts. DSDP*, 83: Washington (U.S. Govt. Printing Office), 165–181.
- Kempton, P.D., Autio, L.K., Rhodes, J.M., Holdaway, M.J., Dungan, M.A., Johnson, P., 1985. Petrology of basalts from Hole 504B, Deep Sea Drilling Project, Leg 83. In Anderson, R.N., Honnorez, J., Becker, K., et al., *Init. Repts. DSDP*, 83: Washington (U.S. Govt. Printing Office), 129–164.
- Kepezhinskas, P.K., 1989. Ultramafic-mafic inclusions in basalts from the Dol-drums Fracture Zone, Central Atlantic: mantle composition and magma chamber evolution in oceanic transform faults. *Abs., 28th Int. Geol. Congr.*, Washington, 2:176.
- Kikawa, E., and Pariso, J.E., 1991. Magnetic properties of gabbros from the Southwest Indian Ridge. *Proc. ODP, Sci. Results*, 118: College Station, TX (Ocean Drilling Program), 285–307.
- Klitgord, K.D., Huestis, S.D., Mudie, J.D., and Parker, R.L., 1975. An analysis of near-bottom magnetic anomalies: sea-floor spreading and the magnetized layer. *Geophys. J. R. Astron. Soc.*, 43:387–424.
- Kusakabe, M., Shibata, T., Yamamoto, M., Mayeda, S., Kagami, H., Honma, H., Masuda, H., and Sakai, H., 1989. Petrology and isotope characteristics (H, O, S, Sr and Nd) of basalts from Ocean Drilling Program Hole 504B, Leg 111, Costa Rica Rift. In Becker, K., Sakai, H., et al., *Proc. ODP, Sci. Results*, 111:47–60.
- Langseth, M.G., Cann, J.R., Natland, J.H., and Hobart, M., 1983. Geothermal phenomena at the Costa Rica Rift: background and objectives for drilling at Deep Sea Drilling Project Sites 501, 504, and 505. In Cann, J.R., Langseth, M.G., Honnorez, J., Von Herzen, R.P., White, S.M., et al., *Init. Repts. DSDP*, 69: Washington (U.S. Govt. Printing Office), 5–29.
- Langseth, M.G., and Mottl, M.J., 1982. Geochemical and geothermal mapping of crustal circulation patterns near DSDP Sites 501/504. *Eos*, 63:1116.
- Langseth, M.G., Mottl, M.J., Hobart, M., and Fischer, A., 1988. The distribution of geothermal and geochemical gradients near site 501/504: implications for hydrothermal circulation in the oceanic crust. In Becker, K., Sakai, H., et al., *Proc. ODP, Init. Repts.*, 111: College Station, TX (Ocean Drilling Program), 23–32.
- Leake, B.E., 1978. Nomenclature of amphiboles. *Am. Mineral.*, 63:1023–1053.
- Leinen, M., Rea, D.K., et al., 1986. *Init. Repts. DSDP*, 92: Washington (U.S. Govt. Printing Office).
- le Roex, A.P., Dick, H.J.B., Erlank, A.J., Reid, M., Frey, F.A., and Hart, S.R., 1983. Geochemistry, mineralogy and petrogenesis of lavas erupted along the Southwest Indian Ridge between the Bouvet Triple Junction and 11°E. *J. Petrol.*, 24:267–318.
- Liou, J.G., 1971. Stilbite-laumontite equilibria. *Contrib. Mineral. Petrol.*, 31:171–177.
- Lippard, J.J., Shelton, A.W., and Gass, I.G., 1986. *The Ophiolite of Northern Oman*. Geol. Soc. London Mem., 11.
- Lister, C.R.B., 1974. On the penetration of water into hot rock. *Geophys. J. R. Astron. Soc.*, 39:465–504.
- Little, S.A., and Stephen, R.A., 1985. Costa Rica Rift borehole seismic experiment, Deep Sea Drilling Project Hole 504B, Leg 92. In Anderson,

- R.N., Honnorez, J., Becker, K., et al., *Init. Repts. DSDP*, 83: Washington (U.S. Govt. Printing Office), 517–528.
- Lonsdale, P., and Klitgord, K.D., 1978. Structure and tectonic history of the eastern Panama Basin. *Geol. Soc. Am. Bull.*, 89:981–999.
- Lowrie, W., 1974. Oceanic basalt magnetic properties and the Vine and Matthews hypothesis. *J. Geophys. Res.*, 40:513–536.
- Lowrie, W., and Kent, D.N., 1978. Characteristics of VRM in oceanic basalts. *J. Geophys.*, 44:297–315.
- Luyendyk, B.P., Laws, B.R., Day, R., and Collison, T.B., 1982. Paleomagnetism of the Semail Ophiolite, Oman. I. The sheeted dike complex at Ibra. *J. Geophys. Res.*, 87:10883–10902.
- Marsh, N.G., Tarney, J., and Hendry, G.L., 1983. Trace element geochemistry of basalts from Hole 504B, Panama Basin, Deep Sea Drilling Project Legs 69 and 70. In Cann, J.R., Langseth, M.G., Honnorez, J., Von Herzen, R.P., White, S.M., et al., *Init. Repts. DSDP*, 69: Washington (U.S. Govt. Printing Office), 747–763.
- Melson, W.G., Vallier, T.L., Wright, T.L., Byerly, G., and Nelen, J., 1976. Chemical diversity of abyssal volcanic glass erupted along Pacific, Atlantic, and Indian Ocean sea-floor spreading centers. In Sutton, G.H., Manghni, M.H., and Moberly, R. (Eds.), *The Geophysics of the Pacific Ocean Basin and Its Margin*. Am. Geophys. Union, 351–367.
- McFadden, P.L., and Merrill, R.T., 1975. Geomagnetic secular variation over the past 5 m.y. *Rev. Geophys. Space Phys.*, 13:687–708.
- Moos, D., and Zoback, M.D., 1990. Utilization of well bore failure to constrain the orientation and magnitude of crustal stresses: application to continental, Deep Sea Drilling Project, and Ocean Drilling Program boreholes. *J. Geophys. Res.*, 95:9305–9325.
- Morin, R., Gable, R., and Becker, K., 1990. State of lithospheric stress and borehole stability at DSDP Site 504, eastern equatorial Pacific. *J. Geophys. Res.*, 95:9293–9303.
- Morin, R.H., Anderson, R.N., and Barton, C.A., 1989. Analysis and interpretation of the borehole televiewer log: information on the state of stress and the lithostratigraphy at Hole 504B. In Becker, K., Sakai, H., et al., *Proc. ODP, Sci. Results*, 111:109–118.
- Mutter, J.C., and North Atlantic Transect (NAT) Study Group, 1985. Multichannel seismic images of the oceanic crust's internal structure: evidence for a magma chamber beneath the Mesozoic Mid-Atlantic Ridge. *Geology*, 13:629–632.
- Natland, J.H., 1980. Effect of axial magma chambers beneath spreading centers on the composition of basaltic rocks. In Rosendahl, B.R., Hekinian, R., et al., *Init. Repts. DSDP*, 54: Washington (U.S. Govt. Printing Office), 833–850.
- Natland, J.H., Adamson, A.C., Laverne, C., Melson, W.G., and O'Hearn, T.O., 1983. A compositionally nearly steady-state magma chamber at the Costa Rica Rift: evidence from basalt glass and mineral data, Deep Sea Drilling Project Sites 501, 504, and 505. In Cann, J.R., Langseth, M.G., Honnorez, J., Von Herzen, R.P., White, S.M., et al., *Init. Repts. DSDP*, 69: Washington (U.S. Govt. Printing Office), 811–858.
- Natland, J.H., Meyer, P.S., Dick, H.J.B., and Bloomer, S.H., 1991. Magmatic oxides and sulfides in gabbroic rocks from the Hole 735B and the later development of the liquid line of descent. In Von Herzen, R.P., Robinson, P.T., et al., *Proc. ODP, Sci. Results*, 118: College Station, TX (Ocean Drilling Program), 75–112.
- Nehlig, P., and Juteau, P., 1988. Deep crustal seawater penetration and circulation at oceanic ridges: evidence from the Oman Ophiolite. *Mar. Geol.*, 94:209–228.
- Newmark, R.L., Anderson, R.N., Moos, D., and Zoback, M.D., 1985. Sonic and ultrasonic logging of Hole 504B and its implications for the structure, porosity and stress regime of the upper 1 km of the oceanic crust. In Anderson, R.N., Honnorez, J., Becker, K., et al., *Init. Repts. DSDP*, 83: Washington (U.S. Govt. Printing Office), 479–510.
- Newmark, R.L., Zoback, M.D., and Anderson, R.N., 1985. Orientation of *in-situ* stresses near the Costa Rica Rift and Peru-Chile trench: DSDP Hole 504B. In Anderson, R.N., Honnorez, J., Becker, K., et al., *Init. Repts. DSDP*, 83: Washington (U.S. Govt. Printing Office), 511–515.
- Nicolas, A., and Boudier, F., 1991. Rooting of the sheeted dike complex in the Oman Ophiolite. In Peters, T., Nicolas, A., and Coleman, R.G. (Eds.), *Ophiolite Genesis and Evolution of Oceanic Lithosphere*: Boston (Kluwer Acad.), 39–54.
- Nielsen, R.L., 1990. Simulation of igneous differentiation processes. In Nicholl, J., and Russell, J.K. (Eds.), *Modern Methods of Igneous Petrology: Understanding Magmatic Processes*. Mineral. Soc. Am., Rev. in Min., 24:65–105.
- O'Hanley, D.S., Chernosky, J.W., and Wicks, F.J., 1989. The stability of lizardite and chrysotile. *Can. Mineral.*, 27:483–493.
- Pariso, J.E., 1991. Magnetic structure of oceanic gabbros; magnetic properties and downhole magnetic measurements from ODP Hole 735B at the Southwest Indian Ridge [Ph.D. dissert.]. Univ. of Washington.
- Pariso, J.E., and Johnson, H.P., 1989. Magnetic properties of an analog of the lower oceanic crust: magnetic logging and paleomagnetic measurements from drillhole CY-4 in the Troodos Ophiolite. In *Cyprus Crustal Study Project: Initial Report, Hole CY-4*, 278–293.
- , 1991. Alteration processes at Deep Sea Drilling Project/Ocean Drilling Program Hole 504B at the Costa Rica Rift: implications for magnetization of oceanic crust. *J. Geophys. Res.*, 91:11703–11722.
- Pariso, J.E., Scott, J.H., Kikawa, E., and Johnson, H.P., 1991. A magnetic logging study of Hole 735B gabbros at the Southwest Indian Ridge. In Von Herzen, R.P., Robinson, P. T., et al., *Proc. ODP, Sci. Results*, 118: College Station, TX (Ocean Drilling Program), 309–321.
- Pearce, J.A., Alabaster, T., Shelton, A.W., and Searle, M.P., 1981. The Oman ophiolite as a Cretaceous arc-basin complex: evidence and implications. *Philos. Trans. R. Soc. London A*, 300:299–317.
- Pezard, P.A., 1990. Electrical properties of mid-ocean ridge basalt and implications for the structure of the upper oceanic crust in Hole 504B. *J. Geophys. Res.*, 95:9237–9264.
- Pezard, P.A., and Anderson, R.A., 1989. Morphology and alteration of the upper oceanic crust from *in-situ* electrical experiments in DSDP/ODP Hole 504B. In Becker, K., Sakai, H., et al., *Proc. ODP, Sci. Results*, 111: College Station, TX (Ocean Drilling Program), 133–146.
- Pezard, P.A., Anderson, R.N., Howard, J.J., and Luthi, S.M., 1988. Fracture distribution and basement structure from measurements of electrical resistivity in the Cajon Pass scientific drillhole, California. *Geophys. Res. Lett.*, 15:1021–1025.
- Pezard, P.A., and Luthi, S.M., 1988. Borehole electrical images in the basement of the Cajon Pass Scientific Drillhole, California; fracture identification and tectonic implications. *Geophys. Res. Lett.*, 15:1017–1020.
- Pockalny, R.A., Detrick, R.S., and Fox, P.J., 1988. Morphology and tectonics of the Kane Transform from Sea Beam bathymetry data. *J. Geophys. Res.*, 93:3179–3193.
- Pollard, D.D., and Aydin, A., 1984. Propagation and linkage of ocean ridge segments. *J. Geophys. Res.*, 89:10017–10027.
- Ramsay, J.G., 1980. The crack-seal mechanism of rock deformation. *Nature*, 284:135–139.
- Rhodes, J.M., Blanchard, D.P., Dungan, M.A., Rodgers, K.V., and Brannon, J.C., 1978. Chemistry of Leg 45 basalts. In Melson, W.G., Rabinowitz, P.D., et al., *Init. Repts. DSDP*, 45: Washington (U.S. Govt. Printing Office), 447–459.
- Rhodes, J.M., Blanchard, D.P., Rodgers, K.V., Jacobs, J.W., and Brannon, J.C., 1976. Petrology and chemistry of basalts from the Nazca plate: part 2. Major and trace element chemistry. In Yeats, R.S., Hart, S.R., et al., *Init. Repts. DSDP*, 34: Washington (U.S. Govt. Printing Office), 239–244.
- Richardson, C.J., Cann, J.R., Richards, H.G., and Cowan, J.G., 1987. Metal depleted root zones of the Troodos ore-forming hydrothermal systems, Cyprus. *Earth Planet. Sci. Lett.*, 84:243–253.
- Roeder, P.L., and Reynolds, S., 1991. Crystallization of chromite and chromium saturation in basaltic melts. *J. Petrol.*, 32:909–934.
- Sack, R.O., 1982. Spinels as petrogenetic indicators: activity-composition relations at low pressures. *Contrib. Mineral. Petrol.*, 79:169–186.
- Salisbury, M.H., Christensen, N.I., Becker, K., and Moos, D., 1985. The velocity structure of layer 2 at Deep Sea Drilling Project Site 504 from logging and laboratory experiments. In Anderson, R.N., Honnorez, J., Becker, K., et al., *Init. Repts. DSDP*, 83: Washington (U.S. Govt. Printing Office), 217–222.
- Sato, H., Aoki, K.I., Okamoto, K., and Fujita, B., 1979. Petrology and chemistry of basaltic rocks from the Hole 396B, IPOD/DSDP Leg 46. In Dmitriev, L., Heirtzler, J., et al., *Init. Repts. DSDP*, 46: Washington (U.S. Govt. Printing Office), 115–141.
- Saunders, A.D., Fornari, D.J., Joron, J.-L., Tarney, J., and Treuil, M., 1982. Geochemistry of basic igneous rocks, Gulf of California, Deep Sea Drilling Project Leg 64. In Curran, J.R., Moore, D.G., et al., *Init. Repts. DSDP*, 64: Washington (U.S. Govt. Printing Office), 595–642.
- Schiffman, P., Smith, B.M., Vargas, R.S., and Moore, E.M., 1987. Geometry, conditions, and timing of off-axis hydrothermal metamorphism and ore-deposition in the Solea Graben. *Nature*, 325:423–425.
- Schilling, J.-G., Kingsley, R.H., and Devine, J.D., 1982. Galapagos hot spot-spreading center system 1, spatial petrological and geochemical variations (83°–101°W). *J. Geophys. Res.*, 87:5593–5610.
- Scott, D.R., and Stevenson, D.J., 1989. A self-consistent model of melting, magma migration, and buoyancy-driven circulation beneath mid-ocean ridges. *J. Geophys. Res.*, 94:2973–2988.

- Searle, R.C., 1983. Gloria survey over Costa Rica Rift Sites 501, 504, and 505. In Cann, J.R., Langseth, M.G., Honnorez, J., Von Herzen, R.P., White, S.M., et al., *Init. Repts. DSDP*, 69: Washington (U.S. Govt. Printing Office), 217–222.
- Seyfried, W.E., Jr., 1987. Experimental and theoretical constraints on hydrothermal alteration processes at mid-ocean ridges. *Annu. Rev. Earth Planet. Sci.*, 15:317–335.
- Sharaskin, A.Y., Migdisov, A.A., Rostschina, I.A., and Miklishansky, A.Z., 1983. Major and trace element chemistry of Hole 504B basalts and their alteration products (Costa Rica Rift, Deep Sea Drilling Project Leg 69 and 70). In Cann, J.R., Langseth, M.G., Honnorez, J., Von Herzen, R.P., White, S.M. et al., *Init. Repts. DSDP*, 69: Washington (U.S. Govt. Printing Office), 775–790.
- Shipboard Scientific Party, 1985. Site 504: Costa Rica Rift. In Anderson, R.N., Honnorez, J., Becker, K., et al., *Init. Repts. DSDP*, 83: Washington (U.S. Govt. Printing Office).
- , 1988. Site 504: Costa Rica Rift. In Becker, K., Sakai, H., et al., *Proc. ODP, Init. Repts.*, 111: College Station, TX (Ocean Drilling Program), 35–251.
- , 1992. Site 504. In Becker, K., Foss, G., et al., *Proc. ODP, Init. Repts.*, 137: College Station, TX (Ocean Drilling Program), 15–55.
- Sigurdsson, H., and Schilling, J-G., 1976. Spinel in Mid-Atlantic Ridge basalts: chemistry and occurrence. *Earth Planet. Sci. Lett.*, 29:7–20.
- Sigurdsson, H., and Sparks, R.S.J., 1978. Rifting episode in North Iceland in 1874–1875 and the eruption of Askja and Sveinagja. *Bull. Volcanol.*, 41:149–167.
- Sinton, J.M., and Byerly, G.R., 1980. Mineral compositions and crystallization trends in Deep Sea Drilling Project Holes 417D and 418A. In Donnelly, T., Francheteau, J., Bryan, W., Robinson, P., Flower, M., Salisbury, M., et al., *Init. Repts. DSDP*, 51, 52, 53: Washington (U.S. Printing Office), 1039–1054.
- Smith, G.M., and Banerjee, S.K., 1986. The magnetic structure of the upper kilometer of the marine crust. *J. Geophys. Res.*, 91:10377–10354.
- Stakes, D.S., Mével, C., Cannat, M., and Chaput, T., 1991. Metamorphic stratigraphy of Hole 735B. In Von Herzen, R.P., Robinson, P.T., et al., *Proc. ODP, Sci. Results*, College Station, TX (Ocean Drilling Program), 153–180.
- Stephen, R.A., 1983. The oblique seismic experiment on Deep Sea Drilling Project Leg 70. In Cann, J.R., Langseth, M.G., Honnorez, J., Von Herzen, R.P., White, S.M., et al., *Init. Repts. DSDP*, 69: Washington (U.S. Govt. Printing Office), 301–308.
- Tarling, D.H., 1983. *Palaeomagnetism*: London (Chapman and Hall).
- Tarney, J., Saunders, A.D., Weaver, S.D., Donnellan, N.C.B., and Hendry, G.L., 1979. Minor element geochemistry of basalts from Leg 49, North Atlantic Ocean. In Luyendyk, B.P., Cann, J.R., et al., *Init. Repts. DSDP*, 49: Washington (U.S. Govt. Printing Office), 657–691.
- Thompson, R.N., and Humphries, S.E., 1980. Silicate mineralogy of basalts from the East Pacific Rise, OCP Ridge, and Siqueiros Fracture Zone: Deep Sea Drilling Project Leg 54. In Rosendahl, B.R., Hekinian, R., et al., *Init. Repts. DSDP*, 54: Washington (U.S. Govt. Printing Office).
- Thy, P., Schiffman, P., and Moores, E.M., 1989. Igneous mineral stratigraphy and chemistry of the Cyprus Crustal Study Project drill core in the phitonic sequences of the Troodos Ophiolite. In Gibson, I.L., Malpas, J., Robinson, P.T., and Xenophontas, C. (Eds.), *Cyprus Crustal Study Project, Initial Report Hole CY-4*. Pap.—Geol. Surv. Can., 88-9:147–185.
- Tual, E., Jahn, B.M., Bougault, H., and Joron, J.-L., 1985. Geochemistry of basalts from Hole 504B, Leg 83, Costa Rica Rift. In Anderson, R.N., Honnorez, J., Becker, K. et al., *Init. Repts. DSDP*, 83: Washington (U.S. Govt. Printing Office), 201–214.
- Wicks, F.J., and Whittaker, E.J.W., 1977. Serpentine textures and serpentinization. *Can. Mineral.*, 15:459–488.
- Wolter, K.E., Rockel, T., et al., 1990. Core diskling in KTB drill cores and the determination of the in-situ stress orientation. In Emmermann, R., Dietrich, H.-G., et al. (Eds.), *Pilot Hole, Results of Geoscientific Investigation in the KTB Field Laboratory, 0–4000 m*. KTB Rep. 90-8:G1–G13.
- Yeats, R.S., Forbes, W.C., Heath, G.R., and Scheidegger, K.F., 1973. Petrology and geochemistry of DSDP Leg 16 basalts, Eastern Equatorial Pacific. In van Andel, T.H., Heath, G.R., et al., *Init. Repts. DSDP*, 16: Washington (U.S. Govt. Printing Office), 617–640.
- Zijderveld, J.D.A., 1967. AC demagnetization of rocks: analysis of results. In Collinson, D.W., Creer, K.M., and Runcorn, S.K. (Eds.), *Methods in Palaeomagnetism*: Amsterdam (Elsevier).

140A-102

NOTE: For all sites drilled, core-description forms and core photographs have been reproduced on coated paper and can be found in Section 3, beginning on page 203. Thin-section data are given in Section 4, beginning on page 285.

Table 22. Index properties from diabase samples collected during Legs 137 and 140.

Leg, hole, core, section, interval (cm)	Depth (mbsf)	Bulk density (g/cm ³)	Grain density (g/cm ³)	Water content (%)	Wet porosity (%)	Dry porosity (%)	Leg, hole, core, section, interval (cm)	Depth (mbsf)	Bulk density (g/cm ³)	Grain density (g/cm ³)	Water content (%)	Wet porosity (%)	Dry porosity (%)
137-504B							207R-1, 18-22	1768.44	2.988	2.954	0.804	0.276	0.276
173R-1, 114-116	1577.47	2.988	3.004	0.786	0.269	0.270	208R-1, 4-7	1778.04	2.996	2.992	0.548	0.188	0.188
175R-1, 19-21	1585.99	2.999	2.990	0.751	0.256	0.257	208R-1, 85-87	1778.85	2.933	2.912	1.529	0.534	0.537
180M-1, 92-94	1619.32	2.993	3.011	0.738	0.253	0.253	208R-1, 99-101	1778.99	2.958	2.981	0.870	0.301	0.302
180M-1, 94-99	1619.34	2.962	2.955	0.714	0.247	0.248	209R-1, 103-105	1788.53	2.880	2.845	4.219	1.499	1.522
180M-2, 29-31	1620.19	3.000	2.989	0.463	0.158	0.158	209R-2, 9-11	1789.09	2.925	2.870	3.327	1.165	1.179
180M-2, 93-98	1620.83	3.013	3.014	0.427	0.145	0.146	210R-1, 18-20	1795.08	3.015	3.003	1.049	0.357	0.358
180M-2, 99-102	1620.89	2.997	3.014	0.427	0.146	0.146	211R-1, 129-131	1799.79	3.036	3.006	1.359	0.459	0.461
181M-1, 148-150	1623.38	2.978	2.946	1.926	0.662	0.667	212R-1, 4-7	1812.54	3.001	2.988	0.570	0.195	0.195
140-504B							213R-1, 49-51	1812.99	2.948	2.943	2.943	1.484	0.518
186R-1, 40-42	1626.70	2.964	2.922	2.078	0.718	0.723	214R-1, 31-33	1818.91	2.882	2.891	2.891	3.717	1.340
186R-1, 54-56	1626.84	2.929	2.884	2.775	0.970	0.980	214R-1, 132-134	1819.92	3.014	2.981	2.981	0.571	0.196
186R-1, 81-84	1627.11	2.899	2.879	1.992	0.704	0.709	214R-2, 88-90	1820.98	2.988	2.977	2.977	0.856	0.294
186R-2, 42-45	1628.22	2.974	2.938	1.547	0.533	0.536	214R-2, 130-132	1821.40	2.863	2.848	2.848	3.194	1.165
187R-1, 21-23	1641.73	2.895	2.894	2.064	0.730	0.736	215R-1, 0-4	1827.90	2.998	2.980	0.677	0.232	0.232
188R-1, 24-27	1651.24	2.982	2.962	0.355	0.122	0.122	216R-1, 58-60	1837.98	2.928	2.923	1.908	0.668	0.672
189R-1, 96-99	1651.96	2.991	2.975	1.103	0.378	0.379	217R-1, 4-6	1837.44	2.903	2.900	3.025	1.068	1.079
189R-2, 39-42	1652.89	2.999	2.966	1.383	0.473	0.475	218R-1, 24-27	1856.44	2.937	2.922	1.346	0.470	0.472
190R-1, 95-98	1665.35	2.804	2.788	1.490	0.544	0.547	219R-1, 7-11	1865.57	2.992	2.986	0.364	0.125	0.125
191R-1, 48-51	1661.88	2.978	2.983	1.048	0.360	0.362	220R-1, 2-6	1865.52	2.941	2.929	0.753	0.262	0.263
192R-1, 13-15	1674.63	3.014	2.880	1.657	0.563	0.566	220R-1, 27-30	1865.77	3.006	2.948	1.113	0.379	0.381
193R-1, 7-10	1674.57	2.979	2.977	0.515	0.177	0.177	221R-1, 4-7	1875.04	2.991	2.981	0.724	0.248	0.249
193R-1, 48-51	1674.98	2.691	2.705	4.800	1.827	1.861	221R-1, 44-46	1875.44	2.937	2.931	1.207	0.421	0.423
194R-1, 92-95	1681.32	2.882	2.843	2.835	1.008	1.018	222R-1, 17-19	1884.77	2.920	2.910	1.392	0.488	0.491
195R-1, 7-10	1696.57	2.946	2.930	1.142	0.397	0.399	222R-1, 37-39	1884.97	2.921	2.913	1.347	0.472	0.475
196R-1, 33-35	1703.13	2.982	2.966	0.617	0.212	0.213	222R-1, 100-104	1885.60	2.969	2.954	0.951	0.328	0.329
197R-1, 131-134	1704.11	2.998	2.993	0.658	0.225	0.225	222R-1, 129-132	1885.89	2.906	2.864	2.059	0.726	0.731
198R-1, 70-71	1720.10	2.927	2.910	1.151	0.403	0.404	223R-1, 20-23	1894.40	3.025	2.988	0.799	0.270	0.271
199R-1, 121-123	1720.61	2.999	2.995	0.470	0.161	0.161	224R-1, 59-62	1904.29	2.995	2.968	1.047	0.358	0.359
200R-1, 128-131	1729.88	2.999	2.980	0.396	0.135	0.136	225R-1, 137-139	1913.57	3.013	2.990	0.390	0.133	0.133
200R-2, 44-46	1730.54	2.994	2.998	0.378	0.129	0.130	225R-2, 42-44	1914.12	3.000	2.978	0.197	0.067	0.067
200R-2, 140-143	1731.50	3.018	2.997	0.485	0.165	0.165	226R-1, 61-63	1920.61	2.949	2.951	0.782	0.272	0.272
200R-3, 13-16	1731.73	2.989	2.987	0.363	0.124	0.125	226R-2, 77-79	1922.22	2.960	2.959	0.574	0.199	0.199
201R-1, 19-23	1747.39	2.988	2.976	0.759	0.26	0.261	226R-3, 2-4	1923.02	2.970	2.949	0.730	0.252	0.252
202R-1, 20-23	1749.20	2.997	2.989	0.353	0.121	0.121	227R-1, 83-85	1925.33	2.988	2.966	0.460	0.158	0.158
203R-1, 57-59	1749.57	2.958	2.934	1.564	0.542	0.545	227R-2, 10-12	1926.10	2.879	2.868	2.539	0.903	0.912
204R-1, 8-11	1756.58	2.968	2.945	1.559	0.538	0.541	228R-1, 55-57	1934.55	2.996	2.979	0.558	0.191	0.191
205R-1, 3-5	1757.03	2.968	2.943	1.611	0.556	0.559	238R-1, 23-25	1992.33	3.031	2.999	0.380	0.129	0.378
206R-1, 19-22	1760.70	3.023	2.964	1.290	0.437	0.439	Mean		2.963	2.946	1.319	0.524	0.445
							Standard deviation		0.055	0.056	0.98	0.6	0.351

Table 23. Wet and dry compressional-wave velocities from Legs 137 and 140.

Leg, hole, core, section, interval (cm)	Depth (mbsf)	Direction	Wet velocity	Dry velocity
137-504B				
173R-1, 114-116	1577.47	C	5843	5342
175R-1, 19-21	1585.99	C	6031	5451
180M-1, 02-94	1619.32	C	6078	5203
100M-1, 94-99	1619.34	A	5574	5509
100M-2, 29-31	1620.19	C	6159	5602
100M-2, 93-98	1620.83	A	5941	5651
180M-2, 09-102	1620.89	C	6068	5579
181M-2, 149-150	1623.38	C	5928	5409
140-504B				
186R-1, 40-42	1626.70	C	5754	5271
186R-2, 42-45	1628.22	C	5892	5394
189R-1, 06-99	1651.96	C	5285	4823
189R-2, 39-42	1652.89	C	5269	4750
191R-1, 48-51	1661.88	C	5339	5078
193R-1, 46-51	1674.98	C	4950	4755
194R-1, 92-95	1681.32	C	5494	4909
197R-1, 131-314	1704.11	C	5823	4967
199R-1, 121-123	1720.61	C	5648	4457
200R-1, 128-131	1729.88	C	5755	4298
200R-2, 44-46	1730.54	C	5808	4423
200R-2, 140-143	1731.50	C	5609	4459
200R-3, 13-16	1731.73	C	5571	4974
203R-1, 57-59	1749.57	C	5893	5623
204R-1, 8-11	1756.58	C	6106	5715
205R-1, 3-5	1757.03	C	6104	5760
206R-1, 19-22	1760.70	C	5664	5221
208R-1, 4-7	1778.04	C	5698	5252
206R-1, 85-87	1778.85	C	5694	5517
208R-1, 09-101	1778.99	C	5483	4898
209R-1, 103-105	1786.53	C	5519	5146
200R-2, 9-11	1799.09	C	5376	4805
210R-1, 18-20	1795.08	C	5468	4879
211R-1, 129-131	1799.79	C	5611	5195
213R-1, 40-51	1812.99	C	5944	5409
214R-1, 31-33	1818.91	C	5541	5250
214R-1, 132-134	1819.92	C	5747	5497
214R-2, 88-50	1820.98	C	5650	5319
214R-2, 130-132	1821.40	C	5923	5507
217R-1, 4-6	1837.44	C	5650	5477
221R-1, 44-46	1875.44	C	5976	5627
222R-1, 17-19	1864.77	C	5969	5733
222A-1, 37-39	1884.97	C	5955	5931
225R-1, 137-139	1913.57	C	5827	5291
225R-2, 42-44	1914.12	C	5643	5327
226R-1, 61-63	1920.61	C	5979	4933
226R-2, 77-79	1922.22	C	5505	4962
226R-3, 2-4	1923.02	C	5716	4985
227R-1, 83-95	1925.33	C	5479	4902
227R-2, 10-12	1926.10	C	5426	4915
229R-1, 55-57	1934.55	C	5852	5561
Mean			5719	5205
Standard deviation			257	383

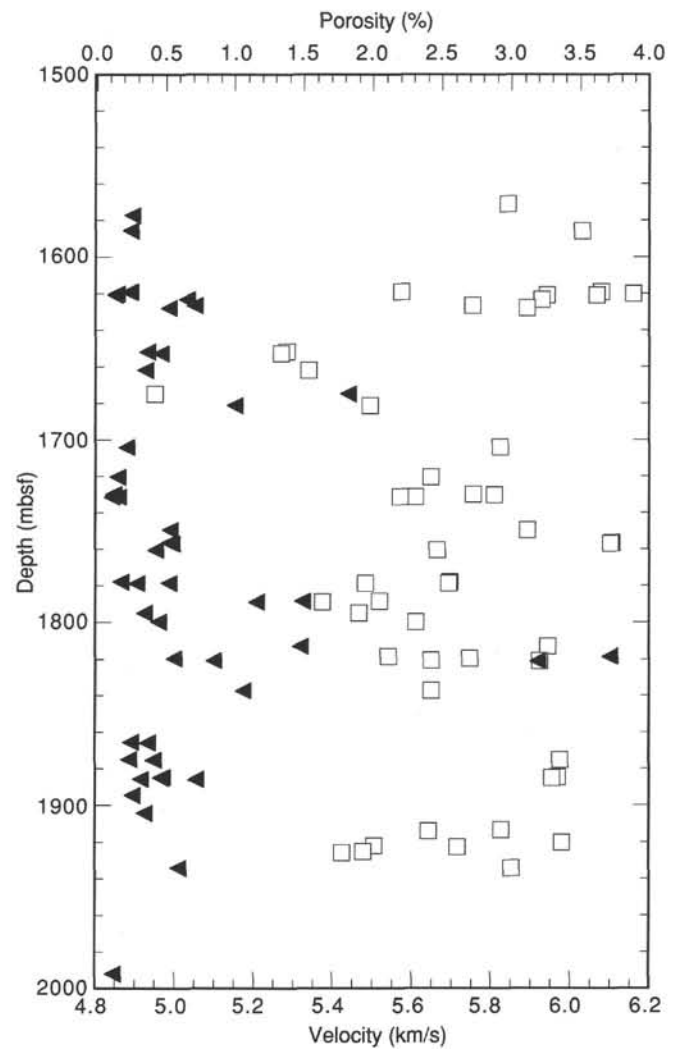


Figure 109. Velocity (triangles) and porosity (squares) vs. depth for the core sections recovered from Legs 137 and 140.

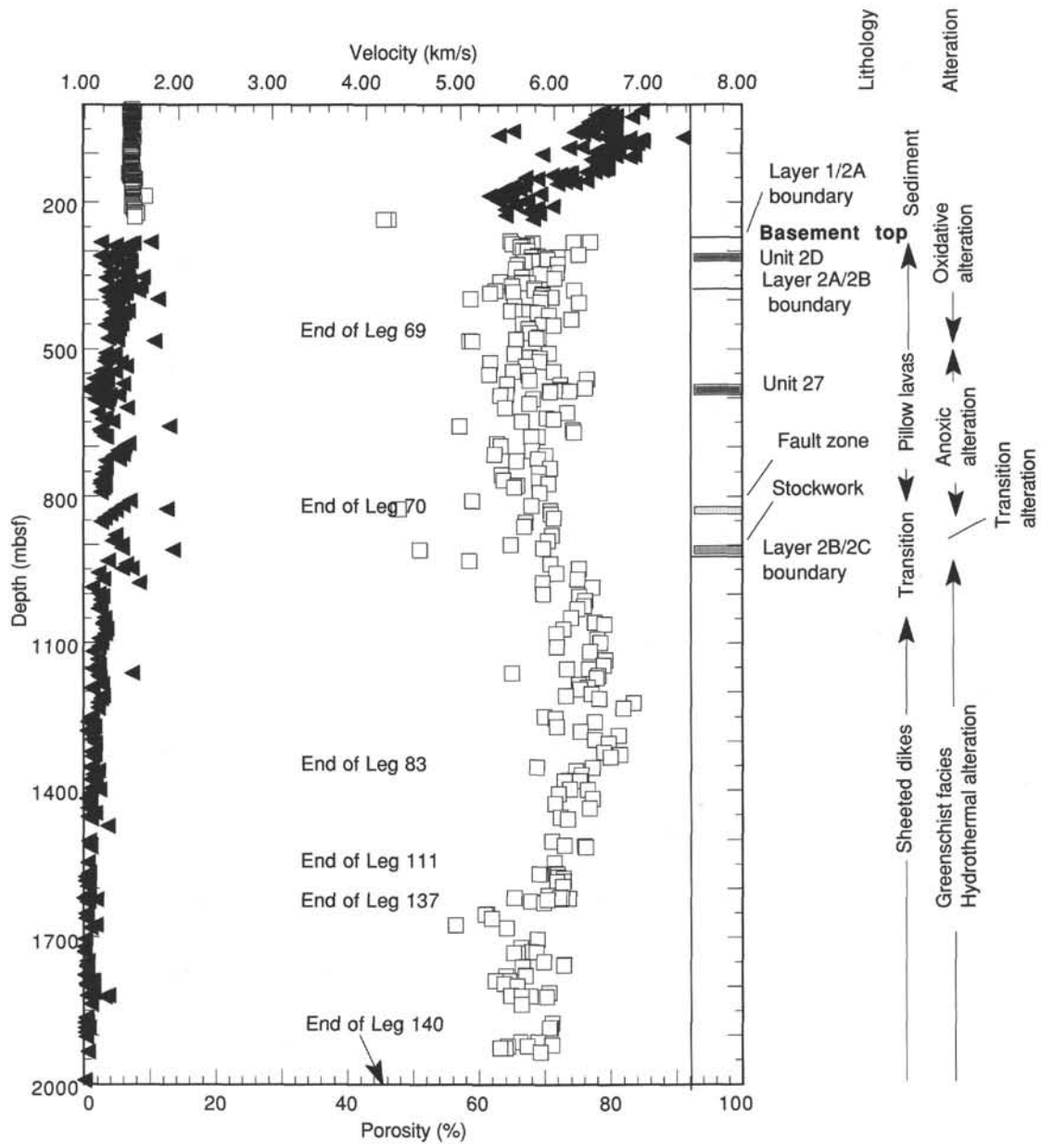


Figure 110. Velocity (triangles) and porosity (squares) vs. depth for the entire section recovered from Hole 504B. Sedimentary section added from Hole 504.

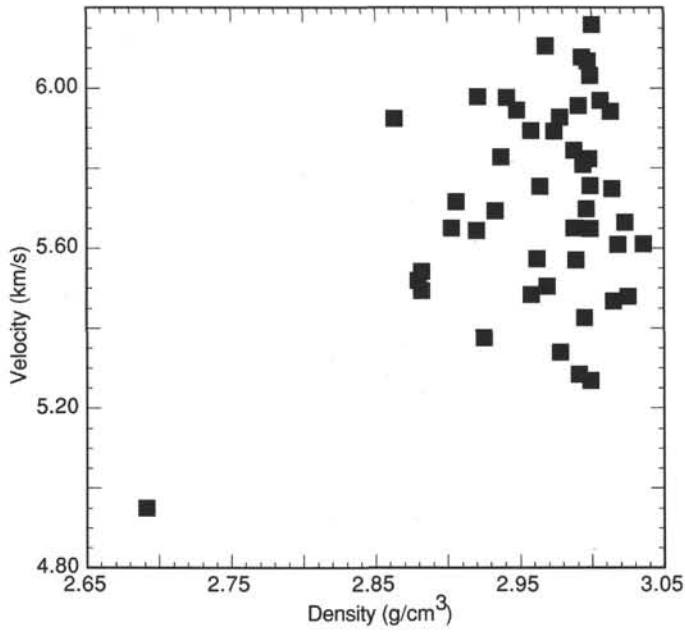


Figure 111. Velocity-density systematics of samples recovered during Legs 137 and 140. Measurements represent wet bulk densities and wet compressional-wave velocities in the C-direction.

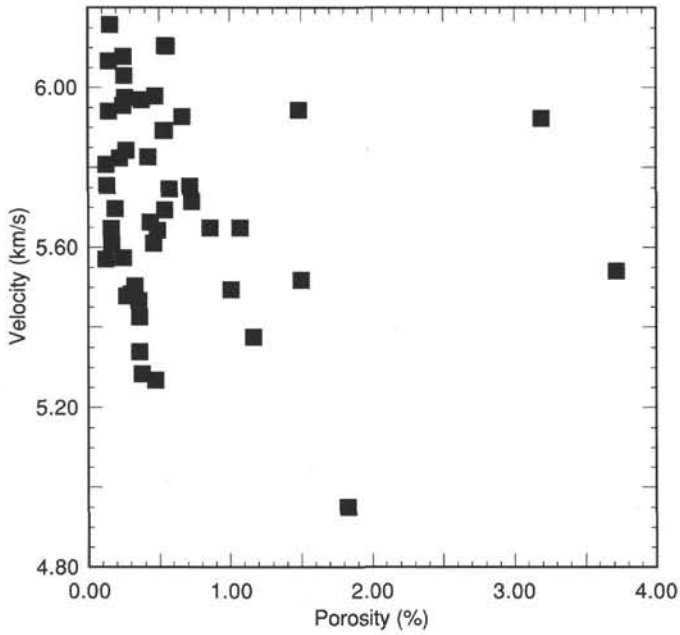


Figure 112. Velocity-porosity relationship for samples recovered from Legs 137 and 140.

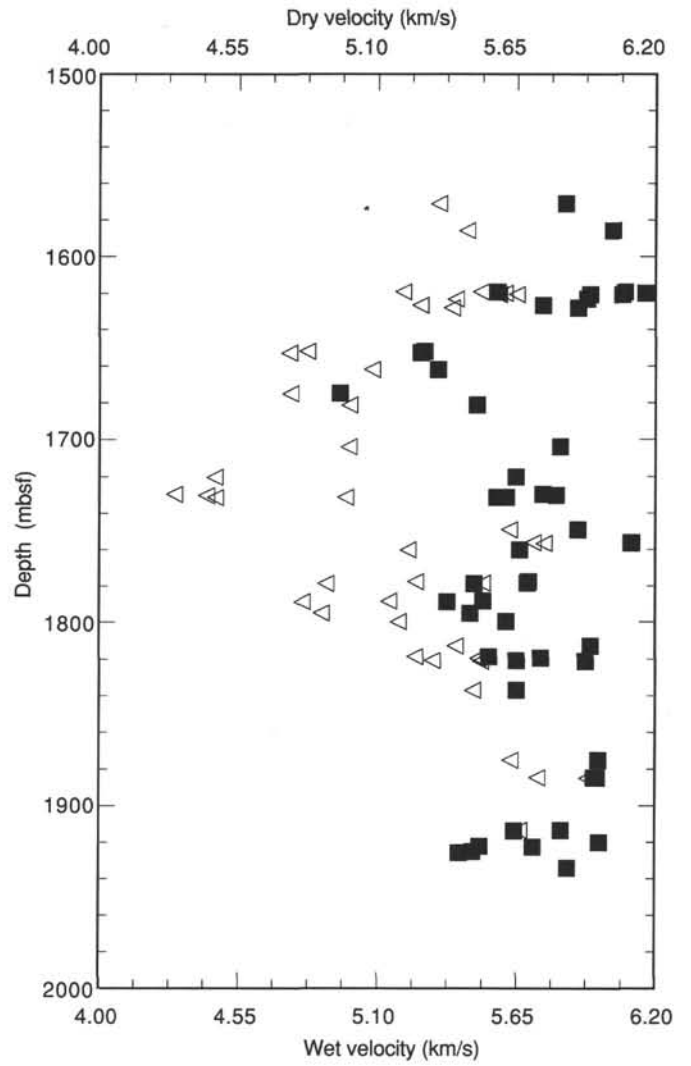


Figure 113. Comparison of wet (■) and dry (◁) compressional-wave velocities.

Table 24. Thermal conductivity (W/m-K) measurements as a function of depth and orientation.

Hole, core, interval (cm)	Depth (mbsf)	Direction of measurement			Comments to other directions
		Vertical	Horizontal	Other	
140-504B					
186R-1, 39-84	1626.69	2.413	2.609		
186R-1, 39-48	1626.69	^a 1.240	^a 1.487		
190R-1, 90-100	1656.00	^b 2.356	^b 2.057	^a 1.859	crack
190R-1, 90-100	1656.00			^a 2.060	heterogenous
190R-1, 90-100	1656.00	^a 1.140	^b 2.343	^b 2.271	45° parallel to veins
190R-1, 90-100	1656.00			^b 2.270	45° parallel to layering
191R-1, 34-45	1661.74	2.731	2.630		
193R-1, 44-54	1674.94	^b 2.244	2.500		
193R-1, 44-54	1674.94	^a 1.285	^b 2.388		
197R-2, 7-18	1704.37	^a 1.478	^b 2.364		
199R-1, 119-126	1720.59	2.653	2.698		
200R-1, 120-132	1729.90	^a 1.429	^b 2.144		
200R-2, 140-148	1731.50	^b 2.526	^a 2.248		
200R-3, 55-63	1732.18	^b 2.248	^a 2.192	2.524	45° homogeneous area
200R-3, 55-63	1732.18			^b 2.353	45° heterogenous area
205R-1, 1-17	1757.00	2.976	2.497		
205R-1, 1-9	1778.00	2.530	2.583		
205R-1, 81-90	1778.81	2.555	2.435	2.439	45° in vein
208R-2, 57-65	1780.07	2.300	^a 1.990	^a 2.020	45° in dark colored area
208R-2, 57-65	1780.07			^a 1.890	45° in light colored area
208R-1, 97-107	1788.47	^b 1.746	^b 2.126	2.640	homogeneous area
209R-1, 97-107	1788.47			^b 2.338	heterogenous area
209R-2, 7-24	1789.07	^b 2.257	^b 2.133		
210R-1, 16-26	1795.06	2.587	^b 2.363	2.440	between two veins
211R-1, 126-133	1799.76	2.617	2.666		
214R-1, 23-39	1818.83	^a 1.852			
214R-1, 23-39	1818.83	^b 2.018	^b 2.053		
214R-2, 86-93	1820.96	^b 2.467	^b 2.360	^b 2.450	45° in light colored area
214R-2, 121-134	1821.31	^a 1.873			
214R-2, 121-134	1821.31	^a 1.942	^b 2.159		
217R-1, 1-7	1828.00	2.450	2.604		
221R-1, 35-48	1875.35	^a 1.180			
225R-2, 99-108	1913.19	^b 1.660	^b 2.050		
225R-2, 99-108	1913.19	^b 1.870			
226R-1, 8-20	1920.80	2.340	2.250		
227R-1, 73-81	1925.23	1.834	2.270		

Needle located in homogenous rock, except where footnoted.

^a Needle located in or close to crack.^b Needle located in heterogenous rock.

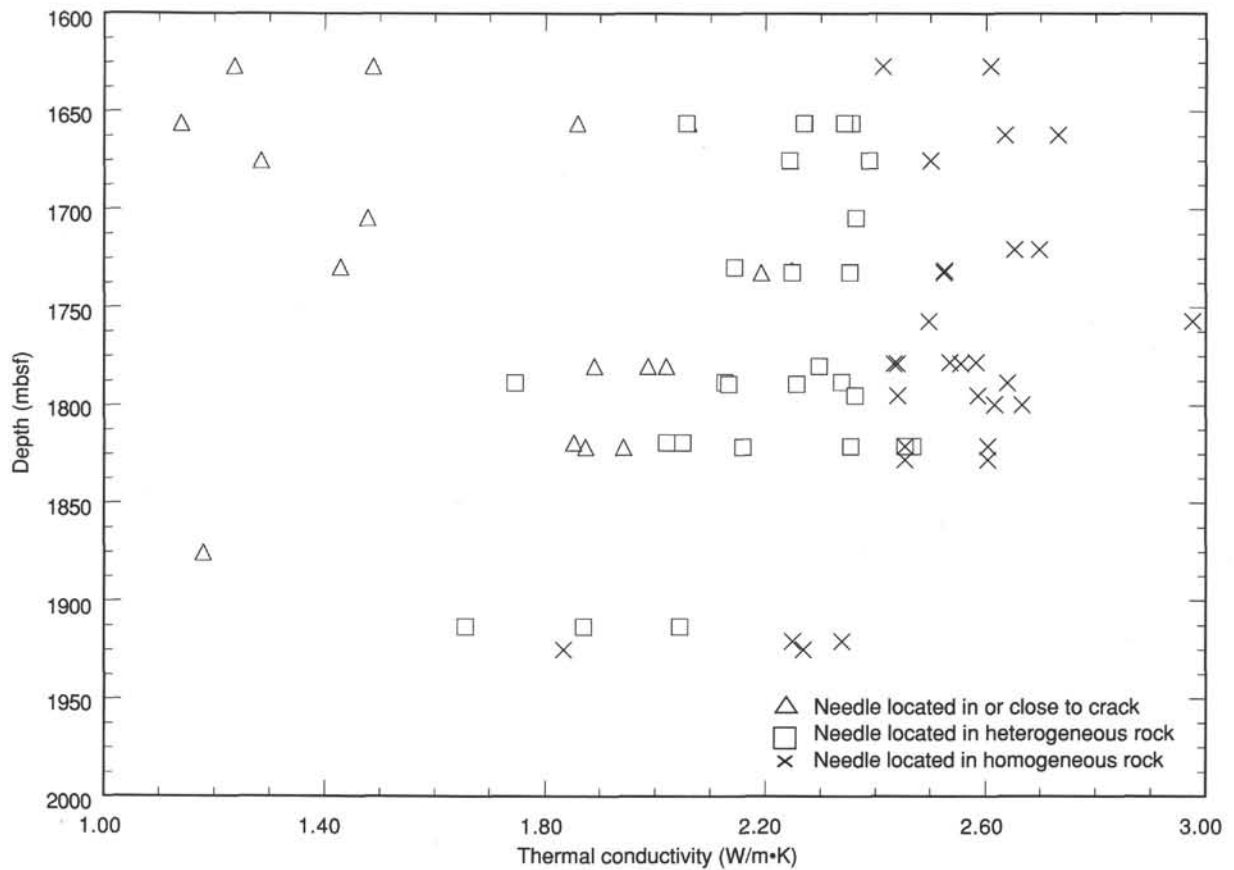


Figure 114. Thermal conductivities as a function of depth.

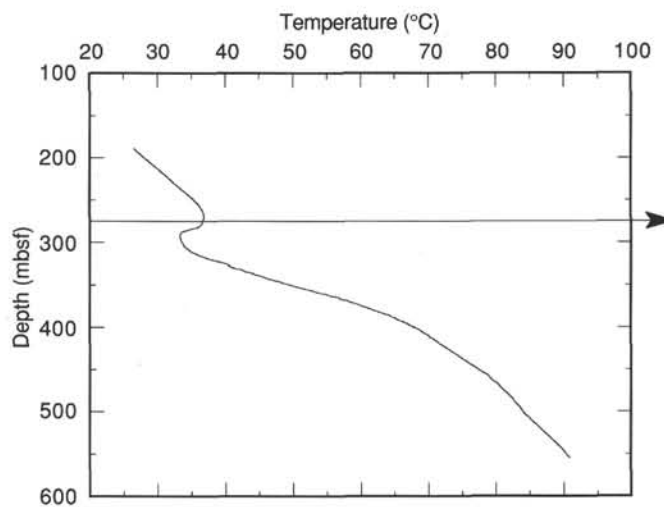


Figure 115. Temperature profile over the hydrologically most active part of the basement recorded on 1 October 1991, after the first re-entry in Hole 504B. The hole is cased through the sedimentary section, (0–275 mbsf) and is hence hydrologically disconnected from the basement.

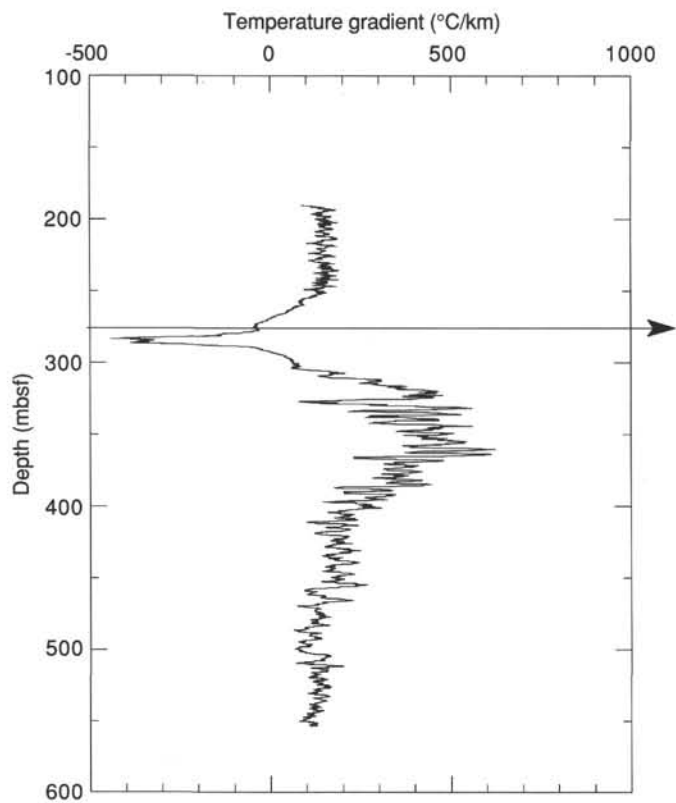


Figure 116. Temperature gradient calculated (moving average of 2.0 m) from the temperature profile recorded on 1 October 1991, prior to drilling in Hole 504B.

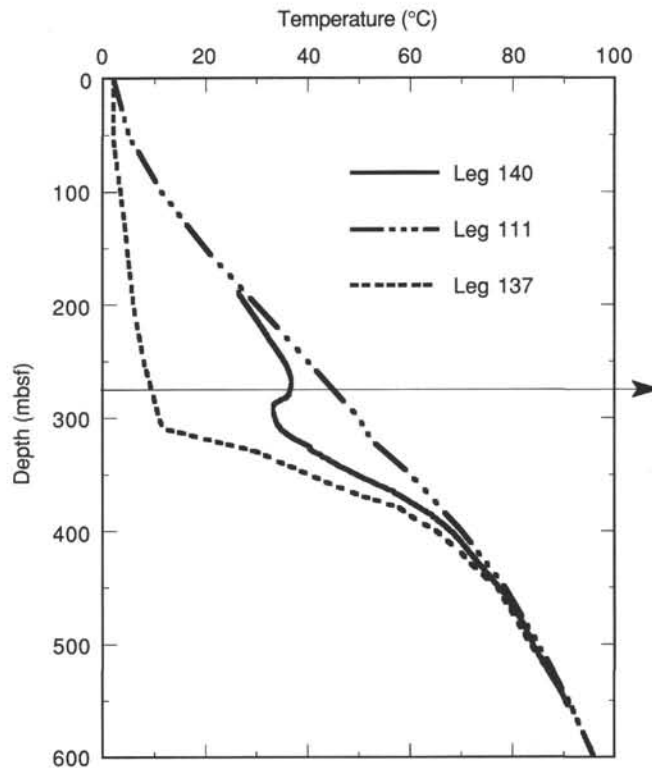


Figure 117. Composite diagram of temperature profiles recorded in Hole 504B with the BRGM high-resolution temperature probe during Legs 111, 137, and 140.

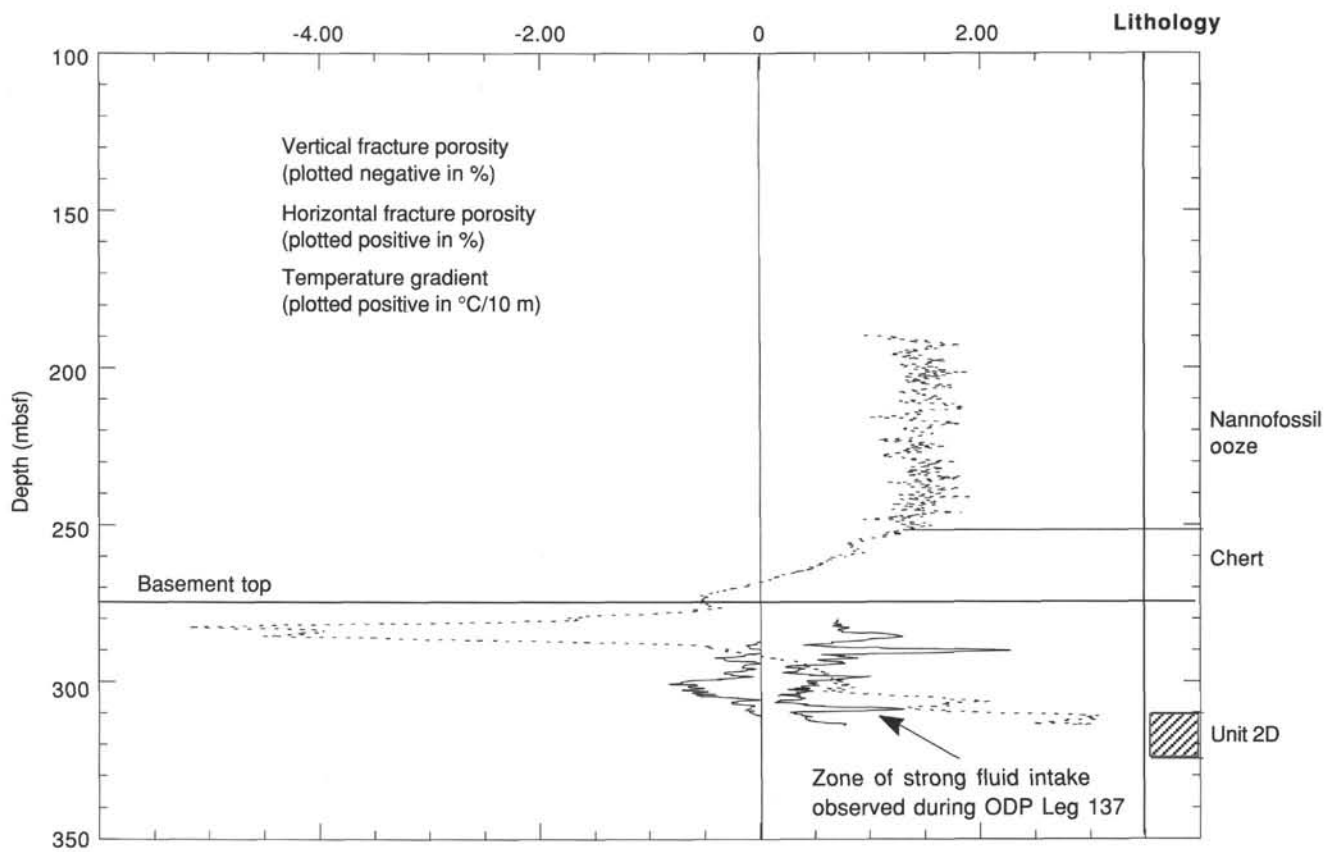


Figure 118. Temperature gradient (expressed in °C/10 m) and fracture porosity (expressed in %) plotted vs. depth over the lower sedimentary column and the upper part of the basement observed to be hydrologically active during Legs 137 and 140. For clarity, the horizontal fracture porosity is plotted using positive values, and the vertical fracture porosity is plotted using negative values.

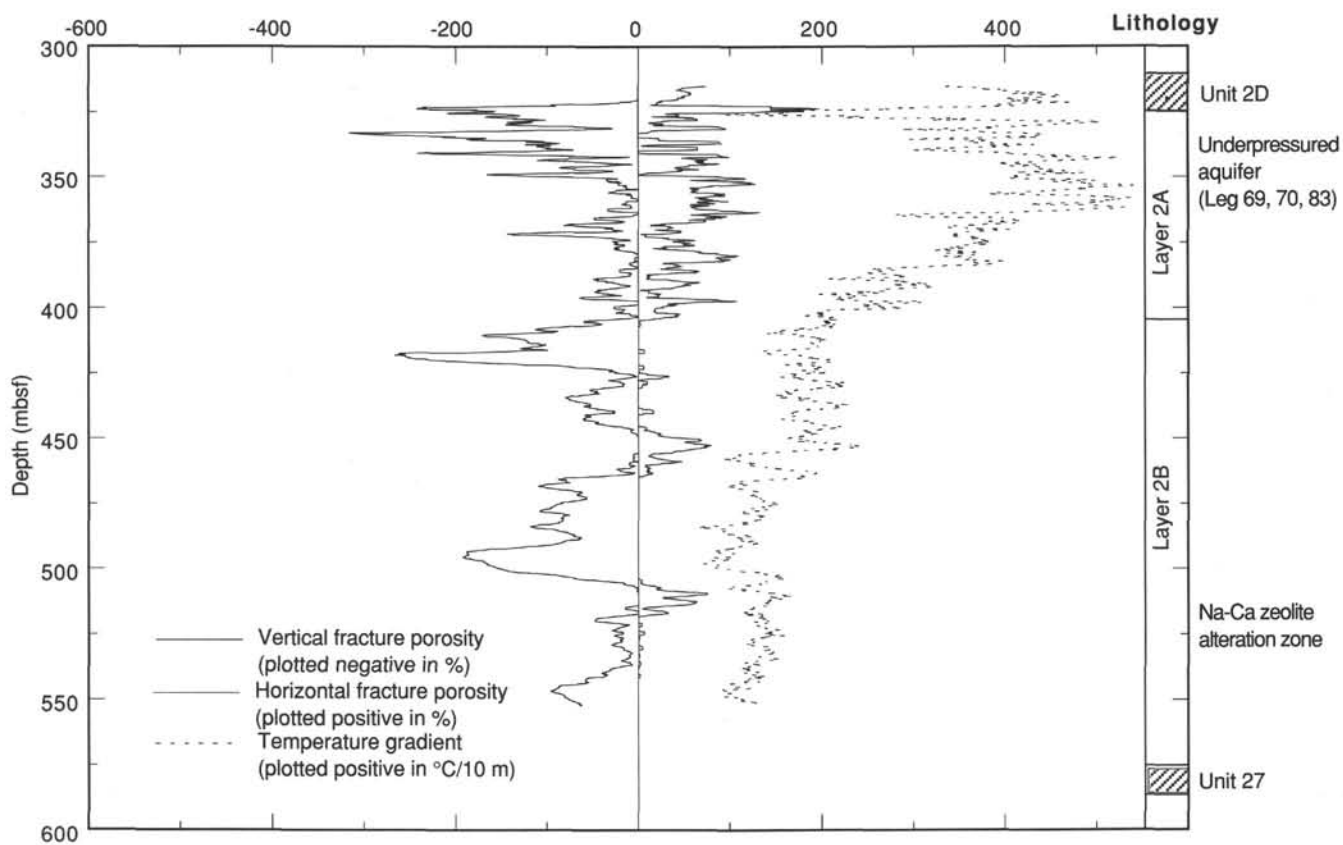


Figure 119. Temperature gradient (expressed in °C/10 m) and fracture porosity (expressed in %) plotted vs. depth over the section of the upper basement constituting the main water inlet after initial drilling of the hole (e.g., during Legs 70, 83, and 92). For clarity, the horizontal fracture porosity is plotted using positive values, and the vertical fracture porosity is plotted using negative values.

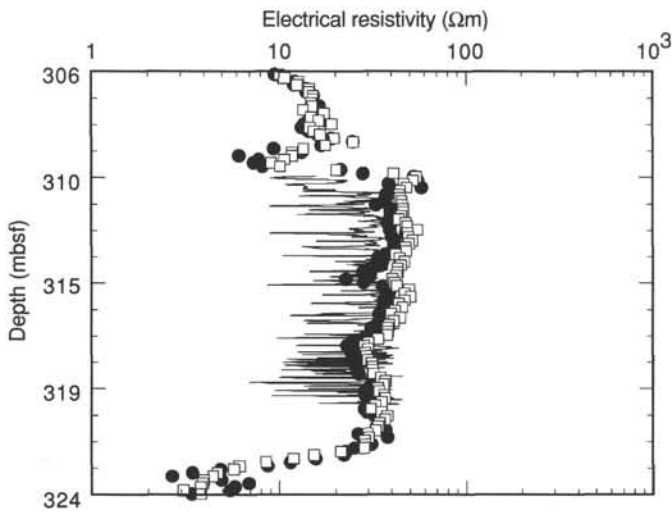


Figure 120. Comparison of resistivities measured through a massive flow (lithologic Unit 2D) using the dual laterolog (LLdc and LLsc plotted as dots and open squares) to resistivities computed from the images recorded with the FMS over the same interval (continuous profile). The plotting technique is justified by the large difference in vertical resolution of the two experiments (that of the DLL is of the order of 600 mm, whereas that of the FMS is equivalent to the footprint of the FMS images, 2.54 mm).

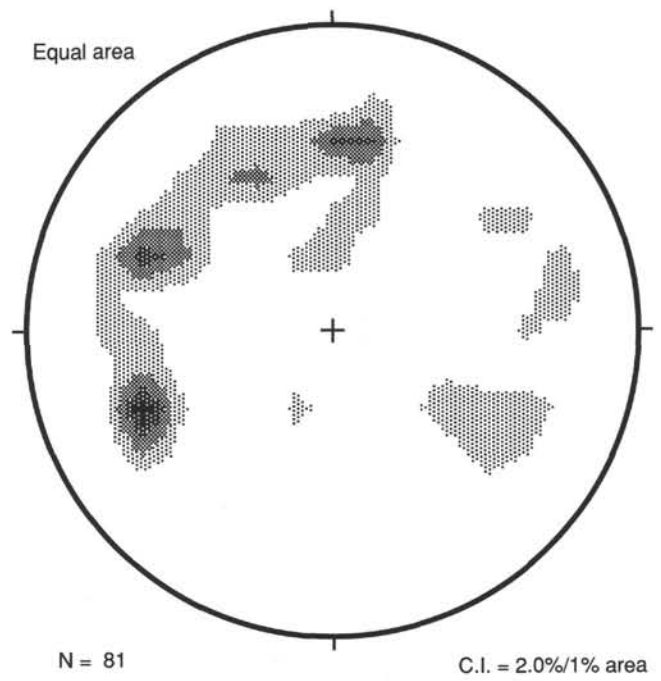


Figure 121. Equal-area stereogram showing the distribution of 81 fractures picked from the FMS images recorded from 1575 to 1563 mbsf in the sheeted dike complex. Fractures are plotted as poles to the fracture planes. C.I. stands for contour interval. N = number of measurements.

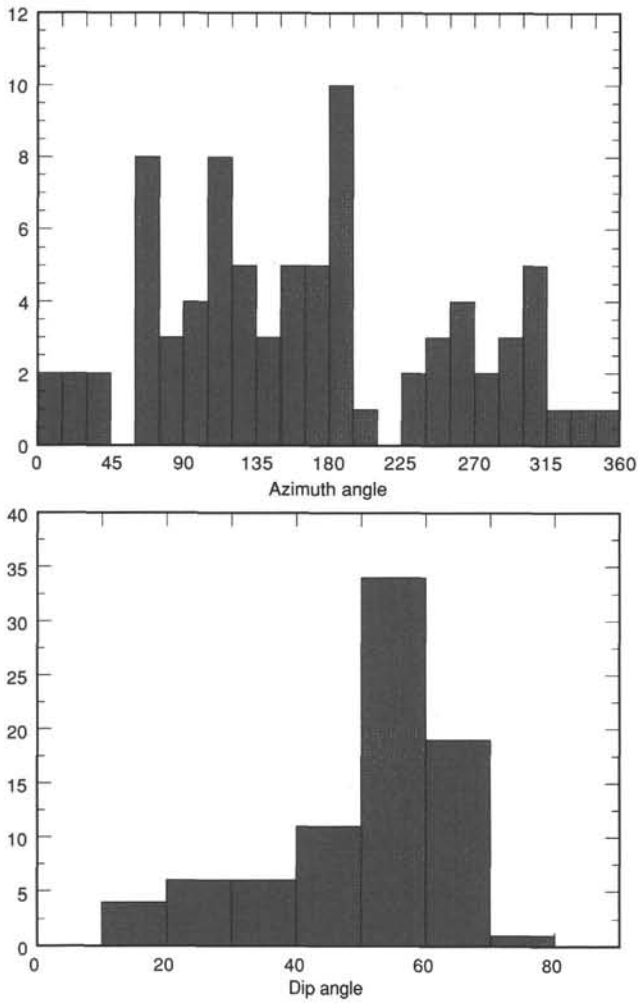


Figure 122. Histograms of dip angles and dip azimuths of fractures mapped from FMS images recorded from 1575 to 1563 mbsf.

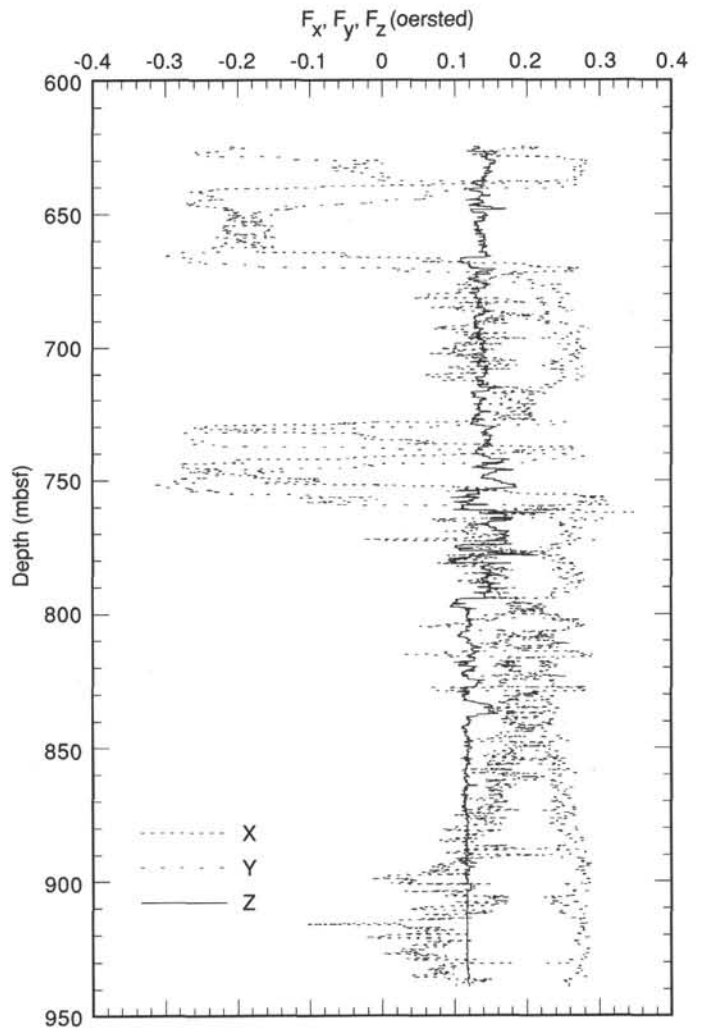


Figure 123. Example of the three-component magnetometer data recorded by the FMS inclinometer over the upper part of the basement.

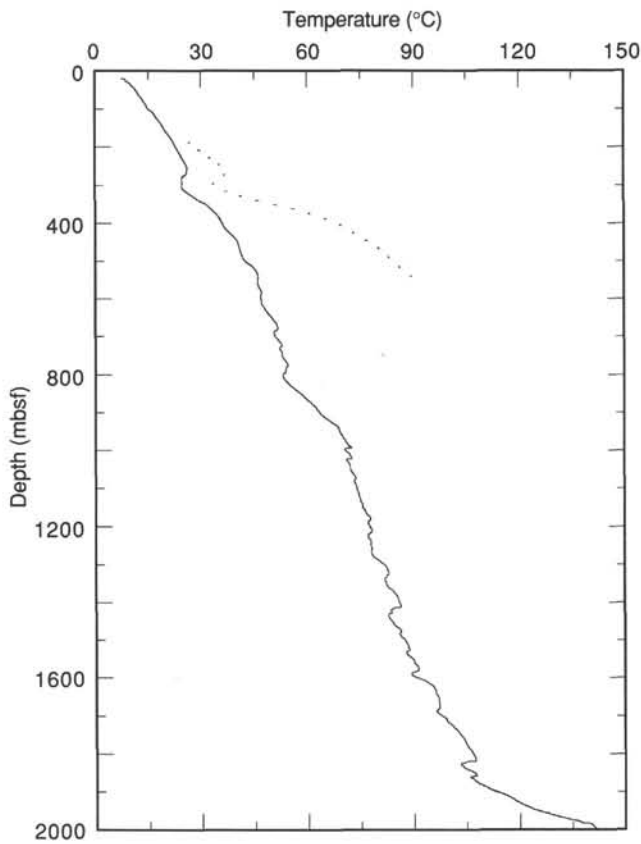


Figure 124. Temperature profile recorded on 7 November 1991, after coring for 4 weeks in the lower section of Hole 504B (solid line). The data span 15 mbsf to total depth (2000.4 mbsf). A sharp temperature increase is noticed over the lower 150 m of the hole. In the upper basement, the temperature profile inversion detected after re-entry (dotted line) is still visible after 4 weeks of continuous coring, emphasizing the presence of strong hydrological activity in this section.

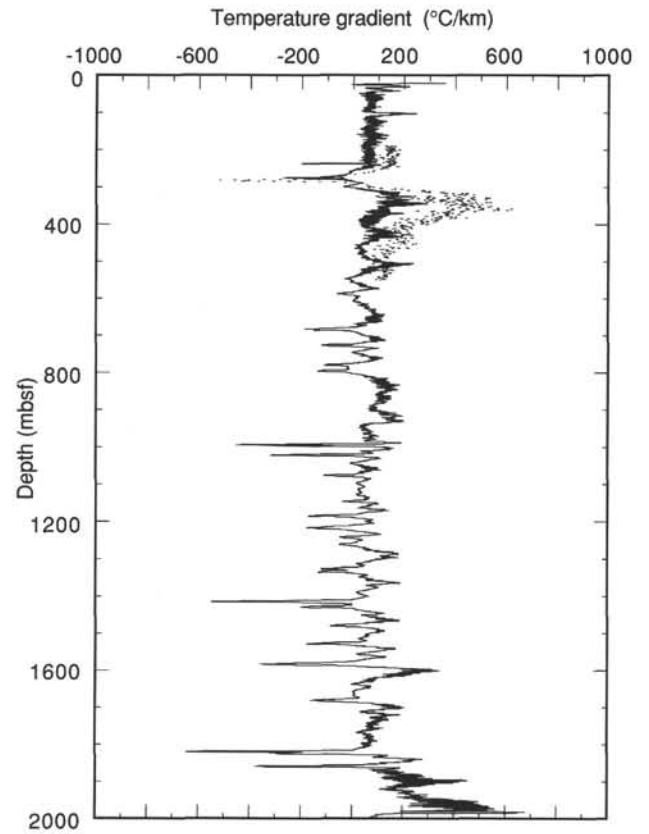


Figure 125. Temperature gradient calculated with a moving average of 2.0 m from the temperature profile recorded throughout the hole after 4 weeks of coring (solid line). Active fluid-movements are still visible in the upper basement, as well as in discrete regions of the dike section where negative values were obtained. Such zones probably correlate to permeable, fractured intervals where fluid was injected during coring, providing more efficient cooling than in the more competent sections. The dotted line represents the temperature gradient calculated from the temperature profile recorded prior to drilling.

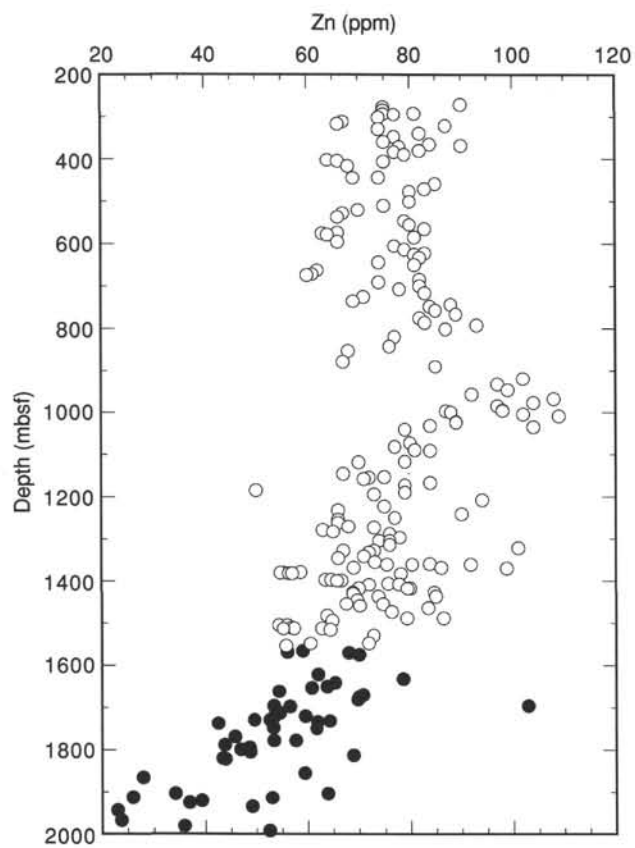


Figure 126. Vertical profile of zinc concentration plotted vs. depth in Hole 504B showing zone of depletion from 1600 to 2000 mbsf. Data from earlier legs (circles), data from Leg 140 (dots).

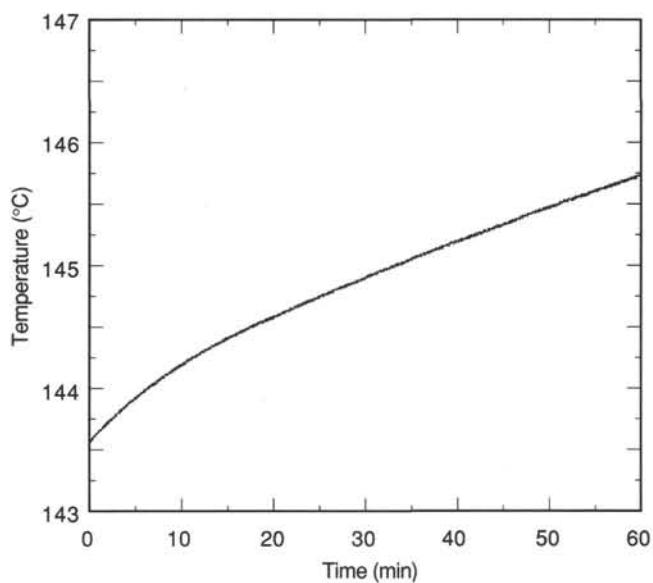


Figure 127. Temperature profile recorded at total depth (2000.4 mbsf) over a time span of 60 min. The recording began 28 hr after the end of coring and circulation at this depth.

APPENDIX A (continued).

Core	Section	Pieces	Interval (cm)	Unit	Plagioclase		Ph GS	Gm GS	Mor	Augite		Ph GS	Gm GS	Mor	Olivine		Ph GS	Gm GS	Mor	Other Min	%Ph	%Gm	Ph GS	Gm GS	Mor	Other Min	%Ph	%Gm	Ph GS	Gm GS	Mor	
					%Ph	%Gm				%Ph	%Gm																					
210R	1	2-19	3-144	241	0.5	55	2	0.9	1c/10c	0.15	40	1	0.5	4b/3b	0.5	-	1	-	1c	Cr-augite	0.2	-	2.5	-	1c							
210R	2	1-7	0-35																													
211R	1	1-30	0-141																													
212R	1	1-17	0-65																													
213R	1	1	0-3																													
213R	1	2-10	3-31	242	0.3	55	1.5	0.3	1c/10c	-	40	-	0.15	3b	0.1	-	1.2	-	1b	Cr-augite	0.1	-	4.0	-	1c							
213R	1	11-36	31-149	243	0.5	60	1.7	1	1c/10c	0.15	35	1.5	0.5	4b/3b	0.5	-	1.2	-	3b	Cr-augite	0.2	-	3.0	-	1c							
214R	1	1-21	0-144	244	2.5	60	3	1.3	1c/10c	0.40	30	1.2	0.5	1b/3b	1.2	-	1.6	-	3b	Cr-augite	0.5	-	3.0	-	1c							
214R	2	1-25	0-135																													
215R	1	1-21	0-90																													
216R	1	1-6	0-24																													
216R	1	7-181	24-89	245	0.8	50	0.8	0.4	1c/10c	0.2	45	0.5	0.1	3b/3b	1	-	1.2	-	1c	Cr-augite	1	-	4.0	-	1c	Dark emerald-green pyroxene	0.5	-	1	-	1c	
217R	1	1	0-8																													
217R	1	2-6	8-27	246	1.5	55	1.5	0.5	1c/10c	0.1	40	1.5	0.4	4b/3b	1	-	1.5	-	1c	Cr-augite	0.75	-	4.0	-	1c							
218R	1	1	0-5																													
218R	1	2-7	5-28	247	0.1	50	1.5	0.25	1c/10c	0.1	45	0.5	0.25	3b/3b	0.1	-	0.5	-	1c													
219R	1	1	0-3																													
219R	1	2	3-7	248	0.5	55	1.6	0.4	1c/10c	0.2	40	0.8	0.15	3b/3b	1	-	1.6	-	1c	Cr-augite	0.5	-	2.0	-	1c							
219R	1	-	7-13	249	-	55	-	0.25	10c	-	40	-	0.25	3b	0.5	-	0.3	-	1c	Cr-augite	0.5	-	0.3	-	1c							
219R	1	4	13-17	250	0.5	55	1.5	0.5	1c/10c	-	40	-	0.4	3b	0.5	-	1.5	-	1c	Cr-augite	0.5	-	2.5	-	1c							
220R	1	1	0-5	251	0.1	60	1.5	0.3	1c/10c	0.2	35	0.5	0.15	3a/3b	0.1	-	0.8	-	4b	Cr-augite	0.5	-	1.2	-	1c							
220R	1	2-7	5-31	252	0.3	55	1.6	0.6	1c/10c	0.5	40	1.5	0.5	3b/3b	0.5	-	1.3	-	4b	Cr-augite	0.1	-	4.0	-	1c							
221R	1	1-3	0-11	253	0.3	55	2	0.3	1c/10c	-	45	-	0.3	3b	1.5	-	1.6	-	1bm	Cr-augite	2	-	2.5	-	1c							
221R	1	4-15	11-67	254	0.5	50	1.6	0.8	1c/10c	0.5	35	1.5	0.6	4a/3b	1	-	1.5	-	1cm	Cr-augite	0.7	-	4.0	-	1c							
222R	1	1-16	0-94																													
222R	1	17-21	94-115	255	0.3	55	1.5	0.4	1c/10c	0.1	40	0.8	0.25	4a/3b	0.5	-	2	-	3cm	Cr-augite	0.3	-	2.0	-	1c							
222R	1	22-24	115-133	256	0.2	50	1.6	0.4	1c/10c	0.5	45	2	0.4	3bm/3b	-	-	-	-	-	Cr-augite	0.1	-	3.0	-	1c							
222R	1	25	133-136	257	0.1	55	0.8	0.4	1c/10c	0.2	40	0.5	0.25	3b/3b	0.1	-	0.7	-	1bm	Cr-augite	0.1	-	2.0	-	1c							
223R	1	1	0-4																													
223R	1	2-10	4-40	258	0.75	55	1.5	1	1c/10c	0.2	35	0.8	0.4	3b/3b	0.5	-	2	-	1cm	Cr-augite	1.5	-	3.0	-	1c							
224R	1	1-14	0-63																													
224R	1	15-19	63-82	259	0.1	55	1.2	0.6	1c/10c	0.1	45	0.8	0.2	3b/3b	0.1	-	2.5	-	1cm													
225R	1	1-32	1-125																													
225R	1	331-37	125-150	260	0.5	55	2.5	1.5	1c/10c	-	35	-	1.5	3b	3	-	1.5	-	3bm	Cr-augite	3	-	2.5	-	1c	Spinel	-	0.2	-	0.40	1b	
225R	2	1-21	0-122																													
226R	1	1-24	0-150																													
226R	2	1-17	1-140																													
226R	3	1-5	0-44																													
227R	1	1-17	0-147																													
227R	2	1-3	0-23																													
227R	2	4-5	23-30	261	0.5	50	2.5	0.4	1c/10c	0.1	45	1	0.3	4b/3b	3	-	1.1	-	1c	Cr-augite	1.5	-	2.5	-	1c							
228R	1	1-17	0-77	262	1	50	2.5	0.5	1c/10c	0.5	45	1.3	0.5	1b/3b	1.5	-	1.5	-	3b	Cr-augite	0.5	-	1.5	-	1b							
229R	1	1-2	0-7																													
229R	1	3	7-11	263	0.5	55	1.5	0.6	1c/10c	0.2	40	0.8	0.4	3b/3b	1	-	0.8	-	1c	Cr-augite	2	-	4.0	-	1c							
229R	1	4-5	11-17	264	0.5	55	2	0.6	1c/10c	-	40	-	0.8	3b	0.8	-	1.2	-	3b	Cr-augite	0.2	-	1.8	-	1b							
229R	1	6-17	17-63	265	1	60	0.8	0.3	1c/10c	0.1	35	0.6	0.3	3b/3b	0.5	-	1	-	1b	Cr-augite	0.3	-	1.5	-	1c							
230R	1	1-4	0-18																													
231R	1	1-2	0-10																													
232R	1	1-3	0-16																													
233R	1	1-6	0-23	266	0.5	60	0.6	0.3	1c/10c	-	35	-	0.25		-	-	-	-	-													
235R	1	1-5	0-17	267	2	50	1.2	0.4	1c/10c	0.5	45	0.8	0.3	3b/3b	1	-	1	-	1bm	Cr-augite	1	-	1.2	-	1c							
235R	1	6	17-21	268	1	55	0.8	0.25	1c/10c	0.5	40	0.8	0.15	4b/3b	-	-	-	-	-													
235R	1	7-8	21-28	269	3	50	1.8	0.4	1c/10c	0.7	40	1.2	0.4	4b/3b	30	-	1	-	1bm	Cr-augite	2	-	1.6	-	1c							
236R	1	1-14	0-84																													
237R	1	1-7	0-27																													
238R	1	1-8	0-26																													

APPENDIX B
Lithology Log: ODP Core Description: Igneous Lithology Leg 140 Hole 504B.

Core	Section	Pieces	Interval (cm)	Unit	Lithology	Texture	Fabric orientation	Color	Ve (%)	Ox (%)	S (%)
182M	1		0-110		Sparsely PC phryic diabase	Fine-grained phaneritic with	-	5B 5/1	-	2	0.1
182M	2		0-150			plagioclase, ophitic augite and					
182M	3		0-22			altered olivine.					
183M	1		0-150		Not described	Not described.	-	-	-	-	-
184M	1		0-133		Not described	Not described.	-	-	-	-	-
185R	1	1-4	0-26	211	Moderately PCO phryic diabase	Fine-grained doleritic with abundant	-	5B 5/1	-	1	0.05
186R		1-6	0-31			plagioclase and ophitic augite.					
186R	1	7	31-35	212	Aphyric diabase	Fine-grained equigranular with rare	-	5B 5/1	-	5	0.05
						plagioclase, ophitic augite and					
						altered olivine.					
186R	1	8-18	35-150	213	Aphyric diabase	Medium-grained equigranular.	-	5B 6/1	-	1	0.05
	2	1-10B	0-54								
187R	1	1-2	0-11	214	Aphyric basalt	Very fine-grained equigranular.	-	5B 5/1	-	1	0.1
187R	1	3-13	11-58	215	Aphyric diabase	Fine-grained equigranular with	-	5B 6/1	-	1	0.2
						extensively sheared zones.					
187R	1	14	58-64	216	Sparsely PC phryic diabase	Fine-grained doleritic with seriate	-	5B 6/1	-	1	0.05
						porphyritic plagioclase, altered					
						olivine and subophitic augite.					
188R	1	1-12	0-41	217	Sparsely CPO phryic basalt	Very fine-grained doleritic with	-	5B 5/1	-	1	0.1
189R	1	1	0-4			plagioclase subophitic augite, and					
						minor altered olivine.					
189R	1	2-28	4-146	218	Moderately POC phryic	Fine-grained doleritic with seriate	-	5B 6/1	-	1	0.1
189R	2	1-16	0-117		diabase	porphyritic plagioclase, subophitic					
190R	1	1-23	0-121			augite, and altered olivine.					
191R	1	1-25	0-150								
192R	1	1-10	0-39								
193R	1	1-4	0-14	219	Moderately PCO phryic	Fine-grained doleritic in middle of	-	5B 6/1	-	1	0.05
					diabase	unit, fine-grained aphanitic in Pieces					
						1 and 4.					
193R	1	5-14	14-58	220	Moderately POC phryic	Fine-grained doleritic with seriate	-	5B 6/1 to	-	0.5	0.01
194R	1	1-23	0-126		diabase	porphyritic plagioclase and altered		5B 5/1			
195R	1	1-2	0-7			olivine.					
195R	1	3	7-10	221	Aphyric basalt	Microcrystalline.	-	5B 5/1	-	2	0.05
196R	1	1	0-6								
196R	1	2-9	6-45	222	Moderately POC phryic	Fine-grained doleritic with seriate	-	5B 6/1	-	1	0.05
197R	1	1-22	0-105		diabase	porphyritic plagioclase and altered					
						olivine.					
197R	1	23-29	105-144	223	Sparsely POC phryic diabase	Fine-grained, seriate doleritic texture.	-	rock	-	2	0.1
197R	2	1-7	0-45					5B5/1;			
198R	1	1-17	0-70					veins			
								5B6/1			
198R	1	18-21	70-85	224	Aphyric diabase	Microcrystalline to fine-grained	-	5B 6/1	-	1	0.05
						aphanitic.					
199R	1	1	0-4	225	Aphyric diabase	Fine-grained aphanitic.	-	N5/	1	3	-
199R	1	2-22	4-96	226	Moderately PCO phryic	Fine-grained seriate doleritic.	-	5B 4/1	-	1	0.2
					diabase			to			
								5B 7/1			
199R	1	22-31	96-150	227	Moderately POC phryic	Fine-grained seriate doleritic.	-	5B 4/1	-	3	0.1
199R	2	1	0-14		diabase			to			
200R	1	1-25	0-150					5B 7/1			
200R	2	1-22	0-148								
200R	3	1-24	0-149								
200R	4	1-13	0-55								
201R	1	1-5	0-23	228	Aphyric diabase	Fine-grained aphanitic.	-	5B 6/1	-	1	0.05
202R	1	1-9	0-36	229	Sparsely POC phryic diabase	Fine-grained doleritic.	-	5B 4/1	-	1	0.05
								contact;			
								5B 6/1			
								interior			
202R	1	10-15	36-71	230	Moderately OPC phryic	Fine-grained doleritic with abundant	-	5B 5/1 to	-	1	0.05
203R	1	1	0-4		diabase	altered olivine.		5B 6/1			
203R	1	2-9	4-32	231	Aphyric diabase	Microcrystalline aphanitic.	-	5B 5/1	-	2	0.05
203R	1	10-15	32-63	232	Sparsely PCO phryic diabase	Microcrystalline to fine-grained	-	5B 5/1	-	1	0.05
204R	1	1-12	0-54			aphanitic.					
205R	1	1-13	0-63								
205R	1	14	63-68	233	Moderately PCO phryic	Fine-grained doleritic.	-	5B 6/1	-	2	0.1
					diabase						
205R	1	15-20	68-87	234	Aphyric basalt	Microcrystalline to very fine-grained	-	N5/	-	2	0.05
						aphanitic.					
205R	1	21-24	87-103	235	Moderately COP diabase	Fine-grained doleritic.	-	5B 6/1	-	3	0.1
206R	1	1-11	0-51								
207R	1	1-16	0-60	236	Aphyric diabase	Fine-grained aphanitic.	-	5B 5/1	-	1	0.05
208R	1	1-8	0-35	237	Moderately COP phryic	Fine-grained doleritic.	0.4	5B 5/1	-	2	0.1
					diabase		vertical				
208R	1	9-12	35-49	238	Sparsely PCO phryic diabase	Phaneritic with microcrystalline to	-	5B 6/1 to	-	1	0.05
						fine-grained groundmass.		N4/ in			
								contact			

APPENDIX B (continued).

Core	Section	Pieces	Interval (cm)	Unit	Lithology	Texture	Fabric orientation	Color	Ve (%)	Ox (%)	S (%)
208R	1	13-28	49-145	239	Moderately OPC phyric diabase	Fine-grained equigranular doleritic; holocrystalline.	-	5B 5/1 to 5BG 5/1 in veins	-	2	0.1
	2	1-23	0-150								
	3	1	0-11								
209R	1	1-17	0-143	240	Moderately OPC phyric diabase	Glomeroporphyritic-doleritic.	-	5B 5/1 to 5BG 6/1 in alteration	-	1	0.1
209R	2	1-25	0-150								
210R	1	1	0-3								
210R	1	2-19	3-144	241	Sparsely POC phyric diabase	Fine-grained equigranular doleritic.	-	5B 5/1 to 5B 6/1 in alteration	-	2	0.1
210R	2	1-7	0-35								
211R	1	1-30	0-141								
212R	1	1-17	0-65								
213R	1	1	0-3								
213R	1	2-10	3-31	242	Aphyric basalt	Microcrystalline.	-	5B 5/1	-	1	0.05
213R	1	11-36	31-149	243	Sparsely POC phyric diabase	Fine-grained glomeroporphyritic.	-	5B 6/1 to 5Y 8/1 in alteration	-	1	0.05
214R	1	1-21	0-144	244	Moderately POC phyric diabase	Medium-grained glomeroporphyritic.	-	5B 6/1 to 5B 7/1	-	1	0.1
214R	2	1-25	0-135								
215R	1	1-21	0-90								
216R	1	1-6	0-24								
216R	1	7-18	24-89	245	Moderately COP phyric diabase	Fine-grained doleritic.	-	5B 5/1; N4/ to 5B 7/1 in alteration	-	3	0.3
217R	1	1	0-8								
217R	1	2-6	8-27	246	Moderately POC phyric diabase	Fine-grained doleritic.	-	5B 5/1	-	1	0.1
218R	1	1	0-5								
218R	1	2-7	5-28	247	Aphyric diabase	Aphanitic-microcrystalline.	-	5B 6/1	-	1	0
219R	1	1	0-3								
219R	1	2	3-7	248	Moderately OCP phyric diabase	Fine-grained doleritic.	-	5B 5/1	-	1	0.05
219R	1	3	7-13	249	Aphyric diabase	Aphanitic-microcrystalline.	Flow alignment	5B 4/1	-	2	0.1
219R	1	4	13-17	250	Sparsely POC phyric diabase	Fine-grained doleritic.	-	5B 5/1	-	1	0.05
220R	1	1	0-5	251	Aphyric basalt	Very fine-grained aphanitic.	-	5B 5/1	-	3	0
220R	1	2-7	5-31	252	Sparsely COP phyric diabase	Fine-grained doleritic.	-	5B 6/1	-	1	0.05
221R	1	1-3	0-11	253	Moderately COP phyric diabase	Fine-grained doleritic.	-	5B 5/1	-	3	0.05
221R	1	4-15	11-67	254	Moderately COP phyric diabase	Fine-grained doleritic.	-	5B 4/1 to 5B 5/1	-	0.5	0 to 100
222R	1	1-16	0-94								
222R	1	17-21	94-115	255	Sparsely OCP phyric diabase	Fine-grained phaneritic.	-	5B 5/1	-	2	0.05
222R	1	22-24	115-133	256	Aphyric diabase	Fine-grained doleritic.	-	5B 5/1	-	1	0
222R	1	25	133-136	257	Aphyric diabase	Fine-grained aphanitic.	-	5B 5/1	-	3	0.2
223R	1	1	0-4								
223R	1	2-10	4-40	258	Moderately CPO phyric diabase	Fine-grained doleritic.	-	5B 5/1	-	3	0.05
224R	1	1-14	0-63								
224R	1	152-19	63-82	259	Aphyric diabase	Fine-grained aphanitic.	-	5B 5/1	-	1	0.5
225R	1	1-32	1-125								
225R	1	33-37	125-150	260	Moderately COP phyric diabase	Medium-grained doleritic.	-	N7/ to 5B 5/1	-	1	0.1
225R	2	1-21	0-122								
226R	1	1-24	0-150								
226R	2	1-17	0-140								
226R	3	1-5	0-44								
227R	1	1-17	0-147								
227R	2	1-3	0-23								
227R	2	4-5	23-30	261	Moderately OCP phyric diabase	Fine-grained phaneritic.	-	5B 5/1	-	3	0.05
228R	1	1-17	0-77	262	Moderately OPC phyric diabase	Fine-grained doleritic.	-	5B 6/1 to N7/	-	1	0.05
229R	1	1-2	0-7								
229R	1	3	7-11	263	Moderately COP phyric diabase	Fine-grained phaneritic.	-	5B 5/1	-	2	0.05
229R	1	4-5	11-17	264	Sparsely OPC phyric diabase	Fine-grained doleritic.	-	5B 6/1	-	1	0.1
229R	1	6-17	17-63	265	Sparsely POC phyric diabase	Fine-grained aphanitic.	-	5B 6/1	-	1	0
230R	1	1-4	0-18								
231R	1	1-2	0-10								
232R	1	1-3	0-16								
233R	1	1-6	0-23	266	Aphyric diabase	Fine-grained doleritic.	-	5B 5/1	-	1	0.05
235R	1	1-5	0-17	267	Moderately PCO phyric diabase	Fine-grained doleritic.	-	5B 6/1	-	2	0
235R	1	6	17-21	268	Sparsely PC phyric basalt	Very fine-grained doleritic.	-	5B 5/1	-	1	0.1
235R	1	7-8	21-28	269	Moderately POC phyric diabase	Fine-grained doleritic.	-	5B 5/1 to 5B 6/1	-	1	0
236R	1	1-14	0-84								
237R	1	1-7	0-27								
238R	1	1-8	0-26								

Abbreviations are defined in the "Petrography" section and Table 1 of the "Explanatory Notes" chapter (this volume).

APPENDIX C
Igneous Contacts Log: ODP Core Description: Igneous Contacts Log-Leg 140 Hole 504B.

Core	Section	Base of unit (cm)	Piece	Unit	Lithology	Character of lower contact	Notes
186R	1	31	6	211	Moderately PCO phyric diabase	NC, small unoriented piece.	End of Unit 211.
186R	1	35	7	212	Aphyric diabase	NC, fine-grained unoriented piece.	End of Unit 212.
186R	2	54	10B	213	Aphyric diabase	NC, no change in grain size through Unit 213. unoriented piece coarser than lower piece.	End of Unit 213.
187R	1	11	2	214	Aphyric basalt	UC, piece of lower unit has fragmented chilled margin.	End of Unit 214.
187R	1	58	13	215	Aphyric diabase	NC, fine-grained unoriented piece.	End of Unit 215.
187R	1	64	14	216	Sparsely PC phyric diabase	NC, unoriented piece coarser than lower piece.	End of Unit 216.
189R	1	4	1	217	Sparsely CPO phyric basalt	NC, no change in grain size through Unit 217. Unoriented piece finer than lower piece.	End of Unit 217.
192R	1	39	10	218	Moderately POC phyric diabase	NC, no change in grain size through Unit 218. Unoriented piece coarser than lower piece.	End of Unit 218.
193R	1	4	1	219	Moderately PCO phyric diabase	NC, unoriented piece finer than lower piece.	Not unit boundary.
193R	1	11	3	219	Moderately PCO phyric diabase	NC, unoriented piece coarser than lower piece.	Not unit boundary.
193R	1	14	4	219	Moderately PCO phyric diabase	NC, unoriented piece finer than lower piece.	End of Unit 219.
195R	1	7	2	220	Moderately POC phyric diabase	UC, unoriented piece coarser than lower unit which is a chilled margin. Boundary is absent.	End of Unit 220.
196R	1	6	1	221	Aphyric basalt	LC, unoriented piece with fine margins chilled against each other.	End of Unit 221.
197R	1	105	22	222	Moderately POC phyric diabase	UC, unoriented piece coarser and more porphyritic than lower piece.	End of Unit 222.
198R	1	70	17	223	Sparsely POC phyric diabase	UC, grain size gradually decreases toward bottom of Unit 223. Lower piece is very fine grained with a fragmented chilled margin, but no boundary obtained.	End of Unit 223.
198R	1	85	21	224	Aphyric diabase	NC, fine-grained unoriented piece. Lower piece is more porphyritic.	End of Unit 224.
199R	1	4	1	225	Aphyric diabase	NC, unoriented piece finer than lower piece.	End of Unit 225.
199R	1	96	22	226	Moderately PCO phyric diabase	NC, unoriented piece coarser than lower piece.	End of Unit 226.
200R	4	55	13	227	Moderately POC phyric diabase	NC, unoriented piece coarser than lower piece.	End of Unit 227.
201R	1	23	5	228	Aphyric diabase	UC, unoriented piece coarser than lower piece.	End of Unit 228.
202R	1	5	1	229	Sparsely POC phyric diabase	NC, unoriented piece finer than lower piece.	Upper chilled margin of Unit 229?
202R	1	33	8	229	Sparsely POC phyric diabase	NC, unoriented piece coarser than lower piece.	Grain size variation within Unit 229.
202R	1	36	9	229	Sparsely POC phyric diabase	LC, unoriented piece finer than upper and lower piece.	Chilled margin at bottom of Unit 229? End of Unit 229.
203R	1	4	1	230	Moderately OPC phyric diabase	NC, unoriented ol-phyric piece coarser than lower aphyric piece.	Gradual coarsening downward within Unit 230.
203R	1	32	9	231	Aphyric diabase	Unoriented piece coarser than lower piece.	End of Unit 231.
203R	1	36	10	232	Sparsely PCO phyric diabase	Unoriented piece intruded by a dike of undefined unit. The piece was still molten when intruded. This is not the unit boundary.	Not unit boundary.
205R	1	63	13	232	Sparsely PCO phyric diabase	NC, unoriented piece less phyric than lower piece.	End of Unit 232.
205R	1	68	14	233	Moderately PCO phyric diabase	NC, unoriented piece coarser than lower piece.	End of Unit 233.
205R	1	87	20	234	Aphyric basalt	NC, unoriented piece finer than lower piece.	End of Unit 234.
206R	1	51	11	235	Moderately COP diabase	NC, unoriented piece coarser than lower piece.	End of Unit 235.
207R	1	61	16	236	Aphyric diabase	NC, unoriented piece finer than lower piece.	End of Unit 236.
208R	1	30	6	237	Moderately COP phyric diabase	Unoriented piece intruded by a fine-grained dike of undefined unit. This is not unit boundary.	Not unit boundary.
208R	1	32	7	237	Moderately COP phyric diabase	Unoriented piece intruded by a fine-grained dike of undefined unit which probably is the same as seen in Piece 6. This is not unit boundary.	Not unit boundary.
208R	1	35	8	237	Moderately COP phyric diabase	NC, unoriented aphyric fine-grained piece.	End of Unit 237.
208R	1	49	12	238	Sparsely PCO phyric diabase	NC, unoriented piece finer than lower piece.	End of Unit 238.
208R	2	11	1	239	Moderately OPC phyric diabase	NC, unoriented piece coarser than lower piece.	End of Unit 239.

APPENDIX C (continued).

Core	Section	Base of unit (cm)	Piece	Unit	Lithology	Character of lower contact	Notes
209R	1	3	1	240	Moderately OPC phyrlic diabase	NC, unoriented piece finer than lower piece. Top of Unit 240.	This piece may be upper chilled margin of Unit 240.
210R	1	3	1	240	Moderately OPC phyrlic diabase	NC, unoriented piece coarser than lower piece.	End of Unit 240.
210R	1	5	2	241	Sparsely POC phyrlic diabase	NC, unoriented piece finer than lower piece. Top of Unit 241.	This piece may be upper chilled margin of Unit 241.
213R	1	4	1	241	Sparsely POC phyrlic diabase	NC, unoriented piece coarser than lower piece.	End of Unit 241.
213R	1	32	10	242	Aphyric basalt	NC, unoriented piece finer than lower piece.	End of Unit 242.
213R	1	54	15	243	Sparsely POC phyrlic diabase	NC, oriented piece intruded by a microcrystalline dike of undefined unit.	Not unit boundary.
213R	1	149	36	243	Sparsely POC phyrlic diabase	NC, highly altered unoriented piece coarser than lower piece which may be a chilled margin of lower unit.	End of Unit 243.
216R	1	24	6	244	Moderately POC phyrlic diabase	NC, unoriented piece coarser than lower piece which has a chilled margin contact with a fractured chilled margin of a undefined unit.	End of Unit 244.
217R	1	8	1	245	Moderately COP phyrlic diabase	NC, unoriented piece more porphyritic than lower piece.	End of Unit 245.
218R	1	5	1	246	Moderately POC phyrlic diabase	NC, unoriented piece coarser than lower piece.	End of Unit 246.
219R	1	3	1	247	Aphyric basalt	NC, unoriented piece finer than lower piece.	End of Unit 247.
219R	1	7	2	248	Moderately OCP phyrlic diabase	NC, unoriented piece coarser than lower piece.	End of Unit 248.
219R	1	13	3	249	Aphyric basalt	NC, unoriented piece finer than lower piece.	End of Unit 249. Presumable chilled margin.
219R	1	17	4	250	Sparsely POC phyrlic diabase	NC, unoriented piece coarser than lower piece.	End of Unit 250.
220R	1	5	1	251	Aphyric basalt	NC, unoriented piece finer than lower piece.	End of Unit 251. Presumable chilled margin.
220R	1	31	7	252	Sparsely COP phyrlic diabase	NC, unoriented piece coarser than lower piece.	End of Unit 252.
221R	1	11	3	253	Moderately COP phyrlic diabase	NC, unoriented piece finer than lower piece.	End of Unit 253.
221R	1	23	1	254	Moderately COP phyrlic diabase	UC, oriented piece penetrated by a fine-grained dike with wavy contact suggesting that this piece was molten when intruded. Shear movement along contact.	Not unit boundary.
222R	1	94	16	254	Moderately COP phyrlic diabase	UC, unoriented piece penetrated by fingers of fine-grained dikes with wavy contact suggesting that this piece was molten when intruded.	End of Unit 254.
222R	1	114	21	255	Sparsely OCP phyrlic diabase	NC, unoriented piece finer than lower piece.	End of Unit 255.
222R	1	133	24	256	Aphyric diabase	NC, unoriented piece coarser than lower piece.	End of Unit 256.
223R	1	4	1	257	Aphyric diabase	NC, unoriented piece finer than lower piece.	End of Unit 257.
224R	1	63	14	258	Moderately CPO phyrlic diabase	NC, unoriented fine-grained piece more porphyritic than lower piece.	End of Unit 258. Lower chilled margin?
225R	1	125	32	259	Aphyric basalt	NC, unoriented piece finer than lower piece.	End of Unit 259. Lower chilled margin? Grain size is coarsest in the middle of the unit and decreases both upward and downward.
227R	2	23	3	260	Moderately COP phyrlic diabase	Unoriented piece coarser than lower piece.	End of Unit 260.
227R	2	30	5	261	Moderately OCP phyrlic diabase	Unoriented piece finer than lower piece.	End of Unit 261.
229R	1	7	2	262	Moderately OPC phyrlic diabase	Unoriented piece coarser than lower piece.	End of Unit 262.
229R	1	11	3	263	Moderately COP phyrlic diabase	Unoriented piece finer than lower piece.	End of Unit 263.
229R	1	17	5	264	Sparsely OPC phyrlic diabase	Unoriented piece coarser than lower piece.	End of Unit 264. This unit may be fallen pieces from Unit 262.
232R	1	16	3	265	Sparsely POC phyrlic diabase	Unoriented piece coarser than lower piece.	End of Unit 265.
233R	1	23	6	266	Aphyric diabase	Unoriented piece finer than lower piece.	End of Unit 266.
235R	1	17	5	267	Moderately PCO phyrlic diabase	Unoriented piece coarser than lower piece.	End of Unit 267.
235R	1	21	7	268	Sparsely PC phyrlic basalt	Unoriented piece finer than lower piece.	End of Unit 268.
				269	Moderately POC phyrlic diabase		

Az = azimuth, ol = olivine. Other abbreviations are defined in the "Petrography" section and Figure 5 of the "Explanatory Notes" chapter (this volume).

APPENDIX D
Spinel Distribution and Cr Content in leg 140 Diabase.

Thin-section sample, interval (cm)	Unit	Spinel	Cr (ppm)
Leg 137			
173R-1, 7-9	193	-	n
173R-1, 103-106	194	-	n
173R-1, 126-127	194	-	n
174R-1, 50-53	195	-	n
174R-2, 85-88	195	-	n
175R-1, 19-21	195	-	252
181M-1, 90-92	210	-	212
181M-2, 40-44	210	-	273
181M-2, 148-150	210	-	n
Leg 140			
185R-1, 15-17	211	-	339
186R-1, 13-14	211	-	n
186R-1, 17-26	211	-	n
186R-1, 53-57	213	RB	n
186R-1, 81-84	213	RB,B	369
187R-1, 5-9	214	-	173
187R-1, 24-27	215	-	n
188R-1, 21-23	217	-	170
189R-1, 13-16	218	-	229
189R-1, 105-106	218	-	n
189R-2, 11-13	218	-	n
189R-2, 39-42	218	-	n
189R-2, 83-86	218	-	330
190R-1, 75-79	218	-	n
190R-1, 95-98	218	-	n
191R-1, 48-51	218	-	n
191R-1, 60-62	218	-	406
192R-1, 1-3	218	-	262
192R-1, 13-14	218	-	n
193R-1, 7-10	219	-	245
193R-1, 28-31	220	-	402
194R-1, 5-9	220	-	345
194R-1, 115-118	220	-	255
195R-1, 7-10	221	-	n
196R-1, 0-3	221	-	164
196R-1, 39-42	222	-	280
197R-1, 99-101	222	-	n
197R-1, 133-138	223	-	n
197R-2, 33-38	223	-	n
198R-1, 21-25	223	RB	n
198R-1, 61-64	224	RB	359
198R-1, 70-71	224	-	n
199R-1, 71-76	226	RB	412

APPENDIX D (continued).

Thin-section sample, interval (cm)	Unit	Spinel	Cr (ppm)
199R-1, 106-110	227	RB	414
199R-1, 121-123	227	RB	n
200R-1, 86-88	227	RB	428
200R-1, 105-107	227	RB	n
200R-1, 128-131	227	RB	n
200R-2, 26-31	227	RB,R,Y	427
200R-2, 44-46	227	RB	n
200R-3, 13-16	227	RB	n
200R-3, 59-63	227	RB	392
200R-3, 106-108	227	RB	n
200R-3, 125-130	227	RB,R,Y	n
200R-4, 23-27	227	RB	409
201R-1, 19-23	228	-	217
202R-1, 25-29	229	RB	369
202R-1, 41-45	230	RB,R,Y	362
203R-1, 4-7	231	-	363
203R-1, 39-42	232	RB	380
203R-1, 57-59	232	-	n
204R-1, 12-14	232	RB,B	n
204R-1, 28-32	232	RB,R,Y	388
205R-1, 14-17	232	-	361
205R-1, 64-67	233	RB	n
205R-1, 87-90	235	RB	n
206R-1, 47-50	235	RB,B	445
207R-1, 0-4	236	-	253
208R-1, 0-3	237	RB	406
208R-1, 50-53	239	-	402
208R-1, 85-87	239	-	n
208R-2, 61-65	239	-	n
209R-2, 9-11	240	RB	n
209R-2, 30-33	240	RB	424
210R-1, 36-39	241	RB	361
210R-1, 73-77	241	RB,R,Y	n
211R-1, 48-51	241	RB	n
212R-1, 4-7	241	RB	373
213R-1, 32-34	243	RB	n
213R-1, 45-47	243	RB	n
213R-1, 79-83	243	-	250
213R-2, 3-6	242	-	149
214R-1, 24-28	244	-	473
214R-1, 126-129	244	RB,R,Y	334
214R-2, 29-32	244	-	384
214R-2, 100-103	244	RB,R,Y	381
215R-1, 0-4	244	B	n

Spinel types are RB = reddish brown; RY = reddish yellow; and B = black. "-" = not observed in thin section. "n" = not analyzed.

[Blank page]

APPENDIX E
Average Maximum Length and Equivalent Diameter of Groundmass Plagioclase and Magnetite in Hole 504 B.

Leg, core, section, interval (cm)	Piece	Unit	Depth (mbsf)	Pl-length (mm)	Pl-E.Q.D. (mm)	Mt-length (mm)	Mt-E.Q.D. (mm)
83-77R-2, 123-126	10	55	894.3	1.3746	0.4234	0.1095	0.1027
83-78R-2, 79-81	1M	58	904.1	1.3195	0.3590	0.0874	0.0870
83-97R-2, 26-29	3A	91	1057.9	1.1078	0.4127	0.1258	0.1183
83-118R-1, 29-33	2C	118	1196.2	1.1380	0.3959	0.2609	0.2491
83-127R-1, 50-53	6	131	1254.0	0.8578	0.2750	0.1706	0.1558
83-129R-1, 35-39	3B	133	1270.4	0.9440	0.3637	0.1545	0.1475
83-130R-2, 9-12	1A	135	1282.5	0.9608	0.3691	0.1328	0.1252
83-132-1, 96-100	13	137	1296.0	0.8587	0.2704	0.0770	0.0741
111-142R-1, 6-8	1A	151	1352.9	0.7250	0.2571	0.0873	0.0825
111-142R-2, 57-59	8A	153	1354.9	0.6554	0.2198	0.1539	0.1533
111-143R-1, 105-107	17	154	1360.4	0.6380	0.2332	0.1023	0.0986
111-145R-1, 96-98		160	1379.3	0.8729	0.3624	0.2065	0.2013
111-145R-3, 44-46	4A	160	1381.8	0.7439	0.3235	0.1806	0.1683
111-147R-1, 39-41	6B	163	1397.8	1.0182	0.4778	0.1909	0.1814
111-147R-1, 96-98	13A	163	1398.4	1.0611	0.4729	0.2049	0.1963
111-147R-2, 44-46	1F	163	1399.0	1.1151	0.4922	0.2068	0.1982
137-173R-1, 7-8	2	193	1570.1	1.2998	0.6244	0.2398	0.2129
137-173R-1, 103-106	11	194	1571.5	1.3027	0.6250	0.2398	0.2129
137-174R-1, 50-53	8	195	1576.8	1.3920	0.5773	0.2842	0.2571
137-174R-2, 85-88	14	195	1578.6	1.1180	0.4753	0.2361	0.2327
137-175R-1, 19-21	3W	195	1586.0	0.7946	0.3283	0.1080	0.0981
137-176R-1, 126-127	23	200	1596.6	0.9773	0.4302	0.2294	0.2119
137-180M-2, 35-39		205	1619.9	0.8976	0.3396	0.1595	0.1458
137-181M-1, 3-5		206	1620.4	0.8416	0.3229	0.1850	0.1836
137-181M-1, 90-92	8W	210	1621.3	0.9208	0.3501	0.2213	0.2245
137-181M-2, 45-47	4W	210	1622.3	0.7204	0.3159	0.1647	0.1535
140-185R-1, 15-17	3W	211	1624.6	0.6856	0.2615	0.1416	0.1266
140-186R-1, 13-14	4W	211	1626.7	0.7166	0.2816	0.0995	0.0891
140-186R-1, 53-57	10W	213	1627.8	1.5443	0.6456	0.2753	0.2549
140-186R-1, 81-84	13B	213	1628.6	1.6475	0.6373	0.2568	0.2557
140-189R-1, 13-16	4W	218	1651.2	1.2699	0.5344	0.1809	0.1785
140-189R-2, 11-13	3W	218	1653.5	1.2818	0.5607	0.1894	0.1892
140-189R-2, 83-86	12W	218	1654.6	1.0913	0.4715	0.1869	0.1722
140-190R-1, 75-79	17W	218	1659.1	1.2514	0.4744	0.1976	0.1901
140-190R-1, 95-98		218	1660.1	1.0974	0.4649	0.2059	0.1922
140-191R-1, 48-51	7B	218	1664.5	1.3589	0.6182	0.1789	0.1678
140-191R-1, 60-62	8W	218	1665.3	1.0681	0.4727	0.1787	0.1747
140-192R-1, 1-3	1W	218	1671.1	1.0829	0.4367	0.1813	0.1837
140-192R-1, 13-14		218	1672.2	1.1461	0.5111	0.1776	0.1704
140-193R-1, 7-10	3W	219	1675.4	1.1223	0.4556	0.1998	0.1841
140-193R-1, 28-31	9	220	1677.5	1.2838	0.5808	0.1661	0.1521
140-193R-1, 44-46	13A	220	1679.1	1.1180	0.4837	0.2128	0.2007
140-194R-1, 5-9	2W	220	1680.9	0.9550	0.4747	0.1776	0.1647
140-194R-1, 95-96		220	1687.4	1.1261	0.4809	0.2028	0.1769
140-194R-1, 115-118	22	220	1688.9	1.0185	0.3953	0.2209	0.2091
140-196R-1, 39-42	9W	222	1702.2	1.3001	0.5051	0.2083	0.1943
140-197R-1, 131-138	28W	223	1709.5	1.2412	0.4640	0.1780	0.1668
140-197R-2, 33-38		223	1711.7	1.1441	0.4496	0.1743	0.1640
140-198R-1, 21-25	6W	223	1714.2	0.8106	0.2801	0.1869	0.1851
140-198R-1, 61-64	16W	223	1717.5	0.9579	0.3474	0.1669	0.1615
140-198R-1, 70-71	18	224	1718.2	1.0872	0.3693	0.2620	0.2399
140-199R-1, 71-76	17W	226	1723.5	1.0156	0.3641	0.2083	0.1987
140-199R-1, 106-110	25A	227	1725.5	0.8004	0.2626	0.1639	0.1534
140-199R-1, 121-123	26B	227	1726.2	0.8648	0.2789	0.1806	0.1714
140-200R-1, 19-23	5	227	1729.0	0.9680	0.3787	0.2165	0.2096
140-200R-1, 86-88	4A	227	1730.2	0.8723	0.3025	0.1797	0.1583
140-200R-1, 105-107	15	227	1730.5	0.8164	0.3058	0.1425	0.1464
140-200R-2, 26-31	4A	227	1731.9	0.8488	0.3311	0.1543	0.1386
140-200R-3, 13-16	2C	227	1734.3	0.8506	0.3002	0.1443	0.1320
140-200R-3, 59-63	8B	227	1735.2	0.8262	0.2706	0.1469	0.1309
140-200R-3, 106-108	17A	227	1736.0	0.8686	0.3077	0.1456	0.1329
140-200R-3, 125-130		227	1736.4	0.8828	0.3046	0.1228	0.1210
140-200R-4, 23-27	6	227	1737.3	0.8862	0.2985	0.1325	0.1243
140-202R-1, 25-29	7	229	1747.9	0.9289	0.3332	0.1989	0.1878
140-202R-1, 41-45	11	230	1748.3	1.0817	0.3624	0.2805	0.2438

APPENDIX E (continued).

Leg, core, section interval (cm)	Piece	Unit	Depth (mbsf)	Pl-length (mm)	Pl-E.Q.D. (mm)	Mt-length (mm)	Mt-E.Q.D. (mm)
140-203R-1, 39-42	12	232	1753.8	1.8024	0.6630	0.3178	0.2697
140-203R-1, 57-59	15B	232	1755.9	1.7348	0.6247	0.2708	0.2717
140-204R-1, 12-14	3	232	1756.6	1.5849	0.6406	0.2990	0.2832
140-204R-1, 28-32	7	232	1756.8	1.5283	0.6007	0.2964	0.2613
140-205R-1, 14-17		232	1757.5	1.6429	0.5456	0.2953	0.2834
140-205R-1, 64-67	14	233	1757.7	0.8633	0.2700	0.1284	0.1215
140-205R-1, 87-90	21	235	1759.6	0.7372	0.2531	0.1251	0.1215
140-206R-1, 47-50	11	235	1760.5	0.7482	0.2660	0.0895	0.0817
140-207R-1, 0-4	1	236	1768.4	1.3485	0.5077	0.3282	0.2990
140-208R-1, 0-3	1	237	1778.0	0.6943	0.2191	0.1273	0.1186
140-208R-1, 30-33	7	237	1779.0	1.3645	0.5598	0.2590	0.2325
140-208R-1, 50-53	13	239	1779.6	0.9956	0.3659	0.2390	0.2244
140-208R-1, 85-87	19A	239	1780.7	1.0208	0.3728	0.1998	0.1896
140-208R-2, 61-65	10B	239	1784.6	1.0109	0.3703	0.1965	0.1827
140-208R-3, 7-10	1	239	1787.6	1.1281	0.4057	0.2168	0.2030
140-209R-1, 98-102	14B	240	1790.0	1.1325	0.4544	0.1665	0.1502
140-209R-2, 9-11	2	240	1791.4	0.8120	0.3219	0.1872	0.1769
140-209R-2, 30-33	4	240	1791.9	0.9164	0.3372	0.2168	0.1963
140-210R-1, 36-39	4C	241	1795.7	1.0605	0.3610	0.2083	0.1940
140-210R-1, 73-77		241	1796.4	1.1629	0.4113	0.2768	0.2585
140-211R-1, 48-51		241	1801.1	1.1035	0.4224	0.2627	0.2494
140-211R-1, 129-131	29B	241	1805.4	1.3848	0.4962	0.2912	0.2655
140-212R-1, 4-7	1B	241	1806.6	1.2717	0.4988	0.2982	0.2613
140-213R-1, 3-6	2	242	1812.7	0.5368	0.2089	0.1011	0.0967
140-213R-1, 32-34	11	243	1813.9	1.0672	0.3718	0.2257	0.2078
140-213R-1, 45-47	15	243	1814.4	1.1832	0.3969	0.2120	0.1985
140-214R-1, 24-28	5A	244	1819.0	1.3645	0.5109	0.2109	0.1953
140-214R-1, 126-129	18	244	1820.6	1.1620	0.4675	0.2294	0.2117
140-214R-1, 130-132	25	244	1820.7	1.1626	0.4850	0.2294	0.2077
140-214R-2, 29-32	7	244	1821.4	1.1803	0.4200	0.2072	0.1865
140-214R-2, 88-90	20	244	1822.3	1.1919	0.4274	0.2139	0.2042
140-214R-2, 100-103	22	244	1822.5	1.4120	0.5732	0.3060	0.2768
140-215R-1, 0-4	1	244	1823.1	1.2551	0.4436	0.2671	0.2382
140-216R-1, 58-60	13	245	1831.2	0.8068	0.2906	0.1857	0.1785
140-216R-1, 66-68	14	245	1831.6	0.8146	0.2771	0.1920	0.1687
140-217R-1, 0-2	1	245	1837.8	0.9553	0.3963	0.2050	0.1876
140-217R-1, 4-6	1	245	1839.2	0.9457	0.3748	0.1691	0.1599
140-217R-1, 23-26	6	246	1846.0	0.8462	0.3148	0.1314	0.1197
140-218R-1, 24-27	7	247	1855.6	0.9219	0.3375	0.2013	0.1822
140-220R-1, 27-30	7	252	1874.1	1.1388	0.4158	0.2479	0.2302
140-221R-1, 11-15	4	254	1877.2	1.8621	0.6713	0.2916	0.2556
140-221R-1, 40-44		254	1882.0	1.8705	0.7758	0.3367	0.3039
140-222R-1, 0-4	1	254	1884.7	1.5298	0.6008	0.2205	0.2042
140-222R-1, 17-19	1E	254	1885.9	1.7429	0.6078	0.2398	0.2228
140-222R-1, 37-39	6	254	1887.3	1.5051	0.5966	0.2673	0.2631
140-222R-1, 129-132	24	256	1897.0	1.5683	0.6412	0.2527	0.2342
140-223R-1, 20-23	6	258	1900.2	0.8433	0.3400	0.1902	0.1598
140-224R-1, 21-24	4	258	1906.8	0.6618	0.2383	0.1846	0.1769
140-224R-1, 59-62	14	258	1912.1	0.7961	0.3008	0.1587	0.1544
140-225R-1, 40-44	10	259	1913.6	0.8085	0.2845	0.1591	0.1482
140-225R-1, 59-61	14	260	1914.2	0.7105	0.2670	0.1571	0.1427
140-225R-1, 137-139	34	260	1916.8	1.0083	0.3962	0.2109	0.1935
140-225R-2, 42-44	7	260	1918.7	1.2383	0.4320	0.2671	0.2460
140-226R-1, 16-20	3	260	1920.3	1.2261	0.5694	0.1913	0.1767
140-226R-1, 61-63	12	260	1920.9	1.1252	0.4594	0.1943	0.1764
140-226R-2, 77-79	10	260	1923.4	1.5066	0.5986	0.2364	0.2208
140-227R-1, 83-85	10	260	1929.8	1.3856	0.5188	0.2449	0.2180
140-227R-2, 0-5	1	260	1933.2	1.3468	0.5525	0.2202	0.2014
140-228R-1, 55-57	13	262	1943.2	1.1226	0.3777	0.2350	0.2129
140-229R-1, 34-37	10	265	1950.7	1.1441	0.4069	0.1550	0.1514
140-233R-1, 4-7	2	266	1961.7	0.5461	0.2111	0.1706	0.1694
140-236R-1, 0-4	1	269	1980.8	1.0339	0.4528	0.2124	0.1935
140-238R-1, 22-25	8	269	2000.2	1.1122	0.4776	0.2309	0.2130

Pl = plagioclase; Mt = magnetite; E.Q.D. = equivalent area.

APPENDIX F
Alteration Log for Legs 137 and 140; ODP Core Description: ALTERATION LOG Leg 137 Hole 504B.

Core	Section	Piece	Interval (cm)		Lithology	After olivine	%	After plagioclase		After augite		After others		After groundmass		Halo	AW (cm)		Amygdules	AD (cm)		Comments
			Top	Bottom				%	%	%	%	%	%	%	%		%	%		%		
173R	1	1-13	0	139	DB	chl.py	100	---	0	---	0	---	0	ac,chl.py cpy.tt	15							Slightly to moderately altered. Amy. are rare w/dark gr act-chl cores and light gray-gr halo of ab,ac,chl,tt.
173R	1	1.2	0	12	DB	chl.py	100	---	0	---	0	---	0	ac,chl.py	15	ab,ac,tt,chl	0.3	10	ac,chl	0.5	3	
173R	1	6.7	54	64	DB	chl.py	100	---	0	---	0	---	0	ac,chl.py cpy.tt	15	ab,ac,tt,chl	0.5	20	ac,chl	0.3	10	Piece 6, 1.5-cm-wide halo + amyg at top of sample.
173R	1	9	72	79	DB	chl.py	100	---	0	---	0	---	0	ac,chl.py cpy.tt	15	ab,ac,tt,chl	0.7	30	ac,chl	0.8	15	Highly alt. due to coalescing amyg. + halo.
173R	1	12.13	116	139	DB	chl.py	100	---	0	---	0	---	0	ac,chl.py cpy.tt	15	ab,ac,tt,chl	0.4	5	ac,chl	0.5	3	Same as Pieces 1 and 2.
173R	2	1-4	0	34	DB	chl.py	100	---	0	---	0	---	0	ac,chl.py cpy.tt	15	---	0.0	0	---	0.0	0	Slightly to moderately altered. Amy. are rare w/dark gr ac-chl cores and light gray-gr halo.
173R	2	2.3	11	27	DB	chl.py	100	---	0	---	0	---	0	ac,chl.py cpy.tt	15	ab,ac,tt,chl	0.3	5	ac,chl	0.4	4	
174R	1	1-22	0	146	DB	chl.py	100	white ab-zeo	20	---	0	---	0	ac,chl.py cpy.tt	15							Slightly altered, locally highly altered due to amyg + halo. Amyg. are rare w/dark gr cores and light gray-gr halo. Dissem. py. Moderately to highly altered due to halo.
174R	1	2.3	6	19	DB	chl.py	100	white ab-zeo	20	---	0	---	0	ac,chl.py cpy.tt	15	ab,ac,tt,chl	0.0	60	ac,chl	0.0	0	
174R	1	5	32	34	DB	chl.py	100	white ab-zeo	20	---	0	---	0	ac,chl.py cpy.tt	15	ab,ac,tt,chl	0.3	5	ac,chl	0.2	2	
174R	1	7-10	43	69	DB	chl.py	100	white ab-zeo	20	---	0	---	0	ac,chl.py cpy.tt	15	ab,ac,tt,chl	0.7	20	ac,chl	0.3	5	Piece 9, moderately altered due to halo, 30-40% diffuse amygdulcs.
174R	1	13	84	87	DB	chl.py	100	white ab-zeo	20	---	0	---	0	ac,chl.py cpy.tt	15	ab,ac,tt,chl	0.3	3	ac,chl	0.0	0	Very thin halo on edge of sample.
174R	1	16-22	100	146	DB	chl.py	100	white ab-zeo	20	---	0	---	0	ac,chl.py cpy.tt	15	ab,ac,tt,chl	0.3	10	ac,chl	0.5	5	
174R	1	17-18	106	118	DB	chl.py	100	white ab-zeo	20	---	0	---	0	ac,chl.py cpy.tt	15	ab,ac,tt,chl	0.3	10	ac,chl	0.8	10	Piece 17, coalescing halo, moderately altered.
174R	2	1-16	0	100	DB	chl,tlc.py FeOx	100	white ab	10	---	0	---	0	ac,chl.py cp,tt	15							Slightly altered, locally highly altered due to amyg + halo. Amyg. are rare w/dark green cores and light gray-green halo. Dis. py.
174R	2	8.9	41	53	DB	chl,tlc.py FeOx	100	white ab	10	---	0	---	0	ac,chl.py cy,tt	15	ab,ac,tt,chl	0.2	3	act,chl	0.4	2	
174R	2	11-14	60	88	DB	chl,tlc.py FeOx	100	white ab	10	---	0	---	0	ac,chl.py cy,tt	15	ab,ac,tt,chl	0.3	15	act,chl	0.4	3	
175R	1	1-6	0	42	DB	chl,tlc.py	100	---	0	---	0	---	0	ac,chl.py cy,tt	15							Slightly altered. No amyg. Disseminated py.
176R	1	1-24	0	133	DB	chl,tlc.py ml-clay	100	white ab	10	---	0	---	0	ac,chl.py cp,tt	15							Slightly altered, locally highly altered due to amyg + halo. Amyg. are rare w/dark gr cores and light gray-gr halo. Mod to highly altered. No amyg. or halo.
176R	1	5-11	24	63	DB	chl,tlc.py ml-clay	100	white ab	10	---	0	---	0	ac,chl.py cy,tt	50	---	0.1	0	---	0.1	0	
176R	1	12	64	67	DB	chl,tlc.py ml-clay	100	white ab	10	---	0	---	0	ac,chl.py cp,tt	15	ab,ac,tt,chl	0.2	3	act,chl	0.1	0	Diffuse amygdulcs.
176R	1	14-17	73	93	DB	chl,tlc.py ml-clay	100	white ab	10	---	0	---	0	ac,chl.py cy,tt	15	ab,ac,tt,chl	0.2	5	act,chl	0.4	3	Pieces 15,16, elongate zone of coalescing halo.
176R	1	20-22	106	121	DB	chl,tlc.py ml-clay	100	white ab	10	---	0	---	0	ac,chl.py cy,tt	15	ab,ac,tt,chl	0.2	10	act,chl	0.3	3	
177R	1	1-17	0	74	DB	chl.py ml-clay	100	---	0	---	0	---	0	ac,chl.py cy,tt	15	---	0.1	0	---	0.1	0	Slightly altered. No amygdulcs. Fine-grained.
178R	1	1-4	0	25	DB	chl,ml-clay ser. ac	100	---	0	---	0	---	0	ac,chl.py cy,tt	15							
178R	1	4	20	25	DB	chl,ml-clay ser, ac	100	---	0	---	0	---	0	ac,chl.py cp,tt	15	ab,ac,tt,chl	0.2	3	act,chl	0.5	4	
180M	1	1-9	0	116	DB	chl,ac.py FeOx,tt,tlc ml-clay	100	---	0	---	0	---	0	ac,chl.py cp,tt	15							Slightly altered, locally highly altered due to amygdulcs + halo.
180M	1	6	65	66	DB	Colorless?? chl,ac.py FeOx,tt,tlc ml-clay	100	---	0	---	0	---	0	ac,chl.py cp,tt	15	ab,ac,tt,chl	0.4	10	act,chl	0.6	2	Halo 80% recrystallized.
180M	1	7-9	76	116	DB	Colorless?? chl,ac.py FeOx,tt,tlc ml-clay	100	---	0	---	0	---	0	ac,chl.py cp,tt	15	ab,ac,tt,chl	0.3	15	act,chl	0.2	2	Halo diffuse, elongate, 80% recrystallized.
180M	2	1-8	0	120	DB	Colorless?? chl.py,FeOx	100	---	0	---	0	---	0	ac,chl.py cp,tt	15							Slightly altered, locally highly altered due to amygdulcs + halo.

APPENDIX F (continued).

180M	2	1-8	0	120	DB	chl.py,FeOx cp,tt	100	---	0	---	0	---	0	ac,chl,py	15	ab,ac,tt,chl	0.3	10	act,chl	0.4	2	Highly diffuse amygdules in some samples.	
181M	1	1-12	0	141	DB	chl,ac,sm tlc	100	---	0	---	0	---	0	ac,chl,py cp,tt	15							Slightly altered, locally highly altered due to amygdules + halo.	
181M	1	5	55	62	DB	chl,ac,sm tlc	100	---	0	---	0	---	0	ac,chl,py cp,tt	15	ab,ac,tt,chl	0.2	3	act,chl	0.8	0	Very diffuse amygdules.	
181M	1	11,12	119	141	DB	chl,ac,sm tlc	100	---	0	---	0	---	0	ac,chl,py cp,tt	15	ab,ac,tt,chl	0.8	10	act,chl	0.4	2	Diffuse amygdules.	
181M	2	1-12B	0	151	DB	chl,py	100	---	0	---	0	---	0	ac,chl,py cp,tt	15							Slightly altered, locally highly altered due to amygdules + halo.	
181M	2	3-12B	0	151	DB	chl,py cp,tt	100	---	0	---	0	---	0	ac,chl,py	15	ab,ac,tt,chl	0.2	5	act,chl	0.5	2		
181M	2	7	87	97	DB	chl,py cp,tt	100	---	0	---	0	---	0	ac,chl,py	15	---	0.0	0	---	0.0	0	50% recrystallized, cut by fine-grained aphyric dark gray material, irreg. shape.	
181M	2	9A	118	123	DB	chl,py cp,tt	100	---	0	---	0	---	0	ac,chl,py	15	ab,ac,tt,chl	0.2	10	act,chl	0.5	7		
181M	2	12A,B	142	151	DB	chl,py	100	---	0	---	0	---	0	ac,chl,py	15	ab,ac,tt,chl	0.2	10	act,chl	0.8	7		
185R	1	1-4	0	22	DB	ac,ml-clay mt,cp,py	100	---	0	---	0	---	0	ac,chl,ab,tt	10							Slightly altered, locally highly altered due to amyg. (dk gr cores) + halo (lt gray gr). Dis. py.	
185R	1	1,2	0	14	DB	chl,py	100	---	0	---	0	---	0	ac,chl,ab,tt	0	ac,chl,ab,tt	0.3	5	chl,ac	0.5	2		
186R	1	1-7	0	34	DB	chl,ac,py,cp ser,mt	100	---	0	---	0	---	0	ac,chl,ab,tt	10	---	0.0	0	---	0.0	0		Piece 4, gabbro xenolith plg to ab, Pieces 4 and 5, FeOx after olivine.
186R	1	8-18	34	148	DB	chl,ac	100	ab	0	---	0	---	0	ac,chl,ab,tt	50	---	0.0	0	---	0.0	0	Coarser-grained material, Piece 14, rare pyrite aggregates after olivine.	
186R	2	1-10	0	54	DB	chl	100	---	0	---	0	---	0	ac,chl,ab,tt	50	---	0.0	0	---	0.0	0	Same as Sample 186R-1-8-18 cm, trace pyrite.	
187R	1	1,2	0	10	DB	chl	100	---	0	---	0	---	0	ac,chl,ab,tt	10	---	0.0	0	---	0.0	0		
187R	1	3	11	15	DB	---	0	---	0	---	0	---	0	ac,chl,ab,tt	40	---	0.0	0	---	0.0	0	Brecciated dike margin, locally highly altered.	
187R	1	4-10	15	46	DB	chl,ac,mt	100	---	0	---	0	---	0	ac,chl,ab,tt	60	---	0.0	0	---	0.0	0	Pieces 4-10, vein network.	
187R	1	11-13	47	58	DB	chl	100	---	0	---	0	---	0	ac,chl,ab,tt	10	---	0.0	0	---	0.0	0	Same as Pieces 1,2, but w/disseminated pyrite.	
187R	1	14	59	63	DB	chl	100	ab,py	80	---	0	---	0	ac,chl,ab,tt	80	---	0.0	0	---	0.0	0		
188R	1	1-12	0	40	DB	ac,chl,mt,py	100	---	0	---	0	---	0	ac,chl,ab,tt	10	---	0.0	0	---	0.0	0		
189R	1	1-28	0	145	DB	ser,chl,tlc ml-clay,mt py,FeOx	100	ab	1	---	0	---	0	ac,chl,ab,tt	10							Slightly alt., locally highly alt. due to halo + amygdules. Disseminated pyrite, FeOx after olivine increasing.	
189R	1	7	30	34	DB	py,FeOx,tlc ml-clay	100	ab	1	---	0	---	0	ac,chl,ab,tt	10	ac,chl,ab,tt	1.0	5	ac	0.1	1	Light gray halo with cores of actinolite.	
189R	1	13	55	58	DB	py,FeOx,tlc ml-clay	100	ab	1	---	0	---	0	ac,chl,ab,tt	10	ac,chl,ab,tt	1.0	20	ac	0.3	2		
189R	1	17	75	79	DB	py,FeOx,tlc ml-clay	100	ab	1	---	0	---	0	ac,chl,ab,tt	10	ac,chl,ab,tt	1.0	20	ac	3.0	7	Moderately to well-developed cores of actinolite coalescing.	
189R	1	18	79	83	DB	py,FeOx,tlc ml-clay	100	ab	1	---	0	---	0	ac,chl,ab,tt	10	ac,chl,ab,tt	0.5	40	ac	0.3	5	Coalescing amygdules.	
189R	1	20	89	94	DB	py,FeOx,tlc ml-clay	100	ab	1	---	0	---	0	ac,chl,ab,tt	10	ac,chl,ab,tt	0.3	10	ac	0.2	3	Centimeter-size vein w/halo.	
189R	1	21A	94	103	DB	py,FeOx,tlc ml-clay	100	ab	1	---	0	---	0	ac,chl,ab,tt	10	ac,chl,ab,tt	0.2	15	ac	0.2	2	Well-developed actinolite core.	
189R	1	24	119	123	DB	py,FeOx,tlc ml-clay	100	ab	1	---	0	---	0	ac,chl,ab,tt	10	ac,chl,ab,tt	1.0	50	ac	0.2	2	Large alteration patch of interconnected fine amygdules with coalescing fine halo.	
189R	1	26	130	136	DB	py,FeOx,tlc ml-clay	100	ab	1	---	0	---	0	ac,chl,ab,tt	10	ac,chl,ab,tt	1.0	75	ac	0.1	10		
189R	2	1-16	0	114		py,FeOx,tlc ml-clay	100	---	0	---	0	---	0	ac,chl,ab,tt	10	---	---	---	---	---	---	Same as Section 189R-1 for groundmass alteration.	
189R	2	1	0	8	DB	py,FeOx,tlc ml-clay	100	---	0	---	0	---	0	ac,chl,ab,tt	10	ac,chl,ab,tt	0.5	60	ac	0.2	15	Cores of well-developed ac w/coalescing fine halo.	
189R	2	3	11	17	DB	py,FeOx,tlc ml-clay	100	---	0	---	0	---	0	ac,chl,ab,tt	10	ac,chl,ab,tt	1.5	60	ac	0.5	7	Concentrated ac zones w/well-developed boundaries.	
189R	2	4,5abc	17	49	DB	py,FeOx,tlc ml-clay	100	---	0	---	0	---	0	ac,chl,ab,tt	10	ac,chl,ab,tt	0.7	35	---	0.0	0		
189R	2	7	54	61	DB	py,FeOx,tlc ml-clay	100	---	0	---	0	---	0	ac,chl,ab,tt	10	ac,chl,ab,tt	0.7	30	ac	0.2	2		
189R	2	10	70	78	DB	py,FeOx,tlc ml-clay	100	---	0	---	0	---	0	ac,chl,ab,tt	10	ac,chl,ab,tt	1.0	15	ac	0.4	2	Well-developed amygdules with actinolite core.	
189R	2	12	63	89	DB	py,FeOx,tlc ml-clay	100	---	0	---	0	---	0	ac,chl,ab,tt	10	ac,chl,ab,tt	0.5	5	---	0.0	0	Halo at edge of sample.	
189R	2	14	100	104	DB	py,FeOx,tlc ml-clay	100	---	0	---	0	---	0	ac,chl,ab,tt	10	ac,chl,ab,tt	0.6	50	ac	0.2	2	Several fine amygdules with actinolite cores.	
189R	2	15	104	110	DB	py,FeOx,tlc ml-clay	100	---	0	---	0	---	0	ac,chl,ab,tt	10	ac,chl,ab,tt	1.0	75	ac	0.5	25	Very well-developed ac amygdules.	
189R	2	16	110	114	DB	py,FeOx,tlc ml-clay	100	---	0	---	0	---	0	ac,chl,ab,tt	10	ac,chl,ab,tt	1.0	90	ac	0.7	5	Large well-developed amygdule.	
190R	1	1-23	0	119	DB	chl,py	100	ab,chl	1	---	0	---	0	ac,chl,ab,tt	10								
190R	1	1	0	4	DB	chl,py	100	ab,chl	1	---	0	---	0	ac,chl,ab,tt	10	ac,chl,ab,tt	0.4	60	ac	0.2	15	Coalescing amygdules.	

APPENDIX F (continued).

Core	Section	Piece	Interval (cm)		Lithology	After olivine	%	After plagioclase			After augite			After others			After groundmass			Halo	AW (cm)		Amygdules	AD (cm)		%	Comments
			Top	Bottom				%	%	%	%	%	%	%	%	%	%	%	%		%	%		%	%		
190R	1	2	5	13	DB	chl.py	100	ab.chl	1	---	0	---	0	---	0	ac.chl.ab.tt	10	ac.chl.ab.tt	0.4	50	ac	0.2	10			Coalescing amygdules.	
190R	1	3	14	18	DB	chl.py	100	ab.chl	1	---	0	---	0	---	0	ac.chl.ab.tt	10	ac.chl.ab.tt	0.5	40	---	0.0	0				
190R	1	4	23	26	DB	chl.py	100	ab.chl	1	---	0	---	0	---	0	ac.chl.ab.tt	10	ac.chl.ab.tt	0.4	20	ac	0.1	8				
190R	1	8	34	37	DB	chl.py	100	ab.chl	1	---	0	---	0	---	0	ac.chl.ab.tt	10	ac.chl.ab.tt	0.4	70	ac	0.1	2				
190R	1	9	38	41	DB	chl.py	100	ab.chl	1	---	0	---	0	---	0	ac.chl.ab.tt	10	ac.chl.ab.tt	0.4	10	---	0.0	0				
190R	1	13	54	57	DB	chl.py	100	ab.chl	1	---	0	---	0	---	0	ac.chl.ab.tt	10	ac.chl.ab.tt	1.0	90	---	0.0	0				
190R	1	14	62	66	DB	chl.py	100	ab.chl	1	---	0	---	0	---	0	ac.chl.ab.tt	10	ac.chl.ab.tt	0.3	8	---	0.0	0				
190R	1	18	82	89	DB	chl.py	100	ab.chl	1	---	0	---	0	---	0	ac.chl.ab.tt	10	ac.chl.ab.tt	1.0	70	---	0.0	0				
190R	1	19	91	101	DB	chl.py,mt,cp	100	ab.chl	1	---	0	---	0	---	0	ac.chl.ab.tt	10	ac.chl.ab.tt	1.5	70	ac	0.1	10			Large halo cut by two veins?	
190R	1	22	110	113	DB	chl.py	100	ab.chl	1	---	0	---	0	---	0	ac.chl.ab.tt	10	ac.chl.ab.tt	1.0	100	ac	0.1	1				
190R	1	23	116	119	DB	chl.py	100	ab.chl	1	---	0	---	0	---	0	ac.chl.ab.tt	10	ac.chl.ab.tt	1.0	95	ac	0.1	5				
191R	1	1-25	0	149	DB	chl.py,FeOx ml-clay,tlc	100	---	0	---	0	---	0	---	0	ac.chl.ab.tt	10										FeOx abundant, disseminated pyrite.
191R	1	1	0	4	DB	chl.py,FeOx ml-clay,tlc	100	---	0	---	0	---	0	---	0	ac.chl.ab.tt	10	ac.chl.ab.tt	0.4	90	ac	0.2	5				
191R	1	3	12	15	DB	chl.py,FeOx ml-clay,tlc	100	---	0	---	0	---	0	---	0	ac.chl.ab.tt	10	ac.chl.ab.tt	0.5	20	---	--	--				
191R	1	7A	34	45	DB	chl.py,FeOx ml-clay,tlc	100	---	0	---	0	---	0	---	0	ac.chl.ab.tt	10	ac.chl.ab.tt	0.5	10	ac	0.1	1				Trace epidote in halo.
191R	1	8	58	66	DB	chl.py,FeOx ml-clay,tlc	100	---	0	---	0	---	0	---	0	ac.chl.ab.tt	10	ac.chl.ab.tt	0.3	5	ac	0.1	1				
191R	1	11	80	84	DB	chl.py,FeOx ml-clay,tlc	100	---	0	---	0	---	0	---	0	ac.chl.ab.tt	10	ac.chl.ab.tt	0.4	40	ac	0.1	2				
191R	1	13	90	96	DB	chl.py,FeOx ml-clay,tlc	100	---	0	---	0	---	0	---	0	ac.chl.ab.tt	10	ac.chl.ab.tt	0.5	15	---	--	--				Diffuse halo.
191R	1	14	97	104	DB	chl.py,FeOx ml-clay,tlc	100	---	0	---	0	---	0	---	0	ac.chl.ab.tt	10	ac.chl.ab.tt	0.5	50	ac	0.1	3				Coalescing amygdules.
191R	1	16	108	113	DB	chl.py,FeOx ml-clay,tlc	100	---	0	---	0	---	0	---	0	ac.chl.ab.tt	10	ac.chl.ab.tt	0.2	3	ac	0.1	1				
191R	1	21	129	132	DB	chl.py,FeOx ml-clay,tlc	100	---	0	---	0	---	0	---	0	ac.chl.ab.tt	10	ac.chl.ab.tt	0.3	70	ac	0.1	10				
191R	1	23	135	139	DB	chl.py,FeOx ml-clay,tlc	100	---	0	---	0	---	0	---	0	ac.chl.ab.tt	10	ac.chl.ab.tt	0.3	10	ac	0.1	1				
191R	1	24	140	144	DB	chl.py,FeOx ml-clay,tlc	100	---	0	---	0	---	0	---	0	ac.chl.ab.tt	10	ac.chl.ab.tt	0.3	15	ac	0.1	2				
191R	1	25	145	149	DB	chl.py,FeOx ml-clay,tlc	100	---	0	---	0	---	0	---	0	ac.chl.ab.tt	10	ac.chl.ab.tt	0.6	50	ac	0.1	1				
192R	1	1-10	0	37	DB	chl.py,FeOx ml-clay mt,cp	100	---	0	---	0	---	0	---	0	ac.chl.ab.tt	10	---	0.0	0	---	0.0	0				No amygdules and no halo.
193R	1	1-14	0	64	DB	chl.py,FeOx ml-clay,tlc	100	---	0	---	0	---	0	---	0	ac.chl.ab.tt	10									Slightly altered, locally highly altered due to amygdules + halo, more green in color.	
193R	1	5,6	14	21	DB	chl.py,FeOx ml-clay,tlc	100	---	0	---	0	---	0	---	0	ac.chl.ab.tt	10	ac.chl.ab.tt	0.2	3	---	0.0	0				
193R	1	7	22	25	DB	chl.py,FeOx ml-clay,tlc	100	---	0	---	0	---	0	---	0	ac.chl.ab.tt	10	ac.chl.ab.tt	1.0	95	---	0.0	0				
193R	1	9	29	32	DB	chl.py,FeOx ml-clay,tlc	100	---	0	---	0	---	0	---	0	ac.chl.ab.tt	10	ac.chl.ab.tt	1.2	90	---	0.0	0				
193R	1	11	36	41	DB	chl.py,FeOx ml-clay,tlc	100	---	0	---	0	---	0	---	0	ac.chl.ab.tt	10	ac.chl.ab.tt	0.5	30	---	0.0	0				
193R	1	13, 14	45	64	DB	chl.py,FeOx ml-clay,tlc	100	---	0	---	0	---	0	---	0	ac.chl.ab.tt	10	ac.chl.ab.tt	0.6	60	ac	0.5	15				Coarse ac amyg. exhibit smooth boundaries cut by fine white + ac veinlets, coalescing amygdules, zones?
194R	1	1-23	0	123	DB	chl.py,FeOx ml-clay,tlc cp,mt	100	---	0	---	0	---	0	---	0	ac.ab.chl.tt	10									Slightly altered, locally highly altered due to amygdules + halo, same as previous cores. Disseminated pyrite.	
194R	1	8	41	47	DB	chl.py,FeOx ml-clay,tlc	100	---	0	---	0	---	0	---	0	ac.ab.chl.tt	10	ac.chl.ab.tt	1.0	40	---	0.0	0				
194R	1	9	48	52	DB	chl.py,FeOx ml-clay,tlc	100	---	0	---	0	---	0	---	0	ac.ab.chl.tt	10	ac.chl.ab.tt	1.5	95	ac	0.2	0.5				
194R	1	10	53	57	DB	chl.py,FeOx ml-clay,tlc	100	---	0	---	0	---	0	---	0	ac.ab.chl.tt	10	ac.chl.ab.tt	0.5	10	---	0.0	0				
194R	1	11A,B	59	67	DB	chl.py,FeOx ml-clay,tlc	100	---	0	---	0	---	0	---	0	ac.ab.chl.tt	10	ac.chl.ab.tt	1.5	60	---	0.0	0				
194R	1	13	72	76	DB	chl.py,FeOx ml-clay,tlc	100	---	0	---	0	---	0	---	0	ac.ab.chl.tt	10	ac.chl.ab.tt	0.4	30	---	0.0	0				
194R	1	14	76	79	DB	chl.py,FeOx ml-clay,tlc	100	---	0	---	0	---	0	---	0	ac.ab.chl.tt	10	ac.chl.ab.tt	1.0	100	ac	0.1	3				
194R	1	15	80	82	DB	chl.py,FeOx ml-clay,tlc	100	---	0	---	0	---	0	---	0	ac.ab.chl.tt	10	ac.chl.ab.tt	0.3	80	---	0.0	0				

APPENDIX F (continued).

194R	1	16	84	87	DB	chl.py,FeOx ml-clay,tlc	100	---	0	---	0	---	0	ac,ab,chl,tt	10	ac,chl,ab,tt	1.2	80	---	0.0	0		
194R	1	18	91	102	DB	chl.py,FeOx ml-clay,tlc	100	---	0	---	0	---	0	ac,ab,chl,tt	10	ac,chl,ab,tt	1.0	80	---	0.0	0	Coalescing halo.	
195R	1	1-3	0	10	DB	chl.py,FeOx ml-clay,tlc	100	---	0	---	0	---	0	ac,ab,chl,tt	10	ac,chl,ab,tt	0.0	0	---	0.0	0	Slightly altered, disseminated pyrite. No halo, no amygdules.	
195R	1	3	7	10	DB	chl.py,FeOx ml-clay,tlc	100	---	0	---	0	---	0	ac,ab,chl,tt	10	ac,chl,ab,tt	0.0	0	---	0.0	0	Bleached dike contact, 3 cm.	
196R	1	1-19	0	45	DB	chl,FeOx.py ml-clay, ser	100	---	0	---	0	---	0	ac,chl,ab,tt	15	---	0.0	0	---	0.0	0	No halo, slightly altered.	
197R	1	1-29	0	143	DB	chl,FeOx.py ml-clay,tlc	100	---	0	---	0	---	0	ac,chl,ab,tt	15	---	---	---	---	---	---	---	Slightly altered, locally highly altered due to halo + amygdules, less py in Pieces 23-29.
197R	1	3	11	13	DB	chl,FeOx.py ml-clay,tlc	100	---	0	---	0	---	0	ac,chl,ab,tt	15	ac,chl,ab,tt	0.3	10	---	0.0	0		
197R	1	6	25	28	DB	chl,FeOx.py ml-clay,tlc	100	---	0	---	0	---	0	ac,chl,ab,tt	15	ac,chl,ab,tt	0.2	5	chl,ac	0.1	0.2		
197R	1	7	29	39	DB	chl,FeOx.py ml-clay,tlc	100	---	0	---	0	---	0	ac,chl,ab,tt	15	ac,chl,ab,tt	0.5	5	chl,ac	0.1	0.2		
197R	1	8	39	44	DB	chl,FeOx.py ml-clay,tlc	100	---	0	---	0	---	0	ac,chl,ab,tt	15	ac,chl,ab,tt	0.2	10	chl,ac	0.1	2		
197R	1	9	45	49	DB	chl,FeOx.py ml-clay,tlc	100	---	0	---	0	---	0	ac,chl,ab,tt	15	ac,chl,ab,tt	0.2	5	chl,ac	0.1	0.5		
197R	1	11	54	58	DB	chl,FeOx.py ml-clay,tlc	100	---	0	---	0	---	0	ac,chl,ab,tt	15	ac,chl,ab,tt	0.2	5	chl,ac	0.1	0.5		
197R	2	1-7	0	44	DB	chl,FeOx.py tlc,ml-clay	100	---	0	---	0	---	0	ac,chl,ab,tt	10	---	0.0	0	---	0.0	0	No halo, slightly altered.	
198R	1	1-21	0	86	DB	chl,FeOx.py ml-clay,tlc sm,ser,mt, cp	100	---	0	---	0	---	0	ac,chl,ab,tt	15	---	0.0	0	---	0.0	0	Slightly to mod. altered. Grain size fines. downward. Disseminated pyrite.	
198R	1	18-21	70	86	DB	chl,FeOx.py ml-clay,tlc sm,ser,mt, cp	100	---	0	---	0	---	0	ac,chl,ab,tt	60	---	0.0	0	---	0.0	0		
199R	1	1-31	0	109	DB	chl,FeOx.py ml-clay,tlc sm,ser,mt cp	100	---	0	---	0	---	0	ac,chl,ab,tt	15	---	0.0	0	---	0.0	0	Slightly altered, no amygdules, no halo. Dis. pyrite, Pieces 27-31 very rare FeOx after olivine.	
199R	1	1	0	4	PB																	Pillow basalt (?).	
199R	1	23-26	96	127	DB	chl,FeOx.py ml-clay,tlc	100	---	0	---	0	---	0	ac,chl,ab,tt	15	---	0.0	0	---	0.0	0	Abundant FeOx after olivine.	
199R	2	1A,B,C	0	14	DB	chl.py ml-clay,tlc	100	---	0	---	0	---	0	ac,chl,ab,tt	15	---	0.0	0	---	0.0	0	Slightly altered, no amygdules, no halo.	
200R	1	1-25	0	148	DB	chl,ac.py tlc,ml-clay sm,mt,cp	100	---	0	---	0	---	0	ac,chl,ab,tt	15	---	0.0	0	---	0.0	0	Slightly altered, no amygdules, no halo. Disseminated pyrite.	
200R	2	1-22	0	149	DB	chl,ac.py tlc,sm,ser mt,cp	100	---	0	---	0	---	0	ac,chl,ab,tt	15	---	0.0	0	---	0.0	0	Slightly altered, no amygdules, no halo. Dis. pyrite, trace FeOx after olivine.	
200R	3	1-24	0	147	DB	chl, ac, py FeOx	100	---	0	---	0	---	0	ac,chl,ab,tt	15	---	0.0	0	---	0.0	0	Slightly altered, no amygdules, no halo.	
200R	3	1-6	0	45	DB	chl, ac, py FeOx,tlc,ser	100	---	0	---	0	---	0	ac,chl,ab,tt	15	---	0.0	0	---	0.0	0		
200R	3	7-24	45	147	DB	chl, ac, py FeOx,tlc,ser sm,mt,cp	100	---	0	---	0	---	0	ac,chl,ab,tt	40	---	0.0	0	---	0.0	0	Disseminated py, 1-4 mm patches of fine- grained chl + ac replacing groundmass	
200R	4	1-13	0	45	DB	chl.py,FeOx ml-clay,tlc ser,sm,mt	100	---	0	---	0	---	0	ac,chl,ab,tt	30	---	0.0	0	---	0.0	0	Greenish mineral after olivine (ac?). 2-5 mm fine-grained extensively altered patches after groundmass (80%).	
201R	1	1-5	0	23	DB	chl.py ml-clay,tlc sm,mt,cp	100	---	0	---	0	---	0	ac,chl,ab,tt	30	---	0.0	0	---	0.0	0	Moderately altered, no amygdules, no halo.	
201R	1	2	4	9	DB	chl.py ml-clay,tlc	100	---	0	---	0	---	0	ac,chl,ab,tt	90	ac,chl,ab,tt	2.0	90	---	0.0	0	60% recrystallized.	
202R	1	1-15	0	70	DB	chl.py,cp ml-clay,tlc	100	---	0	---	0	---	0	ac,chl,ab,tt	15	---	0.0	0	---	0.0	0	Slightly altered, no amygdules, no halo. Minor FeOx after olivine. Disseminated py. Piece 1,9, fine-grained.	
203R	1	1-11	0	39	DB	ser,sm,mt chl.py,tlc?	100	---	0	---	0	---	0	ac,chl,ab,tt	15	---	0.0	0	---	0.0	0	Slightly altered, no amygdules, no halo. Disseminated pyrite.	

APPENDIX F (continued).

Core	Section	Piece	Interval (cm)		Lithology	After olivine	%	After plagioclase	%	After augite	%	After others	%	After groundmass	%	Halo	AW (cm)	%	Amygdules	AD (cm)	%	Comments	
			Top	Bottom																			
203R	1	10	32	36	DB	---	0	---	0	---	0	---	0	ac,chl,ab,tt	75	---	0.0	0	---	0.0	0	Dike margin bounding highly altered diabase. Extensively altered adjacent to margin to ac, chl.	
203R	1	12-15	39	63	DB	chl,ac	100	---	0	---	0	---	0	ac,chl,ab,tt	60	---	0.0	0	---	0.0	0	Highly altered, no amygdules, no halo. Fine coalescing mats of ac rimmed by chl and chl pods replacing groundmass. Dis. pyrite.	
204R	1	1-12	0	54	DB	chl,ac	100	---	0	---	0	---	0	ac,chl,ab,tt	60	---	0.0	0	---	0.0	0	Highly altered, no amygdules, no halo. Same as Pieces 12-15 in Section 203R-1. Pyrite aggregates.	
205R	1	1-13	0	61	DB	ac,chl,tlc py	100	---	0	---	0	---	0	ac,chl,ab,tt	60	---	0.0	0	---	0.0	0	Highly altered, rare olivine, disseminated pyrite. No amygdules, no halo. Piece 17 exhibits the same characteristics.	
205R	1	14	63	65	DB	chl,FeOx, py,tlc	100	---	0	---	0	---	0	ac,chl,ab,tt	10	---	0.0	0	---	0.0	0	Slightly altered, no amygdules, no halo. All centimeter-sized pieces. Pieces 21,23,24 exhibit same characteristics.	
205R	1	15-16	68	73	DB	---	0	---	0	---	0	---	0	ac,chl,ab,tt	20	---	0.0	0	---	0.0	0	Slightly altered, no amygdules, no halo. No olivine, all centimeter-sized pieces. Pieces 18, 20,22 exhibit same characteristics.	
206R	1	1-11	0	51	DB	ac,chl,tlc FeOx,py	100	---	0	---	0	---	0	ac,chl,ab,tt	20	ac,chl,ab,tt	0.3	5	---	0.0	0	Slightly to moderately altered with patchy alteration in Pieces 1,4,7,8, and 9. Disseminated pyrite aggregates.	
206R	1	11	44	51	DB	ac,chl,tlc FeOx,py,mt ml-clay,sm	100	---	0	---	0	---	0	ac,chl,ab,tt	20	---	0.0	0	ac	0.5	0.5		
207R	1	1-16	0	60	db	---	0	---	0	---	0	---	0	ac,chl,ab,tt	60	---	0.0	0	---	0.0	0	Highly altered, no amygdules, no halo. Disseminated pyrite.	
208R	1	1-28	0	145	DB	chl,py,FeOx tlc,ml-clay ac,ser,sm, mt,cp	100	---	0	---	0	---	0	ac,chl,ab,tt	10	---	0.0	0	---	0.0	0	Slightly altered, no amygdules, no halo. Dis. pyrite, minor FeOx after olivine.	
208R	1	5-8	22	35	DB	chl,py,FeOx tlc,ml-clay	100	---	0	---	0	---	0	ac,chl,ab,tt	80	---	0.0	0	---	0.0	0	Pervasive to patchy alteration.	
208R	2	1-22	0	148	DB	chl,py,FeOx tlc,ml-clay ac,mt,cp	100	---	0	---	0	---	0	ac,chl,ab,tt	15	ac,chl,ab,tt ep	4.0	15	---	0.0	0	Slightly altered groundmass with local intense alteration. Dis. pyrite, trace olivine, trace FeOx after olivine. Extensively altered patches (90%) up to 4-8cm in Pieces 1,2,5, 6,10,13,14,17-22. Trace epidote in highly altered zones.	
208R	3	1	0	11	DB	chl,py tlc,ml-clay	100	---	0	---	0	---	0	ac,chl,ab,tt	15	ac,chl,ab,tt, ep	1.0	80	ac	0.7	5	Slightly altered, extensively altered due to halo. Dis. pyrite, trace epidote in halo.	
209R	1	1-17	0	143	DB	ac,py,FeOx tlc,ml-clay	100	---	0	---	0	---	0	ac,chl,ab,tt	15	ac,chl,ab,tt ep	20	---	0.0	0	0	Slightly altered, highly altered locally due to halo (90% recrystallized). Up to 1 cm to 4 x 10 cm in Pieces 3,5,6-14,16. Dis. pyrite, trace epidote in halo. Slightly altered, amygdules in Pieces 15-17.	
209R	2	1-25	0	150	DB	FeOx,tlc,py ml-clay	100	---	0	---	0	---	0	ac,chl,ab,tt	15	---	---	---	---	---	---	---	
209R	2	1-11	0	74	DB	FeOx,tlc,py ml-clay,chl ser,sm,mt, cp,qtz	100	---	0	---	0	---	0	ac,chl,ab,tt	15	ac,chl,ab,tt ep	1.0	20	---	0.0	0	0	Highly altered, locally due to halo 90% recrystallized. Halo in Pieces 1-4, 11.
209R	2	15-17	85	113	DB	FeOx,tlc,py ml-clay	100	---	0	---	0	---	0	ac,chl,ab,tt	15	ac,chl,ab,tt ep	1.5	60	ac	0.2	2		
209R	2	18-24	114	146	DB	FeOx,tlc,py ml-clay	100	---	0	---	0	---	0	ac,chl,ab,tt	15	ac,chl,ab,tt ep	1.0	40	---	0.0	0	0	
210R	1	1-19	0	144	DB	FeOx,py,ac ml-clay,tlc sm,ser,mt cp,qtz	100	---	0	---	0	---	0	ac,chl,ab,tt	10	---	0.0	0	---	0.0	0	0	Slightly altered, no amygdules, no halo. Disseminated pyrite, olivine altered to ac?. Trace FeOx after olivine.
210R	2	1-7	0	32	DB	FeOx,py,ac ml-clay	100	---	0	---	0	---	0	ac,chl,ab,tt	10	---	0.0	0	---	0.0	0	0	
210R	2	1-2	0	12	DB	FeOx,py,ac ml-clay	100	---	0	---	0	---	0	ac,chl,ab,tt	10	---	0.0	0	---	0.0	0	0	Slightly altered with few alteration patches of ac? and chl. Patches 1 cm in diameter, represent 10% of interval.
211R	1	1-30	0	141	DB	chl,FeOx, tlc,ml-clay qtz,mt,cp,py	100	---	0	---	0	---	0	ac,chl,ab,tt	15	Patches	---	15	---	0.0	0	0	Slightly altered, contains bluish-green actinolite-rich patches (1 cm in diameter) in Pieces 3,4,7,13,14,20,21. Patches comprise 3% of 141 cm core. Tr. py in olivine.
212R	1	1-17	0	65	DB	chl,ac,ser py,tlc,sm mt	100	---	0	---	0	---	0	ac,chl,ab,tt	20	---	0.0	0	---	0.0	0	0	Slightly to moderately altered, rare white mineral in olivine.

APPENDIX F (continued).

213R	1	1-10	0	31	DB	chl.py, FeOx qtz	100	---	0	---	0	---	0	ac.chl.ab.tt	30	---	0.0	0	---	0.0	0	Slightly to moderately altered.
213R	1	11-26	31	113	FG	chl.py, FeOx ac.cp	100	---	0	---	0	---	0	ac.chl.ab.tt	30	---	0.0	0	---	0.0	0	Slightly to moderately altered.
213R	1	27-36	113	149	FG	chl.tlc.ac py	100	---	0	---	0	---	0	ac.chl.ab.tt	90	---	0.0	0	---	0.0	0	Pale green xenoliths of chilled glassy margin in Pieces 28,35, and 36.
214R	1	1-13	0	111	FG	ac.chl.tlc	100	---	0	---	0	---	0	ac.chl.ab.tt ep	90	---	0.0	0	---	0.0	0	Some dark gray, less altered zones in Pieces 5 and 7. Patches of fine-grained actinolite (2-12 mm in diameter) in Pieces 5,7-9. Trace epidote.
214R	1	14-21	111	144	FG	ml-clay.cp FeOx.ac.tlc sm,mt.py qtz, ser	100	---	0	---	0	---	0	ac.chl.ab.tt ep	20	---	0.0	0	---	0.0	0	
214R	2	1-25	0	135	FG	tlc.ml-clay chl,FeOx ac.ser,mt.py cp,qtz	100	---	0	---	0	---	0	ac.chl.ab.tt	20	Patches	-	30	---	0.0	0	Less altered patches in Pieces 2,13,16,18-22. Patches, 90% altered, in Pieces 3,5-8,14, and 21-25. Patch forms 5 x 14 mm altered zone in Piece 25.
215R	1	1-21	0	89	DB	chl.ml-clay FeOx.py tlc,sm,mt qtz	100	---	0	---	0	---	0	ac.chl.ab.tt	20	---	0.0	0	---	0.0	0	Slightly to moderately altered. Patch of fine-grained actinolite (1 cm in diameter) in Pieces 4,12, and 20. Trace disseminated pyrite.
216R	1	1-6	0	24	DB	chl, py	100	---	0	---	0	---	0	ac.chl.ab.tt	15	---	0.0	0	---	0.0	0	Slightly altered, no amygdules, no halo. Tr FeOx and abundant pyrite after olivine. Disseminated pyrite.
216R	1	7,8	24	35	DB	chl, py	100	ep, ab	50	---	0	---	0	ac.chl.ab.tt	80	---	0.0	0	---	0.0	0	Highly altered. Dike margin with fragments. 0.1 cm ep-qz-rich pseudomorph occurs in fine-grained host rock.
216R	1	9-18	35	89	DB	chl.py ml-clay chl.py	100	---	0	---	0	---	0	ac.chl.ab.tt	40	---	0.0	0	---	0.0	0	Moderately altered. Coarse-grained pyrite after olivine.
217R	1	1	0	8	DB	chl.py cp,qtz	100	ep, ab	50	---	0	---	0	ac.chl.ab.tt ep	50	---	0.0	0	chl	0.1	5	Highly altered. Abundant epidote and quartz? in groundmass. Abundant py after olivine.
217R	1	2-6	8	26	DB	chl.py,qtz ml-clay,mt	100	---	0	---	0	---	0	ac.chl.ab.tt	15	---	0.0	0	---	0.0	0	Slightly altered, no amygdules, no halo. Disseminated pyrite.
218R	1	1	0	5	DB	chl, py, tlc ml-clay	100	---	0	---	0	---	0	ac.chl.ab.tt	15	---	0.0	0	---	0.0	0	Slightly altered, no amygdules, no halo.
218R	1	2-7	6	28	DB	---	0	---	0	---	0	---	0	ac.chl.ab.tt	75	---	0.0	0	---	0.0	0	Highly altered, no amygdules, no halo.
219R	1	1,3	1	13	DB	---	0	---	0	---	0	---	0	ac.chl.ab.tt	50	---	0.0	0	---	0.0	0	Moderately altered, no amygdules, no halo. Disseminated pyrite.
219R	1	2	3	7	DB	py,chl.tlc	100	---	0	---	0	---	0	ac.chl.ab.tt	15	---	0.0	0	---	0.0	0	Slightly altered, no amygdules, no halo.
219R	1	4	13	16	DB	py,chl.tlc	100	---	0	---	0	---	0	ac.chl.ab.tt	50	---	0.0	0	---	0.0	0	Moderately altered, no amygdules, no halo.
220R	1	1	0	5	DB	---	0	---	0	---	0	---	0	ac.chl.ab.tt	30	---	0.0	0	---	0.0	0	Moderately altered, no amygdules, no halo.
220R	1	2-7	5	30	DB	py,chl.tlc mt,cp,qtz	100	---	0	---	0	---	0	ac.chl.ab.tt	15	---	0.0	0	---	0.0	0	Slightly altered, no amygdules, no halo.
221R	1	1-3	0	10	DB	py,chl.tlc	100	---	0	---	0	---	0	ac.chl.ab.tt	15	---	0.0	0	---	0.0	0	Slightly altered, no amygdules, no halo.
221R	1	4-15	10	66	DB	py,chl.ac	100	---	0	---	0	---	0	ac.chl.ab.tt	80	---	0.0	0	---	0.0	0	Very highly altered, no amygdules, no halo. Blue green actinolite.
222R	1	1-16	0	93	DB	ac.tlc-cores chl-rims py,cp	100	---	0	---	0	---	0	ac.chl.ab.tt	70	---	0.0	0	---	0.0	0	Highly altered, no amygdules, no halo. Ac-chl mats. FeOx after olivine in chilled margin (Piece 1).
222R	1	17-21	94	113	DB	chl, py	100	---	0	---	0	---	0	ac.chl.ab.tt	60	---	0.0	0	---	0.0	0	Highly altered, no amygdules, no halo.
222R	1	22-24	114	132	DB	ac+tlc cores chl rim	100	---	0	---	0	---	0	ac.chl.ab.tt	70	---	0.0	0	---	0.0	0	Highly altered, no amygdules, no halo. Epidote in Piece 22. Edge of sample intergranular chlorite, and actinolite.
223R	1	1	0	4	DB	chl, py	100	---	0	---	0	---	0	ac.chl.ab.tt	50	---	0.0	0	---	0.0	0	Highly altered, no amygdules, no halo.
223R	1	2-10	4	39	DB	chl.py,tlc ml-clay	100	---	0	---	0	---	0	ac.chl.ab.tt	15	---	0.0	0	---	0.0	0	Slightly altered, no amygdules, no halo.
224R	1	1-9	0	45	DB	chl, py,mt ml-clay,cp	100	---	0	---	0	---	0	ac.chl.ab.tt	15	---	0.0	0	---	0.0	0	Slightly altered, no amygdules, no halo. Disseminated pyrite.
224R	1	10-19	45	82	DB	chl, py ml-clay	100	---	0	---	0	---	0	ac.chl.ab.tt	30	---	0.0	0	---	0.0	0	Moderately altered, no amygdules, no halo. Disseminated pyrite.
225R	1	1-37	0	148	DB	tlc,chl, py ser,sm,mt FeOx	100	---	0	---	0	---	0	ac.chl.ab.tt	30	---	0.0	0	---	0.0	0	Moderately altered, no amygdules, no halo. Alteration decreasing downward from 60 to 15% at bottom. Olivine in Pieces 33,34, and 37. Ac, chl form feathery alteration.
225R	2	1-21	0	122	DB	chl, py, tlc ser,sm,mt	100	---	0	---	0	---	0	ac.chl.ab.tt	25	---	0.0	0	---	0.0	0	Moderately altered, no amygdules, no halo. Disseminated pyrite.
226R	1	1-24	0	147	DB	chl, tlc, FeOx ml-clay.py ac,ser,mt	100	---	0	---	0	---	0	ac.chl.ab.tt	20	patches	0.0	7	---	0.0	0	Slightly altered. 1-2 cm extensively altered patches in Pieces 8-11, 17, 19-21, 24.
226R	2	1-17	0	140	DB	chl, tlc, FeOx ml-clay.py mt	100	---	0	---	0	---	0	ac.chl.ab.tt	20	patches	0.0	12	---	0.0	0	Slightly altered. 1-2 cm extensively altered patches in Pieces 1-5, 7-9, 11-14, 16, 17.
226R	3	1-5	0	42	DB	chl, tlc, FeOx ml-clay	100	---	0	---	0	---	0	ac.chl.ab.tt	20	patches	0.0	10	---	0.0	0	Slightly altered. 1-2 cm extensively altered patches in Pieces 1,3.

APPENDIX F (continued).

Core	Section	Piece	Interval (cm)		Lithology	After olivine	%	After plagioclase		After augite		After others		After groundmass		Halo	AW (cm)		Amygdules		AD (cm)		Comments
			Top	Bottom				%	%	%	%	%	%	%	%		%	%	%	%	%		
227R	1	1-17	0	137	DB	chl, tlc, FeOx ml-clay sm,mt,py	100	---	0	---	0	---	0	ac,chl,ab,tt	30	patches	0.0	10	---	0.0	0	Moderately altered. More extensively altered patches in Pieces 3,4,6,8,10-12,13,15.	
227R	2	1-3	0	20	DB	chl, tlc, FeOx ml-clay,py mt	100	---	0	---	0	---	0	ac,chl,ab,tt	20	patches	0.0	60	---	0.0	0	Slightly altered. More extensively altered patches in Pieces 1,2. Epidote after plagioclase in patches.	
227R	2	4-5	23	30	DB	chl, py	100	---	0	---	0	---	0	ac,chl,ab,tt	30	---	0.0	0	---	0.0	0		
228R	1	1-17	0	76	DB	chl, tlc, FeOx ml-clay	100	---	0	---	0	---	0	ac,chl,ab,tt	20	---	0.0	0	---	0.0	0	Slightly altered, no amygdules, no halo. Trace FeOx after olivine.	
229R	1	1-5	0	17	DB	chl, py	100	---	0	---	0	---	0	ac,chl,ab,tt	10	---	0.0	0	---	0.0	0	Fresh olivine in Piece 3?	
229R	1	6-17	17	62	DB	ac	100	ab	90	---	0	---	0	ac,chl,ab,tt	90	---	0.0	0	---	0.0	0	Very highly altered, no amygdules, no halo.	
230R	1	1-4	0	18	DB	ac, chl	100	ab	90	---	0	---	0	ac,chl,ab,tt	90	---	0.0	0	---	0.0	0	Very highly altered, no amygdules, no halo.	
231R	1	1-2	0	10	DB	---	0	---	0	---	0	---	0	ac,chl,ab,tt	80	---	0.0	0	---	0.0	0	Very highly altered.	
232R	1	1	1	6	DB	chl	100	---	0	---	0	---	0	ac,chl,ab,tt	5	---	0.0	0	---	0.0	0	Very slightly altered.	
232R	1	2-3	7	17	DB	---	0	---	0	---	0	---	0	ac,chl,ab,tt	80	---	0.0	0	---	0.0	0	Very highly altered.	
233R	1	1-6	0	22	DB	---	0	---	0	---	0	---	0	ac,chl,ab,tt	60	---	0.0	0	---	0.0	0	Highly altered. amygdules, no halo.	
235R	1	1-8	0	28	DB	chl, py	100	---	0	---	0	---	0	ac,chl,ab,tt	40	Patches	0.0	2	---	0.0	0	Moderately altered. More extensively altered patches in Piece 1 (10% of sample, ~2% of core). Piece 3,7, and 8 contain minor olivine.	
236R	1	1	0	4	DB	chl, py, 100	ab,chl	50	---	0	---	0	ac,chl,ab,tt	30	---	0.0	0	---	0.0	0	Moderately altered.		
236R	1	2-14	4	83	DB	chl, py, 100	ab,chl	50	rare FeOx	---	0	---	0	ac,chl,ab,tt	50	---	0.0	ac	0.2	0	Highly altered. Fine amygdules in Pieces 4,5, 10.		
237R	1	1-7	0	23	DB	chl	100	---	0	---	0	---	0	ac,chl,ab,tt	40	Patches	0.0	1	---	0.0	0	Moderately altered. More extensively altered patches in Pieces 1,2 (1% of core).	
238R	1	1-8	0	26	DB	chl,py	100	---	0	---	0	---	0	ac,chl,ab,tt	30	---	0.0	0	---	0.0	0	Moderately altered. No amygdules, no halo.	

S, section; T, top; B, bottom; Lith, lithology; "Comments" column refers to piece number; AW, average width; AD, average diameter; DB, diabase; dis, disseminated; amy, amygdule; alt, altered; gr, green; chl, chlorite; tlc, talc; yp, pyrite; FeOx, ferric oxide; ml-clay, mixed-layer chlorite-smectite; ser, serpentine; ac, actinolite; sm, smectite; tt, titanite; cp, chalcopyrite; mt, magnetite; ep, epidote; ab, albite; qtz, quartz; zeo, zeolite; lau, laumontite; irreg, irregular, Tr, trace.

[Blank page]

APPENDIX H
Secondary Mineralogy of Thin Sections from Legs 137 and 140.

Sample	Depth (mbsf)	Core	PC	% alt	% ac	% ab	% chl	% tlc	% tlc-sm	% ml-clay	% sm	% ser	% qtz	% ep	% anh	% pr	Trace	Amygdules	Veins
173R-1, 7-8	1570.1	173	a	10	5.0	0.0	5.0	0.0	0.0	0.0	0.0	0.0	0.0	0.0	0.0	0.0			
173R-1, 103-106	1571.5	173	a	13	6.0	0.0	7.0	0.0	0.0	0.0	0.0	0.0	0.0	0.0	0.0	0.0			
173R-2, 24-28	1572.3	173	a	10	4.4	0.0	2.3	0.9	0.0	0.5	0.0	0.0	0.0	0.0	0.0	0.0			
174R-1, 50-53	1576.8	174	a	7	2.0	0.0	5.0	0.0	0.0	0.0	0.0	0.0	0.0	0.0	0.0	0.0	zeo	chl, ac	
174R-2, 85-88	1578.6	174	a	12	8.0	0.0	4.0	0.0	0.0	0.0	0.0	0.0	0.0	0.0	0.0	0.0		1. chl; 2. qtz, zeo	
175R-1, 19-21	1586.0	175	c	37	25.0	6.0	4.4	0.0	0.0	1.6	0.0	0.0	0.0	0.0	0.0	0.0			300 μm ac + tr. ep
176R-1, 74-76	1596.0	176	a	8	6.0	0.0	3.0	0.0	0.0	0.0	0.0	0.0	0.0	0.0	0.0	0.0			
176R-1, 126-127	1596.6	176	a	9	6.7	0.0	1.9	0.0	0.0	0.0	0.0	0.0	0.0	0.0	0.0	0.0			
180M-2, 35-39	1619.9	180	a	9	6.0	0.0	3.2	0.0	0.0	0.0	0.0	0.0	0.0	0.0	0.0	0.0			
181M-1, 3-5	1620.4	181	a	3	1.4	0.0	2.0	0.1	0.0	0.0	0.0	0.0	0.0	0.0	0.0	0.0			
181M-1, 90-92	1621.3	181	d	17	10.4	0.0	7.4	0.6	0.0	0.0	0.0	0.0	0.0	0.0	0.0	0.0			
181M-2, 40-44	1622.2	181	c	27	21.8	0.4	5.6	0.0	0.0	0.0	0.0	0.0	0.0	0.0	0.0	0.0			10-20 μm chl + ac
181M-2, 45-47	1622.3	181	a	37	24.4	9.8	3.2	0.0	0.0	0.0	0.0	0.0	0.0	0.0	0.0	0.0		0.1-0.8 mm: chl, ac, tt	
181M-2, 148-150	1623.3	181	d	37	28.0	0.0	9.4	0.0	0.0	0.0	0.0	0.0	0.0	0.0	0.0	0.0		2-3 mm: chl, ac	800 μm ac
185R-1, 15-17	1624.6	185	c	31	23.8	2.4	5.0	0.0	0.0	0.0	0.0	0.0	0.0	0.0	0.0	0.0		1 mm zoned: 1. chl + ac	100 μm ac + chl
185R-1, 15-17	---	---	---	---	---	---	---	---	---	---	---	---	---	---	---	---		2. qtz	
186R-1, 13-14	1626.7	186	e	22	12.6	5.6	3.8	0.0	0.0	0.0	0.0	0.0	0.0	0.0	0.0	0.0	FeOx	diabase	
186R-1, 13-14	---	---	---	---	---	---	---	---	---	---	---	---	---	---	---	---		gabbro	
186R-1, 17-26	1626.9	186	d	25	15.2	4.0	4.2	0.0	0.0	0.0	0.0	2.0	0.0	0.0	0.0	0.0		50-250 μm chl + ac	ac + chl
186R-1, 53-57	1627.8	186	c	48	35.2	7.8	5.2	0.0	0.0	0.0	0.0	0.0	0.0	0.0	0.0	0.0			1.5 mm grn amph + halo
186R-1, 53-57	---	---	---	---	---	---	---	---	---	---	---	---	---	---	---	---			
186R-1, 81-84	1628.6	186	a	50	28.8	14.0	5.4	0.0	0.0	0.0	0.0	0.0	0.0	0.0	0.0	0.0		0.6 mm interst ac + chl, tt	400 μm ac
187R-1, 5-9	1633.9	187	d	1	0.0	0.0	0.0	0.0	0.0	0.0	0.0	0.0	0.0	0.0	0.0	0.0			No ol observed.
187R-1, 11-14	1633.8	187	a	54	50.0	0.0	4.2	0.0	0.0	0.0	0.0	0.0	0.0	0.0	0.0	0.0			0.1 mm ac + chl
187R-1, 24-27	1635.7	187	a	74	49.0	13.8	9.8	0.0	0.0	0.0	0.0	0.0	0.0	0.0	0.0	0.0		dike margin breccia	50-300 μm ac +
188R-1, 21-23	1647.6	188	a	30	21.8	6.0	2.0	0.0	0.0	0.0	0.0	0.0	0.0	0.0	0.0	0.0			
189R-1, 13-16	1651.2	189	a	17	10.6	0.4	3.8	0.8	0.0	0.8	0.0	0.8	0.0	0.0	0.0	0.0		vein = interconnected vugs?	0.2-0.04 mm ac
189R-1, 96-99	1652.5	189	d	15	11.6	0.0	3.0	0.2	0.0	0.0	0.0	0.0	0.0	0.0	0.0	0.0			
189R-1, 105-106	1652.6	189	a	17	11.2	4.0	1.8	0.0	0.0	0.0	0.0	0.0	0.0	0.0	0.0	0.0			2 mm ac, 5 mm halo
189R-2, 11-13	1653.5	189	a	94	56.8	21.8	5.8	0.0	0.0	0.0	0.0	0.0	0.0	0.0	0.0	0.0	anh	1-4 mm ac + chl, 1 cm halo	
189R-2, 39-42	1653.9	189	a	16	9.2	3.6	3.2	0.0	0.0	0.0	0.0	0.0	0.0	0.0	0.0	0.0	ep, anh	0.2-2.0 mm act, 5 mm halo	
189R-2, 83-86	1654.6	189	a	26	15.0	4.2	6.8	0.0	0.0	0.4	0.0	0.0	0.0	0.0	0.0	0.0			
190R-1, 75-79	1659.1	190	d	11	8.8	0.0	2.0	0.0	0.0	0.0	0.0	0.0	0.0	0.0	0.0	0.0			(ac + chl + qtz + halo)
190R-1, 95-98	1660.1	190	a	19	10.8	4.2	4.2	0.0	0.0	0.0	0.0	0.0	0.0	0.0	0.0	0.0			
191R-1, 48-51	1664.5	191	c	23	17.0	0.4	5.6	0.0	0.0	2.4	0.0	0.0	0.0	0.0	0.0	0.0		1-2 mm ac + chl	
191R-1, 60-62	1665.3	191	a	16	8.6	7.2	5.0	0.0	0.0	0.0	0.0	0.0	0.0	0.0	0.0	0.0		1 mm ac + chl, 2 mm halo	
192R-1, 1-3	1671.1	192	a	21	11.4	5.6	3.2	0.0	0.0	1.6	0.0	0.0	0.0	0.0	0.0	0.0			
192R-1, 13-14	1672.2	192	d	25	14.4	7.8	3.2	0.0	0.0	0.0	0.0	0.0	0.0	0.0	0.0	0.0			
193R-1, 7-10	1675.4	193	c	18	12.2	1.6	4.6	0.0	0.0	0.0	0.0	0.8	0.0	0.0	0.0	0.0		0.4-1 mm ac	1. act; 2. qtz + ep + chl
193R-1, 28-31	1677.5	193	a	43	23.8	13.0	6.4	0.0	0.0	0.0	0.0	0.0	0.0	0.0	0.0	0.0		0.4-1 mm ac + chl	
193R-1, 44-46	1679.1	193	a	60	35.2	18.6	6.4	0.0	0.0	0.0	0.0	0.0	0.0	0.0	0.0	0.4	anh, pr		(0.5 mm pr, ep, chl, ac)
194R-1, 5-9	1680.9	194	c	14	9.4	0.5	3.6	0.0	0.0	5.2	0.0	0.0	0.0	0.0	0.0	0.0		"ser" = ml-clay?	
194R-1, 95-96	1687.3	194	a	67	45.8	15.4	5.8	0.0	0.0	0.0	0.0	0.0	0.0	0.0	0.0	0.0			
194R-1, 115-118	1688.9	194	d	14	13.2	0.0	1.0	0.0	0.0	0.0	0.0	0.0	0.0	0.0	0.0	0.0			
195R-1, 7-10	1695.1	195	c	5	1.4	0.6	2.6	0.0	0.0	0.0	0.0	0.0	0.0	0.0	0.0	0.0			1 mm ep + chl + pren
196R-1, 0-3	1696.8	196	a	5	0.4	1.0	3.4	0.0	0.0	0.4	0.0	0.0	0.0	0.0	0.0	0.0			
196R-1, 39-42	1702.2	196	c	22	16.2	1.8	4.4	0.0	0.0	0.0	0.0	0.0	0.0	0.0	0.0	0.0		0.05-0.1 mm grn amph	
197R-2, 33-38	1711.7	197	a	23	16.2	0.4	0.4	5.8	0.0	0.0	0.0	0.0	0.0	0.0	0.0	0.0			
197R-1, 99-101	1711.0	197	c	29	18.4	7.8	3.4	0.0	0.0	0.0	0.0	0.0	0.0	0.0	0.0	0.0			(0.08-1 mm ac, 5 mm halo)
197R-1, 99-101	---	---	---	---	---	---	---	---	---	---	---	---	---	---	---	---			
197R-1, 131-138	1709.5	197	a	18	8.6	0.8	1.6	4.2	0.0	2.0	0.0	0.4	0.0	0.0	0.0	0.0		1 mm ac + chl, 2 mm halo	
198R-1, 21-25	1714.2	198	a	21	16.0	1.2	1.6	2.2	0.0	0.4	0.0	0.0	0.0	0.0	0.0	0.0			0.1-0.3 mm ac + chl
198R-1, 21-25	---	---	---	---	---	---	---	---	---	---	---	---	---	---	---	---			2 mm halo
198R-1, 61-64	1717.5	198	d	18	14.2	0.0	1.0	3.2	0.0	0.0	0.0	0.0	0.0	0.0	0.0	0.0			
198R-1, 70-71	1718.2	198	d	61	60.4	0.0	0.8	0.0	0.0	0.0	0.0	0.0	0.0	0.0	0.0	0.0		Host rock	

APPENDIX H (continued).

Sample	Depth (mbsf)	Core	PC	% alt	% ac	% ab	% chl	% tlc	% tlc-sm	% ml-clay	% sm	% ser	% qtz	% ep	% anh	% pr	Trace	Amygdules	Veins
198R-1, 70-71	1718.2	198	d	73	9.8	32.0	31.6	0.0	0.0	0.0	0.0	0.0	0.0	0.0	0.0	0.0		6 mm halo around	0.5 mm amph + chl
199R-1, 71-76	1723.5	199	a	15	8.0	0.0	0.4	6.2	0.0	0.0	0.0	0.0	0.0	0.0	0.0	0.0			
199R-1, 106-110	1725.5	199	a	13	7.0	0.0	0.0	5.4	0.0	0.0	0.0	0.4	0.0	0.0	0.0	0.0			
199R-1, 121-123	1726.2	199	a	7	4.4	0.0	0.2	2.6	0.0	0.0	0.0	0.4	0.0	0.0	0.0	0.0			
200R-1, 86-88	1730.2	200	c	13	3.0	0.0	1.2	8.6	0.0	0.0	0.0	0.4	0.0	0.0	0.0	0.0			
200R-1, 128-131	1730.9	200	c	10	0.0	0.0	2.0	0.0	7.8	0.0	0.0	0.0	0.0	0.0	0.0	0.0			
200R-3, 106-108	1736.0	200	a	32	18.0	1.6	4.0	6.8	0.0	0.0	1.4	0.0	0.0	0.0	0.0	0.0		1-3 mm ac + chl	0.1 mm ac + chl
200R-2, 26-31	1731.9	200	c	11	3.0	0.0	2.8	0.4	4.8	0.0	0.0	0.0	0.0	0.0	0.0	0.0			
200R-2, 44-46	1732.2	200	a	10	4.8	0.0	0.6	3.4	0.0	0.0	0.0	1.0	0.0	0.0	0.0	0.0			
200R-1, 105-107	1730.5	200	a	15	7.6	0.2	1.4	5.2	0.0	0.0	0.6	0.0	0.0	0.0	0.0	0.0			(0.3 mm ac, 1 mm halo)
200R-3, 13-16	1734.3	200	a	10	6.4	0.0	0.4	3.6	0.0	0.0	0.0	0.6	0.0	0.0	0.0	0.0			
200R-3, 59-63	1735.2	200	c	16	5.4	0.0	3.6	0.0	5.6	0.0	0.0	0.0	0.0	0.0	0.0	0.0			
200R-3, 125-130	1736.4	200	a	18	7.6	0.0	0.6	9.0	0.6	0.0	0.0	0.4	0.0	0.0	0.0	0.0			
200R-4, 23-27	1737.3	200	a	21	8.2	0.8	4.4	5.6	0.0	0.0	2.0	0.2	0.0	0.0	0.0	0.0		1 mm ac + chl	
201R-1, 19-23	1729.0	201	a	19	17.6	0.8	0.6	0.0	0.0	0.0	0.0	0.0	0.0	0.0	0.0	0.0			
202R-1, 25-29	1747.9	202	a	11	9.2	0.0	0.8	1.2	0.0	0.0	0.0	0.2	0.0	0.0	0.0	0.0			
202R-1, 41-45	1748.3	202	a	16	7.2	2.0	5.6	0.0	0.0	1.2	0.0	0.0	0.0	0.0	0.0	0.0			
203R-1, 4-7	1749.6	203	a	2	1.6	0.0	0.4	0.0	0.0	0.0	0.0	0.0	0.0	0.0	0.0	0.0			
203R-1, 33-36	1753.6	203	a	66	54.6	10.0	1.6	0.0	0.0	0.0	0.0	0.0	0.0	0.0	0.0	0.0			
203R-1, 39-42	1753.8	203	a	42	34.8	6.4	1.0	0.0	0.0	0.0	0.0	0.0	0.0	0.0	0.0	0.0		50-500 µm ac ± æchl	
203R-1, 57-59	1755.9	203	a	47	33.0	13.4	0.6	0.0	0.0	0.0	0.0	0.0	0.0	0.0	0.0	0.0			0.4 mm ac, 4 mm halo
204R-1, 12-14	1756.6	204	a	68	55.2	11.6	0.8	0.0	0.0	0.0	0.0	0.0	0.0	0.0	0.0	0.0			0.20-0.08 mm ac,
204R-1, 12-14	---	---	---	---	---	---	---	---	---	---	---	---	---	---	---	---			50 µm chl
204R-1, 28-32	1756.8	204	a	37	25.4	10.6	1.4	0.0	0.0	0.0	0.0	0.0	0.0	0.0	0.0	0.0			
205R-1, 14-17	1757.5	205	a	72	47.2	24.0	0.6	0.0	0.0	0.0	1.0	0.0	0.0	0.0	0.0	0.0			0.2-0.6 mm ac (ab,chl)
205R-1, 64-67	1757.7	205	a	12	8.0	0.4	0.4	3.0	0.2	0.0	0.2	0.0	0.0	0.0	0.0	0.0			50 µm ac + chl
205R-1, 87-90	1759.6	205	a	8	3.0	0.0	0.4	3.8	0.0	0.0	1.0	0.0	0.0	0.0	0.0	0.0			
206R-1, 47-50	1760.5	206	a	19	13.2	0.0	3.6	1.4	0.0	0.4	0.4	0.0	0.0	0.0	0.0	0.0		0.8 mm ac + chl	
207R-1, 0-4	1768.4	207	a	21	19.0	1.6	0.0	0.0	0.0	0.0	0.0	0.0	0.0	0.0	0.0	0.0			(0.2 mm ac, 5 mm halo)
208R-1, 0-3	1778.0	208	a	9	4.2	0.0	0.4	4.0	0.0	0.0	0.0	0.4	0.0	0.0	0.0	0.0			
208R-1, 36-38	1779.1	208	a	0	0.0	0.0	0.0	0.0	0.0	0.0	0.0	0.0	0.0	0.0	0.0	0.0			
208R-1, 50-53	1778.5	208	a	9	5.4	0.0	1.2	2.2	0.0	0.0	0.0	0.0	0.0	0.0	0.0	0.0			
208R-1, 85-89	1780.7	208	a	62	48.0	4.8	8.4	0.0	0.0	0.4	0.0	0.0	0.0	0.0	0.0	0.0		1 mm ac + qtz	1-4 mm ac + py + cp
208R-2, 61-65	1778.6	208	a	19	15.2	0.8	2.6	0.4	0.0	0.2	0.0	0.0	0.0	0.0	0.0	0.0			
208R-3, 7-10	1787.6	208	a	75	60.4	8.4	6.0	0.0	0.0	0.0	0.0	0.0	0.0	0.0	0.0	0.0			
209R-1, 98-102	1790.0	---	---	---	---	---	---	---	---	---	---	---	---	---	---	---	anh, pr	halo	
209R-2, 9-11	1791.4	209	a	17	6.2	1.2	10.0	0.0	0.0	0.0	0.0	0.0	0.0	0.0	0.0	0.0			
209R-2, 30-33	1791.9	209	a	18	10.8	0.4	5.0	0.8	0.0	0.8	0.0	0.0	0.0	0.0	0.0	0.0			
210R-1, 36-39	1795.7	210	a	10	4.4	0.0	1.0	3.8	0.2	0.0	0.2	0.6	0.0	0.0	0.0	0.0			
210R-1, 73-77	1796.4	210	a	47	44.6	2.0	0.8	0.0	0.0	0.0	0.0	0.0	0.0	0.0	0.0	0.0			(0.1 mm ac)
211R-1, 48-51	1801.1	211	a	24	20.0	1.0	2.6	0.0	0.0	0.0	0.0	0.0	0.0	0.0	0.0	0.0		2 mm: 1. ac + chl, 2. qtz	0.1-0.4 mm ac + chl
211R-1, 48-51	---	---	---	---	---	---	---	---	---	---	---	---	---	---	---	---			3 mm halos
212R-1, 4-7	1806.6	212	a	18	15.6	0.4	0.8	1.2	0.0	0.0	0.0	0.0	0.0	0.0	0.0	0.0			
213R-1, 3-6	1812.7	---	---	---	---	---	---	---	---	---	---	---	---	---	---	---			
213R-1, 32-34	1813.9	213	a	41	36.8	0.6	3.6	0.0	0.0	0.0	0.0	0.0	0.0	0.0	0.0	0.0	pr, ep		
213R-1, 45-47	1814.4	---	---	---	---	---	---	---	---	---	---	---	---	---	---	---	ep		
213R-1, 79-83	1818.3	213	a	0	0.0	0.0	0.0	0.0	0.0	0.0	0.0	0.0	0.0	0.0	0.0	0.0		Unaltered.	
214R-1, 24-28	1819.0	214	a	82	70.4	10.6	1.4	0.0	0.0	0.0	0.0	0.0	0.0	0.0	0.0	0.0			
214R-1, 76-78	1819.8	214	a	79	65.0	13.8	0.0	0.0	0.0	0.0	0.0	0.0	0.6	3.3	3.8	5.4	anh, pr, lm	8.6% laumontite	
214R-1, 126-129	1820.6	214	a	9	4.6	0.4	0.0	3.8	0.0	0.0	0.0	0.4	0.0	0.0	0.0	0.0			
214R-2, 29-32	1821.4	214	a	44	38.0	4.2	1.6	0.0	0.0	0.0	0.0	0.0	0.0	0.0	0.0	0.0	anh, pr, lm	1 mm: 1. chl + ac; 2. laum	
214R-2, 88-90	1822.3	214	a	14	6.6	0.0	4.2	0.6	0.0	0.0	0.0	0.0	2.6	0.0	0.0	0.0			
214R-2, 100-103	1822.5	214	a	12	6.4	0.0	6.0	0.0	0.0	0.0	0.0	0.0	1.0	0.0	0.0	0.0	anh		
214R-2, 130-132	1822.0	214	a	74	53.8	18.2	1.6	0.0	0.0	0.0	0.0	0.0	0.0	0.0	0.2	0.0	anh, lm	0.4% laumontite	
215R-1, 0-4	1823.1	215	a	14	10.8	0.2	3.0	1.2	---	---	0.2	0.0	1.0	0.0	0.0	0.0			

APPENDIX H (continued).

Sample	Depth (mbsf)	Core	PC	% alt	% ac	% ab	% chl	% tlc	% tlc-sm	% ml-clay	% sm	% ser	% qtz	% ep	% anh	% pr	Trace	Amygdules	Veins
216R-1, 58-60	1832.7	216	a	20	8.0	4.6	2.2	0.0	0.0	2.4	0.0	0.0	0.0	2.0	0.0	0.0			(0.8 mm ac, qtz, py, ep, prehn, 1 mm ac, chl, ep, chl, ac, pr, ep, qz, anh) (4% ep, 0.5% pr)
216R-1, 66-68	1833.4	216	a	7	0.8	0.8	5.4	0.0	0.0	0.0	0.0	0.0	0.0	0.0	0.0	0.0	qtz, ep, pr		
217R-1, 0-2	1837.4	217	a	46	6.0	21.6	10.4	0.0	0.0	0.0	0.0	0.0	0.0	5.8	0.4	1.4	anh, pr, ep	1-5 mm, 1. chl, 2. ep	
217R-1, 4-6	1839.0	217	a	57	1.6	25.4	29.8	0.0	0.0	0.0	0.0	0.0	0.0	4.0	0.0	0.5	pr, ep		
217R-1, 23-26	1845.2	217	a	7	0.4	0.0	5.6	0.0	0.0	1.0	0.0	0.0	0.6	0.0	0.0	0.0			
218R-1, 24-27	1856.1	218	a	28	25.8	0.8	0.8	0.0	0.0	0.0	0.0	0.0	0.0	0.0	0.0	0.0	ep	tr ep in rock	
220R-1, 2-6	1866.3	220	a	42	22.0	14.0	5.6	0.0	0.0	0.0	0.0	0.0	0.0	0.0	0.2	0.0	anh, ep		
220R-1, 27-30	1873.7	220	a	16	6.4	3.0	6.4	0.0	0.0	0.0	0.0	0.0	0.0	0.0	0.0	0.4	pr		
221R-1, 4-7	1875.8	221	a	8	0.6	0.2	7.0	0.0	0.0	0.0	0.0	0.0	0.2	0.0	0.0	0.0			
221R-1, 11-15	1877.2	221	a	61	39.8	18.2	3.0	0.0	0.0	0.0	0.0	0.0	0.0	0.0	0.0	0.0	ep, anh		10-300 μm ac, chl, qz
221R-1, 40-44	1882.0	221	a	-	-	-	-	-	-	-	-	-	-	-	-	-	---	too fine	
222R-1, 0-4	1884.8	222	a	60	28.6	9.2	12.4	0.0	0.0	0.0	0.0	0.0	0.6	0.0	0.0	0.0			
222R-1, 17-19	1886.3	222	a	35	17.4	9.4	7.8	0.0	0.0	0.0	0.0	0.0	0.0	0.0	0.0	0.0	anh, ep		
222R-1, 37-39	1888.2	222	a	39	18.6	10.2	10.0	0.0	0.0	0.0	0.0	0.0	0.0	0.0	0.0	0.0			0.2 mm ac
222R-1, 100-104	1894.6	222	a	35	26.0	4.2	4.6	0.0	0.0	0.0	0.0	0.0	0.0	0.0	0.0	0.0	qz, ep, pr, anh		
222R-1, 129-132	1897.0	222	a	66	40.8	19.8	5.6	0.0	0.0	0.0	0.0	0.0	0.0	0.0	0.0	0.0	anh, pr, ep, qz		0.2-1.6 mm pr, ab, qtz
223R-1, 20-23	1899.8	223	a	6	2.6	1.0	2.8	0.0	0.0	0.0	0.0	0.0	0.0	0.0	0.0	0.0			
224R-1, 21-24	1906.6	224	a	4	2.2	0.6	0.8	0.0	0.0	2.0	0.0	0.0	0.0	0.0	0.0	0.0			
224R-1, 59-62	1912.0	225	a	37	37.0	0.4	0.0	0.0	0.0	0.0	0.0	0.0	0.0	0.0	0.0	0.0	ep		
225R-1, 40-44	1913.6	225	a	52	46.2	5.4	0.0	0.0	0.0	0.0	0.0	0.0	0.0	0.0	0.0	0.0			
225R-1, 59-61	1914.2	225	a	55	50.8	4.0	0.0	0.0	0.0	0.0	0.0	0.0	0.0	0.0	0.0	0.0		(0.3 mm ac)	
225R-1, 137-139	1916.9	225	a	11	6.0	0.0	0.8	4.4	0.2	0.0	0.0	0.0	0.0	0.0	0.0	0.0			
225R-2, 42-44	1913.7	225	a	12	11.0	0.0	0.2	1.0	0.0	0.0	0.0	0.0	0.0	0.0	0.0	0.0			
226R-1, 16-20	1920.3	226	a	18	15.0	0.0	1.0	1.8	0.0	0.0	0.0	0.0	0.0	0.0	0.0	0.0			
226R-1, 61-63	1920.9	226	a	28	20.2	1.2	6.8	0.0	0.0	0.0	0.0	0.0	0.0	0.0	0.0	0.0	ep		
226R-2, 77-79	1921.1	226	a	20	12.2	0.2	2.2	3.2	0.0	0.0	2.0	0.0	0.0	0.0	0.0	0.0	ser, qtz		
227R-2, 0-5	1924.7	227	a	23	12.2	0.8	8.4	0.0	0.0	0.0	0.0	0.0	1.2	0.0	0.0	0.0	anh		
227R-1, 83-85	1929.7	227	a	23	9.0	0.2	8.4	1.9	0.0	0.0	3.0	0.0	0.4	0.0	0.0	0.0			
227R-2, 14-16	1933.9	227	a	92	59.4	16.4	0.0	0.0	0.0	0.0	0.0	0.0	0.0	16.0	0.0	0.0	2-5 mm, ac, ep		
228R-1, 55-57	1935.6	228	a	21	13.2	0.0	0.8	2.6	0.0	0.0	0.0	4.0	0.0	0.0	0.0	0.0			
229R-1, 7-11	1945.5	229	a	9	1.0	2.8	2.0	2.0	0.0	0.0	0.0	0.0	0.0	0.6	0.0	0.0			
233R-1, 4-7	1961.5	233	a	59	55.4	3.2	0.0	0.0	0.0	0.0	0.0	0.0	0.0	0.0	0.0	0.0			
236R-1, 0-4	1980.8	236	a	18	13.2	0.0	2.8	0.8	0.0	0.0	1.0	0.0	0.0	0.0	0.0	0.0			
238R-1, 22-25	2000.1	238	a	13	10.4	0.0	0.0	1.0	0.0	0.0	0.0	2.0	0.0	0.0	0.0	0.0			

Modal data is from point counts of thin sections. "Trace" indicates phases present in quantities not detected by point counting. Titanite is not listed, but occurs in every thin section. "Amygdules" indicates mineral phases filling amygdules, and "Veins" indicates minerals filling veins in the thin sections. Parentheses enclosing phases in the "Amygdules" or "Veins" columns indicates that the minerals in veins or amygdules were not included in the point count data. % alt, total percent secondary phases; act, actinolite; ab, albite; chl, chlorite; tlc, talc; tlc-smect, talc-smectite; ML, mixed-layer chlorite-smectite; sm, smectite; ser, serpentine; qz, quartz; ep, epidote; anh, anhydrite; pr, prehnite, lm, laumontite. Sequences of vein and amygdale filling are given with minerals along the rim as "1" and those in the core as "2." Additional abbreviations are listed in the "Alteration and Metamorphism" section and Table 3 in the "Explanatory Notes" chapter (this volume).

[Blank page]

APPENDIX I
Olivine Alteration Products in Legs 137 and 140 Rocks.

Sample	Olivine replacement products			
173R-1, 7-8 cm	chl, ac, py			
173R-1, 103-106	(chl, tlc, Feox, py)			
173R-2, 24-28	chl, ac, cp	1. tlc, mt, (ML)	2. serp	
174R-1, 50-53	(chl, tlc, mt, py, cp)			
174R-2, 85-88	chl, mt, cp			
175R-1, 19-21	chl, ac	ML, mt, py, cp		
176R-1, 74-76	ML, mt, py, cp			
176R-1, 126-127	chl, ac, mt, py, cp			
180M-2, 35-39	1. tlc, mt, py	2. serp		
181M-1, 3-5	1. tlc, mt, py	2. serp		
181M-1, 90-92	1. tlc, mt, py	2. ML	2. serp	
181M-2, 40-44	1. chl, ac, py	2. ML, py	2. serp?	
181M-2, 45-47	chl, ac	ML, qz, mt, cp, py		
181M-2, 148-150	ML, mt, py, cp			
185R-1, 15-17	ML, mt, cp	serp, mt		
186R-1, 13-14	chl, ac, py, cp	chl, qz, Feox	chl, qz, py, mt	
186R-1, 17-26BIG	chl, ac	chl, qz, mt, py, cp		
186R-1, 53-57BIG	chl/interst			
186R-1, 81-84	chl, ac			
187R-1, 5-9	none obs			
187R-1, 11-14	chl			
187R-1, 24-27	chl, ac, mt			
188R-1, 21-23	chl, ac, mt	serp		
189R-2, 11-13	chl, ac	chl		
189R-1, 13-16	chl, qz, ML, mt, py,	ML, serp, mt, py		
	1. tlc, mt	2. chl, qz		
189R-1, 96-99	chl, mt			
	ML/talc?, mt			
189R-2, 39-42	chl, act	ML, qz, mt		
	1. chl, mt, py	2. ML		
189R-2, 83-86	1. chl, mt, py, cp	2. ML		
189R-1, 105-106	1. chl, py, cp, mt	2. ML, mt, py	3. serp	
192R-1, 75-79BIG	1. chl, mt	2. ML		
190R-1, 95-98	chl, py, mt, cp, py			
191R-1, 48-51	1. chl, mt, py, cp	2. ML		
	serp, py	serp, tlc, mt		
191R-1, 60-62	1. chl, py, mt	2. serp, ML		
192R-1, 1-3	chl, act, mt, py, cp	ML, mt, cp		
	1. chl, mt	2. ML, qz		
192R-1, 13-14	chl, ML, py			
193R-1, 7-10	1. tlc, mt, py	2. chl, py, mt	ML along fract	
		2. serp		
193R-1, 28-31	chl, py, cp			
193R-1, 44-46	chl, py			
194R-1, 5-9	ML, py, mt	1. tlc, mt	2. serp	
194R-1, 95-96	chl, act (less alt rock)			
	act (in more alt rock)			
194R-1, 115-118	chl, mt, py, Feox, qz			
195R-1, 7-10	1. ML	2. serp? (green)		
196R-1, 0-3	chl?/interst?			
196R-1, 39-42	1. chl, mt	ML		
197R-2, 33-38	1. tlc, mt, py	2. serp	3. relict olivine	
197R-1, 99-101	chl, py, mt			
197R-1, 131-138	1. tlc, mt, py, cp	2. ML	2. serp	
198R-1, 21-25	1. tlc, mt, py	2. quartz		
-----	1. chl, act	2. tlc-smect		
	1. tlc, mt	2. tlc-smect, qz		
198R-1, 61-64	1. tlc, mt, py, cp	2. tlc-smect	2. serp?	
198R-1, 70-71	ac			
199R-1, 71-76	1. tlc, mt, py	2. tlc-smect, mt	3. serp?, Feox	4. relict olivine
199R-1, 106-110	1. tlc, mt, py	2. tlc-smect	3. relict olivine	
199R-1, 121-123	1. tlc, mt, py, cp	2. relict olivine		
200R-1, 86-88	1. tlc, mt (Feox)	2. tlc-smect	2. serp, Feox	3. relict olivine
	1. tlc-smect, mt	2. serp	3. relict olivine	
200R-1, 105-107	1. tlc, mt, py, (Feox)	2. smect	2. serp, Feox	
	1. tlc-smect, mt	2. relict olivine		
200R-1, 128-131	1. tlc, mt (Feox)	2. tlc-smect	2. serp, Feox	3. relict olivine
	1. tlc-smect, mt	2. relict olivine		
200R-2, 26-31	1. tlc, mt (Feox)	2. tlc-smect	2. serp, Feox, mt	3. relict olivine
200R-2, 44-46	1. tlc, mt, py	2. tlc-smect	2. serp, Feox	3. relict olivine
200R-3, 13-16	1. tlc, mt, py	2. serp?/tlc-smect	3. relict olivine	
		Feox		
200R-3, 59-63	1. tlc, mt, py	2. serp	2. tlc-smect	3. relict olivine
200R-3, 106-108	1. tlc, mt, py, cp	2. smect		
200R-3, 125-130	1. chl	2. talc	3. ML	
	1. tlc, mt, cp	2. smect, py		
	1. tlc, mt	2. serp	2. smect	
	1. tlc, mt	2. relict olivine		

APPENDIX I (continued).

Sample	Olivine replacement products
200R-4, 23-27	1. tlc, mt
201R-1, 19-23	1. tlc, mt, py, act? chl, act, qz, mt, cp, py
202R-1, 25-29	1. ML 1. tlc, mt, cp 1. chl
202R-1, 41-45	1. chl, py, cp
203R-1, 4-7	none observed
203R-1, 33-36	act
203R-1, 39-42	chl, ac/interst
203R-1, 57-59	chl, ac/interst
204R-1, 12-14	ac/interst
204R-1, 28-32	none observed
205R-1, 14-17	ac/interst
205R-1, 64-67	1. tlc, mt, py
205R-1, 87-90	1. tlc, mt, py, (Feox) 1. tlc, mt, serp 1. serp
206R-1, 47-50	1. tlc, py, cp 1. chl, act tlc, mt, serp, py
207R-1, 0-4	ac/interst
208R-1, 0-3	1. tlc, mt, py, cp (Feox)
208R-1, 30-33	ac/interst
208R-1, 36-38	1. tlc, mt, py, serp
208R-1, 50-53	1. tlc, mt, py, cp
208R-1, 85-87	1. chl ML
208R-2, 61-65	1. chl, py, cp, mt, act
208R-3, 7-10	ac/interst
209R-2, 9-11	1. chl, py
209R-2, 30-33	1. chl, mt, cp 1. tlc, mt, cp, py
209R-1, 98-102	ac/interst
210R-1, 36-39	1. tlc, mt, cp, py
210R-1, 73-77	chl, py, mt, serp
211R-1, 48-51	1. chl, (mt) 1. tlc, mt 1. chl
211R-1, 129-131	1. tlc, mt, py
212R-1, 4-7	1. act 1. tlc, mt
213R-1, 3-6	none observed
213R-1, 32-34	chl, act, py, cp
213R-1, 45-47	chl, py, qz
213R-1, 79-83	none observed
214R-1, 24-28	act?/interst?
214R-1, 76-78	chl
214R-1, 126-129	1. tlc, mt, py, cp 1. act, ML act?/interst?
214R-2, 88-90	1. tlc, mt 1. chl, mt, cp, py 1. chl, cp, mt 1. ML
214R-2, 100-103	1. chl, mt, py chl, act, mt, py, cp chl, qz, mt, cp, py 1. chl, qz, mt
214R-2, 130-132	act
215R-1, 0-4	1. tlc, mt, py 1. chl, (mt, py) tlc, mt
216R-1, 58-60	ML, chl
216R-1, 66-68	chl
217R-1, 0-2	chl, py, cp, (qz)
217R-1, 23-26	1. ML, qz, py
218R-1, 24-27	act
219R-1, 7-11	none obs. fine gr
220R-1, 27-30	chl, mt, py, cp 1. chl, mt
220R-1, 2-6	chl, act
221R-1, 4-7	chl, qz, mt, py, cp
221R-1, 11-15	act
	2. ML 2. smect
	2. chl, ML 2. ML 2. qz, mt, py, cp, smect 2. ML
	2. smect, mt, py 2. serp, mt 2. ML 2. smect, Feox 2. serp
	2. tlc-smect, Feox 3. qz 2. ML
	2. tlc-smect, Feox
	2. tlc, mt, py, (Feox) 1. serp 2. tlc, mt, py 2. chl, qz, Feox 2. ML
	2. smect, Feox
	2. ML chl
	2. ML
	2. ML, qz 2. ML, tlc? 2. chl, qz, py
	2. smect, mt 2. serp 2. ML, qz 2. ML
	2. ML chl
	2. ML
	2. ML, qz 2. ML, tlc? 2. chl, qz, py
	3. serp 2. smect, Feox
	2. smect, mt 2. tlc-smect, Feox
	2. serp, Feox 2. serp, mt (py)
	3. relict olivine
	2. mt, py, qz, cp 2. chl 2. ML
	2. smect, Feox 2. serp, tlc 2. smect
	3. qz, mt, py 4. tlc
	2. serp, Feox, qz 2. tlc, mt, py
	2. tlc, mt, qz 2. qz, py, mt, (chl) 2. tlc, mt 2. qz, serp
	3. relict olivine
	2. ML, qz 3. rare relict olivine
	2. smect, Feox 2. chl, qz, tlc
	2. qz, tlc
	2. chl, qz, mt
	2. qz, mt

APPENDIX I (continued).

Sample	Olivine replacement products		
221R-1, 40-44	none obs. fine gr		
222R-1, 0-4	?act, chl/interst?		
222R-1, 17-19	act, chl, py		
222R-1, 37-39	chl, act, cp		
222R-1, 100-104	act, chl, qz		
222R-1, 129-132	chl, ac		
223R-1, 20-23	chl, qz, (ML)		
224R-1, 21-24	chl, py	chl, qz, mt, cp	ML, qz
224R-1, 59-62	none observed		
225R-2, 42-44	1. tlc, mt, py	2. smect 2. serp	3. relict olivine
225R-1, 40-44	none observed		
225R-1, 59-61	act		
225R-1, 137-139	tlc, mt 1. tlc, mt, py 1. tlc-smect	2. talc-smect, Feox 2. serp	3. relict olivine
226R-1, 16-20	1. tlc, mt	2. serp	3. relict olivine
226R-1, 61-63	chl, ac		
226R-2, 77-79	1. tlc, mt, py 1. tlc, mt, py 1. tlc, mt, py 1. tlc, mt, py	2. smect, Feox 2. ML, qz, Feox 2. serp, Feox 2. ML	2. chl 3. chl, (ac) 3. smect
227R-1, 83-85	1. chl, qz 1. tlc, mt, py 1. tlc, mt	2. tlc 2. chl 2. serp	
227R-2, 0-5	chl, qz, Feox		
227R-2, 14-16	act?		
228R-1, 55-57	tlc, mt, py	1. tlc, mt, py	2. serp, Feox
229R-1, 7-11	chl, qz 1. chl, qz, mt, py	ML 2. ML	
229R-1, 34-37	act		
233R-1, 4-7	none observed		
236R-1, 0-4	chl, cp, mt	1. tlc, mt, py	2. smect
238R-1, 22-25	tlc, mt 1. tlc, mt, py	2. serp	3. relict olivine

Data are from shipboard thin-section observations. For each thin section the mineral associations replacing olivine are listed. Where zonations from rim to core are present, these are numbered from "1" at the rim and increasing toward the core. More than one association or type of zonation may be present in a single thin section. Parentheses indicate phases present in trace amounts. Ac, actinolite; chl, chlorite; tlc, talc; tlc-smect, talc-smectite; ML, mixed-layer chlorite-smectite; sm, smectite; serp, serpentine; mt, magnetite; Feox, hematite; py, pyrite; cp, chalcopyrite; frags, fractures; interst, interstitial.

[Blank page]

APPENDIX J

Structural Log: Structural Data ODP Legs 137 and 140-Hole 504B Depth at Top: 1561.3 mbsf.

Core, section, piece	Oriented?	Top-bottom	Depth (mbsf)	Feature	Composition	Dir.	Angle	Dir.	Angle	Angle	Dir.	Mag. dec.	Mag. inc.	Angle	Dir.	Sense	SBA	Comments
173R-1, 2	Y	4-12	1570	Fracture		90	47	0	16	48	75						T	
173R-1, 6	Y	56-57	1570.6	Fracture		270	9											
173R-1, 12	Y	119-	1571.2	Fracture		90	2	180	15	15	173	129.6	-32.4	15	43.4		M	
173R-1, 12	Y	117-	1571.2	Fracture		90	4	180	14	15	164	129.6	-32.4	15	34.4		M	
173R-1, 13	Y	130-131	1571.3	Fracture		270	12	180	6	13	244							
173R-2, 3	Y	21-	1571.6	Fracture		270	2	180	7	7	196						T	
173R-2, 3	Y	19-27	1571.6	Fracture		90	77	0	80	82	37						T	
174R-1, 3	Y	17-19	1576.5	Fracture		270	76	155	0	77	245							
174R-1, 7	Y	47-48	1576.8	Fracture		270	81	170	0	81	260							
174R-1, 8	Y	50-57	1576.8	Fracture		90	75	278	0	78	128							
174R-1, 8	Y	50-55	1576.8	Fracture		270	63	123	0	74	213						T	
174R-1, 15	Y	95-96	1577.3	Fracture		270	30	180	25	37	231							
174R-1, 17	Y	109-110	1577.4	Fracture		270	20	180	25	31	218							
174R-1, 18	Y	117-118	1577.5	Fracture		90	4	0	0	4	90							
174R-2, 7	Y	34-36	1578.1	Fracture		270	38	180	6	38	262							
174R-2, 7	Y	37-38	1578.1	Fracture		270	29	180	0	29	270							
174R-2, 8	Y	42-44	1578.2	Fracture		90	14	180	1	14	94							
174R-2, 8	Y	42-46	1578.2	Fracture		270	32	0	25	38	307							
174R-2, 14A	Y	82-83	1578.6	Fracture		90	27	0	5	27	8							
174R-2, 14B	Y	85-	1578.6	Fracture		270	6	180	7	9	221						T	
175R-1, 3A	Y	11-12	1585.9	Fracture		90	20	180	8	21	111	29.7	-41.6	21	81.3		M	
175R-1, 3A	Y	14-15	1585.9	Fracture		90	6	180	4	10	143	29.7	-41.6	10	113.3		M	
175R-1, 3B	Y	19-22	1586	Dikelet?		270	57										T	1 mm lt minerals cut by fracture
175R-1, 3B	Y	20-21	1586	Fracture		270	3	0	14	14	348	29.7	-41.6	14	318.3		TM	
175R-1, 3A	Y	20-	1586	Vein	Chl					55	0	29.7	-41.6	55	330.3		M	
175R-1, 3A	Y	17-20	1586	Vein	Chl	90	65	180	41	67	112	29.7	-41.6	67	82.3		M	
175R-1, 5	Y	34-35	1586.1	Fracture		90	5	180	1	5	101							
175R-1, 5	Y	34-35	1586.1	Fracture		270	10											
175R-1, 5	Y	35-36	1586.2	Fracture		90	1	180	1	1	135							
176R-1, 18	Y	96-97	1596.3	Fracture		90	12	0	4	13	72							
176R-1, 18	Y	95-98	1596.3	Fracture		90	49	178	0	49	85							
176R-1, 20	Y	106-111	1596.4	Fracture		90	52											
176R-1, 20	Y	106-107	1596.4	Fracture		90	16	180	22	26	145							
176R-1, 24A	Y	128-129	1596.6	Fracture		90	21	180	1	21	93							
176R-1, 24B	Y	129-	1596.6	Fracture		270	11	180	6	13	152							
180M-, 5B, 1	Y	39-44	1618.8	Vein	Chl/Ac	90	70	115	0	81	25							<1 mm cont curvilinear
180M-, 5B, 1	Y	39-40	1618.8	Vein	Chl	270	9	197	0	9	287							<1 mm cont planar
180M-, 5A, 1	Y	39-40	1618.8	Vein	Chl	90	17	180	27	29	147							<1 mm cont planar
180M-, 6A, 1	Y	59-	1619	Vein	Chl/Ac	270	10	0	39	40	347							1 mm lt green core, cont, irreg, 3-5 mm alt halo
180M-, 7, 1	Y	72-76	1619.1	Fracture		270	48	0	28	51	295							
180M-, 7, 1	Y	76-79	1619.2	Fracture		0	15	270	38	40	289							
180M-, 7, 1	Y	73-77	1619.1	Vein	Chl	90	21	180	45	47	159							
180M-, 8, 1	Y	93-95	1619.3	Fracture		270	29	180	5	29	261	294.5	42.5	29	326.5		M	
180M-, 8, 1	Y	90-92	1619.3	Fracture		270	29	150	0	33	240	294.5	42.5	33	305.5		M	
180M-, 8, 1	Y	92-96	1619.3	Vein	Chl/Ac	90	30	180	60	61	162	294.5	42.5	61	227.5		M	
180M-, 1, 2	Y	0-10	1619.6	Vein	Ac/Chl	90	45	0	15	46	75							
180M-, 1, 2	Y	0-8	1619.6	Fracture		90	65	180	0	65	90							
180M-, 3, 2	Y	29-32	1619.9	Vein	Chl	270	3	0	32	32	355	329.1	-32.4	32	25.9		M	
180M-, 4, 2	Y	48-51	1620.1	Vein	Ac	270	4	180	35	35	186							
180M-, 4, 2	Y	48-50	1620.1	Vein	Ac	90	33	295	0	57	25							
180M-, 5, 2	Y	64-67	1620.2	Fracture		90	45	150	0	49	60							
180M-, 5, 2	Y	68-70	1620.3	Vein	Chl	90	50	180	18	51	105							
180M-, 7, 2	Y	96-97	1620.5	Fracture		270	47	180	7	47	264							
180M-, 7, 2	Y	96-97	1620.5	Fracture		90	45	180	10	45	100							
181M-, 7A, 2	Y	84-90	1622.7	Vein	Chl	90	73	160	0	74	70							
181M-, 12, 2	Y	147-148	1623.3	Vein	Chl	90	5	0	29	29	9	72.2	28.1	29	296.8		TM	
181M-, 12, 2	Y	146-147	1623.3	Vein	Ac/Chl	90	8	180	3	9	110	72.2	28.1	9	37.8		M	
181M-, 12, 2	Y	144-149	1623.3	Vein	Chl	270	80	180	42	80	261	72.2	28.1	80	188.8		TM	
186R-1, 5	Y	17-26	1626.5	Fracture		348	0	90	76	76	78							Continuous, planar, smooth. Actinolite?
186R-1, 5	Y	19-20	1626.5	Vein	Chl/Ac	270	5	180	27	27	190							Continuous, curvilinear, smooth.
186R-1, 8	Y	35-37	1626.7	Vein	Chl/Ac	35	0	90	29	34	125							Continuous, sinuous, irregular.
186R-1, 8	Y	34-35	1626.6	Vein	Chl/Ac	90	2	0	5	5	22							Cont. anastomosing, weakly irreg -1 mm thick.
186R-1, 9	Y	45-48	1626.8	Vein	Chl/Ac	270	21	180	20	28	227							Continuous, planar, irregular. HSD.
186R-1, 9	Y	44-48	1626.7	Vein	Chl/Ac					78	90							Cont. planar, irreg; broken surface on bottom corner.
186R-1, 9	Y	44-48	1626.7	Vein	Chl/Ac	90	70	10	0	70	100							Continuous, planar, weakly irregular to smooth. HSD.
186R-1, 9	Y	44-48	1626.7	Vein	Ac?	90	12	0	10	15	50							Continuous, planar, irregular. HSD.
186R-1, 9	Y	44-45	1626.7	Vein	Chl/Ac	90	68	0	57	71	58							HSD.
186R-1, 9	Y	44-45	1626.7	Fracture		180	17	270	8	19	205							Continuous, planar to branching, weakly irregular.

APPENDIX J (continued).

Core, section, piece	Oriented?	Top-bottom	Depth (mbsf)	Feature	Composition	Dir.	Angle	Dir.	Angle	Angle	Dir.	Mag. dec.	Mag. inc.	Angle	Dir.	Sense	SBA	Comments
190R-1, 19	Y	94-97	1656	Vein	Ac	90	27	180	11	29	111	357.5	-27.3	29	113.5		TMP	Continuous, planar to sinuous, smooth.
190R-1, 19	Y	97-99	1656.1	Vein	Ac	90	24	0	6	25	77	357.5	-27.3	25	79.5		TMP	Cont, planar to sinuous, smooth. Cut by fracture.
190R-1, 19	Y	96-100	1656.1	Fracture		270	52	180	47	59	230	357.5	-27.3	59	232.5		TMP	Cont, planar, smooth. Cuts vein descr. above.
190R-1, 19	Y	92-93	1656	Fracture		180	25	270	4	25	189	357.5	-27.3	25	191.5		M	Continuous, sinuous, smooth.
191R-1, 2	N	8-	1661.5	Vein	Ac	90	2	0	5	5								Continuous, planar, smooth.
191R-1, 5	Y	27-28	1661.7	Fracture		90	10	0	26	27	20							Discontinuous, planar, irregular.
191R-1, 5	Y	25-29	1661.7	Vein	Chl	270	55	353	0	55	263							Cont, planar, smooth. Forms bottom corner.
191R-1, 7A	Y	34-45	1661.7	Fracture		270	83	175	0	83	265	47	-9.7	83	218		M	Cont, planar, smooth. Coated on bottom with chl?
191R-1, 7A	Y	41-	1661.8	Fracture		0	22	270	1	22	358	47	-9.7	22	311		M	Discont, planar, smooth. Truncated by above fracture.
191R-1, 7A	Y	39-40	1661.8	Fracture		180	26	270	15	29	209	47	-9.7	29	162		M	Discontinuous, planar, irregular. HSD.
191R-1, 7B	Y	49-53	1661.9	Fracture		90	53	0	0	53	90	47	-9.7	53	43		TMP	Continuous, planar, smooth. HSD.
191R-1, 7B	Y	50-51	1661.9	Fracture		270	8	0	5	9	302	47	-9.7	9	255		TMP	Continuous, planar, smooth. HSD.
191R-1, 7B	Y	47-48	1661.9	Fracture		270	11	180	12	16	222	47	-9.7	16	175		TMP	Continuous, sinuous, smooth. HSD.
191R-1, 7B	Y	45-48	1661.9	Fracture		270	85	352	0	85	262	47	-9.7	85	215		TMP	TWC. Discontinuous, planar, smooth. HSD.
191R-1, 7B	Y	45-48	1661.9	Fracture		28	0	270	77	78	298	47	-9.7	78	251		TMP	TWC. Discontinuous, planar, smooth. HSD.
191R-1, 8	Y	58-62	1662	Fracture		270	54	10	0	54	280						XT	Con, planar, smooth; chl coated?; forms top face.
191R-1, 8	Y	59-64	1662	Fracture		270	55	12	0	56	282						XT	Cont, planar, smooth; chl coated?; forms bottom face.
191R-1, 8	Y	58-60	1662	Fracture		318	0	270	59	66	228						XT	Discont, planar, smooth; chl coated?; forms outside face.
192R-1, 7	Y	23-	1671.1	Fracture		90	5	180	3	6	121							Discontinuous, curvilinear, smooth.
192R-1, 7	Y	24-26	1671.1	Fracture		90	12	180	7	14	120							Discontinuous, weakly sinuous, branching.
192R-1, 10	Y	34-36	1671.2	Vein	Ac	180	69	302	0	72	212							Continuous, planar, smooth.
192R-1, 10	Y	37-	1671.3	Fracture		90	10	180	1	10	96							Continuous, planar, smooth to weakly irregular.
193R-1, 11	Y	37-40	1674.9	Fracture		90	25	28	0	28	118							Continuous, branching planar, irregular.
193R-1, 11	Y	36-40	1674.9	Fracture		345	0	270	76	76	255							Continuous, branching curvilinear, smooth.
193R-1, 13A	Y	44-49	1674.9	Fracture		90	65	7	0	65	97	74.8	1.9	65	22.2		M	TWC; discont, planar, smooth; ends w/ complex fract.
193R-1, 13A	Y	46-	1675	Fracture		90	50	0	8	50	83	74.8	1.9	50	8.2		M	Discontinuous, planar, smooth. HSD.
193R-1, 13A	Y	50-	1675	Vein	Chl	90	25	0	2	25	86	74.8	1.9	25	11.2		M	Discont, planar, smooth; v fine; disappears in alteration.
193R-1, 13A	Y	51-	1675	Vein	Chl	90	49	0	3	49	87	74.8	1.9	49	12.2		M	Discont, planar, smooth; v fine; disappears in alteration.
193R-1, 13A	Y	57-	1675.1	Vein	Chl	90	25	180	12	27	115	74.8	1.9	27	40.2		M	Discont, planar, branch anast; fine; disappears in alt.
193R-1, 13A	Y	51-52	1675	Vein	Chl/Py	90	50	0	10	50	82	74.8	1.9	50	7.2		M	Planar, smooth. Broken lower face; separates Pieces 13A and B.
193R-1, 13B	Y	55-	1675.1	Vein		90	19	0	7	20	70	74.8	1.9	20	355.2		M	TWC. Discontinuous, planar, smooth. HSD.
194R-1, 3	Y	13-	1680.5	Fracture	Ac	90	11	180	5	12	114							Continuous, planar, smooth; cuts Px xtal but no offset.
194R-1, 3	Y	14-15	1680.5	Fracture		90	20	180	18	42	132							Continuous, planar, smooth-wk. irregular, branches.
194R-1, 3	Y	14-	1680.5	Fracture		90	29	0	4	29	87							TWC. Discont, planar, smooth.
194R-1, 3	Y	15-17	1680.6	Fracture		270	70	32	0	73	302							Discont, planar, smooth.
194R-1, 3	Y	11-17	1680.5	Fracture		90	85	358	0	85	88							Continuous, planar, smooth, forms face of core.
194R-1, 10	N	60-	1681	Vein	Ac	270	11	0	4	12								Continuous, weakly curvilinear, smooth.
194R-1, 11A	N	65-	1681.1	Vein	Ac	90	19	0	5	20								Continuous, planar, weakly irregular.
194R-1, 16	N	89-92	1681.3	Vein	Chl/Ac	90	62	58	0	74								Continuous, sinuous, smooth.
194R-1, 18	Y	92-101	1681.3	Fracture		90	85	1	0	85	91	75.6	-14.2	85	15.4		TMP	Continuous, planar to wk. curvilinear, smooth.
194R-1, 18	Y	95-96	1681.4	Fracture		90	7	180	24	25	165	75.6	-14.2	25	89.4		TMP	TWC. Continuous, sinuous, smooth.
194R-1, 19	N	108-112	1681.5	Vein	Chl/Ac	270	43	180	4	43								Continuous, branching planar, smooth.
194R-1, 19	N	110-112	1681.5	Vein	Chl/Ac	90	86	347	0	86								Discontinuous, planar, smooth.
194R-1, 23	N	125-131	1681.7	Vein	Ac	270	75	16	0	76								Continuous, planar, smooth.
194R-1, 23	N	129-	1681.7	Vein	Ac	270	11	180	7	13								Discont, planar, smooth; terminated in chl? of above.
196R-1, 3	Y	10-19	1696.6	Fracture		25	0	90	84	85	175							Continuous, planar, smooth. Forms face of core.
196R-1, 3	Y	12-	1696.6	Fracture		90	12	180	3	12	104							TWC. Discontinuous, planar, smooth.
196R-1, 3	Y	15-	1696.7	Fracture		0	4	270	6	7	304							TWC. Discontinuous, planar to slightly curvilinear.
196R-1, 6	N	29-31	1696.8	Vein	Ac	270	18	180	9	20								Cont, curvilinear, smooth; offset by vein below. HSD.
196R-1, 6	N	30-	1696.8	Vein	Ac	90	85	354	0	85								Continuous, planar, smooth. HSD.
196R-1, 6	N	29-31	1696.8	Vein	Ac	270	59	180	1	59								Continuous, sinuous to curvilinear, smooth. HSD.
197R-1, 6	Y	24-	1703	Fracture		270	11	0	6	12	298							Discontinuous, planar, weakly irregular.
197R-1, 6	Y	23-27	1703	Vein	Chl/Ac	0	65	264	0	65	354							Continuous, planar, smooth.
197R-1, 7	Y	28-32	1703.1	Vein	Ac	90	66	180	49	68	117							Cont, branching curvilinear, weak irregular. HSD.
197R-1, 7	Y	33-38	1703.1	Vein	Ac	90	79	0	45	79	79							Discontinuous, planar, smooth. HSD.
197R-1, 7	Y	30-31	1703.1	Fracture		270	21	180	15	25	235							TWC. Cont, curvilinear, smooth to weak irreg. HSD.
197R-1, 7	Y	28-38	1703.1	Vein	Chl	90	79	3	0	79	93							Cont, planar, smooth. Forms face of core. HSD.
197R-1, 7	Y	35-	1703.2	Fracture		90	4	0	9	10	24							TWC. Continuous, planar, weakly irregular. HSD.
197R-1, 11	Y	56-57	1703.4	Fracture		0	10	270	6	12	329							TWC. Cont, branching curvilinear, weakly irregular.
197R-1, 15	N	68-71	1703.5	Vein	Ac	90	84	349	0	84								Continuous, planar, smooth.
197R-1, 22	N	99-105	1703.8	Vein	Chl/Ac	270	73	26	0	73							T	Cont, planar, smooth. Ac core, chl selvages. HSD.
197R-1, 22	N	99-	1703.8	Vein	Chl/Ac	90	27	17	0	28							T	Cont, planar, smooth. Ac core, chl selvages. HSD.
197R-1, 28	Y	130-	1704.1	Fracture		270	2	180	12	12	189	16.9	-23.5	12	172.1		M	Continuous, planar, weakly irregular.
197R-1, 29	Y	138-142	1704.2	Fracture		90	25	0	20	31	52							Continuous, branching strongly curvilinear, weak irreg.
197R-2, 2	Y	9-16	1704.3	Vein	Ac	0	64	270	42	66	336							Cont, planar to sinuous, smooth. Cut by TWCs. HSD.
197R-2, 2	Y	12-14	1704.4	Vein	Chl	0	29	270	24	35	321							Discont, planar, smooth; cut by above vein and TWC.
197R-2, 2	Y	14-17	1704.4	Vein	Ac	40	0	270	32	39	310							Cont, planar, smooth. Cut by TWCs. HSD.
197R-2, 2	Y	9-	1704.3	Vein	Ac	90	6	180	27	27	168							Cont, planar, smooth; cut by TWCs; very thin. HSD.

APPENDIX J (continued).

Core, section, piece	Oriented?	Top-bottom	Depth (mbsf)	Feature	Composition	Dir.	Angle	Dir.	Angle	Dir.	Mag. dec.	Mag. inc.	Angle	Dir.	Sense	SBA	Comments
200R-3, 2A	Y	4-	1731.6	Fracture		90	8	18	0	8	108	130.4	-32.7	8	337.6	M	Continuous, planar, weakly irregular.
200R-3, 3A	Y	20-24	1731.8	Vein	Chl	270	86	349	0	86	259						Continuous, planar, smooth.
200R-3, 3A	Y	23-24	1731.8	Vein	Chl/Py	6	0	90	81	81	96						Continuous, planar, smooth. Forms face of core.
200R-3, 3A	Y	21-22	1731.8	Vein	Chl					41	14						Planar, smooth. Forms upper surface of core.
200R-3, 3A	Y	21-	1731.8	Fracture		270	4	0	1	4	284						Discontinuous, branching planar, smooth.
200R-3, 5	N	33-38	1731.9	Vein	Chl	270	84	6	0	84							Cont, planar, smooth. Also on Piece 4 (29-31 cm).
200R-3, 6	N	39-40	1732	Vein	Chl	270	9	13	0	9							Continuous, planar, smooth.
200R-3, 7	N	46-49	1732.1	Fracture		270	20	180	4	20							Discontinuous, branching sinuous, moderately smooth.
200R-3, 8B	Y	61-63	1732.2	Vein	Chl/Py	4	0	90	48	48	94						Planar, smooth. Forms lower edge of core.
200R-3, 9	N	64-67	1732.2	Vein	Chl	90	47	107	0	75							Continuous, planar, smooth to strongly irregular.
200R-3, 10	Y	68-72	1732.3	Vein	Chl	270	69	25	0	71	295						Continuous, planar, smooth.
200R-3, 10	Y	71-72	1732.3	Vein	Chl	270	24	0	2	24	274						Discontinuous, planar, smooth to weakly irregular.
200R-3, 10	Y	68-74	1732.3	Vein	Chl	191	0	90	64	64	101						Continuous, planar, smooth. Very fine.
200R-3, 12	N	82-83	1732.4	Vein	Chl	270	13	180	30	32							Continuous, planar, smooth.
200R-3, 12	N	80-83	1732.4	Vein	Chl	81	0	0	55	55							Continuous, planar, smooth. On archive half only.
200R-3, 13	N	85-87	1732.5	Vein	Chl	90	51	31	0	55							Continuous, branching, smooth.
200R-3, 13	N	85-86	1732.5	Vein	Chl	270	44	28	0	48							Continuous, planar, smooth.
200R-3, 14	N	89-95	1732.5	Vein	Chl	90	76	345	0	76							Continuous, planar, smooth.
200R-3, 14	N	89-90	1732.5	Vein	Chl	270	32	338	0	34							Weakly sinuous, weakly irregular. Forms edge of core.
200R-3, 17A+B	Y	104-114	1732.6	Vein	Chl	90	73	171	0	73	81					T	Continuous, sinuous, smooth.
200R-3, 17A+B	Y	104-115	1732.6	Vein	Chl	90	59	346	0	60	76					T	Continuous, planar to weakly sinuous, smooth.
200R-3, 17B	Y	112-115	1732.7	Vein	Chl	90	32	0	18	35	63						Discontinuous, branching planar. Fine.
200R-3, 18	N	117-	1732.8	Vein	Chl	270	28	61	0	48							Continuous, planar to curvilinear, smooth.
200R-3, 20	N	129-130	1732.9	Vein	Chl	270	18	180	14	22							Continuous, planar, smooth.
200R-3, 20	N	127-	1732.9	Fracture		90	13	0	2	13							Continuous, planar, irregular.
200R-3, 20	N	126-	1732.9	Vein	Chl	270	21	304	0	34							Continuous, planar, smooth.
200R-3, 23	N	139-140	1733	Vein	Chl	270	14	0	18	22							Continuous, planar, smooth. Best seen on archive half.
200R-3, 24	N	145-	1733.1	Fracture		0	11	270	21	23							Discontinuous, planar, smooth.
200R-4, 2	N	6-10	1733.2	Vein	Chl	90	64	3	0	64							Continuous, planar to weakly sinuous, smooth.
200R-4, 2	N	7-	1733.2	Fracture		180	2	270	3	4							Discontinuous, planar, weakly irregular.
200R-4, 3	N	11-14	1733.2	Vein	Chl	270	53	330	0	57							Continuous, branching planar, weakly irregular.
200R-4, 6	N	23-24	1733.3	Fracture		90	39	5	0	39							Discontinuous, planar, smooth.
200R-4, 12	N	48-	1733.6	Fracture		90	31	0	7	32							Discontinuous, planar, weakly irregular.
200R-4, 13	N	50-51	1733.6	Vein	Chl/Py					28							Forms planar surface of core on archive half.
201R-1, 1	N	0-3	1737.8	Vein	Chl	90	45	4	0	45							Continuous, planar, smooth. Alteration halo present.
201R-1, 5	N	19-	1738	Fracture		90	8	180	6	10							Discontinuous, planar, smooth to weakly irregular.
202R-1, 1	N	2-3	1747.2	Vein	Chl	270	20	180	4	20							Continuous, planar, smooth. HSD.
202R-1, 12	Y	50-	1747.7	Fracture		270	16	180	14	21	229						Continuous, planar to weakly sinuous, weakly irregular.
202R-1, 12	Y	45-52	1747.7	Vein	Chl/Py	90	75	3	0	75	93						Planar, smooth. Edge of core.
202R-1, 13	Y	53-62	1747.7	Vein	Chl/Ac	90	65	5	0	65	95						Continuous, planar, smooth.
202R-1, 13	Y	53-62	1747.7	Vein	Chl/Py					78	10						Edge of archive half. One patch of remnant ep and qtz.
203R-1, 15A	Y	53-54	1749.5	Vein	Chl	90	12	180	3	12	104	252.8	-4.8	12	211.2	M	Discontinuous, planar, smooth.
203R-1, 15B	Y	57-58	1749.6	Fracture		270	17	180	2	17	263	252.8	-4.8	17	10.2	TMP	Continuous, curvilinear, smooth.
203R-1, 15B	Y	58-62	1749.6	Vein	Chl	270	71	12	0	71	282	252.8	-4.8	71	29.2	TMP	Planar surface of core.
204R-1, 3	Y	12-13	1756.6	Vein	Ac	270	24	0	6	25	283	338.2	11.2	25	304.8	TM	Cont, planar, smooth. Cuts chl/ac vein below. HSD.
204R-1, 3	Y	13-	1756.6	Vein	Ac	90	8	0	4	9	64	338.2	11.2	9	85.8	TM	Cont, planar, smooth. Cut by chl/ac vein below.
204R-1, 3	Y	7-14	1756.6	Vein	Chl/Ac	270	78	354	0	78	264	338.2	11.2	78	285.8	TMP	Cont, planar, smooth. Alteration halo present. HSD.
204R-1, 6	N	26-	1756.8	Fracture		90	2	0	2	3							Discontinuous, planar, smooth.
204R-1, 10	N	40-41	1756.9	Vein	Ac	90	13	180	7	15							Continuous, planar, smooth.
204R-1, 11	N	46-47	1757	Vein	Chl/Ac	270	60	0	27	61							Continuous, planar, smooth. HSD.
204R-1, 11	N	44-49	1756.9	Vein	Chl/Ac	90	33	338	0	35							Continuous, planar, smooth. HSD.
204R-1, 11	N	45-46	1757	Fracture		90	21	13	0	22							Discontinuous, planar, smooth. HSD.
204R-1, 12	N	51-54	1757	Vein	Chl/Ac	90	24	0	5	24							Continuous, planar, smooth.
204R-1, 12	N	51-55	1757	Vein	Chl/Ac	90	79	11	0	79							Continuous, planar, smooth.
205R-1, 1	Y	6-7	1757.1	Vein	Chl	90	14	180	3	14	102	235.9	-3.7	14	226.1	M	Continuous, planar, smooth. HSD.
205R-1, 1	Y	4-9	1757	Fracture		270	75	0	12	75	273	235.9	-3.7	75	37.1	MP	Discontinuous, curvilinear, weakly irregular. HSD.
205R-1, 1	Y	10-14	1757.1	Fracture		90	49	0	30	52	63	235.9	-3.7	52	187.1	XTM	Discontinuous, curvilinear, weakly irregular. HSD.
205R-1, 1	Y	11-15	1757.1	Vein	Ac	90	42	241	0	62	151	235.9	-3.7	62	275.1	XTM	Cont, planar, smooth to wk irreg; v. fine; halo present.
205R-1, 2	N	18-19	1757.2	Vein	Chl/Ac	90	64	7	0	64							Planar, weakly irregular. Forms face of sample.
205R-1, 3	N	21-22	1757.2	Vein	Ac	90	74	6	0	74							Planar, weakly irregular. Forms face of core.
205R-1, 4	N	25-30	1757.3	Vein	Chl/Ac	270	51	180	32	54							Continuous, planar, irregular. Very fine and diffuse.
205R-1, 4	N	25-30	1757.3	Vein	Chl/Py	316	0	180	74	79							Planar to wk curvilinear, smooth; forms surface of core.
205R-1, 14	N	64-	1757.6	Fracture		270	16	0	2	16							Continuous, planar, weakly irregular.
205R-1, 21	N	89-	1757.9	Fracture		270	12	0	50	50							Continuous, planar, irregular.
205R-1, 24	N	98-101	1758	Vein	Chl	90	62	346	0	63							Continuous, planar, smooth.
206R-1, 4C	Y	14-17	1760.8	Fracture		90	81	6	0	81	96	241.7	-9.9	81	214.3	M	Discontinuous, planar, smooth to weakly irregular.
206R-1, 4C	Y	14-17	1760.8	Fracture		90	70	359	0	70	89	241.7	-9.9	70	207.3	M	Discontinuous, planar, smooth.
206R-1, 8	N	33-34	1761	Vein	Ac	90	8	0	1	8							Continuous, planar, smooth.

APPENDIX J (continued).

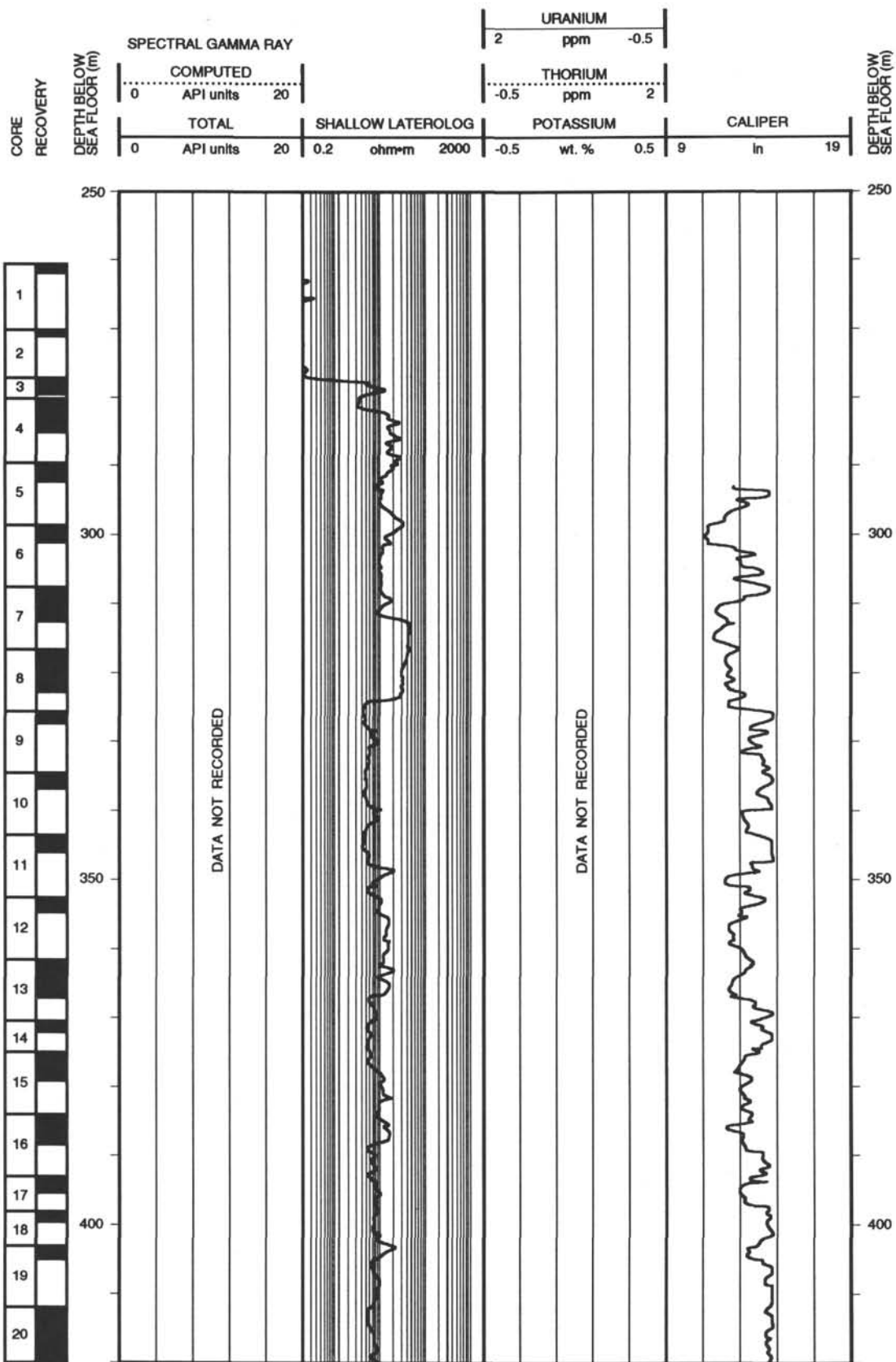
Core, section, piece	Oriented?	Top-bottom	Depth (mbsf)	Feature	Composition	Dir.	Angle	Dir.	Angle	Angle	Dir.	Mag. dec.	Mag. inc.	Angle	Dir.	Sense	SBA	Comments
211R-1, 10	N	46-	1799	Fracture		90	10	0	14	17								Discont, planar to wk sinuous, wk irregular, branching.
211R-1, 11	N	47-52	1799	Vein	Ac	270	64	8	0	64							T	Continuous, planar to weakly sinuous, smooth.
211R-1, 11	N	47-52	1799	Fracture		90	88	357	0	88							T	Continuous, planar, smooth.
211R-1, 11	N	51-	1799	Fracture		90	8	0	21	22							T	Discont, planar, wk irreg. Terminated by fracture above.
211R-1, 12	N	54-56	1799	Vein	Chl/Ac	270	40	8	0	40								Continuous, weakly sinuous, smooth.
211R-1, 12	N	56-	1799.1	Fracture		270	10	0	4	11								Discontinuous, branching planar, smooth.
211R-1, 17A	Y	76-	1799.3	Fracture		270	2	0	2	3	315							Discontinuous, branching planar, weakly irregular.
211R-1, 17C	Y	81-	1799.3	Vein	Ac	270	4	180	24	24	189							Continuous, planar, weakly irregular. Halo present.
211R-1, 17C	Y	82-	1799.3	Vein	Ac	270	3	0	2	4	304							Cont, wk curvilinear, wk anastomosing, smooth; halo.
211R-1, 19	N	89-91	1799.4	Vein	Chl	90	84	359	0	84								Cont, planar, smooth. Continues onto Piece 20?
211R-1, 27	N	118-122	1799.7	Vein	Ac	270	39	337	0	41								Continuous, planar, weakly anastomosing, smooth.
211R-1, 27	N	118-122	1799.7	Vein	Ac	270	40	334	0	43								Continuous, weakly curvilinear, smooth.
211R-1, 27	N	120-121	1799.7	Fracture		90	81	20	0	82								Discontinuous, planar, smooth.
211R-1, 29	Y	125-130	1799.8	Vein	Chl	90	87	359	0	87	89	339	4	87	110		TMP	Continuous, planar, smooth.
212R-1, 1A	Y	0-3	1806	Vein	Chl/Ac	270	33	0	22	37	302							Continuous, planar, smooth.
212R-1, 11	N	36-	1806.4	Fracture		90	23	0	1	23								Discontinuous, branching planar, smooth.
212R-1, 13	N	45-	1806.5	Fracture		0	1	270	4	4								Discontinuous, planar, smooth. Discing fracture?
212R-1, 16	N	57-	1806.6	Vein	Ac	270	13	0	11	17								Continuous, planar, smooth.
212R-1, 17	N	62-63	1806.6	Vein	Ac	90	37	342	0	38								Continuous, planar, smooth.
212R-1, 17	N	63-	1806.6	Vein	Ac	90	11	34	0	13								Continuous, planar, smooth.
212R-1, 17	N	61-65	1806.6	Vein	Chl	90	75	354	0	75								Continuous, planar, smooth. Forms face of core.
213R-1, 15	Y	46-52	1813	Contact		90	78	334	0	79	64	248.5	-13.6	79	175.5		TMP	Chilled margin. Continuous, planar, smooth. HSD.
213R-1, 15	Y	49-	1813	Fracture		270	3	180	1	3	252	248.5	-13.6	3	3.5		MP	Branching planar, confined to chilled lithology. HSD.
213R-1, 15	Y	50-	1813	Fracture		90	6	0	4	7	56	248.5	-13.6	7	167.5		MP	Branching planar. HSD.
213R-1, 15	Y	45-51	1813	Vein	Chl	90	82	352	0	82	82	248.5	-13.6	82	193.5		TMP	Continuous, planar, smooth. forms face of core. HSD.
213R-1, 20	Y	69-77	1813.2	Fracture		90	59	326	0	70	32							Continuous, planar, weakly irregular.
213R-1, 20	Y	73-78	1813.2	Fracture		270	65	12	0	65	282							Planar, wk irreg. Offset by above 1.5-2 mm; normal?
213R-1, 22	Y	86-89	1813.4	Vein	Chl/Ac	270	38	0	3	38	274							Continuous, wk sinuous, smooth. Cut by vein below.
213R-1, 22	Y	87-89	1813.4	Vein	Ac	90	59	0	1	59	89							Continuous, planar, smooth. Cuts vein above. HSD.
213R-1, 22	Y	84-89	1813.3	Fracture		90	69	9	0	69	99							Discont, planar, smooth; cuts chl/ac vein. HSD.
213R-1, 24A+B	Y	97-102	1813.5	Vein	Chl/Ac	270	33	0	68	69	345							Continuous, planar, weakly irregular.
214R-1, 4	Y	16-23	1818.8	Vein	Ac	270	85	17	0	85	287							Continuous, weak sinuous, weak irregular. Very faint.
214R-1, 5A	Y	34-	1818.9	Vein	Ac	270	6	180	34	34	189	69.4	2.7	34	119.6		M	Continuous, planar, weak irregular. Cut by 5A+B vein.
214R-1, 5A	Y	23-31	1818.8	Vein	Ac	90	80	352	0	80	82	69.4	2.7	80	12.6		XTMP	Discontinuous, planar, weakly irregular.
214R-1, 5A+B	Y	34-55	1818.9	Vein	Ac	90	75	0	-43	75	76	69.4	2.7	75	6.6		M	Discont, planar to weak curvilinear, smooth. Very fine.
214R-1, 5B	Y	41-46	1819	Vein	Chl	90	84	358	0	84	88	69.4	2.7	84	18.6		M	Planar, smooth. Fracture from 46 to 49 cm. Face of core.
214R-1, 8	Y	70-	1819.3	Fracture		270	3	180	4	5	217							Discontinuous, planar, weak irregular. Discing fracture?
214R-1, 8	Y	72-	1819.3	Fracture		0	4	270	9	10	294							Discont, branching planar, weak irreg. Discing fracture?
214R-1, 8	Y	68-	1819.3	Vein	Chl	90	17	180	24	28	146							Continuous, weakly sinuous, smooth.
214R-1, 9	N	82-87	1819.4	Vein	Ep/Qtz	90	48	357	0	48								Continuous, planar to weakly sinuous, smooth.
214R-2, 1	Y	1-	1820.1	Vein	Ac	90	1	180	4	4	166							Continuous, planar, smooth.
214R-2, 1	Y	0-8	1820.1	Fracture		270	84	355	0	84	266							Cont, planar, smooth to wk irreg. Forms face of core.
214R-2, 12	N	46-	1820.5	Vein	Ac	270	20	39	0	25								Continuous, planar, smooth.
214R-2, 13	N	52-	1820.6	Fracture		90	1	180	21	21								Discontinuous, branching planar, smooth.
214R-2, 14	N	62-63	1820.7	Vein	Chl	270	26	0	6	27								Discont, planar, smooth. Best seen on archive half.
214R-2, 20	Y	89-92	1820.9	Fracture		270	82	7	0	82	277	32.3	-13	82	244.7		TMP	Discontinuous, planar to weakly curvilinear, smooth.
214R-2, 20	Y	91-93	1821	Vein	Chl/Ac	270	32	0	31	41	314	32.3	-13	41	281.7		M	Discont, planar, smooth. Best seen on working half.
214R-2, 22	Y	99-106	1821	Fracture		2	0	90	76	76	92							Cont, planar, smooth; minor chl coating; edge of core.
215R-1, 1	N	0-5	1823	Fracture		358	0	90	64	64								Cont, planar, smooth. Forms face of core. Chl coated?
215R-1, 11	N	40-43	1823.4	Vein	Chl	90	85	7	0	85								Continuous, planar, smooth. Forms face of core.
215R-1, 12	N	46-	1823.5	Fracture		90	11	180	6	12								Discont, planar to wk curvilinear, branching, wk irreg.
215R-1, 12	N	43-47	1823.4	Vein	Chl	7	0	270	81	81								Continuous, weakly curvilinear, smooth. Face of core.
215R-1, 15	N	58-63	1823.6	Vein	Chl	90	86	6	0	86								Continuous, planar, smooth. chl coated fracture.
216R-1, 9	Y	37-38	1828.3	Vein	Chl	90	9	11	0	9	101							Cont, weak curvilinear, smooth. Weak halo; HSD.
216R-1, 9	Y	39-42	1828.3	Vein	Chl	90	37	180	10	38	103							Continuous, weakly curvilinear, smooth. HSD.
216R-1, 10	N	48-49	1828.4	Vein	Chl	90	15	180	29	32								Continuous, branching planar, weakly irregular.
216R-1, 13	N	59-61	1828.5	Vein	Chl/Ep/Qtz	270	84	23	0	84								Discontinuous, branching? planar, smooth. HSD.
216R-1, 13	N	59-61	1828.5	Vein	Chl/Ep/Qtz	270	42	9	0	42								Cont, planar, smooth to wk irreg. Terminates above.
216R-1, 14	Y	63-	1828.5	Fracture		270	8	180	3	9	250							Discontinuous, branching planar, weakly irregular.
216R-1, 14	Y	65-	1828.6	Fracture		90	2	180	4	4	153							Discontinuous, branching planar, smooth.
216R-1, 14	Y	62-65	1828.5	Vein	Chl/Ep	90	60	358	0	60	88							Cont, planar, smooth; forms face of core; remnant Ep.
216R-1, 15A	Y	70-71	1828.6	Vein	Chl	270	32	311	0	44	221							Continuous, planar, smooth. Cut by vein below.
216R-1, 15A	Y	70-	1828.6	Vein	Chl/Ep/Py	270	14	28	0	16	298							Cont, planar, smooth. Chl rich margin, Ep rich core.
217R-1, 1	Y	6-	1837.5	Vein	Chl	270	48	180	47	57	226	58.9	-2.6	57	167.1		XTMP	Discontinuous, weakly sinuous, smooth. HSD.
217R-1, 1	Y	2-	1837.4	Vein	Chl	270	26	0	36	41	326	58.9	-2.6	41	267.1		TM	Discont, planar, to sinuous, branching, smooth. HSD.
217R-1, 1	Y	0-2	1837.4	Vein	Chl/Ep/Qtz	270	22	340	0	23	250	58.9	-2.6	23	191.1		TM	Cont, planar, smooth; 0.5-2 mm thick; cut by Ep vein.
217R-1, 1	Y	0-	1837.4	Vein	Ep	270	16	54	0	26	324	58.9	-2.6	26	265.1		TM	Cont, weak sinuous, fine. Cuts chl/ep/qtz vein above.
220R-1, 4	N	14-	1865.6	Vein	Chl	90	5	180	3	6								Cont, planar, smooth. Wk halo. Forms fracture surface.

APPENDIX J (continued).

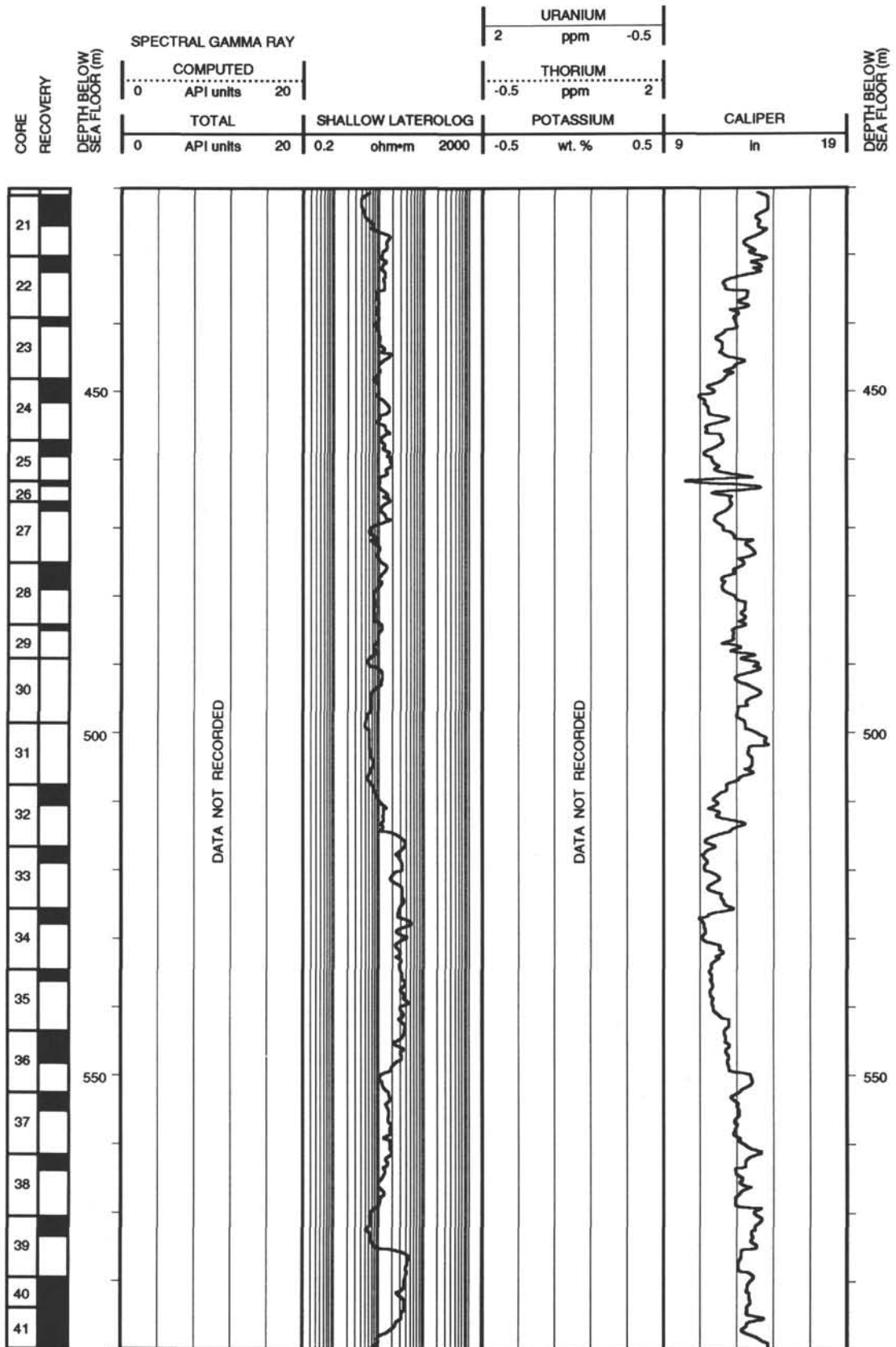
Core, section, piece	Oriented?	Top-bottom	Depth (mbsf)	Feature	Composition	Dir.	Angle	Dir.	Angle	Angle	Dir.	Mag. dec.	Mag. inc.	Angle	Dir.	Sense	SBA	Comments
229R-1, 3	N	7-10	1943.6	Fracture		90	79	8	0	79							TP	Continuous, branching sinuous, smooth.
230R-1, 3	N	10-12	1953.1	Vein	Chl	270	72	0	0	72								Continuous, weakly sinuous, smooth.
235R-1, 7	N	24-	1976.3	Vein	Chl/Ac	270	18	180	15	23								Continuous, planar, smooth.
235R-1, 7	N	24-	1976.3	Fracture		270	1	180	5	5								Discontinuous, planar, weakly irregular.
235R-1, 8	N	28-	1976.4	Vein	Ac	270	9	180	14	16								Continuous, planar, smooth.
236R-1, 2	N	4-8	1980.7	Vein	Ac	90	72	192	0	72								Discontinuous, planar, smooth.
236R-1, 2	N	4-8	1980.7	Vein	Ac	90	11	0	21	23								Continuous, weakly curvilinear, smooth.
236R-1, 5A+B	Y	23-27	1980.9	Vein	Chl/Ac	90	86	214	0	87	124							Cont, planar, smooth. Variable thickness; some offsets?
236R-1, 6	N	40-44	1981.1	Fracture		90	77	206	0	78								Discontinuous, branching planar, smooth.
236R-1, 7	Y	47-	1981.2	Fracture		90	12	0	20	23	30							Continuous, weakly sinuous, smooth.
236R-1, 8	N	57-	1981.3	Vein	Ac	270	89	176	0	89								Continuous, branching planar, smooth.
236R-1, 10	N	64-67	1981.3	Fracture		270	6	180	6	8								Discont, sinuous to planar, branching, weakly irregular.
236R-1, 10	N	63-67	1981.3	Fracture		270	80	182	0	80								Continuous, planar, smooth. Forms face of core.
236R-1, 10	N	63-67	1981.3	Vein	Ac	270	44	0	39	52								Continuous, planar, smooth.
237R-1, 7	N	26-	1984	Vein	Ac	270	3	0	34	34								Continuous, planar, smooth.

Under "Oriented?": Y = yes; N = No. Under composition, Chl = chlorite; Ac = actinide; Ep = epidote; Qtz = quartz; Py = pyrite. Dir. = direction; Mag. dec. = magnetic declination (°); Mag. inc. = magnetic inclination (°); SBA = shipboard analyses; T = thin section, M = paleomagnetism, X = X-ray fluorescence, P = physical properties. Under "Comments," irreg. = irregular, cont = continuous, HSD = hand-specimen description, v = very, pt = point, xtal = crystal, Ab = albite, TWC = thin white crack, descr. = described, discont. = discontinuous, fract. = fracture, Px = pyroxene, wk = weak.

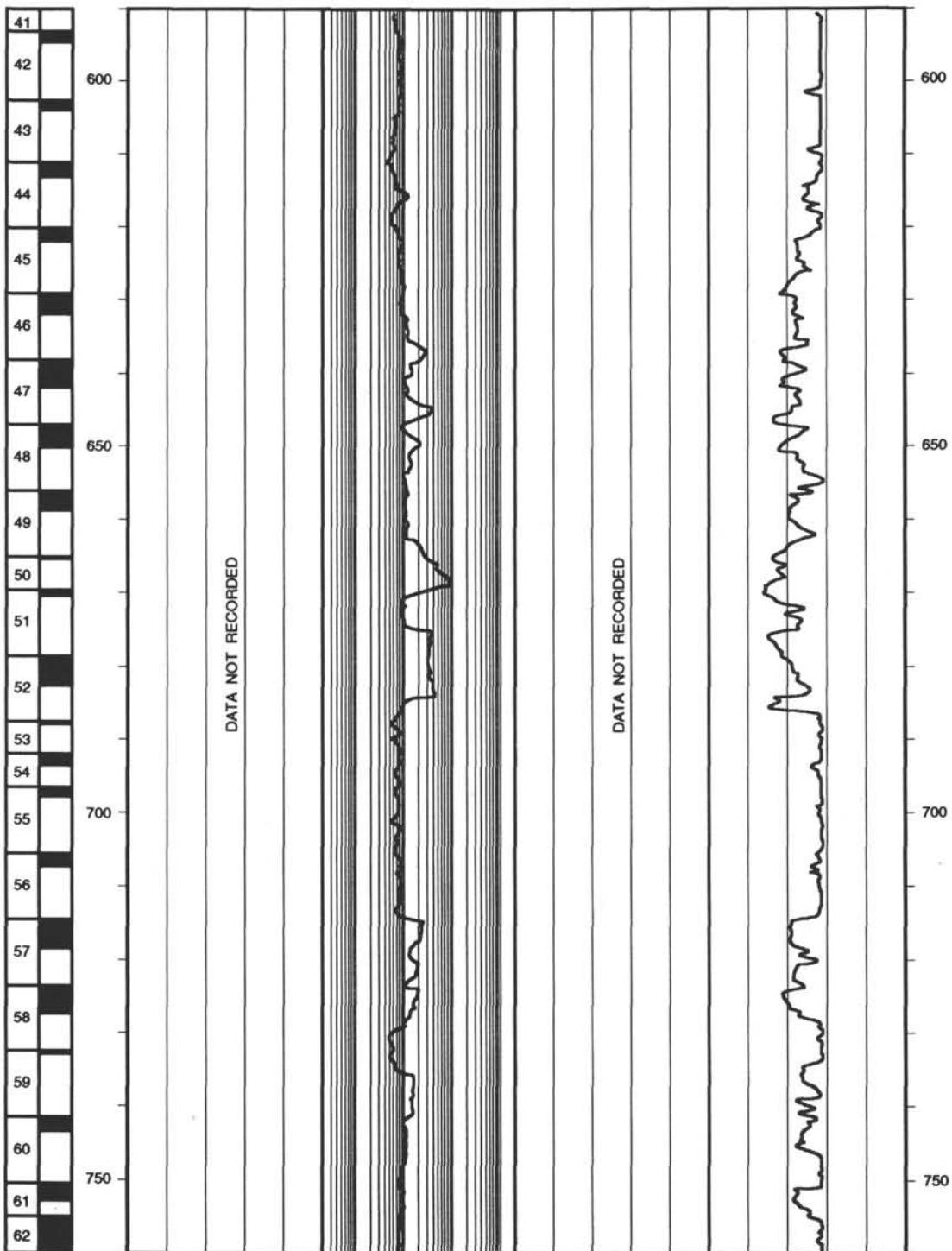
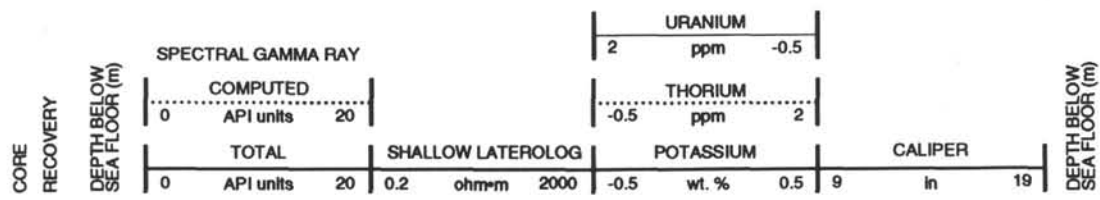
Hole 504B: Resistivity-Natural Gamma Ray Log Summary



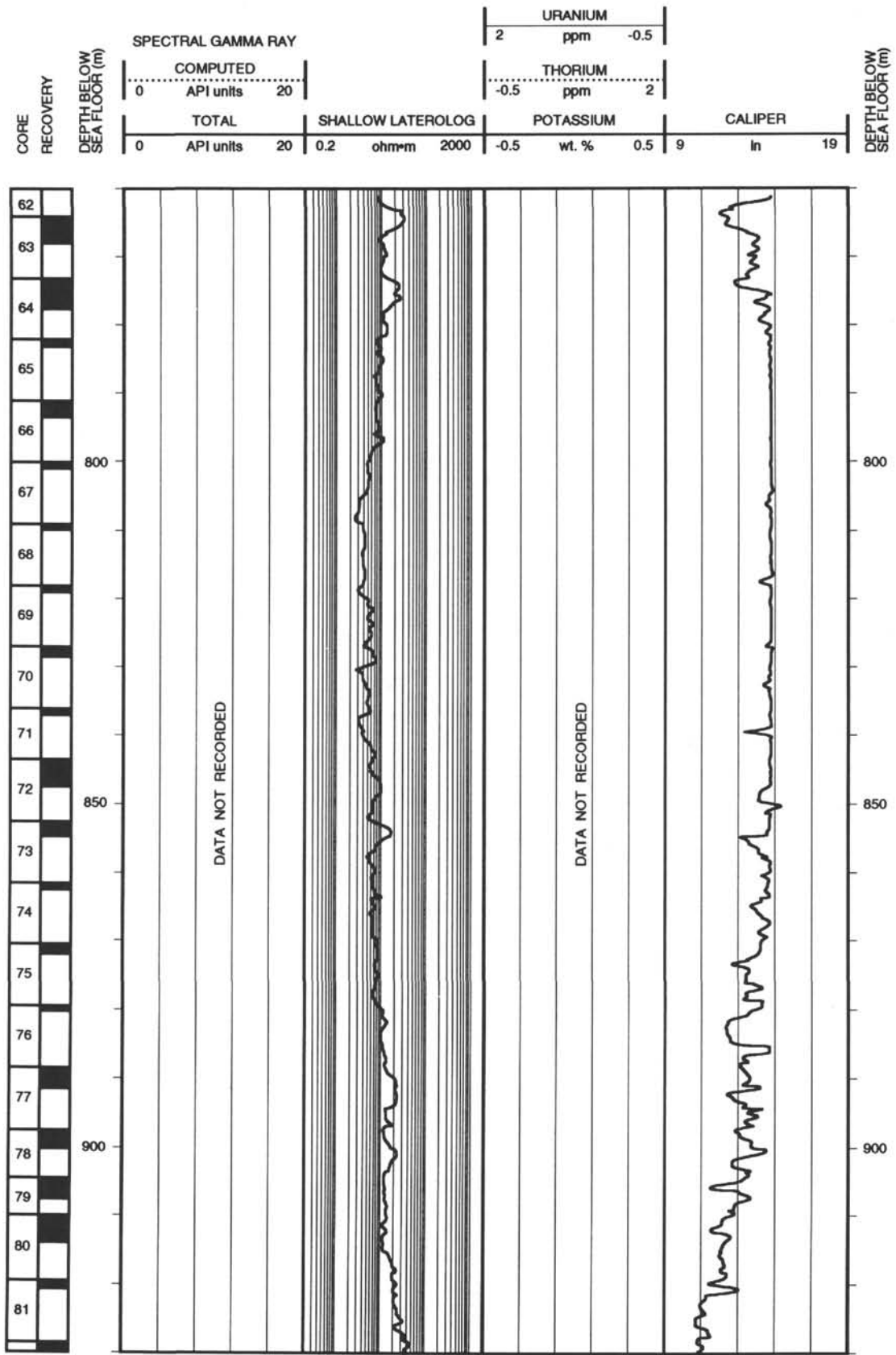
Hole 504B: Resistivity-Natural Gamma Ray Log Summary (continued)



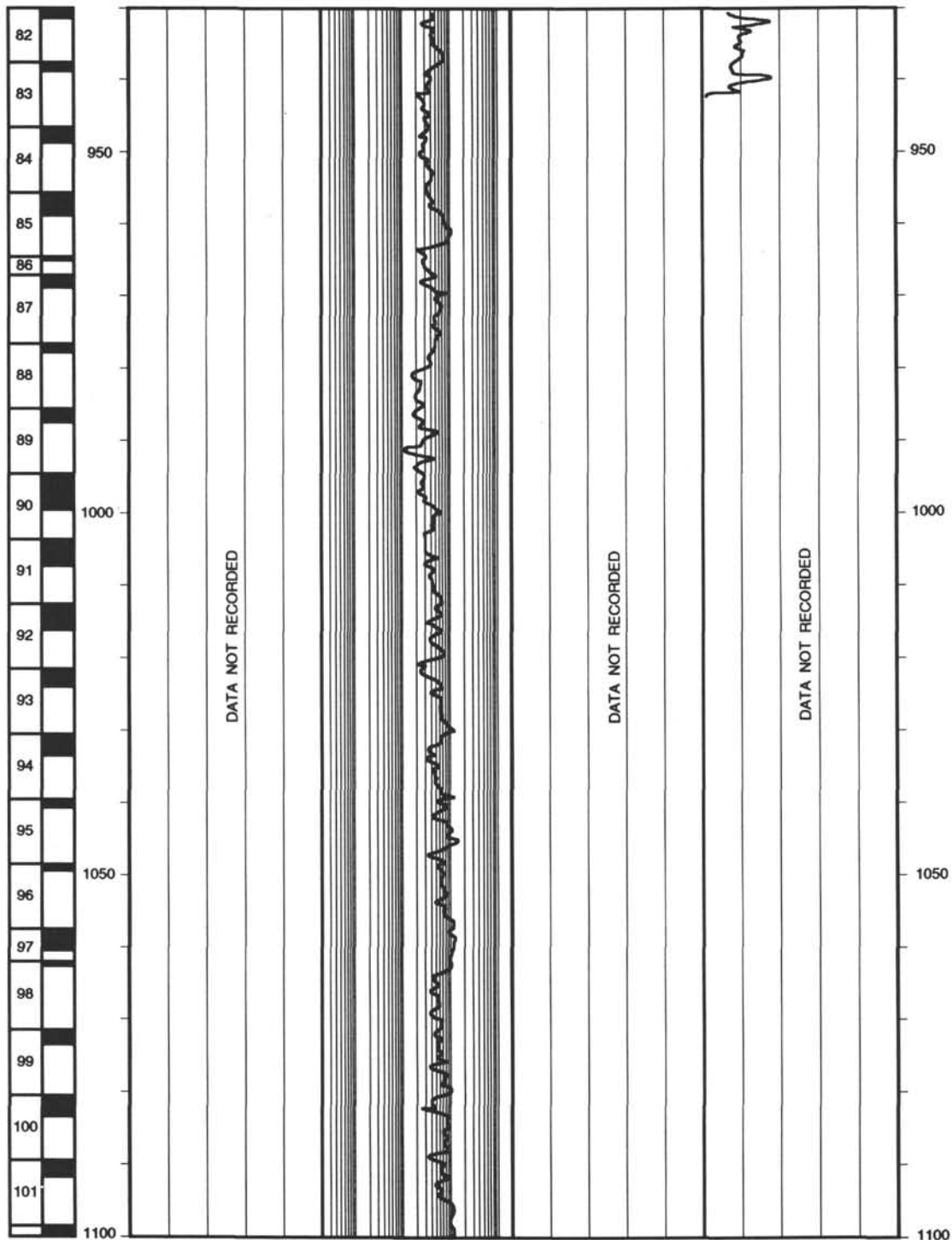
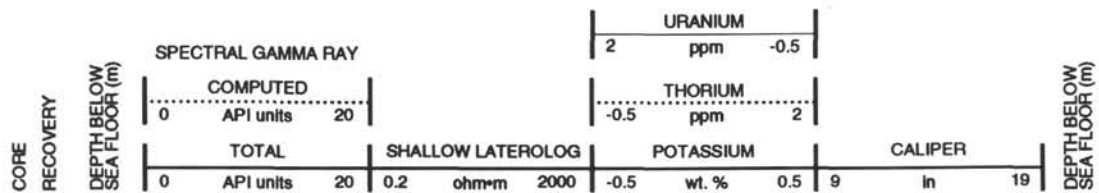
Hole 504B: Resistivity-Natural Gamma Ray Log Summary (continued)



Hole 504B: Resistivity-Natural Gamma Ray Log Summary (continued)



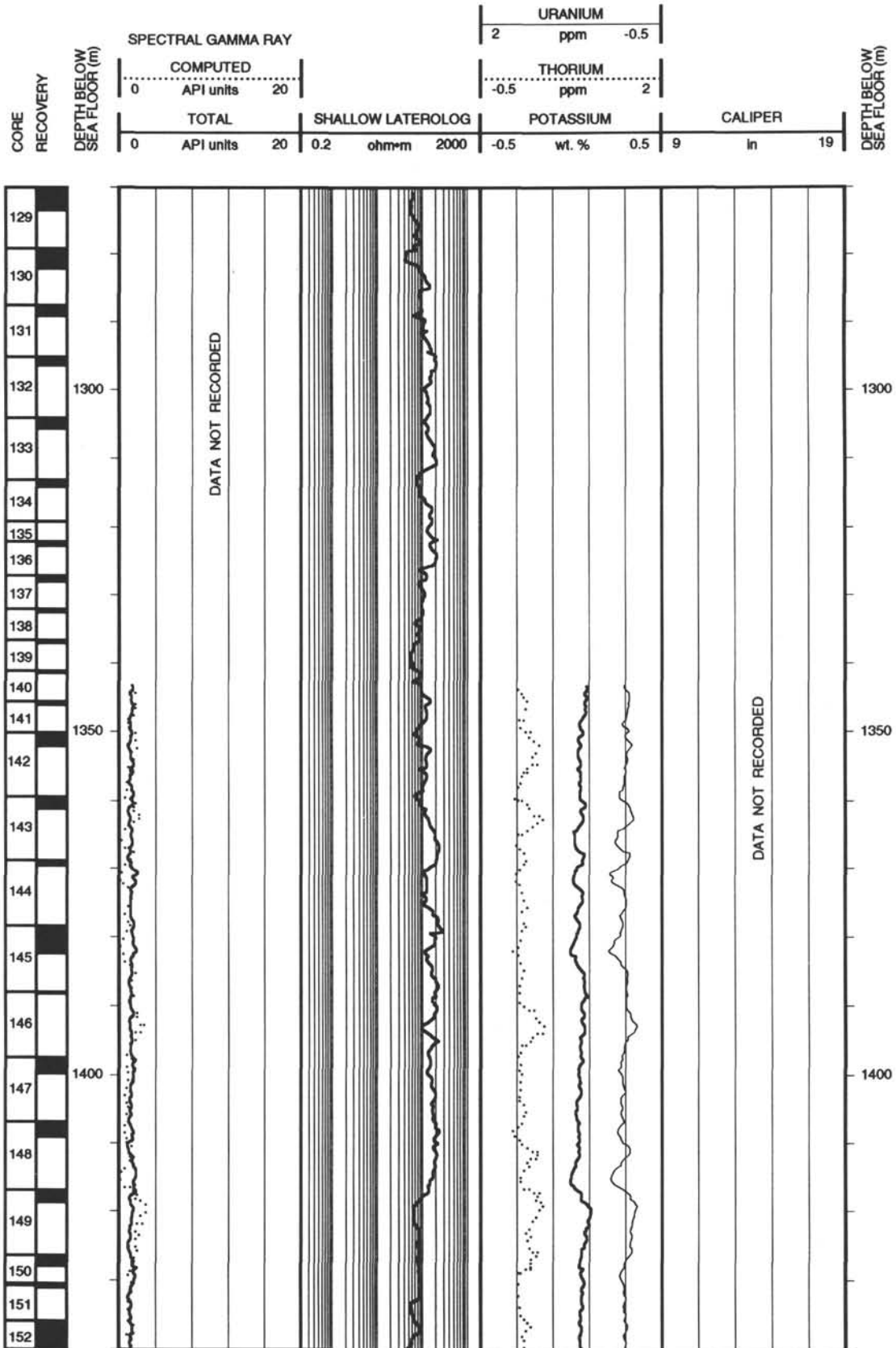
Hole 504B: Resistivity-Natural Gamma Ray Log Summary (continued)



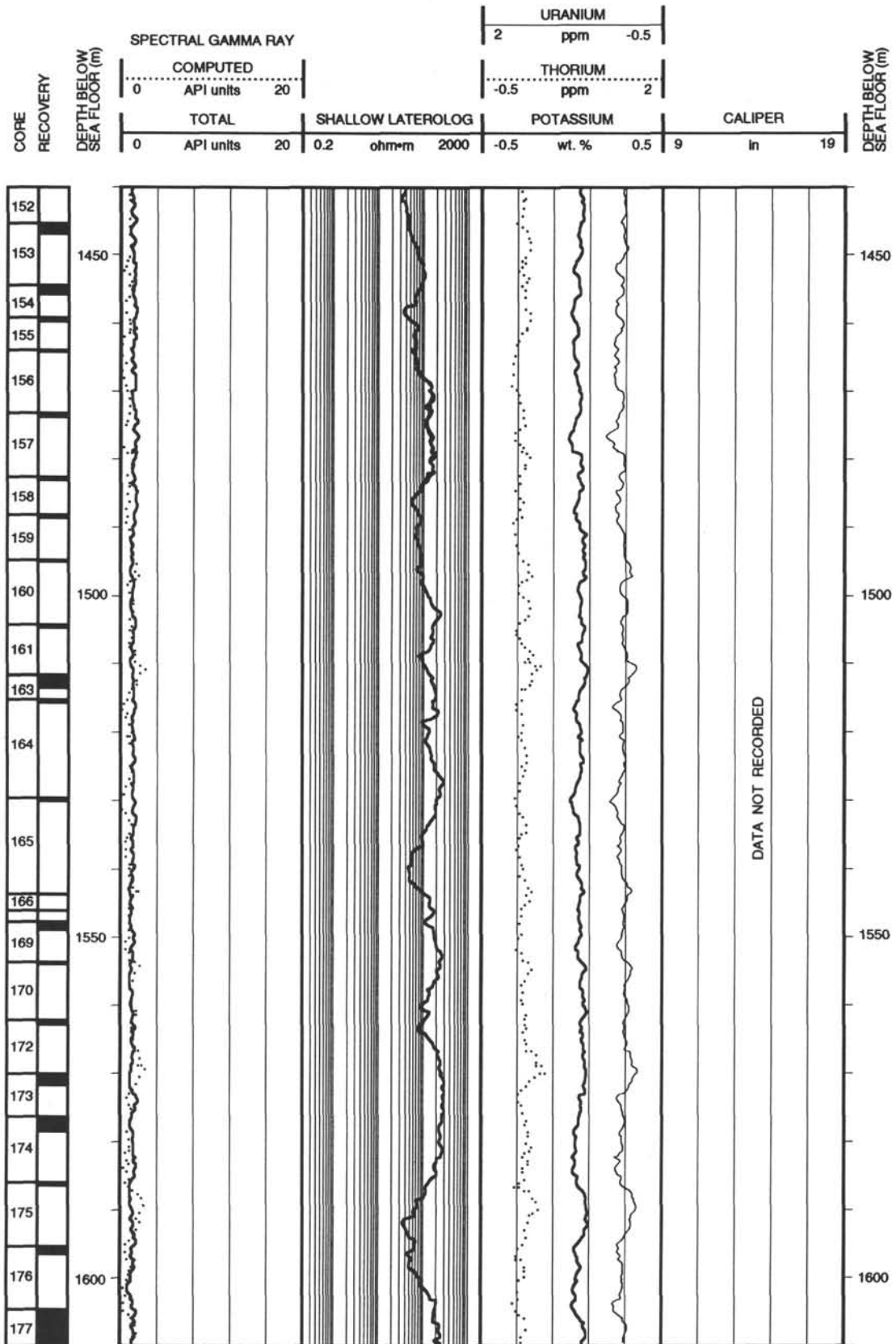
Hole 504B: Resistivity-Natural Gamma Ray Log Summary (continued)



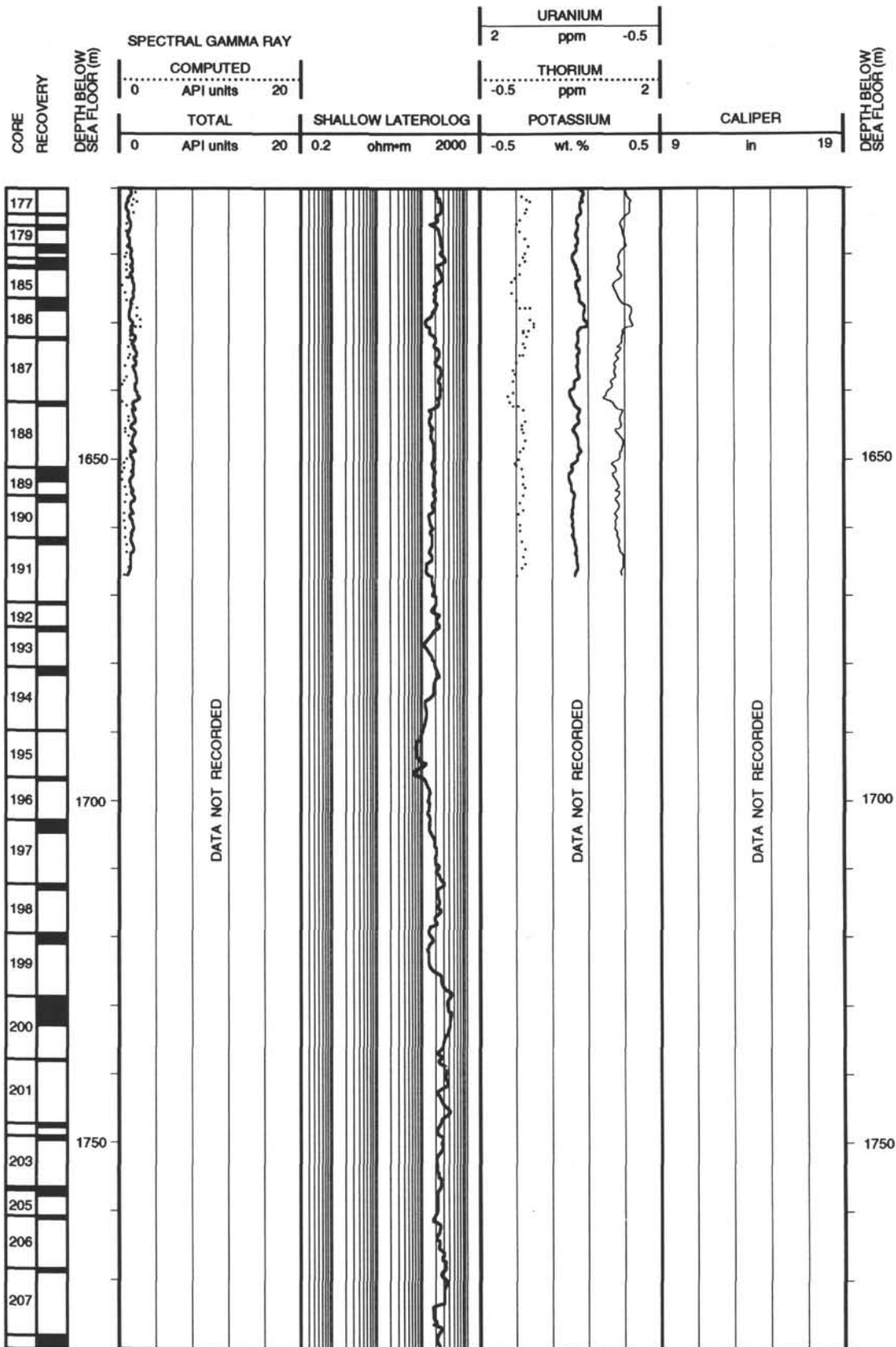
Hole 504B: Resistivity-Natural Gamma Ray Log Summary (continued)



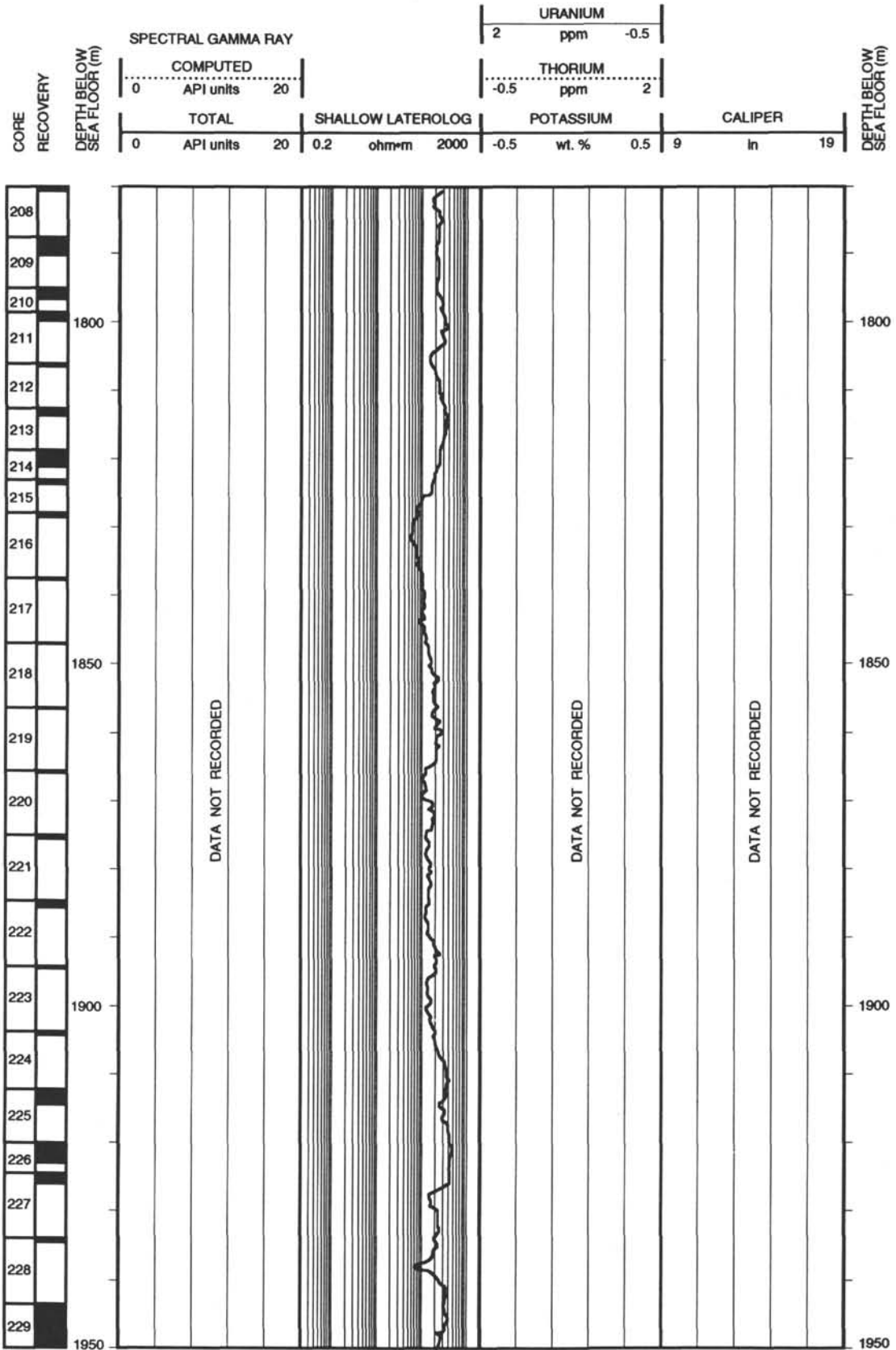
Hole 504B: Resistivity-Natural Gamma Ray Log Summary (continued)



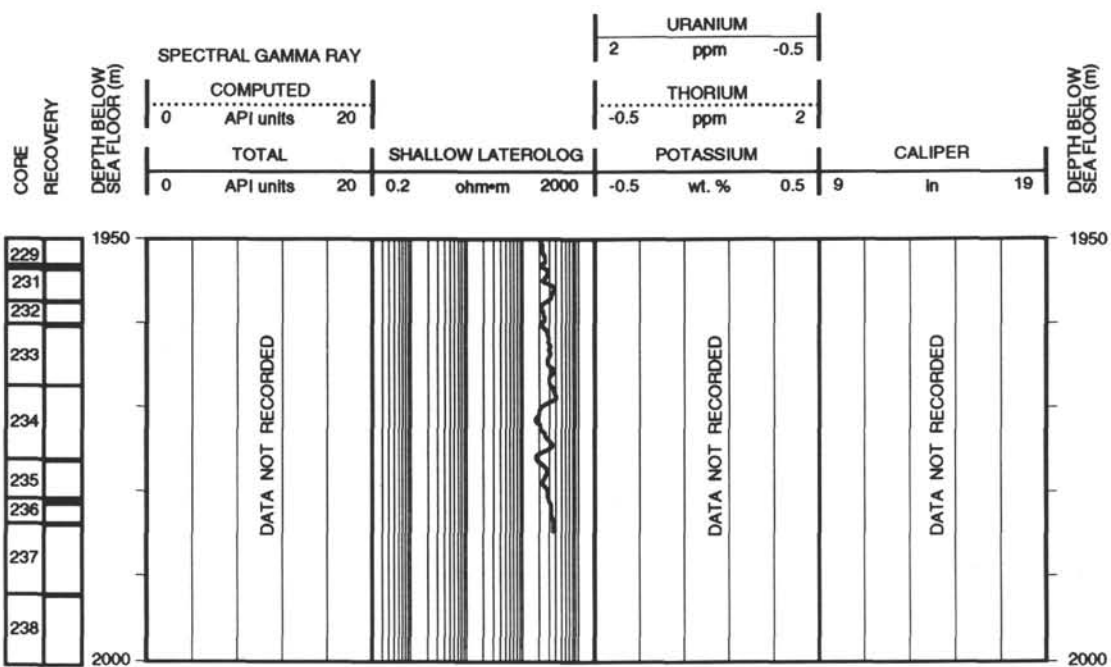
Hole 504B: Resistivity-Natural Gamma Ray Log Summary (continued)



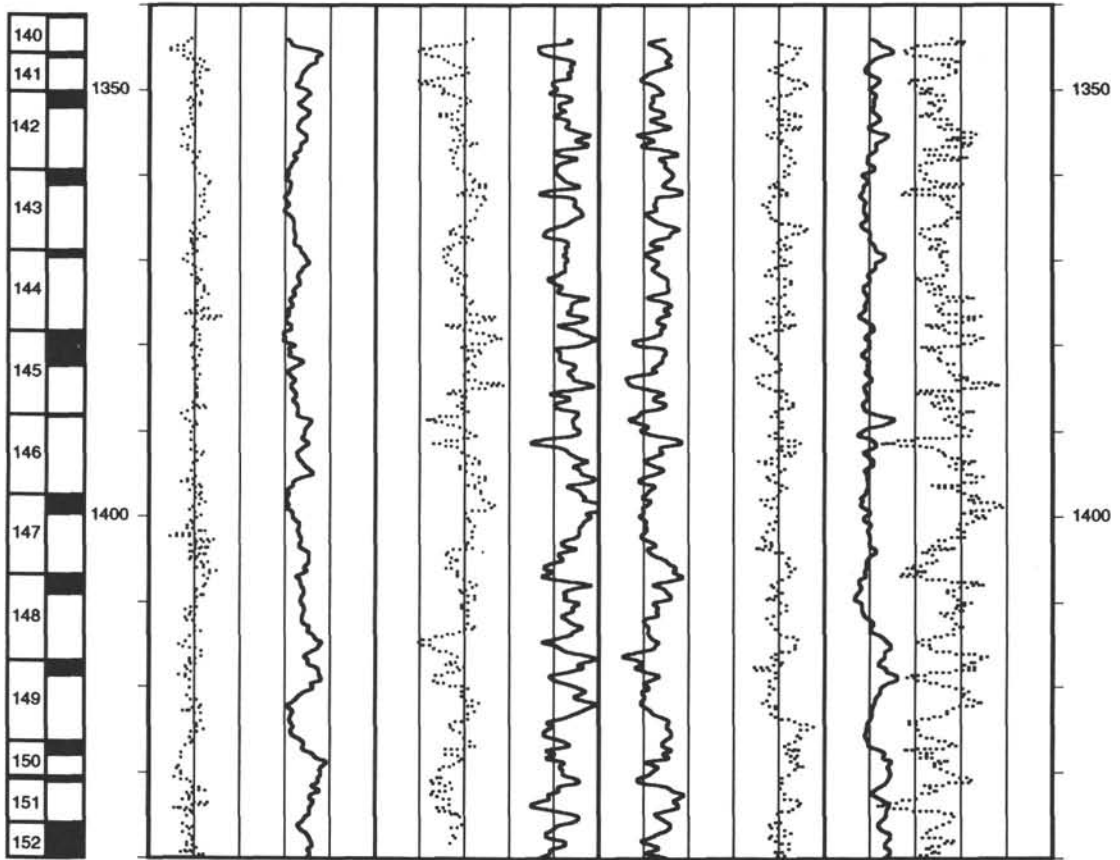
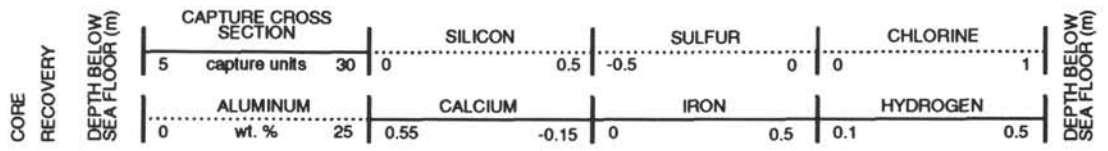
Hole 504B: Resistivity-Natural Gamma Ray Log Summary (continued)



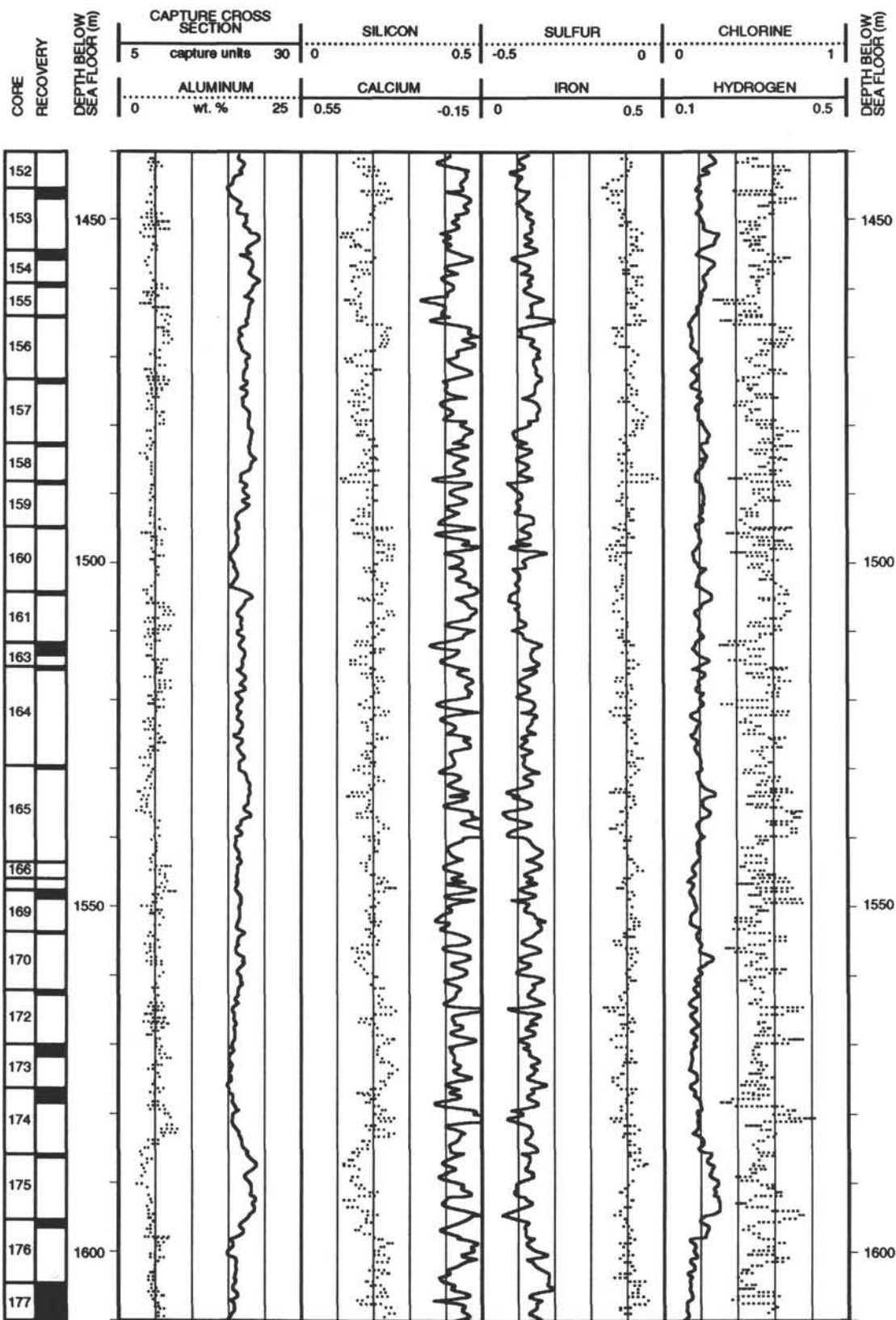
Hole 504B: Resistivity-Natural Gamma Ray Log Summary (continued)



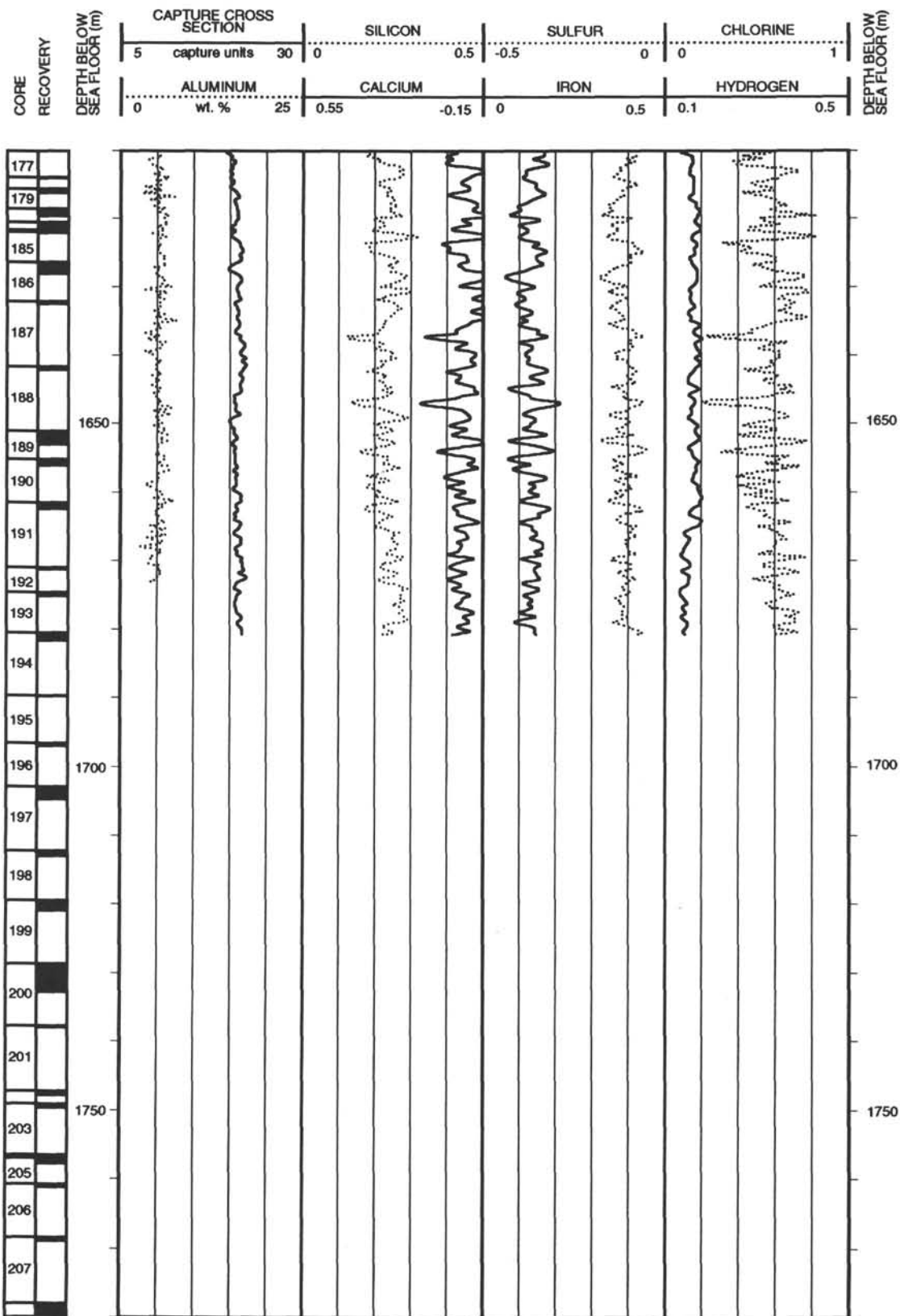
Hole 504B: Geochemical Log Summary



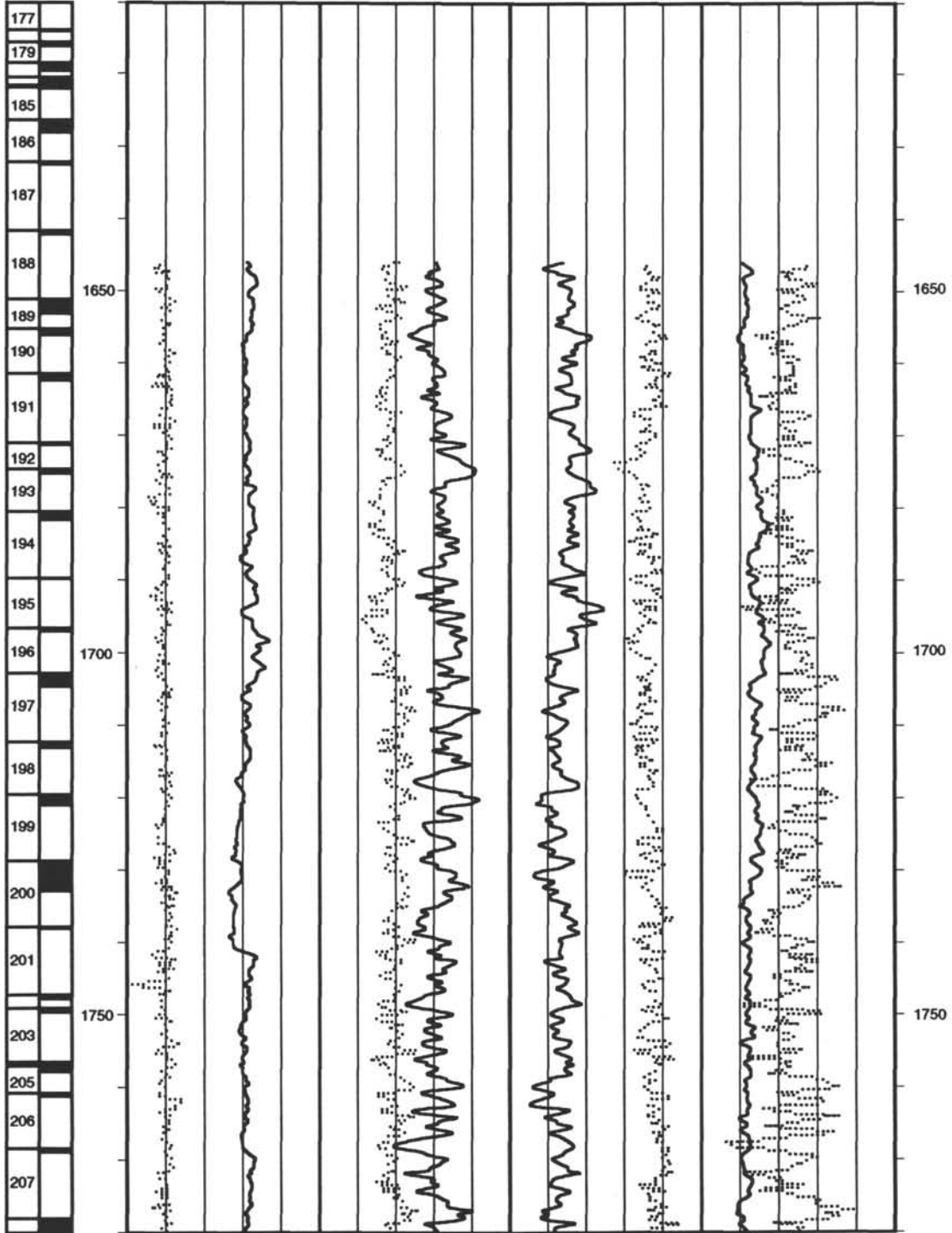
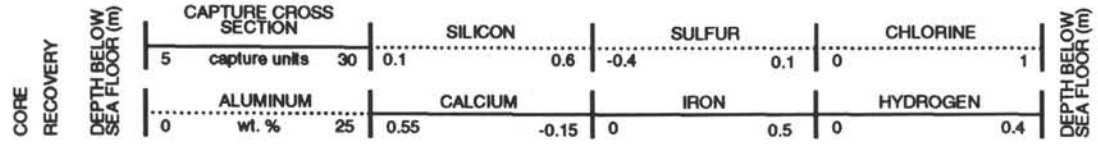
Hole 504B: Geochemical Log Summary (continued)



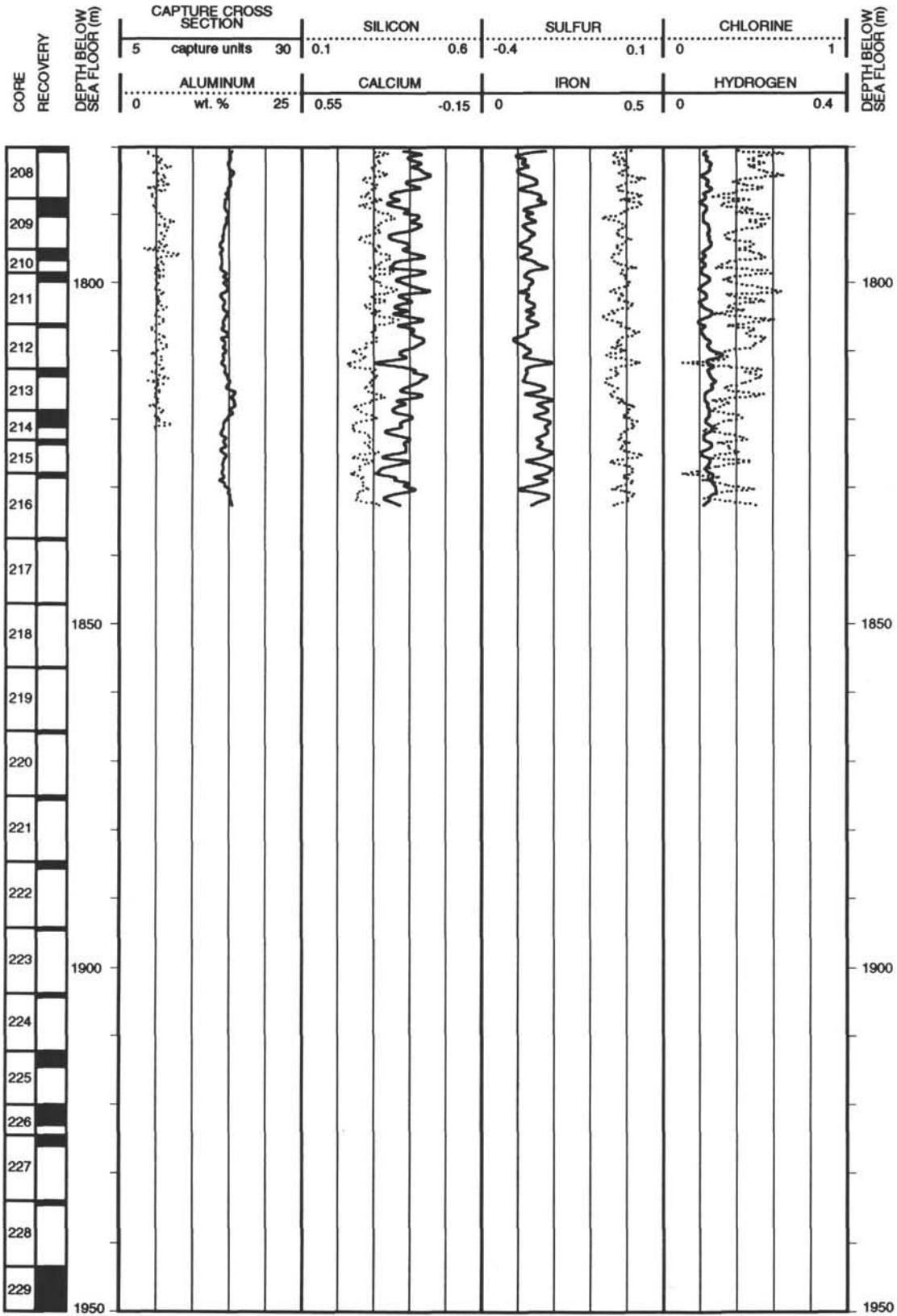
Hole 504B: Geochemical Log Summary (continued)



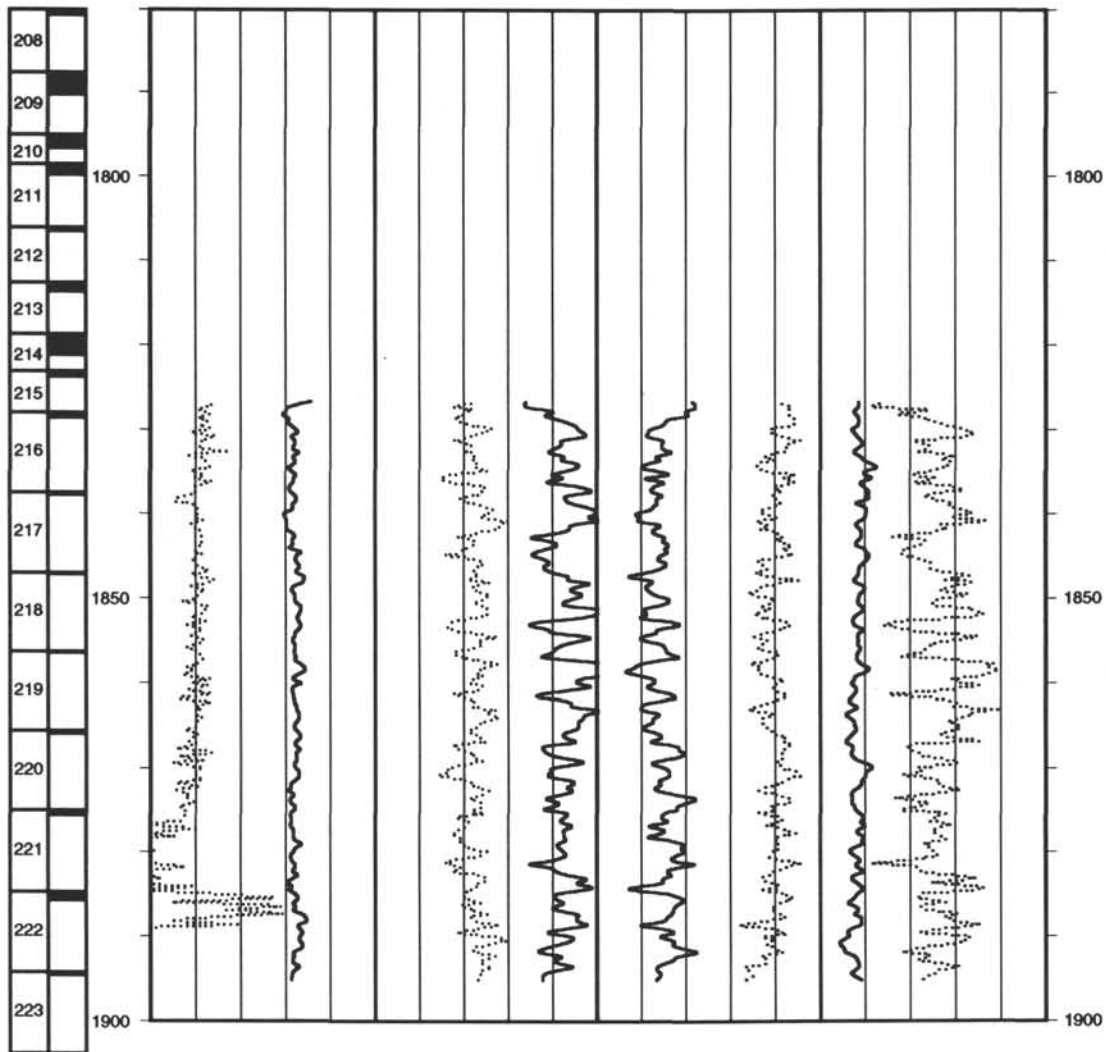
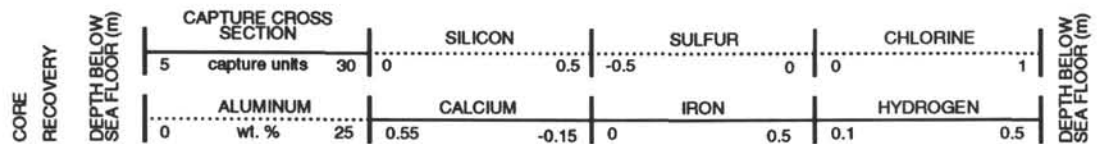
Hole 504B: Geochemical Log Summary (continued)



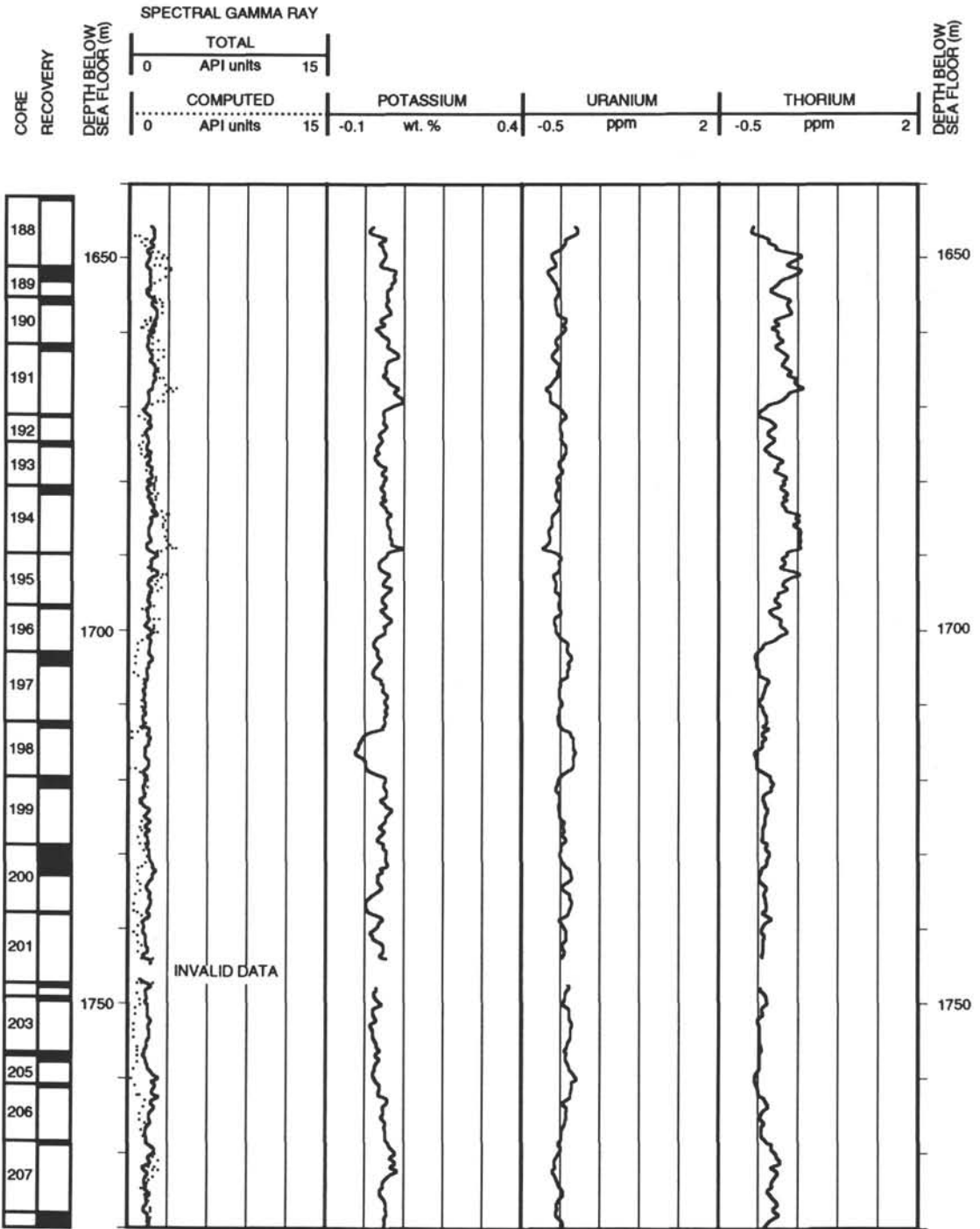
Hole 504B: Geochemical Log Summary (continued)



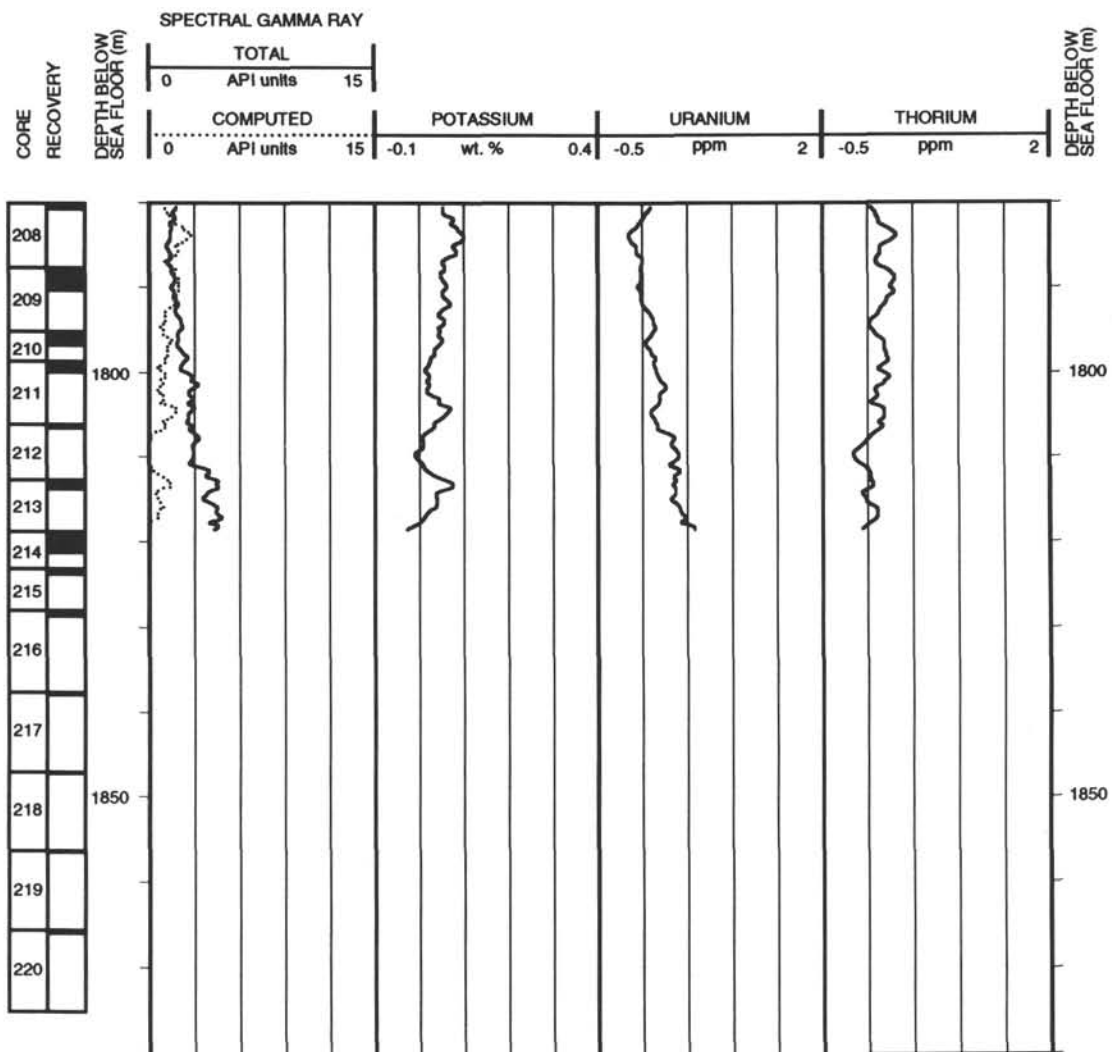
Hole 504B: Geochemical Log Summary (continued)



Hole 504B: Natural Gamma Ray Log Summary



Hole 504B: Natural Gamma Ray Log Summary (continued)



Hole 504B: Natural Gamma Ray Log Summary (continued)

